Vitalii Ivanov · Yiming Rong
Justyna Trojanowska · Joachim Venus
Oleksandr Liaposhchenko
Jozef Zajac · Ivan Pavlenko · Milan Edl
Dragan Perakovic   *Editors*

Advances in Design, Simulation and Manufacturing

Proceedings of the International Conference on Design, Simulation, Manufacturing: The Innovation Exchange, DSMIE-2018, June 12–15, 2018, Sumy, Ukraine

Springer

Lecture Notes in Mechanical Engineering

Lecture Notes in Mechanical Engineering (LNME) publishes the latest developments in Mechanical Engineering—quickly, informally and with high quality. Original research reported in proceedings and post-proceedings represents the core of LNME. Volumes published in LNME embrace all aspects, subfields and new challenges of mechanical engineering. Topics in the series include:

- Engineering Design
- Machinery and Machine Elements
- Mechanical Structures and Stress Analysis
- Automotive Engineering
- Engine Technology
- Aerospace Technology and Astronautics
- Nanotechnology and Microengineering
- Control, Robotics, Mechatronics
- MEMS
- Theoretical and Applied Mechanics
- Dynamical Systems, Control
- Fluid Mechanics
- Engineering Thermodynamics, Heat and Mass Transfer
- Manufacturing
- Precision Engineering, Instrumentation, Measurement
- Materials Engineering
- Tribology and Surface Technology

More information about this series at http://www.springer.com/series/11236

Vitalii Ivanov · Yiming Rong
Justyna Trojanowska · Joachim Venus
Oleksandr Liaposhchenko
Jozef Zajac · Ivan Pavlenko
Milan Edl · Dragan Perakovic
Editors

Advances in Design, Simulation and Manufacturing

Proceedings of the International Conference on Design, Simulation, Manufacturing: The Innovation Exchange, DSMIE-2018, June 12–15, 2018, Sumy, Ukraine

≙ Springer

Editors
Vitalii Ivanov
Department of Manufacturing Engineering,
　Machines and Tools
Sumy State University
Sumy, Ukraine

Yiming Rong
Department of Mechanical
　and Energy Engineering
Southern University of Science
　and Technology
Shenzhen, Guangdong, China

Justyna Trojanowska
Department of Manufacturing
　and Production Engineering
Poznan University of Technology
Poznan, Poland

Joachim Venus
Leibniz Institute for Agricultural
　Engineering and Bioeconomy
Potsdam, Brandenburg, Germany

Oleksandr Liaposhchenko
Department of Processes and Equipment
　of Chemical and Petroleum-Refineries
Sumy State University
Sumy, Ukraine

Jozef Zajac
Faculty of Manufacturing Technologies
　with a seat in Presov
Technical University of Kosice
Prešov, Slovakia

Ivan Pavlenko
Department of General Mechanics
　and Machine Dynamics
Sumy State University
Sumy, Ukraine

Milan Edl
Faculty of Mechanical Engineering
University of West Bohemia
Pilsen, Czech Republic

Dragan Perakovic
Department of Information
　and Communication Traffic
University of Zagreb
Zagreb, Croatia

Preface

This volume of Lecture Notes in Mechanical Engineering contains accepted papers presented at the International Conference on Design, Simulation, Manufacturing: The Innovation Exchange (DSMIE-2018), held in Sumy, Ukraine in June 12–15, 2018. The conference was organized by the Faculty of Technical Systems and Energy Efficient Technologies, Sumy State University, in partnership with Technical University of Kosice (Slovak Republic), Kielce University of Technology (Poland), University of West Bohemia (Czech Republic), Association for Promoting Innovative Technologies—Innovative FET (Croatia). The DSMIE-2018 was organized under the patronage of Prof. Anatoliy Vasylyev, Rector of Sumy State University and Dr. Oleksandr Gusak, Dean of the Faculty of Technical Systems and Energy Efficient Technologies.

DSMIE-2018 is the international forum for fundamental and applied research and industrial applications in manufacturing. The conference focuses on a broad range of research challenges in the fields of Manufacturing, Mechanical and Chemical Engineering, addressing current and future trends in design approaches, simulation techniques, computer-aided systems, software development, ICT tools and Industry 4.0 strategy implementation for solving engineering tasks. DSMIE-2018 brings together researchers from academic institutions, leading industrial companies, and government laboratories located around the world for promoting and popularization of the scientific fundamentals of manufacturing.

The book was organized into three parts, according to the main conference topics. Each part is devoted to research in design, simulation and manufacturing in the areas of Manufacturing and Materials Engineering, Mechanical Engineering and Chemical Engineering.

DSMIE-2018 received 91 contributions from 14 countries around the world. After a thorough peer-review process, the DSMIE-2018 Editorial Board accepted 55 papers, written by authors from 11 countries. Thank you very much to all authors for their contribution. These papers are published in present book, achieving an acceptance rate of about 60%. Extended versions of selected best papers will be published in journals: Management and Production Engineering

Review (indexed by ISI/ESCI, Scopus), Archives of Mechanical Technology and Materials (Poland) and Journal of Engineering Sciences (Ukraine).

We would like to take this opportunity to thank members of Program Committee and invited external reviewers for their efforts and expertise in contribution to reviewing, without which it would be impossible to maintain the high standards of peer-reviewed papers. Fifty-three Program Committee members and 14 invited external reviewers devoted their time and energy for peer-reviewing manuscripts. Our reviewers come from all over the world and represent 17 countries and affiliated with 41 institutions.

Thank you very much to all keynote speakers, who came from Poland, Slovak Republic, Czech Republic and Ukraine, and share their knowledge and experience.

We appreciate the partnership with Springer, Unicheck and EasyChair and our sponsors for their essential support during the preparation of DSMIE-2018.

Thank you very much to DSMIE-2018 Team. Their involvement and hard work were crucial to the success of the DSMIE-2018 conference.

DSMIE-2018's motto is "Together we can do more for science, technology, engineering and education."

June 2018   Vitalii Ivanov
                                                                                        Yiming Rong
                                                                             Justyna Trojanowska
                                                                                     Joachim Venus
                                                                        Oleksandr Liaposhchenko
                                                                                         Jozef Zajac
                                                                                     Ivan Pavlenko
                                                                                          Milan Edl
                                                                                  Dragan Perakovic

Organization

Steering Committee

General Chair

Vitalii Ivanov   Sumy State University, Ukraine

Co-chairs

Oleksandr Gusak	Sumy State University, Ukraine
Oleksandr Liaposhchenko	Sumy State University, Ukraine
Ivan Pavlenko	Sumy State University, Ukraine

Program Committee

Volodymyr Atamanyuk	Lviv Polytechnic National University, Ukraine
Michal Balog	Technical University of Kosice, Slovak Republic
Shahzad Barghi	University of Western Ontario, Canada
Jozef Bocko	Technical University of Kosice, Slovak Republic
Dagmar Caganova	Slovak University of Technology, Slovak Republic
Robert Cep	VSB-Technical University of Ostrava, Czech Republic
Radu Cotetiu	Technical University of Cluj-Napoca, Romania
Alina Crisan	University of Agricultural Sciences and Veterinary Medicine, Romania
Milan Edl	University of West Bohemia, Czech Republic

Joachim Venus	Leibniz Institute for Agricultural Engineering and Bioeconomy, Germany
Emil Hristov Yankov	Angel Kanchev University of Ruse, Bulgaria
Jozef Zajac	Technical University of Kosice, Slovak Republic
Viliam Zaloga	Sumy State University, Ukraine
Volodymyr Zavialov	National University of Food Technologies, Ukraine
Jan Zdebor	University of West Bohemia, Czech Republic

Invited External Reviewers

Vaclav Cerny	University of West Bohemia, Czech Republic
Liviu Adrian Crisan	Technical University of Cluj-Napoca, Romania
Maryna Ivanova	National Technical University "Kharkiv Polytechnic Institute", Ukraine
Svitlana Lugova	JSC "NASOSENERGOMASH Sumy", Ukraine
Ievgen Mochalin	Zhejiang Normal University, China
Dawid Myszka	Warsaw University of Technology, Poland
Andrii Rogovyi	Kharkiv National Automobile and Highway University, Ukraine
Ioana Roman	University of Agricultural Sciences and Veterinary Medicine, Romania
Malgorzata Sokala	Kielce University of Technology, Poland
Anastasiia Symonova	Kremenchuk Mykhailo Ostrohradskyi National University, Ukraine
Iurii Sysoiev	National Aerospace University named after N.E. Zhukovsky «Kharkiv Aviation Institute», Ukraine
Viktor Tkachenko	National Science Center Kharkov Institute of Physics and Technology, Ukraine
Josef Voldrich	University of West Bohemia, Czech Republic
Przemyslaw Zawadzki	Poznan University of Technology, Poland

Contents

Manufacturing and Materials Engineering

Implementation of CALS-Technologies in Quality Management of Product Life Cycle Processes

Yuliia Denysenko[1(✉)] , Oksana Dynnyk[2] , Tetiana Yashyna[2],
Nina Malovana[1], and Viliam Zaloga[1]

[1] Sumy State University, 2 Rymskogo-Korsakova Street, Sumy 40007, Ukraine
uapogor@gmail.com
[2] Konotop Institute of Sumy State University, 24 Myru Street, Konotop 41615, Ukraine

Abstract. The aspects of the usage of CALS-technologies in support of the life cycle of products are considered in this research. The identification of problems and the main ways of creating a unified information space in the quality management system are focused on, due to the principles of ISO standards series 9000. Based on the analysis, a unified methodological approach to the construction of quality management systems for the application of CALS-technologies is introduced. As an example, a conceptual model of the information system for lifecycle management of instrumental production based on the process approach was suggested. The algorithm of construction and implementation of the introduced model with the consideration on the features of this system is developed. It is shown that observance of the recommendations set forth in the research work will allow to improve the quality of technological equipment as well as to facilitate the optimization of its processes, then it will lead to an increase in labor productivity, reducing resource dependence and costs.

Keywords: CALS-technologies · Implementation · Effectiveness · Life cycle

1 Introduction

At present stage of science and technology development, effective management of the products quality of the manufacturing plant (MP) in accordance with the requirements of the international standards of ISO 9000 series involves reducing uncertainty at all stages of the life cycle (LC) products primarily due to automation of measurements and evaluation of changing parameters of external and internal environment.

With the development of information technology (IT), models of quality management system (QMS), implemented with the help of various computer and software network complexes, automated design tools (CAD), information-analytical (IAS) and information management systems, automatic control systems (ACS), etc. [1, 2] are applied. It is IT, along with advanced production technologies, that can significantly increase productivity and product quality, and at the same time minimize costs during LC products and significantly reduce the timing of production of new products that meet the needs and expectations of consumers.

2   Literature Review

From the experience and practice of many foreign companies, it can be concluded [2, 3], that the industrial management system is currently characterized by the use of various information technologies, based on modules that meet the standards of CALS-technologies.

At present Enterprise Resource Planning (ERP) modules and other CALS-based tools (PDM, CRSP, SRM, OLAP, DM, etc.) can be used effectively to manage material resources at the overwhelming majority of enterprises [4–6]. During the research, it was found out that today IT is used mainly to solve, as a rule, the individual tasks of the corresponding phase of the LC: design, development of technologies, preparation, and management of production, etc. However, the analysis of the toolkit of these systems in relation to each stage of the products LC shows that the modules of these systems partially perform the same functions [7].

The main problem here is the underestimation of the difficulties that arise in the process of shifting from the use of IT at individual stages of LC to work in a single information space (SIS), which would cover all the stages of LC products at the same time, including its after-sales support as well as utilization.

Analysis of the information sources showed that at present stage of development, Ukraine strives not to lag behind Western powers in the sphere of automation of all stages of LC. At present, a number of well-known authors [4, 8] of the mentioned issues in the field of introduction of CALS-technologies and their application in the process of development of products are the subject of the study of issues arising on the way of introduction of CALS-technologies and their use at domestic enterprises. At the same time, it has been established that theoretical developments and implementation methods being generalized in nature, are not detailed and cannot be applied in the practical implementation of SIS project.

Thus, an actual task, which is important for the domestic industry in the conditions of constant growth of competition in the world market of high-tech products, is the development of models and methods of formation of the SIS to support the development of product's LC. The use of CALS-technologies in the QMS will provide comprehensive information support for the adoption of sound management decisions on product quality based on the operational collection, processing, and analysis of the information in a single information environment of the enterprise.

3   Research Methodology

3.1   The Development of a Unified Methodological Approach to Building Quality Management Systems Based on the Use of CALS-Technologies

In the course of the research, the main directions in the implementation of information support of QMS based on CALS-technologies were determined. The main ones are [1]:

- definition of the general approach to automated support for QMS on the principles of CALS-technologies.

- modeling and description of the structure of information flows of the QMS, which are subject to management in the UIS of the enterprise.
- creation of a UIS and software for continuous analysis of information about the quality of products and processes of QMS.
- adapted application of technologies of business process re-engineering to the issues of analysis and reorganization of the QMS processes and product quality management within the framework of a modern approach to the implementation of integrated IT and control systems.
- creation of modern information infrastructure, which provides effective management of information resources of the QMS.

The basis of the development of a unified methodological approach to building of an IMS based on the application of CALS-technologies is grounded on the basic principles of quality management, based on the process approach (Fig. 1) [9].
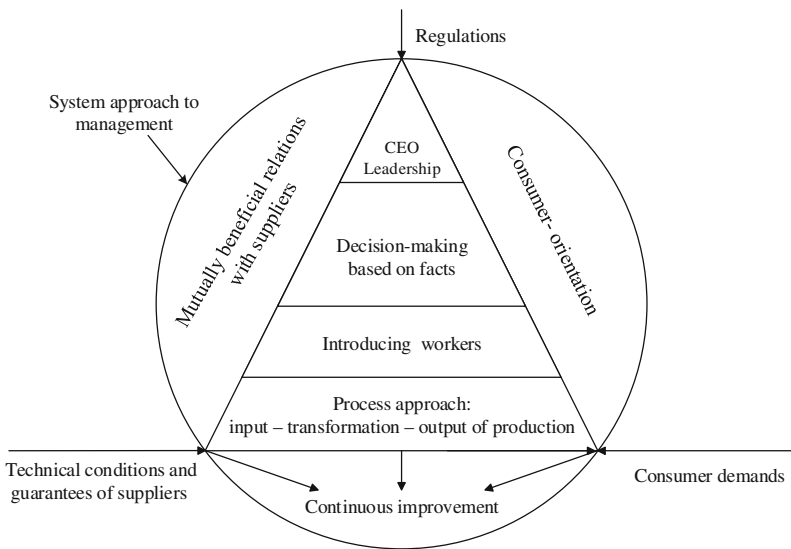
Fig. 1. Principles of quality management.

Realization of the implementation of CALS-technologies scheme consists of several basic stages (Fig. 2):

- organization and preparation;
- analysis and re-engineering of the processes of QMS and processes of the LC products;
- analysis and definition of approaches to the creation of a SIS at an enterprise;
- creation of a SIS in the industry, implementation of software applications for informational support of the processes of production of goods, regulation of the order of interaction of participants of the information exchange of data on the quality of products and processes.

I STAGE	II STAGE
1. Development policy (concepts, strategies) implementation CALS-technologies in QMS	5. Conducting analysis and reengineering of the product's LC processes based on the principles of CALS-technologies
2. Formation of a working group for managing CALS-technologies implementation in QMS	
3. Planning of works on introduction of CALS- technologies in QMS	6. Updating QMS and processes of production's LC in accordance with the principles of technology and methodology of process management
4. Resources to provide CALS-technologies in QMS	

IV STAGE	III STAGE
11. Automation of individual processes QMS and processes of products based on CALS-technologies	7. Defining requirements for information resources
12. Integration of automated processes in SIS, regulated by CALS- standards	8. Analysis of existing information infrastructure and environment in the enterprise
13. Creation in CIC models: products, processes, environment	9. Development of approaches and proposals for creation SIS
14. Development of standards regulating the operation (management) of SIS and the responsibility of the participants of information support of products	10. Development of system architecture and technical project SIS

Fig. 2. Check stage-by-stage introduction of CALS-technologies for the support of LC products and QMS.

The process of production of machine-building products is complex and it is impossible to determine the exact cause of the occurrence of the lack of a real situation. Therefore, it is necessary to improve the QMS and implement statistical methods that make it possible to trace an entire technological process of production and to keep the most responsible stages under constant control.

Due to the application and automation of the use of statistical methods, ultimately, it is possible to improve the effectiveness of quality management at all stages of the production process and make objective managerial decisions regarding the conditions and results of processes and quality of products.

3.2 Introduction of Information Systems on the Example of Production Planning of Tools at the Machine-Building Enterprises

It was established [7], that due to the system of tool preparation for the production of machine-building industry, the modules of CALS-technologies practically do not take into account the specifications and features of the LC of technological equipment and tools. Therefore, the model of a process-oriented production planning of tools (PPT)

management system in terms of information technology can be represented as three interrelated models: organizational model of the PPT, information model of the PPT system and PPT quality management system (Fig. 3).

Information management system of manufacturing tool preparation (IS PPT)

Organizational model of the PPT system	Quality Management System of PPT	Information model of the PPT system
• Organizational structure • The main and ensuring processes • Systems PPT provisions • Regulations on structural units • Job and work instructions	• Compliance with the principles TQM • Compliance with the requirements DSTU ISO 9001-2009 • Process approach	• The provision on the use of information links and databases (workflow, financial, material, equipment, Personnel, normative documentation, protocols and stocks) • Software products

Tools of management systems

| ERP | PDM | PLM | QM | ... |

Fig. 3. Conceptual model of PPT control system under the conditions of information technologies.

Analysis of Fig. 3 shows the availability of a large number of different tools that can be applied in implementing the proposed conceptual model of the PPT management system. Implementation of this model is conditioned by the presence of problems connected, on the one hand, with the development and implementation of PPT quality management systems, on the other hand the implementation of software products and information tools.

The main problem here is the underestimation of the difficulties that arise in the process of shifting from the use of IT at individual stages of the LC to work in a unified information space (SIS), which would cover all the stages of the LC products at the same time, including its after-sales support and recycling. Therefore, in order to minimize the risks associated with the implementation of this model, an algorithm for its development and implementation is proposed (Fig. 4), taking into account those principles discussed in Sect. 2.

According to Fig. 4 the implementation of IS PPT consists of the following steps.

1. Decision-making by the management regarding the implementation of the IS PPT.

At this stage, the management should identify a team of specialists and the project implementation manager, identifying and documenting their functions and responsibilities, and ensuring the competence of the staff members of the team.

2. Formation of the requirements for IS PPT.

A team of experts generates a list of requirements that should correspond to the IS PPT. Based on the list of requirements for the IS PPT and the feasibility study on its implementation, it develops a draft of technical specification and submits it for the approval to the head of the enterprise.
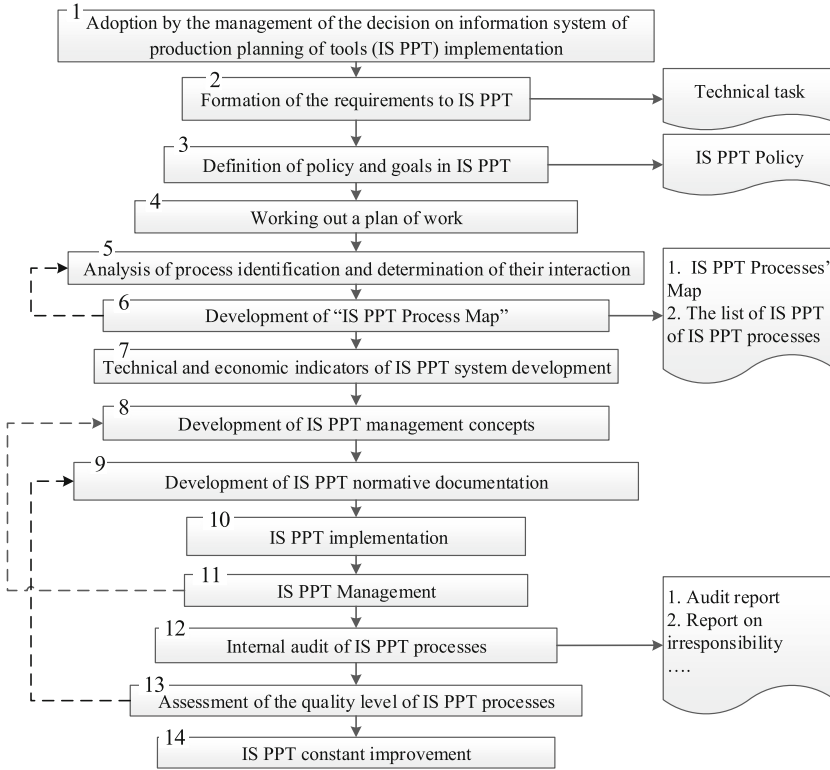
Fig. 4. Algorithm for the implementation of IS PPT.

3. Definition of the policy and goals in IS PPT.

The Working Group formulates the PPT policy and objectives. The project manager coordinates this project with the structural units that are participants in this process and submits it for the approval to the head of the enterprise.

4. Work out a plan of the work.

At this stage, the project manager develops a draft work plan, defines the main stages of the work, the terms of their implementation, and submits it for the approval to the head of the enterprise.

5. Identification, analysis, and identification of the processes acting in the PPT.

The working group defines a list of PPT processes and performs their analysis. Based on a detailed analysis of all the processes operating in the PPT, the working group identifies individual processes, that is owners, consumers and suppliers of each process; goals to be achieved in each of the processes under consideration; who measures (evaluates) the processes results; who initiates at the beginning of each process; input parameters of the processes, who and how to measure them; how and who (responsible persons) each process is realized by; the outputs of the relevant processes, (the result of their

implementation); availability of a description of the of actions (model) algorithm for the transformation of known inputs into the outputs of each process; procedure of actions with changes in the course of its implementation; how (what criteria) each process is evaluated. The basis for the classification and grouping of the processes form the existing regulations on the structural units and job descriptions. The main processes, that is, the processes directly related to the creation of added value, supplemented by supporting processes and management processes. The main processes facilitates, the task of determining, the belonging of all processes of the enterprise to a certain group in the organization should be detected.

After obtaining a list of available PPTs, a project manager analyzes a detailed survey questionnaire to identify the processes required by DSTU ISO 9001: 2009, which are not included in the list. This list should also be agreed with the PPT staff and, if necessary, changes should be made to it. For each new process, it is necessary to carry out the work on its identification. Based on the requirements of the new system, the infrastructure is assessed and the role of the information systems department is determined.

6. Development of "IS PPT Process Map".

Based on the information received about the existing and new processes, the working group is developing an "IS PPT Process Map" in the organization. "IS PPT Mapping" is agreed with the IS PPT staff and, if necessary, makes changes to it. Based on the "Process Maps", the project manager develops the "List of IS PPT in the organization". Then, the "IS PPT Map of Processes" and "IS PPT Processes List in Organization" are approved by the management.

7. Technical and economic indicators of IS PPT system development.

Based on the policy and objectives of the IS PPT, a common system of technical and economic indicators of IS PPT processes is developed, which is approved by the management afterwards.

8. Development of the IS PPT management concepts.

Based on the developed of IS PPT Mapping Cards and the technical specification, a working group together with the representatives of the software provider assesses the necessary resources to implement the IS PPT system, design the interface of the system and create a management concept.

9. Development of the normative documentation of the system IS PPT.

The working group together with the personnel of the IS PPT system carries out work on the development, registration and approval of documentation on the organizational model of IS PPT, information model of the IS PPT system and IS PPT quality management system (Fig. 3).

10. Implementation of IS PPT.

A working group with the representatives of the software provider are in charge of the following: personnel training, provision of technical equipment for workplaces, software implementation, system start-up, testing and experimental exploitation.

11. IS PPT management.

At this stage, IPO executives conduct surveys of the existing forms and methods of the production management, their assessment and benchmarking, identify bottlenecks in the management process, and factors that play the main role both in a positive and negative role in process management and in the search criteria for assessing the effectiveness of process management. Responsible for the process immediately after determining the value of a particular indicator and detecting its deviation transfers the information to the head of the regulatory entity and develops recommendations aimed at improving the process of management efficiency.

12. Internal audit of IS PPT.

The audit team conducts an internal audit of IS PPT procedures in accordance with the schedule of internal audits or management decisions of the PPT management. Auditors conduct data collection (survey methods, document studies, monitoring of activities, etc.), analyze them and record inconsistencies in the "Report on the inconsistency." After the audit, the team forms an "Audit Report", based on which the process managers carry out corrective and preventive actions.

13. Estimation of the quality of IS PPT processes.

The Department of Quality Control within a set period evaluates the level of quality of the processes of the IS PPT, determines the trends of the process changes and, if necessary, formulates recommendations for its correction.

14. Continuous improvement of IS PPT.

Top management of the PPT, in order to continuously improve the IS PPT, systematically reviews and updates PPT policies and objectives in terms of quality, controls the dissemination of information about the policy and objectives in the field of quality to raise awareness, motivation and involvement of staff at all levels of the enterprise, implement the principle of customer orientation (core production) in all units of the PPT, supports the functioning of an efficient and effective quality management system in accordance with DSTU ISO 9001:2009, provides IS PPT with the necessary resources, conducts Thematic analysis of IS PPT develops a system of measures to improve IS PPT.

4   Results

Development and implementation of a unified management information system is one of the ways to improve the effectiveness of the PPT. This system allows collecting and analyzing the sets of data on-time and efficiently planning the enterprise processes. In addition, one of the blocks of such a system is the evaluation of the PPT quality processes at step 13 of the proposed algorithm (Fig. 4). This stage provides for the formation of the quality indicators values process database used for further analysis and decision management aimed at improving the performance of PPT and forming an array of data for the further analysis.

For this stage, the interface of the program was developed to evaluate the generalized indicator of the effectiveness of quality management processes in the PPT (Fig. 5).

Fig. 5. The program interface for calculating the index of processes efficiency of PPT at stage 13 (in Russian).

The program was created using a highly effective LabVIEW software environment (a product of the National Instruments Company), it is a platform for executing programs, created in the graphical programming language "G". LabVIEW is used in collection and data processing systems, as well as for the technical objects and technological processes management.

5   Conclusions

1. Thus, the integrated application of CALS-technologies for automated and informational support of the QMS will allow for the purposeful management of various information resources of the QMS due to their integration into a unified information system and to create a modern information infrastructure that ensures the effective management of product quality at all stages of its JC. Thus, the introduction of CALS-technologies at the MP for informational support of all stages of the production of products is an important task in the QMS.
2. The introduced algorithm of IS PPT implementation is universal. It allows developing IS PPT quality management system taking into account the specific aspects of the enterprise, the totality of technological processes, the nature of the technological equipment being manufactured, and other production features at each machine-building enterprise.
3. Based on the considered principles of creating the information system of a machine-building enterprise, the information support of the PPT effectiveness assessment processes was developed. The main objective of the developed information support is to create conditions that ensure rational processing and timely providsion with the

necessary information about the results of the performance assessment of the quality management system.

4. In the future, normative documentation is planned to be developed, which will allow providing with an information management system for PPT quality at each machine-building enterprise, taking into account the specific aspects of the enterprise, the totality of technological processes, the nature of the technological equipment being produced, and other production features.

References

1. Ovchinnikov, S.A., Talantsev, A.A.: Information support of the quality management system on the principles of CALS-technologies. In: Innovations in the Conditions of the Development of Information and Communication Technologies, pp. 545–547 (2010). (in Russian)
2. Baronov, V.V.: Automation of enterprise management. INFRA-M, Series "Secrets of Management", Moscow (2000). (in Russian)
3. Bakayev, V.V., Sudov, E.V., Homozov, V.A., et al.: Information Support, Support and Support of the Life Cycle of the Product. Publishing house "Mashinostroeniye", Moscow (2005). (in Russian)
4. Vaisman, V.O.: Models, Methods and Mechanisms for the Creation and Operation of a Project-Managed Organization. Science World, Kyiv (2009). (in Ukrainian)
5. Application of IPI technologies in the tasks of ensuring quality and competitiveness of products. Methodical recommendations. Research Center CALS technology "Applied Logistics", Moscow (2004). (in Russian)
6. Kureichik, V.M., Kureichik, V.V., Taratukhin, V.V., Kravchenko, Y.A., Khlebnikova, A.I.: Continuous acquisition and life-cycle support (CALS) simulation models on the basis of ERP and CAD technologies integration. In: Becker, J., Kozyrev, O., Babkin, E., Taratukhin, V., Aseeva, N. (eds.) Emerging Trends in Information Systems. Progress in IS. Springer (2016)
7. Zaloga, V.A., Ivchenko, A.V., Pogorzhelskaya, Yu.A.: Improving the quality of intrusion support based on the principles of modern information technologies. Compres. Power Eng. **2**(16), 48–51 (2009). (in Russian)
8. Repin, V.V., Eliferov, V.G.: Process approach to management. Modeling of business processes. RIA "Standards and Quality", Moscow (2008). (in Russian)
9. Quality management principles. ISO Central Secretariat. ISO (2015) ISBN 978–92-67-10650-2

Variation Coefficient and Some Distribution Laws in the Context of Cutting Tools and Other Technical Objects Reliability Modeling

Mykhaylo Frolov[✉]

Zaporizhzhya National Technical University, 64 Zhukovskogo St.,
Zaporizhzhya 69063, Ukraine
mc.frolov@gmail.com

Abstract. In the paper some practice of the usage of three distribution laws: Gauss, Gamma, and Weibull for reliability modeling of technical objects in general and metal cutting tools in particular are analyzed and arranged. Selection of distribution law and estimation of its parameters based on empirical data are the main tasks in reliability simulation. It is stressed that selection of the above-mentioned laws should be made taking into account the process mechanism; otherwise, it leads to some false conclusions such as equivalence of Gamma and Weibull distribution. Mentioned distribution laws and their usage are analyzed from the position of physical interpretation. The conditions are shown when the above-mentioned distribution laws are similar. The simplified dependence that connects the shape parameter of Weibull distribution and variation coefficient is obtained and confirmed statistically. The variation coefficient defines the shape parameters for both Gamma and Weibull distributions uniquely and reflects the mechanism of the process. The variation coefficient and failure rate in addition to formal criteria are shown to be the main indicators for the distribution law selection.

Keywords: Failure rate · Weibull distribution · Gamma distribution
Shape parameter · Scale parameter · Gauss distribution · Metal cutting tool
Reliability modeling · Empirical data · Object failure

1 Introduction

To simulate the reliability of any technical object and the metal-cutting tool in particular, including: prediction of the failure probability or that of the no-failure operation during certain time; prediction of the no-failure time; determination of the mean time between failures or time to failure; planning of the test programs etc., it is necessary to establish what kind of theoretical distribution law describes available empirical (selective) data referring to the operation time to failure. In other words, it is necessary to establish a correspondence between the empirical and the theoretical distribution laws. From the formal point of view, this correspondence can be established by the Pearson's chi-square, Kolmogorov–Smirnov type, and other criteria. But it is not only the formal side that is important – namely how close the form of the theoretical distribution law to the available

empirical data is, but also the physical interpretation, connecting type of theoretical distribution law and its parameters with the process mechanism [1].

2   Literature Review

Metal cutting tools are wearable and non-repairable though fully restorable objects - for example, the replaceable-insert tools. In this case, one of the reliability parameters is the time to failure - an equivalent parameter, which is the mean time between two failures (MTTF) [2, 3]. In reliability analysis and modeling, it is very important to take into account the period of life cycle at which the object operates: wear-in, normal operation or wear-out, which affects, first, at the nature of the dependence between time and failure rate.

Different theoretical distribution laws can be used to describe the same empirical data [1]; in addition, one distribution law can be a particular case of another. A considerable number of works are devoted to methods for determining the parameters of some theoretical distribution laws, based on empirical data and comparing these methods [4–7]. However, the distribution laws themselves, taking into account their physical interpretation, are not compared, which sometimes leads to some incorrect conclusions. There are also no clear practical criteria and recommendations regarding the application of any particular theoretical distribution laws in reliability analysis. Taking into account the foregoing, the purpose of this paper is as follows: to analyze and compare three most common theoretical distributions (Gauss or Normal, Gamma and Weibull) for the reliability modeling. The laws should be analyzed by arranging available information, from the following positions: object failures; possibility of transition from one law to another; identifying conditions under which a certain law can be applied.

3   Research Methodology

Research methodology, chosen for the purposes of this article, includes general and statistical analysis of the published cutting tools reliability data (including tool life) and theoretical approaches to it as well as simulation experiments based on generating of selections, following the given distribution laws with predetermined parameters, and their further statistical analysis. All selections with defined theoretical parameters have been generated by means of Microsoft Excel program using its inbuilt functions:

– Gamma distribution: GAMMAINV((1-RAND()); <alfa>; <betta>))
– Weibull distribution: *<Cell containing β>*(-LN(RAND()))^(1/*<Cell containing α>*.

4   Results

4.1   Failure Rate and Variation Coefficient

One of the main indicators describing technical objects reliability is the failure rate $\lambda(t)$, as the conditional instantaneous failure probability at time t, referred to the number

of objects that are in good condition at that moment. It can also be defined as the failure probability at a time t, per one object, from those "survived" until that time. Moreover, any integral distribution law can be represented as an exponential function of the failure rate [2]. The nature of the failure rate function determines the phase of the object life cycle:

– Decreasing type - for the wear-in or "child mortality" phase, when failures indicate defects of the object assembly process and/or that of its individual elements caused by violation of production processes;
– Constant - for the phase of normal operation under the conditions of wearing, aging and fatigue absence, when failures occur suddenly because of the reasons not related to the object itself, in accordance with the exponential distribution law. Sometimes it is used for the cutting tools failures analyses [1], but there are no periods without wearing and in general, it is unacceptable to use exponential distribution for the objects that are subject to wear [3]. The only exception for the usage of distribution law similar to exponential is a complete and almost instantaneous restoration of the object after failure [3]. So, for the cutting tools this period could be taken contingently as one of insignificant increase of failure rate
– Increasing – wear-out phase. For the metal cutting tools, it starts just after wear-in due to the distinguishable processes of wearing aging, fatigue, etc. Only for some period, as mentioned above, it is taken as a normal operation. As soon as the tool reaches the certain limiting state, wear rate and thus failure rate will increase sharply and it will be a catastrophic wear period that normally should be avoided for the cutting tools.

Another significant indicator specifying stability or the variable volatility degree, and hence, the time to failure is the variation coefficient:

$$V = \frac{S}{\bar{T}} \tag{1}$$

where S is the standard deviation of the time between failures and $\bar{T}$ is MTTF.

From the viewpoint of the sample homogeneity and therefore the stability of the results obtained, including the objects quality uniformity, certain boundary values of the variation coefficient can be distinguished [8] (see Table 1).

Table 1. Boundary values of the variation coefficient in terms of results stability.

Variation coefficient	Sample characteristics – results stability
Less than 0.17	Sample is absolutely homogenous – the results are stable
From 0.17 to 0.35	Homogeneity is sufficient – the results are stable enough
From 0.35 to 0.40	Homogeneity is not sufficient – the results are not stable enough
Higher then 0.4	Sample is inhomogeneous – the results are not stable

4.2 Gauss Distribution

The distribution probability density is written as follows:

$$f(t) = \frac{1}{\sqrt{2\pi} \cdot S} exp\left(-\frac{(t - \bar{T})^2}{2S^2}\right) \tag{2}$$

It belongs to the two-parameter (S and $\bar{T}$) distribution laws. The distribution curve is the bell-shaped, symmetric relatively $\bar{T}$. Distribution centers: mathematical expectation, median, and mode coincide. 99.8% of the sample is in the range of $\pm 3S$ relatively $\bar{T}$. "Tails" of the curve tend to infinity, but in tools failure analysis we are dealing with the time that cannot be negative. To consider this fact it is recommended sometimes to use the logarithmic Gauss distribution [1]. However, it is not supposed to be correct due to the decreasing time - failure rate function for this law, which is not typical for the technical objects at the wear-out phase. Considering this, the use of the logarithmic Gauss distribution for the metal cutting tools reliability analysis, as well as for other technical objects, is rather questionable [3]. Hence, the only sense to use Gauss distribution is when $\bar{T} \leq 3S$ or for $V \leq 0.33$, thus for the sufficiently stable results.

There is one more limitation for Gauss law. Based on the physical interpretation, the Gauss distribution takes place when there are a large number of independent or weakly dependent random variables with finite variances and practically arbitrary distribution laws affecting object [9]. The basic condition for the Gauss distribution formation is that all factors that act together should play a similar role in the overall result. If the influence of one of the random variables differs sharply from the others, then the distribution law will depend on it and, accordingly, it will not be Gauss. In the practice of technical objects operation, the Gauss distribution is typical for the failures that occur due to the stable progress of wearing and aging processes, which is reflected as a failure rate increase without limits.

4.3 Gamma Distribution

It is a kind of two-parameter distribution: $\lambda_0 > 0$ and $r > 0$ – the scale and the shape parameters respectively. The probability distribution density is described by the following expression:

$$f(t) = \frac{\lambda_0^r}{\Gamma(r)} t^{r-1} \cdot \exp\left(-\lambda_0 t\right) \tag{3}$$

In this equation, $\Gamma(r)$ is the general Gamma function. The importance of Gamma distribution is that it is able to describe failures at various phases of the object life cycle, depending on the value of the shape parameter:

– For r < 1, the failure rate is a decreasing function – wear-in phase;
– At r = 1, the failure rate is constant, distribution goes exponentially and describes sudden failures – normal operation phase;

– For r > 1, the failure rate is an increasing function – wear-out phase. The value of r is interpreted as the amount of damages or peak "emissions" due to which a failure occurs [3] and this fact corresponds to the failure due to the accumulating damages model.

It is shown in [4] that the Gamma distribution approaches the Gauss one when λ_0 is rather large, and in [1], the approximation to the Gauss law is indicated for $r > 12$. Both assertions are not correct because the physical meaning of the scale parameter λ_0 is limiting the failure rate value. For the Gamma distribution, the failure rate curve is convex, bounded from above, which, taking into account the convexity condition as the second derivative of the function, can be written as $\lambda''(t) < 0$. And for the Gauss distribution, it is concave and unbounded - $\lambda''(t) > 0$, although the probability density graphs may be similar. This fact is demonstrated at Fig. 1 - graphs for both distributions are plotted for the same sample. Here $r = 11.9$, $\lambda_0 = 6.9$; variation coefficient – $V = 0.28$. Some basic properties of the Gamma distribution are given in Table 2.

a)   b)
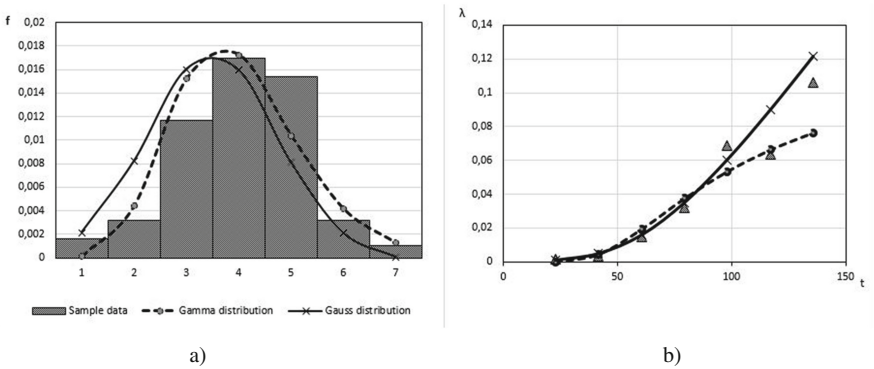
Fig. 1. Behavior comparison for Gauss and Gamma distributions: a – probability density and b – the failure rate.

Table 2. Some properties of the Gamma distribution.

Name	Value
Argument t	$0 \le t \le +\infty$
Variance	$\sigma^2 = r/\lambda_0^2$
Mathematical expectation	$\mu = r/\lambda_0$
Variation coefficient	$V = 1/\sqrt{r}$

In accordance with Table 2 and assuming that the MTTF is an empirical estimation of the mathematical expectation: $\mu = \bar{T}$, empirical estimates of the distribution parameters can be obtained:

$$r = \frac{1}{V^2} \tag{4}$$

$$\lambda_0 = \frac{r}{\overline{T}} \tag{5}$$

Due to Eq. (4): the wear-in phase will be characterized by the variation coefficient $V > 1$; the period of normal operation - $V = 1$; and phase with wear failures - $V < 1$. Moreover, the more the influence of the wear and other mentioned above processes at the object failure, the smaller variation coefficient will be. This is indicated particularly at [10]. Equation (5) also shows the physical meaning of the shape parameter that is the average number of damages resulting in object failure, per unit time.

4.4   Weibull Distribution and Generalization

Weibull is a distribution law, or rather a family of distributions, describing a wide range of processes. The law has wide application for the description of the yield stress of steel distribution [7] as well as for the reliability theory, including the description of the metal-cutting tools failures [10, 11]. As well as the Gamma distribution, it is suitable for all stages of the object life cycle. In [4] it is noted that Weibull and Gamma distributions are competing, and the only difference is the complexity of the distribution parameters empirical estimation. However, as will be shown later, this is not always the case.

The distribution probability density is described as follows:

$$f(t) = \frac{\alpha}{\beta^\alpha} t^{\alpha-1} exp\left[-\left(\frac{t}{\beta} \right)^\alpha \right] \tag{6}$$

where $\alpha > 0$ and $\beta > 0$ are the shape and scale parameters respectively. Some properties of the Weibull distribution are presented in Table 3.

Table 3. Some basic properties of the Weibull distribution.

Name	Value
Argument t	$0 \le t \le +\infty$
Mathematical expectation	$\mu = \beta \cdot \Gamma(1 + 1/\alpha)$
Variance	$\sigma^2 = \beta^2 \cdot \Gamma(1 + 2/\alpha) - \mu^2$
Failure rate	$\lambda(t) = \frac{\alpha}{\beta^\alpha} t^{\alpha-1}$
Median	$Me = \beta ln(2)^{1/\alpha}$
Mode	$Mo = \beta \left(\frac{\alpha - 1}{\alpha} \right)^{1/\alpha}$

The Weibull distribution variety of forms is much wider than that of the Gamma:

– For $\alpha < 1$ and $\alpha = 1$, the behavior of the failure rate function is similar to that of Gamma distribution for $r < 1$ and $r = 1$ respectively. Moreover, for $\alpha = 1$ it completely coincides with the Gamma distribution and both with exponential one;

- For $\alpha > 1$, the failure rate is an increasing function and the distribution law describes failures associated with wear. But here the Weibull distribution offers a much greater variety:
- If $1 < \alpha < 2$ - the failure rate is a convex function bounded above, similar to the Gamma distribution - $\lambda''\,(t) < 0$;
- If $\alpha = 2$ - the failure rate is a straight line - $\lambda''\,(t) = 0$;
- If $\alpha > 2$ - the failure rate is the concave curve and is not bounded from above and $\lambda''(t) > 0$.

Taking the MTTF $\left(\bar{T}\right)$ as an empirical estimate of the mathematical expectation, the conditions when the Weibull distribution transforms to the Gauss one can be written down: $Me = Mo = \bar{T}$. So:

$$\alpha = \frac{1}{1 - ln2} = 3.26 \tag{7}$$

$$\beta = 1.12 \cdot \bar{T} \tag{8}$$

Since the shape parameter $\alpha = 3.26 > 2$, the nature of the failure rate curve is the same as for the Gauss distribution law, i.e. when the Weibull distribution parameters approach the values determined by Eqs. (7) and (8), the distribution itself will approach the Gauss.

Empirical estimation of the distribution parameters can be performed in various ways [5–7] - least-square method (LSM), maximum likelihood, etc. At work [7], the dependencies for the lower and upper limits of α confidence interval can be found. Designating with indexes "L" and "U" lower and upper limits respectively, for a confidence probability of *0.95*, the dependencies will be as follows:

$$\alpha_L = \alpha \cdot exp\left(-\frac{1.53}{\sqrt{N}}\right) \tag{9}$$

$$\alpha_U = \alpha \cdot exp\left(\frac{1.53}{\sqrt{N}}\right) \tag{10}$$

where N is the sample size.

For the estimation of the shape parameter, Eq. (1) and correspondent eq. of Table 3 are used. Then, variation coefficient for Weibull distribution will be as follows:

$$V = \sqrt{\frac{\Gamma\left(1 + \frac{2}{\alpha}\right)}{\Gamma^2\left(1 + \frac{1}{\alpha}\right)} - 1} \tag{11}$$

The approximation of Eq. (11) in the range of α from 0.5 to 25 leads to a simplified empirical dependence of the shape parameter on the variation coefficient that gives determination factor equal to *0.9998*:

$$\alpha = 1.02 \cdot V^{-1.08} \approx \frac{1}{V} \qquad (12)$$

The shape parameter defines the nature and mechanism of the object failures [7], and thus the variation coefficient.

Generating samples with predetermined theoretical parameters, their empirical shape parameters were estimated by LSM and Eq. (12). The theoretical values, values obtained by Eq. (12) as well as those estimated by LSM, happened to be inside the same confidence intervals. Some results of estimation for samples of a size $N = 100$ are shown in Fig. 2, where theoretical parameters are shown in the boxes. Thus, Eq. (12) can be used for the estimation of the shape parameter. According to the presented at [7], some boundary values of the shape parameter α, reflect the nature and mechanism of failures, hence some boundary values of the variation coefficient.
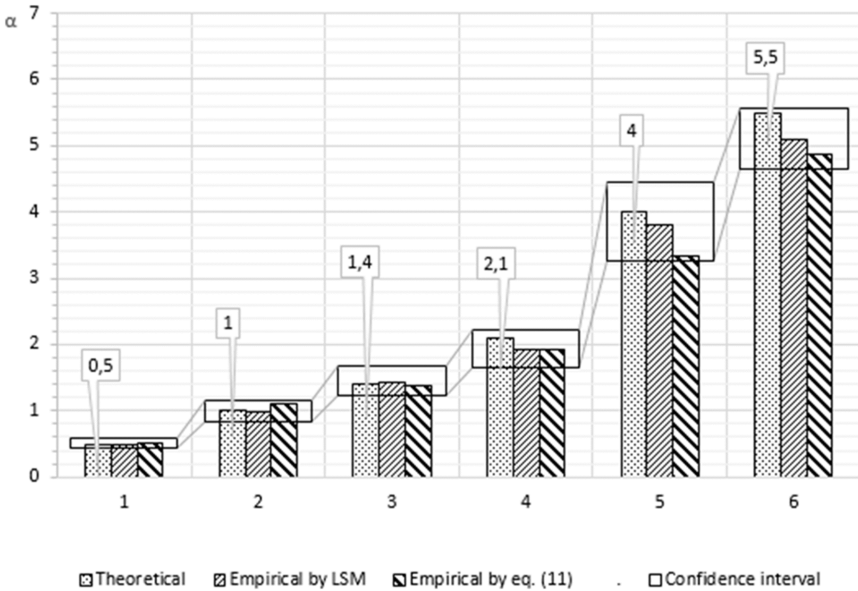
Fig. 2. Comparison of theoretical and empirical shape parameters.

Depending on the variation coefficient, the application areas of the above-mentioned distribution laws can be determined. The summarized data are presented in Table 4. It gives good insight into mechanism involved - the more pronounced the wear nature of failure, including the operation under increasingly unfavorable conditions (for example, with an increase of cutting speed), the smaller the coefficient of variation will be, which is noted at [1, 10, 12]. As Table 4 shows – when variation coefficient is $V > 0.5$ the

Weibull and Gamma distributions are indeed competing and anyone can be used to describe the failures. For $V = 1$, they generally go over into the same exponential distribution, but for $V \leq 0.5$ they describe different physical processes that vary by the nature of the failure rate. The principal difference between failure rates of the Gamma and Weibull distributions is similar to that shown in Fig. 1b. This kind of Weibull distribution behavior also is indicated at [11].

Table 4. Comparison of conditions and application areas for distribution laws

Weibull distribution			Variation coefficient V	Gamma distribution	
α	$\lambda''(t)$	Failure nature		r	$\lambda''(t)$
0.5	>0	Wear-in: inadequate start; misassembly; quality problems	2.00	0.25	>0
1	–	Sudden failures: independent of time; outside influence; maintenance errors; mixtures of problems	1.00	1.00	–
1.5	<0		0.67	2.22	<0
2	=0	Gradual wear-out	0.50	4.00	<0
2.5	>0		0.40	6.25	<0
3	>0	Low cycle fatigue	0.33	9.18	<0
3.26	>0	*Close to Gauss distribution*	0.30	11.11	<0
4	> 0		0.25	16.00	<0
4.5	>0	Rapid wear-out	0.22	20.66	<0
5	>0		0.20	25.00	<0
6	>0	"Old age" wear-out	0.17	34.60	<0

Analysis of empirical data concerning tool life, the variety of which is presented at [1], confirm suggested the approach for distribution law selection and its parameters evaluation. For example, tool-life data for *M10x1.5* screw dies, governed by Weibull distribution on author's estimation, show variation coefficient of *0.76*; shape parameter, defined by LSM - *1.32* and its confidence interval - from *1.06 to 1.64*. Shape parameter, defined by Eq. (12) is equal to *1.36* and by the author – *1.40* that are in above confidence range. At the same time, goodness-of-fit tests by Pearson's chi-square and Kolmogorov-Smirnov criteria with the confidence level of *0.95* indicate that data could also be adequately approximated by the Gamma distribution, that agree with the variation coefficient value.

5   Conclusions

1. Variation coefficient can be used as a simple criterion displaying physical processes underlying failures of the objects and thus defines the shape parameters for both Gamma and Weibull distributions in reliability modeling uniquely.
2. The nature of the failure rate – time dependence should be a decisive factor for the distribution law selection in reliability modeling in addition to formal criteria like Pierson's and Kolmogorov-Smirnov.

3. At $V > 0.5$, the Gamma and Weibull distributions are similar, so they can be used for reliability modeling equally.
4. At $V \leq 0.5$, the Gamma and Weibull distributions have a different character of the failure rate on time dependence that reflects different physical processes.
5. In the conditions of statistical data shortage, having reasonable ground to suppose that failure probability follows the Gauss law the reliability can be estimated by the Weibull distribution with the parameters defined by Eqs. (7) and (8).

References

1. Katsev, P.G.: Statistic Methods of Cutting Tools Research. Mashinostroyeniye, Moscow (1974). (in Russian)
2. Ostreykovskiy, V.A.: Theory of Reliability. Vyschaya Shkola, Moscow (2003). (in Russian)
3. Barrlow, R., Proschan, F.: Mathematical Theory of reliability. Sovetscoye radio, Moscow (1969). (in Russian)
4. Gamma distribution fitting: NCSS Statistical Software. https://ncss-wpengine.netdna-ssl.com/wp-content/themes/ncss/pdf/Procedures/NCSS/Gamma_Distribution_Fitting.pdf. Accessed 17 Nov 2017
5. Akram, M., Hayat, A.: Comparison of Estimators of the Weibull Distribution. Financial Econometrics Series. Deakin University, Geelong (2013)
6. Nielsen, M.A.: Parameter estimation for the two-parameter Weibull distribution. In: All Theses and Dissertations, p. 2509. Brigham Young University, Provo (2011)
7. Abernethy, R.B., Breneman, J.E., Medlin, C.H., Reinman, G.L.: Weibull Analysis Handbook. Pratt & Whitney Aircraft, West Palm Beach, FL (1983)
8. Yudina, A.V.: Statistics. Educational materials of VGUES. https://abc.vvsu.ru/books/pr_stat1/page0010.asp#xex24. Accessed 17 Nov 2017. (in Russian)
9. Bulashev, S.V.: Statistic for Traders. Sputnic+, Moscow (2003). (in Russian)
10. Mironenco, E.V., Vasylieva, L.V.: Research of the machining stability influence at cutting tool operation regulations in the conditions or multi-criteria optimization. In: Bulletin of SevNTU. Mashinopryladobuduvannya ta transport: zb. nauk. pr., vol. 107, pp. 151–154. SevNTU, Sevastopol (2010). (in Russian)
11. Varma, B.S., Kumar, S.S., Madhu, S.: Reliability of ZTA ceramic cutting tools while machining carbon steels. CMR J. Eng. Technol. **1**(2), 1–18 (2016)
12. Dreval, A.V., Litvinenko, A.E.: Scientific works of "Tool equipment and technologies" department of MSTU n.a. N.E. Bauman for improving efficiensy of cutting tools operation. Science and education. http://technomag.bmstu.ru/doc/48836.html. Accessed 18 Nov 2017. (in Russian)

Measurement of Non-rigid Tools Action Force During Finishing

Natalia Honchar[(✉)] , Oleksiy Kachan , Dmytro Stepanov , Mark Kuchuhurov , and Olena Khavkina

Zaporizhzhya National Technical University, 64 Zhukovskogo Street,
Zaporizhzhya 69063, Ukraine
gonchar@zntu.edu.ua

Abstract. The purpose of the research was to design a device (dynamometer) for measuring the action force on work surface (cutting force) during the finishing process with non-rigid tools such as flap wheels, mechanical brushes with metal and nonmetal fibers, or using jet processing with various fillings – sand, grinding materials, metal shot, glass microbeads, etc. The information about force level is used, for example, to select a tool or a method for finishing of thin-walled parts or edges as well as for determination of rational processing modes of the method selected. This device considers special features of action force of some tools and methods: distributed type of loads; rapidly changing force intensity; possibility of rocking sensitive device element; furthermore, different level of loads needs increased sensitivity on the one hand, and on the other hand, the universality of the device. The proposed device provides measuring constant, inconstant and harmonic loads in wide range as well as measuring concentrated and distributed forces with high accuracy. It allows registering information in real time, saving and processing data in a comfortable form. For example, the proposed dynamometer was used to measure action force of brush rotary disc polymer-abrasive tools on work surface. The tools based on polymer-abrasive fiber are used for finishing parts of complex profile, for trimming, cleaning, deburring, etc. They also have a light hardening effect. The results of research determined that force is 20…100 H depending on processing modes and tool options, therefore polymer-abrasive brushes can be used for thin-walled parts.

Keywords: Dynamometer · Action force · Cutting force · Finishing · Polishing
Brush polymer-abrasive tool

1 Introduction

In such industries as aircraft engine building, medical industry (making tools and prostheses), instrument making, etc., most parts are geometrically-complex and thin-walled for a number of reasons. In addition, they often belong to the group of critical or extremely critical parts; they carry a range of loads in operation. As a result, the surface of such parts needs to meet increased requirements. A need for finishing (hardening) machining surface and thin edges of complex configuration arises. This explains a

significant proportion of monotonous and responsible manual labor, and the overall high labor intensity and cost of finish operations.

It must also be taken into account that the materials of parts in the above-mentioned industries are often specific: corrosion-resistant steels of various grades and titanium-based alloys, heat-resistant nickel and titanium alloys, etc., are hard-to-machine. Consequently, their processing requires the application of considerable cutting forces, that can be dangerous for thin-walled elements of parts.

Therefore, it becomes necessary to measure the instrument action force on the surface treated to select or, on the contrary, restrict application of a tool for a finishing method, or to determine rational processing modes.

For hard tools the task of measuring cutting forces is solved by various methods, mainly using dynamometers - spring, hydraulic, mechanical, electrical, combined ones, etc. [1–6].

However, for finishing operations free abrasive, blasting with various fillers (sand, abrasive, balls, etc.), petal circles, rotary brushes with metal and non-metal fibers and other non-rigid tools [7, 8] are often used. Their action is characterized by a relatively small force pressure and distributed force, which changes the intensity rapidly in a short time. Some of these methods allow automating the machining process, which reduces manual labor significantly. Sometimes it can be preferable to choose a certain method, despite some obvious disadvantages or limitations.

In any case, our urgent task is to determine the level of tool action force on the surface to be machined to decide whether this tool can be used for machining specific parts with thin-walled structural elements.

2 Literature Review

Let's look closely at one of modern tools appeared recently at the market - a polymer-abrasive (PA) tool. It has proved to be rather efficient for finishing, including complex products [9, 10]. The difficulty of measuring forces during machining can obviously be seen. Brush tools (Fig. 1) of rotary action are a hub and PA fibers, in the volume of the main polymer fraction of which abrasive grains of a certain granularity are placed evenly [11, 12]. Due to the fibers flexibility they demonstrate the following advantage, which makes them preferable among other alternative tools and methods for machining complex profile parts – that is reduced requirements for the accuracy of the relative positioning of the workpiece and the machining tool, that reduces the complexity of the tool movement and makes mechanization and automation of finishing operations technically and economically viable; the cost of automatic devices and their programming reduces as well as the cost of their maintenance.

In the process of studying PA brushes attempts have been made to estimate the impact energy of a fiber analytically in order to calculate the performance of the PA brushes [12] and the specific pressure on 1 mm^2 of the contact spot [13], the impact force of a single PA fiber [14], using virtual simulation [15, 16], and also to determine the process power [17] and the static pressure of one PA fiber [13] experimentally.
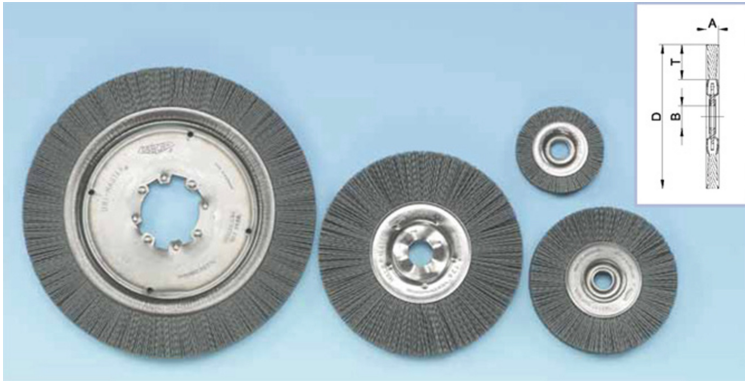
Fig. 1. Polymer-abrasive disc brushes [18].

However, for the experimental determination of the actual value of the action force from a PA tool, as a representative of the above-listed non-rigid tools and methods, it is necessary to have a universal device taking into account their specificity.

As the action force of such tools is much weaker than of traditional cutting tools and abrasive wheels, the sensitivity of the measuring device should be higher. For example, when trying to measure the action force of rotary disc PA brushes with the help of a device [19] (a thin plate fixed with a cantilever served as a sensitive plate receiving the load), another feature arose. Brushes mounted on a surface grinding machine with a slight spindle beat caused considerable vibration and rocking of the sensing element of the measuring device, which measured the action force of a single PA fiber stably [19]. As a result, the secondary dynamic component made it difficult to determine the actual load on the plate.

Taking the above mentioned into account, the purpose of the study was formulated.

3   Research Methodology

The purpose of this work was: (1) to develop a simple and easy-to-use instrument – a dynamometer with high sensitivity in order to determine the forces from permanent, non-permanent and periodic loads, including distributed ones, which can suppress possible excessive fluctuations; it also can monitor measured forces and record them in real time and provide ample opportunities for further result processing; (2) to determine experimentally the vertical component of the action force of the disk PA brush on the machined surface.

In order to perform the tasks set, the initial design of the dynamometer was first worked out in details. The measuring system of the device must have a flexible element, the deformation of which can be easily measured. Therefore, the main element of the dynamometer is the bracket 1 with two upper and lower arms (Fig. 2). Such a principle was applied earlier [20–22] and it is proved to be efficient.
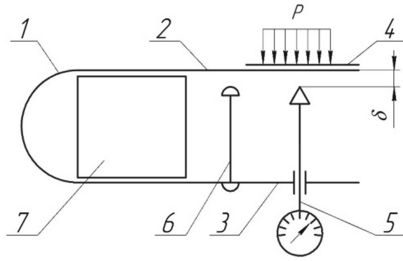
Fig. 2. Scheme of the measuring device: 1 – bracket; 2, 3 – bracket upper and lower arms; 4 – the carriage; 5 – measuring device; 6 – safety device; 7 – vibration damper (buffer pad).

The carriage 4, perceiving both concentrated and distributed load, must be attached to the upper, less massive, arm bracket rigidly. Also, it should be able to move along the staple, changing the arm length to the point where the force is applied (changing the clamp stiffness) in order to measure the loads in different ranges. This increases the device versatility. The arm length must be determined experimentally before the experiment.

The measuring device 5 must also be able to move along the clamp. For this purpose there should be a long slot (Fig. 3) on the bottom of the bracket, which is to be more massive (for its more reliable fixing and additional elements 5 and 6 on the machine); the slot length must equal the entire bracket length. The clearance δ (Fig. 2) was chosen to be a measured parameter as a direct characteristic of the deformation of the flexible clamp upper arm from the load acting on it. The measuring device must be sensitive, quick-response, react to fast processes within a fraction of a second and be relatively inexpensive. These conditions are met by electrical analog devices, for example, widespread contactless inductive sensors.
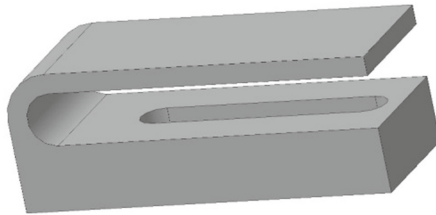
Fig. 3. 3D bracket model.

The safety device 6 should be of the simplest design; it must not allow too much bracket deformation, thus it can result in taking-up of clearance δ, impact, touch or pressure directly on the sensor when the dynamometer is pre-adjusted before the experiment or when the bracket upper arm can be swung because of measured periodic loads. It is necessary to provide a simple method of its fixing and vertical adjustment, as well as the possibility of its rapid removal from the bracket if there is no use in it or, if there is not enough space for a buffer pad – vibration damper 7.

The vibration damper 7 (buffer pads made of various materials – paronite, rubber, etc.) can be placed between the arms (Fig. 2) if necessary, in order to damp the excessive swing of the upper arm when measuring non-permanent or periodic loads.

To solve the problem a dynamometer that makes it possible to measure even a small action force was designed and made (Fig. 4); the dynamometer meets all above-mentioned requirements [23].

a)   b)
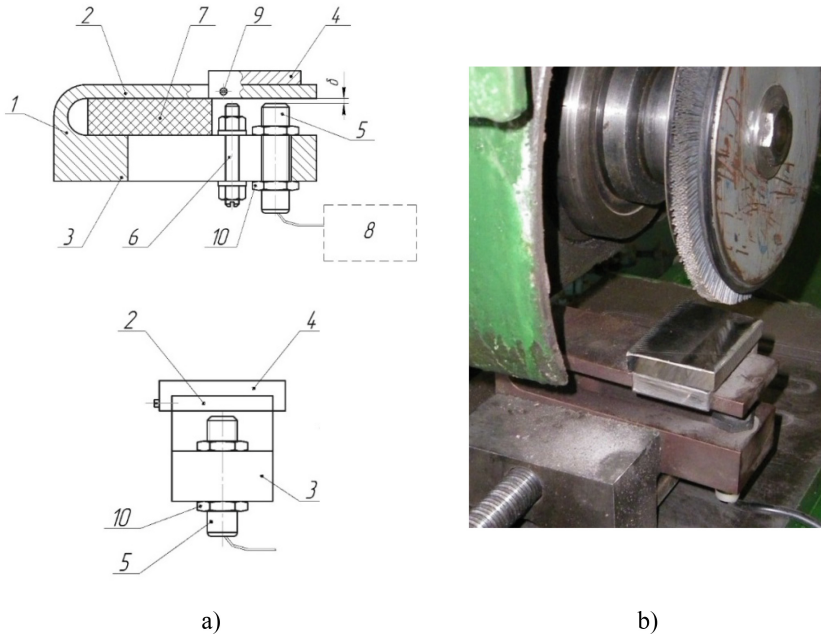
Fig. 4. Draft (a) and appearance (b) of the dynamometer: 1 - bracket; 2, 3 - upper and lower arms of the bracket; 4 - carriage; 5 - XS4P12AB110 eddy current sensor; 6 - safety device; 7 - vibration damper (buffer pad); 8 - recording device; 9 - screw; 10 – nut.

The principle of the dynamometer is as follows. Under the influence of the load on the carriage 4, the upper arm 2 of the bracket 1 is distorted, that causes a change in the size of clearance δ continuously measured by the contactless inductive sensor. The sensor signal is transmitted to the recording device 8, consisting of an amplifier, an analog-digital converter and a PC, with software, for example, "PowerGraph 3.3 Demo" demo version which records the signal in real time, transforms it into force value applied to the carriage, and saves the results obtained to process the gathered information in a convenient form.

The carriage 4 is of U-shape, that makes it possible to move along the upper arm. If the loads are too large, it is moved, reducing the arm length to the point where the force is applied in this way increasing its rigidity. When measuring low force, the carriage is moved closer to the bracket edge, thereby increasing the device sensitivity. The carriage is fixed by three screws 10, preventing its displacement from the possible tangential

component of the load. The sensor 5, if necessary, can be moved along the slot, but its extreme position ensures the highest sensitivity of the measurement.

The calibration for the recalculation of the forces acting on the carriage from the analog signal characterizing the size of clearance δ was carried out using weight measures, obtaining the calibration dependence of the output voltage U on the force P: U = f(P).

The proposed dynamometer can be used to measure the constant forces acting on the carriage, but it is particularly valuable in the measurement of variable forces changing at short intervals.

4   Results

Figure 4 shows the result of measuring the vertical component of the cutting force during the machining with a rotary disc PA brush (Fig. 1). The assembled dynamometer was gripped in a vice, which in turn was fixed on a table of surface grinding machine 3Г71. Little oscillation caused by the minimum spindle wavering and uneven entry of PA fibers into the contact zone did not make it necessary to use a buffer pad. No swinging of the bracket upper arm occurred.

Such oscillograms (Fig. 5) were obtained by carrying out series of experiments with varying processing conditions (cutting speed, feeding, tightness - the degree of brush pressing against the sample surface) and tool parameters (brush diameter, length and diameter of PA fibers, material and grain size of abrasive). The oscillograms were processed using the "Power-Graph" demo version.
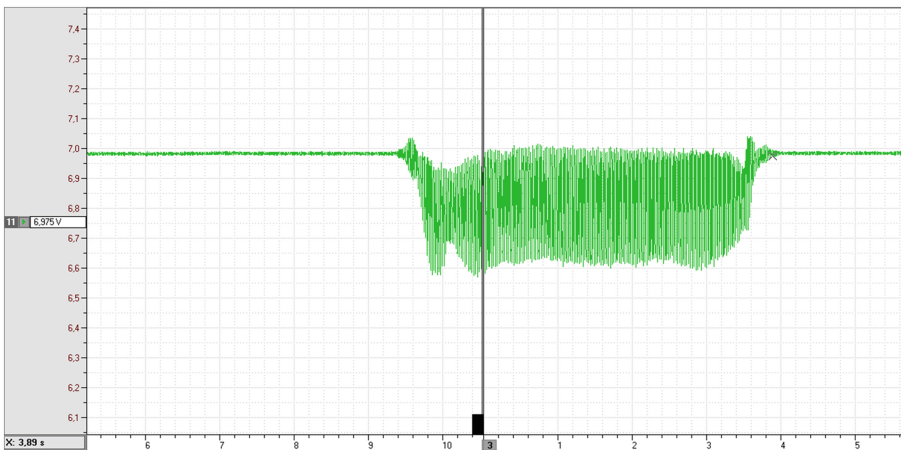
Fig. 5. Oscillogram - graph of clearance δ changes in time.

To study the PA brush action force on the samples, the following tool parameters and processing modes were varied:

– fiber length L = 8; 16; 32 mm;
– feed S = 1.0; 3.5; 5.5; 10 m/min;

– tightness i = 0.5; 1.0; 2.0; 3.0 mm;
– speed V = 17; 27; 40 mps.

The remaining parameters were constant: brush diameter 150 mm; fiber diameter 1.2 mm; 63C abrasive material with F80 grain size. Such abrasive fiber diameter and grain size characterize the hardest PA fiber for PA brushes widely used today.

The results of the experiments of the steel samples 3 (Fig. 6) confirmed a low level of action force on the sample from PA brush. The radial force was 11…67 N in the range of studied brush parameters and processing modes.

With tightness *i* increase the action force level increases too (Fig. 6a): for the fiber length L = 8 mm it is proportional, since the tool becomes similar to a grinding wheel with a polymeric bond in its properties. For length L = 16 and 32 mm, when the tightness is bigger than 2 mm, the flexible fibers are bent, some of them go aside, the number of fibers sliding with their lateral surface increases, the rigidity of the tool as a whole decrease, so the force P grows less intensively with increasing tightness (at a speed V = 17 mps, which is optimal for steel 3).

The fiber length L, as an indicator of rigidity of PA brushes, showed the expected results: the longer a fiber is, the less rigidity an instrument has, and, accordingly, the lower the force action level is (Fig. 6a, c).

In practice, the change in the value of the longitudinal feed S = 0.5…10 m/min does not influence the action force level, as the number of fibers contacting with the sample in the unit of time remains unchanged, only the total contact time of PA brushes with a sample decreases.

An increase of brush circumferential speed slightly increases the level of action force on the sample (Fig. 6b) due to an increase of dynamic and shock components.

Almost similar results were obtained on samples made of nickel alloy ЭИ698-ВД.

The same experiments were carried out for samples of АК7ч aluminum alloy. All regular changes in P were preserved, but because of the slightly higher alloy viscosity part of the brush action energy was dissipated in the sample, so the radial force of PA brushes for this material was smaller (depending on the modes, by 10…30%).

The resulting graphs made it possible to trace the change in the force level at the tool entrance to the contact zone with the machined surface, then during the main machining and in its output - in real time (the abscissa axis - time in seconds) and to obtain the average (constant) force acting from the brush tool during the machining (Pmax did not exceed 100 N, depending on the variable factors).

The dynamometer makes it possible to carry out measurements of the action force of even a single PA fiber (the maximum force is 0.8…1.2 N, depending on modes).

The proposed dynamometer and the developed measuring technique allowed determining the vertical (normal) component of the action force on the machined surface from the disk brush tool with high sensitivity taking into account such peculiarities of a PA brush as distributed amplification (all forces from all the fibers that are simultaneously in contact with the surface are summed): some fibers come into contact the surface, some fibers bounce off it, pressed down with the fibers above forming a contact patch, others don't contact the surface, creating distributed force). Each fiber is within the contact zone with the sample for 0.2…5 ms, the brush rotational speed is 10…255 rps). The form of information recording allowed expanding the oscillogram and
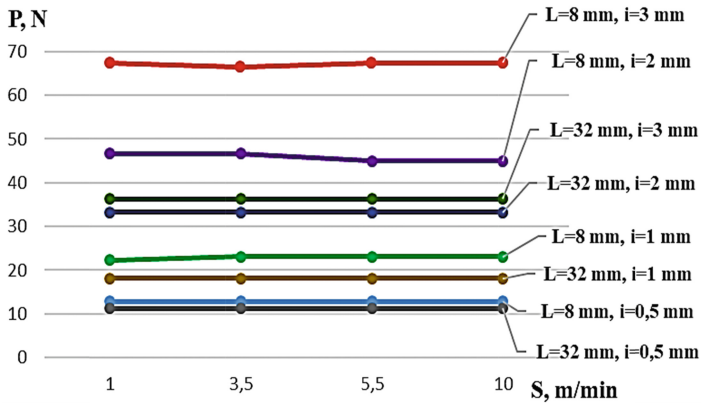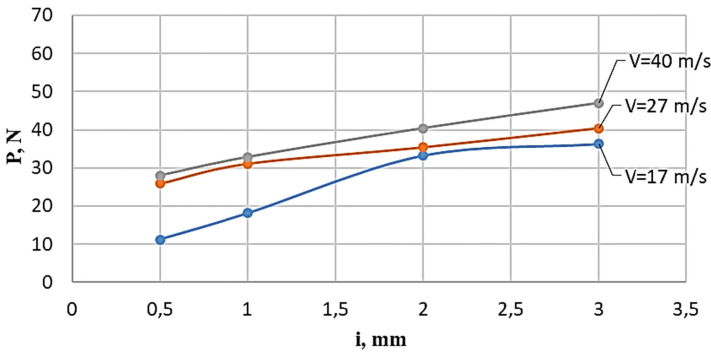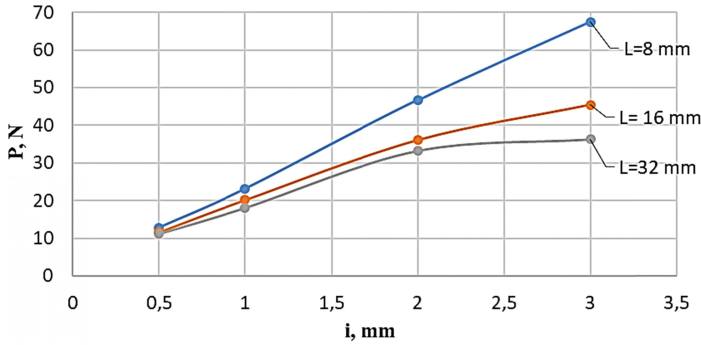
Fig. 6. Dependence of the PA brushes radial force on the sample on: (a) – tightness *i* and length *L*; (b) – tightness *i* and the speed *V*; (c) – on feed S. Steel 3.

analyzing the causes of jumps during the processing of a full PA brush or the force of the first impact of a single fiber.

When comparing the results it was found that the action force of the disk brushes is affected by the speed, brush tightness and stiffness determined by fiber radius and diameter and the number of fibers being simultaneously in the contact zone. But even under experimental conditions, the force action did not exceed 100 N.

5   Conclusions

As a result of the research it was found that the proposed dynamometer can be used in studying the finishing process with various non-rigid tools (petal circles, rotary brushes with metal and non-metal fibers, sisal polishing wheels, blasting with sand, abrasive, balls, etc.). It is quite simple to make it; it has high sensitivity, speed, and the ability to monitor the action force of different characteristics.

With the help of the dynamometer, the action force of disk PA brushes and the influence of the machining conditions and tool parameters on its level were determined. It also was found that due to low force pressure on the workpiece surface, PA brush tools can be widely used for finishing thin-walled parts. Furthermore, the PA brushes make it possible to process parts of a complex profile automatically.

References

1. Youssef Helmi, A., Hassan, E.-H.: Machining Technology: Machine Tools and Operation. CRC Press, Taylor & Francis Group, London (2008)
2. Bray, A., Barbato, G., Levi, R.: Theory and Practice of Force Measurement. Academic Press, San Diego (1990)
3. Wolfer, P., Pfeifer, H.P., Spur, G., Siebert, J.C., Benzinger, K.-J.: Device for measuring the cutting forces on machine tools. Patent No. 4899594 A, United States (1990)
4. Serway, R.A., Beichner, R.J.: Physics for Scientists and Engineers. Saunders College Publishing, Harcourt Brace (2000)
5. Del Taglia, A., Tani, G.: A method for measuring cutting forces in boring operations. Int. J. Mach. Tool Des. Res. **22**, 23–30 (1982)
6. Kistler: E-catalog of the company. http://www.kistler.com
7. Frolov, K.V.: Mechanical engineering. Encyclopedia: in 40 vol. Technology of machine production, V.3: Technology of machine parts manufacturing. Mashinostroenie, Moscow (2002)
8. Boguslaev, V.A., Kachan, A.Y., Mozgovoy, V.D.: Finishing technologies for GTE parts processing. Bull. Engine Build. **1**, 71–78 (2009)
9. Provolotskiy, A.E., Negrub, S.L.: Technological capabilities of polymer-abrasive tools. Research papers of Donetsk National Technical University. Section: Machine Equipment **1**, 125–133 (2004)
10. Burykin, V.V.: Elastic tools with a polymer-abrasive working part. Equipment Tools Prof. [Metalworking] **2**, 30–32 (2014)
11. Abashkevich, Y.D., Machishin, G.M.: Technology of production of polymer-abrasive fiber. Bull. HNADU **73**, 63–67 (2016)
12. Abashkevich, Y.D., Pelevin, L.E., Machishin, G.N.: Polimer-abrasive brush tools for processing metal and non-metallic surfaces. In: Oil and gas of Western Siberia: The International Scientific and Technical Conference, pp. 8–14. TyumGNGU, Tyumen (2013)

13. Yakovlev, D.R.: Theoretical and experimental research of technological possibilities of abrasive-polymeric brushes and determination of effective areas of their use. In: The International Scientific and Technical Conference AAI. Section 7 "Technologies and Equipment of Mechanical Assembly Production", pp. 293–299 (2010)
14. Popovich, A.G., Honchar, N.V., Stepanov, D.N.: Calculation of the impact forces of the elastic fiber on the part at the finish processing. Aviat. Space Techn. Technol. **7**(94), 11–14 (2012)
15. Kurguzov, Y.I.: Analysis of the contact interaction of a rotating brush and a processed surface. News Samara Sci. Center Russ. Sci. Acad. **4**(3), 794–798 (2011)
16. Honchar, N.V., Kondratyuk, E.V., Stepanov, D.N., Kuchugurov, M.V.: Studying of the process of working with a polymer-abrasive tool with modeling. Cut Tools Technol. Syst. **83**, 55–63 (2013)
17. Ustinovich, D.F., Pribylskiy, V.I.: Dependence of power on grinding modes by polymer-abrasive disk brushes. Mech. Mach. Mech. Mater. **1**(18), 75–79 (2012)
18. Osborn. Catalog of the company (2008)
19. Stepanov, D.N.: Method for measuring the pressure force of a polymer-abrasive fiber during the flat sample processing. In: Engineering of Ukraine Through the Eyes of Young Scientists: Progressive Ideas – Science – Production: XII Ukrainian Youth Scientific and Technical Conference, section 2, pp. 110–111. Kyiv (2012)
20. Rapier, A.C.: Cutting force dynamometers. H.M. Stationary Office, NEL Plasticity Report (1959)
21. Sizykh, P.P., Kvashnin, H.R., Zhilitskiy, V.F., Bliznyakov, V.N.: Dynamometer. Patent No. 769369, USSR (1980)
22. Artyukhov, E.S., Suvorov, V.S.: Dynamometer. Patent No. 481800, USSR (1975)
23. Vnukov, Y.M., Stepanov, D.M., Honchar N.V.: Dynamometer. Patent No. 110930, Ukraine (2016)

Implementation of Material Flow Simulation as a Learning Tool

Jozef Husar[✉], Lucia Knapcikova, and Michal Balog

Technical University of Kosice,
1 Bayerova Street, 08001 Presov, Slovak Republic
`jozef.husar@tuke.sk`

Abstract. The paper is focused on the possibility of implementation the simulation of the production process into the education process. Recently, emphasis has been placed on digitizing the production process, using Industry 4.0 and, last but not least, optimizing and minimizing production times. The paper is organized as follows into two sections. Section 1 describes the concrete possibilities of implementation the simulation software and Sect. 2 describes the evaluation of results on a concrete example from production process. After defining the same input data for 4 types of rolling bearings (production times, material flow and Gantt chart), the variety of simulation was followed in order to achieve an optimal distribution of production, transport and storage ratio in the 50:30:20 range. Due to the application of the simulation students are taught how to benefit of a thorough analysis of production process, and all the time the students are very close to the real work environment of the production company.

Keywords: Plant simulation · Education · Student's simulation

1 Introduction

Today's problem is connected with the lack of time and great emphasis on the use of modern technologies. The number of enterprises is not prepared for this and works on the "old" principle. An employee is not forced to rush if he works well and cares for precision. Therefore, the emphasis is focused upon optimizing material flows with a view to shortening transport times between different workplaces and to set the usage of machines correctly. Informational technologies are coming to the fore as the Industry 4.0 trend is also indicative. It uses digitization, virtualization, data collection, analysis, identification technologies in the companies. In simple terms, computer technology can be substituted for the role of a person. In this paper, we try to point out the benefits of simulating manufacture processes as a tool in which we can model changes without a complex change in the production process. For our needs, firstly it is necessary to determine what process should be simulated in order to define its complexity, number of operations etc. [3]. On beginning it is necessary to define the concept of material flow, which is understood as an organized movement of material in a production process. The material is a marking for raw materials, basic and auxiliary materials, semi-finished products, tools, processed and finished products, packaging and waste. Material flow, by its nature, is actually the implementation of the supply chain, where

the consistent application of logistics is manifested by the application of methods and tools in controlling the flow of material flow [4]. Material movement from a logistics point of view is considered as a causal phenomenon resulting from the cooperation of an active and passive logistic element. The active elements (transport and handling machines) have the energy to realize their own movement. Movement of passive elements (materials) is a consequence of the active element moving. The result of these movements is material flow that cannot be changed during the production process. The question arises as to verify the correctness of the proposed production process. We can use simulation programs as Arena, Plant Simulation, ProModel, Quest, Simul8, Witness and others. For simulate production processes, Tecnomatix Plant Simulation was selected for compatibility with the NX CAD software and ergonomic Jack and Jill software that features the author's workplace.

Such implementation allows you to cool down into different enterprise compartments without entering the bottom. In the first part, the paper focuses on the approach of the Tecnomatix Plant Simulation environment, the second part of paper deals with the simulation of inner ring production in a virtual environment [1, 2].

2   Literature Review

Tecnomatix Plant Simulation was used by the research, which is an universal tool from Siemens that serves to simulate and optimize production systems and processes.

The simulation software allows:

- detailed and at the same time clear definition of the system and its surroundings as well as input and output variables;
- detailed identification of the individual components of the system and their interconnection;
- detailed definition of the behaviour of individual components;
- determining all parameters that are critical to tracking the behaviour of the entire system;
- defining variables at the time of the simulation experiment;
- drawing information directly from the enterprise information system.

After complex analyses we can say that the program which is taught to students must provide [6]:

- an appropriate and intuitive user environment;
- interactive communication with the user;
- support for fast search;
- simple correction of errors and collisions;
- multiplatform under multiple operating systems.

Plant simulation software is a tool for designing and optimizing production. It can create scenarios of the future state at the time of planning itself. The ability to use extensive analytical tools such as statistics, charts, and diagrams is the reason why output is always measurable and results are backed. These results will provide you with

the information that you need for quick and correct decisions even in the early stages of planning and shorten the start of production [5].

Advantages of Plant Simulation:

- testing innovative strategies in risk-free virtual environments;
- maximum use of production resources;
- reduction of investment risk through rapid simulation verification;
- optimize system size and storage space;
- quick identification of sources of problems in logistics and production spheres;
- reduction in inventory by 20–60% due to system size;
- the new system costs from 5 to 20% of reduction in investment;
- reduction of staff capacity and handling equipment;
- quickly achieve positive results and identify impacts.

Figure 1 illustrates Plant simulation environment and its basic modeling elements in 2D and 3D versions.
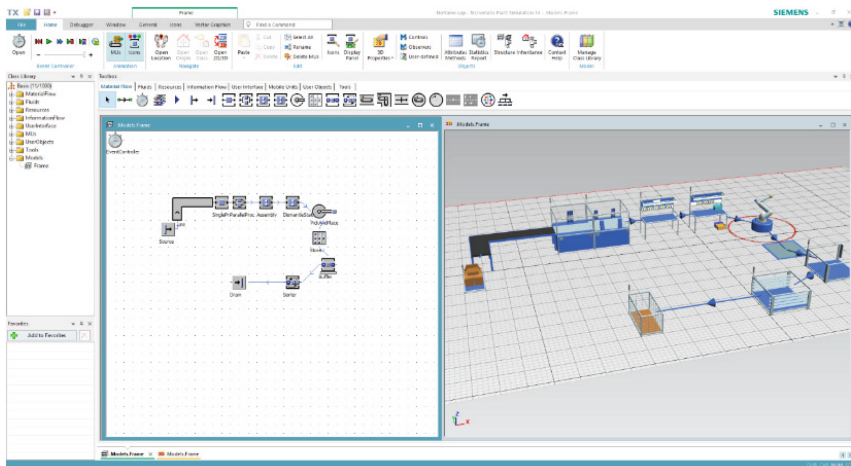
Fig. 1. Plant simulation environment.

The creation of a model of production process is done by storing elements in the modelling window. The elements are saved by clicking on the icon and by double-clicking the model window at the selected location. The element needs to be defined and describes its properties and eventually display [6]. The element's properties are described, in addition to the element type, the name, number and priority of the element, the type and duration of the process, and the number of input entities which we need to initiate the process. The advantage of this software is the opportunity to present students a comprehensive view of production going through supply from production to distribution logistics. An example of a 3D simulation of a manufacturing enterprise is shown in Fig. 2 [11].

The presented model is called "Factory 5" is shown as a content of the Example Models standardly supplied with Tecnomatix Plant Simulation 14. In Fig. 2 it is possible to see the individual stages of the overall production process as it is shown in Table 1.
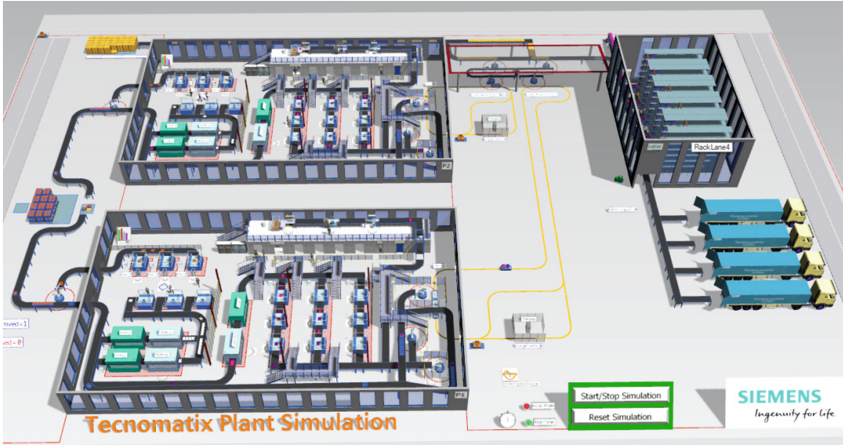
Fig. 2. 3D model of manufacturing enterprise.

Table 1. Using possibilities of simulation in the logistics.

Supply chain logistics	Manufacturing logistics	Distribution logistics
• Cargo loading and unloading • Storage • Dosage on conveyor routes	• Production development • Technological setup • Automated workstations • Handling of goods • Robotic workstations • Control positions • Automatic conveyor systems • Employability of workers	• Machine power supply • Pallets robotic loading • Regal loaders • Automatic storage system • Loading and dispatching of trucks

The great advantage is that students can enter into the simulation process and use the necessary elements in their own lessons. Subsequently, the paper presents how to use simulation in the education process. Their task is to model the production according to defined data (technological process, production times, heuristic rule) [7, 9].

3 Research Methodology

Based on the rolling process production process is shown in Fig. 3, only a certain part of the manufacturing process was selected for the presentation. In this paper, it is concerned primarily with production an inner ring for selected bearings [10]. Since the overall manufacturing process consists of the manufacture and assembly of individual components, which are usually marked as follows: 1-outer ring, 2-inner ring, 3-cone, 4-cage. Other markings which is used in bearing production include: 9-seam, 0-assembly, 5-other components [5].
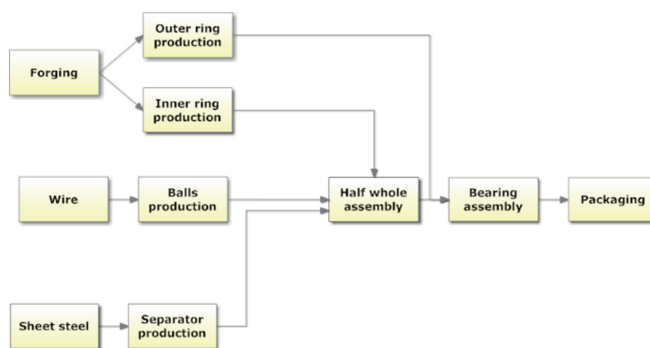
Fig. 3. Bearing process.

Table 2. Production times of inner ring.

Machine/bearing	Bearing 1	Bearing 2	Bearing 3	Bearing 4
SP 50	135,15	78,57	117,228	94,8
SASL 200/500	5,49	5,148	51,48	4,26
ANKL 155	40,284	39,678	37,8	29,22
SASL 200/500	0	0	0	6,72
SPL16	32,796	34,566	32,4	0
Line 400	14400	14400	14400	14400
BDR 60	87,78	11,478	10,632	59,352
SASL 200/500	0	7,932	9,228	0
SWAGL 125	0	84,828	97,8	101,088
SASL 200/500	88,128	0	0	0
SIW 4	88,08	0	0	0
SW 20	27	67,32	66,15	51,75
Hydromatic	60	60	60	60
VLAŠIM	6,96	6,96	6,96	6,96
Hydromatic	60	60	60	60

As it has already mentioned in the paper, priority is given to display the material flow in the production of inner rings. For practical display it is necessary to know the production times (Table 2) and the basic movement of the material in the production process (Figs. 4 and 5). This paper focuses on the production of bearings of the following types: L1 - 32214 A - bearing 1, L2 - 32017 AX - bearing 2, L3 - 32016 AX-bearing 3, L4 - 30212 A- bearing 4.
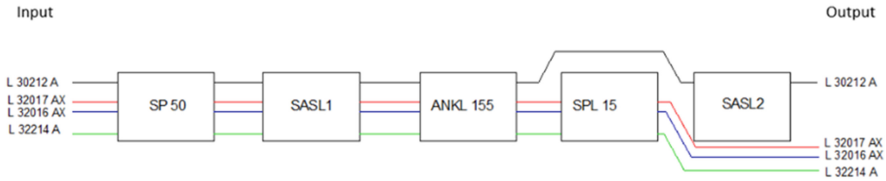
Fig. 4. Material flow of production the inner rings before hardening.
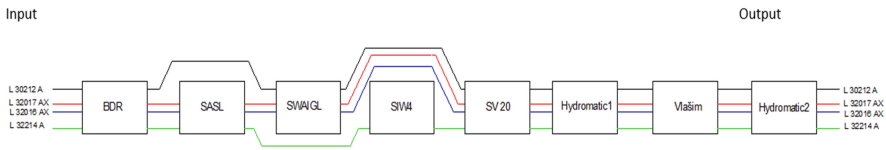
Fig. 5. Material flow of production the inner rings after hardening.

As it is shown in Table 2, operation on line 400 (which is hardening) is time consuming and may involve more than one operation, therefore it is appropriate to divide the total material flow into pre-hardening and quenching operations. Then it is recommended to draw Gantt charts where the total time load of the machines is displayed (Fig. 6).
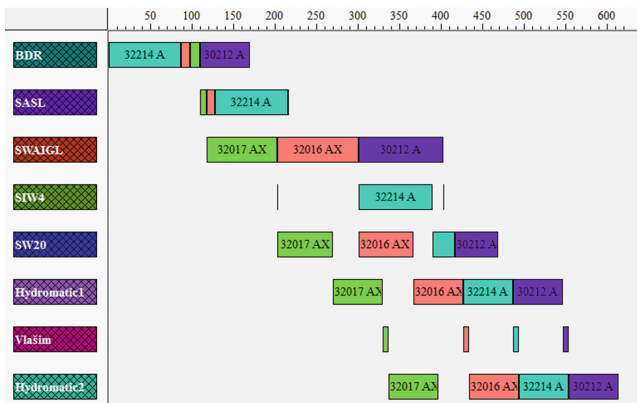
Fig. 6. Gantt charts.

Material flow of inner ring production consists of 4 bearings and 14 operations. As input parameters, the production times were taken from Table 2, and then, on the basis of material flows before and after hardening, a material flow simulation in Plant Simulation was created [8].

4   Results

By creating a simulation of the inner rings, a line consists of 4 bearings: 32214 A, 32017 AX, 32016 AX, 30212 A (Fig. 7).
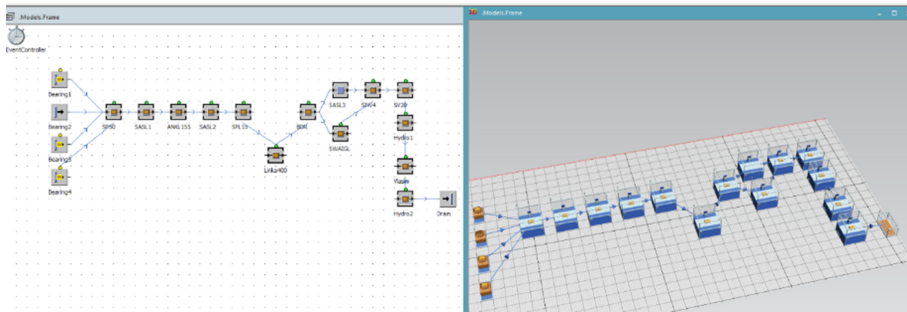
Fig. 7. 2D and 3D view of simulation of inner ring production.

On the basis of the resulting times of the individual operations which is specified in Table 2 below, the production time of the inner rings was determined for the production of 1 piece of each type:

$$T_{vnC} = T_{l1} + T_{l2} + T_{l3} + T_{l4}$$
$$= 14971{,}72 + 14957{,}39 + 15071{,}33 + 14890{,}35$$
$$= 59890{,}79 \text{ s}$$

When simulation is performed, it is possible to change the number of machines, the number of pieces released into the production process and other parameters. These individual elements affect overall production times. The presented simulation was defined by 30 students. Several different types of simulations were created and only 3 simulations were arranged equally. The difference was only in the final time. It was at 3% in the total time from 58093 s to 61686 s. An example of student simulation is shown in Fig. 8.

The task for the students was to create disposition detach operations before (green) and after (blue) hardening. Within the production process, the task was to achieve the most optimal times which can be divided into manufacturing, distribution and storage areas. For this task it was set to achieve manufacturing: transport: storage - ratio in the 50:30:20 range. The best achieved result which is generated from the simulation of the manufacturing process from the whole group is given in the following table (Table 3).
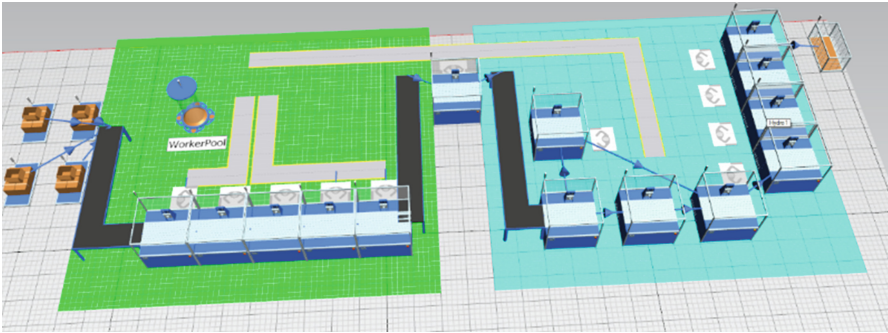
Fig. 8. Simulation of inner ring production – student work.

Table 3. Best results for manufacturing-distribution and storage ratio.

	Manufacturing			Distribution			Storage		
	Work on	Waiting on	Summary	Work on	Waiting on	Summary	Work on	Waiting on	Summary
Simulation	45.2%	3.2%	48.4%	3.28%	27.45%	30.73%	0	20.87%	20.87%

From the presentation it can be concluded that the use of simulation software Tecnomatix Plant Simulation by lectures improves the way of understanding the principles of manufacturing design as it opens up the possibilities of their imagination.

The new knowledge gained will be improved in modelling, designing and optimizing production operations.

5 Conclusion

Material flow simulation must be always an important part of production planning. Most manufacturing businesses pay close attention to this area and try to create the best production programs. A number of businesses are currently starting to use computer simulations to optimize material flows. Simulation can show us how to change the total material flow when we change the layout, after upgrading machines or optimizing production operations. Individual changes are performed without verification and are very complicated, so simulation can be performed where all these elements can be verified. Therefore, it is now necessary to prepare digitization and Industry 4.0 issues for the use by simulation programs. In general we can say, who is learning how to use Plant simulation, as well it will be able to model material flows in other programs.

References

1. Bangsow, S.: Manufacturing Simulation with Plant Simulation and Simtalk. Usage and Programming with Examples and Solutions. Springer, Germany (2010)
2. Bangsow, S.: Tecnomatix Plant Simulation - Modeling and Programming by Means of Examples. Springer, Germany (2015)
3. Thomas, P.: Simulation of Industrial Processes for Control Engineers. Butterworth-Heinemann, Boston (1999)
4. Knapcikova, L., Balog, M., Ruggiero, A., Husár J.: Using simulation software in composites industry. In: SmartCity360 - Gent: EAI, pp. 1–9 (2016)
5. Husar, J., Duplakova, D.: Material flow planning for bearing production in digital factory. Key Eng. Mater. **669**, 541–550 (2016)
6. Babu, B.V.: Process Plant Simulation. Oxford University Press, Oxford (2004)
7. Akkoyun, O.: New simulation tool for teaching–learning processes in engineering education. Comput. Appl. Eng. Educ. **25**(3), 404–410 (2017)
8. Kovalsky, M., Micieta, B.: Support planning and optimization of intelligent logistics systems. In: 12th International Scientific Conference of Young Scientists Sustainable, Modern and Safe Transport, Procedia Engineering 192, pp. 451–456 (2017)
9. Zata, N., van Niekerk, T., Fernandes, J.: A Process Control Learning Factory with a Plant Simulation integrated to Industry Standard Control Hardware. In: 27th Annual Symposium of the Pattern-Recognition-Association-of-South-Africa (2016)
10. Chen, Z., Zhao, Y., Xu, Z.Y.: Design and simulation study on automobile parts production line. ACSR-Adv. Comput. Sci. Res. **71**, 757–762 (2016)
11. Fedorko, G., et al.: Manufacturing process analysis in the mechanical engineering company using Tecnomatix. In: CLC 2015: Carpathian Logistics Congress – Conference Proceedings, pp. 300–306 (2016)

Process-Oriented Approach to Fixture Design

Vitalii Ivanov[(✉)]

Sumy State University, 2 Rymskogo-Korsakova Street, Sumy 40007, Ukraine
`ivanov@tmvi.sumdu.edu.ua`

Abstract. Machining of parts on the metal-cutting machine tools could not be ensured without the use of fixtures. They are an integral part of the closed-loop technological system "machine tool – fixture – cutting tool – workpiece" and make the significant impact on the accuracy and quality of machining of machine parts surfaces. The work presents the structural stages of computer-aided fixture design and determines the data flows between them to ensure the comprehensive approach. The process-oriented model of fixture design process has been developed, which provides the manufacturing analysis of the workpiece, synthesis and optimization of fixture configurations, verification of the mechanical system "fixture – workpiece" for set production conditions, and functional links and data flows between stages have been determined. The above-mentioned allows realizing a comprehensive approach to the computer-aided fixture design in multiproduct manufacturing.

Keywords: Machine tool · Fixture · Computer integrated manufacturing
Data flow · Manufacturing analysis · Multicriteria optimization
Verification · Computer-aided fixture design · CAFD system

1 Introduction

In modern manufacturing engineering, the major challenge is the contradiction between the necessity of decreasing the time required to design and manufacture the products and increasing the complexity of product design. For the last 15 years, the nomenclature of products has been enlarged more than twofold, their complexity is continuously increasing; the requirements for the accuracy and quality of the products are growing up. Today the market requires bigger varieties of products [1, 2], so the equipment and processes should be more flexible to meet the market demands and decrease the time consumption of products output on the market. It stimulates the necessity of development and implementation of innovative solutions for the realization of the processes, which should be directed at the intensification and automation of the production [3]. One of the most perspective directions of intensification of the production planning is the development and implementation of the computer-aided fixture design (CAFD) systems, which allow designing of fixtures in automatic mode, evaluating their efficiency and developing the required design and production documentation. Presently, available CAFD systems are restricted in their functionality that causes the low quality of design, increases the volume of design work and leads to the growing of time consumption for

fixture design. To prevent the above-mentioned problem, a principally new CAFD system should be developed, which could make the design qualitative, ensuring analysis, synthesis, and optimization of fixture configurations.

2   Literature Review

Under the conditions of modern machine-building manufacture, characterized by instability of nomenclature and volume of product output, the key point is a rational selection of fixtures to which the following requirements are set [4–8]: ensuring the given machining accuracy; flexibility sufficient for the machining of parts within the technical characteristic of fixture; mechanized or automated adjustments while transferring to the machining of parts of another standard size; high rigidity of parts and assemblies able to perceive the considerable cutting forces and ensure the maximum use of equipment capacity; tool availability for machining of maximum numbers of surfaces per one setup; high level of unification of parts and assemblies that ensures the decreasing of fixture cost; high functional and technological reliability of fixture and its elements; effectiveness. Main demands on fixture design are reduced to six groups, considering physical and precision possibilities, requirements to the equilibrium state of the system, effectiveness, tool availability, and ergonomics [9].

The design process of the fixture should be considered for the position that the fixture contacts with the external environment during the operation process, with the workpiece, cutting tool, machine tool and operator. The external environment creates certain restrictions, which influence the fixture structure and the engineering process [10].

Today, the obtained long-term experience of the development and implementation of CAFD system, which considerably accelerated and improved the fixture engineering process, allows the designer carrying out the comprehensive analysis of the features of future fixture before its production even at the stage of design.

CAFD-systems according to their application are divided into the systems for designing of dedicated [11], modular [12, 13] and adjustable fixtures [11]. The detailed review of existing CAFD systems is presented in the works [9, 11, 12, 14–19] and others. According to automation level, CAFD systems are traditionally classified on the interactive into (I-CAFD), semi-automatic (Semi-AFD) and automatic (AFCD).

The analysis of the existing CAFD has shown that the typical structure [20] consists of four modules, which ensure a staged solution of the task of forming the technological operation structure, the defining of the production conditions, synthesis of fixture configuration and verification of the designed fixture.

The main tasks of CAFD system, more of which are dedicated to the workpiece machining, are:

– definition of the functional surfaces of workpiece and the selection of the appropriate standard nonadjustable functional elements from the database;
– fixture configuration from the selected functional elements;

- analysis of the fixture configurations mainly by one criterion (for example, the accuracy of workpiece location, rigidity of the configuration, steel intensity, ergonomics, etc.);
- development of engineering drawing (assembly drawings, specification, the scheme of assembly, and adjustment of fixture configuration).

The further development of CAFD-systems is possible, primary by improving their functionality. First, it is the introduction of mathematical algorithms for multicriteria selection of the most appropriate fixture configurations from among the competitive variants [21]; herewith the list and number of criteria could be changed or supplemented according to the given production conditions. The reasonability of libraries formation of functional elements based on the system of modular adjustable fixtures, that is the most efficient under the condition of multiproduct manufacturing, has been proven. To evaluate the errors that appeared because of elastic deformations under the action of the cutting force, the finite-element analysis of the fixture configurations considering the dynamic characteristics should be performed. Equipping CAFD-system with the tool for dimensional analysis of 3D models with the aim of considering an error of production of fixture functional elements during the following calculations is a very advanced direction. The development of 3D animations of the processes of assembly and adjustment of the fixture configurations is very relevant and it allows decreasing the consumption of preparatory and final time, required for the fixture adjustment before its operation. The goal of the proposed research is to define the structural stages of the process of fixture designing and to define the informational links between them for ensuring the complete cycle of design, optimization, and verification of the fixture for the given production conditions

3 Research Methodology

3.1 Computer-Aided Fixture Design in Computer Integrated Manufacturing

Computer-integrated manufacturing (CIM) ensures solving the tasks of design (CAD), analysis and optimization (CAE), process planning (CAPP), manufacturing (CAM), quality control (CAQ), tooling design (CAT). The CAT technology is divided into systems of computer-aided cutting tool design (CACTD) and computer-aided fixture design (CAFD). Figure 1 presents the place of CAFD system in the structure of CIM, which established data flows to ensure the decrease of time consumptions and the cost of design, increasing the quality of developed solutions.

CAFD-systems could be integrated with CAD/CAE/CAPP/CAM systems, therefore to complete the whole cycle of design, analysis, synthesis and fixture manufacturing.

Thus, the process of fixture design should be built by means of considering the integration with the above-mentioned systems. Figure 2 presents the place of CAFD system among other automation systems and their data flows [22].
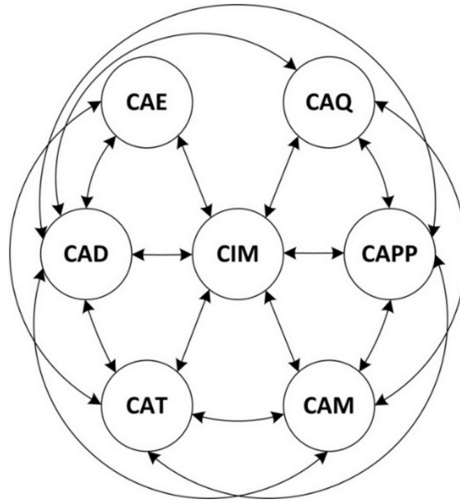
Fig. 1. Data flows in computer-integrated manufacturing system.
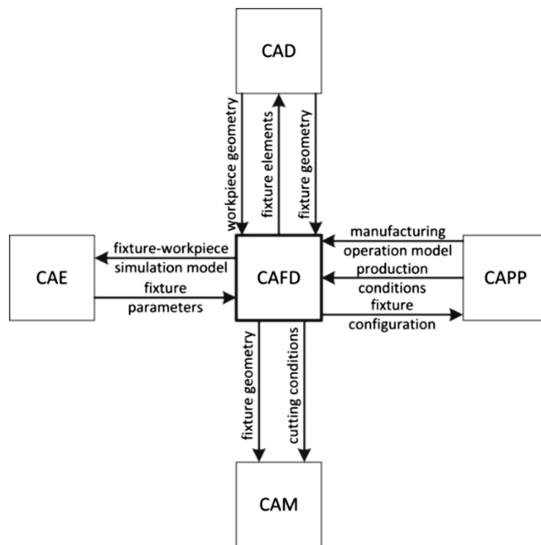
Fig. 2. Place of CAFD system among other systems and their data flows.

3.2   Process-Oriented Model

In the initial stage of CAFD system development, it is important to understand all processes, which should be automated. The process of fixture design is considered from the point of view of design engineer (tooling engineer). The most convenient tool for the simulation of the processes is the process-oriented modeling according to IDEF0

standard. In IDEF0 the system is considered as a set of interaction steps or functions. This approach is principal, as the functions of the system are analyzed independently of the objects, which they operate. It allows modeling the logic and interaction of designing processes more accurately.

The process of fixture design is time-consuming and requires processing of the great value of information, which is classified into constant and variable. The constant information, which could be normative (standards, manuals, catalogs, recommendations, requirements, regulations and managerial documents etc.) and expert (the obtained knowledge of design engineer), characterizes the object, which information is known before the process of fixture design. Variable information is the information that changes with each new design task and is classified into input (task for design), intermediate (generates in the process of work and is used during the interaction of systems modules) and output (results of design).

Informative support of the fixture design process is performed by means of the developed database, which consists of 15 applied libraries and embraces the whole range of the required information: engineering and design, normative-reference, general engineering, optimization, and calculation character.

The All Fusion Process Modeler 7 (BPwin) has been used for the development a diagram of the design process according to the notation of IDEF0. The first step of the modeling process is the development of the contextual diagram of the fixture design process (Fig. 3), which describes the process of fixture design in the most generalized
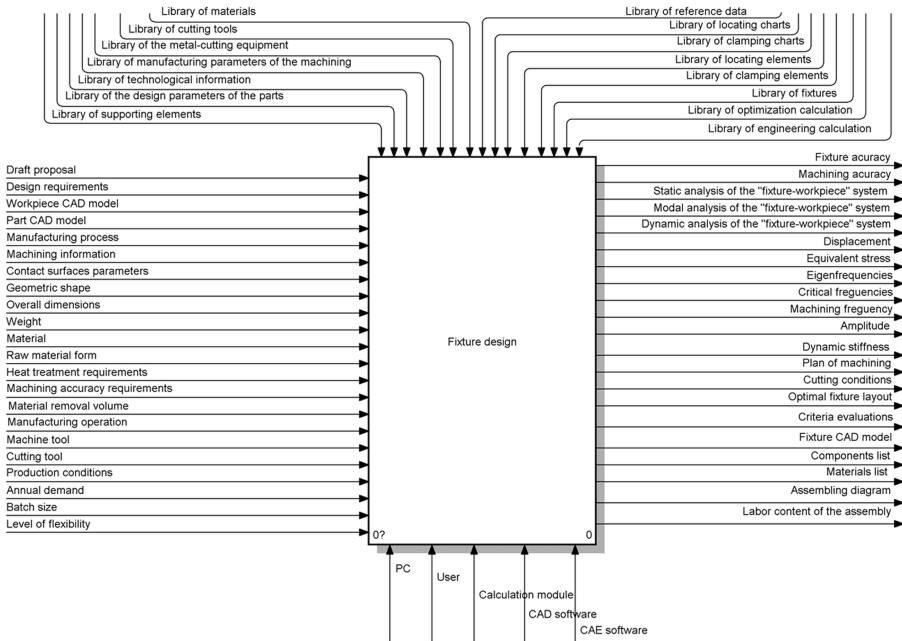
Fig. 3. Contextual diagram of the fixture design process.

form. A complex approach to the fixture design, which consists of three structural steps, each of which is the logical continuation of the previous, is proposed (Fig. 4). Therefore, based on the input data the manufacturing analysis of the workpiece is performed, according to which the synthesis of competitive variants of fixture configurations is carried out and the multicriteria optimization is executed, the result is the basis for verification of the system "fixture – workpiece". This approach is principally new for the fixture design and allows solving tasks of design, optimization and verification of the fixture for the given production conditions in complex and that is the most important for the modern manufacturing engineering.
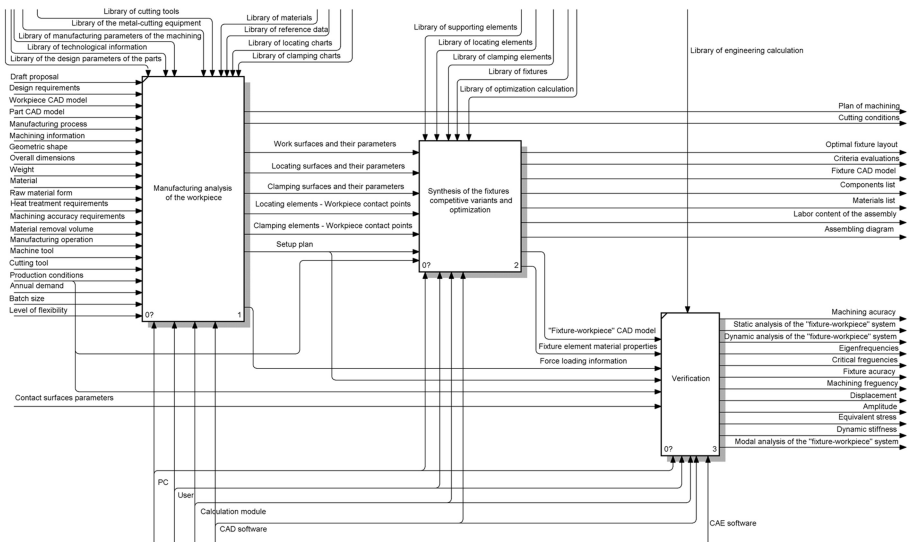
Fig. 4. Decomposition of the fixture design process.

4 Results

4.1 Manufacturing Analysis of the Workpiece

The analysis of 3D model involves the identification of the functional surfaces of workpiece, which could be: work; locating; clamping. It allows obtaining information about: geometry (form) of the surfaces; spatial location of the definite surfaces relatively one each other; dimensional characteristics of the surfaces (length, width, height, diameter).

The following information should be received from the drawing (or another accompanying information): tolerance range for each of the surfaces; rigidity of the surfaces; grade of the material; hardness of the workpiece material; type of thermal treatment; other technical requirements.

The plan of surfaces machining is being developed based on the information about the work surfaces. Within this step, the following points should be determined: the

principal scheme of surfaces machining; the cutting mode (depth of cutting, feed, cutting speed); cutting force; required capacity of the machine tool.

The set of the locating surfaces realizes the theoretical locating chart with the determination of the contact points of workpiece with the locating elements of the fixture. The analysis of clamping surfaces allows selecting of one of the typical clamping chart and contact points of workpiece with the clamping elements.

The developed methodology of determining the contact points with the functional elements of the fixture allows reasonable selecting of the optimal solutions for each project situation.

Based on the plan of machining, a locating chart and a clamping chart of the workpiece, the setup plan of the workpiece with the identification of the value and directions of the cutting and clamping forces in the determined coordination system is formed.

4.2   Synthesis and Optimization of Fixture Configurations

At present stage two processes are performed – synthesis and optimization. Based on the identified interaction, data flows and developed rules and procedures, by means of considering the workpiece configuration, parameters of functional surfaces, selected locating and clamping charts of workpiece, the locating and clamping elements are being chosen, which correspond to the given parameters. According to the overall dimensions and geometrical form of the workpiece and the given requirements to the fixture design, the selection of supporting elements is performed. It allows forming the set of competitive variants of supporting, locating and clamping elements. Hence, considering their basis and previously developed fixture configurations, which are included into the database, the formation of competitive variants of the fixture configurations according to the developed algorithms is performed.

Implementation of the optimization calculations allows the selection of optimal fixture configuration for the specified production conditions based on the multicriteria optimization. Primarily, the optimality criteria are selected, which correspond the project task, range according to the importance, the restriction system is formed. Further on, by using the optimization system and normative-reference information from the database, the selection of fixture configurations is carried out, meeting the system of restrictions. For the fixture configurations, which remained due to the application of technical restrictions, the calculation of the numerous parameters according to each criterion of the optimization is performed. Further on, the multicriteria optimization is performed. A structural formula of optimal fixture configuration and the calculated criterion assessments are being obtained due to the optimization task. Knowing the codes of functional elements, which are included into the structural formula of the optimal fixture configuration, and the information from the libraries of functional elements, the assembly of fixture is performed according to the developed procedure of the spatial positioning of structural elements of the system "fixture – workpiece".

4.3   Verification of the Mechanical System "Fixture – Workpiece"

Carrying out the verification is the most important step, because it allows predicting the parameters of future fixture being at the designing step. For each project task the possibility of task selection and formation of research plan of the system "fixture – workpiece" considering the requirements to the fixture design and production conditions is available. The process-oriented model provides the possibility to perform the calculations: on the accuracy of parts machining; research of the stability of equilibrium state of the system "fixture – workpiece", research of deflected mode, performing of the modal analysis and harmonic analysis.

Based on the proposed process-oriented model of the fixture design process, the structure of CAFD system [28], consisting of 5 modules and sub-system has been substantiated and developed, which ensures the informative support for the design process and includes 15 applied libraries.

5   Conclusions

The process-oriented model of the fixture design process has been developed, which provides the manufacturing analysis of the workpiece, synthesis and optimization of fixture configurations, verification of the system "fixture – workpiece", also the functional and data connections between the stages have been installed, making the realization of the comprehensive approach to the fixture design process possible.

Functional possibilities of the developed CAFD system in the automation mode ensure the search of the optimal fixture configuration for the given production conditions, decrease the terms of performing the project procedures and increase the efficiency of the design.

References

1. Bi, Z.M., Lang, S.Y.T., Verner, M., Orban, P.: Development of reconfigurable machines. Int. J. Adv. Manuf. Technol. **39**(11–12), 1227–1251 (2008)
2. Trojanowska, J., Varela, M.L.R., Machado, J.: The tool supporting decision making process in area of job-shop scheduling. In: Rocha, A., Correia, A., Adeli, H., Reis, L., Costanzo S. (eds.) Recent Advances in Information Systems and Technologies. WorldCIST 2017. Advances in Intelligent Systems and Computing, vol. 571, pp. 490–498. Springer (2017)
3. Duplakova, D., Knapcikova, L., Radchenko, S., Hatala, M.: Software support of modelling using ergonomic tools in engineering. TEM J. **6**(3), 567–571 (2017)
4. Trojanowska, J., Kolinski, A., Galusik, D., et al.: A methodology of improvement of manufacturing productivity through increasing operational efficiency of the production process. In: Hamrol, A., Ciszak, O., Legutko, S., Jurczyk, M. (eds.) Advances in Manufacturing, pp. 23–32. Springer (2018)

5. Brezikova, K., Hatala, M., Duplak, J., et al.: Proposal of measuring fixture for serial production. MM Sci. J., 1082–1085, October 2016
6. Karpus', V.E., Ivanov, V.A.: Universal-composite adjustable machine-tool attachments. Russ. Eng. Res. **28**(11), 1077–1083 (2008)
7. Erdem, I., Levandowski, C., Berlin, C., et al.: A novel comparative design procedure for reconfigurable assembly fixtures. CIRP J. Manuf. Sci. Technol. **19**, 93–105 (2017)
8. Forstmann, R., Wagner, J., Kreiskother, K., et al.: Design for automation: the rapid fixture approach. Proc. Manuf. **11**, 633–640 (2017)
9. Boyle, I., Rong, Y., Brown, D.: A review and analysis of current computer-aided fixture design approaches. Int. J. Robot. Comput. Integr. Manuf. **27**(1), 1–12 (2011)
10. Pehlivan, S., Summers, J.: A review of computer-aided fixture design with respect to information support requirements. Int. J. Prod. Res. **46**(4), 929–947 (2008)
11. Rong, Y., Huang, S.H., Hou, Z.: Advanced Computer-Aided Fixture Design. Elsevier Academic Press, New York (2005)
12. Nee, A.Y.C., Senthil Kumar, A., Tao, Z.J.: An Advance Treatise on Fixture Design and Planning. World Scientific, Singapore (2004)
13. Mihaylov, O., Nikolcheva, G.: An integrated RBR fixture design system. In: Mudrik, R., Vit, O., Basova, P., et al. (eds.) CBU International Conference on Innovations in Science and Education, vol. 5, pp. 1175–1180. CBU (2017)
14. Bi, Z.M., Zhang, W.J.: Flexible fixture design and automation: review, issues and future directions. Int. J. Prod. Res. **39**(13), 2867–2894 (2001)
15. Kang, X., Peng, Q.: Recent research on computer-aided fixture planning. J. Recent Patents Mech. Eng. **2**(1), 8–18 (2009)
16. Vukelic, D., Tadic, B., Luzanin, O., et al.: A rule-based system for fixture design. Sci. Res. Essays **6**(27), 5787–5802 (2011)
17. Parvaz, H., Nategh, M.J.: A pilot framework developed as a common platform integrating diverse elements of computer aided fixture design. Int. J. Prod. Res. **51**(22), 6720–6732 (2013)
18. Parvaz, H., Nategh, M.J.: Development of an efficient method of jamming prediction for designing locating systems in computer-aided fixture design. Int. J. Adv. Manuf. Technol. **86**(9–12), 2459–2471 (2016)
19. Zhang, F.P., Wu, D., Zhang, T.H., et al.: Knowledge component-based intelligent method for fixture design. Int. J. Adv. Manuf. Technol. (2017)
20. Wang, H., Rong, Y., Li, H., Price, S.: Computer-aided fixture design: recent research and trends. J. Comput.-Aided Des. **42**(12), 1085–1094 (2010)
21. Karpus, V.E., Ivanov, V.A.: Choice of optimal construction of modular reusable fixtures. Russ. Eng. Res. **32**(3), 213–219 (2012)
22. Ivanov, V., Vashchenko, S., Rong, Y.: Information support of the computer-aided fixture design system. In: Proceedings of 12th International Conference ICTERI' 2016, vol. 1614, pp. 73–86, CEUR-WS (2016). CEUR-WS.org

Technological Assurance of Complex Parts Manufacturing

Vladyslav Karpus[1], Vitalii Ivanov[2(✉)] , Ivan Dehtiarov[2],
Jozef Zajac[3], and Viktoria Kurochkina[2]

[1] National Academy of National Guard of Ukraine,
3 Zakhysnykiv Ukrainy Sqr., Kharkiv 61000, Ukraine
[2] Sumy State University, 2 Rymskogo-Korsakova Street, Sumy 40007, Ukraine
ivanov@tmvi.sumdu.edu.ua
[3] Technical University of Kosice,
1 Bayerova Street, 08001 Presov, Slovak Republic

Abstract. The ways of intensification of machining complex parts of vehicles on the modern metal-cutting equipment were described. The classification of parts such as levers was developed on the basis of design and technological features. Based on the developed classification the structural code that allows to encode any lever design was proposed. The structural code can be used in computer-aided fixture design and in information retrieval systems for selecting optimal fixture for levers. The reasonability of intensification of parts machining such as levers was substantiated, the typical manufacturing process was analyzed, and opportunities for optimization subject to current trends in machining and technological capabilities of modern equipment were identified. The adjustable locating-and-clamping module characterized by high level of flexibility was proposed for CNC multiaxis machining operation. Comparative analysis of manufacturing processes by labor content, quantity of fixtures and machine tools, number of setups, and production area was performed.

Keywords: Classification · Lever · Manufacturing process · Fixture
Locating · Labor content · Setup time

1 Introduction

At this stage of the development of industry one of the main priority industries is automotive, which is dynamic. The world motor vehicle production in 2015 exceeds 90 million units. Asian manufacturers (China, Japan, and South Korea) made 42% of the world production. According to the 2015 World motor vehicle production statistics the dynamic character is especially noticeable in China, which has increased the production of motor vehicles in 4.3 times since 2005 from 5,717,619 to 24,503,326 units per year. The variety and complexity of new cars has grown multi-fold from "very simple" to "very complex"; while at the same time, the period from conceptual design to market has shrunk [1]. Difficulty increases as car designs by complications of parts and assembly units, and increasing demands imposed by customers to their quality. Traditionally, the best design and technology solutions primarily implemented with the automotive

industry, where the huge industrial experience, better equipment, well-tested technologies. At the same time there is a problem of intensifying, increasing the quality and productivity of manufacturing processes of parts and cars components.

2 Literature Review

Class of complex parts includes such types of components as levers, brackets, forks, connecting rods, rocker and traction parts, and other parts. They are characterized by a complex space form and a great number of surfaces arranged in different planes at an angle to each other. The specified parts are not the rotational parts and they do not belong to the class of prismatic parts. Although the parts are of complex space and geometric shape, the elementary surfaces which compose them are not complex. They are mostly planes, ledges, and cylindrical or conical holes that can have keyways, etc. Parts of this class are characterized by the complexity of setups and insufficient tool accessibility that results from the complex spatial relationship of surfaces. So, even with modern equipment, it is quite difficult to provide multiaxis machining and intensify the manufacturing process. In this regard, the urgent task is to develop fixtures which will ensure maximum tool accessibility and allow multiaxis machining [2–5].

The analysis shows that among all parts machined by a drilling, milling, and boring group of machine tools complex parts make 36% of the total volume, in which 9% are levers, while the labor content makes 24% (including 6% for lever).

Complex parts are a group of parts that are included into car structures, and nowadays this branch of the world industry is dynamically developing. Therefore, it is relevant to perform a component spectrum analysis to identify complex parts and to develop an appropriate classification on design and technological attributes. As a product range of parts in automotive industry is wide [6], the necessity in many different fixtures are in high demand [7]. Traditionally, to setup workpieces dedicated or flexible fixtures are used [8–10]. Modular fixtures, that ensures the desired surface accuracy, but increases labor content and cost due to assembly operations, are used too [11–13]. The development and implementation of the fixtures, which have a high level of flexibility and allow multiaxis machining, are one of the ways to improve the intensification of the machining [14–17]. Fixture requirements were discussed in [18–20].

To obtain the reliable evaluation, the specifications of car mechanisms have been analyzed. In particular, the objects of study became sedan GAZ 3102 and VAZ 2121 (LADA 4 × 4) that were developed at the end of the twentieth century, as well as the foreign cars LIFAN LF-7162 Solano and Hyundai Accent designed in our time. Most cars of the given classes produced by the world's automakers have the similar design elements and differ only in shape and dimension type, but they are available in almost all the cars. This suggests reliability of the analysis and extension of the results for most automobile industry products. When analyzing the percentage of complex parts (levers, forks, brackets, connecting rods, etc.), only original parts (shafts, gears, bushings, etc.) were taken into account excluding standard parts (bearings and fasteners). The analysis of the obtained data showed that in automobiles designed at the end of the twentieth century complex parts make about 10% of all parts. In modern cars, this ratio has increased up to 14%.

Analyzing the ratio of parts on certain car mechanisms designed at the end of the twentieth century, it should be noted that in some mechanisms their number reaches 30%. Most complex parts are available in a front axle mechanism (30%), a frame (25%), a steering mechanism (16%), a clutch mechanism and a transmission (13% and 10% respectively), a front suspension (10%). It should be noted that in some mechanisms of modern cars, the number of complex parts reaches 26%. Most complex parts are contained in such assembly units as a steering mechanism (26%); an engine suspension (25%); a rear and front suspension (21% and 16% respectively); an engine (20%); a clutch mechanism and a transmission (about 15% in each of them).

For most car mechanisms designed at the end of the twentieth century, the obtained data both for sedan and off-road vehicle differed within 0.5%, and for some mechanisms – within 2%, which is explained by the specifics of their functionality. In the considered brands the reading for most modern car mechanisms differ within 1.5%, what can be explained by somewhat different technical solutions of automakers.

The aim of the research is a substantiation of feasibility of using flexible fixtures based on developed design and technological classification of complex parts for automotive industry.

3   Research Methodology

3.1   Classification of Lever-Type Parts

The existing classification based only on the design attributes of the part and did not reflect the technological attributes that are not less important than the design ones. Therefore, based on the complex analysis of the lever-type parts, the above-mentioned part classifier, and the main technological attributes, there was introduced a design and technological classification. The developed classification (Fig. 1) as much as possible considers all possible lever configurations that occur in manufacturing engineering.

When analyzing the parts according to the characteristic "By the number of arms", it was specified that levers can be single-armed, double-armed, of three- or more-armed, that determines their structural complexity and sphere of application. Lever arms may be arranged parallel, perpendicular and at an arbitrary angle with the arm length ratio less than 0.5 and greater than 0.5, that also determines structural complexity and locating.

Levers can have the most common functional elements, such as a fork, a clamp or any other element (e.g. a sector-shaped gearing element) or not have any functional elements at all. Levers can have one or several design datums which can be arranged parallel or non-parallel to each other, that essentially determine the locating chart when machining. Datum surfaces in cross sectional can be circular, noncircular or combined, that specifies the shape of datum surfaces of locating elements. According to the datum surface length, parts are classified as levers with long ($l/d > 1$) and short ($l/d < 1$) datum surface that essentially determines the locating method during machining and consequently, the fixture design.

No.	Classification attributes			
		Levers		
1	By the number of arms	One	Two	Three or more
2	By relationship of arms	Parallel	Perpendicular	At an arbitrary angle
3	By length ratios of arms $l_1/l_2/...l_n$	Less than 0.5	Greater than 0.5	
4	By the availability of functional elements	No functional elemets / Functional element "fork"	Functional element "clamp"	Other functional elements
5	By the number of design datums	One	Two and more	
6	By arrangement of the datum surfaces	Parallel	Nonparallel	
7	Over the form of the datum surfaces	Circular	Noncircular	Combined
8	Over the length of the datum surface	Long (l/d > 1)	Short (l/d < 1)	
9	By accuracy	High accuracy (IT6– IT7)	Medium accuracy (IT8–IT10)	Low accuracy (IT11–IT14)
10	By the overall dimensions	Small (less than 50x50)	Medium (50x50...200x200)	Large (more than 200x200)
11	By mass	Light (less than 1 kg)	Medium (1...10 kg)	Heavy (over 10 kg)
12	By material	Steel / Cast iron	Non-ferrous alloys	Non-metallic

Fig. 1. Design and technological classification of levers.

Depending on the functionality levers are divided according to high, medium, and low dimensional accuracy of datum surfaces, which are usually holes and butts. Manufacturing datum surfaces with high precision, ceteris paribus ensures more reliable and longeval performance of a part and product in general.

According to overall dimensions, levers are divided into small, medium, and large, that determines the fixture dimensions and the required workspace of the machine.

By mass, levers are classified into light, medium, and heavy, that to some extent also determines the technical characteristics of the machine tools which will perform machining. Levers are made of steel (C35, C40, C45, 40Mn4, 41Cr4, 40NiCr6, 50CrMo4, etc.), cast iron (EN-GJL-200, EN-GJL-300, GTS35-10, etc.), light

non-ferrous alloys (ENAB AlSi12(b), ENAW-2024), as well as of non-metallic materials, that influences the choice of cutting tools and cutting conditions during machining.

To enable automated fixture selection for a particular lever design and dimension type, a structural code (Fig. 2) is introduced which includes design and technological attributes. With the help of structural code, it is possible to determine the code of any lever used in manufacturing engineering and automotive industry. The developed coding technique of the lever-type parts will be employed in computer-aided fixture design system, namely, in the module of manufacturing analysis of the workpiece [21]. The mathematical apparatus put into the system based on the analysis of workpiece functional surfaces allows to identify in the automated mode the correspondence between design and technological features of the parts and locating and clamping charts, fixture functional elements (supporting elements, locating elements, clamping elements). This is what provides the automated synthesis of competitive fixture configurations and multicriteria optimization of fixture configurations for specific production conditions. The use of structural codes in fixture computer-aided design helps to reduce the time spent on fixture design, which cuts the final product prime cost as a whole, and makes production competitive in markets.
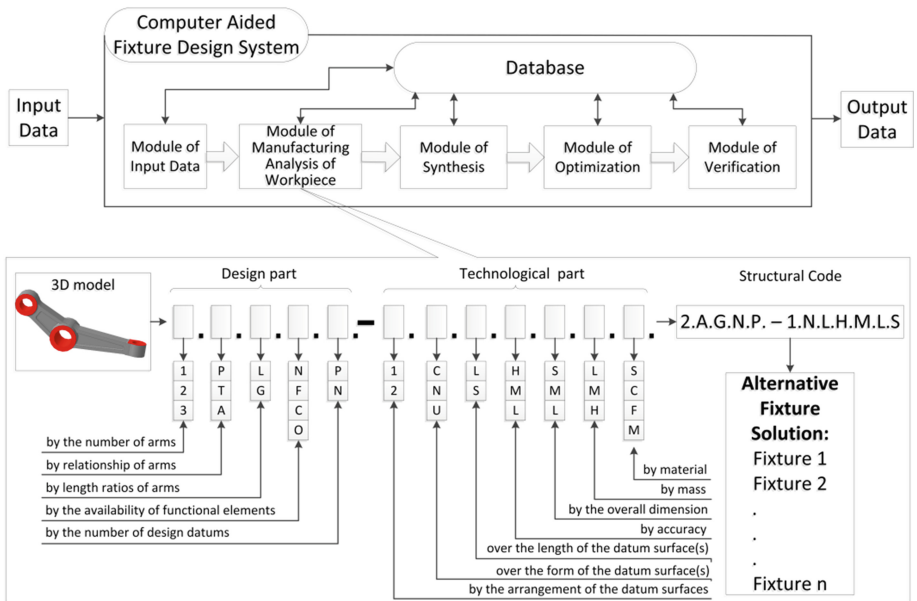
Fig. 2. The structural code of lever-type parts.

When analyzing the structures of various complex parts found in the cars of different brands, it was specified a typical design of lever (Fig. 3) which is mostly common in practice and used in a car front suspension. The lever of this configuration is a part of any vehicle that has a swing-out mechanism and wheels, whether it is a motor car or a truck, a tractor or a bus, and can differ only in dimension types and a slight alteration of form. The

feature of this part is the presence of two arms, usually of different length, a central datum hole of a larger diameter and two smaller holes that can be angled to it, as well as to each other. Parts of this type are very important car design elements that determine their manufacturing cost, because the reliability of levers directly affects the in-traffic safety. For example, such car defect as disturbance of fore wheel alignment angle and deformation of suspension levers can lead to loss of control and emergency on the road. Therefore, it is necessary to pay special attention to quality production of lever-type parts and observe the requirements of the manufacturing process.
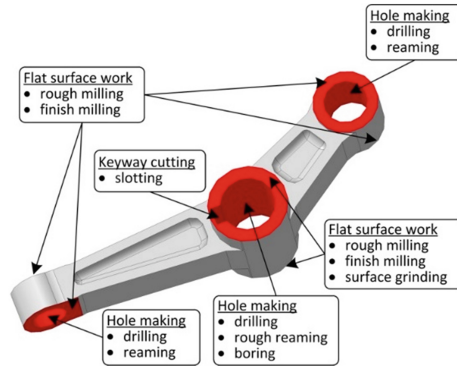
Fig. 3. A typical design and work surfaces of the lever.

3.2   Typical Manufacturing Process of Lever-Type Parts

The quality of any product greatly depends on manufacturing technology of its components. Most parts such as levers are of complex geometric shape that causes some difficulty while locating and clamping workpieces during machining operations. Thus, it is relevant to analyze the typical manufacturing process of lever manufacturing and find the ways for optimization considering the modern trends in machining, as well as functional and technological capabilities of modern equipment.

The typical manufacturing process of lever machining is usually composed of 10 operations, 8 of which are machining operations. Almost in all manufacturing operations, it is carried out a workpiece resetup with the locating charts alteration both between the operations and on different setups within a particular operation. For example, vertical milling operation that causes the accumulation of setup errors in general, and consequently, decreases in surface positional relationship accuracy. When machining, each operation is carried out with a mandatory verification of part location under the similar locating chart that leads to a significant increase in auxiliary time and thus, increased cost per part what is unacceptable in modern manufacturing.

3.3   Expediency Substantiation of Machining Intensification
      of Lever-Type Parts

Taking into consideration the multiproduct manufacturing, as well as the capabilities of modern machine tools that allow to perform the multiaxis machining, it is necessary to

change the approaches to the design manufacturing processes, tending to intensify the machining. In order to achieve this goal, it is proposed to intensify the manufacturing process of lever-type part machining by combining operations 05–30 into one – CNC multiaxis machining, performed on CNC machining center. Thus, the manufacturing process was cut to 5 operations (Fig. 4). The other operations that include heat treatment, surface grinding and slotting are not to be changed or combined, because they are completely different, incompatible with other machining techniques.
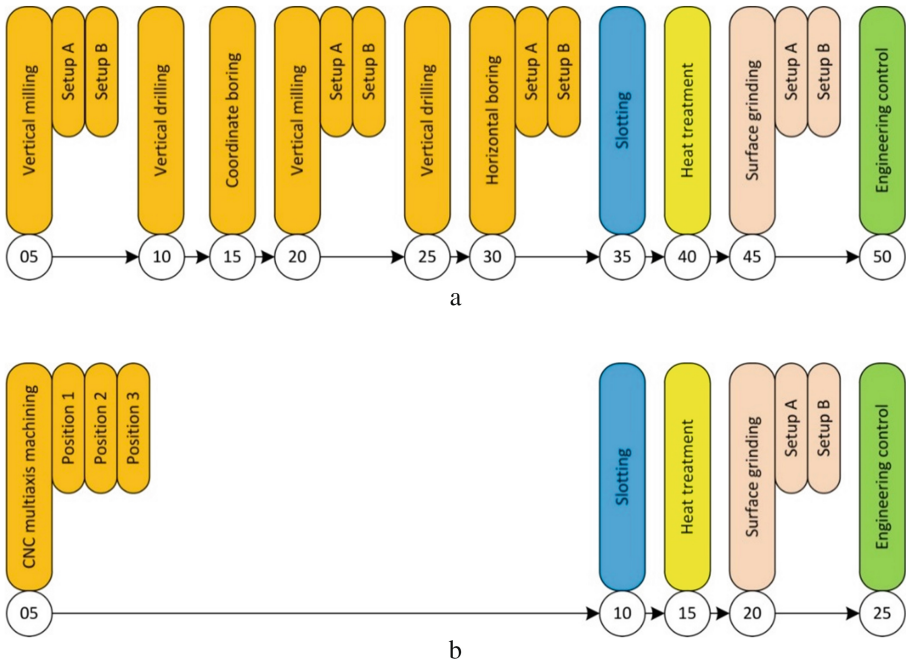
Fig. 4. Comparison of the manufacturing routes for the lever machining: (a) – typical manufacturing process; (b) – proposed manufacturing process.

3.4 Fixture Design for Lever-Type Parts

The main prospect is the development and implementation of flexible fixtures characterized by a high level of flexibility and capable of implementing the entirely new locating charts of parts ensuring the maximum tool accessibility. Machining efficiency greatly depends on the fixture design which should provide the prescribed machining accuracy, shows sufficient rigidity and high flexibility. In order to implement a workpiece locating chart on CNC multiaxis machining operation, it is introduced an adjustable locating-and-clamping module which refers to the system of modular adjustable fixtures. It is designed for locating and clamping parts during machining on drilling, milling, and boring CNC machine tools in multiproduct manufacturing.

Proposed configuration of locating-and-clamping module is assigned for setup the levers in the range of central boss diameters and arm thickness. It is achieved by control of the adjustment mechanisms, which provide changing the distance between locating-and-clamping elements (Fig. 5a). Such engineering solution in conjunction with power-driven rotary table allows carrying out the all drilling, milling, and boring manufacturing operations at one setup (Fig. 5b), which is realized on the CNC machining center. The research based on numerical simulation was confirmed that the proposed fixture corresponds to all the accuracy parameters [15].

a   b
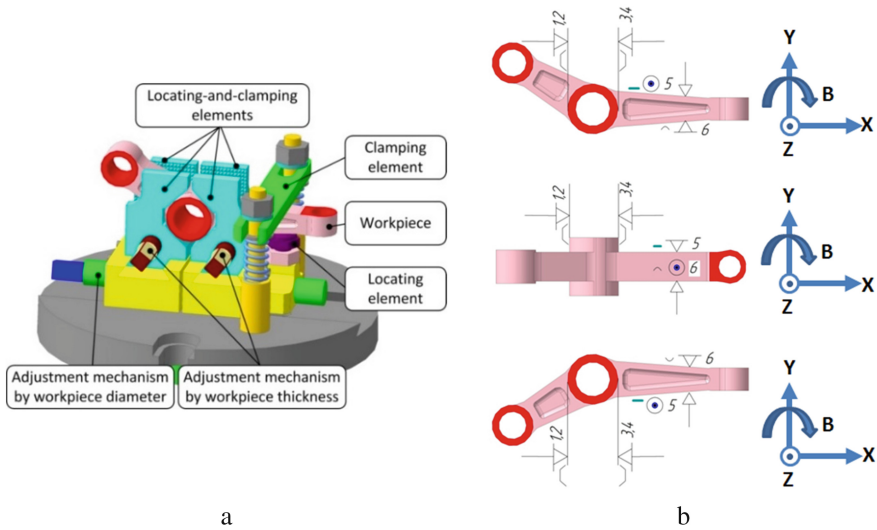
Fig. 5. Adjustable locating-and-clamping module (a) and cut-map for levers machining on the CNC multiaxis machining operation (b).

4 Results

For quantitative comparison of type and progressive manufacturing processes, calculation of standard time was carried out which does not coincide in both manufacturing processes, i.e. operations 05–30 of type and operations 05 of progressive manufacturing processes, respectively, but they are similar by labor content. Moreover, comparative calculation was performed on such parameters as: the number of fixtures used in those manufacturing operations; fixture steel intensity; the number of setups and resetups; the number of machine tools; the production area. Cutting conditions calculation and timing calculation were performed according to the procedure. The production batch was accepted as N = 50 pcs. made of 40NiCr6 structural alloy steel. Cutting conditions and cutting tools are the same for both manufacturing processes. The results of the comparative analysis are summarized in Table 1. The diagrams of time (Fig. 6) provide the following information. Cutting time in both cases is the same since the identical cutting tools and machining conditions are employed.

Table 1. Comparative analysis of manufacturing processes.

№	Parameter	Manufacturing process		Quantitative effect	Percentage effect (%)
		Typical	Progressive		
1	Number of fixtures (units)	2	1	1	200
2	Steel intensity of fixtures (kg)	24.8	4	20.8	620
3	Number of setups and resetups	9	1	8	900
4	Quantity of machine tools (units)	4	1	3	400
5	Production area (m^2)	26.8	8.6	18.1	310

a   b
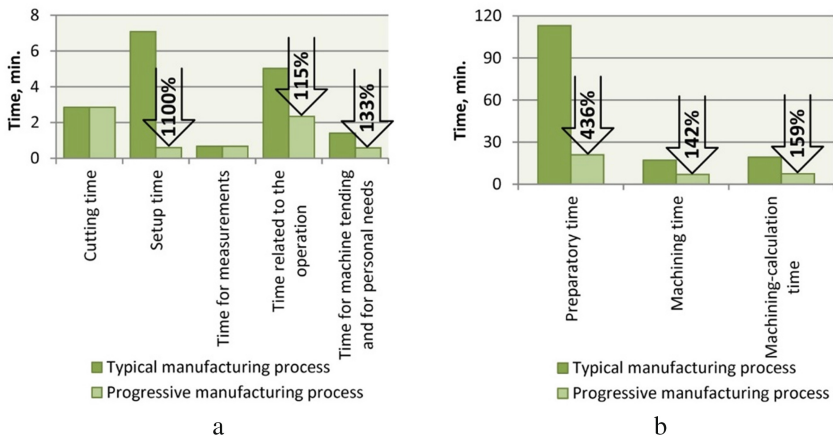
Fig. 6. Norms of time: (a) – for steps that are performed constantly; (b) – for batch workpieces.

Setup time in a typical manufacturing process is characterized by higher labor content because there is the necessity for workpiece setup and resetup in various operations, unlike the only setup in the progressive manufacturing process. Time for measurements in both manufacturing processes is the same, since the number of surfaces for measuring is identical. Time related to the operation, time for machine tending and for personal needs, as well as preparatory time in a typical manufacturing process is greater than in a progressive one due to the greater number of operations and working places. Machining time associated with one-piece machining in a typical manufacturing process is approximately twice more than in a progressive one, as it includes all the previous times, except for preparatory time. Machining-calculation time is inversely proportional to the number of parts in the batch, therefore for small batches it significantly increases in comparison with the machining time.

5   Conclusions

1. Quantitative analysis of complex parts in the structure of a car is completed, it is found out that in modern cars their number reaches 14%, and in some assemblies – 26% (a steering mechanism, an engine suspension, a rear and a front suspension, an engine, a clutch gear, and a transmission). It is developed the lever-type parts classification reflecting the design and technological features that allows identifying groups of parts with the similar characteristics, and so, they can be grouped and referred to certain dimension types of fixtures, that creates the initial conditions for computer-aided fixture design.
2. It is introduced the manufacturing process which allows to reduce time and the amount of tooling, to raise productivity and to ensure the lever-type part machining in one setup. Due to the difficulty of complex parts locating in manufacturing operations and their prevalence in the automobile industry which is undergoing a process of constant renewal, the nearest way to improve the manufacturing process efficiency is to develop flexible fixtures that ensure fundamentally new workpiece locating charts, and accuracy requirement, as well as providing maximum tool accessibility and sufficient stiffness.
3. Our further work is focused on the implementation of the introduced approach for connecting rod- and bracket-type machining under multiproduct manufacturing conditions. The development of flexible fixtures capable of the wide part variety machining in one setup is the major direction of our further research investigations.
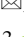
References

1. Bi, Z., Lang, S., Verner, M., Orban, P.: Development of reconfigurable machines. Int. J. Adv. Manuf. Technol. **39**, 1227–1251 (2008)
2. Makwana, R., Gosvami, N.: A study on fixture design for complex part. Int. J. Futur. Trends Eng. Technol. **1**(01), 12–15 (2014)
3. Gameros, A., Lowth, S., Axinte, D., et al.: State-of-the-art in fixture systems for the manufacture and assembly of rigid components: a review. Int. J. Mach. Tools Manuf. **123**, 1–21 (2017)
4. Gameros, A., Axinte, D., Siller, H.R., et al.: Experimental and numerical study of a fixturing system for complex geometry and low stiffness components. J. Manuf. Sci. Eng. **139**(4), 045001-1–045001-12 (2017)
5. Shen, C.-H., Lin, Y.-T., Agapiou, J.S., Bandyopadhyay, P.: Reconfigurable fixtures for automotive engine machining and assembly applications. In: Dashchenko, A.I. (ed.) Reconfigurable Manufacturing Systems and Transformable Factories, pp. 155–194. Springer, Berlin (2006)
6. Kovac, M.: Innovative trends in the automotive industry. Transf. Inov. **22**, 188–192 (2012)

7. Leskova, A.: Reconfigurability of production system by means of modular structure. Int. J. Interdiscipl. Theory Pract. **6**, 15–20 (2015)
8. Posindu, B.A., Janaka, E.B., Kasun, D.T., et al: A novel fixturing system for complex shaped components. In: 2017 Moratuwa Engineering Research Conference, pp. 221–224. IEEE, Moratuwa (2017)
9. Gothwal, S., Raj, T.: Conceptual design and development of pneumatically controlled flexible fixture and pallets. Int. J. Serv. Oper. Manag. **29**(2), 147–162 (2018)
10. Gothwal, S., Raj, T.: Different aspects in design and development of flexible fixtures: review and future directions. Int. J. Serv. Oper. Manag. **26**(3), 386–410 (2017)
11. Tohidi, H., AlGeddawy, T.: Planning of modular fixtures in a robotic assembly system. Proc. CIRP **41**, 252–257 (2016)
12. Hui, L., Weifang, C., Shengjie, S.: Design and application of modular fixture. Proc. CIRP **56**, 528–532 (2016)
13. Mohring, H.-C., Gessler, W., Konig, A., et al.: Modular intelligent fixture system for flexible clamping of large parts. J. Mach. Eng. **17**(4), 29–39 (2017)
14. Ansaloni, M., Bonazzi, E., Leali, F., et al.: Design of fixture systems in automotive manufacturing and assembly. Adv. Mater. Res. **712–715**, 2913–2916 (2013)
15. Ivanov, V., Mital, D., Karpus, V., et al.: Numerical simulation of the system "fixture – workpiece" for levers machining. Int. J. Adv. Manuf. Technol. **91**(1–4), 79–90 (2017)
16. Erdem, I., Levandowski, C., Berlin, C., et al.: A novel comparative design procedure for reconfigurable assembly fixtures. CIRP J. Manuf. Sci. Technol. **19**, 93–105 (2017)
17. Forstmann, R., Wagner, J., Kreiskother, K., et al.: Design for automation: the rapid fixture approach. Proc. Manuf. **11**, 633–640 (2017)
18. Karpus', V.E., Ivanov, V.A.: Universal-composite adjustable machine-tool attachments. Russ. Eng. Res. **28**(11), 1077–1083 (2008)
19. Pehlivan, S., Summers, J.: A review of computer-aided fixture design with respect to information support requirements. Int. J. Prod. Res. **46**(4), 929–947 (2008)
20. Bakker, O.J., Papastathis, T.N., Ratchev, S.M., Popov, A.A.: Recent research on flexible fixtures for manufacturing processes. Rec. Patents Mech. Eng. **6**(2), 107–121 (2013)
21. Ivanov, V., Vashchenko, S., Rong, Y.: Information support of the computer-aided fixture design system. In: Proceedings of 12th International Conference ICTERI'2016, vol. 1614, pp. 73–86, CEUR-WS CEUR-WS.org (2016)

Modeling of Foundry Processes in the Era of Industry 4.0

Jacek Kozłowski[1] , Robert Sika[2(✉)] , Filip Górski[2] ,
and Olaf Ciszak[2]

[1] Warsaw University of Technology, Narbutta 85, 02524 Warsaw, Poland
[2] Poznan University of Technology, pl. Piotrowo 3, 61138 Poznan, Poland
`robert.sika@put.poznan.pl`

Abstract. The paper presents main areas of Industry 4.0 concept with regard to specificity and complexity of foundry processes. Data mining tools are discussed in terms of the possibilities and limitations of their application in Smart Factories. Data acquisition methods are described and the potential areas of restrictions in Internet implementation of things are identified on the example of foundry processes. The methodology of data preparation is also presented, including key tasks and actions to be taken, so that the collected production data are valuable from the point of view of Data Mining tools. As a result, the concept of CPS (Cyber-Physical Systems)/CPPS (Cyber-Physical Production Systems) tool allowing effective implementation of Data Mining tools in complex production processes is presented.

Keywords: Industry 4.0 · Data acquisition · Data mining · Foundry processes

1 Introduction

The idea of the fourth industrial revolution is technology development and, as a result, manufacturing processes based on automation, robotization, communication between machines and digitally supported product management processes. The result of these activities is the creation of Intelligent Factories, where the entire process of producing of an End-to-End product, from prototype due to technology development, production planning and production to control and service, will be digitally integrated in accordance with the principles of horizontal and vertical integration of value stream. In consequence, it will be possible to switch from mass production to individualized production, taking into account individual requirements of customers [1], while maintaining low production costs – this approach is known as mass customization [2].

2 Literature Review

The concept of Industry 4.0 assumes full, digital integration of humans with production machines [3]. In a smart factory, so-called smart manufacturing environment should be created, in which machines communicate with each other in an automated way, transferring a part of key information to a human operator.

The methodology of Industry 4.0 includes several key components i.e.: CPPS – Cyber-Physical (Production) Systems, IoT – Internet of Things, IoS – Internet of Services and finally Smart Factories. Smart Factories are equipped with Social Machines, communicating with each other and with an operator, who is much more capable than a traditional operator, due to the use of digital technologies, such as Augmented Reality (AR) [4]. Some key components of Industry 4.0 are presented in Fig. 1.
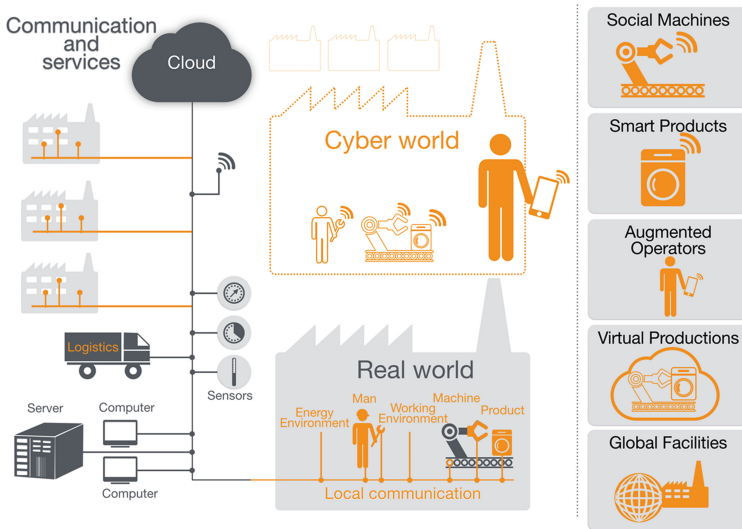
Fig. 1. Main components of Industry 4.0 [5].

An important element of Industry 4.0 concept is virtualization process, which is essential not only for simulation, but also for training. Here, it is worth to mention such concepts as Big Data (management of large data sets) or Cloud Computing (distributed computations), which are helpful for efficient implementation of calculations necessary for decision making, especially in the aspect of predicting possible defects of manufactured products. They are also listed as the key features of Industry 4.0 concept.

IoT is called IIoT in reference to industry (Industrial Internet of Things) and focuses on physical identification and communication between the elements of structural network of the whole process, such as objects, system and server platforms and other applications supporting the process. In the scope of IoT, the significant limitations in implementing of Industry 4.0 concept can be observed in foundry and other processes, in which difficult and demanding conditions occur, e.g. high temperature, high dustiness, manual control, electro-magnetic interference, vibrations or difficult connection and identification between a particular piece of finished product and process parameters.

IoS is the work methodology of service support systems (e.g. delivery of components from different suppliers), which helps analyze their availability at any time on

demand. This includes standardization, which allows building and configuring an offers network for internal and interorganizational services, based on shared resources for all the participants of the value stream.

Smart Factories are treated as a target effect of factory transformation. In the structure of the intelligent factories, physical processes are monitored by CPPS. This digital image is processed on-line into a language understandable for the decision-making systems on subsequent levels. IoT enables and supports communication between CPSs, as well as between CPSs and humans and other parts of system, presented in Fig. 1. This transformed information triggers the decision chains, supported by Internet of Services, finally resulting processes or services, going to the customers along with the whole internal and external value stream.

It is important to emphasize here, that key concepts of Industry 4.0 focus not only on the manufacturing process itself, but also on the planning, design and transport processes [6]. They should all be digitally integrated to allow seamless communication between a client, a producer and a supporter. Some parts of communication can be automated, for example clients can use digital product configurators to create their own variants of products, output from such a system can be then automatically sent further to create a new design and place it to production. This helps realize mass customization concept [2].

Thus, the main factors enabling the development of Industry 4.0 are: mobile communication and digital channels of access for customers, as well as available enough data sets and tools for data analysis, which will be the scope of this paper.

It should be remembered that the concept of Industry 4.0 also has a place for a human operator (especially in case of foundry processes). The concept of so called Operator 4.0 assumes supporting physical and mental work performed by the operator due to various techniques, such as Virtual Reality (for training and CPPS simulations [7]), Augmented Reality (for training directly on production line [4], displaying data on the state of machines, production, resources or hints about decision making directly on production site). Within the concept of Operator 4.0, several functions can be distinguished, namely super-strength operator, augmented operator, virtual operator, healthy operator, smarter operator, collaborative operator, social operator and analytical operator. It also assumes the operator's work directly in the vicinity of automated production machines and his physical cooperation with robots [8]. It can be particularly valuable in processes difficult to be fully automated and requiring current analysis and interpretation of large amounts of data, such as in foundry.

In relation to the above mentioned, foundries and foundry processes seem to be a particular challenge while implementing Industry 4.0 solutions. Complex and difficult process conditions for machines, people and measurement devices, and a wide range of activities realized or controlled by humans can significantly disturb the implementation of even basic IoT solutions. The complexity of foundry processes, the number of input parameters related to the number and type of output parameters (properties of final product) as well as the number and type of casting defects (quality parameters), issues in linking and mathematical description of several process stages significantly limit the implementation of CPPS solutions.

The previous experience indicates that the foundries are at the initial stage of implementing Industry 4.0 concept, hence in this paper, the authors suggest solutions, which allow taking practical steps to implement this concept.

3   Research Methodology

3.1   Data Mining in Foundry Industry 4.0

CPPS implementation requires replacing the existing methods of manual control by a human with automated decision systems, which carry out, lead and control tasks in a repetitive manner and no worse than a human [9]. Recently, it has been particularly noticeable in foundry engineering [10]. In case of processes, where the human factor is an integral part (e.g. in foundry processes), it also requires methods supporting the decision-making processes and other activities physically implemented by humans. In production processes, including foundry ones, it usually boils down to analysis of dependencies between process parameters derived from sensors or DAQ tools (treated as inputs) and other process parameters used for control or product parameters (treated as outputs) [11, 12]. Among the many mathematical models used in Data Mining, two main groups can be distinguished. They are HARD mathematical models, i.e. equations and inequalities describing the analyzed process, phenomenon or object, and SOFT mathematical models, construction and operation of which is based on the data collected in the past. With respect to Industry 4.0 and foundry processes, hard models can only be used at the pre-processing stage for modeling of the selected process steps, e.g. pouring and solidifying of metal in a mold, to determine the initial parameters of the process. At present, there are no known methods allowing a comprehensive mathematical description of all the foundry processes. This raises a need for alternative solutions.

Unfortunately, in relation to Industry 4.0, complex production processes usually require more sophisticated techniques of process state analysis, especially when applying assumptions of mass customization in practice [13]. In such cases, Data Mining methodology and soft mathematical modeling are used. There are 3 main types of soft mathematical models, depending on the complexity of process and knowledge of laws governing it, as well as the complexity of models. Three models are statistical models, artificial intelligence and computational intelligence.

Statistical models are most often used during the first modeling phase. As a result, regression equation is created, enabling prediction of the output variable (e.g. a control variable value or quality characteristics of a finished product) depending on the input variables (e.g. signals from sensors) [14]. Their basic advantage in Industry 4.0 is the speed of their implementation and operation, which can be important when using them on-line. Simplicity of these models allows quick creation of new models, adapted to the changing process conditions, both at the level of augmented operators and social machines.

Artificial Intelligence (AI) models are expert systems, where the knowledge of the process comes from experts and other traditional sources (standards, guides, books, publications) and is intelligently processed by a computer system. They can

significantly support the decision-making processes in foundry, at the augmented operators' level.

Computational intelligence (CI) models are the most complex ones used, where there are large data amounts of different nature for complex processes. This group includes among others: Artificial Neural Networks, Decision Trees and others. In CPPS range, these models can be used anywhere, where a human has decided about the process so far, using his experience, perceptiveness, daytime disposition, as well as where other modeling methods were insufficient as tools directly controlling the process or supporting decisions of augmented operators [15, 16].

For the proper use of soft mathematical models, an appropriate amount of data is needed, prepared in a way allowing its use in the modeling process, with the least interference. Methods of data acquisition and preparation in a specific environment of foundry processes will be presented in the further part of the paper.

3.2 Data Acquisition in Foundry Processes

Almost all diagrams showing Industry 4.0 concepts contain symbols of wireless data transmission, as well as cloud data storage and processing. This assumption is correct for highly automated processes with high IT equipment and high technical capabilities. It is different in foundry processes, where, despite continuous improvement in the methods and tools of quality control at particular stages of processes, quality and availability of production data, as well as continuous technical and IT development, data acquisition in this type of technologically complex processes are still difficult. Although the share of automatic and computer methods of data acquisition is increasing, many production, technical and administrative departments still use various types of paper documents. An especially important source of information is informal documentation, such as entries in personal notebooks, kept by process engineers, quality controllers and other foundry workers. Such data, often valuable and relevant information about the process, are in principle available only to a specific employee. The access to data should be common and quick for authorized persons. However, when they are only at the disposal of the above-mentioned persons, they are unfortunately not available to other departments.

In the era of Industry 4.0, it is necessary to collect data that are used not only for the ongoing monitoring and control of processes, but also for the knowledge capitalization. Production problems cannot always be explained directly with the help of knowledge and experience of an engineer. What is then necessary is production parameters analysis (of the collected historical data) using statistical methods or mathematical models of data mining (Data Mining) [12].

The first requirement, however, is a well-developed and implemented process of data acquisition [8], especially concerning the aspects of data acquisition related to the technical side of casting and associated with complex processes in foundry. Data acquisition in foundries is currently carried out in three ways [17]:

– manually – e.g. parameters of molding sand, such as moisture M [%], permeability p^m [m^2/Pa * s * 10^{-8}] and compressive strength R_c^w [MPa] (in moisture state), which are taken from different places of foundry molding line;

– automatically – e.g. non-contact measurement of pouring temperature of liquid alloy into molds using a pyrometer, non-contact measurement of mold pouring time by means of optical, ultrasound or microwave sensors;
– semi-automatically – occurs most often in case of combining automatic sources and derived from manual entries, e.g. automatic data recording from the Zwick – tensile strength R_m and manual addition of hardness measurement HB to the generated file; such a collective database can be further exported to CAx/ERP computer systems.

In a Smart Factory, guidelines on the frequency of data acquisition should be worked out for each type of data and the means of their acquisition. At further stages of their use in CPPS, this directly translates into efficiency of data processing systems, especially in online mode. Currently, the following data logging modes can be distinguished:

- cyclic mode – changing parameter values are collected in a constant time interval (e.g. every second),
- event mode (delta) – parameter values are collected only when their values change,
- forced mode – parameter values are collected in accordance with the method of data delivery to server (at specified times of the day or with means of extortion – e.g. device failure).

Considering the above mentioned, it seems reasonable that in a Smart Factory it is necessary to collect as much data as possible in electronic form, i.e. in IT databases. It is also important to develop procedures and methods facilitating their issuing "on demand" whenever the necessity of their use arises.

The specificity of foundry processes, the differentiation in the range of data sources and the complexity of this process and the difficult measurement conditions make it difficult to find valuable solutions dedicated to foundry in the marketplace. When implementing original methods and tools for data acquisition in the foundry, it is important to remember often overlooked aspects, such as appropriate supervisory procedures, especially where significant share of data is saved or rewritten manually to database systems. Methods supporting data validation of the collected information will be described below.

3.3   Methodology of Data Preparation for Modeling

Modeling of production processes should be based on reliable data. This requires designing appropriate acquisition system architecture and algorithms including assessment of information sources, data structuring concepts (depending on the type of data) and measurement procedures (from manuscripts to automated measurement systems). The type and class of measuring apparatus, the method of data recording, algorithms for their processing and classification, as well as all disturbances known at the time of measurement should also be taken into account [18].

The methodology of data preparation for modeling consists in the analysis and implementation of selected activities, including 4 main tasks, i.e. cleaning, merging, converging and reducing data [19, 20].

Data cleaning – it aims at elimination of inaccuracies or contradictions in the collected data. The key activities of this task are: deleting outliers and topping up missing data.

Data merging – it aims at combining data from different sources into a single, two-dimensional table. The key activities in this area are: identifying attributes in various databases, removing repetitions and analyzing formats or units compatibility.

Data reduction – it aims at reduction of a database dimensionality, in order to reduce data mining time. The main activities of this task are: analysis of significance and removal of non-essential attributes, deletion of similar records, aggregation, discretization.

Data conversion – it aims at enabling creation of a model and improvement of its accuracy and speed of operation. The main activities related to this are: smoothing, aggregation and normalization.

Apparently, the methodology of preparing data for modeling is a complex process. In the context of Industry 4.0 implementation, it should be mostly automated. Traditional methods, based on paper, should be replaced with digital database systems, including data validation procedures at the time of entering. Therefore, the conscious approach to the quality of data is crucial as early as at the acquisition stage, in order to limit the above-mentioned activities to a minimum.

4   Results

The example of application of the approach presented in this paper within the scope of Industry 4.0 concept, was a feasibility study of the use of Data Mining tools for foundry in ADI production process. The used approach and obtained results were described by the authors in other publications [21, 22].

The methodology and assumptions can be referred to operation of a cyber-physical system shown in Fig. 2.
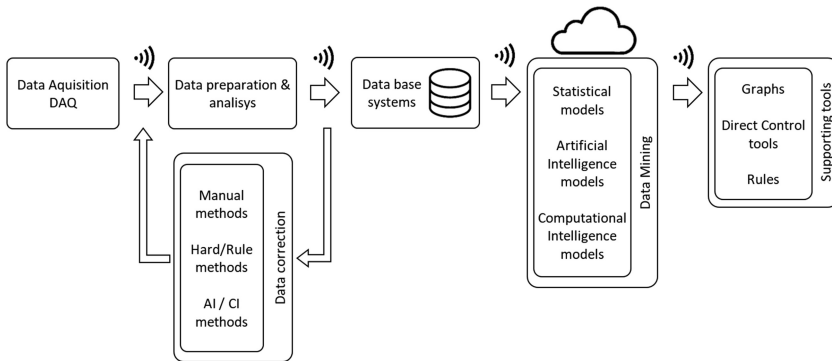
Fig. 2. Exemplary model of a cyber-physical system in foundry Industry 4.0.

The main goal of the analysis of ADI properties modeling was to build a mathematical model predicting mechanical properties such as: tensile strength Rm [MPa] and elongation A5 [%]. In the scope of social machines, it allowed to directly control the process and properly serve as an expert supporting decisions at augmented operators' level to select quasi-optimal process parameters. The effect described above was obtained based on special proprietary procedures for querying of Artificial Neural Networks models learned, taking into account the effect of synergy or competitive influence of process parameters. It is allowed to determine the most important groups of signals to control the process parameters and determination the reverse task, i.e. to search for ranges (intervals) of process parameters, allowing to obtain the values set of the output variables. The research involved the use of MLP Neural Networks with one layer of hidden neurons with the number of hidden neurons equal to the number of input neurons with a logistic activation function. In consequence, this allowed to obtain cast iron with given properties and process parameters control within defined limits. In the research, various mathematical models were used and their analysis was performed in terms of usability as to quality and performance.

The collected ADI database, derived from own research and data available in literature, encompassing over 1,400 records, was analyzed and prepared, taking into account the relevant methodology [20]. This required checking the possibility of implementing automated systems for correctness and data replenishment in on-line process.

Within CPPS in foundry industry, such predictions and suggestions for setting process parameters can be automated, provided that the model is supplied at the right time, along with the right data about the current state of process. In typical foundry processes, it will usually be a set of guidelines, instructions or rules addressed in an appropriate way to Operator 4.0.

5 Conclusions

The paper outlined the main areas of Industry 4.0 concept, taking into account the specific conditions of foundry processes. The implementation of Cyber-Physical (Production) Systems is also possible in these complex processes, however, it is necessary to switch to automatic control systems. Today, more and more often advanced systems supporting the work of operators are installed, such as, for instance, SCADA system (Supervisory Control and Data Acquisition). The example of this is FoMaSys system from Michenfelder which supports selected molding sand parameters control.

The paper shortly presents the stages of production data preparation and includes steps necessary for the data collection from the point of view of Data Mining tools (data cleaning, merging, reducing and transforming). Despite the fact that this paper presents only the concept related to the production process of ADI cast iron, the specific solutions are currently being implemented as a part of the test and development works in another selected foundry, in high-pressure die-casting processes.

It should be noted, that presently, fully automated foundry in accordance with Smart Factory concept is practically unlikely. It should be remembered, however, that quite a lot of production processes have recently been automated in a way that

somewhat reduces operator's participation. In case of foundry processes, a human is still an integral part, although increasingly supplied with methods supporting the decision making processes. The experience gained by the authors, indicates that the implementation of IoT measurement methods and tools may be a significant limitation on the subsequent stages of their connection within CPPS, in relation to various stages of casting production.

The stage of production data acquisition is important, as only on the basis of the data completeness and awareness of the collection frequency, useful knowledge necessary to develop mathematical models can be built.

References

1. Trojanowska, J., Varela, M.L.R., Machado, J.: The tool supporting decision making process in area of job-shop scheduling. In: Rocha, A., Correia, A., Adeli, H., Reis, L., Costanzo, S. (eds.) Recent Advances in Information Systems and Technologies. WorldCIST. Advances in Intelligent Systems and Computing, vol. 571, pp. 490–498. Springer, Cham (2017)
2. Górski, F., Zawadzki, P., Hamrol, A.: Knowledge based engineering as a condition of effective mass production of configurable products by design automation. J. Mach. Eng. **16**(4), 5–30 (2016)
3. Gorecky, D., Schmitt, M., Loskyll M., Zuhlke D.: Human – machine – interaction in the Industry 4.0 ERA. In: 12th IEEE International Conference on Industrial Informatics (INDIN), pp. 289–294 (2014)
4. Górski, F., Wichniarek, R., Kuczko, W., Bun, P., Erkoyuncu, J.A.: Augmented reality in training of fused deposition modelling process. In: Advances in Manufacturing, pp. 565–574. Springer (2018)
5. Ottomotors: Defining the next industrial evolution. https://www.ottomotors.com/blog/understanding-industry-4-0. Accessed 25 Dec 2018
6. Ivanov, V., Vashchenko, S., Rong, Y.: Information support of the computer-aided fixture design system. In: Proceedings of 12th International Conference ICTERI' 2016, vol. 1614, pp. 73–86, CEUR-WS (2016). CEUR-WS.org
7. Żywicki, K., Zawadzki, P., Górski, F.: Virtual reality production training system in the scope of intelligent factory, intelligent systems in production engineering and maintenance. In: Burduk, A., Mazurkiewicz, D. (eds.) Intelligent Systems in Production Engineering and Maintenance – ISPEM 2017. ISPEM 2017. Advances in Intelligent Systems and Computing, vol. 637, pp. 450–458. Springer, Cham (2017)
8. Romero, D., Stahre, J., Wuest, T., Gorecky, D.: Towards an operator 4.0 typology: a human-centric perspective on the fourth industrial revolution technologies. In: International Conference on Computers & Industrial Engineering (CIE46), Tianjin, China, pp. 1–11 (2016)
9. Gramegna, N.: Smart casting process control and real time quality prediction The digitalization of foundry plays a key role in competitiveness introducing new integrated platform to control the process and predict in real-time the quality and the cost of the casting. In: 9th VDI Conference with Specialist Exhibition on Casting Technology in Engine Construction: Potential for the Next generation of Vehicle Propulsion, vol. 2304, pp. 227–234 (2017)
10. Industry 4.0 and what it means to the Foundry Industry. http://www.foundrytradejournal.com. Accessed 20 Dec 2017

11. Perzyk, M., Kochański, A., Kozłowski, J.: Comparison of data mining tools for significance analysis of process parameters in applications to process fault diagnosis. Inf. Sci. **259**, 380–392 (2014)
12. Rogalewicz, M., Sika, R.: Methodologies of knowledge discovery from data and data mining methods in mechanical engineering. Manag. Prod. Eng. Rev. **7**(4), 97–108 (2016)
13. Pavlenko, I.V., Simonovskiy, V.I., Demianenko, M.M.: Dynamic analysis of centrifugal machines rotor supported on ball bearings by combined application of 3D and beam finite element models. In: IOP Conference Series: Materials Science and Engineering, vol. 233, pp. 1–8. IOP Publishing (2017)
14. Andrzejczak, K., Selech, J.: Quantile analysis of the operating costs of the public transport fleet. Transp. Prob. **12**(3), 103–111 (2017)
15. Harding, J.A., Shahbaz, M., Srinivas, M., Kusiak, A.: Data mining in manufacturing: a review. J. Manuf. Sci. Eng. **128**(4), 969–976 (2006)
16. Köksal, G., Batmaz, I., Testik, M.C.: A review of data mining applications for quality improvement in manufacturing industry. Expert Syst. Appl. **38**(10), 13448–13467 (2011)
17. Sika, R., Popielarski, P.: Methodology supporting production control in a foundry applying modern DISAMATIC molding line. In: 13th International Conference on Modern Technologies in Manufacturing, Cluj-Napoca and AMaTUC, MATEC Web of Conference, vol. 137, p. 05007 (2017)
18. Sika, R., Ignaszak, Z.: SCADA systems and theirs connection with statistical process control in foundry. Arch. Foundry Eng. **15**(1), 145–153 (2015)
19. Kochański, A.: Data preparation. Comput. Methods Mater. Sci. **10**(1), 25–29 (2010)
20. Kochański, A., Perzyk, M., Kłębczyk, M.: Knowledge in imperfect data. Advances in Knowledge Representation. InTech (2012)
21. Perzyk, M., Kochański, A., Kozłowski, J.: Control of ductile iron austempering process by advanced data driven modeling. In: Cooper, D., Prat, J., Petzchmann, U. (eds.) Proceedings of 71st World Foundry Congress, pp. 1–11. World Foundry Organization Ltd (2014)
22. Perzyk, M., Kozłowski, J.: Methodology of fault diagnosis in ductile iron melting process. Arch. Foundry Eng. **16**(4), 101–108 (2016)

Ansys Simulation of the Joint Strength with the Interference Fit in the Presence of the Shape Geometry Error

Oleksandr Kupriyanov[(✉)]

Ukrainian Engineering Pedagogics Academy,
16 Universytetska St., Kharkiv 61003, Ukraine
a_kupriyanov@uipa.edu.ua

Abstract. The effect of the shape geometry error on the strength of a cylindrical joint with interference fit was investigated. The strength of the joint without a geometry error was compared with the strength of the joint in the presence of conicity, saddle shape, barrel shape, ovality. The calculation is carried out by the finite element method in Ansys. It is established that for small-bore diameters the strength of a cylindrical joint with interference decreases significantly, i.e. one-third of the initial one. The most unfavorable is a saddle shape, followed by ovality and conicity, and the barrel shape does not lead to a significant decrease. For large diameters, the influence of the shape geometry error on the strength of a cylindrical joint with interference is less significant. It is recommended tightened standardization of the shape geometry error in manufacturing of parts of critical joints with interference.

Keywords: Strength decrease · Cylindrical joint · Finite element method
Conicity · Saddle shape · Barrel shape · Ovality

1 Introduction

Joints with interference are widespread in a mechanical engineering. Their strength, apart from the constructive factors, is also greatly influenced by process ones. It is necessary to ensure the required strength of the interference fit joint with the adopted manufacturing process.

It is known, that the greatest influence on the strength of such joint is exerted by the value of the interference [1]. Other parameters that have a significant effect include the material and characteristics of the surface layer of the mating parts, the roughness and its direction, the presence of grease, glue layers [2]. The influence of the shape geometry error on the joint strength with the interference is not well understood. This is important for responsible joints, such as high-speed machine units.

2 Literature Review

In the classical theory of contacting bodies, it is assumed that the frictional force is proportional to the contact pressure. I.V. Kragelsky constructed a generalized molecular-mechanical theory of the friction coefficient. According to it, friction at

contacting surfaces is formed due to the elastic interaction of the apexes of the irregularity projections of the contacting surfaces. As the contact pressure increases, the number of "pads" that come into contact increases, while the area of everyone "pad" changes insignificantly.

The shape of the mating surfaces has a great influence on the strength during pressing since the actual strength of the contact of the parts decreases [3, 4]. This effect is noticeable both for press joints with interference and for joints assembled with heating or cooling [5].

In work [6] the stress-strain state of interference fits was studied in such joints: fit of an oval shaft in a round hole of the bushing; round shaft fit in the circular bore of the bushing; fit of the oval shaft in the round hole of the bushing; fit of the round shaft in the bushing with eccentricity; fit of the oval shaft in the bushing with eccentricity and angle α between ovality and eccentricity of 0°, 45° and 90°. However, studies of the effect of the stress-strain state assembly on its strength have not been carried out.

Investigation of this problem is currently carried out both by finite element simulation [7–9] and by a model experiment [8].

The author carried out an experimental study [10] and computer simulation by the finite element method [11, 12] with the purpose of estimating of the shape geometry error influence on the Ø60 joint strength with interference. Further refinement of the friction coefficient calculation made it possible to obtain data that coincided with the experiment. The study was carried out for the normal relative geometric accuracy of the Ø60 joints with an interference. It is necessary to expand these studies to other sizes.

The purpose of the study is to determine the effect of the shape geometry error on the strength of the joint with interference, depending on the geometric accuracy and the value of the coupling size.

3   Research Methodology

In this paper, the influence of the shape geometry error on the strength of a cylindrical joint with interference is compared:

– for the normal and high relative geometric accuracy for Ø60;
– for the Ø60 mm and Ø190 mm with normal relative geometric accuracy.

For comparative calculations, the fit H8/u8 was chosen, as one of the rather rough ones used for interference fit joints.

In the GOST 24642-81, a set of deviations of the whole surface (cylindricity tolerance), its individual sections, or individual geometric elements, regardless of the shape of the real surface, are normalized. In order to determine the effect of the real surface shape, the effect on the joint strength of the previously used special forms of shape deviation was investigated. These include such deviations in the cross section profile as conicity, barrel shape, saddle shape, and ovality is a deviation from roundness.

The relative geometric accuracy of the shape can be from 60% of the tolerance range for normal (A) geometric accuracy to less than 25% for extremely high geometric

accuracy. If the geometry error of the part shape is not normalized during assembling with interference, then its value can correspond to normal geometric accuracy.

For the 8th ISO surface accuracy degree, the normal (A) relative geometric accuracy corresponds to the 7th degree of accuracy, which for Ø60 allows the shape geometry error of 32 μm per diameter. The high (C) relative geometric accuracy corresponds to the 5th degree of accuracy, which for Ø60 allows the shape geometry error of 12 μm per diameter. For Ø190, the normal (A) relative geometric accuracy allows a shape geometry error of 40 μm per diameter.

As an example, Fig. 1 shows samples for research, Ø190 with a normal relative geometric accuracy. The shape geometry errors are graphically enlarged for clarity. The bushings were taken cylindrical (Fig. 1a), and the shape geometry error was simulated on the shafts. The cylindrical shaft (Fig. 1b) was compared with cone-shaped, saddle-shaped, barrel-shaped and oval-shaped ones (Fig. 1c–f). The strength of the joint is affected by the geometry of the seating surface, however, shanks were provided for the shafts.

Steel 45 was adopted for the material of the parts. Material characteristics are accepted the same for the shaft and bushing: modulus of elasticity $E = 2 \cdot 10^5$ MPa and Poisson's ratios $v = 0.3$. The friction coefficients for the experimental parts were specially calculated, and their values were within 0.26–0.35.

4   Results

Strength simulation of the cylindrical joint with interference in the presence of a shape geometry error for the initial data of Fig. 1 was carried out by Ansys. The arc of the circle simulated the shape of the saddle and barrel; the oval simulated the ovality in axial section.

When calculating the strength, the offset 1 mm was set for the free edge of the shaft shank, and the opposite edge of the bushing was fixed in the axial direction. The force that caused this offset was displayed after the calculation.

For the cylindricality, conicity, saddle and barrel shapes, the problem was solved in a 2D variant for half of the product (per radius), and for the ovality – in a 3D-one for a quarter of the design. To construct the finite element model of the first four schemes, the element "PLANE82" was used with the "axisymmetric" option enabled, which made it possible to reduce the volume problem to a plane one. On the contact lines, the elements "CONTA172" and "TARGE169" were used. For the ovality, the solid-state finite elements "SOLID95" were used. The interference was simulated by the initial penetration of the elements.

Figures 2 and 3 show examples of equivalent stress profiles obtained by using the von Mises criterion for barrel shape and ovality, respectively, Ø190, normal (A) relative geometric accuracy. Other cases are not shown as they are similar.

Stress diagrams obtained in Ansys are formed for cases of stress-strain state at the time of fit breakage from the action of axial force and for the not the stress-strain state of fit from the interference force. Therefore, the shank is also in a stressed state.

The maximum stresses in all cases are much lower than the yield strength for the selected material and it is 431 MPa in the case of the saddle-shaped Ø190.
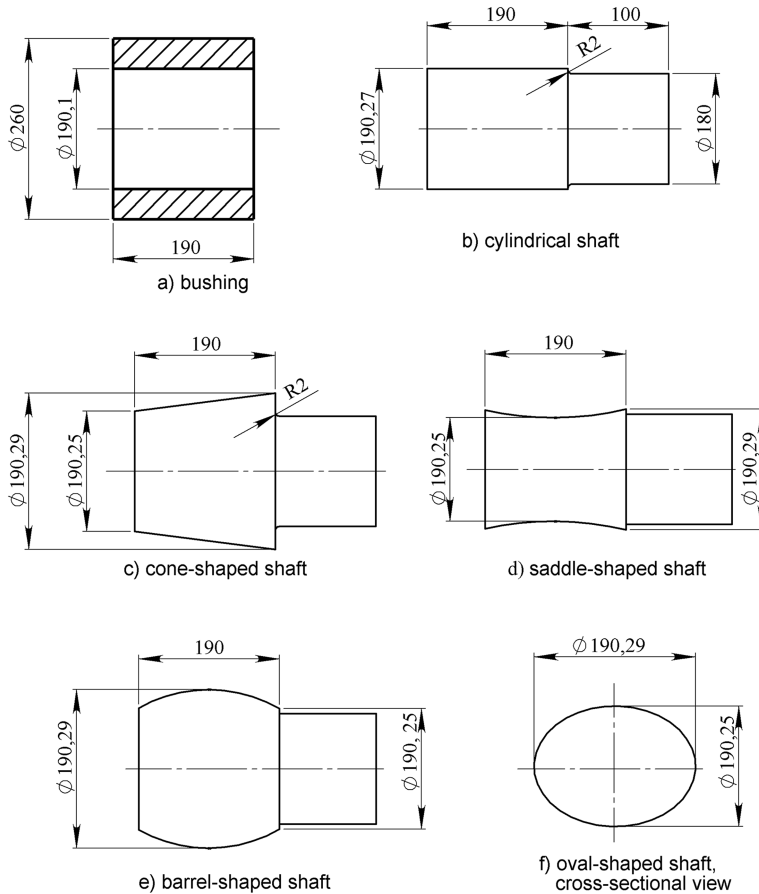
Fig. 1. Investigated shape deviations of the cylindrical surfaces for the Ø190, normal (A) relative geometric accuracy.

The simulation results of the cylindrical joint strength with interference in the presence of a shape geometry error are shown in Fig. 4. The strength of the cylindrical joint without error is taken as one.

The analysis of the obtained results allows to make a conclusion that the strength of a cylindrical joint with interference in the presence of the maximum permissible shape geometry error varies significantly. The presence of conicity and ovality reduces the strength by 20%, the saddle shape reduces the strength of the joint by 36%, and only barrel shape does not lead to a significant reduction. Such a significant reduction in strength cannot be neglected in practice, especially for saddle shape.

If we limit the shape geometry error due to high accuracy, then the reduction in strength becomes much less. In this case, the presence of conicity and ovality reduces the strength by 8%, the saddle shape reduces the strength of the joint by 15%, and the barrel shape does not lead to a significant reduction.
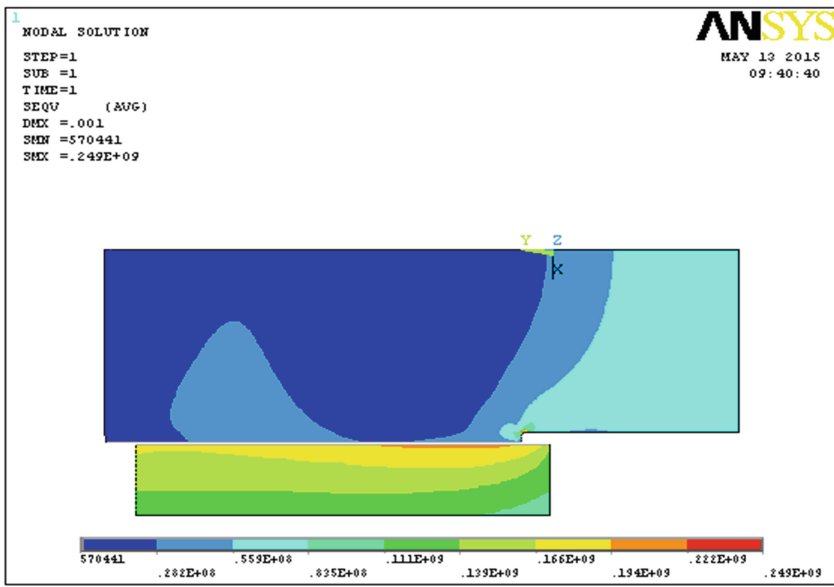
Fig. 2. Equivalent stresses according to the von Mises criterion in the presence of barrel-shape, Ø190 normal (A) relative geometric accuracy.
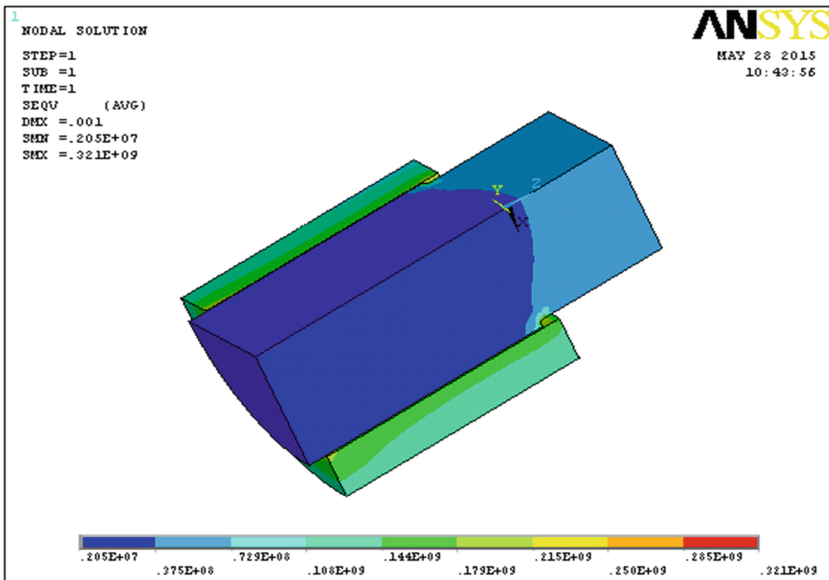
Fig. 3. Equivalent stresses by von Mises criterion in the presence of ovality, 3D image, Ø190, normal (A) relative geometric accuracy.
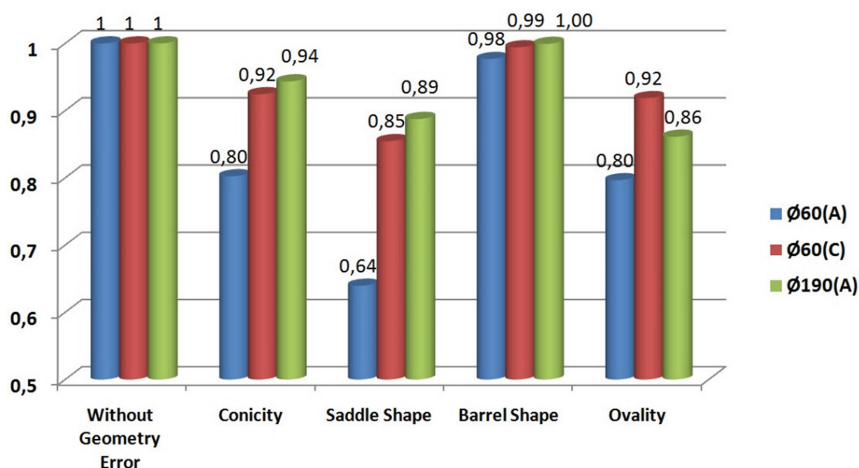
Fig. 4. Relative strength at the axial shift.

For large-format joints, the reduction in strength, even for the maximum allowable shape geometry error, is not so significant. In this case, the presence of a maximum reduction in strength is observed for ovality and it is 14%, and for the remaining errors it is less than 10%. The reason is that according to the standard the larger the connection dimensions, the smaller the permissible ratio of the geometry error to the tolerance limit.

5   Conclusions

1. The calculation allows to make a conclusion that the strength of a cylindrical joint with interference in the presence of the shape geometry error is significantly reduced to about one-third. The most unfavorable is a saddle shape, followed by the ovality and conicity, and barrel shape does not lead to a significant strength decrease.
2. It is recommended tightened standardization of the shape geometry error in manufacturing of parts of critical joints with interference. It precludes a significant reduction in strength.
3. The larger the overall dimensions of the joint, the less the geometry error effect on the joint strength with the interference.

References

1. Andreev, G.Yu.: Thermal assembly of wheelsets. Kharkov University Publishing House, Kharkov (1965)
2. Balatskiy, L.T.: Strength of force-fit joints. Tehnika, Kiev (1982)

3. Gallio, G., Lombardia, M., Rovarinob, D., Finoa, P., Montanaroa, L.: Influence of the mechanical behaviour of different adhesives on an interference-fit cylindrical joint. Int. J. Adhes. Adhes. **47**, 63–68 (2013)
4. Sekercioglua, T., Gulsoza, A., Rendeb, H.: The effects of bonding clearance and interference fit on the strength of adhesively bonded cylindrical components. Mater. Des. **26**(4), 377–381 (2005)
5. Sen, S., Aksakal, B.: Stress analysis of interference fitted shaft–hub system under transient heat transfer conditions. Mater. Des. **25**(5), 63–68 (2004)
6. Perin, A.P., Andreev, A.G.: Calculation of force-fit joints in the ovality and eccentricity of the joined parts based on ANSYS. Bull. NTU "HPI" **38**, 117–123 (2007)
7. Boutoutaou, H., Bouazizb, M., Fontaine, J.F.: Modeling of interference fits taking form defects of the surfaces in contact into account. Mater. Des. **32**(7), 3692–3701 (2011)
8. Chakherlou, T.N., Abazadeh, B.: Experimental and numerical investigations about the combined effect of interference fit and bolt clamping on the fatigue behavior of Al 2024-T3 double shear lap joints. Mater. Des. **33**, 425–435 (2012)
9. Mucha, J.: Finite element modeling and simulating of thermomechanic stress in thermo-compression bondings. Mater. Des. **30**(4), 1174–1182 (2009)
10. Kupriyanov, A.V.: Experimental research of strength of influence of parts shape geometry error on cylindrical joint with interference fit. Mach. Build. Collect. Sci. Pap. **10**, 85–93 (2012)
11. Kupriyanov, A.V.: Strength simulation of joints with interference fit at available inaccuracy of form geometry. Assem. Mech. Eng. Instrum. Mak. **5**(154), 41–44 (2013)
12. Kupriyanov, A.V., Reznichenko, N.K.: Influence of scale factor on the durability of cylindrical joint with interference fit with inaccuracy of geometrical form. Open Inf. Comput. Integr. Technol. Collect. Sci. Pap. **68**, 113–120 (2015)

Adaptive Profile Gear Grinding Boosts Productivity of this Operation on the CNC Machine Tools

Vasily Larshin[1](✉) and Natalya Lishchenko[2]

[1] Odessa National Polytechnic University,
1 Shevchenko Avenue, Odessa 65044, Ukraine
vasilylarshin@gmail.com
[2] Odessa National Academy of Food Technologies,
112 Kanatnaya Street, Odessa 65039, Ukraine

Abstract. The paper is devoted to solving an important scientific and technical problem of increasing the productivity of defect-free profile gear grinding on CNC machines through computer subsystems of grinding operation automated design, monitoring, and grinding diagnostics. The corresponding methodology and theoretical preconditions for these computer subsystems developments are provided to solve the following scientific problem. Despite of the increase in the productivity of gear grinding on CNC machines, a number of attendant factors have appeared that limit the gear grinding productivity: the time of the grinding stock measuring in the tooth spaces which is comparable with the time of gear grinding, the lack of methods for accounting the information about the grinding stock, etc. In this connection, the objective of the paper is to indicate the ways of increasing the productivity of the profile defect-free gear grinding on CNC machines. For this purpose, a set of purposeful methods and means of innovative adaptive gear grinding technology has been developed. For example, a method for restoring information about the grinding stock is proposed with a limited number of measurements to ensure, for example, that the feed can be switched from accelerated one to working and vice versa. Mathematical models have been developed to convert the grinding stock uncertainty into the deterministic value of the grinding wheel retraction from the workpiece, etc.

Keywords: Adaptability · Gear grinding system · Gear grinding stock
Grinding stock model · Designing · Monitoring · Diagnostics

1 Introduction

The property of adaptability in the mechanical engineering is gaining increasing recognition due to the success of its application in practice of automated production on CNC machines. This was the result of a natural process of computer-aided design of high technologies and the corresponding both cutting and grinding machining systems, including the gear grinding systems on the basis of CNC machine tools. The basis of adaptive mechanical machining is its integration with on-machine measurement (monitoring) and process diagnostics (control), which are performed on the same

equipment, i.e. without the error of the workpiece setting and with eliminating the influence of the human factor. As a consequence, it is possible to significantly increase the process productivity, including gear grinding on CNC machine tools. That is why the proposed work, which is the result of many years of experimental and theoretical research, is among the topical in the mechanical engineering.

2   Literature Review

The analysis of labor-intensiveness of the technological process of gears production has been made. A significant amount of time spent on grinding operation (up to 40–70%) is established. Therefore, the task of increasing the productivity of the gear grinding on CNC machines is actual and important, despite of the productivity advantages reached on the CNC machines. The technological possibilities of existing grinding methods are considered. It was established that the most application was made by two kinds of gear grinding: the profile gear grinding (gear quality 3 to 6 to DIN 3961) and the worm wheel one (gear quality 4 to 7) [1]. The appearance of the CNC gear grinding machines allowed increasing the technological operations productivity by ensuring the self-sufficiency, autonomy and mobility of the grinding system with the software and with the minimum participation of the machine operator in the implementation of all stages of the grinding operation. The profile gear grinding compared with the worm wheel gear grinding ensures higher accuracy (DIN 3–6 instead of DIN 4–7), but yields less productivity. That is, we need to find reserves for further increase in productivity. One of these reserves is the use of the individual features of the grinding wheel, pre-machined workpieces of gears as well as disclosing the uncertainty coursed by influences derivable from lubricoolants, the grinding machine, etc. It is known, all elements of the grinding system must be adapted to each other to achieve the goal of the adaptive profile gear grinding. In order to use these reserves, it is proposed to control the process by introducing appropriate adjustments on the basis of the process redesigning, monitoring and diagnosing with the help of corresponding computer subsystems built in an appropriate manner into the CNC structure [2].

The gear grinding stock measurement at the gear periphery on CNC machines allows to take into account the gear individual features when aligning the stock along the lateral sides of their tooth spaces, to ensure the individual removal of the stock, taking into account its value and actual location along the gear periphery. However, the gear grinding stock measurement consumes the auxiliary operation time, so there is a problem reducing this time by optimizing the number of measurements. The feature of the stock to be removed is its unplanned change in the gear periphery, which is influenced by the chosen method of aligning of the stock due to the correction in the gear angular position. It is known that the gear grinding stock determines the productivity of the operation; therefore, studies related to the stock determination which based on the results of its selective measurement in certain tooth spaces are relevant.

The gear grinding temperature is one of the factors limiting the productivity of the grinding operation. In the analysis of temperature field mathematical models during grinding, one of them was used with a phenomenological approach to determine the grinding temperature for a three-, two- and one-dimensional temperature field based on

the Fourier partial differential heat conductivity equation under boundary conditions of the second kind. This approach was started in due time by well-known scientists-thermophysics H. S. Carslaw and J. C. Jaeger. The analysis of the relevant works showed that there are no acceptable solutions to the thermophysical problems for the purpose of gear grinding operation designing, monitoring and diagnosing.

To assess the productivity and for designing the grinding operation, a number of characteristic values are used, among which are: the volume of the material to be removed per unit time (the intensity of the grinding) Q_w (mm³/s), the total amount of removable material V_w (mm³). In the literature, the first two indicators are additionally given to the unit of effective (further active) grinding wheel width and are indicated by: Q'_w in mm³/(s mm) and V'_w in mm³/mm. However, the literature does not describe the applied methods of determining the high-production modes of grinding on the basis of these indicators of grinding operation, there is no information on grinding diagnostics in real time. There is no mathematical dependence to determine the grinding intensity Q_w in mm³/s for an arbitrary curvilinear profile, which differs from the rectangular profile for traditional rectangular grinding schemes. Parameters Q'_w and V'_w affect the grinding temperature and force as well as the grinding wheels wearing in different points of the grinding wheel profile, but the corresponding mathematical dependencies have not yet been installed. The analysis of literature has shown that the relationship between the Q'_w parameter and the thermal burns is still a formal one, because it is not related to the grinding temperature. Therefore, it is necessary to establish this relationship.

The urgency of monitoring and grinding diagnostics subsystems in gear grinding is due to the lack of deterministic relationships between the grinding system output (accuracy and quality of machining) parameters and the input control (grinding modes) ones. The output parameters, i.e. operation result, are determined after the end of the machining (control of the result), when there is no possibility of correction of the result, which creates a control problem by the grinding operation. Therefore, the control of the relevant grinding system state parameters, i.e. process parameters, may be useful to make the necessary corrections for obtaining the output parameters desired.

3   Research Methodology

The methodology of scientific researches, which includes modeling, optimization and control in the grinding system, is given. These directions characterize the investigated grinding system as an object of control, which has input parameters u, state parameters x and output parameters y [3].

The interconnections between these parameters are not deterministic ones; therefore, the task of the research is to identify these parameters, based on ensuring the least number of grinding stock measurements that gives minimum measurements time. This requirement satisfies the representation of the grinding system in the form of an object of control in which it is necessary to provide the necessary output parameters at the highest machining efficiency with automated control of this object using the computer-aided design, monitoring, and grinding diagnosis subsystems [1, 2]. Monitoring and grinding diagnostics of the grinding system state partly compensate for the

lack of adaptive control of the output parameters, which is impossible due to the lack of information about the output parameters which are available continuously. At the same time, the diagnostics of the grinding system state allows indirect characterization of its output parameters through deterministic-stochastic relations, in which the information is distributed from the input parameters through the state parameters to the output ones. Unlike the output parameters, information about the state parameters can occur continuously, providing the possibility of indirect adjustment of the output parameters and thus the solution of the problem.

The deterministic-stochastic nature of the profile gear grinding requires appropriate approaches and methods for solving the tasks; therefore, the theoretical-probabilistic approach is used in the work. In turn, the approach to dividing the information signal into elementary harmonic components is called the frequency approach in the work. According to this approach, any signal in the function of time can be transformed according to the Fourier algorithm into the corresponding dependence of the amplitudes and phases of the signal harmonic components from their frequency (direct Fourier transform) and back from the frequency dependence in the time one (inverse Fourier transformation). On the basis of these approaches (theoretical-probabilistic and frequency), methods of determining the gear grinding stock to be removed are developed, which allow determining the maximum value of the stock along the gear periphery. It has been established that the grinding stock includes constant z_0 and variable Δz parts, i.e. $z = z_0 + \Delta z$. In accordance with the theoretical-probabilistic approach, the variable part Δz of the stock is considered, assuming that it has a systematic (periodic) Δz_{sys} and random (aperiodic) Δz_{ran} components. Consequently, the structural formula for determining the stock $z(n)$ for gear grinding for both sides of the profile of the tooth space has the form

$$z(n) = z_0 + \Delta z(n) = z_0 + \Delta z_{sys}(n) + \Delta z_{ran}(n) \tag{1}$$

where n is the current number of the gear tooth space, $1 \leq n \leq N_{max}$ (N_{max} is the number of gear teeth. The gear grinding stock distribution on the left and right sides of the tooth spaces as the serial number of the teeth changes has a sinusoidal nature of the change (Fig. 1). The stock instantaneous values are the sum of the constant, i.e. z_0^L or z_0^R, and the variable, i.e. $\Delta z^L(n)$ or $\Delta z^R(n)$, components of the stock. The instantaneous magnitude of the variable component of the stock in formula (1) can be positive and negative. In the first case, the instantaneous value of the corresponding stock on the right or left side of the tooth spaces is greater than its constant component, while in the second case is less than it.

Consequently,

$$z^L(n) = z_0^L + \Delta z^L(n) = z_0^L + \left[\Delta z_\beta^L(n) + \Delta z_\gamma^L(n) \right] \tag{2}$$

$$z^R(n) = z_0^R + \Delta z^R(n) = z_0^R + \left[\Delta z_\beta^R(n) + \Delta z_\gamma^R(n) \right] \tag{3}$$
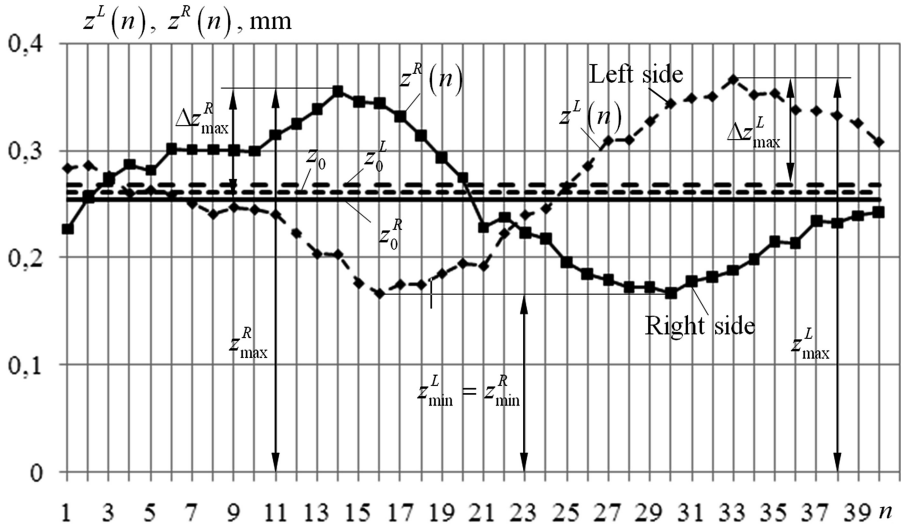
Fig. 1. Distribution of a stock to be removed on the right and left sides of the gear tooth spaces after aligning the stock minimum values.

where $\Delta z_\beta^L(n)$ and $\Delta z_\gamma^L(n)$ are systematic and random components of the variable part of the left-hand stock, mm; $\Delta z_\beta^R(n)$ and $\Delta z_\gamma^R(n)$ are systematic and random components of the variable part of the right-hand stock, mm.

In Eqs. (2) and (3), the systematic component of the variable part of the stock can be replaced by the first harmonic of the corresponding Fourier series, that is,

$$\Delta z_\beta^L(n) = A_1^L \cos(\omega_1 t) + B_1^L \sin(\omega_1 t) \tag{4}$$

$$\Delta z_\beta^R(n) = A_1^R \cos(\omega_1 t) + B_1^R \sin(\omega_1 t) \tag{5}$$

where A_1^L, B_1^L, A_1^R, B_1^R are Fourier coefficients; $\omega_1 t$ is observation interval at the central angle, $0 \leq \omega_1 t \leq 2\pi$.

The stochastic and deterministic models of the stock are developed, on the basis of which the algorithms for determining the maximum stock based on the results of its selective discrete measurements in certain gear tooth spaces are synthesized depending on the number of measurements performed. For up to four measurements are made through the difference between one-sided stocks, that is, accumulated circumferential step and for more eight ones – through a one-sided stock and an accumulated circumferential step.

The maximum stock for the number of measurements $N \leq 4$ is determined by the formula

$$z_{\max} = z_0 + \Delta z_{ran},$$

where $\Delta z_{ran} = \varepsilon$, $\varepsilon = t_\gamma S_{\bar{x}}$, t_γ is confidence coefficient; $S_{\bar{x}} = \frac{s}{\sqrt{k}}$ is mean square deviation of the result, mm; $s = \frac{1}{\sqrt{k-1}} \sqrt{\sum_{n=1}^{k} (x_n - \bar{x})^2}$ is selective mean square deviation, mm. And $x_n = \Delta P(n) = z^L(n) - z^R(n)$, $\bar{x} = \Delta P_0 = \frac{1}{N} \sum_{n=1}^{N} \Delta P_n$ is deflection of the circumferential step and the mean deviation of the circumferential step, respectively.

The maximum stock for the number of measurements $N \geq 8$ found through an accumulated circumferential step is determined by the formula

$$z_{\max} = z_0 + \Delta z_{sys} + \Delta z_{ran} + c_0 \tag{6}$$

where $\Delta z_{sys} = A/2$ is a systematic component that is equal to half the amplitude of the sinusoid recovered by the least squares method at discrete values of the circumferential step; $\Delta z_{ran} = \varepsilon$ for a random component of the deflection of the circumferential step $\Delta P_\gamma(n)$. And $x_n = \Delta P_\gamma(n)$, $\bar{x} = \Delta P_0 = \frac{1}{N} \sum_{n=1}^{N} \Delta P_{\gamma n}$. The amplitude of the deflection of the circumferential step is counted upwards or downwards from the level of the constant component c_0. And $c_0 = z_0^L - z_0^R$.

A large number of measurements lead to additional time expenditures for these measurements, especially for the gear with a large number of teeth. Therefore, reducing the number of measurements is a resource for increasing productivity at the CNC grinding machine setting stage. In turn, the reduction of the number of measurements is accompanied by loss of accuracy of the definition of the maximum allowance value. In this case, the grinding wheel is retracted to a certain distance for a non-predefined grinding, which is due to the maximum allowance value uncertainty. In this regard, the reduction in the number of measurements should be substantiated and investigated.

The theoretical preconditions for optimization of the operation of profile grinding on a CNC machine are developed and tested, according to which the optimization is performed with the help of developed evaluation functions. The first of which is the sum of squares of the difference of the stock extreme values, found by both the limited and maximum number of measurements; the second is the difference of the ordinal numbers of the tooth spaces with the maximum stock, which are found for both the limited and maximum number of measurements. Data on maximum ($z_{\max}^L$ and $z_{\max}^R$) and minimum ($z_{\min}^L = z_{\min}^R$) stocks are used to determine the dispersions D_1 ($z_{\max}^L$), D_2 ($z_{\max}^R$), and D_3 ($z_{\min}^L = z_{\min}^R$), respectively.

Dispersions D_1, D_2, D_3 represent the square of the difference of the corresponding stock, found on the maximum number of measurements for $N = N_{\max}$ (base version) and

the same stock, found for a limited number of measurements at $N < N_{max}$ (compared option version). Evaluation function, i.e. the sum of dispersions D_Σ is determined by the formula

$$D_\Sigma = \left(z_{max}^L(N_{max}) - z_{max}^L(N)\right)^2 + \left(z_{max}^R(N_{max}) - z_{max}^R(N)\right)^2$$
$$+ \left(z_{min}(N_{max}) - z_{min}(N)\right)^2 \tag{7}$$

For example, D_Σ is defined for three gear wheels (GW1, GW2, and GW3) each of them have 29 teeth; the optimal number of measurements of the stock is 9 (Fig. 2a).
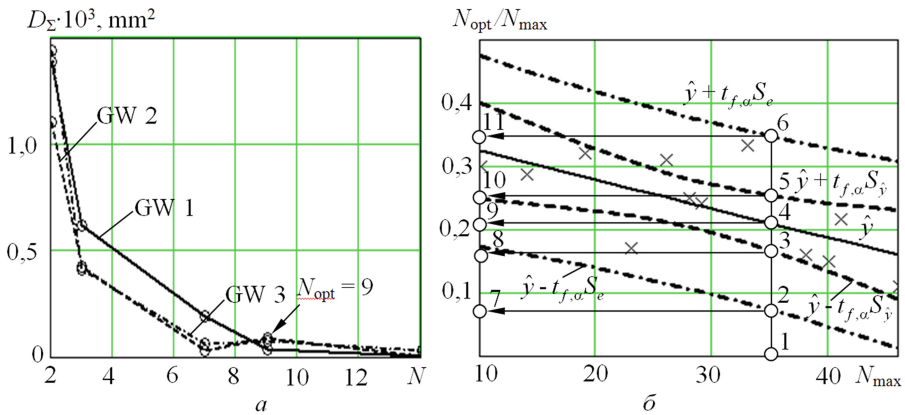
Fig. 2. Evaluation functions (a) and nomogram for determining the optimal number of measurements (b).

A nomogram based on the statistical processing of twenty gears has been developed to select the number of measurements of the stock (Fig. 2b) at the setting up stage of a CNC grinding machine equipped with a Renishaw company's measuring tactile system or a measuring system based on control of acoustic emission signal. Regression analysis has established the linear regression equation: $\hat{y} = 0.36834 - 0.00454N$ (solid line in Fig. 2b). Confidence intervals $\pm t_{f,\alpha}S_{\hat{y}}$ and $\pm t_{f,\alpha}S_e$ (Fig. 2b) to the regression line $\hat{y}$ depend on the following variables: $S_{\hat{y}}$ is standard deviation of regression value $\hat{y}$; S_e is standard deviation of forecast error; $t_{f,\alpha}$ is quantile of t - distribution with f degrees of freedom and at significance level α. For example, it is necessary to find the number of measurements of the allowance on the GW with the number of teeth $N_{max} = 35$ (point 1 in Fig. 2b). Through point 1, the vertical is carried out to intersect with the lines of confidence intervals (points 2, 3, 5 and 6) and the regression line (point 4). Determine the ordinates N_{opt}/N_{max} of all points: for point 7 – 0.072; for point 8 – 0.167; for point 9 – 0.211; for point 10–0.254; for point 11 – 0.349. From here we find $N_{opt} = (N_{opt}/N_{max}) \cdot N_{max}$. We get for N_{opt}: 2.52; 5.85; 7.37; 8.90; 12.22. Thus, the desired result with confidence intervals will be: 7.37 ± 1.53 and 7.37 ± 4.85.

For the grinding operation design, both the parameters of the grinding intensity (Q_w, Q'_w) and the grinding wheel life ones (V_w, V'_w) are used. In the analysis of the profile gear grinding scheme an analogy with the profile rectangular grinding scheme is found as for the volume of material removed per unit time. Consideration of this analogy allowed to formulate and prove the theorem about an equivalent rectangular profile, which at the same grinding depth creates the same cross section area $S_{i+1} = W_{a(i+1)} t_{i+1}$, where $W_{a(i+1)}$ is the active profile width, which is determined on the basis of the known geometric parameters of the profile grinding before $(W_{a\min(i+1)})$ and after $(W_{a\max(i+1)})$ the grinding wheel's profile installation for the next $(i + 1)$-th working stroke. This area depends on the next grinding depth t_{i+1}. A method for determining the active width of an equivalent rectangular profile $W_{a(i+1)}$ for each $(i + 1)$-th working stroke is developed, when the stroke is performed from the previous position of the involute profile $\sum_{k=1}^{i} t_k$ to the its current position $\sum_{k=1}^{i} t_k + t_{i+1}$, after which the stock to be removed value $\sum_{i+2}^{n} t_k$ remains.

According to the theorem on an equivalent rectangular profile the intensity of grinding or material removal rate (in mm^3/s) is determined by the formula

$$Q_{w(i+1)} = S_{i+1} V_f = t_{i+1} W_{a(i+1)} V_f, \tag{8}$$

where $S_{i+1} = W_{a(i+1)} t_{i+1}$ is the section cross area on $(i + 1)$-th stroke, mm^2; V_f is axial feed, mm/s. Knowing the current intensity of the grinding $Q_{w(i+1)}$ (mm^3/s), i.e. during the $(i + 1)$-th stroke, one can find the specific intensity per unit of active grinding wheel width $Q'_{w(i+1)}$ in mm^3/(s mm) and the current amount of removable material $V'_{w(i+1)}$ in mm^3/mm, and regardless of the shape of the profile. These two parameters of the cutting material layer are known as specific material removal rate $(Q'_{w(i+1)})$ and specific material removal $(V'_{w(i+1)})$ [1]. With reference to the Eq. (8) we get for the spur gear:

$$Q'_{w(i+1)} = \frac{Q_{w(i+1)}}{W_{a(i+1)}} = t_{i+1} V_f; \; V'_{w(i+1)} = \frac{Q_{w(i+1)}}{W_{a(i+1)}} \frac{B}{V_f} = B t_{i+1} \tag{9}$$

The conducted theoretical and experimental analysis allowed formulating and proving the following theorem of the gear grinding stock extreme values aligning: the left and the right side gear grinding stocks which aligned by their minimum or maximum values do not depend on the location of the initial tooth space, from which the measurement of the stocks on two sides begins.

4   Results

Theoretical preconditions for the development of built-in automated design, monitoring and profile gear grinding diagnostics subsystems are given [4, 5] to take into account the gear individual characteristics during the gear grinding operation on the CNC grinding machines. On the basis of the research carried out in the workflow, a system of five independent equations has been formed, which is transformed into a system of three equations for automated design, monitoring and grinding diagnostics subsystems development. Introducing the following notation

$$f(W'_w, A_{num}, V_f) = 2 \cdot 10^6 e_c \psi \frac{Q'^{0,75}_w V_f^{-0,25} \sin \alpha}{D^{0,25} \lambda} \sqrt{\frac{a}{\pi}};$$

we get

$$
\begin{cases}
Q'_w = t_v \, V_f \\
q = e_c \psi \frac{V_f t_v \sin \alpha}{\sqrt{D t_v}} \\
T_H = \frac{2 \, q \, \sqrt{a \, \tau_H}}{\lambda \, \sqrt{\pi}} \\
\tau_H = \frac{\sqrt{D} \, t_v}{V_f} \\
V'_w = t_v \, B
\end{cases}
\Rightarrow
\begin{cases}
T_H = f(Q'_w, A_{num}, V_f) \\
V'_w = \frac{Q'_w}{V_f} B \\
Q'_w = t_v \, V_f
\end{cases}
\tag{10}
$$

where e_c is the specific grinding energy in J/mm^3; α is the profile angle in rad.

In accordance with Eq. (10), a block diagram of automated design, monitoring and gear grinding diagnostics computer subsystems is developed, which differs from the existing monitoring system on the CNC machine Höfler Rapid 1250 by the possibility of determining both the specific gear grinding work in J/mm^3 and the gear grinding temperature in °C.

Input parameters for the gear grinding system unit: part drawing data; material thermal diffusivity a in m^2/s; material thermal conductivity λ in W/(m °C); heat partition factor ψ. Input parameters for the calculating device unit: a grinding depth t_v in mm; an axial feed V_f in mm/min; a gear width B in mm, the stock to be removed $\Delta z^L(n)$ and $\Delta z^R(n)$ in mm, AE signal in relative units, and grinding power in W.

The computer subsystem configuration may consist of both hardware and software or may be integrated to the CNC device on the basis of already existing software there. It may comprise a memory and a processor coupled to the memory, etc.

5   Conclusions

1. The paper gives theoretical bases for gear grinding operation automated design, monitoring, and grinding diagnostics computer subsystems to model the gear grinding stock and restore it on the basis of selective equidistant measurements of the stock and to define both the specific material removal rate and the specific material removal. The relationship between these parameters was established as well as that with the temperature of gear grinding.

2. The methods and the computer subsystems that implement them are provided to boost the productivity of the profile gear grinding operation on the CNC machines tools. For example, three such subsystems are considered based on the same generalized computer subsystem configuration: for automated design of gear grinding modes (first), for gear grinding process monitoring (second) and for the process diagnosis (third).

3. The disclosed methodology of gear grinding operation designing, monitoring, and diagnosing may be applicable to any grinding operation. This will help increase the productivity of the corresponding grinding operations in automated production on CNC machines.

References

1. Klocke, F.: Manufacturing Processes 2. Springer, Berlin (2009)
2. Tönshoff, H.K., Friemuth, T., Becker, J.C.: Process monitoring in grinding. CIRP Ann. Manuf. Technol. **51**(2), 551–571 (2002)
3. Freeman, H.: Discrete-Time Systems: An Introduction to the Theory. Wiley, New York (1965)
4. Difference between modelling and simulation. http://www.differencebetween.com/difference-between-modelling-and-vs-simulation/. Accessed 16 Dec 2017
5. Larshin, V.P., Lishchenko, N.V.: Grinding system modelling to simplify decision making. In: XVIIth International Scientific and Technical Conference "The Progressive Techniques, Technology and Engineering Education", pp. 307–309. National Technical University of Ukraine "KPI", Kiev (2017)

Provision of the Quality of Manufacturing Gear Wheels in Energy Engineering

Vladimir Lebedev [ID], Vladimir Tonkonogyi[(✉)] [ID],
Alexey Yakimov [ID], Liubov Bovnegra [ID], and Nataliya Klymenko [ID]

Odessa National Polytechnic University,
1 Shevchenko Avenue, Odessa 65044, Ukraine
vmt47@ukr.net

Abstract. Mathematical modeling of thermal processes during grinding and of the process of formation of residual stresses and cracks is done. On this basis the technique of calculation of thermal processes and of internal residual stresses arising during grinding of wheels made of cemented steels is offered. It is shown that the grinding temperature when machining gears from cemented steels should not exceed the temperature at which the reverse martensitic transformation occurs-the formation of austenite. The formed austenite during grinding does not completely turn into martensite, since the cooling temperature does not overlap the interval Ms-Mf as a result the so-called burnings of hardening are formed. Burnings of hardening 3–4 times reduce the strength and durability of the ground surface, and therefore of the whole part. On the basis of performed calculations, ways of improving the quality of manufacturing of work surfaces of teeth of tooth gears, which are used in aggregates of thermal and nuclear power plants, are proposed and substantiated.

Keywords: Cemented layer · Residual stresses · Solid lubricant
Intermittent circle

1 Introduction

The development of modern power machine engineering goes along the line of continuous increase of speeds, efficiency and power of aggregates. In all cases, when the optimum engine speed is significantly different from the speed of the actuator, a gear reducer is used. Gear transmissions and gearboxes are responsible parts of modern mechanisms and occupy an important place in the domestic power engineering industry. Strength and wear resistance of gears, in addition to design factors, largely depends on the processing techniques. Heavy-loaded cogwheels are made from cemented chromium-nickel and chromium-nickel-tungsten steels 12XH3A (0.12% carbon, 11% chromium, 3% nickel, high-quality), 12X2H4A (0.12% carbon, 2% chromium, 4% nickel, high-quality), 20X2H4A (0.2% carbon, 2% chromium, 4% nickel, high-quality) and 18X2H4MBA (0.18% carbon, 2% chromium, 4% nickel, 1% molybdenum, 1% tungsten, high quality). The final stage of manufacturing of such wheels is the operation of gear grinding. In the process of teeth-grinding in a thin surface layer, complex thermomechanical processes can occur. As a result of short-term

heating to high temperatures in the surface layer the phase and structural transformations occur, called burns, and in some cases even micro and macro-trunks. In addition, there are cases of manufacturing gears with hidden grinding defects (for example, the appearance of large tensile stresses in the surface layer of the tooth), which reduces the service life, and in some cases causes tooth failure under operating conditions. The development of effective measures to ensure the quality of the surface layer in the operation of gear grinding largely depends on the possibility of predicting (or calculating) temperatures and residual stresses over the depth of the cemented layer of teeth.

2   Literature Review

Problems of mathematical modeling of the thermal and stress-strain state of the material of a part during grinding are discussed in [1, 2]. The problems of analytical determination of the values of tensile residual stresses taking into account the heterogeneity of the carbon content in the cemented layer have not been given sufficient attention. The reasons for the formation of surface burns and cracks in the grinding of cemented gears are also analyzed. The harmful effects of grinding are suggested to be reduced by optimizing the parameters of the cutting regime, and the problems of forming the stress-strain state of the surface layer during abrasive processing are considered mainly from the qualitative point of view or are devoted to the experimental study of residual stresses.

The results of mathematical modeling of thermal fields during grinding are shown in [2], but there are no questions of the reason for the appearance of temperature and the change in its values depending on the grinding parameters.

In [3], questions of internal transformations of martensite-nesting steels under different heating conditions are considered, however, the transformations at surface heating, which takes place during grinding, are not illuminated.

In [4], the results of creep tests of martensitic-aging steel are cited for prolonged heating, which also does not correspond to the conditions of heating during grinding.

The sources [5] deal with the effect of alloying elements on the hardening processes of martensitic aging steels, but it is practically impossible to correlate the results with the heating conditions during grinding.

The problems of structural heredity and the conditions for the release of dispersed intermetallic particles from a solid solution under the effect of temperature are considered in [6], which also do not explain the behavior of these steels when heated by grinding.

The results of studies on the change in the strength properties of martensitic-aging steels as a result of structural changes, which, in turn, are the results of temperature changes, are presented in [7]. Despite the interesting data, these materials cannot be used to predict the behavior of these steels when they are heated by the grinding temperature, since in the sources under consideration the heating is volumetric and long, and in the case of grinding, there is a surface and short-term heating.

Thus, by analyzing the data available in the literature, it can be concluded that the behavior of steels is sufficiently well covered when the operating temperature is changed. Practically there is no data on how the characteristics of steels and alloys

change after exposure to a grinding temperature, the values of which can be higher than the operating temperatures.

The objective of the research is to develop a procedure for calculating temperatures and residual stresses that arise during teeth grinding at different levels of the cemented layer, and to suggest ways how to improve the thermal and stress-strain state of the surface layer of the teeth in abrasive processing.

3 Research Methodology

Mathematical modeling of thermal processes during grinding, modeling of the process of formation of residual stresses and cracks is done. The advantage of this method is that, computing experiment can be covered the steels of a different chemical composition.

In the surface layers of cemented parts during grinding, stresses of a different magnitude and sign are formed. Residual stresses arise as a result of the interaction of plastically and elastically deformed layers. If the plastically deformed layers after cooling tend to increase their length in comparison with the initial one, then the elastic-deformed layers tend to return to the original length. Consequently, some layers will experience compressive stresses, while others will stretch. These stresses remain in the part after grinding and are therefore called residual. The main danger in grinding is the occurrence of residual tensile stresses of considerable magnitude, which can lead to cracking of the surface cemented layer. The cause of the occurrence of residual stresses during grinding with an unchanged phase-structural composition of the cemented layer is the grinding temperature, which leads to uneven thermal expansion of its individual microlayers, which causes the formation of residual stresses. In addition, it should be borne in mind that in the phase and structural transformations, additional causes for the formation of residual stresses are created because the density of each phase and structure formed is different.

When calculating the grinding temperatures, two things must be considered:

1. The intensity of the heat flow is unevenly distributed over the contact spot of the grinding wheel with the workpiece. At the beginning of the trajectory of the cutting grain passing through the material being treated, the intensity of the thermal current is smaller, and at the end of the trajectory, where the cross section of the chip is maximal, it is higher. Thus, it is necessary to determine the temperature of the cutting surface, taking into account the heat flux density, which is unevenly distributed over the contact spot of the grinding wheel with the metal.
2. It is of practical interest to know the temperatures that arise not only on the cutting surface (that is, on the surface where the chips are currently being formed), but also on the machined surface located below the cutting surface. In addition, to calculate the thermal residual stresses, it is necessary to know how the temperatures are distributed deep into the cemented layer.

To solve the first problem, we choose a coordinate system X, Y, Z on the surface of a semi-infinite body. Let us agree that heat is supplied to a certain region bounded by a rectangle whose sides are parallel to the X and Y axes:

$$-a \leq x \leq a, -b \leq y \leq b, \tag{1}$$

where $a = \frac{\sqrt{D_w \cdot t}}{2}$, $b = \frac{S}{2}$, D_w – diameter of grinding wheel, t - depth of grinding, S - transverse feed. Outside this region, there is no heat flow through the surface of the part. The heat source is assumed to be immovable, and the surface of the workpiece is moving with the velocity V_p in the direction of decrease of the coordinate.

Let us consider the steady-state thermal regime when $\tau \to \infty$. For an elementary area with a center with coordinates, the distribution of temperatures is described by the dependence [9]:

$$T_1(z) = \frac{q(x)}{2\pi\lambda_1} \cdot \frac{1}{R} exp\left(-\frac{V_p \cdot r + V_p \cdot (x_0 - x)}{2a_1\tau}\right) \tag{2}$$

where T_1 is the temperature at the cutting surface, °C; x, y, z - current coordinates of the position of the part, m; $q(x)$ - the specific intensity of the heat flux at a given point of the contact spot of the grinding wheel with the workpiece, Bt/m²; λ_1 - coefficient of thermal conductivity of the cutting surface, W/m · °C; $R = \sqrt{(x_0 - x)^2 + (y_0 - y)^2 + z^2}$ - radius-vector of coordinates; V_p - speed of moving parts relative to a fixed thermal source, m/min; τ - the moment of time, s; x_o - coordinate at time τ_0, m; r - radius of curvature of the cutting grain, m; a_1 - coefficient of thermal diffusivity of the cutting surface, m²/s.

Integrating expression (2) we obtain:

$$T_1(z) = \frac{1}{2\pi\lambda_1} \int\limits_{-a}^{+a} q(x)dx \int\limits_{-b}^{+b} dy \left\{ \frac{1}{R} \cdot exp\left[-\frac{v_P^r + v_p(x_0 - x)}{2a_1\tau} \right] \right\} \tag{3}$$

where a, b are the half-width and half-length of the contact spot of the circle with the detail, m.

To solve the second problem means, to bring the temperature on the surface to the temperature of the worked surface, it can be imagined that a certain body, heated to temperature T_1 and consisting of the material of the part, abrasive grains and the bundle of the circle, moves along this surface. Each point of the treated surface is in contact with this body for a period of time $\tau = \frac{\sqrt{D_w \cdot t}}{V_p}$.

To simplify the problem, it can be imagined that two semi-bounded bodies with heat-insulated lateral surfaces are brought into contact with each other at the initial moment of time τ_0 the temperature of the first body T_1 is equal to the surface temperature of the cutting surface, and the temperature of the second body is equal to the temperature of the treated surface T_2. It is necessary to find the temperature of the second body at times from $\tau = 0$, to $\tau = \frac{\sqrt{D_w \cdot t}}{V_p}$ (Fig. 1).
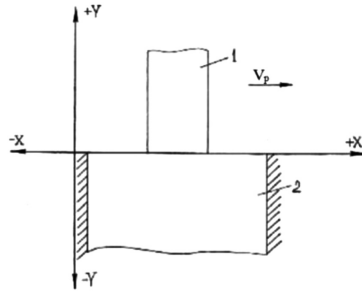
Fig. 1. The scheme of contact of two solid bodies (boundary conditions of the fourth kind).

Thus, the problem reduces to solving the heat equation under boundary conditions of the fourth kind, which corresponds to the contact of two solids with different temperatures.

The solution of this problem is given in the source [10]. Using this data, we have

$$T_2(z, \tau) = \frac{T_{01}\, \varepsilon_1}{\varepsilon_2 + \varepsilon_1} \left(1 - erf \frac{|z|}{2\sqrt{a_2\tau}}\right) \qquad (4)$$

where $T_{01} = T_1$ is the temperature at the cutting surface, °C.

Thus, considering the temperature at the cutting surface (2), the grinding temperature $T_2(z, \tau)$ applied to the treated surface, taking into account that the power of the heat source is unevenly distributed over the contact spot of the grinding wheel with the workpiece, and the thermal power at a given point of the contact spot depends on the certain coordinate x is:

$$T_2(z, \tau) = \frac{\varepsilon_1 \cdot \int\limits_{-a}^{+a} q(x)dx \int\limits_{-b}^{+b} dy \left\{\frac{1}{R} \cdot exp\left[-\frac{v_p^2 + v_p(x_0 - x)}{2a_1\tau}\right]\right\}}{2\pi\lambda_1(\varepsilon_2 + \varepsilon_1)} \left(1 - erf \frac{z}{2\sqrt{a_2\tau}}\right) \qquad (5)$$

where $\varepsilon_1, \varepsilon_2$ - the coefficients of thermal activity, respectively, of the thermal source and the treated surface, $\varepsilon = \sqrt{\lambda c\gamma}\cdot 10^3$ J/m² °C · s$^{0.5}$, λ - coefficient of thermal conductivity j/m °C · s, c - specific heat-J/kg °C, γ - density-kg/m³

The values of the residual stresses arising at different levels of the cemented layer can be determined using the expression:

$$G_2(z) = \frac{E_2\alpha_2\varepsilon_1 \int\limits_{-a}^{+a} q(x)dx \left\{\frac{1}{R} \cdot exp\left[-\frac{V_p^2 r + V_p^2(x_0 - x)}{2 \cdot a_1 \cdot \sqrt{D_{kp}\cdot t}}\right]\right\} \left(1 - erf \frac{z \cdot \sqrt{V_p}}{2\sqrt{a_2\sqrt{D_w\cdot t}}}\right)}{(2 - 2 \cdot \mu_2)\cdot 2\pi\lambda_1(\varepsilon_2 + \varepsilon_1)} \qquad (6)$$

where E_2 is the modulus of elasticity of the cemented layer, MPa; α_2 linear coefficient of thermal expansion of the cemented layer, 1/°C; μ_2 Poisson's coefficient of the cemented layer.

The values of the power of the heat source which are necessary both for solving the temperature problem and for solving the problem of determining residual stresses can be determined from the source, depending on the processing modes
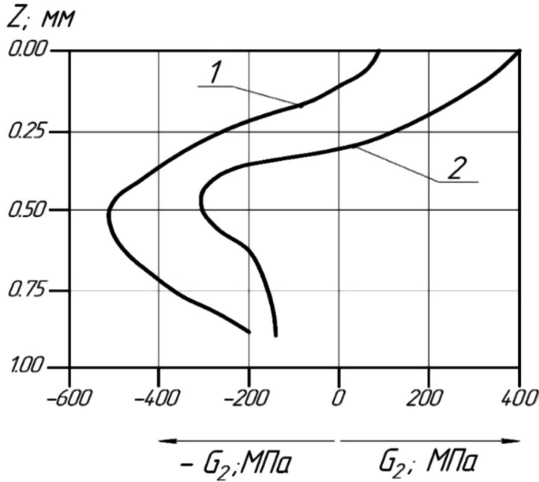
Fig. 2. Distribution of internal residual stresses in the depth of the cemented bed for two grinding modes: $1 - t = 0,015$ mm; $2 - t = 0,1$ mm.

Figure 2 shows the calculated curves describing the distribution of internal residual stresses over the depth of the cemented layer after grinding 18X2H4BA steel with cutting depths of $t = 0,1$ mm (without cooling) and $t = 0,015$ mm (with cooling).

The cemented layer consists of three zones [11] - the hypereutectoid zone, with a carbon content of up to 1.2%, a eutectoid zone with a carbon content 0.8%, a pre-eutectoid zone with a carbon content of 0.3–0.7%. The thermophysical characteristics vary slightly depending on the carbon content and doping.

As the distance from the surface increases, the tensile stresses decrease and become compressive. When grinding according to the most severe regime (curve 2), the compressive stresses are obtained as the least. The appearance of tensile stresses during the grinding of gears leads to a decrease in their fatigue strength.

The calculation of internal residual stresses was carried out considering the change in the thermophysical characteristics in the zones of carburization. The appearance of grinding cracks is facilitated not only by the residual, but also by the time tensile stresses that arise during grinding upon cooling to the temperatures at the onset of the martensitic transformation [8]. The cause of crack formation are high contact temperatures and temperature gradient in the cutting zone, as well as high cooling rates of the treated surface after it leaves the contact zone with the abrasive wheel.

To reduce internal tensile stresses and the likelihood of crack formation, it is necessary to reduce the temperature in the cutting zone and the cooling rate by all available means [8]. This can be achieved with the use of various lubricating-cooling agents, solid lubricants and pastes.

4   Results

Most often, thermal grinding defects are formed in cementitious, improved high-carbon steels, low- and medium-alloyed, with a martensite structure or tempered martensite. With rapid heating by the grinding temperature of the surface of the grinded part of the hardened steel above the Ac_1 line, the martensitic structure of the surface layer transforms into an austenitic structure, that is, an inverse martensitic transformation takes place. This transformation is even more facilitated by the fact that as a result of the high specific pressures exerted by the abrasive grains on the surface of the metal, the point Ac_1 may decrease to lower temperatures.

After a rapid heating of the surface layer, rapid cooling follows with rates significantly exceeding the critical quenching rates. The points Mk for these steels are mostly below 20 °C, that is, at the same temperature, to which the metal cools during grinding. As a result, the martensitic transformations do not take place completely, as a result of which a structure of austenite of the secondary quenching is fixed in the surface layer, resulting in the name of the grinding burn of quenching.

The final cooling of the austenite structure takes place at a temperature interval of 20 °C and lower. The cooling process ends between points Mn and Mk. The temperature interval until the end of the martensitic transformation does not overlap, which causes incompleteness of this transformation and fixation of a significant part of the austenite.

Phase-structural changes in the surface layer of hardened steel during grinding are called grinding burns. Burns are caused by high residual stresses and cracks in the surface layer, a decrease in the wear resistance of the ground surface. This reduces the strength, reliability and durability of the ground surface, and, consequently, of the entire part.

To reduce internal tensile stresses and the likelihood of crack formation, it is necessary to reduce the temperature in the cutting zone and the cooling rate by all available measures.

5   Conclusions

A technique for calculating the internal residual stresses arising when gears are grinded from cemented steels is proposed.

Based on the performed calculations and experiments, ways to improve the quality of manufacturing of the working surfaces of tooth gears used in thermal and nuclear power plants are proposed and justified.

Using the proposed mathematical models allows to assign grinding modes that provide temperatures lower than the austenite formation temperatures, which completely eliminates grinding rejection.

Scientific novelty lies in the fact that the proposed mathematical models make it possible to solve the problem comprehensively for grinding any steel, depending on its chemical composition.

References

1. Korchak, S.: Theory of machinability of steels and alloys in abrasive processing. Herald South Ural State **9**(4), 82–90 (2003)
2. Melnikova, E.: Influence of technological factors of finishing abrasive treatment on the surface quality. Technol. Mach. Build. **3**, 13–16 (2003)
3. de Carvalho, L.G., Andrade, M.S., Plaut, R.L., Souza, F.M., Padilha, A.N.: A dilatometric study of the phase transformations in 300 and 350 maraging steels during continuous heating rates. Progr. Nat. Sci. Mater. Int. **24**, 35–41 (2013)
4. dos Reis, A.G., Reis, D.A.P., Abdalla, A.J., Otubo, J.: Creep properties evaluation at 600 °C of maraging 300 steel solution treated. Technol. Metal. Mater. Miner. **11**, 22–26 (2014)
5. Rao, M.N.: Progress in understanding the metallurgy of 18% nickel maraging steels. Int. J. Mater. Res. **97**, 1594–1607 (2006)
6. Sha, W.: Thermodynamic calculations for precipitation in miraging steels. Mater. Sci. Technol. **19**, 1434–1436 (2013)
7. Nizhnik, S., Usikova, G.: Investigation of structural conditions for improving the characteristics of strength, plasticity, and fracture toughness of maraging steels. Strength Mater. **32**, 141–148 (2000)
8. Leitnera, H., Schoberb, M., Schnitzera, R., Zinnerc, S.: Strengthening behavior of Fe–Cr–Ni–Al–(Ti) maraging steels. Mater. Sci. Eng. **528**, 5264–5270 (2011)
9. Yakimov, A.: Thermal processes during tooth grinding and their effect on the durability of gear wheels. Equipment and tools for professionals (series - metalworking). Int. Inf. Technol. **1**(144), 68–70 (2012)
10. Tritt, T.M.: Thermal Conductivity. Theory, Properties, and Applications. Springer, New York (2004)
11. Gulyaev, A.P.: Metal Science. Aliance, Moscow (2011)

Combined Laser-Ultrasonic Surface Hardening Process for Improving the Properties of Metallic Products

Dmytro Lesyk[1(✉)] , Silvia Martinez[2] , Bohdan Mordyuk[3] ,
Vitaliy Dzhemelinskyi[1] , and Oleksandr Danyleiko[1]

[1] Department of Laser Systems and Physical Technologies, National Technical
University of Ukraine "Igor Sikorsky Kyiv Polytechnic Institute", 37 Peremohy
Avenue, Kyiv 03056, Ukraine
`lesyk_d@ukr.net`
[2] Department of Mechanical Engineering, University of the Basque Country,
Alameda Urquijo s/n, 48013 Bilbao, Spain
[3] Department of Physical Principles for Surface Engineering, G.V. Kurdyumov
Institute for Metal Physics of the NAS of Ukraine, 36 Academician Vernadsky
Boulevard, Kyiv 03680, Ukraine

Abstract. Combined laser-ultrasonic hardening and finishing process of large-sized products using laser heat treatment (LHT) followed by the ultrasonic impact treatment (UIT) is proposed. In this study, a medium carbon and chromium tool steels were heat treated by a 1 kW fiber laser with scanning optics and heating temperature control system to improve their surface hardness. A number of experiments are carried out by changing the heating temperature and specimen feed rate while keeping a constant scanning speed and width to produce the hardened layers of different depths. After the LHT, the specimen surfaces were severely deformed by an ultrasonic tool equipped with a seven-pin impact head supplied by a 0.3 kW ultrasonic generator and controlled by a computer-driven machine to form a regular surface microrelief and compressive residual stresses. The results indicate that the combined treatments provide more than triple increase in the surface hardness and formation the compressive residual stresses. Additionally, the LHT + UIT leads to a formation of the regular surface microrelief with minimum surface roughness and high oil holding capacity.

Keywords: Laser-ultrasonic hardening · Scanning optics
Multi-pin impact head · Temperature control · Regular microrelief
Hardness

1 Introduction

The quality of metallic surfaces is one of the important characteristics that affect the reliability as well as durability of the end-products. An increase of operational life of the surface layer of products by forming a regular microrelief with minimized roughness and a grained microstructure with high surface hardness reduces the cost of energy and material resources. It is, therefore, an important criterion for the increased competitiveness of the manufactured products. Consequently, the advanced combined

or hybrid methods applied to the surface hardening of products using the heat treatment combined with severe plastic deformation may significantly improve the surface roughness and physical-mechanical properties of the modified surface layer.

2 Literature Review

Traditional thermal methods of the surface hardening have been used in the industrial processes for decades. However, novel methods for the surface hardening, cladding or alloying using the highly-concentrated energy sources, such as plasma arc and laser beam are developed to improve the operational properties of the large-sized products at their production or repair [1–4]. In particular, plasma processing of steel parts without surface melting may harden the surface layer to ~ 850 HV to the depth of 0.5… 2.5 mm depending on the processing regimes and the workpiece type [5]. As a result, it allows 2…4 times increasing the wear resistance of the treated surfaces. Herewith, the parameters of the surface microrelief remained practically unchanged.

Another technological solution is the use of laser heat treatment (LHT) [2, 6]. Depending on the chemical composition of the treated materials and the duration of laser exposure the LHT can cause microstructural changes in the surface layers of the steel products at a laser power density of $10^3…10^4$ W/cm^2. In this case, the hardening depth is 0.02…0.5 mm, and microhardness of the surface layer is up to ~ 1000 HV [7]. It should be noted that high-power fiber, diode, and disk lasers have been developed to accelerate the implementation and competitiveness of LHT in mechanical engineering industry for the last decade [8–11].

However, the use of a plasma/laser surface modification combined with surface-plastic deformation (SPD) methods allows a significantly greater effect in increasing the strength, reliability, and durability of the surface layer due to the high hardness, ultrafine-grained microstructure, the formation of compression residual stresses and surface microrelief with a minimum surface roughness [7, 12, 13]. A deep rolling [14], shot peening [15] or cavitation peening [16], as well as ultrasonic impact treatment (UIT) [8, 17] are the most common SPD methods, which can be used in combination with LHT. The UIT has several advantages over other SPD methods.

The purpose of this work is to improve the combined laser-ultrasonic surface hardening process for processing of the large-sized steel products.

3 Research Methodology

The carbon steel AISI 1045 and tool steel AISI D2 were studied. Initially, the specimens of these steels were annealed and further machined. The chemical composition and the initial hardness of the materials used are summarized in Table 1.

The laser transformation hardening of the specimens was performed using a laser technological complex (Fig. 1). The laser technological complex contained a Rofin Sinar FL010 fiber laser with a maximum output power of 1 kW, a Kondia Aktinos B500 milling center with a computer numerical control (CNC) and a Scanlab Hurryscan25 scanning optics [7, 18].

Table 1. Chemical composition and initial hardness of the materials used.

Chemical composition (wt.%)										Initial HRC$_1$
Name	C	Mn	Cr	Mo	V	Si	Ni	Cu	Fe	
AISI 1045	0.45	0.65	0.18	–	–	0.25	0.20	0.23	Bal.	18.6
AISI D2	1.55	0.46	11.3	0.83	0.72	0.42	0.15	0.06	Bal.	19.6
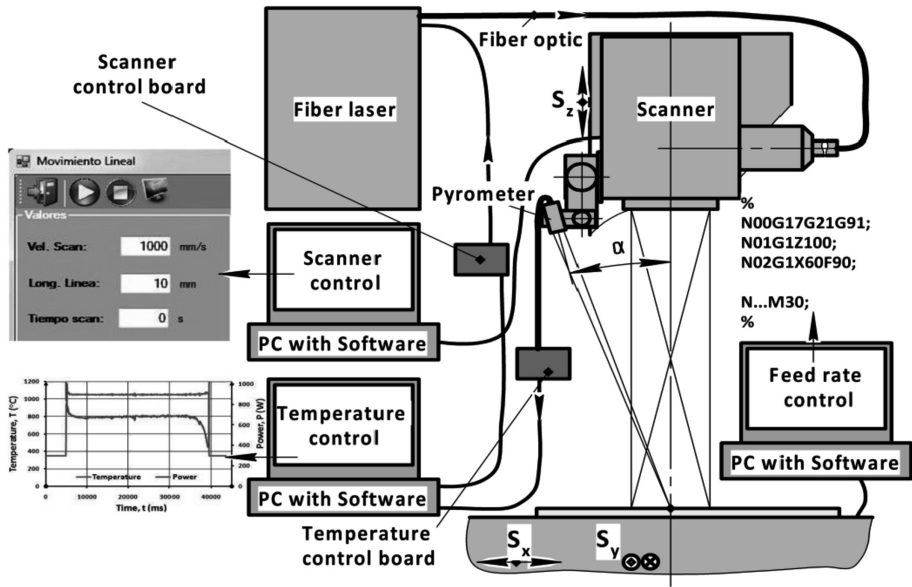
Fig. 1. Block-scheme of the equipment for the laser surface hardening.

Measurement of the surface temperature in the laser affected area was performed using the two-colored Impac Igar 12LO pyrometer. The heating temperature control was carried out using a special proportional-integral-differential (PID) controller and software. The LHT of the studied specimens was performed by changing the heating temperature (900…1340 °C) and specimen feed rate (40…140 mm/min) while keeping a constant scanning speed (1000 mm/s) and scanning amplitude (10 mm) to produce different sizes of the hardened layer.

The ultrasonic strain hardening of the specimens was conducted using a technological equipment [7, 18], which consisted of a DYNAMITE 2800 milling machine with CNC, an ultrasonic generator (power of 0.3 kW), an ultrasonic vibration system (ultrasonic tool) and an electromotor (Fig. 2a). The machine was controlled by the Mach3 system. The ultrasonic tool contained a piezoceramic transducer, a cylindrical waveguide horn, and a seven-pin impact head. UIT was carried out at the vibration amplitude and frequency of ultrasonic horn of 15…18 μm and 21 kHz, UIT durations of 60…240 s, static load of the ultrasonic tool of 50 H, and a rotational speed of 76 rpm. The UIT was conducted with an overlapping of tracks of approximately 10% to avoid overstraining (Fig. 2b).
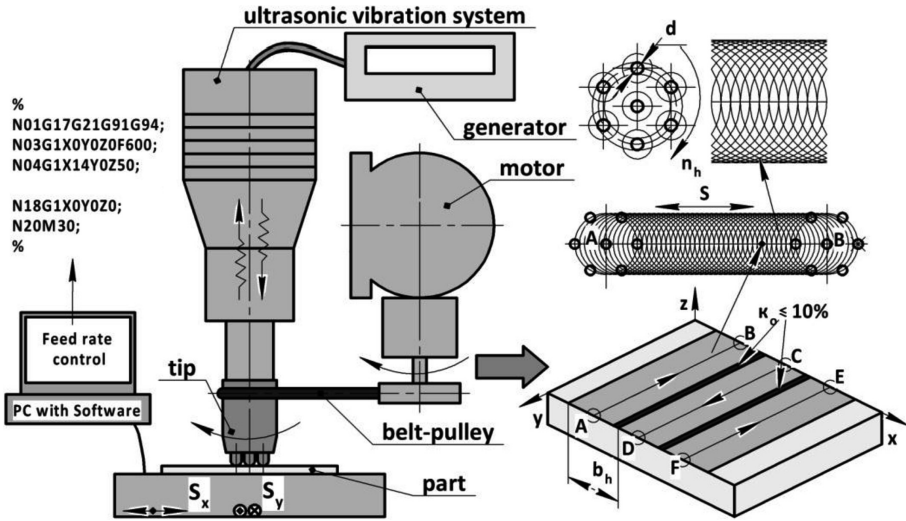
Fig. 2. Block-scheme of the equipment for the ultrasonic surface hardening.

Surface microrelief was studied by means of an optical 3D profilometer Leica DCM3D. Surface hardness/microhardness measurement was performed using a Computest SC and FM800 digital hardness testers respectively.

4 Results

4.1 Laser Transformation Hardening Process with Heating Temperature Control

To improve the laser transformation hardening process a system consisted of the non-contact pyrometer, a special board, and the software was applied together with the LTH methodology allowing the maintenance of a constant heating temperature. In this case, during the LHT, the surface temperature measured by the pyrometer was trans-mitted through the PID controller to a special board that converts digital signals into the analog ones and vice versa. Then, these analog signals (that are proportional to a power of the laser radiation) came to the laser control system (Fig. 3).
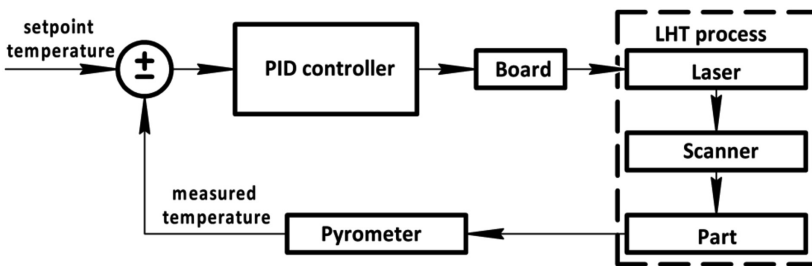
Fig. 3. Block diagram of the heating temperature PID algorithm.

Consequently, the LHT applying the constant temperature strategy is carried out, which, in contrast to the constant power strategy, allows avoiding undesirable surface melting in the sites where the work piece dimensions are markedly changed (Fig. 4).

Thus, the implementation of the PID control loop for the LHT allows maintaining the set-point temperature Ts in the laser affected area, adjusting the laser power:

$$P(t_{i+1}) = k_p e(t_i) + k_i \int_{t_0}^{t_1} e(t)dt + k_D \frac{de(t_i)}{dt_i}, \qquad (1)$$

where P is the laser power, k_p is the proportional constant, k_i is the integrative constant, k_D is the derivative constant, $e(t)$ is the error signal, which is defined as the difference between the measured surface temperature T_m and the set-point temperature T_s $(e(t_i) = T_s - T_m(x(t_i), t_i))$.
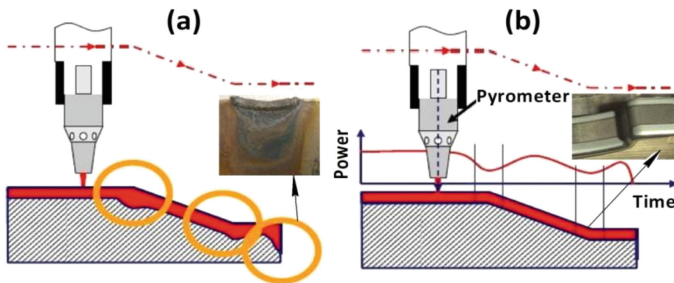
Fig. 4. Laser transformation hardening process applying the constant power strategy (a) and the constant temperature strategy (b).

The visualization of the heating temperature control and the change in the laser power at the LHT speed of 90 mm/min are shown in Fig. 5a.
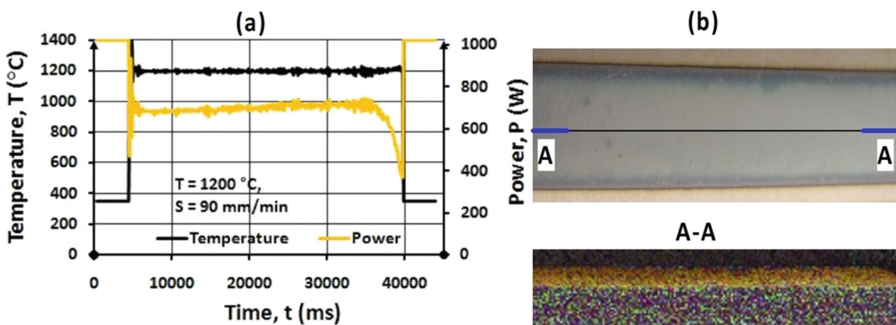
Fig. 5. PID control of the heating temperature (a) and hardened track of AISI 1045 steel (b).

Thus, the LHT applying the constant temperature strategy, using a fiber laser and scanning optics, can be successfully implemented in the industry to process flat/cylindrical as well as complex shaped metallic products without the surfaces melting. In contrast to the LHT, applying the constant power strategy [2], the LHT with the maintaining of constant temperature in the laser affected area avoids undesirable melting of the work piece surfaces. Herewith, the hardening depth uniformity is achieved (Fig. 5b). The laser systems for hardening of the metallic surfaces were shown to be controlled using a fiber, diode or disk laser with special scanning optics [7–11].

The aforementioned laser hardening systems allow conducting the LHT without absorbent coatings and significantly improve the LHT productivity, providing the desired uniform hardened zone and surface layer properties, which might hardly be obtained by other thermal processing methods.

4.2   Formation of the Regular Microrelief by the Ultrasonic Tool with CNC

The UIT applying the mono-pin or multi-pin head (Fig. 6) is successfully used in the industry to form a regular Microrelief. In this case, an ultrasonic tool can be kinematically moved both in a simple and complex manners according to the treated surface by means of application of the control programs. It allows producing the surface microreliefs of the known and new types and realizing any law of their change. It should be noted that the surface microrelief after the UIT is characterized by high uniformity and a specific number of impacts due to the rotation of the multi-pin impact head (Figs. 2c, 6e, f) [7, 18].
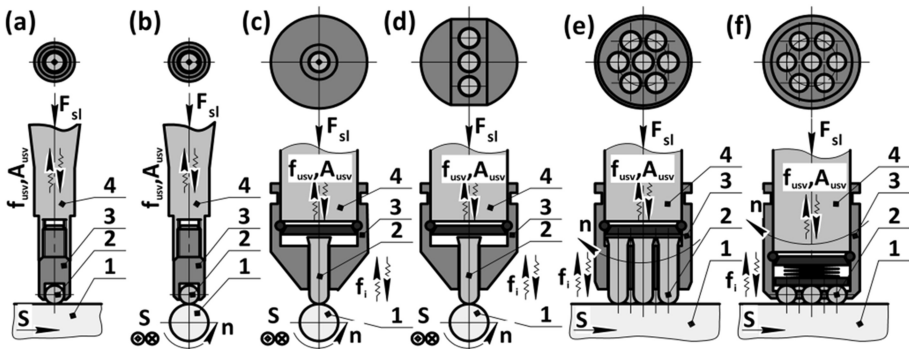
Fig. 6. Kinematic schemes of UIT of the flat (a, e, f) and cylindrical (b–d) surfaces using mono-pin and multi-pin head: 1 – part, 2 – pin(s), 3 – head, 4 – horn.

The most common schemes of linearly regular microreliefs (Fig. 7) on a flat surface were produced using control programs. It allows creating the desired movement trajectory of an ultrasonic tool along the treated surface.
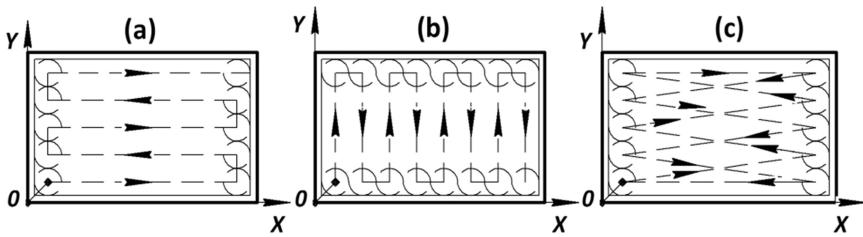
Fig. 7. Schemes of the movement trajectories of an ultrasonic tool along the length (a), along the width (b), and inclined to the length (c).

Figure 8 shows the movement trajectory of the multi-pin impact head and control program developed for the ultrasonic processing of the roller conveyor.
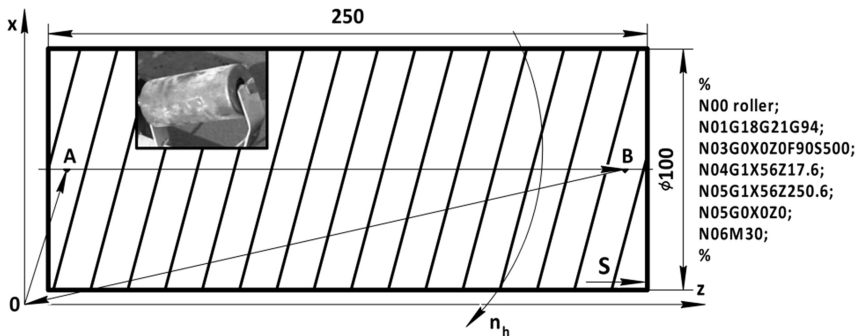
Fig. 8. Scheme and control program for UIT of the roller conveyor.

Thus, the kinematic schemes of UIT and the schemes of the movement trajectories of the ultrasonic tool, as well as the developed control programs allow automating the ultrasonic hardening and finishing process, and increase the UIT productivity.

4.3   Surface Topography and Hardness

The experimental results (Fig. 9) show that the LHT followed by UIT using a multi-pin ultrasonic tool leads to the formation of a regular microrelief on the surface due to the forced rotation of the impact head and the specimen feed rate in accordance with the control program. In this case, the surface roughness is decreased, and the surface waviness is increased due dynamic as well as rotational action of the pins. In particular, the combined treatment leads to a double or higher reduction in Ra parameter depending on the initial state of the surface.

It is shown in [18] that an increase in the UIT duration causes a decrease in the surface roughness parameters and simultaneous enhancement of the waviness parameters of the surface. Additionally, increasing the vibration amplitude of the ultrasonic horn slightly leads to an increase in roughness as well as waviness parameters of the surface due to the high-frequency recurrent impact action of the pins. Thus, the combination of LHT + UIT provides favorable conditions to trap oil on the product

surface due to the formation of a wavy regular microrelief with a low roughness parameter Ra in the range 0.4…0.2 μm. Consequently, it promotes less intensive wear of the treated surfaces.
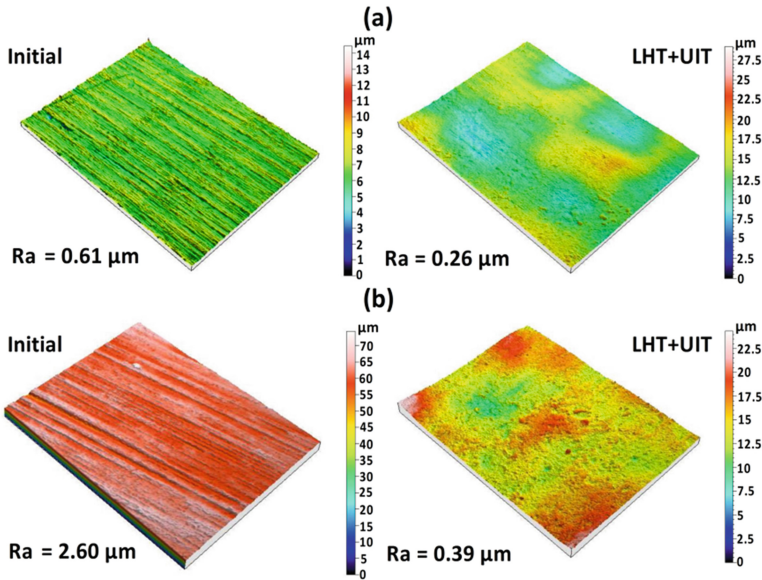
Fig. 9. Surface topography after the combined treatment of AISI 1045 (a) and AISI D2 (b) steels.

The LHT combined with UIT increases the surface hardness more than three times as compared to the initial state due to the formation of ultra-fine grained microstructure [7], providing the hardening depth of 200…450 μm (Fig. 10). It is of interest that the LHT regime used results in the higher surface hardness of AISI 1045 than those of, AISI D2. It is due to the fact that the heating/cooling rates used were either high enough to form ultrafine-grained microstructure fixed with fine carbides (AISI 1045) or, conversely, insufficient for the carbides dissolution/precipitation (AISI D2). It is well known that the more carbide-forming elements the steel contains, the more processing time is needed to obtain a homogeneous microstructure and high hardness.

Figure 11 shows the microstructure and heat/strain affected zone in the cross section of AISI 1045 steel at a heating temperature of 1300 °C and speed LHT of 50 mm/min as well as the corresponding microhardness distribution. A severe ultrasonic surface–plastic deformation (Ausv = 18 μm, t_{UIT} = 120 s) of the hardened surface by LHT leads to form a complex distribution of microhardness and 10…15% increase in the surface hardness by additional strain induced refinement of martensitic grains in the near-surface layer.

Moreover, the magnitude of the compression residual stresses after a combined processing (σ_R = − 405 MPa) is increased 2 times as compared to a single LHT. These
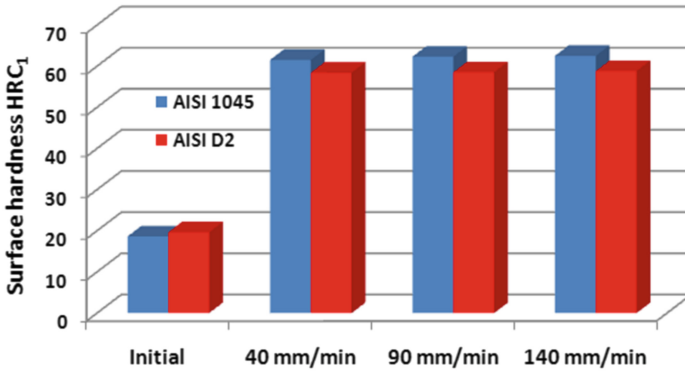
Fig. 10. Surface hardness after a combined treatment.
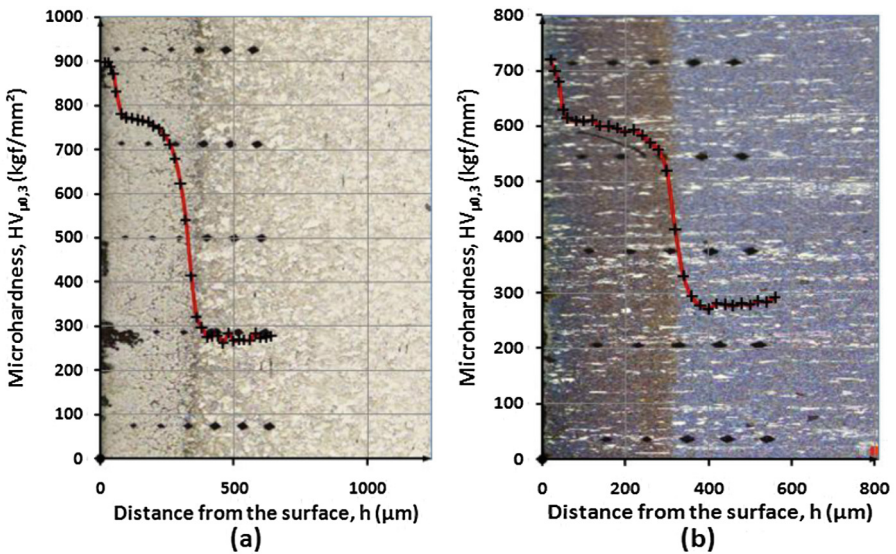
Fig. 11. Microstructures and depth distributions of microhardness in the hardened layers of AISI 1045 (a) and AISI D2 (b) steels after a combined LHT + UIT treatment.

factors lead to an increase in the friction force and wear resistance both in the quasi-static and dynamic test conditions [7].

As a result, a formed refined microstructure and regular microrelief on the surface allow double or higher increase in the wear resistance of the studied steels. Moreover, a combined treatment would provide the high oil capacitance and the corrosion resistance of the treated surfaces.

5   Conclusions

Laser transformation hardening process combined with the ultrasonic strain hardening process was carried out to improve the surface microrelief and hardness of AISI 1045 and AISI D2 steels. The following conclusions can be drawn:

1. A uniform hardened zone can be produced using the LHT by applying a constant temperature strategy. The depth of the hardened layer (200…450 μm) was established to meet the industrial application requirements.
2. The developed technological solutions allow automating the combined laser-ultrasonic surface hardening process, forming a regular micro relief on the surface (Ra = 0.4…0.2 μm), increasing the surface hardness on 10…15% compared to LHT and the productivity of the LHT + UIT.
3. The proposed combination of LHT + UIT can be used for local hardening of the large-sized parts in the mechanical engineering industry.

References

1. Wagiman, A., et al.: Effect of heat treatment parameters in plasma arc surface hardening of AISI 4340 steel. Appl. Mech. Mater. **699**, 105–110 (2015)
2. Guarino, S., et al.: High Power Diode Laser (HPDL) surface hardening of low carbon steel: fatigue life improvement analysis. J. Manuf. Proc. **28**(1), 266–271 (2017)
3. Santhanakrishnan, S., et al.: An experimentally based thermo-kinetic hardening model for high power direct diode laser cladding. J. Mater. Proc. Technol. **211**, 1247–1259 (2011)
4. Klachuk, S., Bamberger, M.: Laser surface alloying of 1045 AISI steel using Ni–CrB$_2$ powder. J. Mater. Sci. Technol. **26**(9), 1059–1067 (2010)
5. Ismail, M.I.S., Taha, Z.: Surface hardening of tool steel by plasma arc with multiple passes. Int. J. Technol. **5**, 79–87 (2014)
6. Kusinski, J., et al.: Laser modification of the materials surface layer – a rewire paper. Int. Tech. Sci. **60**, 710–728 (2012)
7. Lesyk, D.A., et al.: Microstructure related enhancement in wear resistance of tool steel AISI D2 by applying laser heat treatment followed by ultrasonic impact treatment. Surf. Coat. Technol. **328**, 344–354 (2017)
8. Liua, A., Previtali, B.: Laser surface treatment of grey cast iron by high power diode laser. Phys. Procedia **5**, 439–448 (2010)
9. Klocke, F., et al.: Optimization of the laser hardening process by adapting the intensity distribution to generate a top-hat temperature distribution using freeform optics. Coatings **7**, 1357–1366 (2017)
10. Qiu, F., Kujanpaa, V.: Surface hardening of AISI 4340 steel by laser linear oscillation scanning. Surf. Eng. **28**, 569–575 (2012)
11. Schuöcker, D., et al.: Improved laser hardening process with temperature control avoiding surface degradation. In: 8th International Conference on Photonic Technologies, pp. 108–120. LANE (2014)

12. Tian, Y., Shin, Y.C.: Laser-assisted burnishing of metals. Int. J. Mach. Tools Manuf. **47**, 14–22 (2007)
13. Wanga, Z., et al.: Influence of shot peening on the fatigue life of laser hardened 17-4PH steel. Int. J. Fatigue **33**, 549–556 (2011)
14. Balland, P., et al.: An investigation of the mechanics of roller burnishing through finite element simulation and experiments. Int. J. Mach. Tools Manuf. **65**, 29–36 (2013)
15. Soady, K.A., et al.: The effect of shot peening on notched low cycle fatigue. Mater. Sci. Eng. A **528**, 8579–8588 (2011)
16. Gill, A., et al.: Comparison of mechanisms of advanced mechanical surface treatments in nickel-based superalloy. Mater. Sci. Eng. A **576**, 346–355 (2013)
17. Li, L., et al.: Influence of multiple ultrasonic impact treatments on surface roughness and wear performance of SUS301 steel. Surf. Coat. Technol. **307**, 517–524 (2016)
18. Lesyk, D.A., et al.: Laser hardened and ultrasonically peened surface layers on tool steel AISI D2: correlation of the bearing curves' parameters, hardness and wear. J. Mater. Eng. Perform. **27**, 764–776 (2018)

Influence of the Scale Factor of Fibers and the Temperature of Structuring on the Physical and Mechanical Characteristics of Hemp Fiber Biocomposites

Mykola Melnychuk[✉] and Oksana Andrushko

Lutsk National Technical University, 75 Lvivska St., Lutsk 43018, Ukraine
m.melnychuk@lntu.edu.ua

Abstract. According to sustainable development approaches in the world, there are tendencies to save renewable resources, or resources with a long recovery time. This research aims to develop new composite materials based on the renewable resource in the form of hemp fibers. The article shows the results of research of mechanical characteristics (impact toughness, tensile strength, hardness) of polymer composite that is fiber-reinforced by technical hemp. The effect of size of fibers and method of structuring the polyester matrix on the mechanical properties is studied. The optimal composition of the composite, which provides better mechanical properties, is defined. It is determined that the investigated composites can be used as construction material based on renewable source.

Keywords: Technical hemp · Fiber · Polymer composite
Mechanical properties · Renewable resources

1 Introduction

At present, the development of technology of composite polymer materials is determined by scientific research in the field of polymer material science, since the problem of the interaction of fillers and matrix is very diverse.

Applied and scientific aspects of polymer material science have been developing quite rapidly during the last decade. In one of his works, MIT Professor Albert Dietz wrote: "Science and technology, like literature and art, have their own fashionable phrases and stamps. One of the most fashionable in our time is the expression "composite materials", containing in a new form of a very old and simple idea that the joint work of heterogeneous materials gives an effect that is an equivalent to the creation of a new material whose properties are quantitatively and qualitatively different from the properties of each from its components". Currently, polymers and materials on their basis pushed seriously such basic structural materials as reinforced concrete, metal, wood. Possibilities of polymer materials are wide due to a variety of polymers and fillers, as well as the variability of composition of composites and methods for their modification.

In recent decades, natural fibers as an alternative to reinforcement in polymer composites attracted the attention of many researchers and scientists due to their advantages over glass and carbon fibers. Apply such natural fibers: flax, hemp, jute, sisal, kenaf, coconut, kapok, banana, and many others.

The advantages of natural fibers over artificial glass and carbon fibers are low cost, low density, comparison of specific properties of tension, reduced energy consumption, lower health risk, recovery, processing and biodegradation; they are nonabrasive to the equipment, do not cause skin irritation.

2 Literature Review

In the course of the research, the author analyzed papers by Suardana, YingjunPiao (South Korea) [1], AmirEtaati, SelvanPather (Australia) [2], Hughes and Mott (USA) [3], Anand (India) [4]. Many researchers studied composites based on various natural fibers, and thermoplastic materials for the matrix were preferably used.

Phenolic, epoxy and polyester resins are the most common thermosetting material for polymer composite matrix [4]. The matrix of a constructional composite material has at least two functions: to inhibit the propagation of the crack from fiber to fiber and to convey the effect of external forces on fibers in the best way. Most studies relate to the hybridization of natural fibers with glass fibers to improve properties. Some studies show that natural fibers have the potential to replace fiberglass in polymer composite materials [1–5]. The main parameters that influence the mechanical properties of biocomposites are the length of the fibers, the mass ratio, the orientation of the fiber, and the interfacial adhesion between the fiber and the matrix.

3 Research Methodology

On the basis of the foregoing it is possible to formulate the research objective, which is to determine the influence of the size and orientation of fibers on mechanical characteristics, the method of composite formation, studies on determining the impact strength, tensile strength and hardness.

In this work a number of studies were conducted to determine the relationship between the composition, the structure of the structure and the mechanical properties of the composite reinforced with technical cannabis - the design purpose. In this paper polyester resins of two brands CRYSTIC 2-446 RH was used as a binder used. Composites are filled with cannabis fibers with chaotic and unidirectional continuous fibers. The fiber content varied from 5 to 40 wt%. The samples were dried at a temperature of 100–180 °C during the formation.

Table 1 shows the characteristics of long hemp fiber from the abrasive wetting truss used for reinforcement, and Fig. 1 shows a general view of hemp fiber.

The optimal composition of the composite was determined empirically by the main mechanical characteristics of the material. For this purpose, the following parameters were taken into account: the size and shape of the filler, the mass ratio of the

Table 1. Characteristics of long hemp fiber from the trust of water wetting (greens).

Indicator	Value
Length, cm	163
Breaking load, N	430
Linear density, tex	42

Fig. 1. The hemp fiber is long with the trust of water wetting (greens).

components, the method of mixing, the order of adding the components, the method and temperature of drying.

A fiber of technical cannabis of two types was used for reinforcement according to the dimensional parameters:

I. Diameter of 420...470 μm and a length of 150 mm;
II. Diameter of 80...120 μm and a length of 20 mm.

The shock strength of the Sharp method was determined according to GOST 4647 at a temperature of +20 °C. The results of the study on impact strength are shown in Fig. 2. The models were made with two types of filler: thicker and longer fibers - type I and more subtle and short - type II.

The first type fibers were oriented along rectangular models and respectively perpendicular to the axis of the hammer of the pendulum, while fibers of the II type are chaotic in the matrix of the polymer.

Strength of fibers (time boundary of strength) depends on the length of the sample. The longer the fiber, the greater the probability of a large defect in it (time, splash, crack, etc.). It can be said that the free fiber is similar to the chain: there are strong links and there are weakened areas in which these links are connected. If the fiber is perfect (it has no defects), then in CM (composite material) it is still unevenly loaded, for example, there are ineffective areas of the fiber. Therefore, the ideal fiber in CM should also be considered like a chain.

The model [6] used to evaluate the effect of the properties of components on the tensile strength limits takes into account that at the individual ruptures, a portion of each fiber can be considered ineffective. Then CM can be considered as consisting of layers which height is equal to the length. The fiber that collapses inside such a layer can transfer the load through the formation. Then the load applied in this cross-section
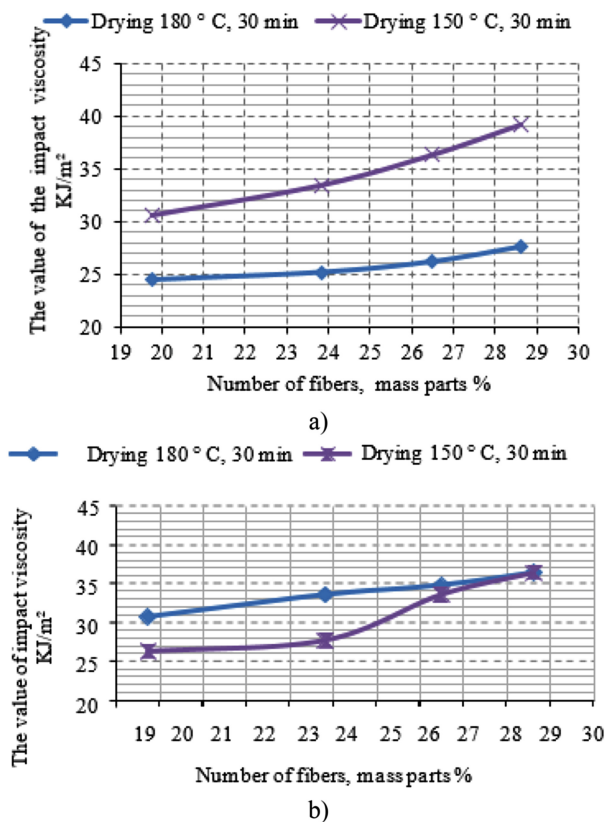
Fig. 2. Dependence of the impact strength on the amount of reinforcing fiber II-type at different temperatures polymerization: (a) the resin "Crystic"; (b) the resin "2000".

must be evenly distributed between the whole fibers in each layer. Segment of a fiber within one of the layers can be regarded as a chain link. Then each layer in CM is a packet (a sheaf) of such units, and CM itself consists of a series of packages. We can assume that the strength of the links is subject to a statistical distribution, equivalent to the statistical distribution of defects along the length of the fiber. The probability that in long chains there is a weakened link is greater than in short chains.

4   Results

The results of the study are presented in Figs. 2, 3 and 4 show that as the temperature of polymerization of compositions decreases, it can be assumed that with increasing temperature there is deterioration of the properties of hemp fibers, through drying of lignin, organic resins and other components as the fracture work (a) that falls on the polyester matrix is small.
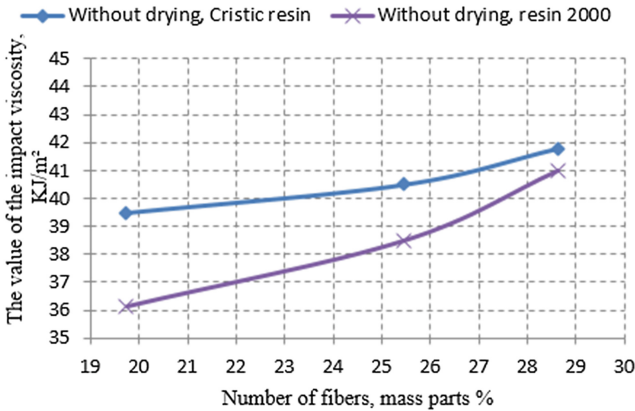
Fig. 3. Dependence of impact strength on the amount of type II reinforcing fiber without drying.
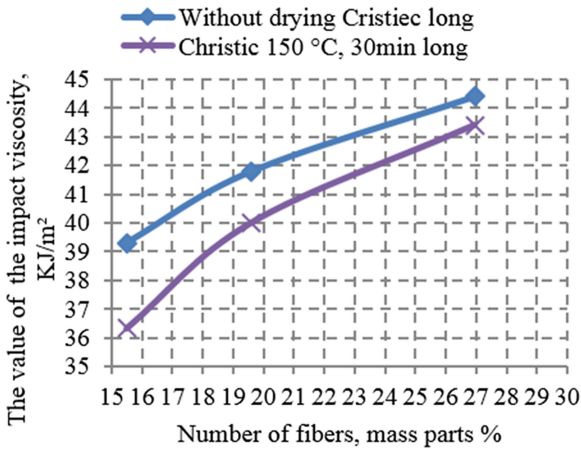
Fig. 4. Dependence of impact strength on the amount of I-type reinforcing fiber at different polymerization temperatures.

In general, the viscosity of the composite material depends on the transverse strength of the fibers, the strength of the fiber-matrix section and other parameters. Most importantly, during the cooling of the CM from the polymerization temperature $Tp > 423$ K, the resin compresses more intensively than the fibers. In the KM material there is thermal stress, since the matrix is stretched, then the shear strength of the CM will be smaller compared to the case where the CM does not have thermal stresses.

According to the obtained results, the highest impact strength of 44.5 kJ/m^2 is in samples with the highest degree of filling and perpendicularly oriented fibers to the axis of destruction, they inhibit the propagation of the crack, branching it in directions parallel to the fiber; the sample is destroyed in the entire volume, and this requires a great work. However, in samples with chaotic arrangement of smaller fibers, the impact

strength is 93% of the impact strength of the samples with the parallel arrangement of the fibers to the sample axis. The chaotic distribution provides better isotropy of the mechanical characteristics of the composite.

According to the results, the best impact strength is in samples with the highest amount of fiber.

The study of the tensile strength (according to GOST 1497) was carried out for a composite based on a crystal matrix of polyester resin "Crystic" with a one-sided orientation of the I-type and a chaotic distribution of II-type fibers, all samples were polymerized at room temperature, the models were manufactured in accordance with the standard, the general appearance is depicted in Fig. 5.

Fig. 5. Samples of composite with fibers I-type (a) and II-type (b) after tensile tests.

The temporal resistance of the gap increases almost linearly with the increase in the amount of reinforcing fiber. In the visual inspection of the fracture site, Fig. 5 of the Type II models under study did not show any discontinuity of the fibers, indicating a good interaction between the binder and the reinforcement, but stratification of the samples was observed in the samples with fibers along the axis of stretching during loading.

We consider our composite material to be a chain of beams (links), to which we can apply the weakest link theorem (Rosen theory), which states that the greater the proportion of fibers in structural material, the less ineffective fiber length in it [6].

According to the obtained results of the tensile strength of composites reinforced with fine fibers II-type is close to the strength of I-type composites. In general, the results of the experiment are confirmed as the theory of destruction based on the rule of mixtures and the Rosen theory on the inefficient length of the fiber and it is possible to achieve the strength of the longitudinal fibers with a certain ratio between the diameter and length of the fiber, in our case, this ratio is 1: 15…20.

Also, the location and nature of the destruction of specimens of type II fibers were investigated with an increase of 200 times using a MICROTEX 14C metallographic

microscope. With such an increase, Fig. 5 shows that fracture occurs as a result of fiber breaking and no disconnected fibers are observed.

Determination of hardness was carried out using the Brinell method (GOST 9012). The results of the tests are presented in the form of dependencies in Fig. 6. It was experimentally determined that the increase in the amount of binder in the material increases the hardness of the samples proportionally. It is obvious that the hardness of the composite is provided by the polymer matrix, and the hardness is reduced for the increase in the number of fibers. Also, with a slight increase in the temperature of the structuring, hardness rises, since according to the dependencies for composites reinforced with fibers I and II type practically it does not differ. It can be stated that the length, diameter and character of the placement in the polymer matrix do not significantly affect the hardness (Figs. 7 and 8).

In Fig. 9 it can be seen that the samples have the highest hardness, which are subjected to a drying temperature of 180 °C for 10 min.
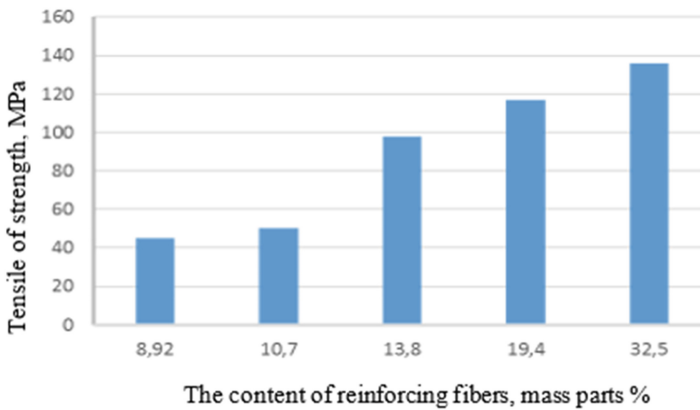
Fig. 6. Dependence of change of strength on the content of reinforcing fibers I-type.
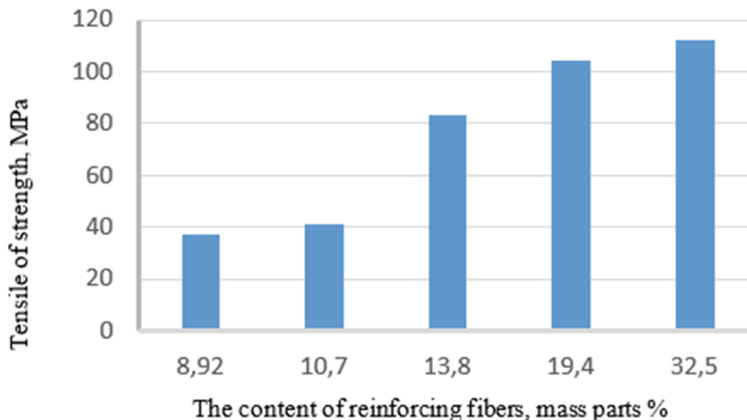
Fig. 7. Dependence of change of strength limit on the content of reinforcing fibers II-type.
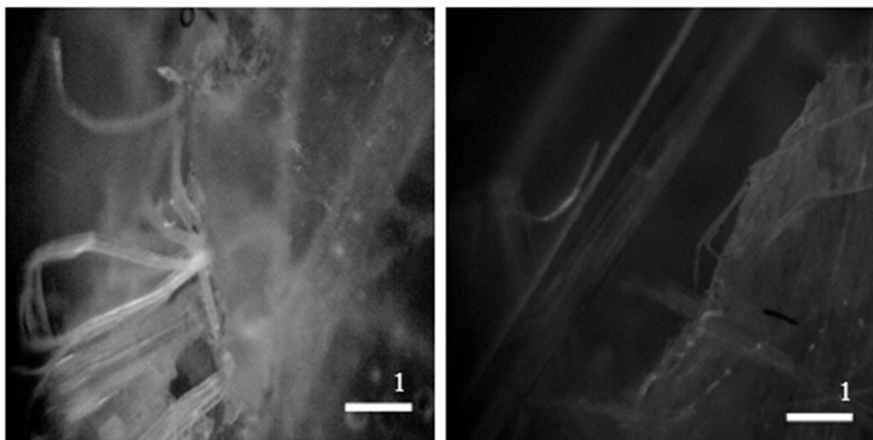
Fig. 8. Place of destruction of the composite, ×200.

a)

b)
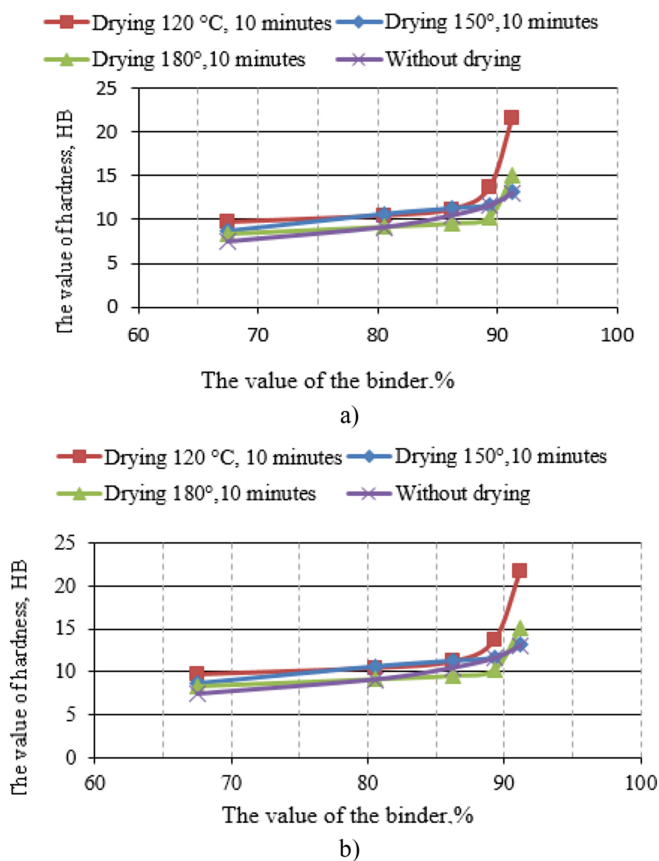
Fig. 9. Dependence of the composite hardness on the quantity of polyester resin CRYSTIC 2-446 RA: a – fibers of the I-type; b – II-type fibers.

5   Conclusions

According to the results of the studies described in the article, the best mechanical properties are detected in polymeric composite with a distribution of (I - type) hemp fibers oriented along the sample axis. In particular, the composition with a fiber content of about 30% by weight has a toughness $a_v = 44$ kJ/m^2; $\sigma_v = 138$ MPa; HB = 90 MPa, but also the composition with small type II fibers at high filling rates yields only 5–7% in mechanical characteristics. To determine the nature of the interaction on the boundary between the phase interaction of the fibers and the matrix, it is necessary to conduct a study using electron microscopy. It is also necessary to conduct a study on the effect of the previous chemical treatment of fibers to provide better adhesion to the polymer matrix. Based on the conducted studies, it has been shown that the introduction of fillers can influence the morphology of materials and, thus, achieve the necessary complex of mechanical properties of composites for practical use.

References

1. Suardana, N.P.G., Piao, Y., Lim, J.K.: Mechanical properties of hemp fibers and hemp/PP composites effects of chemical surface treatment. Mater. Phys. Mech. **11**, 3–9 (2011)
2. Etaati, A., Pather, S., Rahman, M.: Ground hemp fibers as filler/Reinforcement for thermoplastic biocomposites. Adv. Mater. Sci. Eng. **1**, 24–35 (2015)
3. Hughers, M., Mott, L., Hague, J., Hill, C.A.S.: Procudings of the Sth International Conference on Woodfiber-Plastic Composites, Madison, WI, USA (1999)
4. Anand: Silver Jubilee Celebrations: Souvenir Volume, vol. 2. Institute of Agriculture, India, December 1966
5. Yan, Z.L., Wang, H., Lau, K.T., Pather, S., Zhang, J.C., Lin, G., Ding, Y.: Reinforcement of polypropylene with hemp fibres. Compos. B Eng. **46**, 221–226 (2013)
6. Kopan, V.: Composite Materials. University Publishing House "Pulsari", Kiev (2004)

On the Application of N-2-1 Locating Principle to the Non-rigid Workpiece with Freeform Geometry

Hadi Parvaz[1(✉)] and Seyyed Ali Sadat[2]

[1] Shahrood University of Technology,
P.O. Box 3619995161, Shahrood, Iran
`h.parvaz@shahroodut.ac.ir`
[2] K. N. Toosi University of Technology,
470 Mirdamad Avenue, West, 19697 Tehran, Iran

Abstract. Fixture design for non-rigid workpieces is performed based on the N-2-1 locating principle (with N > 3 base locators). Determination of the position and orientation of the application points of the locators are among the most challenging processes that fixture designers are encountered with, especially in case of the freeform workpiece without specific datum features. In this paper, the N-2-1 locating principle has been applied to a non-rigid freeform workpiece which is chosen from the aerospace industry. In this regard, four distinctive locating plans have been designed by alternating of two parameters: the quantity of the base locators (N) and the position of the locating points on the base locating surface. Numerical analyses have been conducted using finite element software in order to investigate the effects of the mentioned parameters on the fixturing characteristics under the application of the clamping forces. The output parameters can be elaborated as workpiece deformation, displacements of the locating points, stress values and the reaction forces generated on the locating agents. The best locating plan has been chosen by the application of the suggested decision-making model by incorporation of the calculated fixturing characteristics. Based on the results, reductions of almost 41.6% and 66% were observed respectively on the workpiece maximum deflection and cumulative locating points' displacements by switching from the 3-2-1 to the N-2-1 (with N = 6) locating system without sensible change in the stress values.

Keywords: Fixture design · Fixturing layout · Finite element analysis
N-2-1 locating principle · Sheet metal part

1 Introduction

The traditional 3-2-1 principle is widely used to design the locating systems for the rigid workpieces. For the non-rigid workpieces, however, the N-2-1 locating principle has been suggested which incorporates N (N > 3) base locators on the workpiece base surface. Towards the determination of the position and orientation of the locating and clamping points on the non-rigid workpieces, several types of research have been published by incorporating different meta-heuristic optimization methods (such as GA,

PSO, ACO, etc.) with various objective functions. In the real world application, however, several technical limitations usually emerge during the design of fixture for this kind of workpieces, which can't be mathematically modeled and considered, especially in cases of workpieces with freeform geometry. Some of these limitations can be named as the lack of appropriate datum feature on the workpiece geometry, the unavailability of application of the point-contact locators on the workpiece, the lack of appropriate base locating surface, etc. Based on the mentioned limitations, the fixture designer usually considers several heuristic models to design the locating and clamping systems and chooses the best solution by taking into account the most critical parameters of both workpiece and fixture systems. From the viewpoint of workpiece, these parameters can be named as the accuracy of the fabricated workpiece to be within both dimensional and geometrical requirements, the surface quality of workpiece, residual stress of workpiece, etc. Hence, finite element software is one of the indispensable tools that the fixture designer utilizes in order to determine the required parameters and select the best solution between several alternatives. Based on the above-mentioned challenges in the real world application of fixture design process, in the present study, the design of locating system is considered for the workpiece selected from aerospace industry by taking into account the N-2-1 locating principle. For this purpose, four distinctive layouts have been suggested as a locating system of the workpiece and using the numerical analysis, the best solution has been chosen based on the suggested decision-making model.

2   Literature Review

Among the most recently published research works in the field of application of FEM at investigation of the fixture-workpiece system, Ivanov et al. [1] employed numerical analysis to design an innovative fixture for the lever machining in single set up considering the tool access problems that emerge at the multi-axis machining and ensuring of the manufactured part tolerances that meet the required values through the application of several FE analyses: workpiece-fixture deformation analysis, fixture-workpiece modal analysis, and harmonic analysis under the effect of oscillatory machining forces. Integration of the FEM application in the modeling of fixture-workpiece system with the heuristic and evolutionary optimization techniques have been recently focused on by several researchers. Sundararaman et al. [2] combined FEM, RSM and evolutionary optimization models of GA, PSO and their combinations for optimization of the locating layout of fixture aimed at machining of a hollow shaped workpiece. The presented model employed response surface methodology and developed a quadratic model to enable the suggested methodology to search for the optimized locating layout on the continuous spaces of the workpiece surfaces. Integration of the PSO with RSM was concluded to generate more realistic results at optimization process. Literature of the locating system design can be surveyed based on the workpiece geometry and rigidity. Hurtado and Melkote [3] optimized the quantity, dimension, and position of the pins with the clamping force intensity at the pin-array configuration method by considering the objective function as the maximum conformation of pins to the workpiece with freeform surfaces. Three heuristic ideas were

suggested in [4] for fixturing of the freeform workpiece: fixturing with the magnetorheological fluid, moving arms with the pneumatics powered bladder strips and a motor driven pin-array like configuration. Parvaz and Nategh [5, 6] suggested a mathematical analysis to design the locating and clamping systems for the workpiece with the freeform surfaces. The fixture design activities are going to be more challenging by adding flexibility to the workpiece. Having suggested the N-2-1 locating plan for these kinds of workpieces by Cai et al. [7], a combined GA and FE model was developed by Xiong et al. [8] for the optimization of locating positions in non-rigid aerospace workpieces aimed at minimization of the total and partial workpiece elastic deformation near the active machining regions. In [9], the optimization of the N-2-1 locating system for non-ideal sheet metal part was conducted by considering the variations of workpieces in the production batch. Li et al. [10] proposed a non-rigid fixture based on the controlled motor-driven modular elements for non-rigid workpieces with introducing the follow-up support idea. Yang et al. [11] proposed an efficient concept for optimization of locating plan by application of cuckoo search algorithm. Sample sets were were generated from few FE calls based on the N-2-1 scheme. More recently, Calabrese et al. [12] suggested the optimization of the fixture topology into the mixture of solid-lattice topology with the objective function of maximizing fixture stiffness.

At the real-world application of the fixture design, lots of limitations occur and constrain the incorporation of the mathematical analysis such as optimization methods reviewed above in the design of locating system for the workpiece. These limitations make the designer use finite element packages to obtain the necessary information for choosing the best solution as the locating plan between the alternatives. The main contribution of this paper is to investigate the effective fixturing parameters in selecting the best solutions between the alternatives and how these parameters should be manipulated when selecting the best solution. Specifically, the aim of the paper is to study the applicability of the N-2-1 locating principle to design the fixture aimed at riveting a freeform non-rigid workpiece through determining the best quantity, layout and configuration of the N base, twoside and single stop locators by taking into account effective fixturing parameters. For this purpose, a sheet metal model was chosen from the aerospace industry. Four locating plans were designed as alternatives using the N-2-1 locating principle with varying quantity and pose of the base-locating agents. The effective parameters in the selection of the best alternative were chosen to be the workpiece elastic deformation, displacements of the workpiece locating points, stress values and the reaction force values generated on the locating agents. Numerical analyses were conducted using FE software and the best solution was chosen based on a decision-making algorithm.

3   Research Methodology

Abaqus software was utilized for numerical analysis and determination of the output parameters for the chosen model represented in Fig. 1. The workpiece is selected as one of the parts used in aerospace industry, which is made of AL7075-t6 material with the thickness of 2 mm. The CAD model of the workpiece was prepared and imported

for the software using the neutral file format as a deformable body. Locators were chosen to be tip-sphered due to the freeform nature of the workpiece geometry and made up of steel material. Rigid body constraint was applied to all of the locators to ensure that no deflection occurs on them during the workpiece fixturing. Since plastic deformation is not allowed in the fixturing phenomenon, the elastic data of the materials were just submitted as Young's modulus, Poisson's ration and density equal to 200 GPa, 0.29 and 7800 kg/m^3 for Steel and 71.7 GPa, 0.33 and 2810 kg/m^3 for the aluminum, respectively. By applying the locators at the mentioned positions of Table 1, friction was defined between the mating surfaces of the locators and the workpiece with Coulomb's friction coefficient equal to 0.6 [13]. The suggested four locating plans have been graphed in Fig. 1 and the corresponding data have been elaborated in Table 1. Since the analysis includes frictional multi-contacts between the freeform surfaces, the dynamic explicit solver was chosen with time period of 0.1. Full DOF constraint was applied to the locators to ensure that the locators remained fixed during the fixturing application. Total of four clamping forces were applied at the mentioned positions and orientation of Table 1 with equal intensity of 500 N. The parts were meshed by explicit element of C3D10M type with a quadratic geometric order using the second order accuracy. This element type is capable of modeling frictional contact between the mating surfaces, especially of the non-ideal geometries. Following the selection of the mentioned element type, the tetrahedron shaped meshes were applied to the workpiece using a free algorithm with the general size of 5 which was refined to 2 mm in the vicinities of the contact regions.
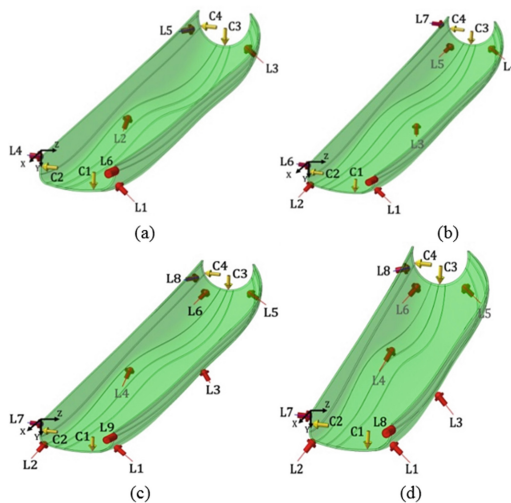
Fig. 1. The model of case study and the suggested (a) first locating plan (3-2-1 system) (b) second locating plan (5-2-1 system) (c) third locating plan (6-2-1 system in three rows) and (d) fourth locating plan (6-2-1 in four rows).

Table 1. The position of the locators at the suggested locating plans.

Locating plan no.	Locating points (mm)	
	Base locators	Side and stop locators
1	(0.43, 29.82, 94.44), (−350, 28.30, 9.72), (−685, 10.9, 55.81)	(−15.37, 10.969, −0.990),
2	(0.43, 29.82, 94.44), (−14.604, 38.877, 3.625), (−350, 34.842, 52.358), (−685, 10.9, 55.814), (−685, 15.212, 5.682)	(−685, −3.43, −6.6), (16.06, 11.87, 97.03)
3	(0.43, 29.82, 94.44), (−14.604, 38.877, 3.625), (−350, 20.934, 99.404), (−350, 28.298, 9.723), (−685, 10.9, 55.814), (−685, 15.212, 5.682)	
4	(0.43, 29.82, 94.44), (−14.604, 38.877, 3.625), (−234, 24.791, 105.555), (−467, 35.571, 15.602), (−685, 10.9, 55.814), (−685, 15.212, 5.682)	

The locators were meshed with the size of 1 mm to ensure the appropriate contact control between the mating surfaces. The model was then solved by requesting the displacements, stress values and reaction forces at the locating agents. It should be mentioned that the clamping points were remained fixed for all of the locating plans as (11.49, 37.05, 69.44), (0.17, 18.78, 1), (−700, 16.12, 26.86) and (−700, −4.02, −4.15).

4   Results

The mentioned output parameters were calculated for all of the locating plans. Typically, Fig. 2 represents the contours of deformation, stress distribution on workpiece, the displacement and reaction forces which are created on the sixth locators and plotted at the local coordinate system ($n - t_1 - t_2$ system) for the third locating plan.

The calculated output parameters for all of the locating plans are demonstrated in Table 2. By referring to the results, the alternatives for the locating plans can be compared from the point of view of each output parameter. The minimum of the maximum deformations calculated on the workpiece is 0.21 mm for the third locating plan which is occurred at the application point of the first clamping unit.

The experimental test has to be performed for verification of the results to the exact real-world data. However, several checks can be performed in order to ensure the results of simulations and confirm the adequacy of the results of FEM analyses. Figure 2(e) represents the typical curves of internal and kinetic energy for the simulation performed on the third locating plan. The kinetic energy is well below the 5–10% of the internal energy which confirms the quasi-static nature of the simulations.

To verify the order of magnitude of the deflection occurred at the free end of the workpiece represented in Fig. 2(a), this part of the workpiece can be roughly modeled by a cantilever beam with a rectangular section with the dimensions of 92.5 mm × 2 mm and the length of 15 mm. It should be noted that the straight distance between the locator No. 1 and 2 at the third locating plan is 92.5 mm. When applying the formula, the deflection occurs at the free end of the cantilever beam to the configured problem,
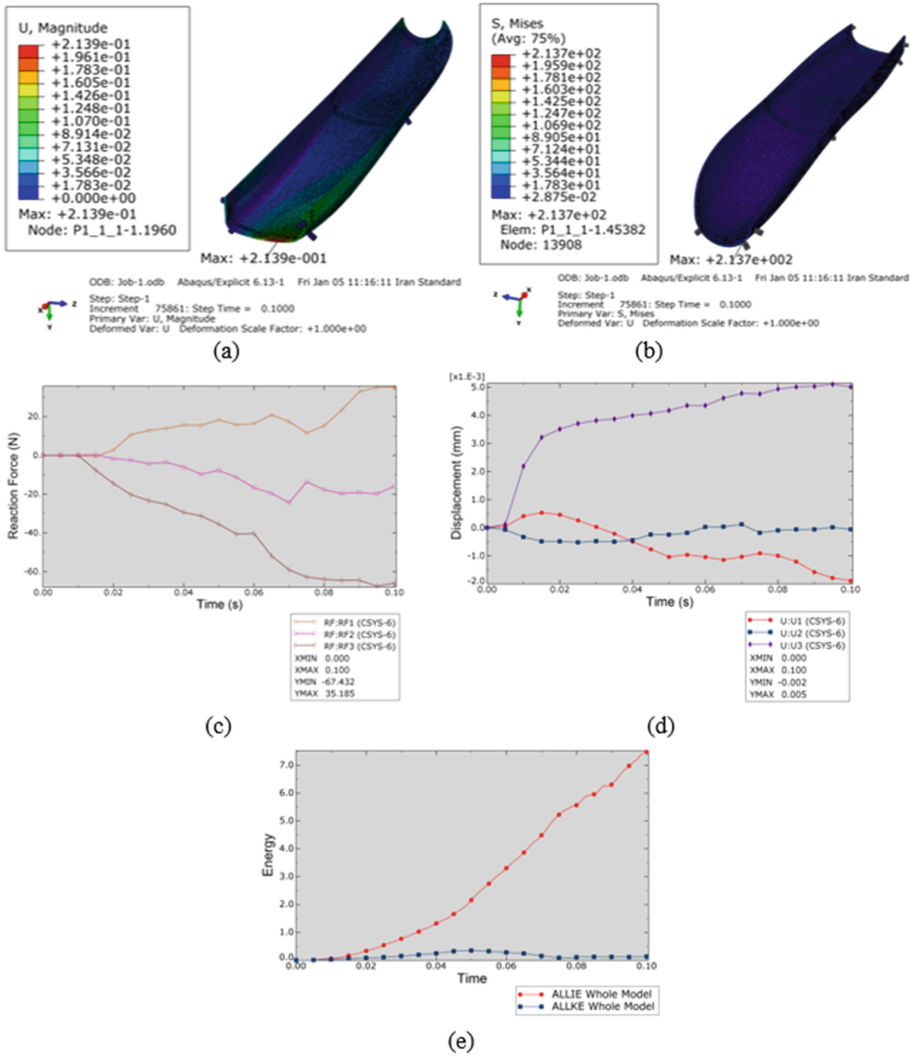
Fig. 2. The output parameters of fixturing the workpiece with the third locating plan (a) contour of deformation (b) contour of Mises stress (c) reaction forces created on locator No. 6 in the normal, first and second tangential directions and (d) the displacement of the third locating point (e) the internal vs. kinetic energy curves (with COF = 0.6 and clamping force intensity of 500 N).

assuming that only the clamping force of 500 N is applied at the free end of this beam at +Y direction, the deflection can be calculated as 1.272×10^{-1} mm.

The calculated deflection shows that the order of magnitude of the displacement obtained from FEM analysis is quite reasonable. The difference between the FEM result and the calculated value from the modeled equivalent beam can be justified by assumptions admitted during the beam modeling process: considering only one of the

Table 2. The calculated fixturing output parameters for the locating plans.

Plan no.	Max. deformation (mm)	Max. Mises stress (MPa)	Locating point displacement (mm) $(U_{L1}, U_{L2}, U_{L3}, U_{L4}, U_{L5}, U_{L6})$	Reaction force values (N) $(U_{L1}, U_{L2}, U_{L3}, U_{L4}, U_{L5}, U_{L6})$
1	0.36	133.7	(0.23, 0.07, 0.25, 0.11, 0.09, 0.25)	(20.12, 75.72, 6.12, 26.7, 45.14, 114.23)
2	0.22	196.4	(0.09, 0.01, 0.05, 0.03, 0.00, 0.02, 0.05, 0.10)	(27.08, 28.19, 0.00, 10.95, 77.47, 20.61, 7.00, 141.70)
3	0.21	213.7	(0.09, 0.01, 0.03, 0.02, 0.03, 0.00, 0.01, 0.05, 0.10)	(27.62, 27.31, 17.93, 17.15, 11.97, 78.64, 19.88, 7.49, 97.22)
4	0.247	129.6	(0.13, 0.02, 0.1, 0.07, 0.08, 0.03, 0.04, 0.03, 0.15)	(57.08, 36.84, 0.00, 0.00, 18.55, 76.92, 20.67, 24.61, 84.92)

clamping force with the intensity of 500 N and neglecting the other clamping forces, assuming the boundary conditions as cantilever beam and changing of the geometry of workpiece from U-section to simple rectangular one. Since these parameters had been considered by the FEM analysis, the results were altered in the same order of magnitude.

To investigate the adequacy of the FEM results and its relationship to the mesh size, simulations were repeated three times each with a different number of elements. 12 simulations were conducted for the mesh independence investigation. The results are elaborated in Fig. 3.
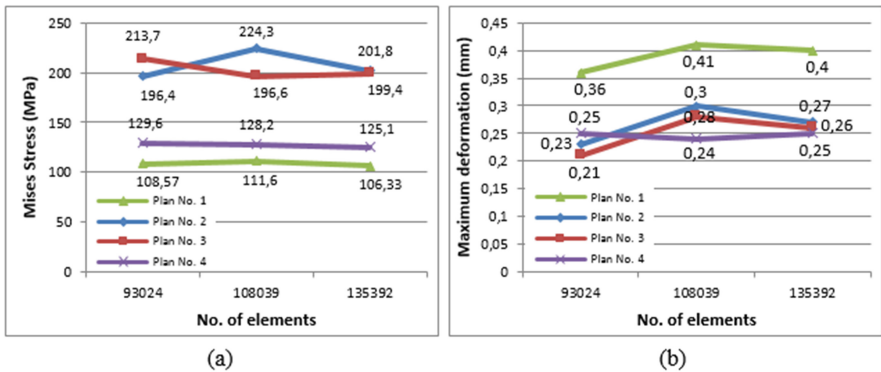
Fig. 3. The results of mesh independence analyses on (a) maximum Mises stress and (b) maximum deformation of the workpiece.

Curves in Fig. 3 indicate that the results of simulations are almost independent of the mesh size within an acceptable range. Since, the position of maximum Mises stress changes with different element sizes for the first locating plan, stress was measured at the position of the contact between locator No. 5 (Fig. 1c) and the workpiece for this plan. The standard deviations of the results of maximum Mises stress were calculated as 2.16, 12.08, 7.49 and 1.88 from the first to the fourth locating plans, respectively. In

addition, standard deviations for the maximum deformations of the workpiece were calculated as 0.02, 0.03, 0.03 and 0.005 from the first to the fourth locating plans, respectively. Based on these results, it can be concluded that the simulations and results were mesh-independent, approximately. It should be noted that the element quantity numbers (horizontal axis in Fig. 3) correspond the mesh sizes of 5, 4 and 3 mm, respectively.

The minimum of maximum Mises stress was obtained as 129.6 MPa in the fourth plan at the contact point of locator No. 6 and the workpiece surface. According to the diagrams of Fig. 4, it can be seen that the minimum cumulative displacement of locating points occurred at the third locating plan which was equal to 0.34 mm. The reduction of almost 41.6% in w/p maximum deformation and 66% in the cumulative locating point displacement can be observed in Fig. 4(b) by switching from 3-2-1 locating system to the third plan (N-2-1 with N = 6).
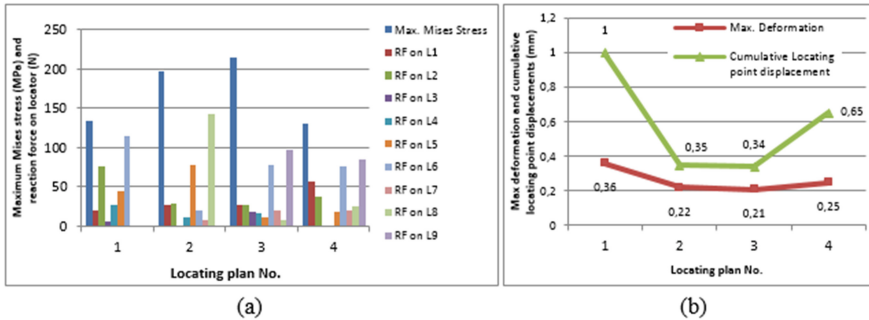
Fig. 4. The diagrams of the output parameters regarding the locating plan No.

From the point of view of the reaction forces on the locating agents, it should be considered that the reaction force should be created on all of the locators to ensure that no separation occurs between either of the locators and the workpiece surfaces at the contact points. Considering this principle, it can be observed that zero reaction forces were calculated at the second and fourth locating plans for some of the locators. From the diagram in Fig. 4b, the minimum of the maximum deformations was calculated for the third locating plan which was equal to 0.21 mm.

A decision-making procedure should be performed to select the best solution for the locating system between the four alternatives based on the output parameters. Between the four output parameters, the parameter corresponding the reaction forces on the locating agents is a prerequisite rule which should be satisfied by all of the alternatives. An alternative would be removed from the list if the reaction force was zero in (at least) one of the locators. A scoring and weighting method based on Eq. (1) is incorporated for the decision-making model.

$$S_i = \sum_{j=1}^{3} w_j \times (s_i)_j; \ i = 1, 2, 3, 4; \ j = 1, 2, 3; \ \sum_{j=1}^{3} w_j = 1, \ 0 < (s_i)_j < 1 \quad (1)$$

Where, S_i is the score of the ith locating plan, w_j is the weight of the output parameter, $(s_i)_j$ is the score obtained by the ith locating plan from the j-th output parameter, i and j stands for the number of locating plans and the output parameters. Between the four output parameters, the fixturing accuracy mostly depends on the two parameters of displacements of the locating points and the workpiece maximum deflection. So, weights w_j were increased for these two output parameters according to Table 3. It should be mentioned that $(s_i)_j$ is calculated based on the linear relationship between the obtained best and worst conditions of the jth parameter and normalized between the 0 and 1. Also, the scores of the alternatives from the third rule were calculated based on the yield stress of the workpiece material which was equal to 530 MPa for the case study [14]. Table 3 demonstrates the details of the scores and results.

Since zero reaction forces were observed at some locators of the second and fourth alternatives, they were removed from the list of candidates. According to the results in Table 3, it was concluded that the third locating system should be chosen as the best solution with score of 0.94. So, the 6-2-1 system in the ordered array layout is the best solution for locating the represented non-rigid freeform workpiece.

Table 3. The score of locating plans from the decision-making model.

Plan no. (i)	Score $(s_i)_j$ from the jth output parameter				
	Reaction force values	$j = 1$ Locating point displacement $(w_1 = 0.5)$	$j = 2$ Maximum deformation $(w_2 = 0.4)$	$j = 3$ Maximum Mises stress $(w_3 = 0.1)$	S_i
1	Passed!	0.00	0.00	0.75	0.07
2	Not passed!	0.98	0.93	0.63	N. A.
3	Passed!	1.00	1.00	0.40	0.94
4	Not passed!	0.53	0.75	0.75	N. A.

5   Conclusions

In this study, a realistic procedure was suggested for the design of locating system for non-rigid freeform workpieces. A case study was chosen from the aerospace industry and four locating systems were designed as alternatives. Numerical analyses were conducted for the calculation of four main fixturing parameters including displacement of the locating points, workpiece maximum deformation, reaction force values on the locators and maximum stress value generated on the workpiece. A decision-making model was suggested based on the scoring and weighting method and the third alternative was chosen with the score of 0.94 as the best solution for the specific case study. Also, the results showed the reductions of 41.6% and 66% at the N-2-1 locating system (with N = 6) in comparison with the 3-2-1 system in the workpiece maximum deformation and cumulative locating point displacement, respectively. It can be concluded that the suggested generic combined FE and decision-making algorithm can be utilized

for design of locating/clamping systems for the workpieces regardless of its geometry and level of rigidity. For the further studies, the experimental verification of the calculated parameters is suggested for the validation of the results and the selected locating system.

References

1. Ivanov, V., Mital, D., Karpus, V., et al.: Numerical simulation of the system "fixture–workpiece" for lever machining. Int. J. Adv. Manuf. Technol. **91**(1–4), 79–90 (2017)
2. Sundararaman, K.A., Padmanaban, K.P., Sabareeswaran, M., Guharaja, S.: An integrated finite element method, response surface methodology, and evolutionary techniques for modeling and optimization of machining fixture layout for 3D hollow workpiece geometry. J. Mech. Eng. Sci. **231**(23), 4344–4359 (2017)
3. Hurtado, J.F., Melkote, S.N.: A model for synthesis of the fixturing configuration in pin-array type flexible machining fixtures. Int. J. Mach. Tools Manuf. **42**(7), 837–849 (2002)
4. Rukshan, K., Chaminie, W., Madushan, M.D., Jayaweera, N.: Design and development of flexible fixturing system for handling irregular shaped components. In: Moratuwa Engineering Research Conference (MERCon), IEEE, Sri Lanka (2015)
5. Parvaz, H., Nategh, M.J.: Analytical model of locating system design for parts with free-form surfaces. Modares Mech. Eng. **15**(13), 129–133 (2016). (in Persian)
6. Nategh, M.J., Parvaz, H.: Development of computer aided clamping system design for workpieces with freeform surfaces. CAD **95**, 52–61 (2018)
7. Cai, W., Hu, S.J., Yuan, J.: Deformable sheet metal fixturing: principles, algorithms, and simulations. J. Manuf. Sci. Eng. **118**(3), 318–324 (1996)
8. Xiong, L., Molfino, R., Zoppi, M.: Fixture layout optimization for flexible aerospace parts based on self-reconfigurable swarm intelligent fixture system. Int. J. Adv. Manuf. Technol. **66**(9–12), 1305–1313 (2013)
9. Das, A., Franciosa, P., Ceglarek, D.: Fixture design optimisation considering production batch of compliant non-ideal sheet metal parts. Procedia Manuf. **1**, 157–168 (2015)
10. Li, H., Chen, W., Shi, S.: Design and application of flexible fixture. Procedia CIRP **56**, 528–532 (2016)
11. Yang, B., Wang, Z., Yang, Y., Kang, Y., Li, X.: Optimum fixture locating layout for sheet metal part by integrating kriging with cuckoo search algorithm. Int. J. Adv. Manuf. Technol. **91**(1–4), 327–340 (2017)
12. Calabrese, M., Primo, T., Del Prete, A.: Optimization of machining fixture for aeronautical thin-walled components. Procedia CIRP **60**, 32–37 (2017)
13. Brunelli, K., Dabalà, M., Martini, C.: Surface hardening of Al 7075 alloy by diffusion treatments of electrolytic Ni coatings. La Metall. Ital. **7–8**, 37–40 (2013)
14. Torabi, A., Berto, F., Razavi, S.: Tensile failure prediction of U-notched plates under moderate-scale and large-scale yielding regimes. Theor. Appl. Fract. Mech. (2017, in Press). https://doi.org/10.1016/j.tafmec.2017.07.009

Information and Communication Technologies Within Industry 4.0 Concept

Dragan Peraković(✉) , Marko Periša ,
and Rosana Elizabeta Sente

Department of Information and Communication Traffic, University of Zagreb,
Faculty of Transport and Traffic Sciences,
4 Vukelićeva St., 10000 Zagreb, Croatia
{dperakovic,mperisa,rsente}@fpz.hr

Abstract. Internet of Things provides connectivity and interoperability between transport entities, transported entities and product entities in Industry 4.0 concept. The market requirements are changing on daily basis and for the business processes of manufacturing organizations to be successful, it is necessary to link all the supply chain stakeholders and ensure their real-time informing, by forming an ecosystem for connecting stakeholders of Industry 4.0 concept. By implementing contemporary information and communication technologies in the production line it is possible to ensure the flexibility of production and adaptation of product entities to end user requirements. The problem of providing real-time information to all participants in supply chain has been identified by analyzing the traditional supply chain in the manufacturing industry. Based on the analysis of information and communication technologies in Industry 4.0 concept, the aim of this research is to propose optimal information and communication technologies for connecting stakeholders of logistic production chain. This extends the opportunity for all logistic production chain participants to inspect the stage of product entities from the stage of the development of product materials to the delivery stage of the product to the end users.

Keywords: Internet of Things · Cloud Computing · Automatization
Wireless Technology

1 Introduction

Contemporary Information and Communication Technologies (ICT) and concepts such as wireless sensor networks, Internet of Things (IoT), Big Data, and Cloud Computing (CC) are used in the manufacturing environment. With the development of Industrial IoT (IIoT) and Industry 4.0 concept, it is possible to link automated remote control of manufacturing machines and enable rapid response to incident situations in real-time, to provide real-time information to users or to ensure smart inventory tracking in manufacturing organizations, automated resource ordering and automated production. This research is focused on exploring the possibilities of using IoT in the manufacturing industry. The possibilities of ICT in Industry 4.0 concept were analyzed based on the available scientific literature and research. The aim of the research is to select the optimal ICT to connect all the stakeholders in the logistic production chain. The purpose of the

research is to increase the efficiency of manufacturing organizations by linking all logistic production chain stakeholders. To provide customers with quality informing service it is necessary to monitor their activities and needs.

2 Literature Review

By analyzing the available scientific literature and previous researches, information about the contemporary ICT which are used in Industry 4.0 concept was obtained. Customer requirements and needs change daily, and for this reason it is necessary to adapt the production of manufacturing organization to meet their needs, thereby to increase the profit and reduce the costs of manufacturing organizations [1]. Market requirements and the development of new ICT change the way of manufacturing organizations' business activities. The previous research on ICT and technological solution areas related to processing, data storage, information delivery, automation of business processes, supply chain and information transfer between stakeholders who are a part of logistic production chain were analyzed.

Industry 4.0 concept is the fourth generation of the manufacturing industry and includes the processes of automation and data exchange in manufacturing organizations. The integral parts of Industry 4.0 are IoT and smart manufacturing which refer to the ability of manufacturing machines to collect data and forward them in real-time [2]. Nine technological solutions in the field of automation of business processes, data collection, processing, storage and delivery, security of information and communication (IC) system and the abilities of remote control are as follows: autonomous robots, simulations, horizontal and vertical integration systems, IIoT, cybersecurity, CC, Big Data, Additive Manufacturing and Augmented Reality [3, 4]. Autonomous robots will become represented in the manufacturing industry and will have a great impact on customer expectations that are aimed at delivery of orders [4, 5]. The available research indicates that autonomous decisions can improve business processes within the organization, reduce the probabilities of risk appearance, improve the way data are collected from the environment, and reduce long-term costs [6]. 3-D product and material simulations are already used in manufacturing organizations, and it is expected to be used in other areas of operational processes of organizations [7]. With it, it will be possible to test business processes before their implementation in a physical environment [8]. This will affect product quality and optimization of production process. Horizontal and vertical integration of the system involves connecting all system participants and manufacturing business processes. Its implementation will have a great impact on the currently existing problems related to the responsibility control, safety, confidentiality, standardization and infrastructure configuration [9]. By adopting Industry 4.0 concept into the manufacturing process and business, the functions they perform and the features they provide will become more coherent [1]. IIoT is often compared with Industry 4.0 concept but it needs to be analyzed separately. IIoT implies the use of Big Data, data collection using sensors, Machine to Machine (M2M) communication and automatization technologies within the industrial area [10, 11]. Industry 4.0 concept is focused on the manufacturing while the IIoT refers to all elements, objects, devices that can be connected to Internet and that can provide feedback and increase the business efficiency [12]. When connecting all parts of

the manufacturing organization, it creates space for cyber-attacks on all data that are constantly transmitted through the entire IC system [13]. For this reason, cybersecurity strategies must ensure secure and reliable communication across the entire IC system. According to 2016 Symantec Internet Security Threat Report, the manufacturing sector is among the top three industries that have most frequently executed spear phishing attacks [14]. Latency can represent a problem for systems that require quick responses on collected data [15]. In Industry 4.0 concept, CC is used for data processing and storage, meeting the conditions of network requirements so that the collected data could be analyzed in real-time and provide the necessary feedback [16, 17]. Fog Computing has features which can solve problems that arise within CC environment, regarding latency and traffic congestion which occur during the transmission of data over Internet. Big Data represents the amount of data that can not be processed by using simple database tools. Manufacturing organizations need to analyze different types of data from different sources to benefit from the implementation of IoT within their business processes. Based on the collected data, manufacturing organizations need to make quick decisions to increase their productivity [18, 19]. With implementation of Big Data into manufacturing organization business processes, it is possible to improve the product development and market expansion, operational efficiency, market demand forecasting, and improved customer experience [20]. The key components of Industry 4.0 concept are devices which can produce fast, flexible and accurate parts/materials that are important for production [21]. These devices are a part of Additive Manufacturing, and 3D printing is one of them. 3D printing enables creation of new product solutions and solutions for the supply chain [22]. This implies a faster delivery of the product and their reduced number in the warehouse. Apart from the above, it affects new business models in terms of changing the supply chain participants and integration of users [23, 24].

3   Research Methodology

By analyzing technical characteristics of CC and Fog Computing, improvement by implementing Fog Computing into manufacture organizations business in Industry 4.0 concept has been noticed. Fog Computing influences on efficiency and flexibility of business as well as on resource management, and the advantages compared to CC are shown in Table 1. One of the advantages of Fog Computing is that it can be accessed by Wi-Fi, mobile network, Bluetooth and ZigBee network which provides support on

Table 1. Comparative analysis of Cloud Computing and Fog Computing.

	Cloud Computing	Fog Computing
Client and server distance	Multiple hops	Single hop
Latency	High – 5 [s]	Low – 1.5 [s]
Delay jitter	High	Very Low
Real time interaction	Yes	Yes
Mobility	Limited support	Supported
Access	Wi-Fi, Mobile Network, Ethernet	Wi-Fi, Bluetooth, Mobile Network, Ethernet, ZigBee

many devices. According to Gartner, 25 billion of devices will be connected and demand data processing by 2020 [25]. In total, 600 [ZB] of IoT data will be generated by 2020 which will require a sufficient data processing speed for avoiding latency in delivering data and information [26].

In Fog Computing, the data is sent directly from the client to the server, while in CC it passes through several points, thus affecting the slower response to the forwarded data and information. Due to the amount of generated data, Fog Computing is more efficient for the business environment to collect and process the data and forward it to CC environment [27].

ZigBee technology, in comparison to Wi-Fi and BLE technologies, can work on 868 [MHz] and 915 [MHz] which lowers the possibilities of interference of other devices that work on 2,4 [GHz] and is shown in Table 2. It is suitable for use at moment when low power consumption and transfer of collected sensor data are required. Automated manufacturing processes require communication for monitoring the work progress. ZigBee can provide low power consumption and low communication costs and increase overall control over the working processes. Implementation of Industry 4.0 concept into manufacturing organizations can provide interoperability, transparency of information, decentralization of business decision making and technical support. It is also possible to plan to increase or reduce the production output, thereby affecting the optimum and efficient production. Real time informing requires high reliability and availability of information which can provide Wi-Fi communication network. The biggest advantage of Wi-Fi technology is availability, and the biggest disadvantage is high power consumption. It is advisable to combine Wi-Fi technology with other ICT to ensure business efficiency in terms of low latency, power consumption and high reliability. BLE technology is suitable for usage because of low energy consumption. It can be used in form of BLE transmitters and tags placed on transported and product entities, but also for marking indoor areas. Barcodes require more time to scan of each delivered transported entity and do not have the ability to provide information about their real-time location. RFID devices do not have the mentioned ability, require more finances for installing the infrastructure and require workers to come on each floor and each part of warehouse area to collect data on RFID tags about transported entities. For this reason, Beacon transmitters and BLE tags have

Table 2. Communication and AIDC technologies

	Wi-Fi	BLE	ZigBee	NFC	RFID	Barcode
Frequency	2,4 GHz, 5 GHz	2,4 GHz	2,4 GHz, 868 MHz, 915 MHz	13,56 MHz	125–134,2 kHz, 13,56 MHz, 860–960 MHz 2,45 GHz	–
Range	Up to 100 [m]	Up to 77 [m]	10–100 [m]	Up to 10 [cm]	Up to 20 [m]	Up to 15 [m]
Two-way data transfer	Yes	Yes	Yes	Yes	Yes	No
Power consumption	High	Very low	Low	Very low	Very low	–

the advantages over above mentioned technologies in terms of scalability of service and cost efficiency. BLE Gateway collets data from BLE tags and forwards them to Fog Computing or CC environment. User device connects to CC or Fog Computing and reads data on BLE tags. BLE technology is better in comparison to RFID and barcodes because it can provide greater coverage within the warehouse. NFC technology is suitable for mobile transactions, which affects security and time savings when making payments [28, 29].

4   Results

Optimal communication technologies provide users to reduce costs in power consumption and ensure real-time communication between required entities. Figure 1 shows communication technologies used for communication between entities in logistic production chain.
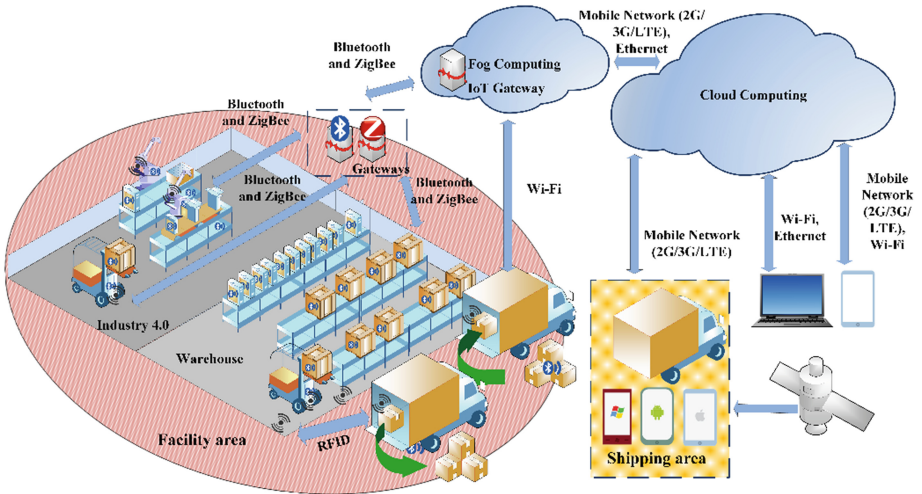
Fig. 1. ICT for communication between entities in logistic production chain.

Entities in manufacturing organizations and warehouses are connected via ZigBee and Bluetooth technologies and collected data is sent to Fog Computing. The data is processed there and forwarded to CC environment if needed for providing information to end user (consumers or business organizations). Fog Computing is used to link manufacturing facilities and warehouses, so that collected data could be processed before CC environment to reduce the latency in providing required information. ZigBee technology is used because of low power consumption for communication between sensors, indoor vehicles and production line. Transported entities are marked with BLE and RFID tags so that they could be detected while entering the warehouse.

While the transportation entity is in the field of warehouse, data is sent to Fog Computing via Wi-Fi technology. Locating transported entities within the warehouse area is possible because of BLE tags and transmitters. During the delivery of transported entities, mobile phone devices inside transporting entities can be used for location of (GPS technology) transported entities. Communication to CC environment is realized via Mobile Network. End users can, in real-time, check the information about the location of their product by using mobile phone which can connect to CC via Wi-Fi, Ethernet or Mobile Network, and computers/laptops which are connected via Ethernet or Wi-Fi.

Figure 2 shows proposition of optimal ICT for each stakeholder of logistic production chain and required information. The palette of production resources, within the procurement phase, which are brought to manufacture organization, are marked with BLE tags and placed in warehouse. Wi-Fi technology is used for sending information about storage changes to CC database. This provides real-time access to information about development of production entity. Temperature, humidity, fire, proximity and distance sensors located inside the warehouse communicate via ZigBee technology, but LoRa and Zwave technologies can also be used. This enables M2M communication between sensors and ZigBee Gateway if ZigBee communication technology is used.
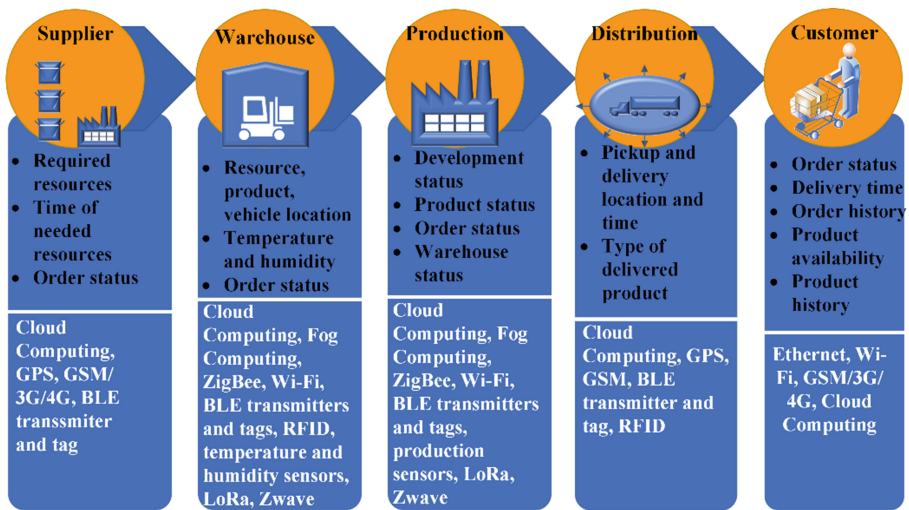
Fig. 2. Optimal ICT for stakeholders of logistic production chain.

5   Conclusions

Industry 4.0 concept offers possibility to change the way manufacturing organizations do business with the use of contemporary ICT. The available literature and scientific research were used to analyze possibilities of using ICT within Industry 4.0 concept. The traditional supply chain analysis has identified a problem in used ICT for

managing business processes which affected efficiency and effectiveness of manufacture organizations' business. By using contemporary ICT, CC and Fog Computing concepts, it is possible to connect all stakeholders of logistic production chain to ensure the delivery of information without delays. By connecting the stakeholders, it is possible to influence their distribution in new business activities.
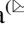
References

1. PWC: Industry 4.0: building the digital enterprise. https://www.pwc.com/gx/en/industries/industries-4.0/landing-page/industry-4.0-building-your-digital-enterprise-april-2016.pdf. Accessed 22 Nov 2017
2. Lopez Research: Building smarter manufacturing with the Internet of Things (IoT). http://cdn.iotwf.com/resources/6/iot_in_manufacturing_january.pdf. Accessed 15 Nov 2017
3. Cheng, G., Liu, L., Qiang, X., Liu, Y.: Industry 4.0 development and application of intelligent manufacturing. In: 2016 International Conference on Information System and Artificial Intelligence, pp. 407–410. IEEE-CPS, Hong Kong (2016)
4. The Boston Consulting Group: Industry 4.0 the future of productivity and growth in manufacturing industries. https://www.zvw.de/media.media.72e472fb-1698-4a15-8858-344351c8902f.original.pdf. Accessed 15 Nov 2017
5. Deloitte: Using autonomous robots to drive supply chain innovation. https://www2.deloitte.com/content/dam/Deloitte/us/Documents/manufacturing/us-manufacturing-autonomous-robots-supply-chain-innovation.pdf. Accessed 15 Nov 2017
6. Bi, Z.M., Xu, D., Wang, C.: Internet of Things for enterprise systems of modern manufacturing. IEEE Trans. Ind. Inf. **10**(2), 1537–1546 (2014)
7. Posada, J., Toro, C., Barandiaran, I., Oyarzun, D., Stricker, D., de Amicis, R., Pinto, E.B., Eisert, P., Döllner, J., Vallarino Jr., I.: Visual computing as a key enabling technology for Industrie 4.0 and industrial internet. IEEE Comput. Graph. Appl. **35**(2), 26–40 (2015)
8. Wan, J., Cai, H., Zhou, K.: Industrie 4.0: enabling technologies. In: Proceedings of 2015 International Conference on Intelligent Computing and Internet of Things, pp. 135–140. IEEE, Harbin (2015)
9. Heng, S.: Industry 4.0 upgrading of Germany's industrial capabilities on the horizon. https://www.dbresearch.com/PROD/RPS_EN-PROD/PROD0000000000451959/Industry_4_0%3A_Upgrading_of_Germany%E2%80%99s_industrial_ca.PDF. Accessed 25 Nov 2017
10. PWC: The industrial Internet of Things. https://www.pwc.com/gx/en/technology/pdf/industrial-internet-of-things.pdf. Accessed 28 Nov 2017
11. World Economic Forum: Industrial Internet of Things: unleashing the potential of connected products and services. http://www3.weforum.org/docs/WEFUSA_IndustrialInternet_Report2015.pdf. Accessed 28 Nov 2017
12. Bloede, K., Mischou, G., Senan, A., Tilow, A.: The industrial Internet of Things: making factories "smart" for the next industrial revolution. http://www.woodsidecap.com/wp-content/uploads/2017/04/WCP-IIoT-Report-Spring-2017-1.pdf. Accessed 28 Nov 2017
13. Deloitte: Industry 4.0 and cybersecurity: managing risk in an age of connected production. https://www2.deloitte.com/insights/us/en/focus/industry-4-0/cybersecurity-managing-risk-in-age-of-connected-production.html. Accessed 28 Nov 2017
14. Symantec: Internet security threat report. https://www.symantec.com/content/dam/symantec/docs/reports/istr-21-2016-en.pdf. Accessed 28 Nov 2017

15. Bonomi, F., Militio, R., Zhu, J., Addepalli, S.: Fog Computing and its role in the Internet of Things. In: Proceedings of the First Edition of the MCC Workshop on Mobile Cloud Computing, pp. 13–16. ACM, Helsinki (2012)
16. Oracle: CLOUD: opening up the road to Industry 4.0. https://www.oracle.com/webfolder/s/delivery_production/docs/FY16h1/doc30/reportIaas.pdf. Accessed 29 Nov 2017
17. Givehchi, O., Trsek, H., Jasperneite, J.: Cloud Computing for industrial automation systems—a comprehensive overview. In: 2013 IEEE 18th Conference on Emerging Technologies & Factory Automation (ETFA), pp. 10–13. IEEE, Caligari (2013)
18. Lee, J., Kao, H.A., Yang, S.: Service innovation and smart analytics for Industry 4.0 and big data environment. Procedia CIRP **16**, 1–6 (2014)
19. Yin, S., Kaynak, O.: Big data for modern industry: challenges and trends. Proc. IEEE **103**(2), 143–146 (2015)
20. ISACA: Big data impacts & benefits. White paper (2013)
21. Deloitte: Industry 4.0 challenges and solutions for the digital transformation and use of exponential technologies. http://www.industrie2025.ch/fileadmin/user_upload/ch-en-delloite-ndustry-4-0-24102014.pdf. Accessed 30 Nov 2017
22. PWC: Turning additive manufacturing into business. https://www.pwc.nl/en/assets/documents/pwc-turning-additive-manufacturing-into-business.pdf. Accessed 30 Nov 2017
23. KPMG: The factory of the future, Industry 4.0—the challenges of tomorrow. https://assets.kpmg.com/content/dam/kpmg/es/pdf/2017/06/the-factory-of-the-future.pdf. Accessed 16 Dec 2017
24. McKinsey & Company: Industry 4.0: how to navigate digitization of the manufacturing secor. https://www.mckinsey.de/files/mck_industry_40_report.pdf. Accessed 22 Dec 2017
25. Gartner: https://www.gartner.com/newsroom/id/2905717. Accessed 27 Dec 2017
26. Forbes: https://www.forbes.com/sites/gartnergroup/2015/02/12/gartner-predicts-three-big-data-trends-for-business-intelligence/#3284874c6de4. Accessed 27 Dec 2017
27. Al-Doghman, F., Chaczko, Z., Ajayan, A.R., Klempous, R.: A review on Fog Computing technology. In: 2016 IEEE International Conference on Systems, Man and Cybernetics, pp. 001525–001530. IEEE, Budapest (2016)
28. Peraković, D., Periša, M., Sente, R.E.: New challenges of ICT usage in transport and logistics. In: The Sixth International Conference Transport and Logistics, pp. 9–16. University of Niš, Faculty of Mechanical Engineering, Department for Material Handling Systems and Logistics, Niš, Serbia (2017)
29. Periša, M., Cvitić, I., Kolarovszki, P.: Challenges of information and communication technologies usage in E-business systems. In: E-Business—State of the Art of ICT Based Challenges and Solutions. InTech (2017)

Computer Modeling Application for Predicting of the Passing of the High-Speed Milling Machining Hardened Steel

Alexander Permyakov ⓘ, Sergey Dobrotvorskiy ⓘ,
Ludmila Dobrovolska ⓘ, Yevheniia Basova ⓘ,
and Maryna Ivanova(✉) ⓘ

National Technical University «Kharkiv Polytechnic Institute»,
2 Kyrpychova St., Kharkiv 61002, Ukraine
`e.v.basova.khpi@gmail.com, ivanovamarynal@gmail.com`

Abstract. A high-speed milling of hardened steels at multi-coordinate machining centers in individual and small-series production has become of special interest because of the ability to provide high-quality characteristics of products. To ensure the surface layer quality with extremely small values of residual roughness, surface microhardness, and structural phase composition, a computer-aided simulation of the high-speed milling process by computational-logical algorithms based on the finite element method was performed. The experiments with computer simulation research of high-speed milling were done for two objectives: the process of rectangular cutting and the process of oblique-angled cutting of materials. Two-dimensional and three-dimensional computer modeling was used for the research. The connection between the chip formation process, the stress–strain state of the material, and the angle of inclination of the chip-forming groove of the end mill was established. The maximum value of the energy contribution to the cutting process was offered to choose for the determination of the maximum limit cutting conditions in high-speed milling.

Keywords: Computer simulation · Finite element method · High-speed milling
Cutting conditions

1 Introduction

Nowadays, machine-building industry is characterized by an increase in the requirements for quality and accuracy of manufacturing complex surfaces parts [1]. Particularly the area of high-quality surface treatment of hardened parts is the most difficult. An urgent need for the simultaneous provision of high quality, the precision of the machined part and a reduction in its cost has arisen to ensure the competitiveness of Ukrainian products. Under the conditions of individual and small-series production development, this problem is solved due to using of the high-speed multi-axis machining centers. On such equipment, the part undergoes a complete production cycle. Particular interest and, at the same time, the complexity is represented by the surface process area of hardened steel parts on machining centers that provides production quality parameters that correspond to similar parameters after grinding.

The application of existing finishing technologies in advance determines the possible change in the physical and mechanical state of the surface of the part and the formation of residual tensile stresses in it. Such phenomena negatively affect the operational properties of the machine parts. In this connection, there is a necessity to search for the new technological solutions that would ensure high quality and accuracy of processing complex surfaces of hardened steels by using the capacities of multi-axis machining centers [2]. However, the creation of such technology requires, on the one hand, the consideration of a through cycle from the design to the manufacturing of a part using CAD /CAE /CAM /CAPP systems for automated production, and on the other hand a deep understanding and study of the features of the technology and the processes in the cutting zone as well as the effect to the roughness formation and changes in the physical and mechanical state of the surface. Though, despite a large number of existing scientific works, it has not been possible to find studies that represent a systematic approach to the planning process for the development of a competitive technology for the manufacture of engineering products from hardened steels in an economically reasonable and reliable manner. Thus, we concluded that the formation of high-quality high-speed milling (HSM) of hardened parts requires an integrated approach taking into account all the stages of the through cycle from the design of accurate 3D-models to their fabrication at a machining center, including the characteristics of the fracture and surface formation processes, that is, within the CAD/CAE /CAM/CAPP systems (Fig. 1) [3–5].
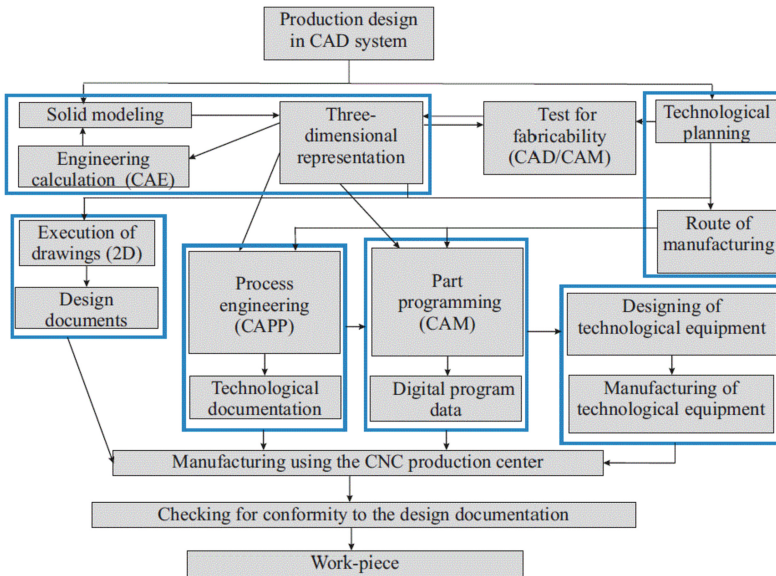
Fig. 1. End-to-end parallel workpiece manufacturing cycle.

2   Literature Review

A high-speed milling is one of the most promising methods of hardened steel surface treatment. This method allows ensuring the smoothness of the cutting tool movement and the accuracy of manufacturing complex surfaces that are not subjected to bedding-in during operation [5–7]. When planning the adoption of the high-speed milling of the surfaces of hardened steel parts, it is necessary to take into account the fact that the transformations that occur during quenching, tempering, and further heat treatment are of great technological importance. An author [8] states that hardened steel acquires good elastic properties and a relatively high viscosity. In the paper [9], fundamental differences in the treatment of hardened steel are given, namely: sawtooth chips are formed by breaking the material being processed; the chip formation process is characterized by a small material shear angle in the working plane, etc. In 1988 Professor Nakayama et al. carried out an analysis of the hardened steels treatment and identified issues that still require deep understanding and study. They are the presence of an innovative angle in the processing of brittle material and its correlation with the direction of the propagation of fracture, which from the point of view of engineering technology can ensure the integrity and durability of machine parts during the operation. It can also ensure the quality of the working surfaces. It is necessary to understand the nature of the sources of high temperature in the treatment zone of the hardened steel, its effect on the cutting process and, as a result, on the formation of the physic-mechanical characteristics of the processed material.

The basic ideas and a model of the chip formation process, proposed in the article [10], were successfully developed by the subsequent research. Studying the chip formation process [11], researchers determined that the formation of the segment chips is not a linear dynamic process. That can affect the cutting forces, the accuracy of machining and the quality of the surface. A mathematical model of the chip formation process in the treatment of hardened steels takes into account both the fracture and the plastic deformation of the thick section of the chips. That has made it possible to explain the structure of the chips.

Currently, the study of the quality characteristics of hardened steels after high-speed milling has received very little attention. Practically there is neither theoretical nor experimental research to apply the high-speed milling of the details from the hardened steels [12, 13]. For a deep insight into the phenomena occurring by the high-speed milling, a non-replaceable instrument is a finite element analysis, which allows getting fairly accurate predictions in a convenient graphical interface. Beker et al. widely adopted this method for modeling and optimization of the cutting processes [14–17]. The application of the finite element method for a three-dimensional (3D) analysis is extremely rare, although it allows obtaining a comprehensive picture of the processes and has a significant advantage in solving the complex of optimization problems.

The article purpose is to improve the quality of hardened steels part process by a computer design and simulation of the high-speed milling processes.

3   Research Methodology

According to the existing recommendations of the technology of hardened steels high-speed milling, cutting speeds of 250–600 m/min and above are required. This fact extremely limits the possibilities of using the traditional manufacturing processes. High-speed milling of the complex surfaces occurs under the conditions of localization of thermal zones and distribution of the strain–stress state of the part material. Therefore, to ensure the quality of the surface layer with extremely small values of the residual roughness, surface micro hardness, and structural phase composition, it is necessary to perform computer-aided design and simulation of the process.

Studies show that the basis of the cybernetic approach to solving the mechanical engineering problems is a system analysis. According to that the research, analysis and calculation tasks of individual technological processes, computer modeling and optimization of complex technological processes and phenomena, as well as the optimal design of technological complexes are solved in close connection with each other. e They are united by a common strategy and are subject to a single goal - the creation of a highly efficient technology production of competitive products.

The development of a high-quality products manufacturing from hardened steels by the high-speed milling requires material cost and time expenditure to find reasonable process conditions for a new material, which has unfavorable effect to the cost of production.

Computer-aided design and simulation of the process objects images under study on the computational-logical algorithms based on the finite element method were decided to use in order to determine the area of existence of the reasonable process conditions for high-speed milling of hardened steels (Fig. 2).
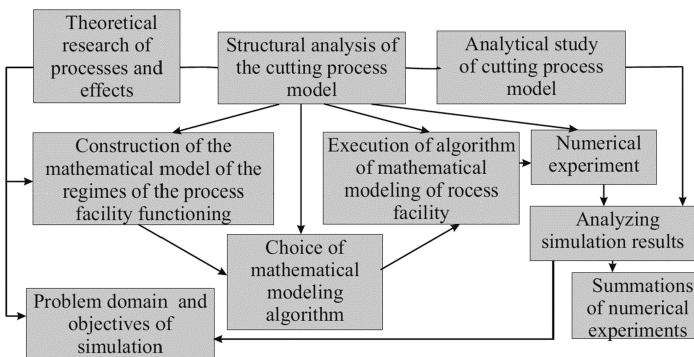
Fig. 2. Scheme of organization of computer simulation of the high-speed milling process.

Due to the computer simulation of the research HSM, the optimization and design of the real technological tasks for the manufacturing of high-quality products from hardened steel, two research objects were selected: the process of rectangular cutting and the process of oblique-angled cutting of the materials.

2D modeling of the two-component system "tool – workpiece" in DEFORM-2D (Fig. 3) was applied to analyze the rectangular cutting process.
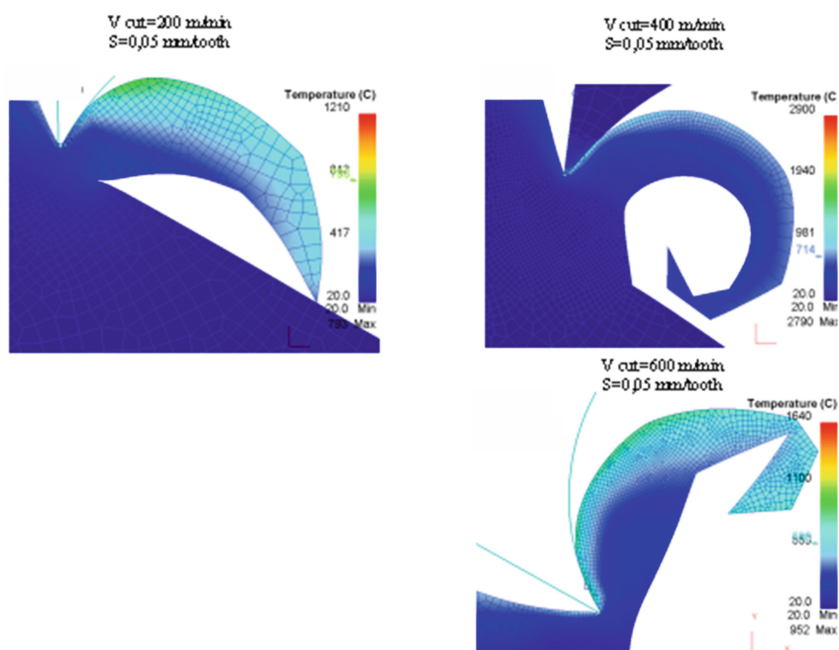
Fig. 3. 2D modeling of the process of rectangular cutting of the hardened steel (S-feed, Vcut-cutting speed).

In DEFORM, the stresses and deformations that are used in stress–strain curves are shown as effective stresses and effective deformations. The processor uses the following effective stress and strain equations:

$$\bar{\sigma} = \frac{1}{2} \cdot \sqrt{(\sigma_x - \sigma_y)^2 + (\sigma_y - \sigma_z)^2 + (\sigma_z - \sigma_x)^2 + 6 \cdot \left(\tau_{xy}^2 + \tau_{yz}^2 + \tau_{zx}^2\right)}, \qquad (1)$$

$$\bar{\varepsilon} = \frac{\sqrt{2}}{3} \cdot \sqrt{(\varepsilon_x - \varepsilon_y)^2 + (\varepsilon_y - \varepsilon_z)^2 + (\varepsilon_z - \varepsilon_x)^2}, \qquad (2)$$

where σ - the normal mechanical stress applied to the unit area of the cross section, normal to the cross section (Pa), ε - active deformations used by program solvers in stress-deformed curves.

In the plastic deformation processes, essentially all of the deformation energy converts into heat, and this causes the irreversibility of the processes. The only reversible energy that is restored is the energy caused by the elastic deformation. According to the fact that the elastic deformation energy is small, we can assume that

the reversible energy equals approximate zero. Thus, the specific thermal energy can be presented as:

$$Q_p = \frac{1}{J} \cdot \int\limits_{\bar{t}_1}^{\bar{t}_2} \bar{\sigma} \cdot d\bar{\varepsilon},$$

(3)

where J—the amount of specific heat per unit time during the plastic deformation.

At very high deformation rates, provided that there are no thermal losses, the adiabatic temperature can be calculated as follows

$$T = T_0 + \frac{Q_p}{c \cdot p},$$

(4)

where T_0—the initial temperature, °C; c—specific thermal capacity; p—specific material weight.

4   Results

Understanding the mathematical processes taking place in the selected CAE system, the search for the area of existence of the reasonable cutting conditions was carried out by numerical experiments with changeable cutting speed (m/min), tool feed (mm/tooth) and cutting depth (mm). The experimental analysis was performed on constructing the model by an updated Lagrangian, which uses the method of automatic reconstruction of the grid. This allowed to ensure continuous reconstruction of the grid and to exclude the use of the separation criterion in the process of chip formation.

The chosen model of the manufacturing process simulation allows in case of distorted elements to trigger automatically the generation of a new grid that divides the contact boundaries, connects adequate internal nodes, smoothes the elements, and then interpolates the stresses and deformations for the new grid. As a result of numerical calculations, it was possible to establish lower limits of technological conditions for the transition from conventional to high-speed cutting. It is determined that the transition from conventional cutting to high-speed cutting is characterized by an increase in the time shift between the deformation wave and the temperature wave taking place in the material destruction zone by 10^{-7}–10^{-8} s [5].

The analysis of the influence of various technological factors on the qualitative changes in the plastically deformed layer of the material showed that there is a direct correlation between the chip formation and the stress–strain state of the material depending on the slope of the chip-shaped groove of the tool. This fact has been confirmed by a number of numerical calculations with diverse variants of changes of the cutting tool 3D models.

Simulation of the oblique-angled cutting was carried out in the DEFORM-3D modeling system (Fig. 4). The boundary conditions were the heat exchange between the tool, the material and the external environment.
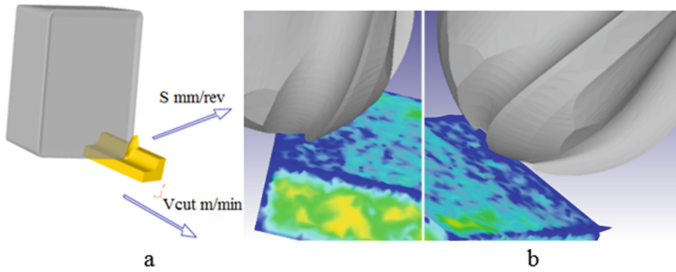
Fig. 4. 3D modeling of the rectangular cutting of the hardened steel process (a) and the oblique-angled cutting of the hardened steel process (b).

Due to realizing the multi-criterion optimization of the high-speed milling process and ranking its technological parameters, the sufficiently accurate forecasts of the physical and physical-mechanical characteristics of the high-speed material destruction was obtained [5]. Analyzing the results of the experimental computer simulation data of the high-speed milling process, it becomes possible to state that the maximum processing conditions, where cutting conditions can be assigned, are between maximum energy contribution to the process of material destruction and the amount of energy contribution to the cutting process that corresponds the moment of material inertial flow.

Thus to achieve the estimated purpose of the maximum limit processing condition, it is necessary to use the maximum value of the energy contribution to the cutting process.

The disrupted layer depth of the material test sample was estimated by the results of visualization of the material deformation distribution and the graphic representation of their distribution in high-speed milling process. The acquired results were considered to define the process condition range of high-speed milling (Figs. 5, 6, 7, 8, 9).

Computer simulation results of rectangular and oblique cutting show that the temperatures for the oblique cutting are much lower than for the rectangular cutting. In this case, rectangular cutting is accompanied by phase transformations. These facts allow to state, that oblique high-speed milling will avoid the drawbacks of materials during processing and the appearance of unfavorable structural characteristics in the disturbed-deformed layer (Figs. 5, 6, 7, 8, 9).

From the mechanical engineering point of view, this makes it possible to ensure a stable dislocation nature of the damaged material accumulation, during manufacturing as well as operation processes products. The result can be adopted as a wear resistance criterion of treated surfaces.
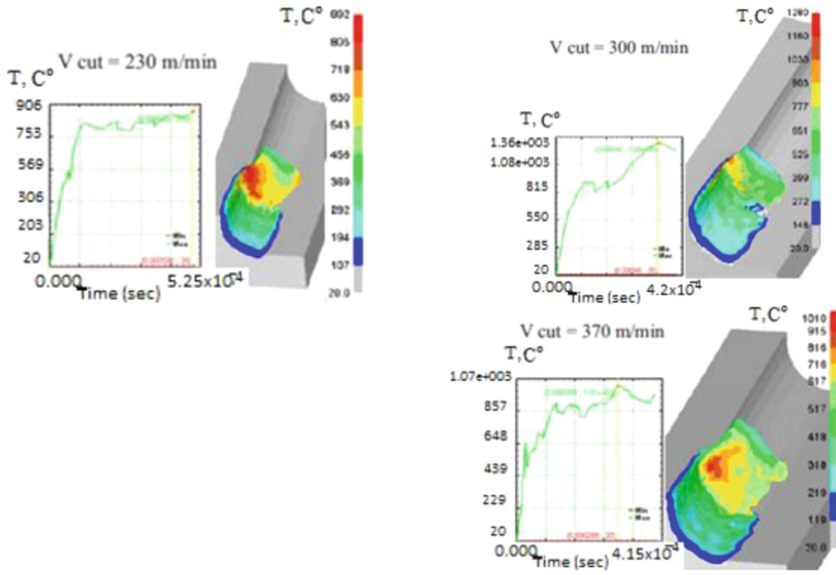
Fig. 5. Dependence of the temperature in the zone of orthogonal cutting on the processing time at different process speeds (S = 0.15 mm/rev).
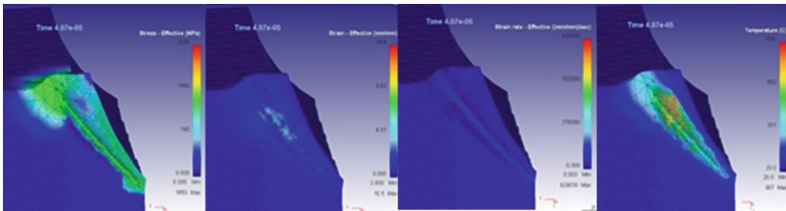
Fig. 6. Window postprocessor with the image of the diagrams (an angle of inclination of the helical line 35°).
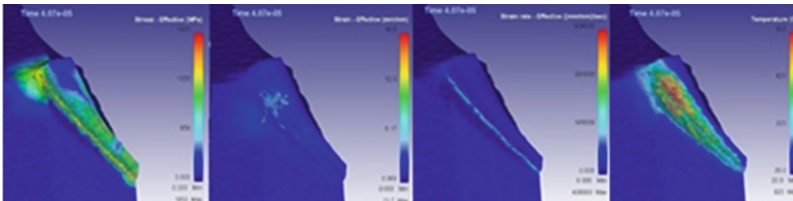
Fig. 7. Window postprocessor with the image of the diagrams (an angle of inclination of the helical line 40°).
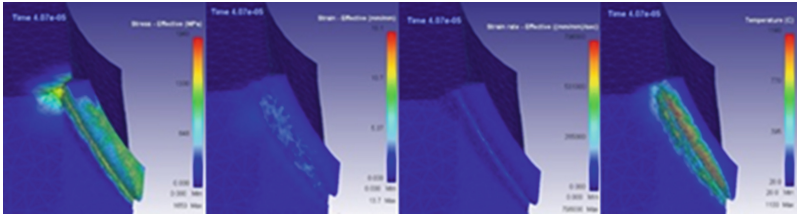
Fig. 8. Window postprocessor with the image of the diagrams (an angle of inclination of the helical line 45°).
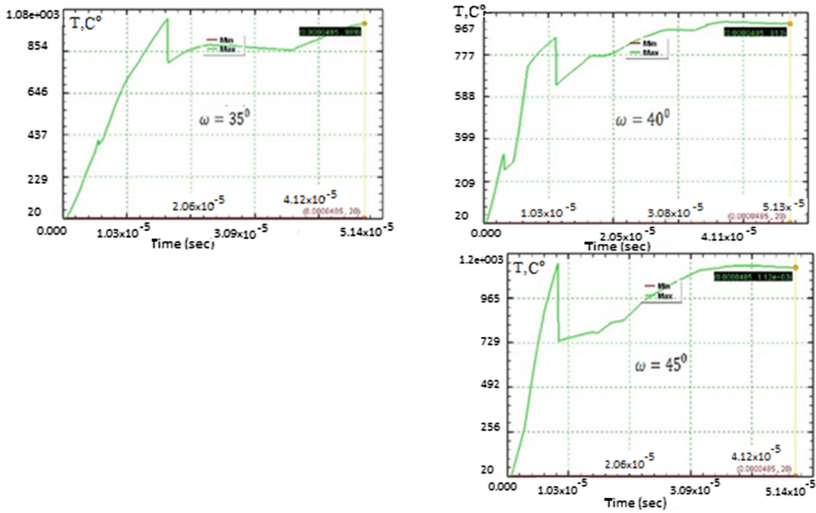
Fig. 9. Graphs of temperature versus time.

5   Conclusions

1. Computer modeling of different engineering processes is an integral stage in the manufacturing of quality products. Computer modeling allows reproducing the cutting process with a high degree of isomorphism and obtaining sufficiently accurate predicted results of processes and phenomena. In addition, it has been determined that computer simulation of the high-speed milling process is sufficient for determining the technological conditions of processing the part at the stage of planning the production process, eliminating the stages of cutting conditions development in the manufacturing environments and reducing the cost of production.

2. Computer simulation of HSM allowed defining the fact that the maximum processing conditions, where cutting conditions can be assigned, are between maximum energy contribution to the process of material destruction and the amount of

energy contribution to the cutting process that corresponds to the moment of inertial flow of material.

3. A comparison of the results of computer modeling of rectangular and oblique-angled cutting showed that it is possible to avoid the drawbacks of materials and unfavorable structural characteristics in the disturbed-deformed layer with the oblique-angled cutting.

References

1. Vieira, G., Reis, L., Varela, M.L.R., Machado, J., Trojanowska, J.: Integrated platform for real-time control and production and productivity monitoring and analysis. Rom. Rev. Precis. Mech. Opt. Mechatron. **50**, 119–127 (2016)
2. Ivanov, V., Mital, D., Karpus, V., et al.: Numerical simulation of the system "fixture–workpiece" for levers machining. Int. J. Adv. Manuf. Technol. **91**(1–4), 79–90 (2017)
3. Karwasz, A., Trojanowska, J.: Using CAD 3D system in ecodesign—case study. In: Golinska-Dawson, P., Kolinski, A. (eds.) Efficiency in Sustainable Supply Chain, Part II, pp. 137–160. Springer, Cham (2017)
4. Ivanov, V., Vashchenko, S., Rong, Y.: Information support of the computer-aided fixture design system. In: Proceedings of 12th International Conference ICTERI'2016, vol. 1614, pp. 73–86. CEUR-WS, online CEUR-WS.org (2016)
5. Dobrotvorskiy, S.S., Basova, YeV, Dobrovolska, L.G.: Increase of competitiveness of domestic machine-building production in modern conditions. Bull. Natl. Tech. Univ. Kharkiv Polytech. Inst. Ser. Technol. Mech. Eng. **42**(1085), 25–31 (2014). (in Russian)
6. Dhandapani, N.V., Thangarasu, V.S., Sureshkannan, G.: Investigation on effect of material hardness in high speed CNC end milling process. Sci. World J. **2015**, 1–6 (2015)
7. Mebrahitom, A., Rizuan, D., Azmi, M., Nassif, M.: Effect of high-speed milling tool path strategies on the surface roughness of Stavax ESR mold insert machining. IOP Conf. Ser. Mater. Sci. Eng. **114**, 1–6 (2016)
8. Fetisov, G.P.: Materials Science and Technology of Metals. High School, Moscow (2001) (in Russian)
9. Singht, D.A., Rao, P.V.: A surface roughness prediction model for hard turning process. J. Mater. Process. Technol. **189**, 192–198 (2007)
10. Nakayama, K., Arai, M., Kanda, T.: Machining characteristic of hard materials. CIRP Ann. Manuf. Technol. **37**(1), 89–92 (2007)
11. Davies, M.A., Burns, T.J., Evans, C.J.: On the dynamics of chip formation in machining hard metals. CIRP Ann. Manuf. Technol. **46**(1), 25–30 (1997)
12. Twardowski, P., Wojciechowski, S., Wieczorowski, M., Mathia, T.: Surface roughness analysis of hardened steel after high-speed milling. Scanning **33**(5), 386–395 (2011)
13. Hajdarevic, D.B., Cekic, A., Kulenovic, M.: Experimental study on the high speed machining of hardened steel. In: 24th DAAAM International Symposium on Intelligent Manufacturing and Automation, 2013. Procedia Engineering, vol. 69, pp. 291–295. Faculty of Mechanical Engineering, University of Sarajevo, Bosnia and Herzegovina (2014)
14. Baker, M., Rosler, J., Siemers, C.: A finite element model of high speed metal cutting with adiabatic shearing. Comput. Struct. **80**(5), 495–513 (2012)
15. Bil, H., Kilic, S.E., Tekkaya, A.E.: A comparison of orthogonal cutting data from experiments with three different finite element models. Int. J. Mach. Tools Manuf. **44**(9), 933–944 (2014)

16. Özel, T., Sima, M., Srivastava, A.K., Kaftanoglu, B.: Investigations on the effects of multi-layered coated inserts in machining Ti–6Al–4V alloy with experiments and finite element simulations. CIRP Ann. Manuf. Technol. **59**(1), 77–82 (2010)
17. Arrazola, P.J.: Investigations on the effects of friction modeling in finite element simulation of machining. Int. J. Mech. Sci. **52**(1), 31–42 (2010)

Computer Simulation of the Processes of Mixing in Multilayer Nitride Coatings with Nanometer Period

Oleg Sobol$^{(\boxtimes)}$, Andrey Meylekhov, and Anna Postelnyk

National Technical University «Kharkiv Polytechnic Institute»,
2 Kyrpychova St., Kharkiv 61002, Ukraine
`sool@kpi.kharkov.ua`

Abstract. Using the complex of methods for the structural state attestation in combination with the computer simulation and measurement of mechanical properties (hardness), the influence of the period Λ on the mixing process on the interlayer boundaries of multilayer coatings TiN/ZrN, CrN/ZrN and MoN/ZrN is studied. The coatings were obtained by the vacuum arc method on the upgraded "Bulat-6" installation. By means of the computer simulation method the depth of impact was estimated, which for the systems under investigation is about 2 and 3.5 nm, respectively. It is established that for the period $\Lambda = 20$ nm the highest hardness is 44 GPa. At Λ less than 20 nm, the hardness decreases, this can be related to the formation of a solid solution in the border regions due to the radiation-stimulated mixing. Computer simulation results obtained in the work allow to define the regimes for the optimal structural state. This is the basis of the direction of the structural engineering of nonequilibrium systems.

Keywords: Computer calculation · Multilayer coatings · Bias potential
Structure

1 Introduction

In recent years the structural engineering has become the main way of obtaining the materials with specified properties. The use of the structural engineering principles has shown high efficiency during the highly nonequilibrium conditions deposition of the coatings. The use of the ion-plasma and vacuum arc technologies coating deposition leads to such processes.

2 Literature Review

The deposition of the vacuum-arc coatings occurs under the action of the radiation factor due to the bombardment of the material surface by the charged accelerated particles [1, 2]. The most typical types of radiation damage in the surface layers during the bombardment by the accelerated ions are shown in Fig. 1.
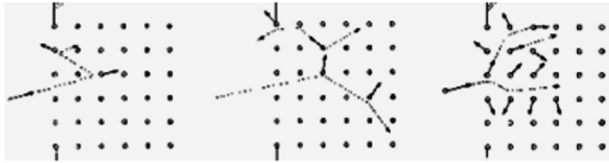
Fig. 1. Schematic processes in the "sputtering" mode bombarding the surface of the particles during the formation of the coating: (a) single-knock-on, (b) linear cascade, (c) spike.

Vacuum arc methods are characterized by a high degree of ionization and therefore most particles in the source field are accelerated. This determines the relatively high average energy of the deposited particles and their high mobility and the ability to form defects. In this case, new types of structures [3, 4] are formed, the preferential arrangement of structural elements [5] and the development of structural stresses [6] in the coatings during their deposition. The prediction and control of structural states in PVD (physical vacuum deposition) coatings is of constant interest [7]. This is connected with the determining influence of the structure on a number of the most important technological properties of the material [8].

Therefore, in this paper, the goal was to investigate the influence of the "radiation factor" on the structure and hardness of the multilayer coatings with a nanometer thickness of the period. For this the experimental data on the attestation of the structural state of the coatings were compared with the results of the computer simulation of radiation-stimulated structural changes by ion implantation during the growth.

3   Research Methodology

The coatings were obtained by the vacuum arc method on the upgraded "Bulat-6" installation. The pressure of the working (nitrogen) atmosphere during precipitation was $P_N = 4 * 10^{-3}$ Torr, the deposition rate was about 2 nm/s. The deposition was carried out from two sources to the surface of the samples with dimensions of $20 \times 20 \times 2$ mm from austenitic steel 12Cr18Ni10Ti (the analog of stainless steel SS 321).

One source was Zr, and the other was Cr or Ti or Mo (depending on the type of the multilayer coating). The used cathode materials are: chromium, titanium, molybdenum and zirconium, obtained by the electron-beam melting (ELF); Active gas - nitrogen (99.95%). The thickness of the layers in the coating (h) was determined by the holding time at the source and on the average for the layer was 7, 10, 20, 40, 75, and 150 nm, which corresponded to a bilayer period with an average thickness of about 14, 20, 40, 80, 150, and 300 nm.

The phase composition, structure, and substructural properties were determined by the X-ray diffractometry (DRON-4) using Cu-Kα radiation. For the monochromatization of the recorded radiation, a graphite monochromator was used, which was

installed in a secondary beam (in front of the detector) with a high degree of colli-
mation [9]. For decoding the diffractograms, the tables of the international diffraction
data center Powder Diffraction File [10] were used.

Microindentation was carried out at the Micron-gamma facility at a load of up to
$F = 0.5$ N with the Berkovich diamond pyramid with an angle of sharpening of $65°$,
with the automatic loading and unloading for 30 s.

To understand the spatial distribution of radiation-stimulated changes in the
boundary (interlayer) regions during the deposition of the high-energy particles, the
computer simulation was used in the work. For this purpose, the program based on the
approximate method of double collisions, TRIM, was used in the work. The calculation
is based on the Monte Carlo method for describing the trajectory of the incident particle
and the damage created by this particle (Figs. 2 and 3). TRIM uses the maximum
exposure parameters determined by the density of the medium and by the constant
mean mileage between collisions [11].
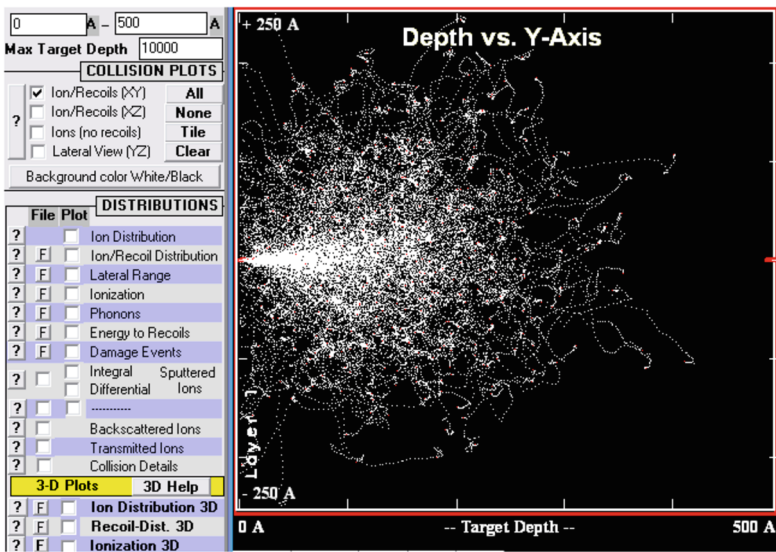
Fig. 2. Window of calculation of parameters.
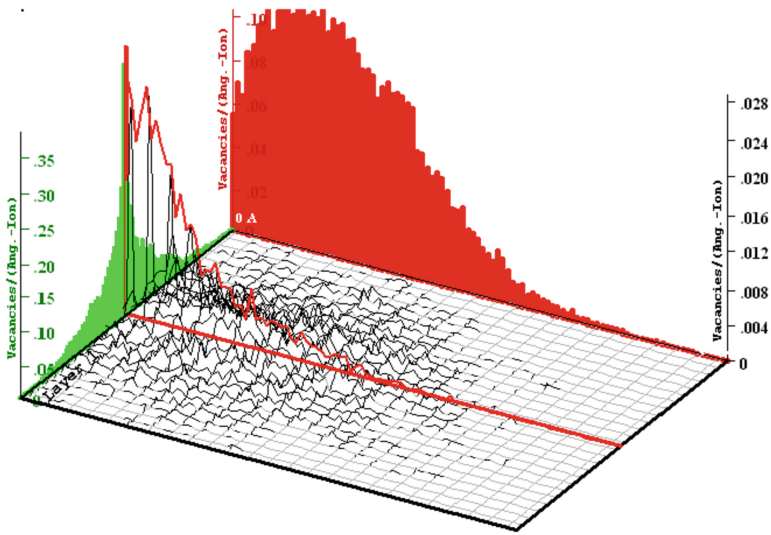
Fig. 3. Simulation results.

4 Results

The phase composition of the layers was determined by the XRD method. The X-ray diffraction (XRD) spectra of the multi-period system ZrN/TiN coatings are shown in Fig. 4. The use of the complex profile separation program showed that at a large Λ (about 300 nm), two systems of the diffraction peaks from ZrN and TiN phases (card PDF 38-1420) Fig. 4a, c) are identified.
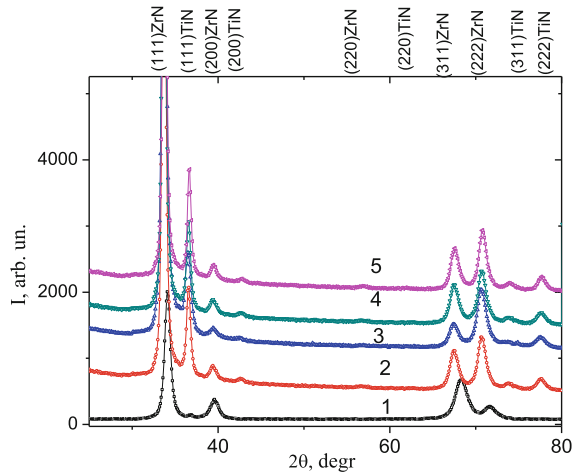
Fig. 4. XRD patterns of coatings ZrN/TiN with different Λ: (1) 10 nm; (2) 20 nm; (3) 80 nm; (4) 150 nm; (5) 300 nm.

Isostructural phases (structural type NaCl) of ZrN and γ-Mo$_2$N are formed in the ZrN/MoN coatings. With the smallest potential $U_b = -70$, crystallites with predominant orientation are formed in the coating layers (the [100] axis is perpendicular to the growth plane, the axial texture). The formation of this orientation in the deposition of the vacuum-arc nitride coatings with the structural type of the NaCl crystal lattice is usually associated with the condensate depletion over the light nitrogen atoms [12]. In the coatings deposited at a larger $U_b = -110$ V, the predominant orientation of the crystallites is practically not detected (Fig. 5, spectrum 1). And the asymmetrical form of the reflexes (shown in Fig. 5 by arrows) indicates the formation of transition layers by mixing Mo and Zr components. The mean crystallite size determined by the Scherrer formula [13] is about 5 nm for ZrN. Crystals of the γ-Mo$_2$N phase are much smaller (with an average size of about 2.3 nm).
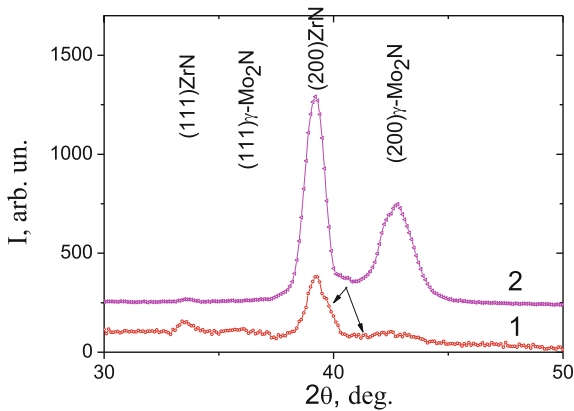
Fig. 5. XRD patterns of the ZrN/MoN coatings obtained at a constant bias potential of -110 V (1) and -70 V (2) with a period of 15 nm.

The formation of a solid solution at the interface is even more pronounced on the diffraction spectra of the CrN/ZrN system (Fig. 6). In this case, the supply of $U_b = -70$ V is sufficient for the explicit formation of a solid solution (in the spectrum, 2 is shown by arrows). The formation of such mixed zones is possible only on the contacting surfaces of the CrN/ZrN layers, i.e. on the interphase boundary.

The most important factor in the multilayer composition is the state of its interphase boundary [14]. As was shown above, the formation of a solid solution occurs precisely at the interphase boundary and is associated with the action of the radiation-stimulated processes. This necessitates the simulation of the processes that can occur at the border. This is especially important for the nanometer scale of the layers, when the radiation effect is comparable to the thickness of the layer.
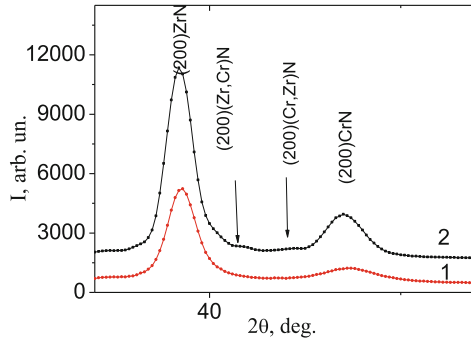
Fig. 6. XRD patterns of the multilayer coatings of CrN/ZrN obtained at $P_N = 1.5 \times 10^{-3}$ Torr with a number of layers of 564 and a period of about 20 nm without applying a constant potential to the substrate (1) and $U_b = -70$ V (2).

To assess the depth of impact in the work, the modeling of the implantation processes was carried out. The simulation of the processes that can occur at the boundary at the nanometer scale of the layers is based on the radiation-stimulated effects upon the deposition. For the ZrN/MoN system, the simulation showed that in the case of irradiation with Mo ions with an average energy of 110 eV (corresponding to the average particle energy for the deposition with $U_b = -110$ V) of the ZrN (Mo $\rightarrow$ ZrN) coating, the maximum concentration of the implanted particles should be at a depth of ≈ 0.9 nm (at the total depth of exposure up to 2 nm (Fig. 7a)). Under the influence of Zr $\rightarrow$ MoN, the maximum ion distribution is also at a depth of ≈ 0.9 nm with the total depth of impact of ≈ 1.85 nm (Fig. 7b).
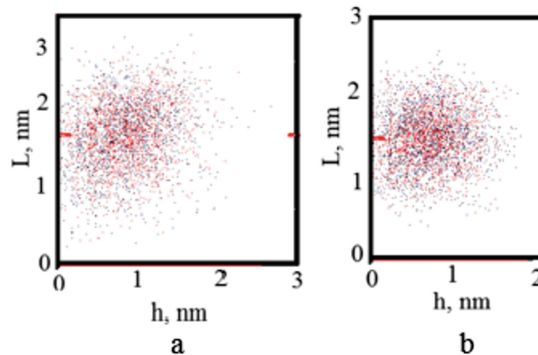
Fig. 7. Type of the distribution of the embedded ions obtained by the modeling: (a) Mo $\rightarrow$ ZrN, (b) Zr $\rightarrow$ MoN (1000 iterations).

Thus, during the deposition of the coating at the boundaries, a layer about 2 nm in thickness is formed in which the radiation-stimulated mixing plays a decisive role. Since there are two such boundaries in the period Λ, the total depth of influence of the radiation defect formation in the period is about 4 nm.

The modeling for the CrN/ZrN system has shown that the depth of the penetration of Cr ions is larger in comparison with Zr (Fig. 8). For the energy of the accelerated ions of about 100 eV, the average depth of the penetration of Cr ions is 2.0 nm (the number of the initiated vacancies is 0.37 vac./ion, the total depth of the action reaches 3.5 nm), and for Zr ions is 1.8 nm (the number of the initiated vacancies is 0, 47 vac./ion, the total depth of exposure reaches 2.8 nm).
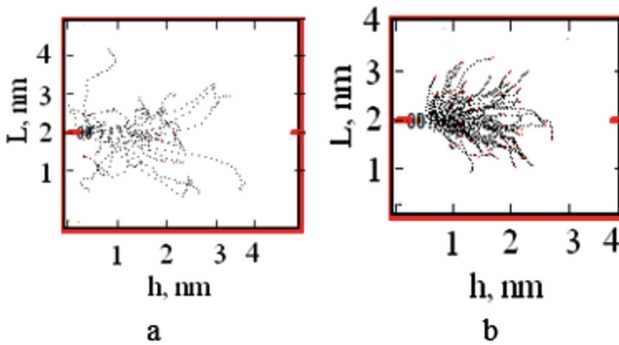
Fig. 8. The depth of the penetration of chromium ions (a) and zirconium ions (b), CrN/ZrN (100 iterations).

Thus, in the case of the CrN/ZrN system, the total depth of impact can reach 5.6–7 nm in the border region. This is almost 1.5 times greater than the same indices of mixing in the ZrN/MoN system, which determines the greater degree of the manifestation of mixing (the formation of solid-solution reflections is observed) on the XRD-spectra (see Figs. 5 and 6).

Using the software package TRIM, the simulation showed that in the case of irradiation with ions with an average energy of 110 eV, which corresponds to the deposition under the action of $U_b = -110$ V, in the TiN/ZrN system, the penetration depth of Ti ions is larger in comparison with Zr (as more straggling, Fig. 9). For the accelerated ion energy of about 100 eV, the average penetration depth of Ti ions is 1.9 nm (the number of the initiated vacancies is 0.35 vacancies per ion, the total depth of the action reaches 3.5 nm), and for Zr ions is 1.8 nm (the number of the initiated vacancies is 0.46 vacancies per ion, the total depth of exposure reaches 2.9 nm).

The most universal and express characteristic of the determination of the mechanical properties is hardness. Figure 7 summarizes the results of the change in hardness of the multiperiod coatings from Λ. It can be seen from the obtained results that in the CrN/ZrN system the hardness of the coatings obtained at $U_b = -70$ V at small Λ (less than 40 nm) practically does not increase, remaining at the level of 40 GPa. For the ZrN/MoN system with a large $U_b = -110$ V (in contrast to the small U_b,

Fig. 10, curves 2 and 3) and a period Λ less than 20 nm, a significant decrease in hardness is observed. For a small $U_b = -70$ V (Fig. 10, curve 2), the maximum hardness ($\approx$41 GPa) in the ZrN/MoN system is achieved in the coatings with the smallest Λ.

The decrease in hardness observed at small Λ (less than 20 nm) can be related to the effect of the boundary mixing. If compared with the XRD-data (Figs. 5 and 6), then it is at $\Lambda = 20$ nm that peaks appear from the solid-solution component.
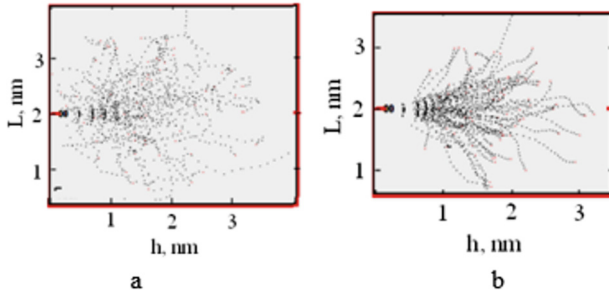
Fig. 9. The depth of the penetration of titanium ions (a) and zirconium ions (b), TiN/ZrN system (100 iterations).
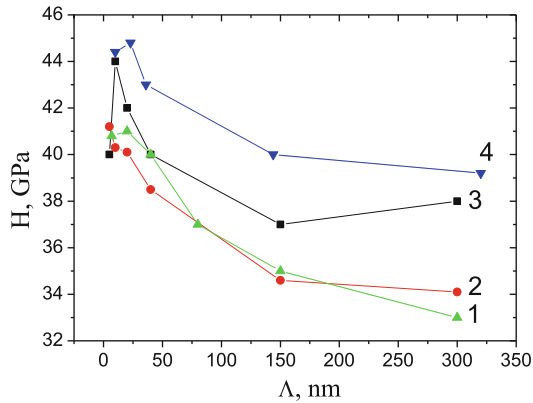
Fig. 10. Dependence of the hardness of the coatings (H) on the thickness of the bilayer period (Λ) for the multilayer coatings of the CrN/ZrN system at $U_b = -70$ V (1) and the ZrN/MoN system obtained at $U_b = -70$ V (2) and $U_b = -110$ V (3) and TiN/ZrN system (4).

5   Conclusions

1. At $\Lambda = 20$ nm (or less), the formation of solid solutions for the ZrN/MoN system at $U_b = -110$ V appears on XRD-spectras, and for the CrN/ZrN system at $U_b = -70$ V.
2. The use of the method of modeling the radiation-stimulated damage during the ion irradiation has made it possible to determine the critical mixing thickness in the bilayer systems. This thickness is about 4 nm for the ZrN/MoN system about 7 nm for the CrN/ZrN and TiN/ZrN systems.
3. It is established that at $\Lambda = 20$ nm the highest hardness is 44 GPa. At Λ less than 20 nm, the decrease in hardness is observed, which can be related to the formation of a solid solution in the border regions due to the radiation-stimulated mixing.
4. To reduce the effect of mixing between the layers (i.e., reducing the critical thickness), it is possible to reduce U_b to -20 V (the mixing region will be less than 1 nm in this case), and to use the nitrides based on Ti and Cr (with the close atomic masses).
5. Computer simulation results obtained in the work allow to define the regimes for the optimal structural state. This is the basis of the direction of the structural engineering of nonequilibrium systems.

References

1. Berish, R.: Solid Objects Sputtering by Ions Bombardment. Transl. from English. Mir, Moscow (1984)
2. Elstner, F., Kupfer, H., Richter, F.: Activation energy of point defect diffusion in low-temperature deposited TiN. Phys. Status Solidi **147**, 373–377 (1995)
3. Ivashchenko, V.I., Dub, S.N., Scrynskii, P.L., Pogrebnjak, A.D., Sobol', O.V., Tolmacheva, G.N., Rogoz, V.M., Sinel'chenko, A.K.: Nb–Al–N thin films: structural transition from nanocrystalline solid solution nc-(Nb, Al)N into nanocomposite nc-(Nb, Al)N. J. Superhard Mater. **38**(2), 103–113 (2016)
4. Sobol', O.V.: The influence of nonstoichiometry on elastic characteristics of metastable β-WC1–x phase in ion plasma condensates. Tech. Phys. Lett. **42**(9), 909–911 (2016)
5. Barmin, A.E., Zubkov, A.I., Il'inskii, A.I.: Structural features of the vacuum condensates of iron alloyed with tungsten. Funct. Mater. **19**(2), 256–259 (2012)
6. Mayrhofer, P.H., Mitterer, C., Hultman, L., Clemens, H.: Microstructural design of hard coatings. Prog. Mater. Sci. **51**, 1032–1114 (2006)
7. Cavaleiro, A., De Hosson, J.T.M.: Nanostructured Coatings. Springer, Heidelberg (2006)

8. Kumar, P., Patnaik, A., Chaudhary, S.: A review on application of structural adhesives in concrete and steel–concrete composite and factors influencing the performance of composite connections. Int. J. Adhes. Adhes. **77**, 1–14 (2017)
9. Klug, H.P., Alexander, L.E.: X-ray Diffraction Procedures for Polycrystalline and Amorphous Materials, 2nd edn. Wiley, New York (1974)
10. Jenkins, R., Snyder, R.L.: Introduction to X-ray Powder Diffractometry. Wiley, New York (1996)
11. Ziegler, J.F.: SRIM – the stopping and range of ions in matter. Nucl. Instr. Methods Phys. Res. B **268**, 1818–1823 (2010)
12. Kuo, L.-Y., Shen, P.: On the condensation and preferred orientation of TiC nanocrystals—effects of electric field, substrate temperature and second phase. Mater. Sci. Eng. **276**(1–2), 99–107 (2000)
13. Karabacak, T., Senkevich, J.J., Wang, G.C., Lu, T.: Stress reduction in sputter deposited films using nanostructured compliant layers by high working-gas pressures. J. Vac. Sci. Technol. A **23**(4), 986–990 (2005)
14. Wu, Y.G., Cao, E.H., Wang, Z.S., Wei, J.M., Tang, W.X., Chen, L.Y.: Stress anisotropy in circular planar magnetron sputter deposited molybdenum films and its annealing effect. Appl. Phys. A **76**, 147–152 (2003)

Model of Thermal State of the System
of Application of Coolant in Grinding Machine

Mykhaylo Stepanov[1] , Larysa Ivanova[2(✉)] ,
Petro Litovchenko[2] , Maryna Ivanova[1] ,
and Yevheniia Basova[1]

[1] National Technical University «Kharkiv Polytechnic Institute»,
2 Kyrpychova St., Kharkiv 61002, Ukraine
[2] National Academy of the National Guard of Ukraine,
3 Maidan Zahysnykiv Ukrainy, Kharkiv, Ukraine
`larisanangu@gmail.com`

Abstract. A high grinding performance and ensuring the accuracy and quality of processing depend on a stable thermal regime in the cutting zone, which is carried out by efficient removal of the released heat. Application of lubricating and cooling fluid allows reducing the power and cutting forces, accelerates heat transfer, provides a reduction in temperature in the cutting zone. It's found out, that the most instability is characteristic for the heat entering the machine tool from the coolant system. Potentialities of decreasing of heat fluxes influence at the grinding machine on the accuracy by improving cooling ability of coolant tank are researched. The heat exchange processes in the coolant tank of the grinding machine are studied. A mathematical model describing the temperature regime of coolant in the grinding machine tank is proposed. The model makes it possible to estimate the steady-state and non-stationary temperatures of the coolant in the tank, depending on the course of the stages of the grinding cycle and to define the rational volume of the coolant, considering the cooling of cutting zone, the grinding parameters, and the characteristics of the grinding wheel. The dependence of the value of the average coolant temperature in the grinding machine tank from volume of coolant is determined.

Keywords: Coolant application system · Stationary mode
Nonstationary mode · Temperature gradient · Heat transfer coefficient
Coefficient of thermal conductivity

1 Introduction

An important condition of high grinding performance and ensuring the accuracy and quality of processing is the maintenance of a stable thermal regime in the cutting zone, which is carried out by efficient removal of released heat. This function is performed by coolant—a lubricating and cooling fluid, which reduces the power and cutting forces, accelerates heat transfer, provides a reduction in temperature in the cutting zone.

Thermal deformations of machines disturb their geometric accuracy and cause errors in the dimensions and shapes of the machined workpieces [1–4]. In addition, the temperature deformations of the grinding machine lead to a deviation from the perpendicular axis of the spindle to the plane of the table [5, 6]. When the temperature changes by 5 °C, the change in the angular position of the spindle axis can be 0.1 mm over a length of 1000 mm. Because of this deviation from the parallelism of the ends of the ground workpiece is 0.012 mm at a length of 300 mm [7]. The factor of the effect of coolant in this process is practically not detected [8].

Analysis of the heat fluxes of the grinding machine shows that the most instability is characteristic for the heat entering the machine from the coolant system [9–11]. For this reason, it is obviously that the actual problem is the reduction of the effect of the heat flows of the machine on the accuracy of grinding, which can be ensured by improving the cooling capacity of the coolant tank.

2   Literature Review

The influence of coolant on the efficiency of the grinding process has been devoted to a large number of studies [6, 7, 12–14].

Shakhnovsky [13] tried to predict the effect of heat fluxes not only directly in the cutting zone, but also as a whole in the technological system of the grinding machine, including in the coolant supply system.

It is established, if the final temperature, returned together with the coolant in the cutting zone, exceeds the ambient temperature by 20 °C, then deviations from the parallelism of the faces of the prismatic part can reach 20 μm. If there is no excess, the deviation from parallelism does not exceed 5 μm.

The reason for this phenomenon is the change in the angular position of the grinding wheels under the influence of excessive temperatures in the reservoirs of the coolant systems [10, 13, 15, 16]. If the excess temperature exceeds 30 °C, the change in the angular position of the circle can reach 0.3 mm, one of the main reasons for the deviation of the position of the grinding spindle from the machine bases is the insufficient heat dissipation capacity of the reservoirs of the coolant system.

The aim of the research is to improve the parameters of the heat exchange processes in the coolant tank of the grinding machine with an individual feeding into the cutting zone.

3   Research Methodology

3.1   Characteristics and Parameters of the Cooling System Operation Cycle

The temperature of the coolant in the reservoir depends on many factors, the most important of which are:

– overall dimensions and spatial geometric shape of the tank;
– the material of the walls of the reservoir and its heat transfer capabilities;
– the nature of the process of heat exchange between the coolant and the walls of the reservoir, and also between the reservoir and air;
– the properties of the used coolant.

In the process of research, the system of coolant application is considered as the one that works in the following sequence.

The machine is switched on for the first time after a long time and operates for a period of time t_d, that is, during the auxiliary time. The initial temperature of the coolant in the tank is equal to the ambient temperature $T_{01} = T_{at}$: (Fig. 1).
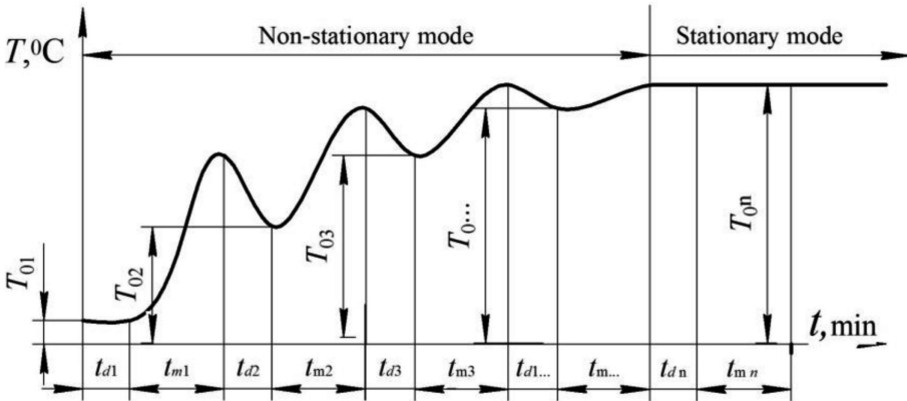
Fig. 1. Diagram of the operation of the coolant system.

After continuous operation for a period of time t_d in the transmission mode, the machine goes into the grinding operation mode, and the coolant application system is operational and operates in it during the main operating time t_m. The temperature at the entrance to the pump is the one that was set at the time of the system's transition to the operating mode – t_d.

Then, the system returns to the throughput mode and is in it during the auxiliary operating time t_d, and the temperature at the pump inlet $T_0 = T_{td}$ is the same as that set in the tank after the first grinding operation, i.e.: $T_0 = T_{m1}$.

Then, the system again goes into the operating mode, etc., that is, the process repeats cyclically n times, where n is the number of processed blanks.

Total operating time of the system in such cyclic mode can be determined from the dependence:

$$t_\Sigma = \sum_{i=1}^{n} (t_{di} + t_{mi}), \tag{1}$$

where is t_{di}, t_{mi} – respectively, the auxiliary and machine times with i - therefore the repetition of the cycle, min.

The coolant system operates in two thermal modes:

- non-stationary when the current coolant temperature in the tank during the operation of the system for a finite time do not reach a constant value and grows after each next run of the cycle (grinding operation), that is $T_0 \neq const$;
- stationary, when the current coolant temperature in the tank reaches a constant value and remains constant even at $t \to \infty$, that is $T_0 = const$.

When working in non-stationary mode, the temperature at a certain point depends not only on the coordinates of the point, but also on time, that is:

$$T = f(x, y, z, t), \quad \frac{dT}{dt} \neq 0, \tag{2}$$

where is $\frac{dT}{dt}$ - the temperature gradient over time.

When operating in a stationary mode, provided the reservoir is of sufficient volume, the temperature does not depend on time, that is:

$$T = f(x, y, z, t), \quad \frac{dT}{dt} = 0. \tag{3}$$

In a real coolant application system, the intake part of the pump is located in the reservoir at a horizontal distance from the main heat source - the coolant shower point from the working circuit (Fig. 2).
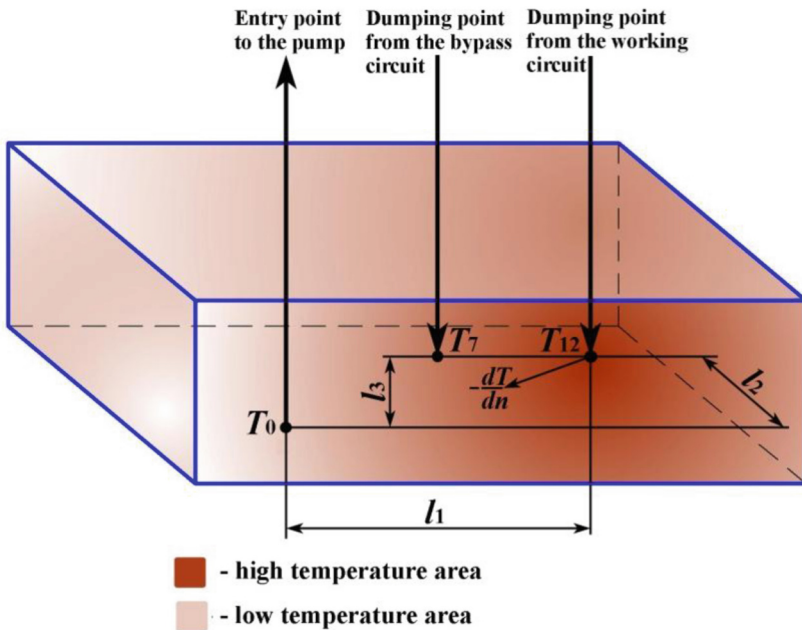
Fig. 2. Diagram of variation of the temperature field in the coolant reservoir.

The temperature decreases with the gradient $-\frac{dT}{dn}$ as you move away from point 12 of the drain from the working circuit. In this case, we assume that the tank used in the system has a sufficient volume, which ensures that the permissible value of the constant temperature is not exceeded.

Considering the above, it is necessary:

- to obtain dependencies for determining the current coolant temperature in the reservoir for a certain value t when the system is operating in non-stationary mode;
- to obtain dependencies for determining the constant coolant temperature in the tank when the system is in steady state operation.

3.2   Mathematical Model of the Thermal State of the Coolant System

In the studies, the heat balance equations in the coolant reservoir were used:

$$Qdt = (cm + c_1 m_1)dT + kF \cdot dt \left(\frac{dT}{2} + T_p - T_{nc}\right), \tag{4}$$

where is Q - the amount of heat that receives coolant in the current (throughput or operating mode), kJ; dT - temperature increase over time dt, °C; T_{nc} - ambient temperature, °C; T_p - coolant temperature in the considered time interval, °C; c - heat capacity of coolant at the current temperature kJ kg^{-1} · °C^{-1}; m - mass of coolant in the tank, kg; c_1 - heat capacity of the tank material, kJ·kg^{-1} · °C^{-1}; m_1 - the calculated mass of the dry reservoir, kg; F - the estimated surface area of the tank, m$_2$; k - coefficient of heat transfer from the tank to the air, W m^{-2} · °C^{-1}.

The calculated surface area for a known volume of the reservoir is determined by the empirical formula:

$$F = 0.065\sqrt[3]{V^2}, \tag{5}$$

The coefficient of heat transfer from the reservoir to the air is determined from the dependence:

$$k = \frac{1}{\frac{1}{\alpha_1} + \frac{\delta}{\lambda} + \frac{1}{\alpha_2}}, \tag{6}$$

where is α_1 – the coefficient of heat transfer from the coolant to the tank wall, W m^{-2} · °C^{-1}; α_2 – coefficient of heat transfer from the tank wall to air W m^{-2} · °C^{-1}; $\delta = 0.003...0.004$ – thickness of the tank wall, m; λ – coefficient of thermal conductivity of the material of the tank wall, W m^{-1} · °C^{-1}.

The values of heat transfer coefficients α_1 and α_2 depend on the type of used coolant and the speed of its movement in the tank, the temperature of the coolant, the walls of the reservoir and the environment, and can vary within fairly wide limits.

The coefficient λ for the most used water-emulsion coolants is usually taken within the limits of $\lambda = 0.15 \dots 0.65$ W m^{-1} · °C^{-1} [12].

In practical calculations of the coolant supply systems for convective heat transfer, with sufficient accuracy, the following coefficients can be adopted:

– $k = 75$ W m^{-2} · °C^{-1};
– $c_1 = 300...500$ kJ kg^{-1} · °C^{-1} - for welded steel tanks;
– c – is accepted depending on the temperature according to the reference tables in the range $2 ... 4.5$ kJ kg^{-1} · °C^{-1}.

With the continuous operation of the coolant supply system for the time t, h, the current coolant temperature in the reservoir is determined from the relationship obtained from the heat balance Eq. (4):

$$T = T_{nc} + (T_0 - T_{nc})e^{-\frac{kF}{cm+c_1m_1}t} + \frac{Q}{kF}\left(1 - e^{-\frac{kF}{cm+c_1m_1}t}\right), \tag{7}$$

where T_0 the initial temperature of coolant in the tank.

Using Eq. (7), it is possible to determine the temperature of the coolant in the reservoir for anyone when the system is operating in a non-stationary mode.

By the transformation of Eq. (7), with $t \to \infty$ a dependence is obtained for determining the constant temperature in the reservoir when the system is operating in a steady state:

$$T_0 = T_{nc} + \frac{Q}{\sqrt[3]{V^2}}, \tag{8}$$

where is T_{nc} - the ambient temperature, °C; V - volume of liquid in the tank, dm^3;

The value Q is determined by the formula:

$$Q = 860N_{pid}t, \quad \text{kJ}, \tag{9}$$

where is N_{pid} - the system power input, kW; t - pump running time in the current mode, h.

As previously stated, the system operates in two modes, throughput and operating ones, respectively, the power input in the coolant application system has different values for each of these modes.

When working in the admission mode, formula (9) takes the form:

$$Q = 5,85\frac{pQ_nt}{\eta_{com}}, \quad \text{kJ}, \tag{10}$$

where is p – the pressure, develops the pump, kg cm^{-2}; Q_n – pump capacity, dm^3 min^{-1}; t – operating time in the transmission mode, min.; η_{com} – full efficiency of the pump.

When the system is operating in the operating mode, in addition to the heat released from its own losses in the coolant supply system, the heat released during the cutting

process is added. In this case, the total heat released in the system is determined by the formula:

$$Q = 5.85 \frac{p Q_n t_{\text{cut}}}{\eta_{com}} + Q_{LCL}, \tag{11}$$

where is Q_{LCL} – the heat that the coolant receives as a result of cooling the workpiece and the wheel during grinding and is transferred to the tank, kJ; t_{cut} – the main time of this stage of the operation, min.

The value Q_{LCL} depends on the stage of the technological cycle of grinding (tie-in, preliminary, final, grooming), and for the entire operation - it is defined as the total heat at all its stages.

4   Results

The dependencies obtained to determine the temperature are realized as a separate calculation module in the computer program Heat, previously developed by the authors to determine the parameters of the thermal regime of the coolant system. Cycle of computational and analytical studies was conducted with the help of the program.

The studies were carried out for the following data: flow rate 45 dm^3/min, operating pressure 0.06 MPa; type of coolant – Ukrinol-1 with a concentration of 3%.

For this study, the parameters of the cutting regime for grinding were taken as in Table 1.

Table 1. Range of parameter values in determining the cutting force at different stages of the grinding cycle.

Preliminary infeed speed $V_{vr\ n}$ (mm/min)	End infeed speed $V_{vr\ oc}$ (mm/min)	Speed of the part V_{det} (mm/min)	Grain circle number z	Speed diamond with straightening S_{pr} (mm/min)	Cutting depth when adjusting the circle t_{pr} (mm)	Circle hardness (sound index) ZI
1…2	0.1…0.25	30…70	16…40	60…300	0.01…0.03	1.38…1.6

Grinding was performed around a circle with a width of $B = 40$ mm, hardness of SM2. The preliminary grinding time is 60 … 90 s, the final grinding time is 40 … 60 s.

In order to determine the transition points from non-stationary to stationary, the continuous operation of the coolant system in the operating mode (without transition to the throughput) was investigated.

The results of the studies are shown in the form of graphs of these temperatures in the screenshot of the graphic window of the Heat program (Fig. 3).
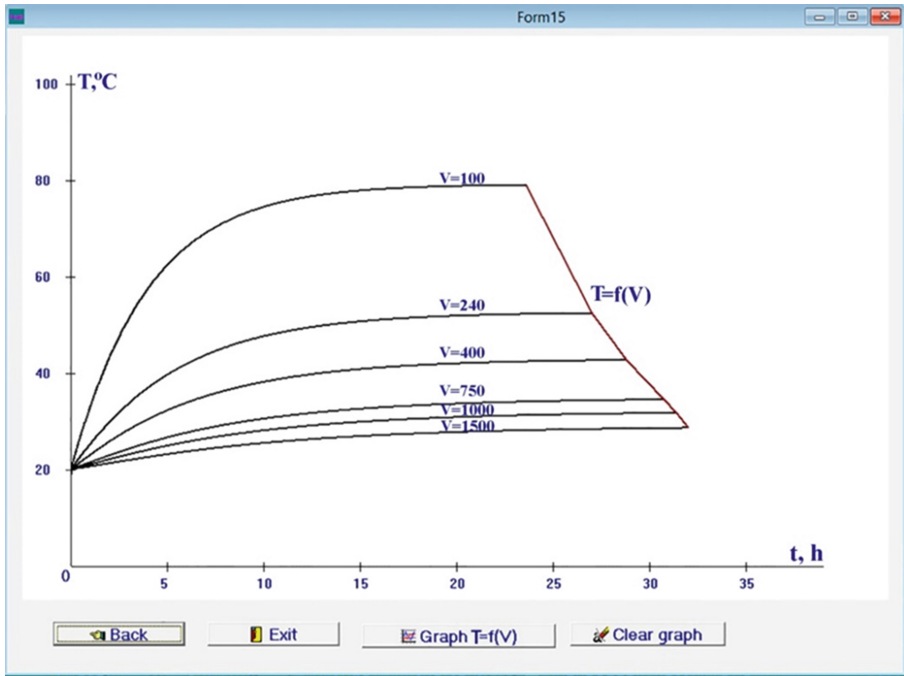
Fig. 3. Graphs of temperature change of coolant in the tank.

Analysis of the temperature graphs in the coolant tank shows that they have a special shape, which consist of two sections: a curve characterizing the operation of the coolant application system in a nonstationary regime and almost a straight line, asymptotic approaching a horizontal line of stable temperature characterizing the operation of the system in a steady state.

Analysis of the results shows that the increase in the coolant temperature after heat exchange with the billet and the ring is explained by the high heat transfer in the grinding process, especially in the preliminary grinding stage, where the temperature even in the application of coolant fluctuates in the range 200 … 900 °C.

Obviously, for the adopted parameters of the coolant application system, the condition for maintaining the average temperature of the coolant within 25 … 35 °C in the reservoir should be 400 … 1500 dm^3.

The transition points from the nonstationary regime to the stationary one are established (Table 2).

As can be seen from the graphs, with the accuracy of the calculation of the temperature 0.001, the coolant supply system operates in a non-stationary mode from 24 to 32 h, and this time increases with the increase in the volume of the reservoir, due to the greater inertia of heat exchange in a larger volume of liquid. At the same time, at practically reasonable accuracy of calculation of temperature 0.5 … 1.5 the time of system operation in non-stationary mode will decrease to 5 … 12 h.

Table 2. Parameters of the transition points of the coolant application system from nonstationary to stationary.

Reservoir volume V (dm^3)	Time to exit non-stationary mode (h)	The value of stable coolant temperature (°C)
100	23.58	82.39
240	27.00	54.69
400	28.81	44.58
750	30.73	36.02
1000	31.40	33.15
1500	32.02	29.91

The study shows that the tools for ensuring a rational thermal regime of the coolant system are the selection of the required volume of the reservoir and the corresponding characteristics of the pump based on the automated calculation of the temperature conditions of the coolant with the help of the developed software.

5   Conclusions

1. The research described a mathematical model describing the temperature regime of coolant in the grinding tank in the working and throughput modes. The model makes it possible to estimate the steady-state and non-stationary temperatures of the coolant in the reservoir, depending on the course of the stages of the grinding cycle.
2. The results of calculations and analytical studies carried out on the basis of the model make it possible to determine the rational volume of the coolant in its application system, taking into account the cooling zone cooling rate, the grinding parameters, and the characteristics of the grinding wheel.
3. It is established that the stabilization of the thermal regime of coolant comes after
4. 5 … 30 h of operation of the grinding machine with an accuracy of determining the steady-state temperature of 0.5 … 0.001, which allows using the results of studies in the development of algorithms and means for compensating the temperature deformations of machines during processing precision parts.
5. The results of the studies are recommended for application in the development of standards for the volume of coolant in its application systems for grinding machines.

References

1. Oh, S.-Y., Jang, J., Choi, W.C.: Analysis of a high-precision grinding machine. Int. J Emerg. Trends Eng. Res. (IJETER) **3**(1), 12–16 (2015)
2. Krajnik, P.: High-performance industrial grinding: recent advances and case studies from automotive industry. Wiener Produktionstechnik Kongress, Vienna, 8 May (2014). http://www.produktionstechnik.at/fileadmin/wpk/doc/2014_Vortraege/3a_Technologies_I/5_High-Performance_Industrial_Grinding.pdf. Last accessed 21 Oct 2017

3. Lattner, R., Holešovskỳ, F., Karel, T., Lattner, M.: Abrasive machining of Ti6Al4V alloy. Manuf. Technol. **15**(4), 571–575 (2015)
4. Karpus, V.E., Ivanov, V.A.: Locating accuracy of shafts in V-blocks. Russ. Eng. Res. **32**(2), 144–150 (2012)
5. Kondratyuk, O.L.: Influence of temperature deformations of knots of multicircular circular grinding machines on accuracy of processing. Mech. Eng. **17**, 68–73 (2016). (in Ukrainian)
6. Martsinkevicius, A-GYu.: Reduction of temperature deformation of a circular grinding machine. Mach. Tools **5**, 7–10 (1991). (in Russian)
7. Yagopolsky, A.G., Krikunov, D.E.: Analysis of the correction of thermal deformations in machine tools. Bull. MSTU. N.E. Bauman Ser. Mech. Eng. **5**, 98–105 (2015). (in Russian)
8. Nosenko, S.V., Nosenko, V.A., Kremenetsky, L.L., Serdyukov, N.D.: Influence of COTS and the hardness of a circle on the grinding coefficient and surface roughness in the processing of a titanium alloy. Int. Sci. Res. J. **12**(54), 156–161 (2016). (in Russian)
9. Lebedev, V., Klimenko, N., Chumachenko, T., Uryadnikova, I., Ovcharenko, A. : Definition of the amount of heat released during metal cutting by abrasive grain and the contact temperature of the ground surface. East. Eur. J. Enterp. Technol. **5**(7(83), 43–50 (2016). https://doi.org/10.15587/1729-4061.2016.81207
10. Lischenko, N.V., Larshin, V.P.: The effect of forced cooling on the grinding temperature. Sci. Vector TSU 3-1 **33**(1), 47–53 (2015). (in Russian)
11. Kundra'k, J., Fedorovich, V., Markopoulos, A.P., Pyzhov, I., Kryukova, N.: Diamond grinding wheels production study with the use of the finite element method. J. Adv. Res. **7**, 1057–1064 (2016)
12. Stepanov, M.S.: Influence of grinding modes on the specific useful flow rate of coolant through the contact zone. Bull. Natl. Tech. Univ. Kharkiv Polytech. Inst. Ser. Technol. Mech. Eng. **1**(9), 71–76 (2002). (in Russian)
13. Shakhnovsky, S.S.: Balance of heat flows in the face grinding machine. Mach. Tools **6**, 13–15 (1989). (in Russian)
14. Kim, B.-S., Bae, G.-T., Kim, G.-N., et al.: A study on the thermal characteristics of the grinding machine applied hydrostatic bearing. Trans. Can. Soc. Mech. Eng. **39**(1), 717–728 (2015)
15. Vekteris, V.Yu.: Stabilization of the temperature field of cylindrical grinding machines. Mach. Tools **7**, 17 (1986). (in Russian)
16. Novikov, F.V., Ryabenkov, I.A.: Increase in the efficiency of tooth gear grinding operations. Bull. Natl. Tech. Univ. Kharkiv Polytech. Inst. Ser. Technol. Mech. Eng. **33**(1205), 139–144 (2016). (in Russian)

Technology of Effective Abrasive Jet Machining of Parts Surfaces

Viktor Sychuk$^{(\boxtimes)}$, Oleg Zabolotnyi, and Dmytro Somov

Lutsk National Technical University, 75 Lvivska St., Lutsk 43018, Ukraine
svamator@gmail.com

Abstract. Presented scientific work is devoted to increasing the efficiency of abrasive jet machining through the development and implementation of a new, wear-resistant and progressive abrasive jet tool, namely a new designed assembled Venturi type nozzle. A developed design of a nozzle provides the formation of a special air layer on its internal working surface, which allows significantly decrease the contact of the abrasive air blast with the working surface of the nozzle, which increases its durability and the efficiency of the abrasive jet machining. Such kind of effect was reached by using a permeable porous insert in the narrowest part of Venturi type nozzle. An additional air flow is fed in radial direction to the outer surface of the insert and then penetrates through porous wall to the inner working surface of the nozzle. The desired design of developed product was obtained using titanium powder metals which were pressed and sintered in conditions of self continues high temperature synthesis because of its energy-efficient properties. Besides, if one of components of assembled nozzle is worn off, it is easy to fix by replacing to a new one.

Keywords: Sand blasting · Nozzle · Porous material

1 Introduction

Increasing the efficiency of parts machining ensuring specified characteristics is an extremely important task of machine-building enterprises. Solving and researching this issue will significantly increase the machining efficiency, reduce the cost of manufacturing parts, and promote scientific development in this field of the national economy.

2 Literature Review

On the basis of information sources of leading scientists such as A.V. Provolotsky, Sh. M. Bilik, V.N. Podurayev, I.R. Kleis, P.P. Paley, I.V. Krakhelsky, E.P. Nepomnyaschy and others [1] it was analyzed the features of the technology of abrasive jet machining, the interaction of the abrasive with the processed surface, the interconnection of the technological parameters with the abrasive jet machining, the nozzles for the abrasive jet machining, the modern technology of producing nozzles for the abrasive jet machine, the technology of machining surfaces of foundry parts, the quantitative characteristics of technological parameters of the abrasive jet machining.

While making billets of body parts of the foundry production, certain defects are formed on their surfaces, such as tides, strangles, remains of forms (in the case of sand forms), corrosion traces. All these should be eliminated, as they adversely affect the operation of the assembled mechanism, where these parts will be applied.

It was carried out the analysis of surfaces of body parts made by foundry production, which according to the basic technological processes were not subject to machining, which in turn worsens their performance characteristics.

Abrasive jet machining is a modern, progressive method of machining, which becomes more and more relevant in the technological processes of machining various parts.

With considerable advantages, this machining technology also has certain disadvantages. An integral part of the abrasive jet equipment, in particular the abrasive jet nozzle, has the ability to quickly wear out during operation. The worldwide trend towards extending the life of this tool is to use super-hard materials that are expensive and difficult to process. Nowadays the use of classic materials in the manufacture of abrasive jet nozzles does not meet the requirements of wear resistance, operational properties and, as a consequence, significantly deteriorates the effectiveness of abrasive jet machining. Therefore, an actual scientific and practical task is increasing the efficiency of the technological operation of this type of machining by improving the nozzle of the abrasive jet machine, and as a consequence, changing the modes of abrasive jet machining.

3 Research Methodology

The reasons for reducing the productivity of abrasive jet machining are changes in the internal geometry of the nozzle because of its wear out. Venturi shape nozzle UDC32-450 (Fig. 1) was chosen as an experimental abrasive jet tool and after its wear out we got the following internal profile (Fig. 2).
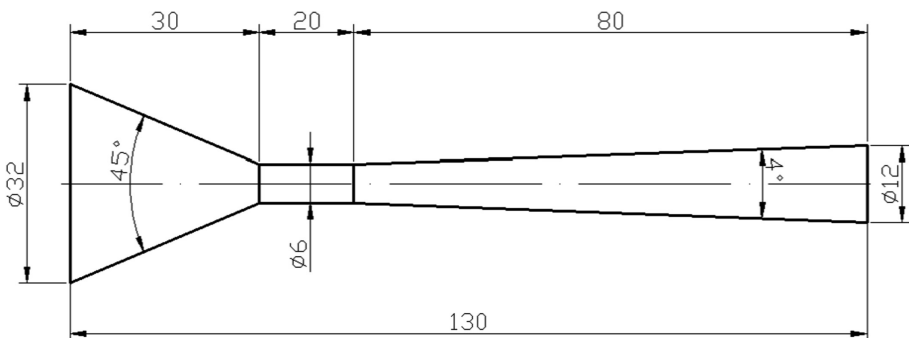
Fig. 1. Geometric dimensions of the inner surface of Venturi nozzle UDC32-450.
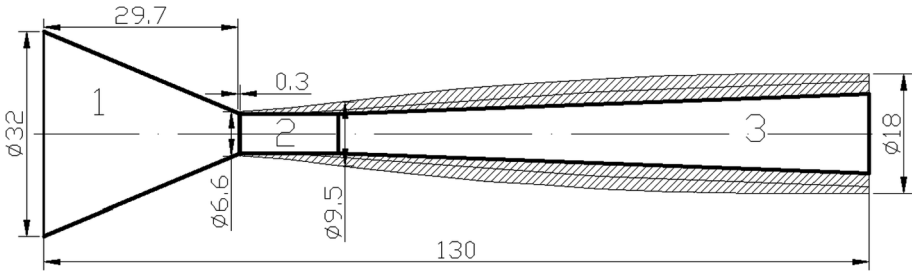
Fig. 2. Overlapped contours of the inner surface of new and wornout abrasive jet Venturi type nozzles: 1 - inflow conical wide neck; 2 - cylindrical acceleration zone; 3 - outflow conical narrow neck.

Analyzing the wear out of the internal profile, the authors of the scientific work developed an improved new design of abrasive jet nozzle [2, 3] (Fig. 3).
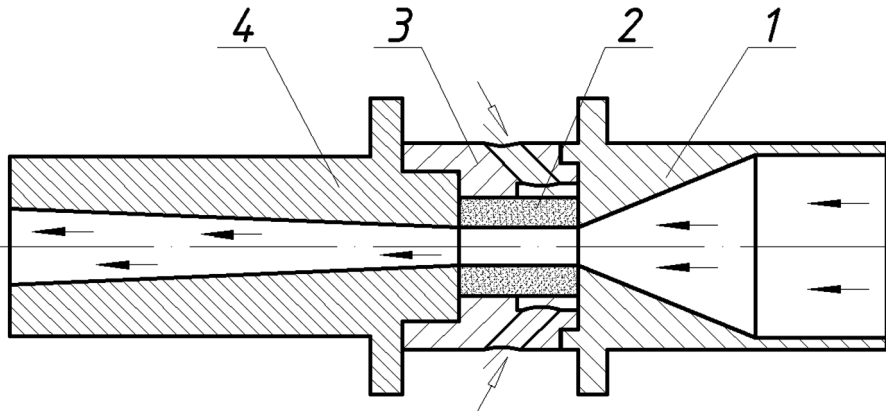
Fig. 3. Developed assembled design of the abrasive jet machine nozzle: 1 - inflow conical wide neck; 2 - porous permeable insert (acceleration zone); 3 - housing for placing porous permeable insert; 4 - outflow conical narrow neck; ——▶ – air flow with abrasive particles; ——▷ – additional air flow.

The principal difference of abrasive jet nozzles from other designs is that the wear resistance of the internal working surface of the nozzle is achieved not by the use of super-hard materials, but by the formation of air layer on the working surface of the nozzle, which prevents the contact of abrasive particles with the inner working surface during the operation of the abrasive jet machining (Fig. 4).
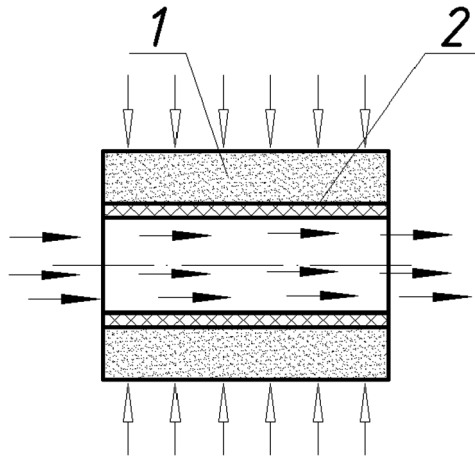
Fig. 4. A scheme of forming an air layer on the inner surface of the nozzle: 1 - cylindrical porous permeable insert of a nozzle; 2 - air layer; ▬▶ - air flow with abrasive particles; ▭▷ - additional air flow.

The form of the internal profile was chosen as in Venturi nozzle. The fundamental difference between our design of the abrasive jet nozzle and others is that it is assembled, that means, the internal form of Venturi consists of at least three parts. It is worth noting that such design provides a quick recovery of the tool by replacing only the worn part with the new one. To provide the necessary air pressure in the working zone of the nozzle, it is fed there through a porous permeable element in the radial direction.

Undoubtedly, the assembled nozzle should function while providing defined technological conditions for its operation, which contributes to the reduction of the operation not in contradiction with the machining performance.

For the practical manufacture of assembled nozzle of a new design, it is necessary to find the parameters of the porous permeable insertion of the nozzle.

A scheme with necessary variables that play a key role in the appearance of the desired air layer (Fig. 5). Under this scheme, it is necessary to find the pressure drop of the air flows passing through the porous permeable element of the nozzle and the mixture of air and abrasive material.

So we get the following dependence:

$$\Delta P = f(\rho, h, Q, U_{nou}, P_1, k) \tag{1}$$

where ΔP - pressure drop;
ρ - fluid density (in our case air);
h - thickness of the wall of the porous material;
Q - flow rate of fluid (in our case air) by volume;
$\overline{U}_{nou}$ - the velocity of entry of the fluid into the porous material;
P_1 - fluid pressure at the entrance to the porous material;
k - coefficient of filtration of the porous element.
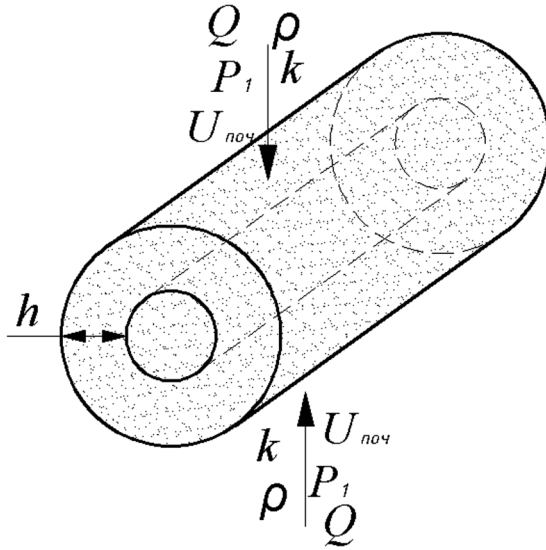
Fig. 5. Variables which influence the formation of the air layer on the inner surface of the porous permeable element.

To determine the conditions for the formation of the air layer, which will prevent the contact of abrasive particles with the inner working surface of the Venturi nozzle of abrasive jet machine, we use the theory of dimensions and researches of Doctor of Technical Sciences Yakhno Oleg [4].

After the necessary transformations, we obtain the formulas of the coefficients (2)–(4) that characterize the occurrence of the necessary conditions of the nozzle operation:

$$K_1 = \frac{h^2 \cdot U_{no4}}{Q} \tag{2}$$

$$K_2 = \frac{P_1}{h \cdot \rho} \tag{3}$$

$$K_3 = \frac{h^2 \cdot k}{Q} \tag{4}$$

Where our coefficient will be equal to:

$$K_{no\partial} = K_1 \cdot K_2 \cdot K_3 \tag{5}$$

After calculations, combining theoretical and practical data, we obtain required coefficient (6), in case of which the condition of efficiency of the instrument will be achieved.

$$K_{no\partial} \leq 0,047 \tag{6}$$

As a result, obtained coefficient means that before providing the abrasive jet machining we must choose certain values of parameters in dependence (1) to get the most suitable durability mode of the sand blasting nozzle.

To create a necessary permeable insert we choose powder metallurgy with its inherent methods of manufacturing products, namely, pressing of powder materials with subsequent sintering [5]. After experiments (Fig. 6) with permeability of porous samples (31 pieces) using different particle sizes of powder metal we got necessary characteristics of the porous permeable insert for its manufacture. So, we choose using powder metal based on titan with the size of particles 0.63 mm to 1 mm to create products with porosity of 50% because the pressure drop was the smallest.
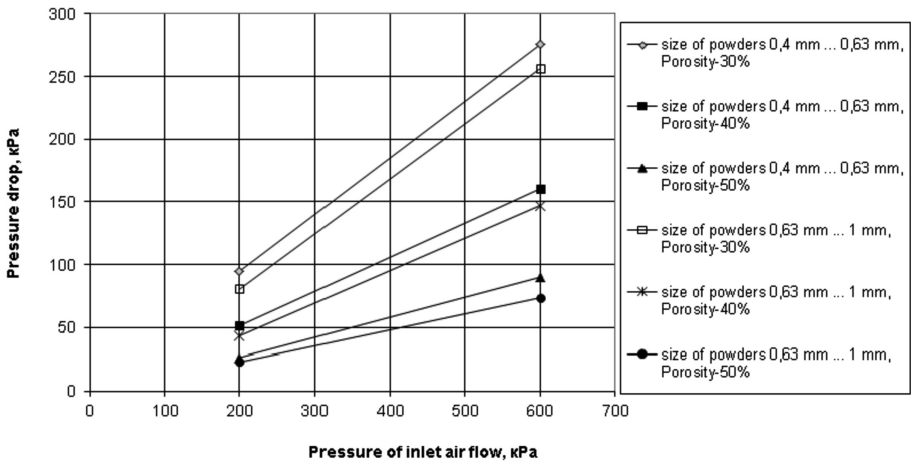
Fig. 6. An averaged dependence of the pressure drop of all experimental samples taking into account the pressure of inlet air flow.

The manufacturing process was carried out according to the scheme presented below (Fig. 7).

We place auxiliaries on a stationary plate 6 of vertical-screw press. In the cavity between the matrix 4 and the mandrel 5 we fill the metal powder 3. Then press the moving plate 1 of the press onto the punch 2, which in turn creates pressure on the metal powder 3 and thereby compresses it. After sintering the result is a product (Fig. 8).

The rest of the parts were made (Fig. 9) after manufacturing of a permeable part of the assembled nozzle.
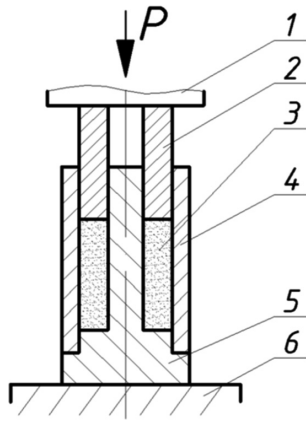
Fig. 7. A scheme of porous permeable insert pressing.

a)   b)
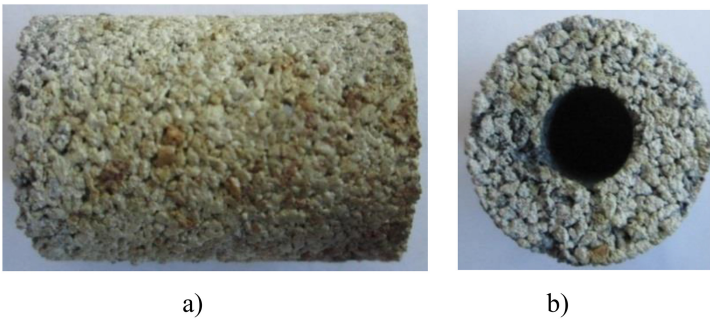
Fig. 8. Pressed and sintered porous permeable insert of a nozzle: (a) side view; (b) front view.
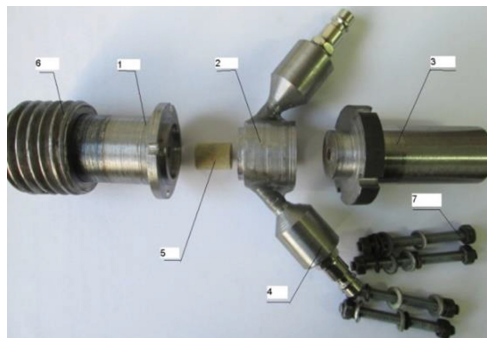
Fig. 9. General view of the finished unit of the nozzle of new design (in disassembled condition): 1 - confuser; 2 - housing; 3 - diffuser; 4 - connecting pipe; 5 - porous permeable insert; 6 - connecting thread; 7 - turnbuckle.

Parts that were chosen to be processed were obtained by casting. The effectiveness of surface treatment of such parts is provided by two methods:

– the first is to apply a more advanced method of machining with the assurance of necessary quality of the surface of the workpiece. For example, the replacement of the basic machining method, such as shot blasting treatment on abrasive jet machining;
– the second one is to apply a more durable tool that can perform a larger amount of work. As a result, the tool is to be replaced less frequently, which consequently significantly affects the final cost of machining. Also, an important factor in this case is the shortening of the time periods spent on re-adjusting the equipment to replace worn out tool to a new one, which will allow machining more parts (surfaces) for the defined time period.

In order to provide an effective abrasive jet machining of the surfaces of the foundry parts, it is necessary to perform the machining according to the following scheme (Fig. 10).
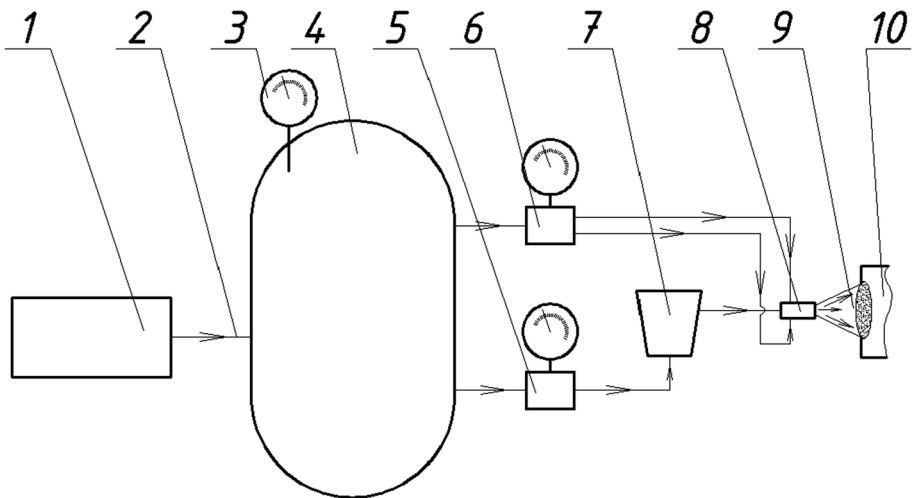
Fig. 10. A scheme of abrasive jet machining of parts using assembled nozzle of a new design: 1 - compressor; 2 - hose; 3 - pressure gauge; 4 - receiver; 5 - regulator of air pressure of the main flow; 6 - air pressure regulator of the additional flow; 7 - a mixer of abrasive and air; 8 - assembled nozzle of new design; 9 - a mixture of air flow with abrasive, so called working flow; 10 - the surface of the workpiece.

Suggested abrasive jet machining with increased efficiency can work according to the following procedure:

– the compressor 1 pumps air through hose 2 into the receiver 4 to a certain pressure ($\approx$ 0.75…0.8 MPa), pressure monitoring is carried out with the help of pressure gauge 3, while functioning, that is, with air flow, compressor 1 in automatic mode completes the required volume of air to maintain a certain pressure in the receiver 4;
– from the receiver 4 the air under pressure through the hose flows into the pressure regulator 6, which is adjusted to a pressure of air of 0.75 MPa, further this air enters through the connecting pipes into assembled nozzle 8. Here air flows through a porous permeable insert and creates an air layer on the inner working surface of the nozzle;
– from the receiver 4 the air under pressure through the hose flows into the pressure regulator 5, which is adjusted to an air pressure of 0.55 MPa, further this air flows into the mixer of abrasive and air. Flow of a mixture of air with abrasive through the hose-arm flows into the inflow wide neck of assembled nozzle of a new design, passes through it, acquiring performance characteristics;
– as a result, the mixture 9 of a stream of abrasive with air which flows out of the assembled nozzle processes the surface of the part 10.

It is important to note that first of all it is necessary to apply the air that forms air layer on the inner working surface of the assembled abrasive jet nozzle, and only then feed the flow of a mixture of air and abrasive.

In general, in order to obtain the required roughness (given in the drawing of the experimental part) of the surface got by casting using abrasive jet machining, it is necessary to use obtained by author formula (7), which describes the necessary technical regimes, such as the pressure of the main flow and the machining time of the surface area:

$$Ra = 2{,}358 \cdot 10^{-8} \cdot d_{абраз}^{6,6299\,(1-0,9868\,\lg P - 0,321\,\lg t)} \cdot P^{8,4736} \cdot t^{2,7566} \qquad (7)$$

where $d_{абраз}$ – the size of the abrasive fraction, mm;
   P – air pressure of the main flow, bar;
   t – time of abrasive jet machining, sec.

4   Results

After experiments on machining of surfaces we have got the following results (Fig. 11).

While comparing the basic method of machining of the part and the developed technology of abrasive jet machining with the use of a new design nozzle with an air layer, we also have experimentally established that the machining time was reduced by 2.8 times with the provision of all similar technological machining parameters and quality characteristics.
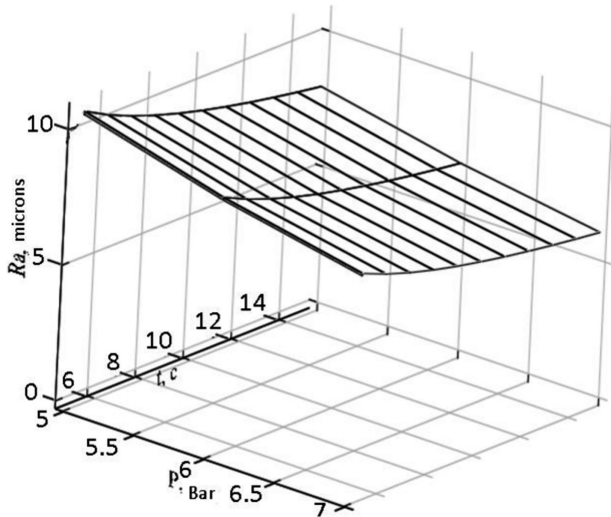
Fig. 11. Dependence of the obtained roughness of the surface on the time and air pressure with the abrasive during abrasive-blasting sand with a predominant diameter of the particle of 0.26 mm.

5 Conclusions

Thus, the technology of abrasive jet machining developed by us with the use of a new assembled Venturi nozzle allows us to substantially increase the efficiency of abrasive jet machining by significantly reducing the wear out of the working surface of the nozzle and, consequently, increasing its service life, saving the material cost of the nozzle, reducing material, labor and time costs of machining parts and adjusting the equipment, while providing the required quality of surfaces.

Further researches will be devoted to creating permeable insert of assembled sand blasting nozzle with defined direction and shape of pores [6]. Also, it is planning to develop a design with multiple inlet pipes of additional air flows. All these implementations should influence on durability of a nozzle and on the abrasive jet process in general.

References

1. Spencer, L.F.: Abrasive blasting. Met. Finish **7**, 67–68, 70–75 (1975). (Gvideb. Direct., Hackensack)
2. Sychuk, V., Zabolotnyi, O., McMillan, A.: Developing new design and investigating porous nozzles for abrasive jet machine. Powder Metall. Met. Ceram. **9–10**, 600–605 (2015)
3. Sychuk, V., Zabolotnyi, O., Golodjuk, R., Koljadunskyj, M.: Modular nozzle of abrasive jet machines. Patent No. 104492, Ukraine (2016)

4. Jakhno, O., Matijeva, V., Odajskyj, S.: Technical Hydrodynamics and Hydrodynamic Theory of Lubrication. Zoloti Lytavry, Chernivtsy (2010)
5. Povstyanoy, O.Y., Sychuk, V.A., McMillan, A., Rud, V.D., Zabolotnyi, O.V.: Metallographic analysis and microstructural image machining of nozzles for sandblasting produced by powder metallurgy methods. Powder Metall. Met. Ceram. **54**(3–4), 234–240 (2015)
6. Rak, A.L., Illyuschenko, A.F., Maziuk, V.V., Pilinevich, L.P.: New technology for production of high-effective porous materials with adjusted pore structure, designed for filtration of gases and liquid. In: Proceeding of the 1998 Powder Metallurgy World Congress & Exhibition, pp. 225–231. Granada, Spain (1998)

Choice of the Optimal Parameters
of the Ultra-Fine Grained Cooper Machining

Anastasiia Symonova[1]([✉]) [iD], Valerii Havin[2], and Dmitrii Savelov[1]

[1] Kremenchuk Mykhailo Ostrohradskyi National University,
20 Pershotravneva St., Kremenchuk 39600, Ukraine
NSymonova@gmail.com
[2] National Technical University "Kharkiv Polytechnic Institute",
2 Kyrpychov St., Kharkiv 61002, Ukraine

Abstract. This article is focused on the features of the structure of ultra-fine grained metals and the influence of the machining on its changes. The search for optimal parameters was carried out for machining of pure copper, obtained by the method of several plastic deformations. The objective function, which includes a new criterion of optimization, was proposed. Limitations of the function for turning ultra-fine grained copper were obtained from experimental data. As a criterion of optimality, a general combining criterion is proposed, which is based on the linear convolution, two particular criteria the productivity and size of the grain size of nano- and ultra-fine grained metals, each with its own weight coefficients. The optimization problem was solved by the penalty function method in the MATLAB software environment using the method of unconditional mini-mization of several variables. Optimal decisions on the selection of the cutting speed and feed during the rotation of ultra-fine grained copper with different initial grain sizes are obtained.

Keywords: Ultra-fine grained · Pure copper · Machining · Optimization
MATLAB

1 Introduction

With newly developed materials being produced for their superior properties of high strength, high ductility, low weight, etc., a need for implementing them into practical use has arisen. Because of these features, many advanced materials show potential in engineering applications such as medical devices and aerospace structural components, but an adherent gap exists between the research and industrial fields to push these materials into usage. For newly produced materials which is shaped and formed into their final dimensions, further machining research is typically required [1].

The recent development of ultra-fine grained (UFG) or nanostructured materials, with strengths up to twice stronger has created greater interest in research fields than their coarse grained counterparts. Various methods of producing nanostructured materials are existed. Substantially large samples can be produced easily from bulk form with little internal porosity making SPD materials boasted the greatest potential for an industrial impact of all UFG materials [2, 3]. Because of this, all UFG materials,

referred to this thesis, are considered as being constructed using SPD. The exceptional properties yielding from these materials can be attributed solely to their defect structures. Along with the extremely small grains in the range of 100–1000 nm, numerous dislocations and subgrains, which are existed throughout the microstructure, with the aid in blocking slip, thus, increase material strength. However, these defects in the polycrystalline structure exhibit high internal energy, and as a result, thermally induced grain growth or subsequent changes in defect structure may occur at considerably low temperatures. These changes will naturally indicate a loss of strength, and thus limit SPD materials to low temperature applications [4, 5].

Since heating UFG materials may change their microstructures, it may be difficult to find means of forming and shaping these materials into their final dimensions. Given that machining is a heat dissipating process, the thermal stability of nanostructured materials must be considered carefully to save their unique properties. The major motive for conducting machining research is to discover the interaction between the cutting tool and the workpiece material, so that the machining costs can be minimized while still optimizing part quality [6].

The effect of machining conditions on the change in grain size in metals with UFG structure has been observed in numerous studies [7–9].

Therefore, optimal cutting conditions will be able to ensure the preservation of the initial grain size in the manufacture of products from blanks with bulk nano and UFG structure. Studies, which determined such cutting conditions are an urgent task.

The problem of determining the optimum cutting conditions is given to a large attention in the scientific works [10–12]. The task of optimizing the cutting conditions has been studied quite fully to the present. This allows us to develop not only new mathematical models for calculating cutting modes, but also to implement them in the form of various control computer programs. Such programs are executed both in the form of separate applications, and in the form of modules of different CAM and TDM systems.

2 Optimization Model

2.1 Optimization Criterions

One of the generally accepted criteria of optimality for cutting modes is the productivity of processing Q - the volume of metal (allowance), taken from the workpiece per time unit. Varying parameters are the cutting speed (s) and the feed (f) [11].

$$Q = s \cdot f \rightarrow \max \text{ or } Q^{-1} = \frac{1}{s \cdot f} \rightarrow min, \qquad (1)$$

where s – cutting speed, f – cutting feed.

The main difference and peculiarity of the processing of nanostructures is the appearance of a new optimization criterion is the grain size. This criterion is very important because it will minimize the effects of cutting conditions on the structure. And the grain size should tend to a minimum, as the smaller the grain size, the higher

the physical and mechanical properties of the nanomaterial. However, it should not reach the boundary values, which are stipulated by the Hall-Petch equation [13].

This criterion for turning can be written in the following form [5]:

$$D = \sqrt{D_0^2 + A \cdot \frac{\pi \cdot d \cdot L}{s \cdot f}} \rightarrow min, \qquad (2)$$

where L – length of the surface to be machined; d – the diameter of the workpiece to be machined; D_0 – initial grain size in UFG or NC metal; D – admissible critical grain size, at which high physical and mechanical properties of metal are preserved; A – a parameter that characterizes the intensity of grain growth, taking into account the properties of the material being processed.

Expressions (1) and (2) are optimization criteria for the problem under consideration.

2.2   Technical Limitations

Technical limitations of the machining are represented in the form of a system of inequalities (Table 1).

Table 1. Technical limitations for tuning [14].

Restrictions	Mathematical expressions
Kinematic	$\begin{cases} f - f_{min} \geq 0 \\ f_{max} - f \geq 0 \end{cases} \begin{cases} s - s_{min} \geq 0 \\ s_{max} - s \geq 0 \end{cases}$
Roughness	$R_{amax} - C_{Ra} \cdot s^{xRa} \cdot f^{yRa} \geq 0$
Microhardness	$C_{Hv} \cdot s^{xHv} \cdot f^{yHv} - H_{vmin} \geq 0$
Power machine	$N_{max} - \frac{F_c \cdot s}{60 \cdot 1000} \geq 0$
Cutting temperature	$T_{max} - C_t \cdot s^{xT} \cdot f^{yT} \cdot d^{zT} \geq 0$

2.3   Method of Optimization

Optimization can be single-purpose, an extremum of one objective function is defined, and a multi-criteria (multi-objective) search for an extremum for a combination of several optimization criteria.

The problem under consideration is a multicriteria optimization problem. To solve it, the linear convolution method was chosen. Using this method, individual criteria were combined, the productivity $Q^{-1}(s, f)$ and grain size $D(s, f)$ into one [14]:

$$J(Q^{-1}, D) = k_1 \cdot f(Q^{-1}) + k_2 \cdot f(D), \qquad (3)$$

where, Q^{-1} – a particular performance criterion; D – a particular criterion grain size; k_1 – the weighting coefficient of the grain size criterion; k_2 – the weight coefficient of the performance criterion.

This method allows us to reduce the problem of multicriteria optimization to the problem of one-criterion optimization, the solution of which depends on the selected weight coefficients of the partial criteria.

The method of penalty functions was chosen to solve the optimization problem. Using the penalty function, the initial problem of conditional minimization is transformed into a sequence of unconditional minimization tasks [14]. The idea of transforming a constrained problem in this way seems the best, mainly in connection with the existence of effective and reliable methods of unconditional minimization. To apply this method, the following objective function was formulated:

$$F = k_1 \cdot Q^{-1} + k_2 \cdot D + R \cdot \sum_{i}^{i=8} q_i^2, \tag{4}$$

where R – penalty parameter; q_i – the i-th technical constraint.

In practical calculation, a penalty was used such as the square of the cut [10]:

$$\Omega = R \cdot \sum_{i}^{i=8} \langle q(x) \rangle^2$$

$$\langle q(x) \rangle = \begin{cases} q(x), & if, q(x) \leq 0 \\ 0, & if, q(x) \geq 0 \end{cases}, \tag{5}$$

If $q(x) \geq 0$, then the vector of variable variables x belongs to an admissible set, and otherwise does not belong. In this case, the objective function is "punished" by a penalty, i.e., decreases, so long as the point x does not enter the admissible set, and the objective function does not begin to increase again.

The penalty of the type of the cut-off square is very convenient, in particular, the function is defined and continuous throughout the range of values. Calculations are carried out with some given positive P. After solving the next subtask, the penalty R is increased and the search for the next more accurate solution is performed until the specified accuracy is achieved.

3   Realization of Optimization Model in MATLAB

The material for research was selected from technically pure copper C10100 (standard ASTM B359, USA), 2.0040 (standard WNr. Germany). Chemical composition: Cu + Ag min 99.93%. UFG structure is obtained by the method of overall forging [15]. The study of changes in the quality of the surface layer (microhardness and roughness) was carried out during the turning process with varying processing conditions: cutting speed from 30 to 100 m/min, feed from 0.1 to 1.2 mm/rev. T11302 (standard UNS, USA), 1.3343 (standard WNr, Germany) were used as instrumental material.

Table 2. Limitations obtained by processing experimental data.

Restriction criterion	Mathematical expressions
Roughness	$R_{a\,max} - 7.5 \cdot s^{0.04} \cdot f^{0.6} \geq 0$
Microhardness	$1374 \cdot s^{-0.3} \cdot f^{-0.15} - H_{v\,min} \geq 0$
Cutting temperature	$T_{max} - 183 \cdot s^{0.5} \cdot f^{0.2} \cdot d^{0.1} \geq 0$

Using the experimental data which is given in [9, 15, 16], the obtained analytical dependencies were reduced to the canonical form for specifying the main limitations of the model (see Table 1). The final form for the constraints obtained on the basis of the experimental data is given in Table 2.

For the correct application of the imposed constraints, it is necessary, that the corresponding constraint parameter (Ra, Hv, $Tmax$) does not exceed the maximum or minimum values to maintain the high physico-mechanical and operational properties of the corresponding workpiece material.

The parameter which is limited (Ra, Hv, $Tmax$) corresponding to the imposed restrictions should not exceed the maximum or minimum values for preserving the original grain size. This allows us to apply the imposed restrictions correctly.

Thus, we have received the main components of the optimization problem - these are particular criteria for optimality (productivity and grain size), a general criterion for optimality and a system of constraints.

Table 3. Initial data for the search for optimal processing conditions.

Designation	Name	Parameter values
L	Length of the surface to be machined (m)	0.1
d	Diameter of the workpiece (m)	0.01
A	The index, which takes into account the properties of the processed material (m/min)	2.5×10^{-12}
D_0	Initial grain size (nm)	100
s_{min}	Minimum speed (m/min)	30
s_{max}	Maximum speed (m/min)	160
f_{min}	Minimum feed (mm/rev)	0.1
f_{max}	Maximum feed (mm/rev)	0.24
d	Depth of cut (mm)	0.5
$Nmax$	Cutting power (kW)	12
$Ramax$	Allowable maximum roughness value (µm)	3.2
$Hvmin$	Allowable minimum value of microhardness (MPa)	600
$Dmax$	Maximum permissible grain diameter (µm)	1
$Tmax$	Permissible maximum cutting temperature (K)	623

The numerical solution of the problem was carried out in the MATLAB software environment using the method of unconditional minimization of the function of several variables *fminsearch*.

The values given in Table 3 were accepted as input data for the calculation.

The general view of the target function for implementation in MATLAB is:

$$F(s,f) = k_1 \cdot s \cdot f + k_2 \cdot \sqrt{D_0^2 + A \cdot \frac{\pi \cdot d \cdot L}{s \cdot f}} + P_{en} \tag{6}$$

$$
\begin{aligned}
P_{en} = R \cdot \Big(& (f_{max} - f)^2 + (f - f_{min})^2 + \cdot (s_{max} - s)^2 + (s - s_{min})^2 \\
& + \left(7.5 \cdot s^{0.04} \cdot f^{0.6} - R_{a\,max}\right)^2 + \left(1374 \cdot s^{-0.3} \cdot f^{-0.15} - H_{v\,min}\right)^2 + \\
& + \left(\frac{F_{c \cdot s}}{60 \cdot 1000} - N_{max}\right)^2 + \left(183 \cdot s^{0.5} \cdot f^{0.2} \cdot d^{0.1} - T_{max}\right)^2 \Big)
\end{aligned}
\tag{7}
$$

where *Pen* – the penalty term.

When solving a multicriteria problem, the problem of normalization and scaling arises - bringing the criteria to a single scale and dimensionless is formed.

The most frequent usage is the replacement of the absolute values of their criteria dimensionless relative values:

$$\overline{F_k(x)} = \frac{F_k(x)}{F_k^*}, F_k^* = \max_{x \in D} F_{k(x)} \tag{8}$$

Thus, after normalization, the original function will have the following form:

$$F(s,f) = k_1 \cdot \frac{s_{max} \cdot f_{max}}{s \cdot f} + k_2 \cdot \frac{\sqrt{D_0^2 + A \cdot \frac{\pi \cdot d \cdot L}{s \cdot f}}}{D_{max}} + P_{en} \tag{9}$$

$$
\begin{aligned}
P_{en} = R \cdot \Big(& \left(1 - \frac{f}{f_{max}}\right)^2 + \left(\frac{f}{f_{max}} - \frac{f_{min}}{f_{max}}\right)^2 + \cdot \left(1 - \frac{f}{s_{max}}\right)^2 + \left(\frac{s}{s_{max}} - \frac{s_{min}}{s_{max}}\right)^2 \\
& + \left(\frac{7.5 \cdot s^{0.04} \cdot f^{0.6}}{R_{a\,max}} - 1\right)^2 + \left(\frac{1374 \cdot s^{-0.3} \cdot f^{-0.15}}{H_{v\,min}} - 1\right)^2 + \left(\frac{F_{c \cdot s}}{60 \cdot 1000 \cdot N_{max}} - 1\right)^2 \\
& + \left(\frac{183 \cdot s^{0.5} \cdot f^{0.2} \cdot d^{0.1}}{T_{max}} - 1\right)^2 \Big)
\end{aligned}
\tag{10}
$$

4   Results and Discussion

As a starting point for the optimization process, we selected: $s = 65$ m/min; $f = 1.2$ mm/rev. As the initial value of the penalty, $R = 10$ is taken. The weights for the derived results are $k_1 = 0.7$ (for the grain size of the structure) and $k_2 = 0.3$ (for productivity).

Table 4. The change in the optimum solution near the optimum for the machining of cooper with an initial grain size of 100 nm.

Penalty function R	Cutting speed s (m/min)	Feed rate f (m/rev)	Productivity Q (m²/min)	Grain size D (nm)	min F (s, f)
10000	30.0000	0.0001	0.0042	1830	0.0050

Table 5. The change in the optimum solution near the optimum for the machining of cooper with an initial grain size of 300 nm.

Penalty function R	Cutting speed s (m/min)	Feed rate f (m/rev)	Productivity Q (m²/min)	Grain size D (nm)	min F (s, f)
10000	30.0000	0.0001	0.0045	1900	0.0030

Tables 4 and 5 show the results of the calculation of the optimum parameters of the cutting process for UFG copper with different grain sizes of the structure.

The developed program, as a result, derives the optimal solution for the selected objective functions when constraints are satisfied. Increasing the penalty allows you to obtain results with increasing accuracy. When the value of changeable variables (cutting speed and feed) on the two subsequent fine values coincide to the first decimal place, the optimal solution is considered to be received.

The results which is given in Tables 4 and 5 show us that during processing of nano (initial grain size of the billet 100 nm) and UFG (initial grain size of the blank 300 nm), the copper cutting speed does not exceed 30 m/min with a feed of 0.1 mm/rev. At the same time, the grain size of the billet is increased to more than 1 μm, which will lead to a decrease in the physical and mechanical properties and the operational properties acquired when the billet is produced by intensive plastic deformation.

The obtained values of cutting conditions for UFG copper significantly lower than recommended for coarse-grained copper [17].

The developed program allows to vary the significance of particular objective functions (coefficients k_1 and k_2), thus, in advance it is possible to determine the degree
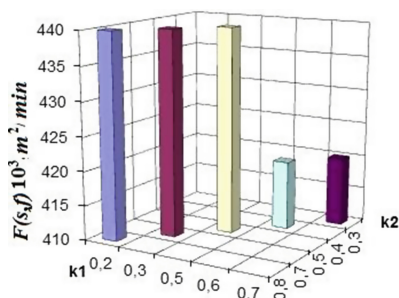
Fig. 1. Dependence of the objective functions on the values of the weight coefficients for copper with an initial grain size of 100 nm.
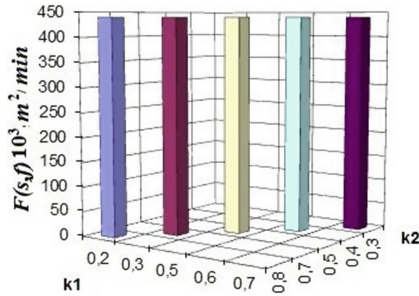
Fig. 2. Dependence of the objective functions on the values of the weight coefficients for copper with an initial grain size of 300 nm.

of the necessity to maintain a certain grain size of the workpiece or the level of productivity for each product individually.

Graphs of the dependence of the objective function on the values of the weight coefficients for nano- and UFG copper with an initial grain size of 100 nm and 300 nm are presented in Figs. 1 and 2.

The graphs (see Figs. 1 and 2) show the values of the objective functions when the weights are changing. Due to the fact that optimal conditions were not found for processing without cutting fluid, the developed program received the least value of the grain size after machining at a practically constant speed and feed, so it has no significant changes.

5   Conclusions

The work has explored and mastered the possibilities of solving optimization tasks in the MATLAB software environment. The method *fminsearch* was chosen as the crucial. A subroutine for the MATLAB software environment has been developed, which makes it possible to search for optimal parameters for machining in the manufacture of products from workpiece with a nano- or UFG structure. The proposed objective function allows us to counter the intensity of grain growth, which is very important when processing this group of materials.

As a result of solving the task, the following values of the cutting and feeding speeds were obtained. For copper with the initial grain size of the workpiece both 100 nm and 300 nm, optimal values for machining were not obtained. Since copper has a high thermal conductivity, the machining without coolant gives a lower productivity and does not allow preserving the original grain size.

Thus, the proposed optimization model works correctly and is consistent with the experiments. For copper, it is necessary to perform a series of investigations of machining with coolant and the use of diamond tools to reduce the amount of heat accumulated in the workpiece.

References

1. Lowe, T., Valiev, R.: Investigations and Applications of Severe Plastic Deformation. Springer, Dordrecht (2012). https://doi.org/10.1007/978-94-011-4062-1
2. Dyakonov, G., Mironov, S., Semenova, I., Valiev, R., Semiatin, S.: Microstructure evolution and strengthening mechanisms in commercial-purity titanium subjected to equal-channel angular pressing. Mater. Sci. Eng. A **701**, 289–301 (2017)
3. Dragobetskii, V., Shapoval, A., Zagoryanskii, V.: Development of elements of personal protective equipment of new generation on the basis of layered metal compositions. Steel Transl. **45**(1), 33–37 (2015)
4. Gubicza, J., Chinh, N., Dobatkin, S., et al.: Stability of ultrafine-grained microstructure in fcc metals processed by severe plastic deformation. Key Eng. Mater. **465**, 195–198 (2011)
5. Symonova, A., Verezub, O., Sytcheva, A., Verezub, N., Havin, V., Kaptay, G.: Surface grain coarsening and surface during machining of ultra-grained titanium. J. Min. Metall. Sect. B **48**, 378–389 (2012)
6. Dipeshkumar, B.: Machining of difficult-to-cut super alloys: a review. Int. J. Adv. Eng. Res. Dev. **4**(10), 120–125 (2017)
7. Rodrigues, A., Balancin, O., Gallego, J., et al.: Surface integrity analysis when milling ultrafine-grained steels. Mater. Res. **15**(1), 125–130 (2012)
8. Symonova, A., Filippi, E., Kmec, J., Majerník, J., Karkova, M.: The mechanics of machining ultrafine-grained Ti–6Al–4Mo alloy processed severe plastic deformation. Manuf. Technol. **17**(4), 592–597 (2017)
9. Moreheada, M., Huanga, Y., Hartwigb, K.: Machinability of ultrafine-grained copper using tungsten carbide and polycrystalline diamond tools. Int. J. Mach. Tools Manuf. **47**, 286–293 (2007)
10. Deepak, D., Rajendra, B.: Optimization of machining parameters for turning of Al6061 using robust design principle to minimize the surface roughness. Procedia Technol. **24**, 372–378 (2016)
11. Oxley, P.L.B.: Modeling machining processes with a view to their optimization and to the adaptive control of metal cutting machine tools. Robot. Comput. Integr. Manuf. **4**(1/2), 103–119 (1988)
12. Lebaal, N., Nouari, M., Ginting, A.: A new optimization approach based on Kriging interpolation and sequential quadratic programming algorithm for end milling refractory titanium alloys. Appl. Soft Comput. **11**, 5110–5119 (2011)
13. Weertman, J.: Hall-Petch strengthening in nanocrystalline metals. Mater. Sci. Eng. A **166**, 161–167 (1993)
14. Fletcher, R.: Practical Methods of Optimization, 2nd edn. Wiley, New York (1987)
15. Kuznetsov, P., Rakhmatulina, T., Belyaeva, I., Korznikov, A.: Energy of internal interfaces as a characteristic of the structural evolution of ultrafine-grained copper and nickel after annealing. Phys. Met. Metall. **118**(3), 241–248 (2017)
16. Huang, Y., Morehead, M.: Study of machining-induced microstructure variations of nanostructured/ultrafine-grained copper using XRD. J. Eng. Mater. Technol. **133**(2), 21–28 (2011)
17. Klocke, F., Lung, D., Gerschwiler, K., et al.: Recommended machining parameters for copper and copper alloys. DKI Monograph i.18, Düsseldorf Germany (2010)

Obtaining of Porous Powder Materials by Radial Pressing Method

Oleg Zabolotnyi$^{(\boxtimes)}$, Viktor Sychuk , and Dmytro Somov

Lutsk National Technical University,
75 Lvivska St., Lutsk 43018, Ukraine
z.o.v@i.ua

Abstract. The article presents the results of theoretical and experimental investigations of the radial-isostatic pressing process of powder materials (PM) in order to improve its effectiveness, to create the new and improve the existing technologies, equipment, tools and PM with the improved properties. For analytical description of the pressing processes we propose a new improved equation of pressing, which takes into account the properties of PM, powder consolidation during pressing, the loading schemes and allows general authentical description of the deformation behavior of the porous material. We improved the construction of the machine press-block for dry radial-isostatic pressing of enclosed volume and also developed a number of new technical solutions which can solve the problem of obtaining high-quality and long powder products (simple and complex shapes) with a uniformly distributed density by volume. Proposed solutions also allow reducing the volumes of intermediate environments, power inputs of the pressing process, sizes and metal content of equipment, costs, which raises the productivity of work and reduces the cost of manufactured products.

Keywords: Powder metallurgy · Porous powder material
Dry radial isostatic pressing · Yield surface · Plasticity model

1 Introduction

In the development of modern industry the role of powder metallurgy is estimated differently. On the one hand, in the manufacture of products for constructional purposes it has been slightly losing position due to a significant energy costs for obtaining starting material - powders. On the other hand, in the manufacture of products with unique properties, its role has increased and in many cases it is the only possible way of obtaining them. Therefore, we must strive for increasing the efficiency at all stages of the manufacture and use of products.

Further development of powder metallurgy depends on the improvements of the pressing processes because they determine the operational characteristics of the finished product and has hereditary influence on a number of the most important physical and mechanical properties. The irregularity distribution of the density in briquettes after compression is often seen at the sintering stage as warping sample, the formation of

micro- or macro cracks or even its destruction. Moreover, it leads to irregularity of mechanical, filtering, electrical and other properties [1–4].

2   Literature Review

In the modern engineering there is a growing interest to porous penetrable materials with high and well-controlled porosity [5]. The main parameters that determine their suitability for work is the porosity, regularity of its distribution by volume and penetrability. The efficiency, suitability for work and application field of such materials is determined by the presence of interconnected pore structure. This structure is formed and provided for all the operations of the technological process, but the final stage of technology - a stage of briquettes forming, which determines not only the size, shape, density, performance, safety and work culture, but also affects many most important properties of the finished product. Analysis of the modern technological processes of powder metallurgy also shows that the processes of PM consolidation at the stage of forming briquettes have a decisive impact on the quality and economic characteristics of the finished products manufacture [3, 4, 6].

From all the variety of penetrable PM we need to allocate long products, as with increase of their length we have a corresponding increase of their working surface, intensification of heat transfer and chemical processes [7, 8]. Powder metallurgy has a number of technologies for obtaining this class of products. The choice forming method of powder products is defined by the modern requirements for properties products, energy-power consumption, type of production, complexity shapes, geometric dimensions of the product, its performance properties, etc. Traditional pressing methods have many limitations and therefore not fully solve the problem of high-quality PM production [1, 3]. Highly advanced technology should complexly satisfy modern requirements applicable to the properties of products, their manufacture, safety work and should provide minimal energy-power parameters, production flexibility, etc.

As a result of information and patent researches, analytical analysis of traditional processes of powders compaction we found that for producing the long powder products the most rational schemes are a radial pressing scheme and a multilateral pressing scheme, because in their development they will implement the main positive benefits, which are inherent in traditional pressing methods, taking into account the current requirements, and complexly satisfy the needs of the production and the quality of products [9]. Therefore, they are, in our opinion, may be the basis for creating the new and improving the existing technologies, equipment and tools.

The optimal process for the implementation of radial compaction scheme is dry radial-isostatic pressing (DRIP), when the form with powder is isolated from the fluid by elastic medium, which allows to automate the process more efficiently, raise production standards and reduce power inputs [9]. Small volumes of intermediate environments to DRIP allow to significantly reduce metal content, sizes and cost of equipment. But along with the undisputed advantages of applying DRIP for long PM pressing this technology has several limitations: the problem of PM production with regularity distribution of density by volume, high complexity of manufacturing tools

and their low reliability, additional power inputs for the working environment deformation, etc. [1]. Therefore, the aim of the article is investigation of the PM compaction regularities directed towards the efficiency increasing of the DRIP PMprocesses, creation and implementation of improved technologies, equipment, tools, and PM with improved properties.

Studying of the yield surface forms in the deformation process is associated with determination of powders compaction laws with consideration of PM structural characteristics, which is urgent for the further improvement of DRIP theory and practice. From the conducted analytical review of researches and developments of progressive technologies it follows that the description of multi factor compaction process of powder environments may be based on a study of contact interaction particles of environment or using the continuous representations about its theological properties. Existing theoretical regularities describe the processes of compaction of metal powders and on the one hand have a general character based on the interconnection of stress tensor, strain tensor and porosity parameters and do not take into account the structural features of the materials. On the other hand, there are many models based on structural approach, where the main limitation is the difficulty of practical application, since they contain many structural parameters which are quite difficult to consider [10–15].

Analysis of the existing types of loading surfaces shows that the yield surface in the form of rotation ellipsoid would extend understanding the mechanism of deformation's behaviour of porous mediums [16]. These models have adequately described the behavior of porous materials under complex loading taking into account the micromechanical characteristics of the material and macro mechanics of the deformation process. On the other side, many parameters included in these criteria limit to some extent their practical application. As an alternative approach in such cases, not multi parametric models can be used [17] that is advisable for the numerical analysis of various pressing schemes or describing a specific technological scheme of deformation. So, it is obvious that the real model of PM plasticity must be multi parametric and should take into account the peculiarities of powdered environment that is compacted. Therefore, in our opinion, the prospective direction is the development and application of new continuum models that take into account the structural construction of porous PM.

3 Research Methodology

3.1 Theoretical Investigations of the Powder Materials Pressing Process

In the technological processes of pressing details from powders, materials under study may be processed by pressure along the loading trajectories which is in the range of deposition schemes to the uniform hydrostatic compression. Therefore, it is necessary to increase the accuracy of accepted interpolation of yield criterion using two definable stresses from this technological range of loading schemes. As two unknown allowable stresses we chose the deformation resistance of powder briquettes in two extreme loading schemes: hydrostatic loading (compression) and axial pressing in a tight matrix without external friction [1]. Experimental researches [18] indicate that the shape of loading surface in the p–T plane (here p – hydrostatic pressure; T – intensity of

tangential stresses) is represented as ellipse which shifted along the hydrostatic axis. However, for the chosen range of powders compaction schemes it is appropriate to use the models of plasticity in the form of central ellipsoid. This will be got with sufficient accuracy for practical calculations of technological parameters and properties of PM dependence, which don't contain very complex parameters of the ellipsoid displacement center along the hydrostatic axis.

Existing plasticity models, which are based on the hypothesis that the plasticity conditions are described on the ellipsoidal loading surface, are usually associated with the assumption that the mechanical reaction of the material is determined by only one parameter - the porosity. In the case when we are talking about porous sintered material, it is known that there are two factors which affect its deformation resistance. The first one - structural (geometric) factor determines the direct dependence on porosity (appears as logarithm in the equations like K.A. Konopytskyi–S.Torre, R.D. Green etc.). The second factor is determined by the contribution which makes the deformation of the solid phase. In porous materials, as opposed to free-flowing, the matrix is coupled and is going on a plastic deformation. The magnitude of this deformation determines the second component of porous material's resistance [14, 19–21].

In the case the powder material matrix doesn't exist, that does not permit to use the second parameter to its characteristics. In the meantime, due to breaking the particles during compaction and their mutual slippage, in the powder medium it is also observed the dissipation of energy, which nevertheless cannot be described in the same way as in the case of the plastic matrix presence. To take this into account, we propose to use the assumption that this factor exponentially depends on density:

$$\sigma_T = \sigma_{T_0} \left(\frac{v}{v_0} \right)^k, \tag{1}$$

where σ_T i σ_{T_0} – yield limits of powder material before and during pressing, respectively; v i v_0 – current and starting relative density of briquette, respectively; k – hardening index which depends on the properties of the powder material and pressing scheme (determined experimentally). This assumption can be justified when we talking about a narrow range of loading trajectories - from uniform hydrostatic compression to axial pressing in a tight matrix. This dependence is obtained on the basis of the experimental-empirical approach, which is based on the conducting of ray loads.

So, for the analytical description of the pressing processes in the range of compaction schemes from axial compression in a tight matrix without external friction to uniform hydrostatic pressure, we propose to use our improved equation of pressing, which is based on the equation of K.A. Konopytskyi–S. Torres and takes into account the properties of PM and its consolidation (strengthening) during pressing, loading schemes and allows to correctly describe the deformation behavior of the porous PM [22]:

$$p = 2\sigma_{T_0} \left(\frac{v}{v_0} \right)^k \ln \frac{1 - v_0}{1 - v} \tag{2}$$

Now we can define the explicit form of the ellipsoidal loading surface via calculated estimates of deformation resistance of powder briquettes of varying density in the selected range of loading schemes [9, 22]. The loading surface in the form of rotation central ellipsoid has the view:

$$\frac{3p^2}{\psi^2} + \frac{2T^2}{\varphi^2} = 1, \tag{3}$$

where p – hydrostatic pressure; T – intensity of tangential stresses; ψ i φ – functions of the mechanical and structural characteristics of compacted materials.

As a result, the joint solution of Eq. (3) and calculated dependencies to determine the deformation resistance in the selected loading schemes, taking into account the Eq. (2), was refined by the yield criterion, which is determined by the dependencies:

$$\psi = 2\sqrt{3}\sigma_{T_0}\left(\frac{\upsilon}{\upsilon_0}\right)^m \ln\frac{1-\upsilon_0}{1-\upsilon}; \quad \varphi = \frac{2\sqrt{6}\sigma_{T_0}(1-\xi)\left(\frac{\upsilon}{\upsilon_0}\right)^{m+l}\ln\frac{1-\upsilon_0}{1-\upsilon}}{\sqrt{9\left(\frac{\upsilon}{\upsilon_0}\right)^{2m}-(1+2\xi)^2\left(\frac{\upsilon}{\upsilon_0}\right)^{2l}}}; \tag{4}$$

$$p^2\left(\frac{\upsilon_0}{\upsilon}\right)^{2m} + \frac{T^2\left[9\left(\frac{\upsilon}{\upsilon_0}\right)^{2m}-(1+2\xi)^2\left(\frac{\upsilon}{\upsilon_0}\right)^{2l}\right]\left(\frac{\upsilon_0}{\upsilon}\right)^{2(m+1)}}{3(1-\xi)^2} = 4\sigma_{T_0}^2\left(\ln\frac{1-\upsilon_0}{1-\upsilon}\right)^2, \tag{5}$$

where ξ – coefficient of lateral pressure, which depends on the density and material properties of powder and briquette that is, to some extent, the carrier of information about the structural features of powder body (particles shape, method of producing powder, hardening of the material, etc.); m i l – strengthening indicators under hydrostatic and axial compaction respectively (determined experimentally). It is known that the main parameters that affect the coefficient of lateral pressure ξ, are the density and type of powder material. Sizes and shape of powder particles, method of powder producing and other factors have smaller influence. For its definition we use the results of studies to determine the coefficient of lateral pressure ξ, which is described in [1].

3.2 Experimental Verification of New Pressing Equation and Yield Surface

To determine the explicit form of the ellipsoidal loading surface except the coefficient of lateral pressure it is necessary to have the calculated or empirical dependencies of deformation resistances in the selected loading schemes. Experimental verification of the obtained and improved pressing equation and yield criterion was performed using the original experimental complex (up to 1 GPa) (Fig. 1).

Resistance to hydrostatic pressure was determined by using aforementioned experimental complex based on the standard hydraulic press 1 model PSU500 (ПСУ500). This complex designed and manufactured in Lutsk National Technical University allows to realize both simple and complex loading trajectories [23]. Resistance to deformation at axial pressing in a tight matrix was determined by recording the compaction diagrams on
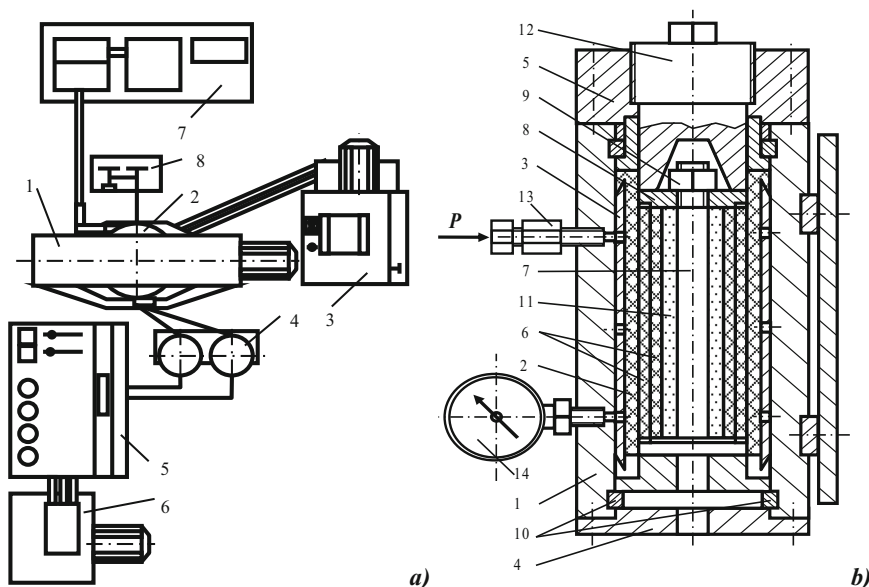
Fig. 1. Structural scheme of experimental complex (a) and press-block of machine for DRIP (b). (a) Experimental Complex: 1 - hydraulic press mod. PSU500; 2 - high pressure camera; 3 - remotes controls of press; 4 - block of multiplication; 5 - remotes controls of hydraulic system; 6 - hydraulic system drive; 7 - measuring & recording equipment; 8 - press-block for DRIP (see b). (b) Press-block for DRIP: 1 – hull; 2 – polyurethane elastic insertion; 3 – reinforcing element; 4, 5 – lids; 6 – internal elastic shells; 7 – mandrel; 8 – shim; 9 – nut; 10 – cut cams; 11 – powder; 12 – shutter; 13 – connecting pipe; 14 – manometer.

the universal testing machine "Instron-1195" (England). In order to reduce external friction, the inner surface of the matrix is greased MoS_2 and ratio of height to diameter of a briquette was 0.3. Psychometric density and bulk density were determined by the SSU19440-74.

Figure 2 shows the received by us dependencies of the functions of mechanical and structural characteristics from the relative density of briquettes obtained from titanium powder brand PTS-1 (ПТС-1), which are constructed by the Eq. (4).

In Fig. 3 it is shown the kind of yield surface in the plane p–T for briquettes of titanium powder brand PTS-1 constructed according to the Eq. (5). Obtained dependences to the definition yield criterion in good agreement with the experimental data and with sufficient accuracy for practical calculations describe the processes of PM deformation in the selected range of loading schemes.

Thus, from the position of continuum theory the plasticity model of powder environments had been improved, which is based on a yield condition with the loading surface as a central ellipsoid and differs in that, which establishes link components of stress tensor not only with density and mechanical properties of the material, but also includes parameters that contain information about the structural features of the PM and
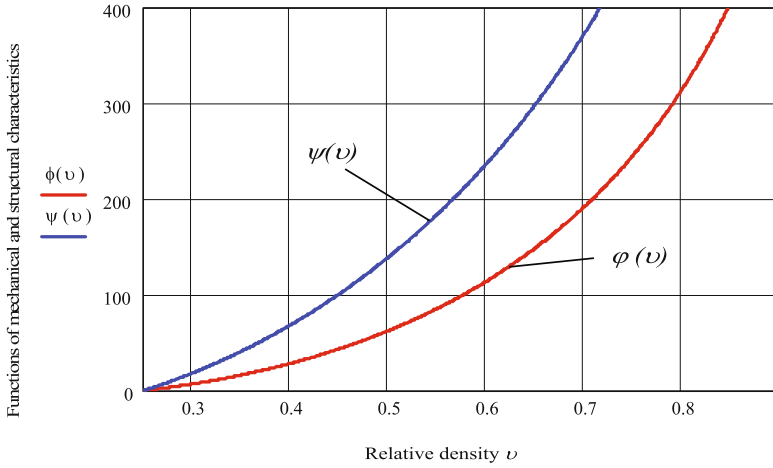
Fig. 2. Dependencies functions of mechanical and structural characteristics $\psi(\upsilon)$ and $\varphi(\upsilon)$ depending on the relative density of briquettes from titanium powder (PTS-1, $\upsilon_0 = 0.25$).
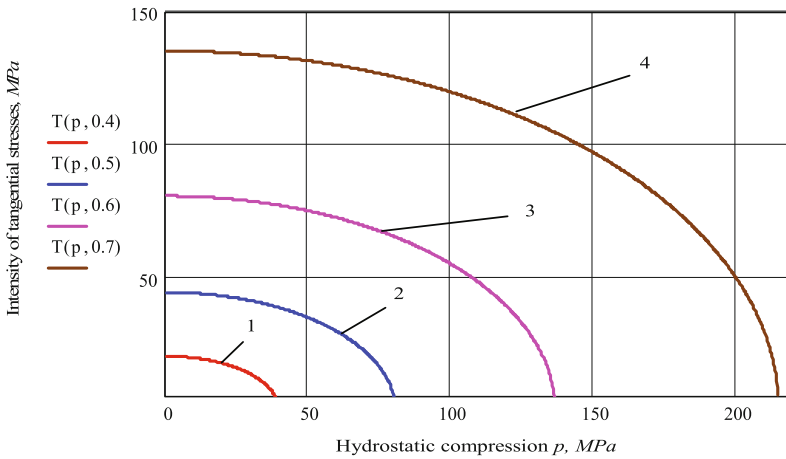
Fig. 3. Form of yield surfaces in the p–T plane for briquettes from titanium powder brand PTS-1 ($\upsilon_0 = 0.25$) with the final relative density: (1) $\upsilon = 0.4$; (2) $\upsilon = 0.5$; (3) $\upsilon = 0.6$; (4) $\upsilon = 0.7$.

PM strengthening during pressing. Improved plasticity model (5) is a multi parametric and can be used to calculate the technological parameters of DRIP [9, 22].

On the basis of the improved plasticity model we define the stress-strain state in briquettes under a radial compaction of powders. The joint solution of the system of equations (the plasticity conditions, the equation of equilibrium and associated flow law at the boundary conditions ($\tau_{rz} = 0$, $\varepsilon_z = 0$) has allowed us to set the value of stress tensor components for radial loading scheme [22]:

$$\sigma_r = p_{np} = 2\sigma_{T_0}\left(\frac{\upsilon}{\upsilon_0}\right)^m \ln\frac{1-\upsilon_0}{1-\upsilon}\sqrt{1 + \frac{\left(\frac{\upsilon}{\upsilon_0}\right)^{2l}(1-\xi)^2}{9\left(\frac{\upsilon}{\upsilon_0}\right)^{2m} - (1+2\xi)^2\left(\frac{\upsilon}{\upsilon_0}\right)^{2l}}} \tag{6}$$

$$\sigma_z = \frac{2\left(\psi^2 - \varphi^2\right)}{\sqrt{6\left(2\psi^2 + \varphi^2\right)}}. \tag{7}$$

Figure 4 shows the obtained dependence of the stress tensor components depending on the relative density of briquettes from titanium powder brand PTS-1 constructed by the Eqs. (6) and (7). We need to know axial stresses (7) to calculate strength components for the equipment, tools and pressing machine (press-block). Equation (6) does not include power inputs on radial deformation of elastic shells. However, the work [1] showed that for real sizes of elastic shells with thickness of 5–30 mm which are made of polyurethane brand SKU-7L, additional power inputs for shells deformation are constituted at 2–4% of the working pressure of pressing. With increasing compacting pressure the share of power inputs on shells deformation decreases. This allows us to assume for such shells $\sigma_r \approx \sigma_t \approx \sigma_z$, that is, as the fluid uniformly transmits pressure. At the same time pressure change at 2–4% leads to a change in density to 0.3–0.5%, that guarantees the stability properties of briquettes.

Radial-isostatic pressing process of powder tubes is performed using the radial compaction of powder with the restriction longitudinal deformation (Fig. 1b).
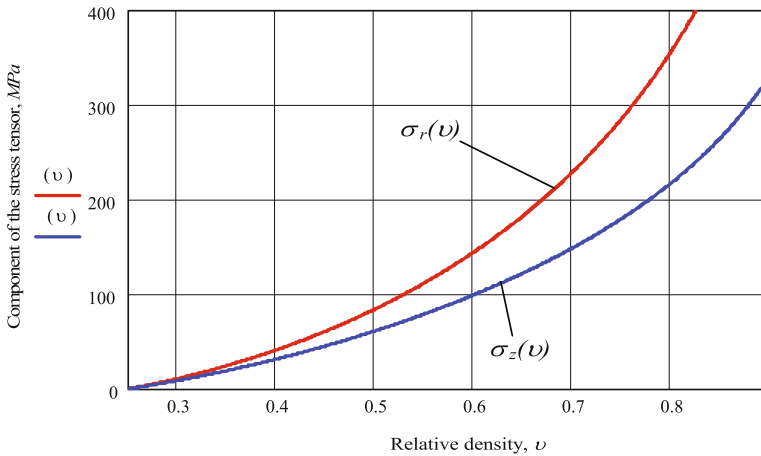
Fig. 4. Dependencies component of the stress tensor depending on the relative density of briquettes from titanium powder brand PTS-1 ($\upsilon_0 = 0.25$).

Figure 5 describes the curves of powders ability to compaction at static radial loading. To calculate the pressure pressing for radial scheme we used Eq. (6). The results of calculations by Eq. (6) agree well with the obtained experimental data (see dots).
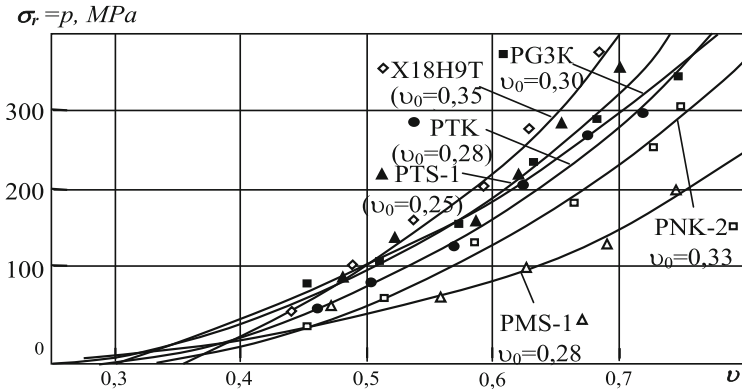
Fig. 5. The dependence of pressure on the relative density at the radial pressing according to the Eq. (6). Dots - the experimental data.

Thus, based on our new, improved by us plasticity model, have determined the stress-strain state in briquettes for radial loading scheme. We have determined the impact of starting and final density, geometry of briquette, physical and mechanical properties of powders material on energy-power parameters of DRIP. In calculations that allows to predict the distribution of physical and mechanical characteristics of briquettes by volume, predict the energy-power parameters of compaction process, as well as conduct a power calculation of equipment and tools for DRIP process.

4 Results

4.1 Improving Equipment and Tools for Drip of Powder Materials

To conduct experimental researches in order to determine the energy-power parameters of radial pressing we have designed and manufactured an improved experimental press-block for DRIP (see Fig. 1b). It allows to obtain products from sealing materials of different nature and shape with the limiting dimensions of $\emptyset 60 \times 320$ mm ($p \leq 150$ MPa). Flexible tools (insertion, shells, corks) placed inside press-block perform the leading role in the pressing process. To them it is put forward a set of requirements that focused on providing the reliability of work, process ability constructions (minimum labor inputs) and providing the necessary PM properties. In the basic version of press-block [1] elastic insertion with cuffs were used, which had been received using the machining.

This is not good because during the cutting machining micro irregularities (surface roughness, microtears) are formed on the cuffs surface, which depends on the physical

and mechanical characteristics of the processed material and processing modes. These micro irregularities act as stress concentrators, which leads to the emergence of macro- and microdamages in the working area of the cuffs and as a result, significantly reduces the reliability of elastic insertion work and press-block as a whole.

They have especially great influence on the durability of details under cyclic loading we have in radial-isostatic pressing. As a result, sustainability of the basic element of the press-block (elastic insertion) was less than 1000 cycles of loading. Therefore, it became necessary to improve the design of elastic insertion to improve manufacturability, which guarantees its reliability and as a result, reduces the cost of the basic elements of the press-block [23]. We have developed a new design and producing technology of reinforced elastic insertion (Fig. 6), which involves the presence of a reinforcing element from steel in it, which forms the high-pressure cuffs of elastic insertion at the stage of its casting [23].
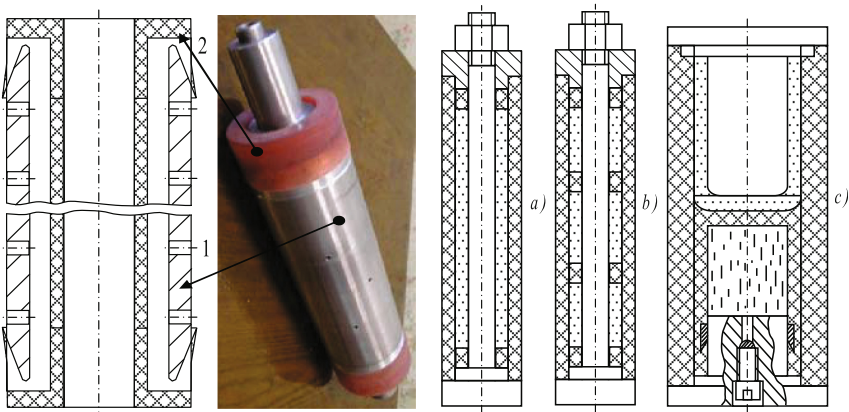
Fig. 6. Construction scheme and general view of improved reinforced elastic insertion to press-block for DRIP (1) - reinforcing steel element; (2) - improved elastic insertion) and a, b, c – improved adaptations (tools) for pressing powder products of different sizes and forms.

The use of casting instead of processing by cutting the elastic insertion for manufacturing helped us to avoid the negative effects of the cutting process. This allows improving the quality of its manufacturing, reliability and durability of the press-block work, provides sealing at high pressures, reduces the volumes of intermediate environments that transmit pressure, saves elastic material and improves manufacture ability by reducing labor inputs in its manufacture.

The main parameters of the PM, which determine its performance characteristics are density and regularity of its distribution by the volume of the product. As a result of theoretical and experimental researches conducted by us we found that the change in density along the radius of briquettes is in the range of the experiment accuracy (1–1.5%). Density along the length of products at the traditional scheme of DRIP is distributed regularity, but observed the "marginal" effects in the ends of the briquette. It is connected with the presence of the external friction – it's a negative phenomenon.

To fix these problems, we proposed a new technical solution – special elastic plugs (Fig. 6a, b) [23], which using allows us to create an additional axial force on the end of briquette and thus provides the uniform distribution of density along the length of the product.

At DRIP and manufacturing of "glass" type products with axial non-through hole, by traditional technology is observed irregularity density in the bottoms region of the product, which leads to defects both at the pressing stage and sintering. To fix these problems, we proposed a new technical solution – elastic cork, which is hermetically filled with fluid (Fig. 6c) [23]. This cork, by creating the conditions of quasi-isostatic pressing, provides uniform pressure distribution over the whole surface of the briquette, which provides uniform distribution of density throughout the volume of the product.

Developed design and technology for obtaining the adaptations for DRIP PM (Fig. 6) to get products like tube and "glass" type products of complex shape with axial non-through hole, allow providing constancy of working pressure across the surface of the product, which greatly reduces the number of defects, saves expensive powder material and allows obtaining high quality PM with uniform distribution density by volume of the product and stable operational characteristics.
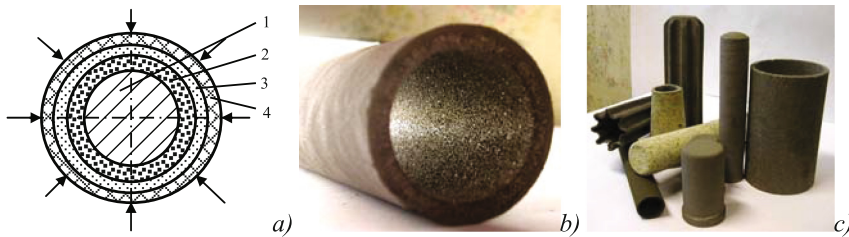
Fig. 7. Gradient filtering materials: a – technology scheme of staged DRIP of multilayered FM: 1 – mandrel; 2 – first layer (carcass); 3 – next layer(s); 4 – elastic shell(s); b – general view of two-layer FM based on carbide titanium powders; c – general view of different types of FM obtained by DRIP.

5   Conclusions

As follows, DRIP using the proposed improved technical solutions (Fig. 6), solves the problem of obtaining high-quality long products with a uniformly distributed density by volume both products of simple and complex shapes. Using our solutions allows reducing volumes of intermediate environments, power inputs of process, sizes, metal content, equipment costs and increases the productivity of work. Based on the obtained results we developed the new technology of obtaining the gradient filtering materials (FM) of simple and complex shapes (Fig. 7) based on titanium carbide powders.

We tested the obtained multilayer FM under production conditions for filtration the lubricating and cooling fluids and technical water. The results of the carried out tests shows that the using our FM allows increasing the duration of filtering material

operation 1.5–2.0 times as much. This confirms the expediency of using these technologies to production of other types of PM including powder nozzles for abrasive-jet machines [24, 25].

References

1. Reut, O., Boginskyi, L., Petiushik, Y.: Dry Isostatic Pressing of Compactable Materials. Debor, Minsk (1998)
2. Hernández, J.A., Oliver, J., Cante, J.C., Weyler, R.: Numerical modeling of crack formation in powder forming processes. Int. J. Solids Struct. **48**(2), 292–316 (2011)
3. Bortzmeyer, D.: Dry pressing of ceramic powders. In: Terpstra, R.A., Pex, P.P.A.C., de Vries, A.H. (eds.) Ceramic Processing. Springer, Dordrecht (1995)
4. Sethi, G., Myers, N.S., German, R.M.: An overview of dynamic compaction in powder metallurgy. Int. Mater. Rev. **53**(4), 219–234 (2008)
5. Jabur, A.: Effect of powder metallurgy conditions on the properties of porous bronze. Powder Technol. **237**, 477–483 (2013)
6. Oberacker, R.: Powder compaction by dry pressing. In: Riedel, R., Chen, I.-W. (eds.) Ceramics Science and Technology, vol. 3, pp. 1–37. Wiley-VCH, Weinheim (2011)
7. Cristofolini, I., Pederzini, G., Rambelli, A., Molinari, A.: Densification and deformation during uniaxial cold compaction of stainless steel powder with different particle size. Powder Metall. **59**(1), 73–84 (2016)
8. Cristofolini, I., Molinari, A., Pederzini, G., Rambelli, A.: From experimental data, the mechanics relationships describing the behaviour of four different low alloyed steel powders during uniaxial cold compaction. Powder Metall. **61**(11), 10–20 (2018)
9. Boginsky, L., Reut, O., Piatsiushyk, Y., et al.: The development of processes of pressing of articles from powders on the bases of metals. Ceramics and graphite. In: 15 International Plansee Seminar, vol. 3, pp. 197–209, Reutte, Austria (2001)
10. Bozhydarnik, V., Rud, V.: Plasticity criteria of porous solids: global and national trends. Rheology, structure, properties of powder and composite materials: collection of scientific papers, pp. 68–80. LNTU, Lutsk (2004)
11. Lee, S.C., Kim, K.T.: Densification behavior of aluminum alloy powder under cold compaction. Int. J. Mech. Sci. **44**(7), 1295–1308 (2002)
12. Al-Qureshi, H.A., Galiotto, A., Klein, A.N.: On the mechanics of cold die compaction for powder metallurgy. J. Mater. Process. Technol. **166**(1), 135–143 (2005)
13. Carlone, P., Palazzo, G.S.: Cold compaction of ceramic powder: computational analysis of the effect of pressing method and die shape. Int. Appl. Mech. **43**(10), 1174–1178 (2007)
14. Montes, J.M., Cuevas, F.G., Cintas, J., Torres, Y.: Powder compaction law for cold die pressing. Granul. Matter **12**(6), 617–627 (2010)
15. Hadadzadeh, A., Whitney, M.A., Wells, M.A., Corbin, S.F.: Analysis of compressibility behavior and development of a plastic yield model for uniaxial die compaction of sponge titanium powder. Mater. Process. Technol. **243**, 92–99 (2017)
16. Shtern, M., Serdiuk, G., Maksimenko, L., et al.: The Phenomenological Theory of Powders Pressing. Scientific Thought, Kiev (1982)
17. Shtern, M., Mikhailov, O.: Numerical modeling of pressing processes powder products with complex shapes in tough matrices: influence of pressing scheme on the density distribution. Powder Metall. **11**(12), 29–36 (2002)

18. Midukov, V., Rud, V.: About Status of Experimental Researches of Porous Metals Plastic Deformation. Rheological Models and Deformation Processes of Porous Powder and Composite Materials. Scientific Thought, Kiev (1985)
19. Yousuff, M., Page, N.W.: Die stress and internal friction during quasi-static and dynamic powder compaction. Powder Technol. **76**(3), 299–307 (1993)
20. Poquillon, D., Lemaitre, J., Baco-Carles, V., Tailhades, P., Lacaze, J.: Cold compaction of iron powders—relations between powder morphology and mechanical properties Part I: Powder preparation and compaction. Powder Technol. **126**(1), 65–74 (2002)
21. Aryanpour, G., Farzaneh, M.: Application of a piston equation to describe die compaction of powders. Powder Technol. **277**, 120–125 (2015)
22. Zabolotnyi, O.: Improving of the plasticity conditions of compactable powder medium with particles of complex shape. Bulletin of Zhytomyr ETI 19/Tech Sciences, 14–17 (2001)
23. Zabolotnyi, O.: Improving elastic tools for dry radial isostatic pressing of powder materials. Sci Notes **10**, 77–84 (2002)
24. Sychuk, V., Zabolotnyi, O., McMillan, A.: Developing new design and investigating porous nozzles for abrasive jet machine. Powder Metall. Met. Ceram. **53**(9–10), 600–605 (2015)
25. Povstyanoy, OYu., Sychuk, V.A., McMillan, A., et al.: Metallographic analysis and microstructural image processing of nozzles for sandblasting produced by powder metallurgy methods. Powder Metall. Met. Ceram. **54**(3–4), 234–240 (2015)

Methods for Calculating the Grain Boundary Adsorption Capacity of Nanostructured Copper Based Condensates

Maria Zhadko[(✉)] , Oleg Sobol , Galina Zelenskaya ,
and Anatoly Zubkov

National Technical University "Kharkiv Polytechnic Institute",
2 Kyrpychova St., Kharkiv 61002, Ukraine
maglushchenko@gmail.com

Abstract. The structure of vacuum Cu-Ta and Cu-Mo condensates in the form of foils approximately 50 μm thick was studied by transmission electron microscopy and X-ray diffractometry. The samples were obtained by electron-beam evaporation from various sources in vacuum of $\sim 10^{-3}$ Pa. It is established that alloying of copper condensates with tantalum or molybdenum in the amount of 0.4–0.5 at. % disperses the grain structure of copper matrix from micro- to nanoscale dimension. It is shown that this effect is due to the blocking effect of adsorption layers of tantalum or molybdenum atoms formed on the surface of growing copper grains during the condensation of two-component vapor. Based on the experimental data and theoretical calculations carried out in different approximations, the conclusion about the monolayer character of grain-boundary segregations of tantalum or molybdenum atoms on the grain boundaries of copper matrix was made. Numerical methods for calculating the concentrations of tantalum or molybdenum that are necessary for the formation of monoatomic adsorption layers at grain boundaries of matrix metals of specified sizes are developed. Concentration dependencies of grain sizes of copper matrix calculated theoretically by the proposed method are in good agreement with the experimental data.

Keywords: Thermal stability · Grain size · Grain boundary segregation

1 Introduction

The development of technologies for the production of metallic materials with a nano-sized thermally stable structure is an urgent problem of up-to-date materials science. The most common methods of synthesis of these objects are powder metallurgy, various kinds of intensive plastic deformation, crystallization from amorphous state, vacuum plasma technologies. The latter, despite the shortcomings associated with the problems of obtaining bulk materials, have a number of advantages, which are as follows. Firstly, the crystallization front during the formation of condensate is a free surface, which makes it possible to use theoretical representations describing adsorption processes on free surfaces [1, 2] to interpret the experimental results and to determine the degree of activity of the alloying elements to the surface of matrix metal.

Secondly, upon obtaining objects by condensation from the vapor phase, the veiling effect on the adsorption processes of foreign impurities that are always contained in the melts is eliminated. Thirdly, it becomes possible to use the experimental results to evaluate the ability of certain alloying elements to form equilibrium grain-boundary segregations in matrix metals during their crystallization from melts. Despite a large number of experimental and theoretical works dealing with these issues, at present there is no information on the optimal phase-structural state and the amount of these elements that are necessary for the formation of the adsorption layers.

In this regard, the aim of this paper was to investigate these processes experimentally and theoretically and to develop mathematical methods for calculating the number of atoms of alloying elements, necessary for the formation of the optimal state of equilibrium adsorption layers.

2   Literature Review

The research direction chosen in this paper is based on the concept of "useful" and "harmful" impurities [3, 4], which consists in concentrating the atoms of certain alloying elements on the grain boundaries of matrix metal in the form of adsorption layers, which is usually called equilibrium grain-boundary segregations [3]. These processes can occur during crystallization from various media [5–7] or as a result of subsequent heat treatment. Theoretical basis of this direction are the works of Gibbs [1], Langmuir [2], McLean [8], Sean [9], as well as numerous experimental results and commercially developed technologies for modifying various alloys, for example, [10]. The important conclusion of these studies is that the general regularities of the adsorption processes that occur on free surfaces must also be saved, when grain boundaries are formed during the crystallization of metals from various media [9, 11, 12].

3   Research Methodology

The research objects were foils of two-component Cu–Ta and Cu-Mo condensates up to 50 µm thick obtained by electron-beam evaporation from different sources and subsequent crystallization at nonorienting glass ceramic substrates in vacuum at a pressure of $\sim 10^{-3}$ Pa.

The condensates were prepared at fixed technological parameters, while only tantalum and molybdenum content was ranged from 0.1 to 2.5 at. %.

The structure of condensates was studied by transmission electron microscopy using PEM-100 and JEM-2100 instruments and by X-ray diffractometry using DRON-3M X-ray apparatus.

Tantalum and molybdenum concentration was controlled using energy dispersive X-ray spectroscopy (EDS).

4   Results

Figure 1 displays experimental dependences of the average conditional grain size (*D*) in condensates on molybdenum (1) and tantalum (2) concentration. These curves exhibit two sections: when the alloying element content is approximately to 0.4–0.5 at. %, a sharp decrease in *D* with subsequent attainment of saturation is observed.
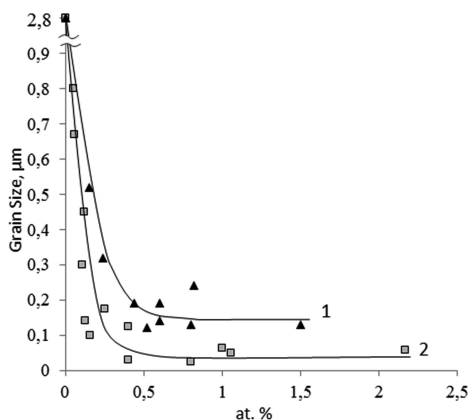
Fig. 1. Dependences of the average conditional grain size of copper matrix on the concentration of molybdenum (1) and tantalum (2).

The signs indicating the presence of tantalum or molybdenum particles in the volume of the matrix copper metal are absent on the electron-microscopic images of structures of the objects that correspond to the falling branches of the experimental dependences (Figs. 2 and 3), whereas on electron diffraction patterns, the diffraction reflections that belong only to FCC copper crystal lattice are present.
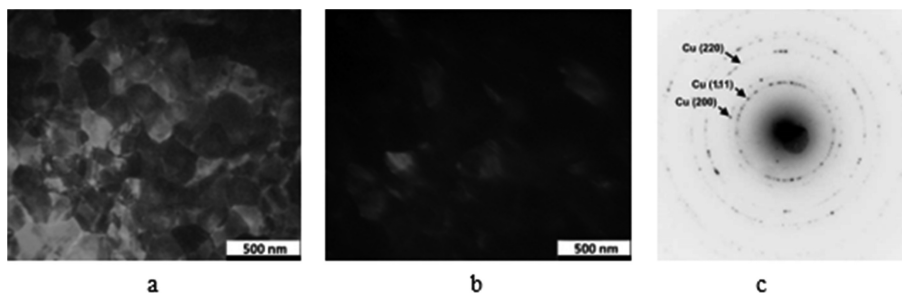
Fig. 2. Electron microscopic images of the condensate structure containing 0.25 at. % Ta: a – bright field image, b – dark field image, c – electron diffraction pattern.
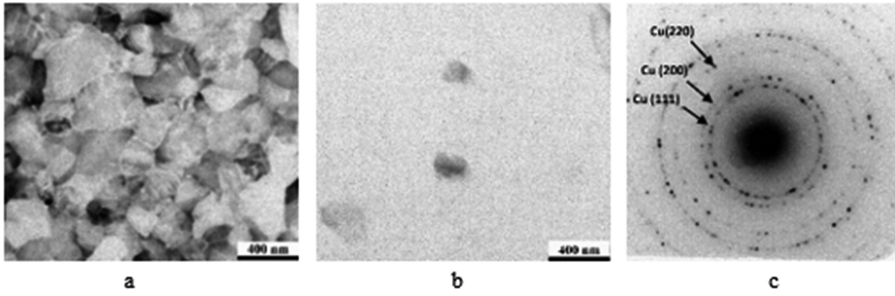
Fig. 3. Electron-microscopic negative images of the condensate structure containing 0.4 at. % Mo: a – bright field image, b – dark field image, c – electron diffraction pattern.

The second element concentrations are above 0.4–0.5 at. %, the structure of condensate changes substantially (Figs. 4 and 5). The observed fragmented granular structure of copper matrix is evidenced by bright- and dark-field images, where tantalum particles, fringed with chains, are seen inside grains. On the electron diffraction patterns, the diffraction reflections that belong to the phases of tantalum and molybdenum appear (Figs. 4c and 5c).
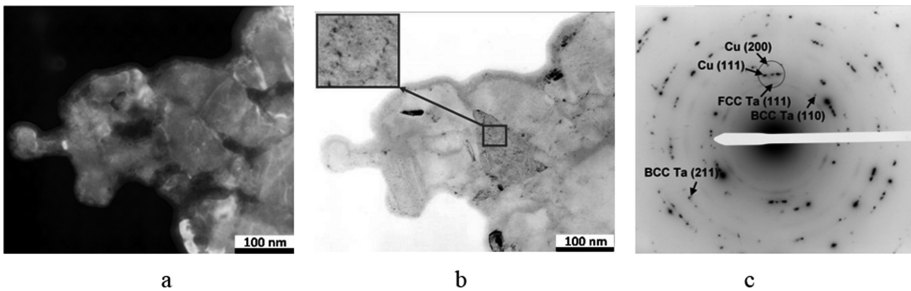
Fig. 4. Electron-microscopic negative images of the condensate structure containing 1.3 at. % Ta: a – bright field image, b – dark field image, c – electron diffraction pattern.
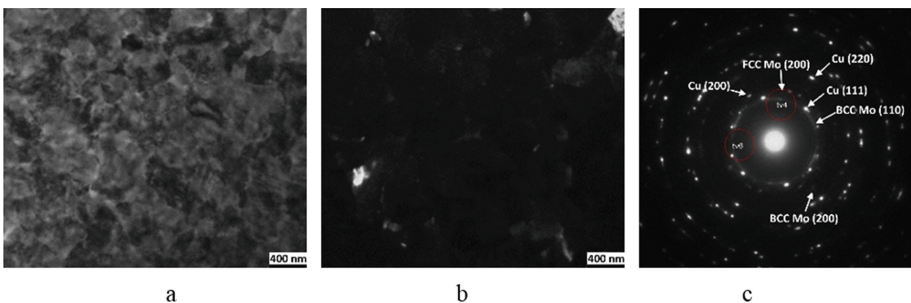
Fig. 5. Electron-microscopic images of the condensate structure containing 1.6 at. % Mo: a – bright field image, b – dark field image, c – electron diffraction pattern.

Figure 6 shows the concentration dependences of the parameter of FCC copper crystal lattice (*a*) in condensates, for which the curves *D–f* (*C*, at. %) were obtained (Fig. 1). It can be seen from Fig. 6 that, at low tantalum or molybdenum contents, no noticeable change in the crystal-lattice parameter occurs. The increase in tantalum or molybdenum concentration leads to growth in parameter *a*, which indicates the formation of a supersaturated solution in copper crystal lattice.
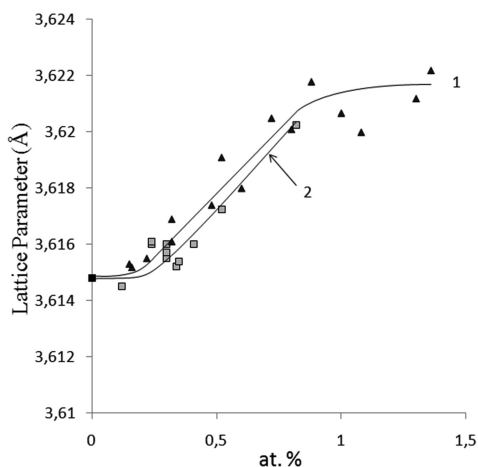
Fig. 6. Dependence of parameter of FCC crystal lattice of copper matrix on molybdenum (1) and tantalum (2) concentration.

The character of concentration dependences of the grain size and crystal lattice parameter of copper matrix (Figs. 1 and 6) and electron-microscopic images of the structure (Figs. 2 and 3) allows us to conclude that at tantalum or molybdenum concentrations corresponding to the descending branch of the dependence *D–f* (*C*, at. %), Ta and Mo are localized in grain boundaries in the form of monatomic adsorption layers. The enhancement in tantalum or molybdenum content in condensates leads to the redistribution of their atoms between grain boundaries, solid solution, and second-phase particles. This sequence of tantalum and molybdenum distribution between condensate-structure elements suggests that the reduction in grain size is connected with the blocking action of Ta or Mo atoms adsorbed at the surface of growing grains of copper matrix [13].

It should be noted that tantalum has a stronger effect on grain size than molybdenum. This can be caused by a greater difference in melting temperatures and atomic radii of copper and tantalum compared with molybdenum. In addition, the region of inflection on *D–f* (*C*, at. %) curves (Fig. 1) for Cu-Mo and Cu-Ta samples is observed at different alloying element concentrations. This, apparently, is due to the different adsorption capacity of grain boundaries for tantalum and molybdenum atoms.

As an example, the grain size values for Cu-Ta system (Fig. 7, curves 1, 2) and schemes of the arrangement of adsorbed tantalum atoms on various crystallographic copper planes obtained in various approximations (Fig. 8) were calculated. Note that the dependence 1 is calculated according to the procedure described in [5], and the scheme of atoms arrangement is on Fig. 8a, while the area of adsorption cells for different crystallographic planes of matrix metals is not taken into account.
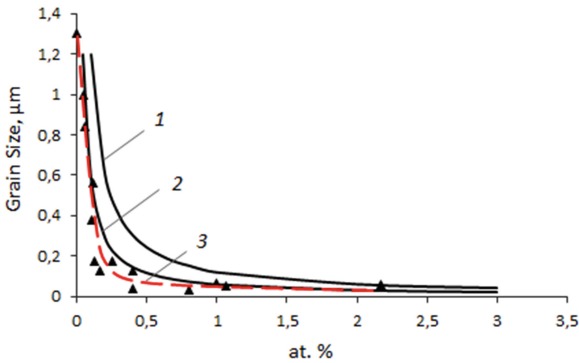
Fig. 7. Dependence of the average conditional grain size in copper matrix on tantalum concentration: *1* - theoretical dependence calculated according to the procedure in [5]; *2* - theoretical dependence calculated with allowance for the adsorption-cell area; and *3* - experimental curve.
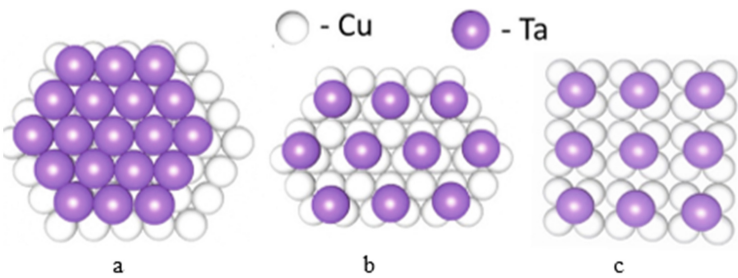
Fig. 8. Schemes of the arrangement for adsorbed tantalum atoms on crystallographic copper planes: a, b – (111), c – (100).

If this factor is taken into account [14], then the calculated D–f (C, at. %) dependences will better correspond to the experimental data. This is demonstrated by the example of curve 2, Fig. 7, in the construction of which the expression was used:

$$Cat = \frac{\pi d^3}{nSD} \cdot 100\% \tag{1}$$

where d is the diameter of the matrix metal atom, n is the coefficient taking into account atomic packing factor of the crystal lattice of the matrix metal; S is the calculated area of the adsorption cells, which for (111), (100), (110) copper crystallographic planes are

$5.7 \cdot 10^{-2}$ nm^2, $6.6 \cdot 10^{-2}$ nm^2 and $9.3 \cdot 10^{-2}$ nm^2, respectively (Fig. 8b, c), D is the specified grain diameter.

Thus, the monolayer nature of grain-boundary segregations, which suggest strong interatomic interaction between adsorbed atoms of tantalum, molybdenum or copper [15], is the reason for the decrease in grain size of copper matrix during condensate formation and the thermal stability of the original highly disperse structure [13].

The results open the possibility of structure refinement, increasing strength properties and thermal stability of metals obtained using different technologies. For this purposes, it is necessary to select the appropriate elemental composition with certain physicochemical properties of the components and create such technological conditions for obtaining the structure of metals in which the possibility of grain-boundary segregation by alloying elements in the form of monolayer adsorption layers will be possible.

5   Conclusions

1. Alloying of copper condensates with tantalum or molybdenum to ~ 0.5 at. % leads to a decrease in the grain size from 3 μm to 50 nm and 100 nm, respectively.
2. Upon the condensation of the vapor mixture of atoms of copper and tantalum or molybdenum, the distribution of atoms of alloying element occurs between an adsorption layer at the surface of growing copper grains, the supersaturated solution, and second-phase particles. The monolayer nature of the adsorption layers, which suggests strong interatomic bonds between tantalum, molybdenum and copper atoms, explains high thermal stability of the initial nanodispersed structure of two-component Cu-Ta and Cu-Mo vacuum condensates.
3. Methods for calculating the necessary concentrations of alloying element to obtain needed dimension of the grain structure of copper matrix metal by forming grain-boundary segregations by atoms of alloying elements in the form of monoatomic adsorbed layers have been developed.

References

1. Gibbs, J.W.: Collected Works, vol. 1. Yale University Press, New Haven (1948)
2. Langmuir, I.: The constitution and fundamental properties of solids and liquids. Part I. Solids. J. Am. Chem. Soc. **38**(11), 2221–2295 (1916)
3. Glikman, E.E., Bruver, R.E.: Equilibrium segregation at grain boundaries and intercrystalline cold brittleness of solid solutions. Metallofizika **43**, 42–63 (1972). (in Russian)
4. Firstov, S.A., Lugovskoy, Yu.F: Features of the influence of microstructure on the strength of composite materials under static and cyclic loading. Electron Microsc. Strength Mater. **15**, 83–88 (2008). (in Russian)
5. Barmin, A.E., Sobol', O.V., Zubkov, A.I., Mal'tseva, L.A.: Modifying effect of tungsten on vacuum condensates of iron. Phys. Met. Metallogr. **116**(7), 706–710 (2015)
6. Schuler, J.D., Rupert, T.J.: Materials selection rules for amorphous complexion formation in binary metallic alloys. Acta Mater. **140**, 196–205 (2017)

7. Rjagopalan, M., Darling, K., Turnage, S., Koju, R.K., Hornbuckle, B., Mishin, Y., Solanki, K.N.: Microstructural evolution in a nanocrystalline Cu-Ta alloy: a combined in-situ TEM and atomistic study. Mater. Des. **113**(5), 178–185 (2017)

8. McLean, D.: Grain Boundaries in Metals. Oxford University Press, London (1957)

9. Sean, M.P.: Adsorption-induced interface decohesion. Acta Metall. **28**(7), 955–962 (1980)

10. Goldstein, Ya.E., Misin, V.G.: Inoculation of Iron-Carbon Alloys. Springer, Moscow (1993)

11. Thomas, M.T., Baer, D.R., Jones, R.H., Bruemmer, S.M.: Sulfur and oxygen chemistry at free surfaces and grain boundaries of iron alloys. J. Vac. Sci. Technol. **17**(1), 25–28 (1980)

12. Grabke, H.J.: Surface and grain boundary segregation on and in iron. ISIJ Int. **57**(4), 178–185 (1986)

13. Zubkov, A.I., Zubarev, E.N., Sobol', O.V., Hlushchenko, M.A., Lutsenko, E.V.: Structure of vacuum Cu-Ta condensates. Phys. Met. Metallogr. **118**(2), 158–163 (2017)

14. Brune, H.: Metals on metals. In: Bonzel, H.P., Bornstein, L. (eds.) New Series III/42A1: Physics of Covered Solid Surfaces, pp. 217–258. Springer, Heidelberg (2001)

15. Zangwill, A.: Physics at Surfaces. Cambridge University Press, New York (1988)

Investigation of the Influence of Electro-Impulse Current on Manganiferous Liquid-Alloy

Olena Zhbanova[(✉)], Levan Saitgareev, Igor Skidin,
Nonna Shapovalova, and Genadiy Gubin

State Higher Educational Institution "Kryvyi Rih National University",
11 Vitalii Matusevych St., Kryvyi Rih 50027, Ukraine
zhbanova.olena@gmail.com

Abstract. The article shows that for improving the quality of castings, more and more often, technical solutions are used related to the influence of electric current on the melt during its crystallization. The positive results of such a modification are improved processes of heat and mass transfer and structuring. However, these results only concern the electrical treatment of non-ferrous metals and alloys, as well as some castings. The influence of the electric current limits on the degree of modification of manganese-containing steels during their crystallization in the foundry, as well as on the physical and mechanical properties of the casting requires careful research that would be close to real conditions. The authors compared the macro and microstructures of steel 35GL doped with manganese and modified during crystallization in the foundry form of the electro-impulse current with different current parameters: intensity, duration of impulses, frequency, squinting. It has been established that the modification of an alternating polarity with an electric pulse current of more than $10–3$ s, a frequency of 5–33 Hz, a force of 30–40 A, a vacuum of 5–24, at a voltage in the power line of 180–240 V provides a reduction in structural inhomogeneity (the crystallite of the metal base and manganese carbides are reduced respectively from 280 to 82–85 microns and from 6.7 to 0.3–0.5 microns). These structural changes lead to a significant increase in the basic mechanical properties of cast structural steel 35GL: strength limits – 9%, impact strength – 21%, hardness (HB) – 6%.

Keywords: Electroprocessing · Alloy · Microstructure of steel

1 Introduction

The problem of improving the structure of cast products is the subject of many studies. To improve the quality and properties of casting the electric current impact method is increasingly used to melt during crystallization [1].

The research was mainly carried out on non-ferrous metals and alloys [2–4]. Electricity treatment of these melts contributes to reducing the probability of occurrence of macro and microflaw of the structure and causes directional crystallization in the inter-electron space.

2   Literature Review

Positive results of the application of electroprocessing also exist in the manufacture of pig iron castings [5, 6]. Electricity treatment also has a positive effect on the processes of heat and mass transfer and structure formation.

The study shows the results of the first experiments on the impact of current on steel grade 40L [7]. The modifying effect of constant voltage on alloyed and manganiferoussteel melts was studied by the authors of this study [8].

The urgent task is conducting a complex of studies to analyze the effect of modifying the pulsed current of manganiferousmelts during their crystallization in the casting-form. According to preliminary data, repetitively-pulsed current modification of the melts has some advantages compared to treatment of direct and alternating current. The first one is lower energy consumption while simultaneously reducing the losses on metal heating.

The obtained theoretical and practical results of researches of different authors testify that under the influence of a constant electric current on the alloy an alloying elements move from a body of a casting to its surface. However, the only clear and universally accepted theory of current influence on the melt has not existed yet. Nowadays the question of the influence of current on the mechanisms of phase formation in rare-solid states with different types of conductivity of solid inclusions is not sufficiently unexplored. Particularly many contradictions are expressed regarding the mechanism of mass transfer of elements in the inner layers of the casting under the action of a constant and electrical impulse current.

3   Research Methodology

3.1   Analysis of Current Influence on Crystallite Size

The authors carried out a large volume of experimental studies on the influence of electro-impulse current in the process of crystallization of the casting during the study of steel grade 35GL.

The treatment of the melt with an electro-impulse current was carried out from the beginning of the casting of the metal in the form to the end of the encryption, with the parameters of the current strength varying from 20 to 80 A, squelching from 1 to 24, and also the frequency from 5 to 33 Hz. 4 modifications were selected (Table 1) to conduct research.

Table 1. Routines of electro-impulse current influence.

Current parameters	Routine 1	Routine 2	Routine 3	Routine 4
Current strength	20, 40, 60, 80			
Squelching	2	5	15	24
Frequency	5	10	33	33

All four routines of modification have an effect on the morphology of crystallite of the metal base (Fig. 1) and the crushing of manganese carbides (Fig. 2).
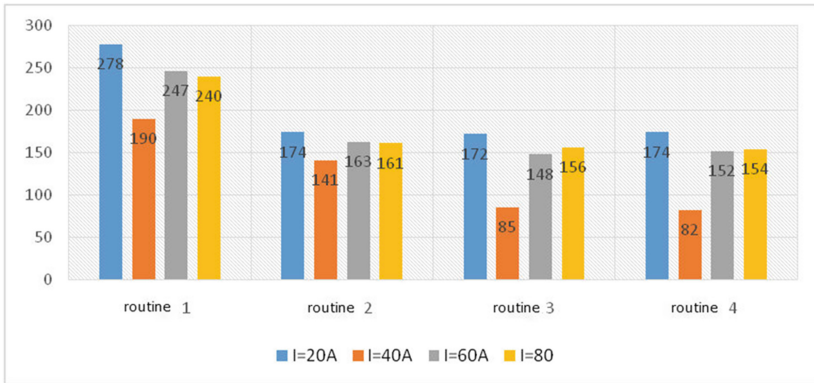
Fig. 1. Influence on the size of the crystallite of the metal base of different routines of electro-impulse processing of manganiferous steel 35GL. A figure caption is always placed below the illustration. Short captions are centered, while long ones are justified. The macro button chooses the correct format automatically.

	I=20A	I=40A	I=60A	I=80A
Routine 1	4,3	3,1	3,5	4,5
Routine 2	2,4	1,4	1,8	2,8
Routine 3	3	0,3	0,9	1,2
Routine 4	4,7	0,5	1,3	1,4
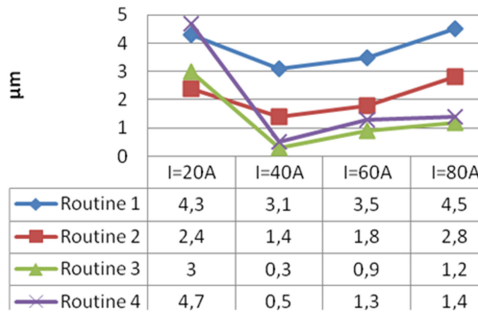
Fig. 2. The magnitude of manganese carbide crystallite, depending on the strength and routines of modification with the electro-impulse current of steel.

When modifying according to the routine 1, the crystallite of the metal base has the largest size, while in routine 2 the crystallite is significantly reduced and is 156 μm, manganese carbides are located along the boundaries of the crystallite of the metal base (Fig. 3). Treatment in routines 3 and 4 reduces the size of the crystallite from 278 μm to 82–85 μm, the distribution of manganese carbides becomes more even. They are mainly located not in the boundaries, but in the center of the crystallite of the metal base.

unmodified   routine 1   routine 2   routine 3   routine 4

x 150
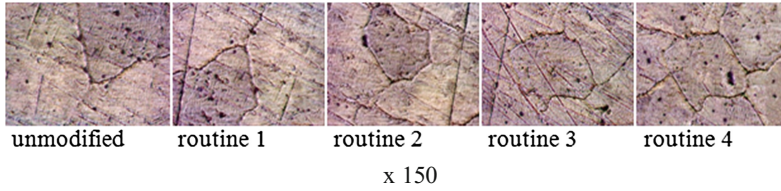
Fig. 3. Comparison of microstructures in different modes of electro-impulse processing.

a   b

x 50
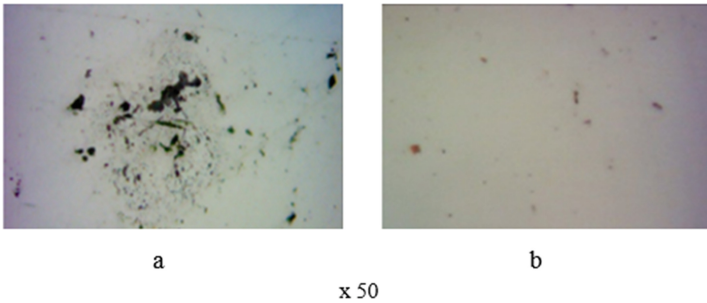
Fig. 4. Nonmetallic: a - an unmodified sample of steel 35GL, and b - a modified sample.

Modification routines 3 and 4 are the most appropriate since the smaller the austenitic crystallite is, the larger the total area is between the crystallites, and consequently the less specific content of harmful impurities is located on the boundaries of the crystallites.

With a current of 40 A (routine 3) in 35GL steel samples the crystallite size of manganese carbides is the smallest: crystallites are 10 times smaller than unmodified specimens and 2 times smaller than when treated under routine 4. Thus, the smallest structure is obtained in samples at modulating the electro-impulse current of variable polarity with the following parameters: duration of impulses - more than 10–3 s, frequency – 5–33 Hz, strength – 30–40 A, squareness – 5–24, with voltage in the power line 180–240 V (routine 3).

3.2   Influence of Electro-Impulse Current on Chemical Discontinuity

On the unfertilized polished section of the unmodified sample accumulations of non-metallic inclusions (exogenous) are revealed.

Disoriented inclusions of FeP, MnP, Fe_3P, Mn_3P up to 10 microns (Fig. 4) are observed in most fields of view of a polished section modified by the selected sample routine and their number is reduced by 2.5 times.

Data on the "migration" of the elements was found (Fig. 5) on the basis of the generalization of the results of the chemical analysis of the contents of the elements near the anode and cathode of 35GL steel samples. As a result indicator, the relative change in Mn concentration between the anode and the cathode (electromigration) is

used. The mechanism of ion division with mutual diffusion in the melts in the presence of electromigration was determined by a change in the set of interconnected parameters: atomic volume, partial diffusion coefficients and effective charges of the components of the melt.

	routine 1	routine 2	routine 3	routine 4
ΔMn	0,9	0,5	0,2	0,4
ΔC	0,6	0,4	0,5	0,7
ΔFe	0,3	0,2	0,2	0,25
ΔSi	0,7	0,7	0,9	0,65
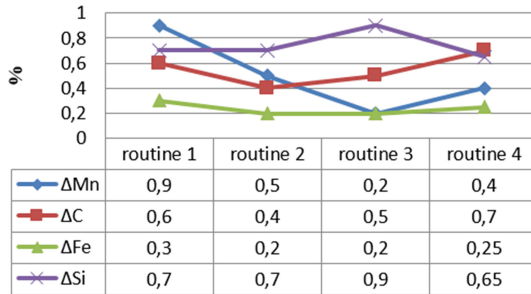
Fig. 5. Relative change in the concentration of the elements between the cathode and the anode in samples of steel 35GL when modified by an electro-impulse current of 40 A.

The electromigration of all chemical elements is rather low, the relative change in their concentration between the cathode and the anode at a current of 40 A does not exceed 0.9%, what is a positive result.

Consequently, the electro-impulse current of an alternating polarity provides a reduction of chemical discontinuity across the intersection of the casting, in contrast to the modification by a direct current [8].

3.3   Influence of Electro-Impulse Modification on Physical Discontinuity

As a result of the electrodes, the structure of the cast manganese-containing alloy has not only less, but physical discontinuity, compared with the basic (not modified current) chemical sample: the content of gases decreases significantly (in 1.4–2.5 times) (Fig. 6, Table 2).

a   b

x 20
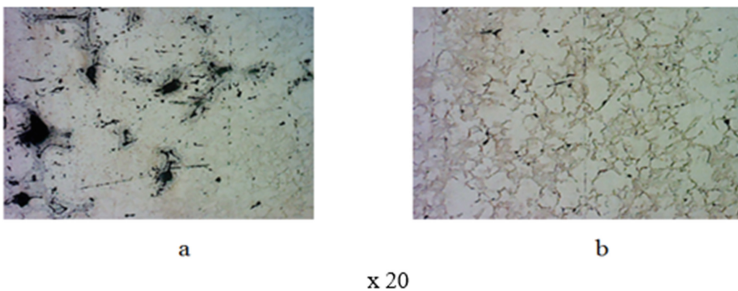
Fig. 6. Macrostructure of cast steel 35GL: a - basic sample; b - a sample modified with current.

Table 2. Changes in porosity in 35GL steel before and after modification with an electro-impulse current of variable polarity with a force of 40 A.

Characteristics of gas bubble	Unmodified samples	Modified samples
Volume ratio of gas bubble, %	6.5	2.7
Distance between gas bubble, μm	306	789
Number of gas bubble per cm^2, pcs	10–15	6–8
Diameter of gas bubble, μm	<0.6	<0.1
Crack length, μm	89–116	12–18

The electro-impulse current passing through liquid steel run away of formation of critical nucleus. This leads to active volumetric crystallization. The dendritical crystallization is discontinued much earlier than the unmodified casting. Metal in the volumetric crystallization zone has a finer structure and a higher density. In the modified casting the internal shrinkage is insignificant.

4   Results

The above mentioned structural changes, which are caused by the electro-impulse modification, provide an opportunity to increase the physical and mechanical properties of castings made of steel alloyed with manganese (Table 3).

Table 3.   Physical and mechanical properties of quenched specimens.

Characteristics of the studied specimens	Limit of fluidity, MPa	Strength, MPa	Percentage extension, %	Contraction ratio, %	Impact hardness, kJ/m^2
Unmodified	230	503	11.00	19	243
Modified	302	540	12.05	21	296

Increase of enduring quality of steel occurs as a result of crushing crystallite of austenite and grain boundary strengthening. Electroprocessing reduces the proportion of manganese carbides in the structure, especially on the boundaries of the crystallite of the metal base. In the crystallite of austenite manganese carbides appear having high microhardness, preventing the formation of pinhole.

5   Conclusions

Reduction of physical discontinuity is contributed by electric discharge machining of a liquid-alloy steel 35GL with a current of variable polarity with an impulse time of more than 10–3 s, a frequency of 5–33 Hz, a strength of 30–40 A, a squareness of 5–24, at a voltage in the power line 180–240 V during crystallization in the casting-form:

- the content of gases and other nonmetallic inclusions is reduced, their distribution becomes more uniform, the crack length in castings is reduced by 7 times, the distance between gas bubble is reduced by 3.3 times, the number of gas bubble per cm^2 – by 1.8 times, and their diameter is 5 times;
- reduction of structural discontinuity: the size of the crystallite of the metal base decreases from 280 to 82–85 microns, and the size of manganese carbides, from 6.7 to 0.3–0.5 microns;
- significant increase in the basic mechanical properties of cast structural steel 35GL: the strength is increased by 9%, the impact hardness – by 21%, the hardness (HB) – by 6%.

References

1. Yakimov, V.I.: The effect of electric current on liquid aluminum alloy. Metall. Mach. Build. **3**, 36–39 (2003)
2. Kishchenko, O.M.: Bull. Krivoy Rog Natl. Univ. **30**, 220–223 (2012)
3. Ivanov, A.V.: Electron. Mater. Process. **5**(47), 89–98 (2011)
4. Timchenko, S.L.: Investigation of crystallization of an alloy under the action of an electric current. Melt **4**, 53–61 (2011)
5. Kolchuryna, Y.U.: The influence of external influences on the microstructure of a crystallizing alloy. Foundry Prod. **8**, 13–15 (2009)
6. Minenko, G.N.: On the energy impact on a metallic melt. Metall. Mach. Build. **3**, 10–12 (2006)
7. Minenko, G.N.: The physical model of the effect of electric current on the crystallization process of an alloy. Metall. Mach. Build. **3**, 48–49 (2009)
8. Zhbanova, O.M.: Influence of a direct current on macrostructure and microstructure of manganese-containing steels. Metallofiz. Noveishie Tekhnol. **39**(11), 1457–1469 (2017)

Forecasting Real Option Price Model by Means of Evolutionary and Genetic Algorithms

Mykyta Zubrii , Anastasia Mazur , and Vitaliy Kobets$^{(\boxtimes)}$

Kherson State University, 27 Universitetska St., Kherson 73000, Ukraine
vkobets@kse.org.ua

Abstract. Research goals and objective: to predict real option prices using evolutionary and genetic algorithms which affect the accuracy of price forecasting. The object of research: real option price model. The subject of research: forecasting evolutionary and genetic algorithms for real option price model. Research methods are genetic algorithm, evolutionary algorithm, statistical technique. Results of the research: in options trading one of the main tasks is to determine the fair price option, using which we can estimate what options are undervalued, and which ones are overvalued at the moment. The decision on the purchase or sale of a particular option is made according to these algorithms. In this paper we apply genetic and evolutionary algorithms in the areas of financial instruments in order to create software intended for analysis and forecast of real price option.

Keywords: Genetic and evolutionary algorithms · Options
Financial instruments · Optimization · Forecasting

1 Introduction

The highly dynamic nonlinear and volatile nature of real option price model has remained a challenge for the investors in financial instruments and financial forecasting. Despite a number of financial and software computational methodologies for real option forecasting available nowadays, there is still a gap between existing and required techniques for an accurate forecasting model. Although a wide range of genetic and evolutionary algorithms have been developed and applied successfully in the field of real option price model forecasting, their performance can vary significantly.

In options trading, one of the main tasks is to determine the fair price option, using which we can estimate what options are undervalued, and which ones are overvalued at the moment. The decision on the purchase or sale of a particular option is made according to these algorithms. In this paper we apply genetic and evolutionary algorithms in the areas of financial instruments, in order to create software intended for analysis and forecast of the options.

The problems that are solved with the help of evolutionary algorithms are the problems of optimization, i.e. the gradual improvement of certain populations (decisions, strategies, etc.) based on the given criteria. Evolutionary algorithms are used in a situation where it is possible to formulate criteria for an acceptable solution, but it is

difficult to offer such a solution. Each task can be optimized due to the improvement of its components.

So, the purpose of the paper is to predict real option prices using evolutionary and genetic algorithms which affect the accuracy of financial instruments price forecasting.

The paper is organized as follows: Sect. 2 describes related works; Sect. 3 explains mechanism of genetic and evolutionary algorithms; Sect. 4 applies genetic and evolutionary algorithms for prediction of optimal solution; Sect. 5 is devoted to real option price model forecasting; the last part concludes the paper.

2 Literature Review

Philip Mirowski, a leading economist, considers the market processes as a form of computations and algorithms. He calls the market processes a computational evolutionary economics or Markomata theory [1].

Genetic and evolutionary algorithms are the forms of Metaheuristic algorithms which solve high-dimensional optimization problems for important applications in business, finance and economics [2]. Genetic algorithms are a relatively modern optimization technique which can he applied to economic and finance problems, including NP-hard. Authors [3] propose a novel method of Mean-Capital Requirement portfolio optimization through nondominated sorting genetic algorithm (NSGA). Improvements of the algorithm are achieved at the expense of reduced cardinality of Pareto-optimal portfolios and thus portfolio diversification. The simulation experiments using a genetic algorithm illustrate that the influence of competitive conditions on investment behavior and attitudes towards risk is significant. Intense competitive pressure generates risk-seeking behavior (accepted excessive risk), creates inefficient investment and undermines the predominance of the most skilled fund managers [4].

Instead of using genetic algorithm to maximize a payoff function of agents, their processes are used to select the best adjusted agents' strategies and produce a new generation of strategies using genetic operators and mutation. If the mutation rate is infinitely small, the crossover rate has no effect on the long-run behavior of a GA. Individual chromosomes contain the information about strategies of agents like life span, life expectancy and causes of death. These individuals' characteristics are used to evaluate an individual success in comparison with alternative strategies [5].

Author [6] investigates possible impact of binary encoding of strategies on the performance of genetic algorithms in agent-based modeling of economic and finance systems. Genetic algorithm can lead to premature convergence if population size is insufficient. At the same time this approach depends crucially on strategies which are encoded in a binary form. Premature convergence can be avoided even during simulation experiments with small populations if actual values in EA instead of binary ones in GA are used. Alternative specification of mutation may also decrease the occurrence of premature convergence in case when actual values of strategies are not sufficient. Experiments for portfolio optimization in the context of high frequency environment with dynamic changes of financial assets are obtained from the London Stock Exchange Rebuilt Order Book database and the FTSE100 index. It is aimed at providing Pareto optimal portfolios and updating them when estimating returns rates or

risks of real option change. The problem is determined in terms of dynamic optimization and solved using evolutionary algorithm [7].

In paper [8] portfolio optimization involves the optimal distribution of limited fund of investors to different available financial instruments planning to achieve a reasonable trade-off between investors' profit and risk by using Markowitz's mean-variance portfolio optimization model. The proposed algorithm, that as a rule uses experimental results, is compared with existing multi-objective evolutionary algorithms to prove its higher effectiveness, such as Non-dominated Sorting Genetic Algorithm (NSGA-II), Strength Pareto Evolutionary Algorithm (SPEA-2), Pareto Envelope-based Selection Algorithm (PESA-II) and Pareto Archived Evolution Strategy (PAES). Particle swarm optimization (PSO) algorithm is a powerful optimization method that relies on exploiting analogues of biology interaction. PSO is a model of individual adaptation in an agent-based computational model, in which agents' strategies must adapt interdependently. In some research fields PSO has advantage over evolutionary algorithms. For example, decreasing volatility in market prices does not require an election operator or additional parameter in contrast to evolutionary algorithm [9].

Bankruptcy prediction is a popular research area in finance, the importance of which lies in probability assessment of investors' bankruptcy. As companies become complex, they develop elaborate plans to conceal their real profit. Evolutionary algorithms have shown to be an excellent tool to minimize the number of irrelevant features and maximize quality measure, such as forecasting accuracy [10]. Application of evolutionary algorithms to credit scoring is used for assessment of the credit solvency of loan applicants too. The simultaneous development of multiobjective evolutionary algorithms and the emergence of complex problem formulation in the finance and economics areas have led to a mutual interest from both research communities.

In some studies, however, there is no clear reason for the use of a binary encoding of agents' strategies. Thus, some authors [11] believe, that since GAs do not have a meaningful economic interpretation, they should be regarded as artifacts. At the same time it is important to employ evolutionary algorithms with a reasonable economic interpretation. From our point of view GAs can forecast trends for different strategies of agents, whereas EAs can predict result of agents' interaction in actual values. Empirical results have shown the superiority of the cooperative algorithms over individuals in terms of forecasting accuracies for real option prices in microeconomic system [12, 13].

3   Methodology

3.1   Mechanism of Genetic and Evolutionary Algorithms

Let us assume that the function is unknown and we only have an algorithm that allows calculating its value at any arbitrarily selected point. This process of building is new and new populations x (k) j will continue with expectation that at a certain point we will find a point in which the function f (x) reaches its extremum. What can confirm that our expectations were met and that we really got a coordinate value for the sought-for extremum at certain iteration? For example, it can be confirmed by the fact that new iterations do not already improve the results, or that from the expert's point of

view the entire area of definition of the function, the extremum of which we are looking for, is thoroughly inspected. These and many other criteria for completing the process of iteration of the evolutionary algorithm obviously have nothing in common with the formal strict mathematical proofs of the results obtained.

In order to obtain the points of a new population based on the analysis of the points of the previous population, we use crossover and mutations. The choice of good points and the rejection of bad ones by the chosen criterion is called selection.

Here is a simple example. Note that if we choose only good points to produce a new population - the genomes of the previous population - there is a high probability of "looping" around the point of the local extremum and lose a population that contains the global extremum. To avoid such a phenomenon, living nature invented a mutation - a random change of a particular genome, which causes variability in an individual, either for the better or for the worse. According to this mechanism of variability, an operation of mutation is used in genetic algorithms, which provides, as a rule, a way out of looping around good genomes. A more complex crossing operation can be interpreted as an attempt to produce a child by mixing the characters of two other persons (parents).

Technically, the crossover operation involves a formation of genomes of several children from selected genomes of parents. According to some rules that resemble cross-pollination (in order to produce children a part of the chromosomes (blocks of genes) is taken from one of the parents, the other part, from another parent), they are united, in a way that their total number, and sometimes the location, is the same as their parents'.

In 1975, J. Holland proved a theorem known as the schemata theorem. In a very rough approximation, schemata theorem asserts that the increase in the number of iterative steps in the genetic algorithm qualitatively increases the probability of approaching the function extremum. The theorem relies on the fact that the genome is a binary sequence in which each gene (binary bit) can vary independently of others as a result of crossover and mutation operations. The theorem argues that from generation to generation selection operations stabilize a group of digits in a genome that remains unchanged from generation to generation.

Let us explain the statement of the theorem in the example. Let us assume that the genome is a sequence of n binary digits and analyze the population of some generation, consisting of M individuals that have the best values of quality functions. Each category of the genome we will match with the frequency of its value. For example, the value of 0 of the genome with the number i is repeated in population k times, the value of 1 of this gene is repeated $M - k$ times. If k $\approx$ M − k, then we will consider such a gene "random" or non-informative, and denote its uncertain value by the symbol *, if k m $\gg$ −M, then we assume that the probability of the genome getting some value is proportional to the frequency of its occurrence in the population. This allows us to construct a "scheme" of the genome, which will reflect the degree of attachment of certain values of genes in the population. Scheme of the genome is shown in Fig. 1.

Significant variables of the scheme can be interpreted as the definition of significant variables of the Boolean function, which distinguish the class of points of space, where the sought-for extremum is located. The acceleration given by the genetic algorithm in comparison with straightforward enumeration, as well as 1012, reaches billions of

0	0	*	*	1	0	1	1	*	0

Fig. 1. "Scheme" of the genome.

times. If N is large, for example, 300, then even a very powerful modern supercomputer will fail to perform a straightforward enumeration. In order to solve problems of the type described, genetic algorithms are successfully used.

3.2   Application of Genetic Algorithms for Prediction of Optimal Solution

The accumulated information as a result of the task execution and the purposeful change of the probability vector components can be used to predict the optimal solution - if at a certain stage of the algorithm the desired value of the components becomes clear, their future value can be fixed and evaluate the produced individual. This can produce a solution that is much better than the current one and will save resources that should be spent on finding such a solution during the regular operation of the algorithm. The forecast algorithm can be implemented in many ways, but it should be quite simple, since it will be used repeatedly during the work of the Probabilistic Genetic Algorithm. Proceeding from the conducted numerical experiments, the following procedure was proposed:

1. For this task, select a specific scheme of the genetic algorithm, determine the prediction step K.
2. Through every K generations with the obtained statistics:

$$\left(\rho_j\right)_i, \mathrm{j} = \overline{1, N_k}, N_k = \mathrm{t} \cdot K, t \in N \tag{1}$$

    Calculate changes in the components of the probability vector:

$$\left(\Delta\rho_j\right)_i = \left(\rho_j\right)_i - \left(\rho_j\right)_{i=1}. \tag{2}$$

3. Give weight to each generation according to its number:

$$\sigma_i = \frac{i}{\sum_{i=1}^{N_k} n}. \tag{3}$$

4. Calculate the predicted vector:

$$\left(\rho_j\right) = \sum_{i=1}^{N_k} \sigma_i \cdot \left(\Delta\rho_j\right)_i \tag{4}$$

5. Compute:

$$x_j^{opt} = \begin{cases} 1, \rho_j \geq 0, \\ 0, \rho_j < 0. \end{cases} \tag{5}$$

The Probabilistic Genetic Algorithm with the proposed prediction algorithm has been tested on a number of test tasks, and showed a higher efficiency than the PGA without a forecast. This prediction algorithm can also be used for standard GA.

In steps 2 and 5 (selection of parents and formation of a new population) of both algorithms, the choice of an individual from a population depends on its degree of sustainability i.e., the more suitable the individual is, the more likely it is to be selected. The degree of sustainability is calculated through the sustainability function. The suitability calculations by means of the objective function value are quite simple in case of unconditional optimization, but we require special approaches when we have constraints in place. There is a large number of such approaches, but ones mentioned below are the ones that were selected after numerous experiments on test tasks.

Let us look at the problem of conditional optimization:

$$\begin{cases} f(x) \rightarrow extr, \\ g_j(x) \leq 0, j = \overline{1, r}, \\ h_j(x) = 0, j = \overline{r+1, m} \end{cases} \tag{6}$$

In general, the sustainability or fitness of an individual x_I is calculated with the formula:

$$\text{Fitness}(x_i) = f(x_i) + \delta \cdot \lambda(t) \cdot \sum_{j=1}^{m} f_j^{\beta}(x_i), \tag{7}$$

where t is the current generation number, $\delta = 1$, if the minimization problem is solved, $\delta = -1$, if the maximization problem is solved, – is a penalty for violation of the j limit for the i-th individual, $\lambda(t)$, β-parameters.

In particular, using the method of dynamic penalties:

$$\text{Fitness}(x_i) = f(x_i) + \delta \cdot (C \cdot t)^{\alpha} \cdot \sum_{j=1}^{m} f_j^{\beta}(x_i),$$
$$f_j(x) = \begin{cases} max\{0, g_j(x)\}, j = \overline{1, r}, \\ |h_j(x)|, j = \overline{r+1, m} \end{cases} \tag{8}$$

Parameters α, β are often accepted in practice as 2. Parameter C for each task is selected individually (if it fails, then most often it is $C = 0.5$). This method was chosen as most effective in the tasks considered after testing and comparison with other methods.

In some problems of conditional optimization, it is quite difficult to get even a feasible solution. In majority of cases it happens due to a large number of conditions in a task and/or an admissible area is sufficiently small in relation to the entire search area. This statement is also valid in case of stochastic algorithms applied in complex optimization tasks. In order to solve this problem there is a method of behavioral memory.

1. Generation of the initial population.
2. The counter of the accounted conditions j = 1.

3. The current population is the starting point for the next phase of evolution, during which all points that do not correspond to at least one of the j − 1 accounted conditions are discarded. Stop criterion is satisfaction of all j − 1 restrictions of the given part of the population.
4. j = j + 1; repeat the last two steps until j equals the number m +1.

For this algorithm, the order of adding the considered constraints is very important. In many cases, this method works better than penalty techniques, since often small value of the penalty in comparison with the value of the objective function conceals the admissible area among the peaks of the "penalized" objective function.

On the other hand, as experiments have shown, this method is good at swift localization of a population within the admissible area if a sequence of conditions account is successfully selected.

4   Results

Options are financial derivatives with non-linear value. Option is the right to buy/sell certain financial instruments, stocks or currency at a specified price on a specified date. In order to obtain this right, the buyer (the holder) pays a certain premium to the seller, i.e. the market price of the option, at the time of contract conclusion. Thus, the right itself becomes a commodity in this operation.

The basis of options is the basic asset (BA). There are 2 types of options: CALL options, the cost of which increases with the rise in the price of basic asset, and PUT options, the cost of which increases with lowering the price of basic asset.

Figure 2 shows the position of buyer and seller correspondingly in the case of optional CALL. You can see that the seller's gain/loss of the option is "symmetric" to the loss/profit of the buyer of the option: where the buyer has income, the seller is at loss, and vice versa. The maximum profit is 50, the amount of damage is unlimited. If the stock price of a company exceeds 950, then the seller is at loss.
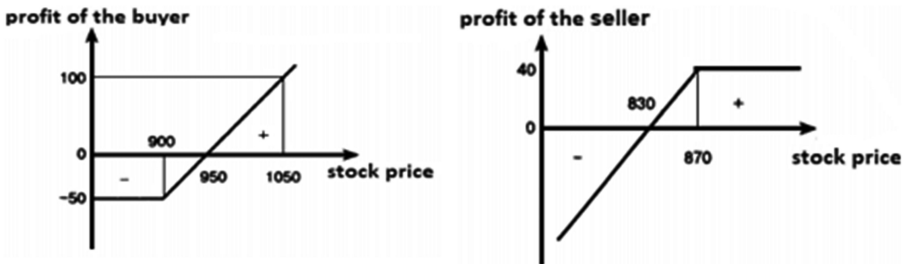
Fig. 2. Profit and loss of buyer and seller in CALL options.

The pattern "profit-share price" for the buyer of the PUT option in this situation changes dramatically (Fig. 3). If the market price of the stock is less than $870 - 40 = 830$, the buyer of the option gains profit. For example, at a stock price of 810, the profit will be $870 - (810 + 40) = 20$. At the price of 830, the profit is zero, since $870 - (830 + 40) = 0$, and at a price exceeding 830 there is a loss, the maximum value of which is 40. The profit/loss of the seller of such option can be seen in Fig. 4.
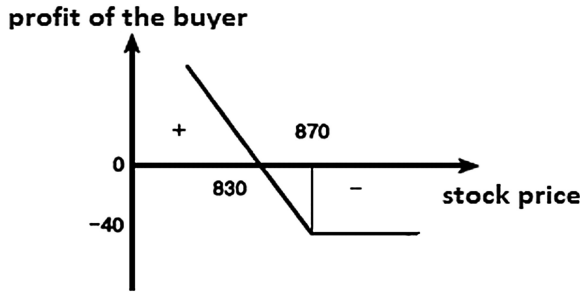
Fig. 3. Profit and loss of buyer in PUT options.
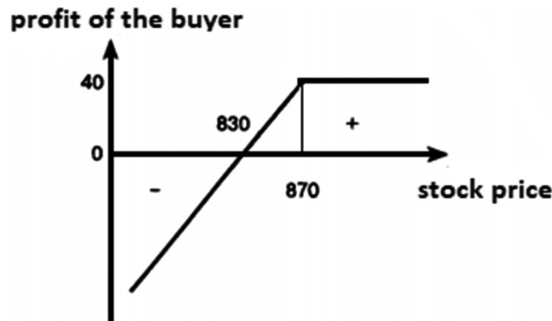
Fig. 4. Profit and loss of seller in PUT options.

For example: an importer who possesses Swiss francs and has to pay some amount in US dollars, buys an option to purchase dollars at a rate of 1 USD = 2 CHF and pays a premium of 0.03 CHF for 1 USD. At the time of value date, the following options determined by the dollar price range are possible for completing the transaction:

1. The dollar falls to 1.9 CHF. In this case, the buyer does not use the option and buys dollars in the market. His results:

   - the difference between the option rate and the spot rate: 2.0 CHF − 1.9 CHF = 0.1 CHF;
   - premium: 0.03 CHF;
   - imputed profit from an option in the amount of 1 USD: 0.07 CHF.

2. The dollar rate rises to 2.15 CHF. The buyer of the option uses his right to purchase currency at the strike price. His result: real profit in the amount of 2.15 − (2.00 + 0.03) = 0.12 CHF for 1 USD;
3. The rate is 2 CHF. Option buyer can use it, or refuse it and buy currency in the market. In both cases, his losses are 2.03 CHF (losses in relation to the market rate equal the premium level: 0.03 CHF);
4. The rate exceeds the strike price, but this excess is less than the premium. If the buyer still exercises the option, the losses are also less than the premium. Let us assume that the rate is 2.02 CHF, then the loss will be 2.03 CHF − 2.02 CHF = 0.01 CHF per 1 USD.

Acquisition of the right to purchase an option is feasible when an increase in its price is anticipated. The right to sell, obviously, is bought with the expectation of lowering the price. In order to calculate the theoretical option price the Black-Scholes formula is used.

We introduce the following notation to record it: C - option price; S - underlying price; E – strike price; $e^{-\partial t}$ - present value factor for the term t at the continuous rate ∂; T – the time to maturity; ∂ - continuous interest rate (growth force) adopted for discounting; N (d_1) and N (d_2) - normal distribution functions; σ^2 - volatility (return is measured as a continuous interest rate);

Black-Scholes Formula:

$$C = S \times N(d_1) - E \times e^{-\partial t} \times N(d_2). \tag{9}$$

In every options of BA market, there are appropriate futures. So for the US dollar options, BA is the US dollar futures (Si). Options, as well as futures, expect life. The date when the option expires is called the expiration date. At this moment, the final calculation on the options that the trader has in the basket is performed.

Despite the complexity of these instruments, they have properties that are not available in other financial instruments. One of these features is that they allow trading of the same instrument (the underlying asset) at the same time, but for different expected prices (strikes), which makes it possible to build complex combinations of options of different types (CALL/PUT) and different prices (strikes).

Conditionally, trade options can be divided into 2 types: static and dynamic. In *static* trading the trader makes some assumptions about the price of BA in the future, according to which he builds a strategy. For example, if the trader believes that the price will remain in some range, he can sell the CALL and PUT options and profit on the premium from sale. However, if the price of BA is closer to the edge of such position, then it must be "regulated" in order not to have loss. In *dynamic* trade the stake is placed not on of the price of BA, but rather on the price variation, i.e. volatility. With high volatility, prices for options can vary significantly, which makes the profit possible.

When trading options, one of the main tasks is to determine the fair option price, using which it is possible to understand what options are undervalued by the market, and which ones are overvalued at the moment. On this basis, decisions are made to buy or sell a particular option. With the use of the Genetic Algorithm you can create a

program that will automate the process of choosing options for sale and purchase. Such a program, unlike trading robots (or Mechanical Trading Systems - MTS), does not perform transactions, it can only give advice to a trader who has control over the decision whether to carry out an operation or not.

The main function of the software mentioned is the search for a combination of purchased/sold options, in which the "positive" position area will be maximized at a given length of one gene, that is, when the maximum number of options for a single strike price is limited.

The result based on the input data and its analysis will be obtained in the form of a current position plot, as well as the ability to perform a genetic search of the optimal position and to correct the result manually if necessary.

5   Conclusions

In options trading we proposed to find real option price using genetic and evolutionary algorithms, using which it is possible to understand what options are undervalued by the market, and which ones are overvalued at the moment. On this basis we can make a decision about purchase or sale of a particular CALL or PUT option. In this paper we applied genetic and evolutionary algorithms in the areas of financial instruments, in order to create software intended for analysis and forecast of real price option. Within this framework we plan to study the additional criteria that affect prices of cryptocurrencies and are able to explain price variation using machine learning forecasting algorithms.

References

1. Lash, S., Dragos, B.: An interview with Philip Mirowski. Theory Cult. Soc. **33**(6), 123–140 (2016)
2. Mandavi, S., Shiri, M.E., Rahnamayan, S.: Metaheuristics in large-scale global continues optimization: a survey. Inf. Sci. **295**, 407–428 (2015)
3. Drenovak, M., Rankovic, V., Ivanovic, M.: Market risk management in a post-Basel II regulatory environment. Eur. J. Oper. Res. **257**(3), 1030–1044 (2017)
4. Witte, B.-C.: Fund managers-why the best might be the worst: on the evolutionary vigor of risk-seeking behavior. Economics **6**(201224), 31–49 (2012)
5. Schimit, P.H.T.: Evolutionary aspects of spatial prisoner's dilemma in a population modeled by continuous probabilistic cellular automata and genetic algorithm. Appl. Math. Comput. **290**, 178–188 (2016)
6. Maschek, M.K.: Economic modeling using evolutionary algorithms: the influence of mutation on the premature convergence effect. Comput. Econ. **47**(2), 297–319 (2016)
7. Filipiak, P., Lipinski, P.: Dynamic portfolio optimization in ultra-high frequency environment. In: 20th European Conference on the Applications of Evolutionary Computation (EvoApplications), pp. 34–50. LNCS, Amsterdam (2017)
8. Lwin, K., Qu, R., Kendall, G.: A learning-guided multi-objective evolutionary algorithm for constrained portfolio optimization. Appl. Soft Comput. **24**, 757–772 (2014)

9. Maschek, M.K.: Particle swarm optimization in agent-based economic simulations of the cournot market model. Intell. Syst. Account. Finance Manag. **22**(2), 133–152 (2015)

10. Gaspar-Cunha, A., et al.: Self-adaptive MOEA feature selection for classification of bankruptcy prediction data. Sci. World J. **314728**, 31–49 (2014)

11. Waltman, L., et al.: Economic modeling using evolutionary algorithms: the effect of a binary encoding of strategies. J. Evol. Econ. **21**(5), 737–756 (2011)

12. Nayak, S.C., Misra, B.B., Behera, H.S.: Cooperative optimization for efficient financial time series forecasting. In: 8th International Conference on Computing for Sustainable Global Development, pp. 124–129. IEEE, New Delhi (2014)

13. Kobets, V., Weissblut, A.: Nonlinear dynamic model of a microeconomic system with different reciprocity and expectations types of firms: stability and bifurcations. In: CEUR Workshop Proceedings, vol. 1614, pp. 502–517 (2016)

Mechanical Engineering

Experimental Study of the Power Characteristics Influence on the Hydraulic Efficiency

Pavlo Andrenko[1]([✉]) [iD], Iryna Grechka[1] [iD], Sergey Khovanskyy[2] [iD], and Maksym Svynarenko[3] [iD]

[1] National Technical University "Kharkiv Polytechnic Institute", 2 Kyrpychova St., Kharkiv 61002, Ukraine
andrenko1947@gmail.com
[2] Sumy State University, 2 Rymskogo-Korsakova St., Sumy 40007, Ukraine
[3] Kharkiv National University of Civil Engineering and Architecture, 40 Sumska St., Kharkiv 61002, Ukraine

Abstract. The hydraulic unit of rotation control system is improved. It is based on the use of a hydraulic distributor with a hydraulic vibration circuit and the injection of a hydraulic feedback for pressure. Due to this, the efficiency during winding operations increases. A model of the experimental installation for hydraulic unit of rotation for winding is developed and made. It provides a constant wire tension force. Hence, the hydraulic stiffness and reliability are increased. The choice of control and measuring equipment and experimental data processing methods are substantiated. The influence of the working parameters for hydraulic unit for winding of the electric motors wound on its efficiency is investigated. The results of a two-factor active experiment are presented. It was conducted using a rotatable plan of the second order. The response function is obtained and its adequacy is proved. The graphic dependencies of the hydraulic motor shaft moment from the wire tension force at different values of its shaft rotational speed are built. The optimum values of the wire tension force and the hydromotor shaft rotation frequency are defined. The hydromotor linear mathematical model is developed. The operating time for the hydraulic unit of rotation is set.

Keywords: Hydromotor · Two-factor experiment · Wire tension force
Rotational speed · Operating time · Optimization

1 Introduction

Rapid development of the machine-building industry requires the improvement of electrical and electronic automation means. The elements made by winding (electric motors, electromagnets, relays, inductors, transformers, etc.) are the essential components of these tools. Part of winding operations in the technological processes of these tools production reaches 15–20% of their total labor intensity, and for some products is up to 50%. Output characteristics, and hence, the technical level of these products, depend on the wire tension force fluctuations in the winding operations. The change in

the electric motor winding tension force affects the wire wound density. It determines the coefficient of the electric motor rotor or stator slot filling. The power and efficiency factors depend on these factors.

Hydraulic units have a small volume and mass per unit of established power, the possibility of smooth gradual adjustment of speed and effort, small inertia of executive mechanisms, simple and reliable overload protection; they allow to construct both simple and complex systems, to receive variables in time modes of operation, automatically with the given regularity it is easy to organize internal feedback. Thus the hydraulic units are widely used in winding machines to perform work and auxiliary functions.

2   Literature Review

Electric motors are the main consumers of electricity in industrial and commercial facilities. Their demand is almost a half of the total electricity used in the UK and nearly two-thirds of industrial electricity consumption [1]. According to article [2], mobile equipment consumes about two thirds of the electricity. Improving the electric motor efficiency will lead to significant energy savings. The importance of solving this problem is given in [3].

The influence of mixed stator windings on the formation of rotational moment is observed in article [4]. A production method, using industrial robots for automation of the cable winding operation for the stators electric machines, is presented in [5]. The operating characteristics of the winding machine depend on its accuracy, namely: the geometric shape, mechanisms and devices that providing wound shaping, kinematic chains, as well as wire tension, speed and filing. Machines for winding ordinary wounds, both single-row and multi-row, are the most widely used among winding machines. The process and technologies of fiber winding for fiber-reinforced composites are observed in article [6]. However, the majority of analyzed sources does not consider the insurance of the constant wire tension during the winding operations.

The hydraulic unit for adjusting the rotation speed of the hydraulic motor with the LS system [7] has a low sensitivity of the locking and regulating flow and pressure elements to the hydraulic control signals for the presence of significant rest frictional forces, obliteration, hydrodynamic and regulating springs forces. Hysteresis of the flow and pressure regulators is about 4%.

An electrohydraulic rotation unit with perturbation compensation has been developed in [8] to regulate the rotational speed. This hydropower unit provides high accuracy of maintaining the speed rotation. However, its drawbacks are the use of two types of energy: electric and hydraulic (reducing reliability) and an electronic control system (increasing the cost and maintenance). Thus, existing designs of hydraulic units of rotation in winding machines for electric motors do not provide high-voltage tension forces. Their circuit designs and layouts need improvement. Results of experimental studies for hydraulic units of rotation using other types of hydro motors are not found.

The article purpose is to increase the efficiency of the hydraulic unit of the machine for winding electric motors wounds. The following tasks were formulated to reach this goal: development and manufacture of the physical model of the hydraulic unit of the

machine for winding electric motors wounds; planning and running an experiment, receiving a response function; seting the optimum values for the wire tension force and the hydraulic motor shaft rotation speed; making up the mathematical model of the hydraulic unit of rotation hydromotor and determinate its operational time.

3   Research Methodology

Methods of mathematical and physical modeling, the theory of automatic control, planning of the experiment were used to solve the problem. The results reliability is determined by using of proven research methods, compliance of accepted assumptions with the tasks nature, adequacy of mathematical models, the meaningful choice of control and measuring equipment and methods for processing experimental data, mathematical statistics and the small samples theory.

4   Results

A principally new scheme of the hydraulic unit for electric motors winding machine (Fig. 1) was developed. It provides the constant wire tension force and rotation frequency on the hydromotor output shaft by using a hydraulic distributor with an advanced hydraulic vibration circuit and the implementation of a hydraulic pressure feedback [9].

In the course of experimental studies, the wire tension force was determined by changing the distance between the sheaves 10 and 16 and the loading device 12, changing the arm l_1 (the distance between the tension force center and the load $G = 5$ kg). The pressure in the hydraulic unit was regulated by safety valve 4 and controlled by a pressure gauge 6.

Control throttling valves 7 set the pressure at the hydromotor inlet and outlet 8. Recording were provided using pressure transducers and a multichannel measuring kit 14 based on the laptop. The flow was measured using a measuring tank 17 and a stopwatch. The displacement change of the lever 13 end (the sudden change in the wire tension force set by the load G) was controlled by a motion sensor. The motion sensor signal was sent to the multi-channel measuring kit 14. Rotational frequency n (s^{-1}) was found through the known dependence using the hydraulic motor 8 flow

$$n = \frac{q}{V_0} \qquad (1)$$

where q – actual hydraulic motor flow, m^3/s; V_0 – hydraulic motor displacement, m^3.

Mineral oil IGP–30 ($\rho = 885$ kg/m^3, $v_t = 3\ 10^{-5}$ m^2/s) was used as a working fluid. Its temperature was controlled by a thermometer 18.

The wire tension force $F_t = 50$ N and the shaft rotational frequency $n = 2.62$ s^{-1} were taken as zero points. Variability interval for the wire tension force was 30 N, and for the rotational speed – 1.36 s^{-1}.
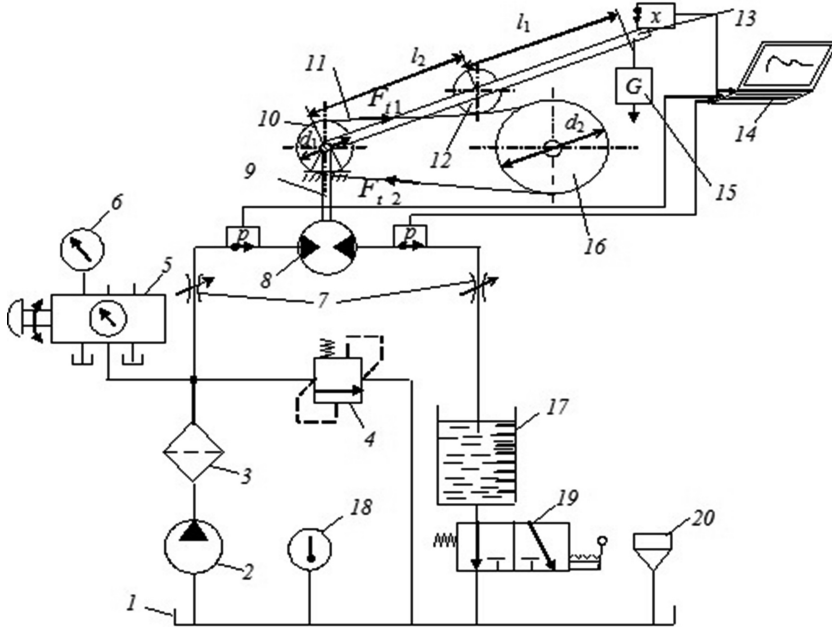
Fig. 1. Scheme of the experimental installation for determining of the hydraulic motor working fluid pressure change depending on the wire tension force change: 1 – tank; 2 – volume pump G15-21M; 3 – filter 8-80-1K; 4 – hydraulic pressure valve PG54-32M; 5 – pressure gauge switch; 6 – pressure gauge; 7 – control throttling valve PG77-12; 8 – hydromotor G15-21N; 9 – hydromotor shaft; 10, 16 – sheaves; 11 – wire; 12 – loading device; 13 – lever; 14 – multi-channel measuring kit, based on the laptop; 15 – cargo; 17 – measuring tank; 18 – thermometer; 19 – hydro distributor; 20 – pouring neck.

The actual value of wire tension was determined using calibration with a dynamometer and the dependence based on the formulas for the belt transmission calculation

$$F_t(t) = \frac{N(t)}{v} \left(\frac{0.85 C_p C_l}{C_\alpha C_i} - 0.5 \right) \tag{2}$$

where $N(t)$ – power at the hydromotor shaft, kW; C_p, C_l, C_α, C_i – coefficients: load mode, belt length, grip-hold angle, gear ratios; v – wire winding speed, m/s, which is determined from the formula

$$v = \pi d_1 n$$

where n – the hydromotor shaft rotation frequency, s^{-1}; d_1 – sheave diameter, m.

Standard methods and devices were used to measure the pressure, flow, temperature and displacement. They had to ensure high accuracy of the measurements. For pressure: pressure gauges (type MO, measurement error according to a passport – 0.05%)

and aneroid barometer [type M67, range of measurements (0.61–0.79) mm Hg, measurement error $\pm 8 \cdot 10^{-4}$ mm Hg]; for temperature – thermometers (measurement error less than 1 °C); for the working fluid flow – a measuring tank (scale division – $8 \cdot 10^{-6}$ m³/mm) and a stopwatch.

Pressure transducers PD/20/2 (measurement error $\pm$ 0.5%, pass frequency according to a passport is 1200 Hz) were used to determine the output hydro unit characteristics. An inductive sensor of a solenoid type was used to measure displacements. It had a linear dependence between the coil inductance and displacement. Converters, pressure and displacements sensors had been pre-calibrated.

Planning of the experiment was made to reduce the number of experiments. A two-factor active experiment were conducted. A rotatable plan of second order was used. It allowed to predict the response function with the same dispersion at equal distances from the plan center.

It is known that the output power and operating torque on the shaft of a volumetric hydraulic motor, and hence the wire tension force, essentially depend on the difference in pressure on it, the rotational speed of the shaft and leaks. Using of hydraulic feedback allows compensating the leaks. Thus two factors were chosen: wire tension force and hydromotor shaft rotation frequency.

A central compositional rotatable planning of the second order was conducted for a two-factor experiment (Table 1). Parallel experiments were supposed to evaluate their reestablishment and to determine the statistical estimates. Student's criterion excluded rough measurements.

Table 1. Central composite rotatable planning of the second order for a two-factor experiment.

Experiment	x_0	x_1	x_2	x_1^2	x_2^2	$x_1 x_2$	y
Planning type 2^2	+1	−1	−1	+1	+1	−1	5.2
	+1	+1	−1	+1	+1	+1	5.1
	+1	−1	+1	+1	+1	+1	5.5
	+1	+1	+1	+1	+1	−1	5.3
Star points	+1	−1.414	0	2	0	0	5.5
	+1	+1.414	0	2	0	0	5.1
	+1	0	−1.414	0	2	0	5.2
	+1	0	+1.414	0	2	0	5.2
Zero points	+1	0	0	0	0	0	5.7
	+1	0	0	0	0	0	5.4
	+1	0	0	0	0	0	5.2
	+1	0	0	0	0	0	5.4
	+1	0	0	0	0	0	5.3

Changes in pressure at the hydromotor inlet and outlet and wire tension force were recorded at each experimental point. Transient processes oscillograms were received (Figs. 2 and 3).

Fig. 2. Transient processes oscillogram for the working fluid pressure at the hydraulic motor inlet and outlet at the hydraulic unit of the machine for winding the electric motors wounds in the sudden change of tension forces $F_t = 20$ N and $n = 2.28$ s^{-1}: 1 – hydraulic motor inlet pressure; 2 – hydraulic motor outlet pressure; 3 – lever 13 displacement change.
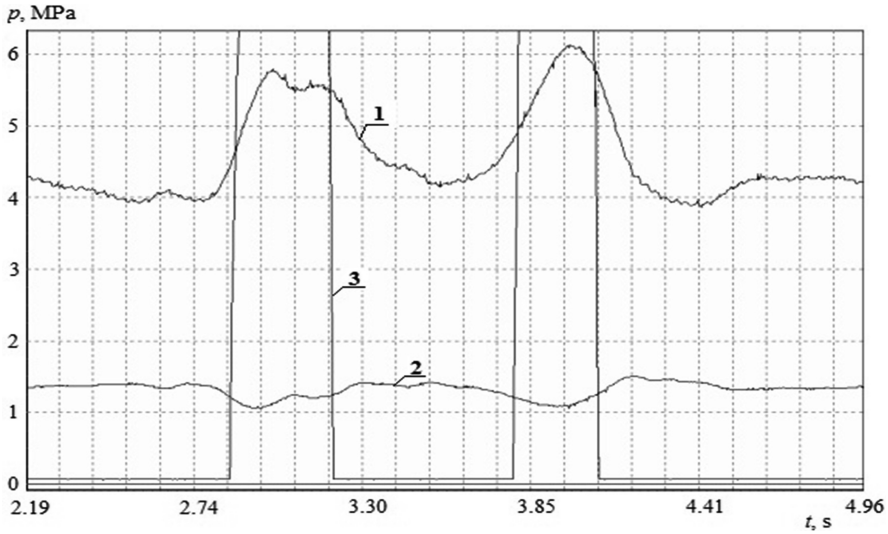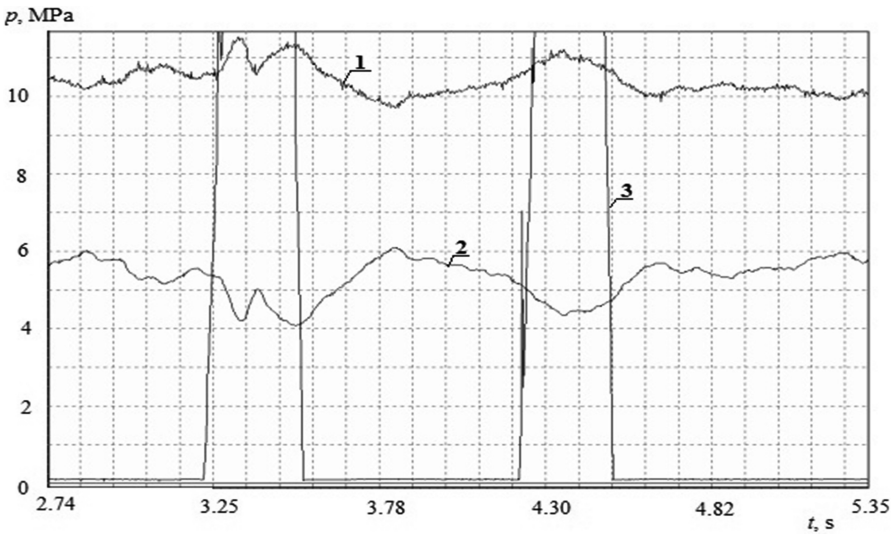

Fig. 3. Transient processes oscillogram for the working fluid pressure at the hydraulic motor inlet and outlet at the hydraulic unit of the machine for winding the electric motors wounds in the sudden change of tension forces $F_t = 80$ N and $n = 2.48$ s^{-1}: 1 – hydraulic motor inlet pressure; 2 – hydraulic motor outlet pressure; 3 – lever 13 displacement change.

The last column of the Table 1 was completed with experiment results, y was replaced by its value – the hydraulic motor differential pressure Δp. The response functions were determined by the polynomial [10]

$$y = b_0 + \sum_{i=1}^{k} b_i x_i + \sum_{i<1} b_{ij} x_i x_j + \sum_{i=1}^{k} b_{ii} x_i^2 \tag{3}$$

where b_0, b_i, b_{ij}, b_{ii} – regression equation coefficients; x_i, x_j – variable factors.

A response function was received as a result of the experimental data processing

$$y = 5.4 + 0.108\, x_1 + 0.0625\, x_2 + 0.025\, x_1 x_2 - 0.044\, x_1^2 - 0.094\, x_2^2 \tag{4}$$

The formula (4) was used to obtain the response function values – the hydraulic unit of rotation running quality through the natural factors

$$\Delta p = 5.0706 - 0.0004\, F_t + 0.3089\, n + 0.0038\, F_t n - 0.0005\, F_t^2 + 0.0507\, n^2 \tag{5}$$

where Δp – the hydraulic motor shaft differential pressure, MPa.

The hydraulic motor shaft moment was determined from the formula

$$M = \frac{\Delta p V_0}{2\pi} \tag{6}$$
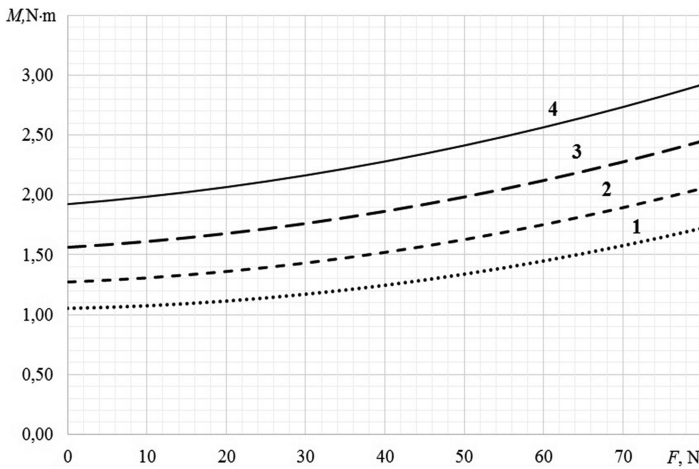
Fig. 4. Graphs for dependence of the hydraulic motor shaft moment M from the wire tension force F_t at different values of the rotational frequency n: $1 - n = 2\ \text{s}^{-1}$; $2 - n = 4\ \text{s}^{-1}$; $3 - n = 6\ \text{s}^{-1}$; $4 - n = 8\ \text{s}^{-1}$.

Dependency graphs $M = f(F_t)$ were plotted at different values of n according to the experimental results (Fig. 4).

The calculation of measurement errors was carried out using statistical methods. The error of the experiment was determined from the experiment in the center of the plan, using the method shown in [10]. A dispersion was calculated. It characterizes the scattering of the experimental results.

$$D_0^2 = \frac{D_0}{n_0 - 1} \tag{7}$$

where $D_0 = \sum_{u=1}^{n_0} (y_{0u} - \bar{y}_0)^2$; n_0 – number of experiments in the plan center; y_{0u}, $\bar{y}_0$ – respectively, the result of the u-th experiment and the average experiments result in the plan center.

The total residual sum of the plan squares

$$D_{tot} = \sum_{u=1}^{n} (y_u - y_{uc})^2 \tag{8}$$

where y_u – experimental result for the u-th experiment; y_{uc} – result of calculation for the u-th experiment.

The dispersion of adequacy was calculated. It is characterized by sum $D_{ad} = D_{tot} - D_0$ and degree of freedom $f_{ad} = n - \frac{(k+2)(k+1)}{2} - (n_0 - 1)$, $f_{ad} = 3$. Thus, the adequacy dispersion $D_{ad}^2 = D_{ad}/f_{ad}$.

Cochrane criterion tested the process reproduction. It was established that the condition for the process reproduction works. Compassion testing of experimental results and data obtained using a mathematical model was carried out according to Fisher's criterion. The Fisher's criterion was calculated from formula $F = D_{ad}^2/D_0^2$ and compared with the table. Fisher's criterion for our case is $F = 3.26$ (Table 2). Criterion selected according to the tables $F = 4.3468$ [10]. Hence, the model is adequate.

Table 2. Calculation of measurement errors.

Criterion	D_0^2	D_0	D_{tot}	D_{ad}	f_{ad}	D_{ad}^2	F
Value	0.035	0.14	0.38	0.34	3	0.11	3.26

The relative average quadratic error during experimental research was: for pressure – 2.5%, for loading device lever displacement – 3.3%, for liquid flow – 1.5%. Moreover, it can be said that the measured values are in the confidence interval with the probability of 0.95. It means that the maximum deviation from their average measured value is less than: for pressure – 4.6%; for displacement – 6.3%; for flow – 5.8%.

Surface extremum $Y = f(x_1, x_2)$ can be found using the obtained equation for the response function (4):

$$\begin{cases} \frac{\partial y}{\partial x_1} = 0; \\ \frac{\partial y}{\partial x_2} = 0, \end{cases}$$

which gives the optimal value: $x_{1opt} = 1.22$ and $x_{2opt} = 0.05$. It corresponds with $F_r = 19.72$ N; $n = 4.18$ s^{-1}.

Response time is an important characteristic of the hydraulic unit. Parameters of G15–21H and the tracking hydraulic distributor are used to determine it. Pipelines were considered to be absolutely rigid. Wave processes were neglected because of the large pipeline diameter. Temperature and density of the working fluid are constant and correspond the catalog. Moment of load resistance $M_R = const$. Equation for the hydromotor shaft moments

$$(J_M + J_R)\frac{d\omega}{dt} + \frac{k_\mu V_0}{2\pi}\omega = \frac{\Delta p V_0}{2\pi}(1 - k_p) - M_R \qquad (9)$$

where J_M and J_R – hydromotor moment of inertia and load. They were determined from the known formulas: $J_M = 16 \cdot 10^{-6}$ kg $\cdot$ m^2 and $J_R = 8 \cdot 10^{-6}$ kg $\cdot$ m^2; ω – hydromotor shaft frequency of rotation; k_μ and k_p – proportionality constant, which are determined from the equation

$$\eta_{mech} = 1 - k_p - k_\mu \frac{2\pi n}{\Delta p} \qquad (10)$$

where η_{mech} – mechanical efficiency factor for the hydromotor, which is determined from the catalog.

Equation (9) is a differential equation of the first order. Coefficients for this equation are constant values at constant Δp. Initial conditions: $t = 0$ i $\omega = 0$. The operating time τ was found from the Eq. (8) solved from ω.

$$\tau = \frac{2\pi(J_M + J_R)}{k_\mu V_0} \qquad (11)$$

When $\eta_{mech} = 0.85$ from formula (10) $k_\mu = 3.47$ (s $\cdot$ m)/kg and $k_p = 0.145$. Hence, the operating time is $\tau = 0.04$ s.

According to the transient processes oscillograms for the working fluid pressure at the hydraulic motor inlet and outlet at the hydraulic unit of the machine for winding the electric motors wounds in the sudden change of tension forces (Fig. 2) the operating time is $\tau = 0.045$ s.

5 Conclusions

The developed experimental installation model of the hydraulic unit of rotation for winding allows to establish the effect of the structural and operating parameters to its initial characteristics. It provides a constant wire tension force, which significantly

influences the groove-filling coefficient. The electric motor power and efficiency depend on it.

The response function value (operating characteristic of the hydraulic unit) was found as a result of the active two-factor experiment. It adequacy was proved by Fisher's criterion. The optimum values of the hydromotor operating parameters were found by its optimization. They were: wire tension force F_t = 19.72 N and hydraulic motor shaft rotational frequency n = 4.18 s^{-1}.

The operational time τ = 0.045 s was determined according to the developed linear mathematical model of the investigated hydraulic unit of rotation. When comparing the operating time determined experimentally with the calculation results, the error does not exceed 10%. Thus, the mathematical model can be used to study the hydro unit dynamic characteristics.

The obtained results will allow to establish the rational structural and operating parameters for the developed hydraulic unit of rotation.

References

1. Cirstea, M., Dinu, A., Khor, J., Mc Cormick, M.: Electric motors and power systems. In: Neuraland Fuzzy Logic Control of Drive sand Power Systems, pp. 18–55 (2002)
2. Europump and Hydraulic Institute: Chapter 6—Motors. In: Variable Speed Pumping, pp. 47–58 (2005)
3. Bonig, J., Bickel, B., Spahr, M., Fischer, C., Franke, J.: Simulation of orthocyclic windings using the linear winding technique. In: 2015 5th International Electric Drives Production Conference (EDPC) (2015)
4. Muteba, M., Nicolae, D.V.: Influence of mixed winding arrangements on torque ripples of five-phase induction machines. Electr. Power Syst. Res. **151**, 154–165 (2017)
5. Hultman, E., Leijon, M.: Utilizing cable winding and industrial robots to facilitate the manufacturing of electric machines. Robot. Comput. Integr. Manuf. **29**(1), 246–256 (2013)
6. Gonzalez Henriquez, R., Mertiny, P.: Filament winding applications. In: Reference Module in Materials Science and Materials Engineering, Comprehensive Composite Materials II, vol. 3, pp. 556–577 (2017)
7. Avrunin, G., Gritsay, I., Kirichenko, I.: Fluid Power Drive and Hydropneumoautomatics: Tutorial. KhNAHU, Kharkiv (2008)
8. M. REXROTH Enterprise: Proportional technique and pilot valves technique. Hydraulic training course, vol. 2. RSU 00303/10.86 (2009)
9. Andrenko, P., Grechka, I., Bilokin, I., Stetsenko, Yu.: Hydraulic unit of machine for winding of the electric motors wound. Patent No. 45554, Ukraine (2009)
10. Rogoviy, A.: Features of operating modes of vortex chamber superchargers. Bull. Kharkiv Natl. Automob. Highw. Univ. **75**, 120–128 (2016)

Increase of Efficiency of Turbine Setting Based on Study of Internal Flows

German Bondarenko [ID], Serhiy Vanyeyev [ID], Vadim Baga$^{(\boxtimes)}$ [ID],
Tetiana Rodymchenko [ID], and Iryna Bashlak [ID]

Sumy State University, 2 Rymskogo-Korsakova St., Sumy 40007, Ukraine
{s.vaneev,v.baga}@kttf.sumdu.edu.ua

Abstract. Turbo efficiency largely depends on the internal overflows. Labyrinth seals are used as internal ones. To determine their flow characteristics a simplified calculation model of the opening with a sharp edge is used. It is supplemented with the experimental coefficients obtained under conditions which are significantly different from as-build. These ratios do not take into account the ring gap shape, flow vortexes on the inlet, eccentricity, shaft rotation, scale factor. When designing, simplification data do not allow using a labyrinth seal with a minimum leak value. The aim of this work is to upgrade knowledge about the workflow in the labyrinth seals using the modern methods of computational fluid dynamics (CFD), which are going to increase the efficiency of the internal labyrinth seals. At the same time, the numerical and experimental studies of the labyrinth seal element were carried. The research tasks are to establish the correctness of CFD methods application for studying the flows in the essentially narrow slits and obtaining the visualizations of the workflow under various geometric and regime parameters, to give practical recommendations on the design of such seals. Velocity fluctuations in the labyrinth seal are identified. They result from the uneven distribution of pressure along its length. The seal design with a variable pitch that allows reducing the leakage to 30% is proposed. Shaft rotation causes leakage reduction to 20%.

Keywords: Labyrinth seal · Physical and numerical study
Performance characteristics · Defining parameters

1 Introduction

Labyrinth seals are applied as interstage ones in the flow part of turbo-machines. These seals do not have alternatives for simplicity, cheapness and reliability. However, leaks and therefore energy losses in such seals are sufficient enough. Their values are extremely high especially in the stages of the flow channels with the small cross sections.

Despite the simplicity of the labyrinth seals device, the way it operates is still poorly understood. Nobody knows for sure the impact of the ring gap, eccentricity, rotation, scale factor on the amount of the leakage through the seal.

2   Literature Review

Up till now, the developers use rough leak calculations according to the formula of Stodola [1, 2], with the experimental coefficients obtained for various structural performances of the seals [3]. On the basis of the flow from the hole with a sharp edge model the Stodola formula was built [4]. A. Schegljaev suggested considering the labyrinth seal as a number of sequentially fixed holes with a sharp edge [5]. Influence of the crests edge shape is counted by the correction index obtained by Trojanovskiy [6]. In the works of Orlik [7] the effect of the crest edge shape and the form of intermediate cells are shown.

When designing new compressors the calculation accuracy for the leakage through a seal is unacceptably low and sometimes exceeds 30%. Experimental coefficients are obtained with the idealized physical models, usually flat, excluding the shaft rotation, eccentricity and effects of gases properties. Traditionally used seal model consists of a series of sequentially installed holes with sharp edges, an analogue which has very little in common with the real seals: instead of a circular slit there is an opening of the same cross-section; the sharp edges occur only on one surface of the slits (crests), and the other surface is formed by a smooth shaft.

Working conditions are significantly different: flowing out from the holes implies the unlimited space on the outlet, and in the seal each slit is followed by a limited chamber, where the kinetic energy isn't completely damped. Well-known experimental data were obtained on the simplified models, which do not fully describe the physical processes.

In the labyrinth seals calculation the equal distribution of pressure difference between the chambers is expected, the gas density is considered to be mid-range, the effect of changes in the compressibility, rotation, eccentricity of the gap is not taken into account.

The aim of this work is to upgrade knowledge concerning the work process in the labyrinth seals using the modern methods of computational fluid dynamics (CFD), which allow increasing the efficiency of the internal labyrinth seals.

3   Research Methods

The labyrinth seal for centrifugal compressors with full-scale dimensions is taken as the base investigated seal.

While investigating, the outlet pressure was taken as equal to atmospheric, the operating environment was air. The seal testing was performed on the test bench that ensured the following conditions for its work: engine speed from 0 to 7000 rpm; sealed pressure ratio from 1.05 to 1.25; shaft diameters 80, 240 mm; radial clearances 0.225, 0.37 mm; eccentricity from 0 to 1 [8].

The test-bed consists of a stage controlled drive and a test head, a shield of water gauges, a compressor with a receiver, an air filter, valves and piping mounted on the node frame of the stage controlled drive.

Determination of the actual leakage value through the seal was performed on the test bench by measuring with RG counters. Temperature was measured by means of a

mercury-thermometer, pressure in the test head- by water manometers, barometric pressure – by a barometer-aneroid. Measurement errors do not exceed 5%.

As the test bench doesn't allow obtaining the flow visualization in the seal flow section, the advantages of the numerical value simulation flow visualization were used. It was done in the axis symmetrical setting; the flow model was a fully compressible fluid, the turbulence model k-e.

Considering the small size of the gap, the computational grid is selected so that the gap $s = 0.225$ mm could fit about 10 estimated square cells. The number of estimated cells for the sector $\alpha = 3^0$ is $N = 150000$. Smaller values of the estimated cells result in the inaccurate leak value (Fig. 1).
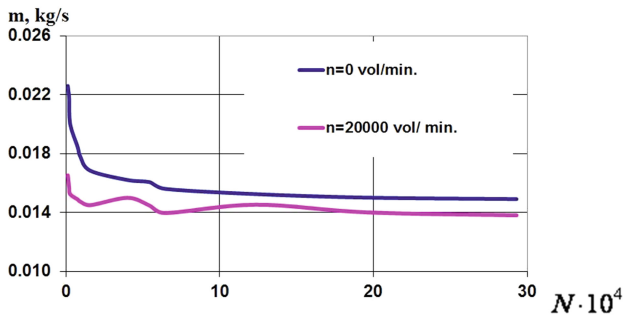
Fig. 1. Effect of the estimated cells on the leak value through the seal.

Discrepancies between the experimental and calculated values of the leakage amount through the seal do not exceed 5% (Fig. 2).
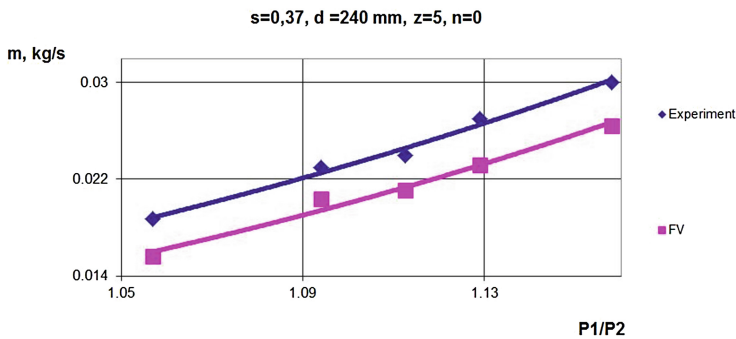
Fig. 2. Comparison of the calculated and experimental values of the leakage.

4   Results

Application of the hole model with a sharp edge requires more careful study. To confirm this hypothesis a series of coherent models has been investigated: an opening with a sharp edge, a flat gap, an annular gap with unlimited and limited jet release, a single crest (with or without rotation), two crests. In all cases, there are significant differences in visualizations of flowing out from hole with a sharp edge model (Fig. 3). Stodola formula should be considered an artificial structure rather than analogy, and the consumption coefficients obtained using this formula are imputed and require clarification [9].
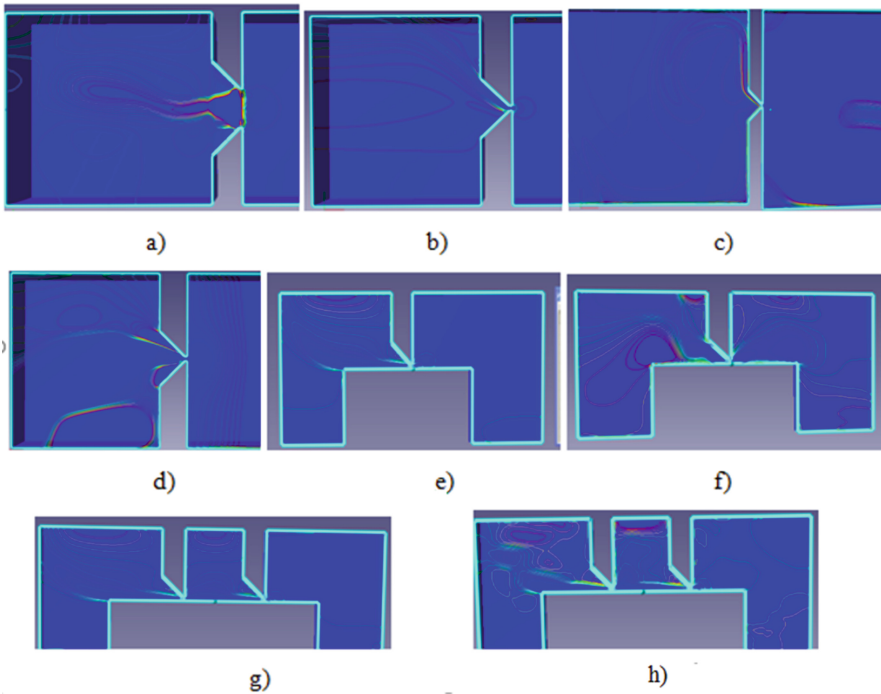
Fig. 3. Isolines for different models of the seals ($p1/p2 = 1.21$): (a) a hole with a sharp edge ($D = 2$ mm); (b) a flat gap ($l = 1.6$ mm); (c) an annular slit with unlimited jet release; (d) an annular slit with limited jet release; (e) a slit which is formed by a single crest and a smooth shaft ($n = 0$); (f) a slit formed by a single crest and a smooth shaft ($n = 15000$ rpm); (g) two crests with a smooth shaft ($n = 0$); (h) two crests with a smooth shaft ($n = 15000$ rpm).

Here are some results of the pilot study given as a lustration (Table 1). Experiments based on pressure distribution measurement by the length of the seal under different variations of pressure have shown that with the increasing frequency of rotation, there is a tendency to reduction of the coefficients $\bar{\mu}$ and μ, that is not taken into account in the existing computing techniques.

Table 1. Imputation rates of the investigated seals consumption μ ($D = 240$ mm, $z = 5$, $s = 0.225$ mm).

№ experiment	$p1/p2$	n, rpm	$s = 0.225$ mm		$s = 0.37$ mm	
			$\bar{\mu}$	μ	$\bar{\mu}$	μ
1	1.06	0	1.093	1.11	1.418	1.311
2		2910	1.087	1.09	1.369	1.271
3		4336	1.032	1.03	1.346	1.225
4		6693	0.924	0.92	1.277	1.053
5	1.12	0	1.083	1.05	1.449	1.338
6		2910	1.150	1.11	1.454	1.332
7		4336	1.133	1.103	1.398	1.264
8		6693	1.060	1.07	1.304	1.177
9	1.21	0	1.378	1.135	–	–
10		2910	1.197	1.1	–	–
11		4336	1.0895	1.06	–	–
12		6693	0.953	0.92	–	–

When comparing the average consumption coefficient of the seal $\bar{\mu}$, with its integral value μ it turned out that there were discrepancies, which increase with the increasing frequency n and the value of the radial clearance s. In some cases the divergence is up to more than 10%. This data demonstrates the impact of additional factors which have been ignored until now. It should be noted that the usual computing techniques for all the proven options should take a constant value μ, while the results of the experiments indicate its change ranging from 0.92 to 1.21 for s = 0.225 mm and from 1.05 to 1.39 for s = 0.37 mm which is equivalent to the difference in the amount of the leakage, about 24%.

The local consumption coefficients μ_i (calculated for each crest) are unevenly distributed along the length of the seal Fig. 4.
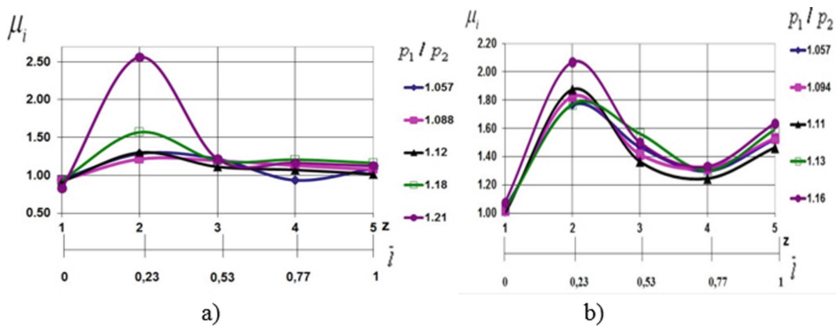

Fig. 4. Distribution of the consumption coefficients μ_i along the length of the seal where $n = 0$ ($D = 240$ mm, $z = 5$): (a) $s = 0.225$ mm; (b) $s = 0.37$ mm.

There has been a dramatic increase in the coefficient μ_i of the slit under the second crest, it is especially sustainable when the gap is large. For the slits under the rest of the crests the coefficients retain approximately the same values.

The shaft speed effect on the sealing characteristics is worth paying attention to. Figure 5 gives the experimental dependencies of the shaft speed effect on the value of the flow seal coefficients under each crest of a base sealing.
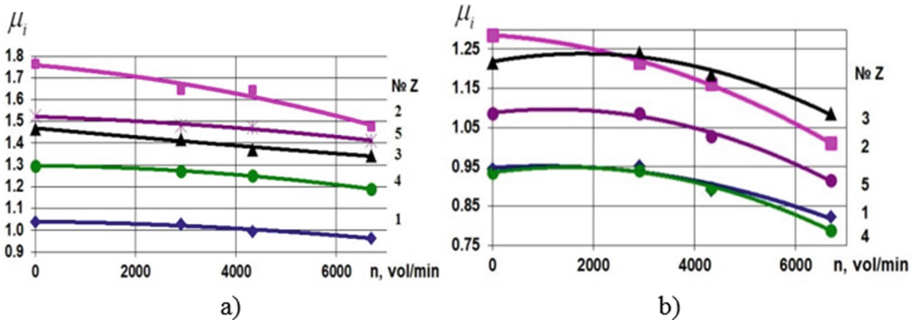
Fig. 5. The effect of the shaft rotation on the local flow seal coefficients μ_i ($D = 240$ mm, $z = 5$, $p1/p2 = 1.06$): (a) $s = 0.225$ mm; (b) $s = 0.37$ mm. Figures indicate the numbers of the seal crests.

These results confirm the existence and the rotation frequency impact on the coefficient value μ obtained previously for the integral values μ (Table 2). The shaft rotation effect in the explored limits is estimated by the value of reduction in the leakage as (10–20)%.

Table 2. Comparison of the coefficients μ and $\bar{\mu}$ ($n = 0$ rpm).

z	1	2	4	5	7	9	11	15
$\bar{\mu}$	0.76	0.755	1.031	0.878	0.928	0.917	0.942	0.961
μ	0.78	0.866	0.908	0.886	0.865	0.833	0.842	0.841

With the view of a more detailed study of the uneven coefficient μ_i changes, the research of the seals with different number of crests was conducted: for $D = 80$ mm, $t = 4$ mm, $h = 5$ mm. According to accepted assumptions [1, 2] the pressure drop along the length of the sealing is implied to be stepped and steady. To verify this situation the computing study of the seals with $z = 15$ crests was carried out, some study results are shown in Fig. 8. It should be noted that the pressure drop is extremely uneven along the length of the seal. A significant redistribution of differences between the crests is noticeable when the shaft rotates.

On the whole the charts (see Fig. 6) confirm the data Tables 1 and 2: the reduction of Δp_i on the crest corresponds to the increase of the coefficient μ_i on the same crest and vice versa. Experimentally obtained pressure distribution in the seal with $z = 5$ and
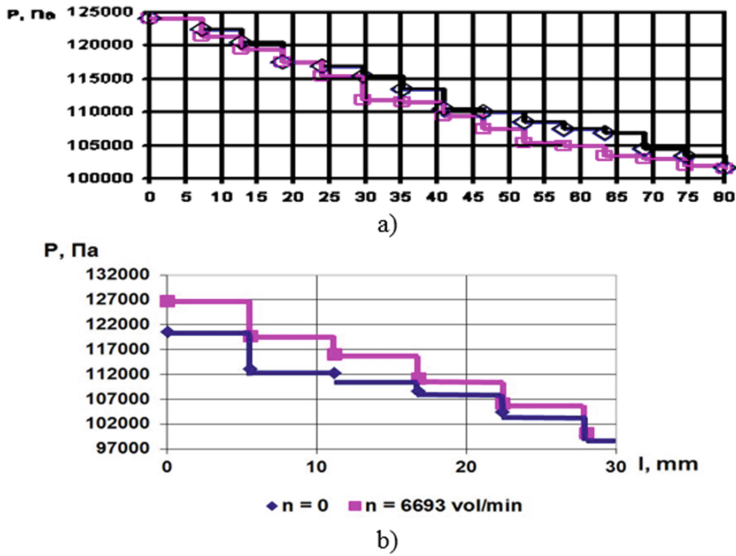
Fig. 6. Distribution of pressure along the seals: (a) calculation ($D = 80$ mm, $s = 0.225$ mm, $z = = 15$, $p1/p2 = 1.25$); (b) experiment ($D = 240$ mm, $s = 0.225$ mm, $z = 5$, $p1/p2 = 1.21$).

$D = 240$ mm is given in Fig. 6, *b* for comparison. Similar conclusions follow from this experiment.

The accepted postulate of even distribution of pressure differences between the crests is confirmed by neither experiments nor calculations (Fig. 6). In the seals with 5 crests there occur the specific zones of intensive torispherical vortices which alternate with the zones of smooth movement (Fig. 7) [10, 11].
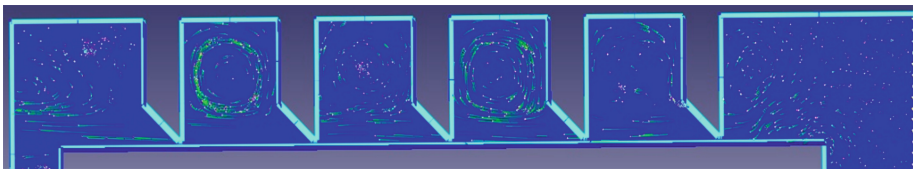
Fig. 7. The trajectory of particles movement in the sealing ($D = 240$ mm, $s = 0.225$ mm, $n = 6700$ rpm).

Wavelike change of the μ_i coefficient along the length of the sealing occurs due to a burst of the local values μ_i spaced at every 2–3 crests. An increase of μ_i occurs up to 2.5 times, and the absolute values exceed 1, that is difficult to explain in terms of physics. So this suggests an uneven distribution of load on the crests of the labyrinth seals. In Fig. 8 we observe the occurrence of four coefficient μ_i values jumps and position of the peaks is shifted to the outlet at the shaft rotation. This is caused by uneven vortex-formation along the length of the seal (Fig. 9).
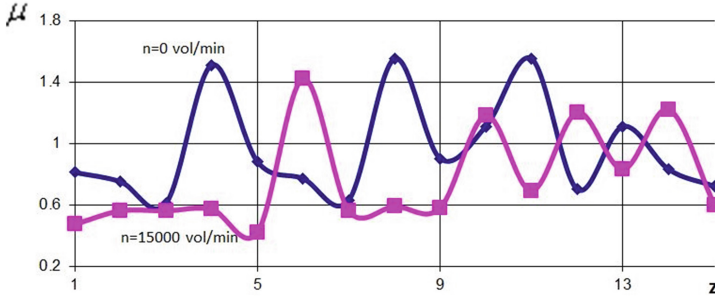
Fig. 8. Change of the imputed flow seal coefficients along the length of the seals ($D = 80$ mm, $s = 0.225$ mm, $z = 15$, $p1/p2 = 1.25$).
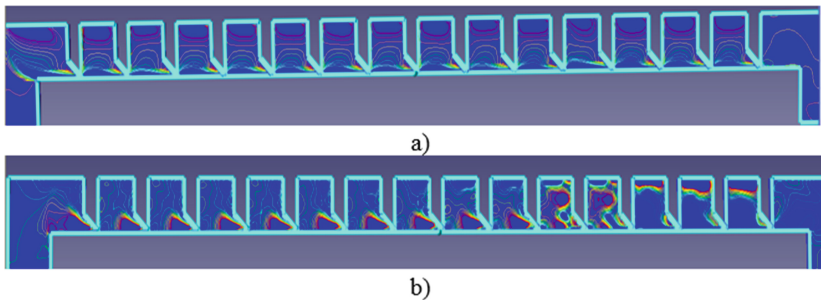
Fig. 9. The velocity contours in seal $z = 15$: (a) $n = 0$; (b) $n = 15000$ rpm.

Discrepancies between the values of coefficients $\bar{\mu}$ and μ increase with the number z increasing. We note that the integrated and average values of the imputed flow seal coefficients are less than one, despite the occurrence of the peak values, significantly exceeding one.

In the seal with 15 crests (Figs. 7, 8) with the shaft motionless, the flow structure in all the chambers is the same, but when the shaft rotates, there are a fluctuations-simultaneous existence of zones without turbulence (the first three chambers), transitional (the next two chambers) and zones of stable vortex structure (the remaining chambers). µi coefficients peaks correspond to those crests, before which the flow is being rebuilt.

With the change in diameter of the shaft and in the presence of rotation the vortex zones structure in the chambers alter. It refers to the effect of a large scale factor and shaft rotation on the labyrinth seal characteristics.

As seen from the above, as gas flows through the seal, it is necessary to increase the volumes of the chambers geometrical parameters because of gas expansion that apparently should facilitate a more complete flow velocity suppression resulting from under the crest. The construction of the labyrinth seals with a variable pitch is proposed (Figs. 10, 11).
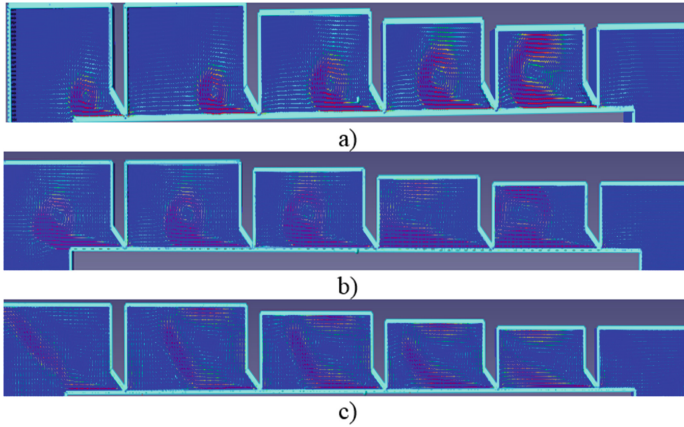
Fig. 10. Velocity vectors: (a) $D = 240$ mm, $n = 0$ rpm; (b) $D = 80$ mm, $n = 0$ rpm; (c) $D = 80$ mm, $n = 6700$ rpm.
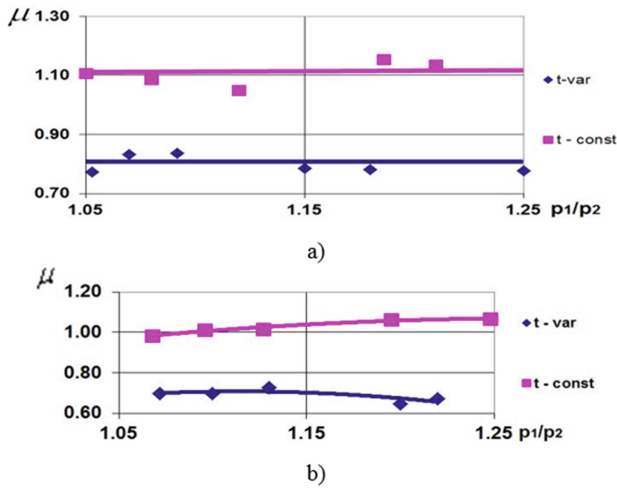
Fig. 11. The experimental study of the developed seal construction (version 7): (a) D = 240 mm, s = 0.225 mm; (b) D = 80 mm, s = 0.225 mm.

For $D = 240$ mm the flow seal coefficient with a variable pitch is lower in comparison with the source by nearly 30%, and for $D = 80$ mm – by 35%.

5 Conclusions

According to the results of the numerous and experimental investigations of various structural performances of the labyrinth seals, new data were obtained:

1. Shaft rotation leads to a decrease in the leakage through the labyrinth seal. The higher the speed is (up to 20%) the greater decrease in the leakage is.
2. The structure of a flow in the labyrinth seals of various types is not uniform, it depends on the scheme and geometric sizes.
3. Increase of the chamber volumes downstream the flow helps to reduce the leakage up to 30%.

References

1. Stodola, A.: Dampf- und Gasturbinen. Springer, Berlin (1924)
2. The Basic Data for Centrifugal Compressor. Dresser Machinery, Ltd. (1975)
3. Shlyahtenko, S: Efficiency of different labyrinth seals forms. Aircr. Constr. Rev. Newsl. **2**(3) (1947)
4. Deitch, M.: Technical Gas Dynamics, 2nd edn. Energy, Moscow (1974)
5. Scheglyaev, A.: Steam Turbines, 4th edn. Energy, Moscow (1967)
6. Troyanovsky, B.: Steam consumption through labyrinth seal steam turbines. News **1**(1), 19–24 (1950)
7. Orlik, V.: Flow characteristics of seals with a single and a group throttle. Heavy Mach. **9**, 4–7 (1993)
8. Bondarenko, G., Baga, V., Bashlak, I.: Flow simulation in a labyrinth seal. Appl. Mech. Mater. **630**(2044), 234–239 (2014)
9. Cangioli, F., Pennacchi, P., Vannini, G., Chatterton, S., Dang, P.V.: On the thermodynamic process in the bulk-flow model for the estimation of the dynamic coefficients of labyrinth seals. J. Eng. Gas Turbines Power **140**(3), 032502 (2018)
10. Cangioli, F., Chatterton, S., Pennacchi, P., Nettis, L., Ciuchicchi, L.: Thermo-elasto bulk-flow model for labyrinth seals in steam turbines. Tribol. Int. **119**, 359–371 (2018)
11. Duenas Dobrowolski, J., Gawliński, M., Paszkowski, M., Westerberg, L., Höglund, E.: Experimental study of lubricating grease flow inside the gap of a labyrinth seal using microparticle image velocimetry. Tribol. Trans. **61**(1), 31–40 (2018)

Effect of Abnormal Operation of Turbine Generator on the Resource of Steam Turbine Shafting

Anatoliy Bovsunovsky[(✉)]

National University of Food Technologies of Ukraine,
68 Volodymyrska St., Kyiv 01601, Ukraine
apbovsunovsky@gmail.com

Abstract. The results of evaluation of fatigue damage caused by the intense vibrations of steam turbine shafting at abnormal operation of turbine generator are presented. The abnormal operation of turbine generator may be caused by the sudden short-circuit in turbine generator or by the connection of turbine generator to the electric network. The evaluation of fatigue damage is based on the 3D finite element model of turbine shafting of steam turbine K-215-130. The fatigue properties of rotor steel were experimentally determined and used in the model. The fatigue damage of steam turbine shafting was evaluated for different scenarios of connection of turbine generator to the electric network and in account for experimentally determined damping properties of turbine shafting in operation.

Keywords: Turbine shafting · Fatigue damage · Torsional vibrations
Coarse synchronization

1 Introduction

The ensuring of safe operation of heavily-loaded structural elements of steam turbines is an important problem in modern power engineering. Its significance increases in Ukraine every year with the exhaustion of service life of power generating equipment of thermal and nuclear stations [1].

The strength and reliability of steam turbine elements in operation is extremely dependent on the dynamic conditions of loading at critical rotation speed of the turbine shaft (transverse vibrations) and at abnormal regimes of turbine generator operation (torsional vibrations). The abnormal operation of turbine generator may be caused by the sudden short-circuit in turbine generator, by the connection of turbine generator to the electric network or by the interaction of turbine generator with the power network [2–5].

2 Literature Review

The turbine generator short-circuit can occur several times over the time of turbine operation. Under some operating conditions turbine shafting can fail suddenly as a result of short-circuit [4]. However, the long-term fatigue damage accumulation in

turbine shafting is hardly probable in this case. At the same time, the analysis of crack propagation in turbine shafting has shown [3, 6] that cracks propagated during several years. For this reason, a catastrophic failure of the medium pressure rotor of the 225 MW steam turbine occurred at the Gallatin power plant (USA) in 1974 [3].

The accumulation of fatigue damage in turbine shafting is rather caused by multiple start-ups, which are typical for steam turbine units operating in a flexible manner. The predetermined number of such start-ups during the operation time is 2000, but in some cases it can be prolonged to 2500 and more. At least one connection of turbine generator to electric network occurs at each start-up. At this because of the difference of the phase shift angle between the vector of electromotive force of turbine generator and the vector of electric network voltage the short-term reactive electromagnetic shaft's torque arises, resulting in the turbine shafting torsional vibrations of various intensity. At this, the short-term reactive electromagnetic shaft's torque arises, resulting in the turbine shafting torsional vibrations of various intensity, because of the difference of the phase shift angle between the vector of electromotive force of turbine generator and the vector of electric network voltage. In some cases the intensity of torsional vibrations may be so high that they cause the fatigue damage of the shafting.

If turbine generator is connected to the power network with coarse synchronization, the amplitudes of torsional vibrations of shafting can considerably exceed those under the condition of sudden short-circuit [7, 8]. The vibrational process occurring at each start-up can continue from several tens to several thousand cycles with the maximum stresses exceeding the fatigue limit of rotor steel. It results in cyclic damage of the material that is gradually accumulated during the period of turbine operation.

The amplitudes of shafting vibrations are strongly dependent on the level of damping in the system. Damping governs the rate of decay of free vibrations of shafting after the short-term action of the electromagnetic torque and in such a way affects the number of damaging cycles of vibrations. Experimental study on turbine shafting vibrations [9] have made it possible to determine modal damping the for several mode shapes of shafting.

The aim of the research was to evaluate possible level of fatigue damage of the turbine K-215-130 shafting due to vibrations occurring at connection of turbine generator to the power network with account of real level of damping in the mechanical system. This work is the development of study [10], where the level of damping was assumed to be in a wide range because the its real level was unknown.

3   Research Methodology

The steam turbine K-215-130 is a complex mechanical system consisting of high, middle and low-pressure rotors (HPR, MPR and LPR, respectively) and turbine generator. The study on forced vibrations of such mechanical system was performed numerically with a 3-D finite element model (Fig. 1), which was the mesh of 50000 eight-node elements. The detailed description of the model and the numerical methods used for the solution of the problem can be found in ref. [5].

The loading of shafting is presented in Fig. 1, namely the torques acting in HPR, MPR and LPR, and the electromagnetic torque (Mel) which arises at the connection of
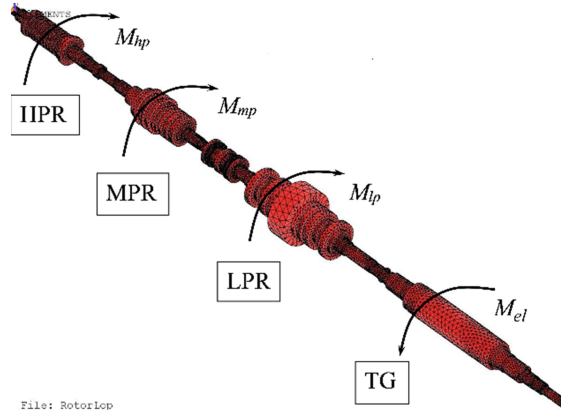
Fig. 1. 3D finite element model of the K-215-130 shafting.

turbine generator (TG) to electrical network. Total operating shafting torque is determined as follows

$$M_{oper} = M_{hp} + M_{mp} + M_{lp}. \tag{1}$$

where M_{hp}, M_{mp}, M_{lp} are the torques acting in high, middle and low pressure rotors, respectively.

The electromagnetic torque is strongly dependent on the phase shift angle θ between the vector of electromotive force of the turbine generator and the vector of electrical network voltage. The equation for calculation of time dependence of the relative value of electromagnetic torque is as follows [10]

$$M_{el}/M_{oper} = a_0 + [a_1 \sin(314t) + a_2 \sin(628t)] \cdot e^{-a_3 t} \tag{2}$$

For instance, at connection of the turbine generator TGV-200 to the electric network of voltage 110 kV with the angle $\theta = 30°$ coefficients in Eq. (2) were determined to be a0 = 2.04; a1 = 6.85; a2 = 0.4; a3 = 1.7. The same coefficients were determined for different values of angle θ as well. In such a way, the electromagnetic torque may exceed the operating torque up to 9 times.

4   Results

The level of damping of mechanical system was estimated by the logarithmic decrement of vibration δ. Tests on damping of turbine shafting [9] determined damping of torsional vibration for several mode shapes as a function of generator's power loading (Fig. 2).

The turbine generator in the process of connection to the electric network operates at full power. That is why in calculations of the first four modes of vibrations there
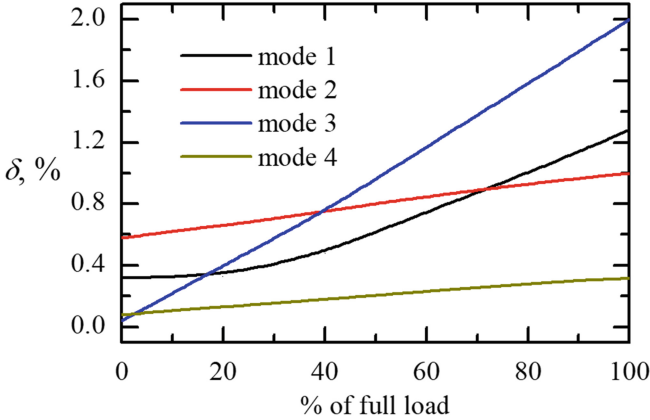
Fig. 2. Logarithmic decrement of turbine shafting torsional vibrations versus the power of generator loading at different mode shapes [9].

were used the levels of damping related to the full power of the turbine generator, that is δ1 = 1.28%; δ2 = 1.0%; δ3 = 2.0%; δ4 = 0.32%.

The connection of turbine generator to the electrical network can be successful and unsuccessful. In case of successful connection the turbine generator is not disconnected from the electrical network and the electromagnetic torque gradually vanishes. However, if in the process of connection the intense vibrations of the shafting arise, the turbine generator is immediately disconnected from the electrical network. As a result, the electromagnetic torque disappeared. This is the case of unsuccessful connection. The attempt of connection is repeated for as long as it would be a successful one.

Thus, at successful connection of turbine generator torsional vibrations of the shafting are maintained at relatively high level for almost the entire duration of the electromagnetic torque action (Fig. 3). The most intense vibrations are excited in the case of the angle θ = 30°, as far as the electromagnetic torque has maximal value.

The most intense stresses are observed in the area between LPR and TG. The fatigue limit of R2MA rotor steel at normal temperature is τ − 1 = 230 MPa (it is shown in Fig. 3 by a horizontal line). At certain conditions the stress level may exceed the fatigue limit of rotor steel. This is the main reason of fatigue damage of shafting. The higher the angle θ, the more intense is the fatigue damage of shafting.

In case of unsuccessful connection of turbine generator to the electrical network the intensity of torsional vibrations of shafting depends not only on the angle θ, but also on the duration of the electromagnetic torque tel. The duration of the electromagnetic torque strongly affects free vibrations of the shafting.

The fatigue damage of turbine shaft in a result of torsional vibrations was evaluated based on the hypothesis of Palmgren-Miner [11, 12]

$$D = \sum_{i=1}^{n} \frac{1}{N_{id}}, \qquad (3)$$
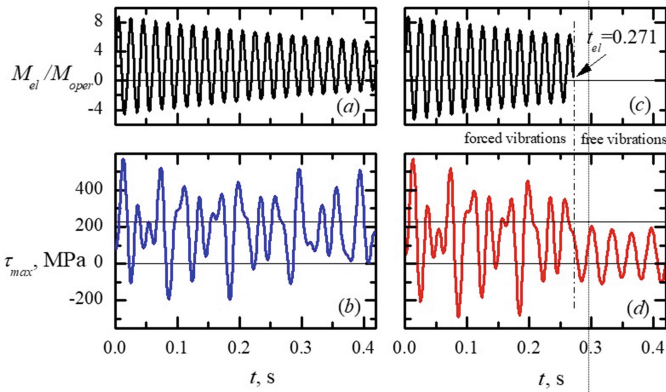
Fig. 3. Time dependences of the electromagnetic torque (*a, c*) and maximal shear stresses (*b, d*) in the area between LPR and TG at successful (*a, b*) and unsuccessful (*c, d*) connection of turbine generator to the power network in case of angle $\theta = 30°$.

where n is the number of damaging cycles of vibration, in which shear stresses exceed the fatigue limit of rotor steel $\tau - 1$; Nid is the number of cycles till the fracture under the stress τimax. In 2000 connections of a turbine generator the total fatigue damage was determined as Dtotal = 2000D. The limiting state of the rotor steel is attained in condition Dtotal = 1.

Calculations of cyclic damage of the shafting were performed with the fatigue curve for the rotor steel R2MA, which was obtained at symmetric cycle of loading and at normal temperature (Fig. 4). The influence of scale effect, temperature and asymmetry of cyclic deformation on the fatigue properties of the steel was taken into account by means of correction factors

$$\tau_{max} = K_s K_a K_t [\eta_0 + \eta_v(N)^c + \eta_u(N)^b], \tag{4}$$

where $\eta_0 = 208.3$; $\eta_v = 3176.2$; $\eta_u = 1.86105$; $c = -0.3114$; $b = -0.8348$; N is the number of loading cycles; Ks is the scale factor; Ka is the asymmetry factor; Kt is the temperature factor.

Based on the experimental research [13] the values of scale and temperature factors were excepted to be Ks = 0.58 and Kt = 0.78. The asymmetry factor was determined by the formula

$$K_a = \frac{\sqrt{\tau_{-1}^2 - \kappa^2 \psi_\tau^2 \tau_m^2}}{\tau_{-1}}, \tag{5}$$

where $\tau - 1 = 230$ MPa; $\kappa = 0.922$; $\psi\tau = 0.505$ [14, 15]; τm is the mean stress.

At unsuccessful connection of turbine generator to the electrical network it is necessary to take into account the effect of the duration of electromagnetic torque on free vibrations of shafting arising after the disconnection of turbine generator from the electrical network.
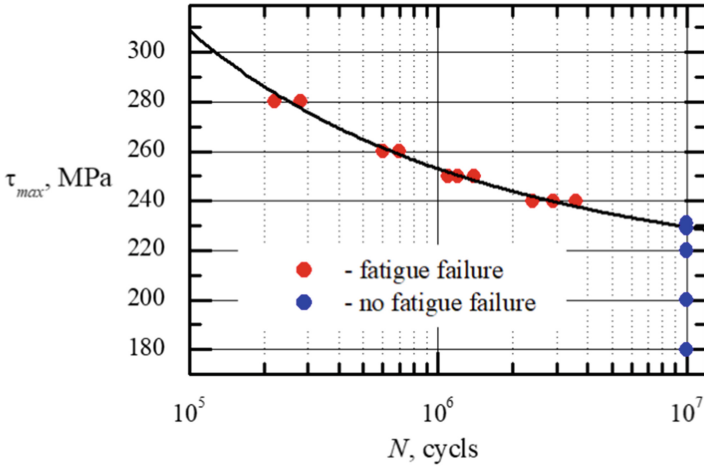
Fig. 4. The curve of the high-cycle fatigue of R2MA steel at cyclic torsion.

The assessment of damage was performed based on the assumption that the duration of electromagnetic torque tel is distributed equiprobably in a certain range of time Δtel = tel,K − tel,1 (tel,1 and tel,K are the initial and end value of the range, respectively). The initial value of the range was taken to be tel,1 = 0.25 s. The averaged over the range damage was determined by the formula

$$D_{av} = \frac{\sum\limits_{i=1}^{K} D_{total,i}(t_{el,i})}{\Delta t_{el}}, \qquad (6)$$

where $D_{total,i}$ is the total damage at the duration of the electromagnetic torque $t_{el,i}$.

It is practically unlikely that all 2000 connections of turbine generator to the electrical network would be successful. The more realistic scenario should count for possibility of certain number of unsuccessful connections which is different for various steam turbines. In such a way Fig. 5 presents the results of averaged damage assessment for two hypothetical cases: first case considers 2000 successful connections (blue curve) and second one – 2000 unsuccessful connections (red curve). It should be noted that the attempts to connect the turbine generator to electrical network continues until it will be successful. Therefore, in calculations of fatigue damage for 2000 unsuccessful connections there were added fatigue damage caused by the same amount of successful connections.

In all cases presented in Fig. 5 the averaged damage is strongly dependent on the angle θ and on the number of unsuccessful connections. The scenario of damage accumulation presented in Fig. 5 by red curve is optimistic in terms of the number of unsuccessful connections. The real theirs number could be much higher than 2000.

The limiting state of the rotor steel (Dav = 1) can be achieved in condition $\theta \geq 9.7°$, if all connections would be successful, and in condition $\theta \geq 9.7°$, if the number of unsuccessful connections would be 2000 (vertical dash-dot lines in Fig. 5
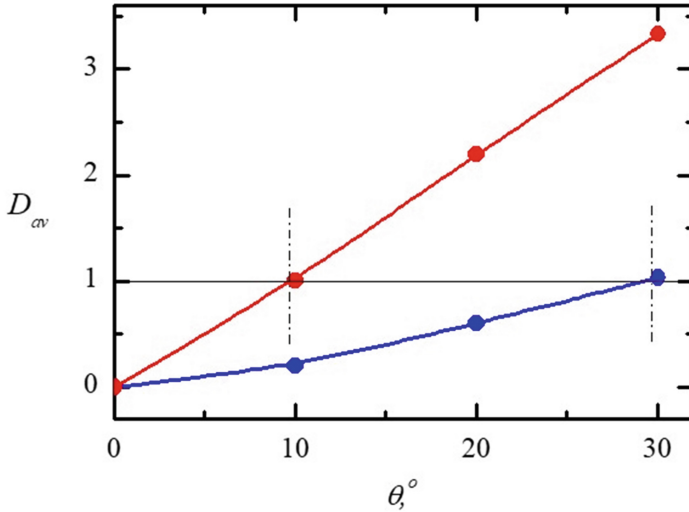
Fig. 5. Dependences of averaged fatigue damage of turbine shafting in area between LPR and TG on the angle θ: 2000 successful connections (blue curve); 2000 unsuccessful + 2000 successful connections (red curve).

demonstrate these critical values of θ). It is evident that the higher is the number of unsuccessful connections the lower should be the angle θ to avoid critical accumulation of fatigue damage in the turbine shafting.

The proposed above procedure can be applied for the real time estimation of fatigue damage of turbine shafting based on the measurement of torsional vibrations of the shafting during operation, especially at abnormal regimes of operation of turbine generator.

5   Conclusions

The evaluation of fatigue damage of turbine shafting should be based on the account not only of the transverse but also of the torsional vibrations caused by the connection of turbine generator to the electrical network. The intensity of torsional vibrations essentially depends on the angle θ and on the duration of electromagnetic torque.

Torsional vibrations of turbine shafting are the main reason of its fatigue damage. In general case the fatigue damage is a function of three parameters: the angle θ, the number of unsuccessful connections and the duration of the electromagnetic torque at unsuccessful connections.

The assessment of fatigue damage of turbine shafting at torsional vibrations for 2000 successful connections of turbine generator to the power network showed that at real level of damping in the mechanical system the limiting state of the rotor steel can be achieved in condition $\theta \geq 29.7°$. This value obtained for the condition of real damping in the mechanical system is much lower than in ref. [10]. Therefore, actual

situation with fatigue damage of turbine shafting is much more dangerous than it was predicted in [10] under the assumption of high damping.

In general, the safety of steam turbines in operation to a great extent is affected by the number of unsuccessful connections and by the angle θ. The value of angle θ should be controlled at every connection of the turbine generator to electrical network and should be as lower as possible.

References

1. Matsevityi, Yu.M., Shul'zhenko, N.G., Goloshchapov, V.N.: Increase of the operational power efficiency of turbine units at combined heat power plants and thermal power plants by way of upgrading, reconstruction and improvement of their operation conditions. Naukova Dumka, Kiev (2008)
2. Zagretdinov, I.Sh., Kostyuk, A.G., Trukhnii, A.D., Dolzhanskii, P.R.: Failure of the 300 MW turbine unit of the state district power station at Kashira: causes, consequences and conclusions. Teploenergetika **5**, 5–15 (2004)
3. Dorfman, L.S., Trubelja, M.: Torsional monitoring of turbine-generators for incipient failure detection. In: Proceedings of the Sixth EPRI Steam Turbine/Generator Workshop, pp. 1–6, St. Louis (1999)
4. Barella, S., Bellogini, M., Boniardi, M., Cincera, S.: Failure analysis of a steam turbine rotor. Eng. Fail. Anal. **18**(6), 1511–1519 (2011)
5. Bovsunovskii, A.P., Chernousenko, O.Yu., Shtefan, E.V., Bashta, D.A.: Fatigue damage and failure of steam turbine rotors by torsional vibrations. Strength Mater. **42**(1), 108–113 (2010)
6. Kakinoki, T., Yokoyama, R., Fujita, G.: Shaft torque observer and excitation control for turbine- generator torsional oscillation. Electr. Power Syst. Res. **68**, 248–257 (2004)
7. Kima, C.-K., Jang, G.: Effect of an excitation system on turbine-generator torsional stress in an HVDC power system. Electr. Power Syst. Res. **77**, 926–935 (2007)
8. Bovsunovskii, A.P.: Numerical study of vibrations of a nonlinear mechanical system simulating a cracked body. Strength Mater. **31**(6), 571–581 (1999)
9. Steam turbine-generator torsional vibration interaction with the electrical network. Final Report. Electric power research institute. Palo Alto, California (November 2005)
10. Bovsunovsky, A.P.: Fatigue damage of steam turbine shaft at asynchronous connections of turbine generator to electrical network. In: Journal of Physics: Conference Series 628 conference 1, 012001 (2015)
11. Palmgren, A.: Life of ball bearings. Z. Ver. Dtsch. Ing. **68**, 339–341 (1924)
12. Miner, M.A.: Cumulative damage in fatigue. J. Appl. Mech. **12**, 159–164 (1945)
13. Kudryavtsev, I.V., Naumchenkov, N.E.: Fatigue strength characteristics of steel 25KhNZMFA in relation to absolute dimensions and stress concentrations. Strength Mater. **10**(4), 386–392 (1978)
14. Troshchenko, V.T.: A "scale effect" in tests of long-term strength. Strength Mater. **1**(1), 22–26 (1969)
15. Troshchenko, V.T., Shestopal, L.R.: Criteria of torsional fatigue strength of metals. Strength Mater. **7**(2), 127–131 (1975)

Experimental Investigation of Physical and Tribological Properties of Engine Oil with Nano-particles Additives

Manoj K. Gaur[1], Sumeet K. Singh[1], Akash Sood[1(✉)] ,
and Dharamveer S. Chauhan[2]

[1] Madhav Institute of Technology and Science,
Race Course Road Gole ka Mandir, Gwalior 474005, Madhya Pradesh, India
akku.sood@live.com
[2] Rustamji Institute of Technology, Race Course Road Gole ka Mandir,
Gwalior 475005, Madhya Pradesh, India

Abstract. Experimental Investigation of physical and tribological properties of engine oil was performed on SAE20W40 lubricant containing CuO and FeO nano-particles and their combination (content of metal 0.875 g/350 ml of oil). This presents an analysis of the variation in properties of lubricants by adding nano-particles and further enhancement in its operational quality. This work also presents a review of the addition of copper and iron metallic nanoparticles in engine oil and the evaluation of changes in their respective physical and tribological properties. Later analysis of the variation in tribological properties has been carried out by conducting tests on the bearing test apparatus. FFT (Fast Fourier Transform) and other operational parameters are used to analyse vibration characteristics for different samples of lubricants. Through comparative analysis, the use of the base oil (SAE20W40) with the mixture of CuO and FeO provides the most effective improvement of physical properties via viscosity, flash and fire point as well as vibration in tribological properties.

Keywords: CuO nanoparticles · FeO nanoparticles · SAE20W40 lubricant
Tribological properties · FFT

1 Introduction

Having considered a lot of research papers it is inferred that the addition of nanoparticles of lubricant is quite effective to improve the anti-frictional, chemical and physical properties of some base oils such as mineral, synthetic, vegetable or animal, which results in improving the lubricant performance and extending the equipment life. Because of the tribological properties of nanoparticles, the concept of Trilogy was enunciated in 1966 in a report of the UK Department of Education and Science. It encompasses the interdisciplinary science and technology of interacting surfaces in relative motion and associated subjects and practices [1].

2   Literature Review

The use of nanoparticles which includes Al2O3, CuO, TiO2, SiC, TiC, Ag, Au, Cu, and Fe nanoparticles are frequently used in nanofluid that shows many typical properties and their typical features offer unprecedented potential for many applications [2]. Under these nanoparticles such as Cu, CuO, Fe, Ni, TiO2, SiO2 a good friction reduction of anti-wear behavior is provided. The tribological properties of the modified TiO2 microcrystals as additives of liquid paraffin improve the anti-wear performance, friction-reduction property, and load-carrying capacity of the liquid paraffin [3]. The nanoparticles, such as SiO2 added into the base oil (SN-500) exhibit a good friction reduction and anti-wear properties. Also, SiO2 nanoparticles in the SN-500 base oil decreased the friction coefficient by 61%, 55% and 43% at 0.5 at.% concentration and 36%, 76% and 17% at 0.75 at.% concentration respectively, as compared with the standard base oil without SiO2 nanoparticles [4].

Cu nanoparticle additives in the oil indicates that the higher the oil temperature is applied, the best the tribological properties of Cu nanoparticles will be and it can be safely inferred that a thin copper protective film with some lower elastic modulus and hardness is formed on the worn surface, which results in better tribological performances of Cu nanoparticles, especially when the oil temperature is quite high [5–7]. When the CuO was added to the engine oil, the thermal conductivity coefficient and the flash point of Nano lubricants with 0.1 wt% concentrations, respectively, had 3% and 7.9% improvement with respect to the base oil. Also, the oil's viscosity, is a very important factor in the lubricating issue, at a lower concentration with respect to the engine oil without which CuO had no appreciable change [8–10].

The purpose of this work is to determine the effect of adding CuO and FeOnano-particles to the engine oil 20w40 on the viscosity, flash point, fire point and friction of automobile parts. In this study, Copper oxide (CuO) and iron oxide (FeO) have been used quite often as Nanoparticles with their tribological, additive and anti-wear properties. With the help of some experiments, three mixtures have been prepared, these are the base oil (SAE 20W40) and CuO, the base oil and FeO, and the base oil and (FeO + CuO). Hence, these prepared lubricating oils have been tested for the flash point, fire point and finally the vibration effect.

3   Research Methodology

3.1   Preparation of Lubricant with Nano-particles

To complete this process, the standard oil (SAE 20W40) is chosen and taken as a base oil and for the emulsion formation nanoparticles, hydrazine powder, and distilled water were used. First, an emulsion of nanoparticles with hydrazine sulfate is prepared. Then, this emulsion is mixed with the standard base oil with the help of a mechanical stirrer. Thus, the Nanoparticles mixed oil is obtained thereafter. The process of preparation of Nano additives, its emulsion and description of properties of base oil is as follows.

a) **Base oil:** The SAE 20W40 engine oil (purified lubricants, India) was used as the base oil. The pure lubricant engine oil contains some additives for the reduction in friction and vibration and to increase viscosity. The base oil Fig. 1 used for Nano additive lubricant is of a particular and that company is an Indian Standard certified company [7]. The properties of the base oil (SAE 20W40) are presented below in Table 1.
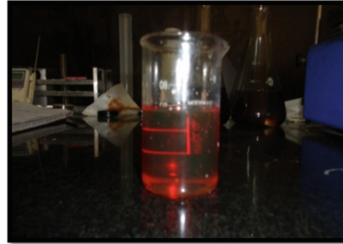
Fig. 1. Base oil 20w40.

Table 1. Properties of the base oil.

S. No.	Properties	Range
1	Appearance	Bar & clear
2	Colour	1.5 ASTM
3	Density@29. 5 D.C.	0.88, GM/ml
4	K.V. @40 D.C.	94cSt
5	K.V. @100 D.C.	10.54cSt
6	Viscosity index	94 (MIN)
7	Flash point (^{0}C)	252
8	Aniline point (^{0}C)	105.5
9	Pour point	L-6

b) **Nanoparticles**: The Nanoparticles of FeO and CuO were used to prepare the Nano additive lubricant oil (Fig. 2). One of the most effective factors of the nanofluid properties is the rate of the dispersion and stability of Nanoparticles in the base fluid. When the dispersion of particles is not good inside the base fluid, there will be
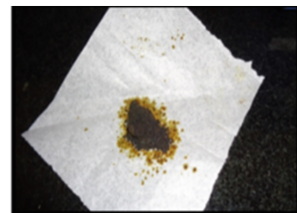
(a) Copper oxide (CuO)   (b) Ferrite oxide (FeO)

Fig. 2. Nano-particles.

Table 2. Properties of nanoparticles.

S. No.	CuO nano-particles	Fe nano-particles
1	Purity- 99.9%	Purity- 99.9%
2	Melting point- 1326 °C	Melting point- 1565 °C
3	Density - 6.49 g/cm^3	Density - 5.24 g/cm^3
4	PH value – 4–6	PH value – 6–7

chances of jumbled collection and precipitation of nanoparticles. The specification of Nanoparticles [11] is shown below in Table 2.

3.2   Procedure for Preparing Nano Additive Lubricating Oil

The three types of Nano additive lubricant oil were prepared viz. SAE 20W40 + CuO, SAE 20W40 + FeO and a mixture of SAE 20W40 + FeO + CuO. The Table 3 below gives the content of Nanoparticles in the lubricating oil.

Table 3. Content of nano oils and nanoparticles.

S. No.	Title of nanooil	Nanoparticles	Content of metal (g/350 ml oil)
1	SAE 20 + CuO	CuO	0.875
2	SAE 20 + FeO	Fe	0.875
3	SAE20 + FeO + CuO	Mixture of FeO and CuO	0.875/0.875

1. First, hydrazine emulsion is prepared by mixing 20 ml of water with 2.6 g hydrazine (NH2OH.HC).
2. Then, 0.875 g of Fe is mixed with CuO in the hydrazine emulsion with the help of a magnetic stirrer to form some Nano additive oil.
3. The Nano additive oil is mixed at room temperature in a base oil by dropping small droplets of Nano additive oil one by one.
4. The whole solution is placed on a magnetic stirrer (Fig. 3) to mix properly Nano additive oil in a base oil. The stirring of the solution is done for 30 min so that Nano additive oil completely mixes with the base oil.
5. In some time, the colours of mixture began to change and this indicates the presence of moisture in the mixture.
6. The moisture from the mixture is removed in the form of vapor by heating it in an oven for 15 min.
7. Finally, the Nano additive lubricating oil is prepared.

   This same procedure will be repeated to prepare other samples of Nano lubricating oil by replacing the Nano-particles. The three samples prepared from the above procedure viz. CuO mix oil, FeO mix oil, and FeO + CuO mix oil as well as the base oil are shown in Fig. 4.
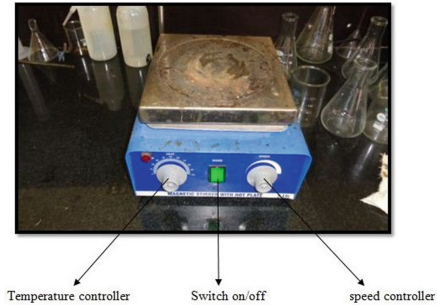
Fig. 3. Magnetic stirrer with hot plate.
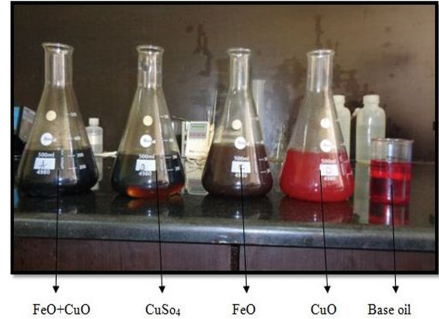
Fig. 4. Prepared sample of lubricating oil.

3.3   Testing of Oils

Viscosity Test

Experimental setup and procedure of testing. The viscosity test is done on the base oil (SAE 20W40) and the three samples of the prepared Nano additive lubricating oil viz. CuO mix oil, FeO mix oil, and FeO + CuO mix oil. The test is done using the viscosity test apparatus Redwood Viscometer No. 1. The test is done at 40 °C and 100 °C for evaluating the kinematic viscosity. The measured viscosity of base oil (SAE 20W40) is compared with the measured values of three samples of Nano additive lubricating oil (Fig. 5).

Fig. 5. Redwood viscosity apparatus.

The time taken in emptying the container of redwood Viscometer is measured in seconds (t). This measured time is converted into centistokes by an empirical formula. The empirical formula for converting the kinematic viscosity from seconds into centistokes

$$V = ct - \beta/_t \ln \text{ cSt} \qquad (2.1)$$

where, V = kinematic viscosity in centistokes (cSt); T = Time of flow in seconds; C and β are constants.

The following values are taken for constants in empirical relation 2.1, the value of $C = 0.25$ and $\beta = 172$.

3.4   Flash and Fire Point Test

Experimental setup and procedure of testing. The flash and fire point of base oil (SAE20W40) of Nano additives lubricating oil were tested using Pensky–Marten's apparatus which is used for the oil having flash and fire point above 100 °C is as shown in Fig. 6. In Pensky–Marten closed-cup flash-point test, a brass test cup is filled with some test specimen and is also fitted with some cover. The 80 ml of oil taken for testing in the beaker of pesky marten's apparatus. This oil is then heated and afterward stirred at specified rates depending upon the material being tested. An ignition source is then directed into the cup at regular intervals of time with simultaneous interruptions of stirring until a flash that spreads throughout the inside of the cup is seen. The related temperature is its flash point. The temperature at which the vapours of the oil give a clear and some distinct blue flash for five seconds is recorded as the fire point of the oil.
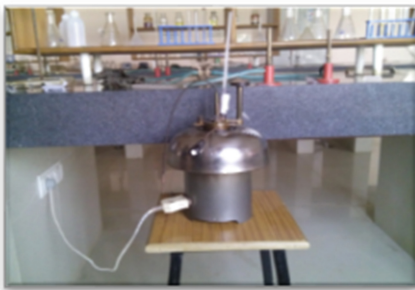
Fig. 6. Pensky–Marten's fire point apparatus.
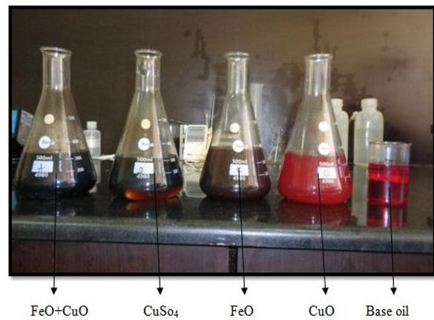
Fig. 7. Experimental setup.

Vibration Test Rig. Nanoparticles lubricating oil is tested on the bearing test apparatus available in tribology and machine dynamic lab of the mechanical engineering department of PDPM IIITDM Jabalpur. Main parts of the test rig are starting a motor, bearing, rotating shaft, dead weight and oil filling chamber. The half of the bearing is immersed in lubricating oil. The outcomes of the analysis for the respective samples of oil are used to evaluate the optimum Nano additives and its effect. The respective position of the major components of the experimental setup is shown in Fig. 7 and technical specifications of vibration test apparatus are listed below in Table 4.

The lubricant to the bearing is supplied through the sump having two chambers - outer chamber and the inner chamber, partitioned by the bearings partially immersed in the lubricant. Lubricating oil is filled in both chambers separately as shown in Fig. 8 and experimental setup with Data Acquisition System is also shown in Fig. 9.

Vibration Analysis. The vibration analysis is performed on the oil operator bearing test rig for evaluating the performance of the Nano additive lubricating oil. The test was

Table 4. Specifications of test apparatus.

S. No.	Specification	Details
1	Motor	Ac motor 3-phase 2.2 kW
2	Bearing	Roller bearing 307 SKF
3	Temperature	Temperature sensing system
4	Vibration	Variable frequency drives DEWE 43A
5	Load capacity	100 kg
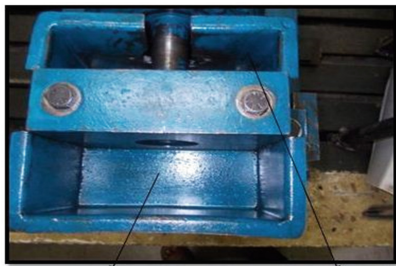
outer oil Filing chamber   inner oil filing chamber

Fig. 8. Oil filling chamber.
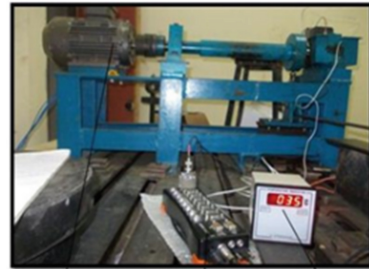
Motor   Data Acquisition System   Temperature indicator

Fig. 9. Experimental setup with data acquisition system.

performed on two load condition 40 kg and 60 kg respectively. These tests were performed on four lubricating oil viz. (a) Base oil, (b) SAE20W40 + FeO, (c) SAE20W40 + CuO and (d) SAE20W40 + FeO + CuO mix oil. The test was performed for 30 min at a data stabilization time and 1 s as a data acquisition time for the vibration characteristics using DEWESOFT 7.1.1 software, besides this, the temperature variations were recorded and analysed. The applied boundary conditions and parameters evaluated are shown below in Tables 5 and 6.

Table 5. Experimental parameters at 40 kg.

S. No.	Lubricating oils	RPM	Applied load (w) kg	Time (t) min.	Temperature (t) °C
1	Base oil	1000	40	30	36–38
2	SAE20W40 + FeO Mix Oil	1000	40	30	34–36
3	SAE20W40 + CuO Mix Oil	1000	40	30	34–37
4	SAE20W40 + FeO + CuO Mix Oil	1000	40	30	37–38

Table 6. Experimental parameters at 60 kg.

S. No.	Lubricating oils	RPM	Applied load (w) kg	Time (t) min.	Temperature (t) °C
1	Base oil	1000	60	30	36–37
2	SAE20W40 + FeO mix oil	1000	60	30	35–36
3	SAE20W40 + CO mix oil	1000	60	30	36–38
4	SAE20W40 + FeO + CuO mix oil	1000	60	30	38–39

The parametric values mentioned as boundary conditions in Tables 5 and 6 clearly indicate that only applied load is taken as a significant varying parameter for the present research work.

4   Results

4.1   The Result of Viscosity Test

The viscosity test was done at 40 °C and 60 °C of base oil and three samples of Nano additive lubricating oil were taken. Table 7 shows that the time taken for emptying the container of Redwood Viscometer is different for all samples. The minimum time takes place in FeO mix oil at both temperatures. And maximum time takes place in the FeO + CuO mix oil at those temperatures. When the kinematic viscosity is evaluated from the formula 2.1 at maximum and minimum time then Feo + CuO mix oil and CuO mix oil show maximum and minimum kinematic viscosity respectively.

Table 7. The result of viscosity test.

S. No.	Type of oil	k. v. @ 40 °C		k. v. @ 60 °C	
		In seconds	* (cSt)	In seconds	* (cSt)
1	Base oil (SAE 20W40)	380	94.54	55	10.62
2	CuO mix oil	384	95.55	57	11.23
3	FeO mix oil	375	93.75	50	9.06
4	FeO + CuO mix oil	386	96.05	58	11.54

4.2   The Result of Flash and Fire Point Test

The flash and fire point of the base oil (SAE20W40) and three samples of Nano additives lubricating oil is measured using Pensky Marten's apparatus and the measured values for three samples of Nano additives oil were compared with respective values of base oil. The result of the test is shown below in Table 8.

Table 8 shows that the flash and fire point of CuO + FeO mixed with Nano oil is comparatively higher than the base oil (SAE 20W40) and the other two samples. Thus, when the base oil is mixed with the mixture of FeO and CuO, the new oil improves the flash and fire point.

Table 8. The result of flash and fire test.

S. no.	Type of oil	Flash point (°C)	Fire point (°C)
1	Base oil (SAE 20W40)	252	258
2	CuO mix oil	220	250
3	FeO mix oil	200	230
4	FeO + CuO mix oil	254	260

4.3   The Result of Vibration Test

The FFT Spectrum for the Vibration Characteristics at 40 kg Load. The FFT Spectrum for the Vibration characteristics was obtained by running the experimental setup at boundary conditions mentioned in Tables 5 and 6. The tests were performed in all the four samples with the data acquisition time of 30 min and got different results as in Tables 9 and 10.

Table 9. Summary of results for 40 kg load.

S. No.	Load	Oil composition	Acceleration amplitude	
			RMS value (ms^{-2})	Peak value (ms^{-2})
1	60 kg	Base Oil	2.17	1.39
2	60 kg	FeO-mix oil	1.99	1.34
3	60 kg	CuO- mix oil	1.92	1.25
4	60 kg	FeO + CuO mix oil	1.64	0.91

The vibration parameters are evaluated in the form of the wave spectrum between acceleration amplitude and corresponding frequencies through the simulation software DEWESOFT 7.1.1. The measured acceleration amplitudes are generated in the form of a spectrum of FFT (Fast Fourier Transforms). The common use of Fourier transforms is to find the frequency components of a signal buried in a noisy time domain signal. Since it is difficult to identify the frequency components by looking at the original signal. Converting to the frequency domain, the discrete Fourier transform of the noisy signal is found by taking the fast Fourier transform (FFT). The FFT vibration spectrum at various concentrations and varying loads are evaluated for 1-minute data acquisition time and are discussed below.

4.4   FFT Spectrum for Vibration Characteristics at 40 Kg Load

The FFT Spectrum for Vibration characteristics were obtained by running the experimental setup at boundary conditions mentioned in Tables 5 and 6. The tests were performed in all the four samples with the data acquisition time of 30 min. The obtained FFT for the respective samples are shown in Figs. 10(a) to 11(d).

Table 10. Summary of result for 60 kg load.

S. No.	Load	Oil composition	Acceleration amplitude	
			RMS value (ms^{-2})	Peak value (ms^{-2})
1	60 kg	Base oil	2.04	1.64
2	60 kg	FeO-mix oil	2.01	1.48
3	60 kg	CuO- mix oil	1.98	1.16
4	60 kg	FeO + CuO mix oil	1.88	0.96

The results obtained through FFT transform spectrum shown in Figs. 10(a) to 11(d) at 40 kg load are mentioned in Table 9.

4.5   FFT Curve for Vibration Characteristics at 60 Kg Load

Similarly, FFT spectrum of vibration characteristics was obtained by running the experimental setup at boundary conditions mentioned in Table 6. The tests were performed in all the four samples with the data acquisition time of 30 min. The obtained FFT for the respective samples are shown in Fig. 11(a)–(d).

(a) FFT Spectrum of Vibration for Base oil (SAE20W40)

(b) FFT Spectrum of vibration for FeO Mix oil

(c) FFT Spectrum of Vibration for CuO Mix oil

(d) FFT Spectrum of vibration for FeO+CuO oil
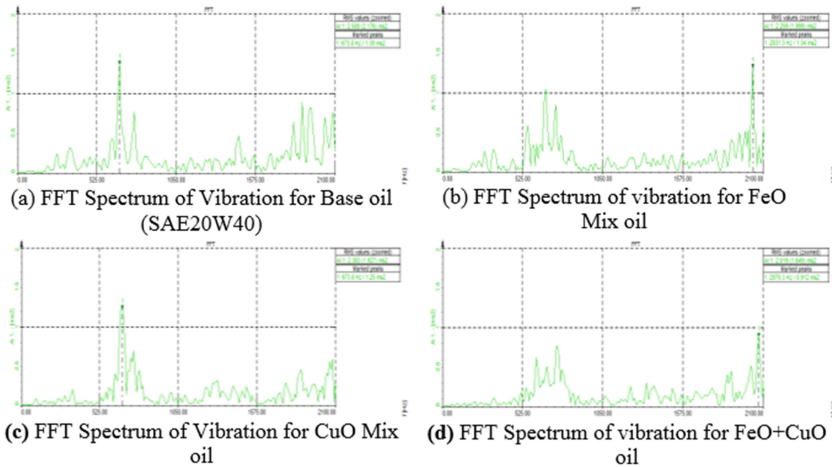
Fig. 10. FFT spectrum of vibration for oil.

Figures 10(a)–(d) and 11(a)–(d) show that the PEAK and RMS values at load 40 kg and 60 kg of FeO + CuO mix oil is minimum and maximum for the base oil. Thus FeO +CuO mix oil is the best lubricating oil. The vibration characteristic is evaluated during the tribological tests. The Figs. 10(a) and 11(a) shows the graph of variation in the vibration of base oil at 40 kg and 60 kg load condition. Further, the FFT Spectrum of vibration at the same loading condition of FeO mixed nano additive lubricant oil is shown in Figs. 10(b) and 11(b). The result indicated that in comparison

(a) FFT Spectrum of Vibration for Base Oil (SAE 20w40)

(b) FFT Spectrum of Vibration for FeO Mix Oil

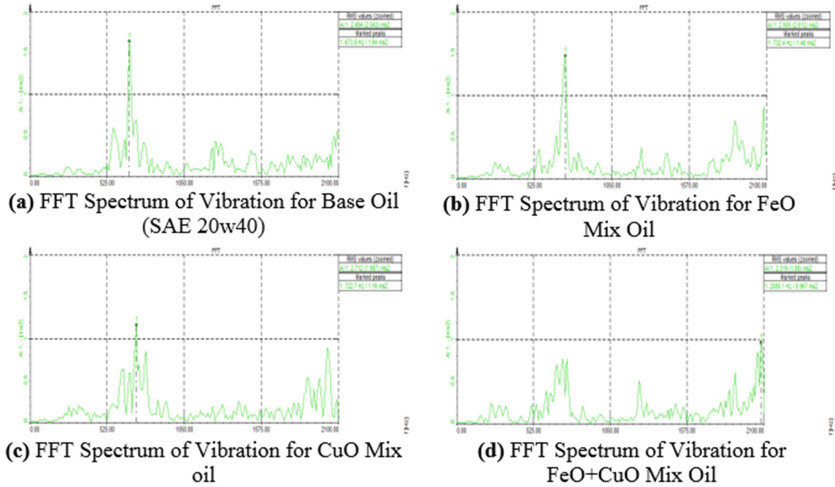**(c)** FFT Spectrum of Vibration for CuO Mix oil

(d) FFT Spectrum of Vibration for FeO+CuO Mix Oil

Fig. 11. FFT Spectrum of vibration for oil.

with the base oil the PEAK and RMS values at the load of 60 kg of FeO mix lubricating oil is lowered by 9.75% and 1.47% respectively and at a load of 40 kg lowered by 3.59% and 8.29% respectively. The FFT (Fast Fourier Transformation) Spectrum of vibration shown in Figs. 10(c) and 11c gives the variation in vibration at a 40 and 60 kg of CuO added Nano additive lubricant oil. The result depicts the reduction of vibration by 2.94% and 11.5% at the load of 40 kg and 60 kg in comparison with the base oil respectively. Similarly, when the FeO and CuO are mixed with the base oil, the PEAK and RMS values as compared with the base oil at a load of 40 kg is lowered by 34.53% and 24.42% respectively and at the load of 60 kg lowered by 41.46% and 7.84% respectively. The comparison of RMS and PEAK Values of amplitudes at the load of 40 kg and 60 kg is shown below in Tables 11 and 12.

Table 11. RMS values of amplitude at 40 kg.

Oil composition	RMS values at 40 load (ms^{-2})
Base oil	2.17
FeO mix oil	1.99
CuO mix oil	1.92
FeO + CuO mix oil	1.64

The comparative analysis of RMS value of amplitude in both conditions the RMS value is maximum for the base oil at 40 kg and 60 kg as shown in Tables 11 and 12.

The above-mentioned tables and graph show that the RMS value of the amplitude of acceleration reduces by addition of Nano additives and is minimum for FeO + CuO mix oil sample irrespectively of the applied load. The Peak Values comparison at load 40 kg and 60 kg is shown below in Tables 13 and 14.

Table 12. RMS values of amplitudes at 60 kg.

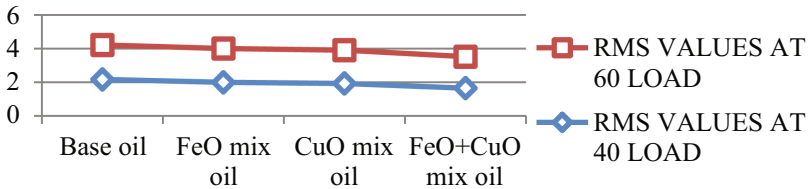| Oil composition	RMS values at 60 Load (ms^{-2})
Base oil	2.04
FeO mix oil	2.01
CuO mix oil	1.98
FeO + CuO mix oil	1.88

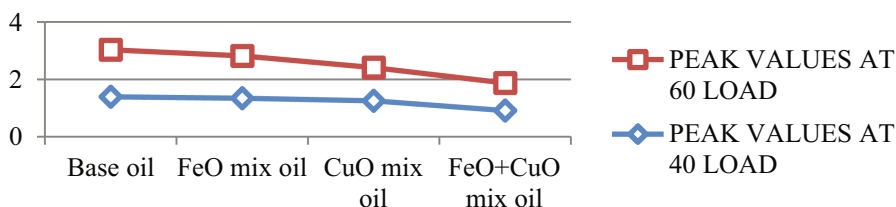**Fig. 12.** The comparative analysis of RMS value of amplitude.

The above comparative analysis of Figs. 12 and 13 shows that the peak value of amplitude at the load of 40 kg and 60 kg of FeO + CuO mix oil is minimum as compared with other base oil. Thus, FeO +CuO mix oil is the best lubricating oil. The vibration characteristic is evaluated during the tribological tests. The results are presented in Figs. 10(a)–(d) and 11(a)–(d). The Figs. 10(a) and 11(a) show the graph of variation in the vibration of the base oil at the 40 kg and 60 kg load condition. Further, the FFT Spectrum of vibration at the same loading condition of FeO mixed Nano additive lubricant oil is shown in Figs. 10(b) and 11(b). The result indicated that in comparison with the base oil the FFT Spectrum of vibration of FeO added lubricating oil is lowered by 1.47% and 8.29%. The FFT (Fast Fourier Transformation) Spectrum of vibration shown in Figs. 10(c) and 11(c) gives the variation in vibration at 40 and 60 kg of CuO added the Nano additive lubricant oil. The result depicts the reduction of vibration by 2.94% and 11.5% at load of 40 kg and 60 kg in comparison with the base oil respectively. The variation in vibration at the respective loading condition of FeO + CuO added Nano additive lubricating oil is shown in Figs. 10(d) and 11(d). The result of the analysis compared with the base oil, revealed that the vibration is decreased by 7.84% and 24.42% in FeO + CuO added Nano additive lubricant oil.

Table 13. Peak values at 40 kg.

Oil composition	Peak values at 40 load (ms^{-2})
Base oil	1.39
FeO mix oil	1.34
CuO mix oil	1.25
FeO + CuO mix oil	0.91

Table 14. Peak values at 60 kg.

Oil composition	Peak values at 60 Load (ms^{-2})
Base oil	1.64
FeO mix oil	1.48
CuO mix oil	1.16
FeO + CuO mix oil	0.96

Fig. 13. The comparative analysis of peak value of acceleration amplitude.

5   Conclusions

In the present research work, some investigation of physical as well as tribological properties of the base oil (SAE 20W40) and a few three-prepared samples of CuO, FeO and CuO + FeO Nano additive lubricant is carried out. This test is done to examine the viscosity, flash point, fire point and the vibration characteristics of the base oil and other three samples of Nano additive lubricating oil. The comparison of the results of these three samples of Nano additive lubricant oil is done with the help of the obtained result of the base oil. The analysis clearly indicates that the use of nanoparticles CuO + FeO 3 enhances the physical and tribological characteristics of the lubricating oil.

References

1. Dongare, A.D., Gite, A.J.: Experimental analysis of tribological properties of various lubricating oils without and with using extreme pressure additives by using four ball extreme pressure oil testing machine. J. Eng. **8**(4), 10–27 (2014)
2. Ramakoteswaa, R.N., Gahane, L., Ranganayakulu, S.V.: Synthesis, applications and challenges of nanofluids—review. IOSR J. Appl. Phys. **2014**, 21–28 (2014)
3. Qian, J., Yin, X., Wang, N., Liu, L., Xing, J.: Preparation and tribological properties of stearic acid-modified hierarchical anatase TiO$_2$ microcrystals. Appl. Surf. Sci. **7**(258), 2778–2782 (2012)
4. Patil, H.H., Sangli, D.: Tribological properties of Sio$_2$ nano-particles added in SN-500 base oil. Int. J. Eng. Res. Technol. **5**(2), 763–768 (2013)
5. He-long, Y., Yi, X., Pei-jing, S., Bin-shi, X., Xiao-li, W., Qian, L.: Tribological properties and lubricating mechanisms of Cu nano-particles in lubricant. Trans. Nonferrous Met. Soc. China **3**(18), 636–641 (2008)

6. Guang-bin, Y., Shan-tao, C., Xiu-juan, X., Sheng-mao, Z., Lai-gui, Y., Ping-yu, Z.: Preparation and tribological properties of surface modified Cu nanoparticles. Trans. Nonferrous Met. Soc. China **2**(22), 366–372 (2012)
7. Padgurskas, J., Rukuiza, R., Prosyevas, I., Kreivaitis, R.: Tribological properties of lubricant additives of Fe, Cu and Co nano-particles. Tribol. Int. Tribol **60**, 224–232 (2013)
8. Ettefaghi, E., Ahmadi, H., Rashidi, A., Mohtasebi, S., Alaei, M.: Experimental evaluation of engine oil properties containing copper oxide nano-particles as a nanoadditive. Int. J. Ind. Chem. **1**(4), 1–28 (2013)
9. Prakash, E., Siva Kumar, K., Muthu Kumar, K.: Experimental studies on vibration characteristics on ball bearing operated with copper oxide nano particle mixed lubricant. Int. J. Eng. Technol. **5**(5), 4127–4130 (2013)
10. Pisal, A.S., Chavan, D.S.: Experimental investigation of tribological properties of engine oil with CuO nano-particles. Int. J. Theor. Appl. Res. Mech. Eng. **2**(3), 34–38 (2014)
11. Mohan, N., Sharma, M., Singh, R., Kumar, N.: Tribological properties of automotive lubricant SAE 20W-40 containing nano-Al_2O_3 particles. SAE Tech. Pap. **2781**, 1–9 (2014)

Simulation and Analysis of Passive vs. Magneto-Rheological Suspension and Seat Dampers

Sulaymon Eshkabilov[✉], Hamdam Jumaniyazov,
and Davron Riskaliev

Dynamics and Control Lab, Tashkent Institute of Design,
Construction and Maintenance of Automobile Roads,
20 Amir Timur St., Tashkent 100060, Uzbekistan
sulaymon@d-c-lab.com

Abstract. This paper presents some analyses and simulation results of the passive and magneto-rheological (MR) suspension and driver's seat dampers. The damper with the MR liquid is modeled via the Bingham model due to its simplicity and high efficiency in comparison with other models. The simulation models of the passive and MR damper suspension and driver's seat models are developed in MATLAB/Simulink. Two road profile data sets are used in simulations, one of which is the road roughness data, collected from the roads, that is interpolated with respect to the vehicle speed, and the time spent to cover the chosen road distance. The other is the Heaviside step function generated numerically. The numerical simulation results have shown that the MR based suspension and seat dampers have outperformed the passive suspension and seat dampers considerably.

Keywords: Bingham model · Comfort ride · Road profile
MATLAB/simulink

1 Introduction

The comfort ride of ground vehicles is defined by several factors and the main one is an enhanced comfort level of a vehicle while driving it on various terrains without causing tiredness or motion sickness for its driver and passengers. The comfort ride is linked with a whole body vibration and how to assess it via experimental studies and numerical analyses are well formulated in the International Standard procedures - ISO2631 [1]. In our studies, we have considered these issues experimentally by measuring terrain roughness and the system (car body and driver's seat) responses on uneven road profile excitation in different speeds (20, 30, 40, 50, 60 km/h) of a vehicle driven in a chosen part of a road. In addition, we have investigated the comfort ride issues by improving damping properties of the vehicle suspension system along with the driver's seat with respect to the road excitations by equipping the passively controlled suspension system of a vehicle with the MR suspension and seat dampers via simulation models developed in MATLAB®/Simulink®. As a test object, we have

chosen a medium size bus – ISUZU-NP70 with a passively controlled suspension and seat damper and used 3-axis accelerometers installed on the floor and seats of the bus to measure vertical and two horizontal accelerations on the floor and seats of the bus.

2   Literature Review

There are many relevant studies carried out within the domain of comfort ride issues and improvement of dynamic and damping properties of the vehicle suspension and driver's seat. For instance, the work [2] is dedicated to studying the effects of stiffness and damping properties of the bus suspension system by performing numerical studies in MATLAB in frequency domain analysis of road excitations. Key attention in this study is given to the estimation of the root mean square values of weighted vertical acceleration in the car body along with the resonant (natural) frequencies of the car body. In the studies of [3], an assessment of road roughness and its influence on the ride comfort and vehicle dynamics is carried out and as an essential excitation of vibration in the comfort ride is found to be in the range of 0.5 Hz to 50 Hz. Another study [4] is dedicated to the method of evaluating the stiffness and damping properties of a cabin suspension system for heavy-duty trucks and is limited with the studies of a linear model for a simplified 3-DOF system for a whole vehicle cabin. In this study, one of the assumptions is to treat the driver's seat and cabin as one rigid body; however, in reality, the driver's seat has its own dynamics and damping properties that all are designed to provide the comfort ride for the driver. Therefore, the proposed model cannot be sufficient for comfort ride studies in the driver's seat. The studies [5] are dedicated to designing integrated controller for a driver's seat and suspension based on a quarter car model, composed of un-sprung mass (axle), sprung mass (car body), seat and a driver's mass, that has been designed to be 4-DOF system representing four main body parts of a human, viz. thigh, lower and upper torsos, and head. The developed control strategies in numerical simulations have demonstrated to be efficient in damping road disturbances. Another study [6] is carried out to investigate the optimization of the non-linear quarter car suspension-seat-driver model by treating human body as a 4-DOF system similar to the work [5]. Similar studies [7–9] with a quarter-car model along with a driver model are performed. In the recent years, there have been many studies with the design applications of magneto-rheological (MR) dampers [10–12] with non-linear hysteresis loop characteristics for semi-active dampers and shock absorbers. The studies [13] of the MR dampers are focused on the comparative analyses and parameter dependencies of the MR dampers in the example of quarter car model with the golden car parameters [14, 15] via modelling MR damper with Bingham [16], Dahl [17], LuGre [18, 19] and Bouc–Wen [20, 21] models.

3   Research Methodology

We have considered a quarter vehicle model in terms of simplicity in our numerical simulations in order to verify and modify our anticipated MR suspension and seat dampers. We have studied three case scenarios, which are passively controlled by

suspension and seat damper model, MR damper is equipped with the suspension and passive seat damper model, and MR damper is equipped with the suspension and seat model. The considered physical models for the quarter vehicle model are shown in Fig. 1. It should be noted in the models that the seat mass includes the driver's mass as well and driver (human body) model is not considered to be a separate system with its own physical and dynamic properties.
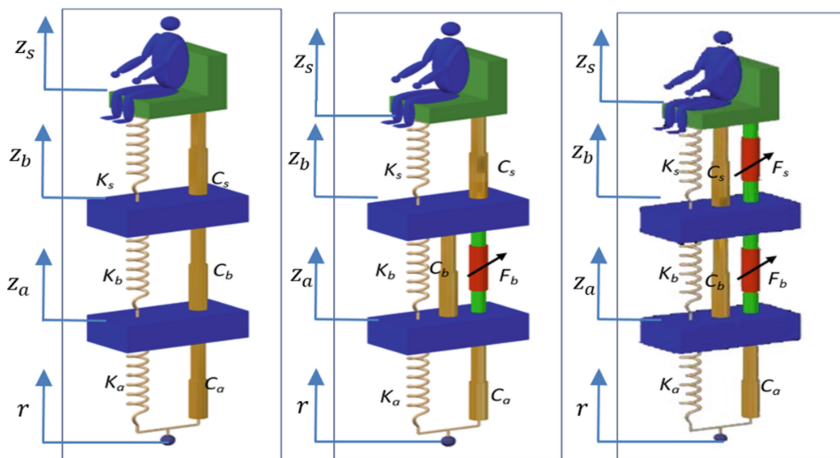

Fig. 1. Quarter Vehicle model configurations: (1) Passive suspension and seat damper model; (2) The MR damper equipped suspension and Passive seat damper model; (3) The MR damper equipped suspension and MR damper equipped seat model.

From the suspension and seat damper configuration shown in Fig. 1, we have derived the equations of motion of the quarter car model as a 3-DOF system with three masses, which are an axle (including tires), a car body and a seat (including driver's mass).

1. Passive suspension and seat model:

$$\begin{cases} m_a \cdot \ddot{z}_a + (c_a + c_b)\dot{z}_a + (k_a + k_b)z_a - c_b\dot{z}_b - k_bz_b = k_ar + c_a\dot{r} \\ m_b \cdot \ddot{z}_b + (c_b + c_s)\dot{z}_b + (k_b + k_s)z_b - c_b\dot{z}_a - k_bz_a - c_s\dot{z}_s - k_sz_s = 0 \\ m_s \cdot \ddot{z}_s + c_s\dot{z}_s + k_sz_s - c_s\dot{z}_b - k_sz_b = 0 \end{cases} \quad (1)$$

2. The MR damper is equipped with the suspension and passive seat model:

$$\begin{cases} m_a \cdot \ddot{z}_a + (c_a + c_b)\dot{z}_a + (k_a + k_b)z_a - c_b\dot{z}_b - k_bz_b = -F_b + k_ar + c_a\dot{r} \\ m_b \cdot \ddot{z}_b + (c_b + c_s)\dot{z}_b + (k_b + k_s)z_b - c_b\dot{z}_a - k_bz_a - c_s\dot{z}_s - k_sz_s = F_b \\ m_s \cdot \ddot{z}_s + c_s\dot{z}_s + k_sz_s - c_s\dot{z}_b - k_sz_b = 0 \end{cases} \quad (2)$$

3. The MR damper is equipped with the suspension and seat model:

$$\begin{cases} m_a \cdot \ddot{z}_a + (c_a + c_b)\dot{z}_a + (k_a + k_b)z_a - c_b\dot{z}_b - k_bz_b = -F_b + k_ar + c_a\dot{r} \\ m_b \cdot \ddot{z}_b + (c_b + c_s)\dot{z}_b + (k_b + k_s)z_b - c_b\dot{z}_a - k_bz_a - c_s\dot{z}_s - k_sz_s = F_b - F_s \\ m_s \cdot \ddot{z}_s + c_s\dot{z}_s + k_sz_s - c_s\dot{z}_b - k_sz_b = F_s \end{cases} \quad (3)$$

Where $z_a, \dot{z}_a$ and $\ddot{z}_a$, z_b, $\dot{z}_b$ and $\ddot{z}_b$, $z_s, \dot{z}_s$ and $\ddot{z}_s$ are displacement, velocity and acceleration of the un-sprung mass (half of the axle mass and one wheel), the sprung mass (quarter vehicle's body mass), and seat mass (including driver's mass), respectively; c_a, c_b, c_s are damping coefficients of tire, suspension and seat; k_a, k_b, k_s are stiffness of tire, suspension, and seat; $r(t)$ and $\dot{r}$ are the terrain profile and its derivative with respect to longitudinal speed of the vehicle; m_a, m_b, m_s are masses of tire (including semi-axle), car body and seat (including the driver's mass). F_b is the damping force (force against the vertical motion of the car body) of the suspension generated by the MR damper that would take into account the terrain irregularities $r(t)$, that is the vertical displacement as a function of time and created as a lookup table with respect to the vehicle's speed. Similarly, F_s is the damping force generated in the seat by the MR damper that functions with respect to the disturbances coming from the vehicle body (floor of the cabin) after damping (by the suspension system) excitations caused by road irregularities. We set our objective to design such a controllable damper, capable of generating control forces F_b and F_s that respond to road profile irregularities adequately by providing a comfortable ride. For the controller model of the MR damper, there are several hysteresis effect models, viz. Bingham [16], Dahl [17], LuGre [18, 19] and Bouc–Wen [20, 21] models. We have chosen the Bingham Model [16] due to its simplicity and relatively high performances for the random road profile irregularities that were studied by [13] for the quarter car model and rational parameter values of the model are found. The Bingham model given in [16] can be expressed with the following first order differential equations to formulate the dynamic hysteresis behaviors of the MR liquid dampers for the suspension and seat dampers.

For the suspension (car body):

$$F_b = F_c sgn(\dot{z}_1) + c_0\dot{z}_1 + K_0z_1 + F_0 \quad (4)$$

For the driver's seat:

$$F_s = F_{cs} sgn(\dot{z}_2) + c_{0s}\dot{z}_2 + K_{0s}z_2 + F_{0s} \quad (5)$$

where z_1, z_2 are the relative vertical displacements of the MR damper pistons corresponding to the vertical displacement (z_b) of a car body mass (m_b) and the displacement (z_s) of a seat mass (m_s); and $\dot{z}_1, \dot{z}_2$ are their derivatives, velocities of the MR damper pistons (installed on suspension and seat); F_c, F_{cs} is frictional (control) forces; c_0, c_{0s} are damping constants; K_0, K_{0s} are stiffness values of the elastic elements of the MR damper in the suspension and seat; F_0, F_{0s} are offset forces (constant force values). The signum function $sgn(\dot{z}_1)$, $sgn(\dot{z}_2)$ resolves the direction of the frictional forces F_c, F_{cs} with respect to the relative velocities $\dot{z}_1, \dot{z}_2$ of the hysteresis (internal) variables z_1, z_2. Note that in the simulation model z_1, z_2 and velocity $\dot{z}_1, \dot{z}_2$ correspond to the

displacements z_b, z_s and velocities $\dot{z}_b, \dot{z}_s$ of the car body (quarter car body) and seat masses (Fig. 1).

The Bingham model includes the Coulomb (dry) friction, plain (constant) damping, stiffness and some constant offset force and its controlled force direction changes with respect to the value of the velocities $\dot{z}_b, \dot{z}_s$. Moreover, its controllable damping forces F_c, F_{cs} contribute in the intensity of damping or on the contrary, releasing the damping force in order to dissipate fast and efficiently potential and kinetic energies induced by the uneven road profiles. In (4) ad (5), there is a discontinuity represented by the signum function $sgn()$ that can be altered by the inverse tangent function to approximate the expressions (4) and (5), that is expressed with the following formulations.

For suspension (car body):

$$F_b = \frac{2F_c \tan^{-1}(d \cdot \dot{z}_1)}{\pi} + c_0\dot{z}_1 + K_0z_1 + F_0 \qquad (6)$$

For seat:

$$F_s = \frac{2F_{cs} \tan^{-1}(d_s \cdot \dot{z}_2)}{\pi} + c_{0s}\dot{z} + K_{0s}z + F_{0s} \qquad (7)$$

where the terms d, d_s are form factors for the MR model in semi-active suspension and seat dampers, respectively.

Simulation Models. For the numerical simulations of the quarter car model with the passively controlled and semi-actively controlled suspension and seat dampers, we have developed MATLAB/Simulink model (Fig. 2) based on our derived formulations (1), (2) and (3) for the quarter vehicle's models along with the Bingham model formulations (4), (5), (6) and (7).

In the generalized model (Simulink) shown in Fig. 2, there are two types of input signals representing road excitations generated from the road profile irregularities. They are the Heaviside step function generated by Simulink block numerically and the measured road profile shown in Fig. 3. In the MR damper suspension model is added, the controllable MR force of the suspension F_b is fed to the summing junction of the forces of the suspension with (−) sign and the one of the axle/tire forces with (+) sign. Similarly, the MR damper is equipped with the suspension and seat models, the controllable force F_b and F_s are connected with the summing junctions with (−) and (+) signs, respectively. Also, the MR damper is added to the suspension and seat models along with the feedback signals from the car body's mass.

4   Results

We have measured road profile or terrain roughness (Fig. 3) on a selected 252.0 m long track along one wheel path by employing the device - Leica™ laser level meter. While measuring the road profile we have split the chosen lane into equally spaced 0.25 m long grids and measured the deviation of each marked point (from the horizontal axis) or unevenness of the road surface w.r.t. the first reference point ('0').
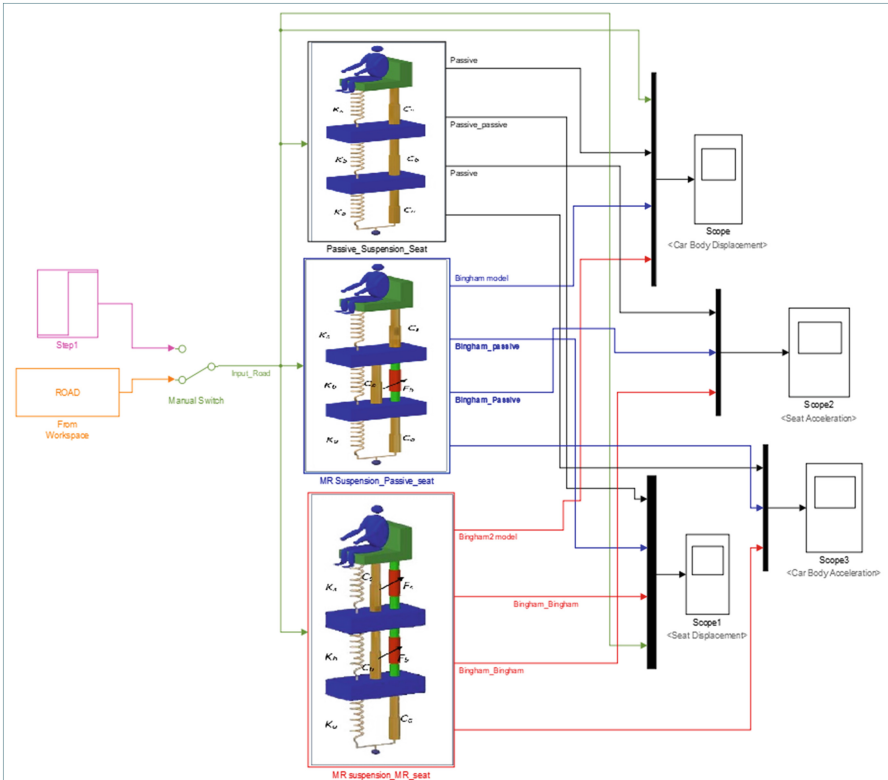
Fig. 2. Simulink model connecting the passive, semi-active (suspension) and semi-active (suspension and seat) models.
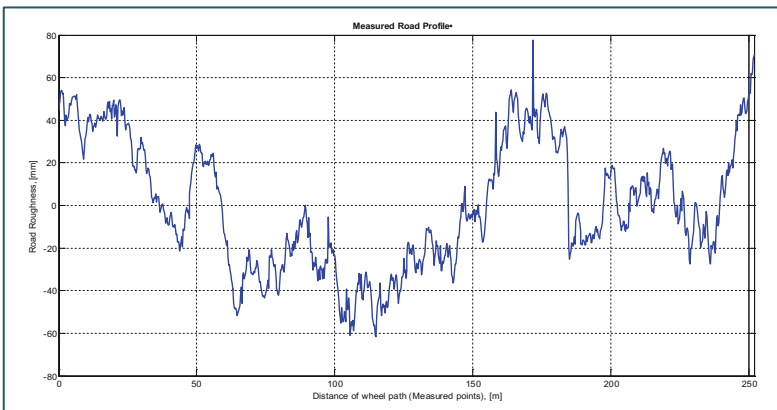

Fig. 3. Measured road profile.

From the plot of the measured road profile, it is clear that the chosen short segment of the road is in considerably poor conditions with many loopholes and bumps. We have also carried out acceleration measurements using one, two, and three-axis accelerometers on the floor and seats (passenger and driver seats) of the bus (Fig. 4) – ISUZU NP70 on the chosen road at different constant velocities – 20, 30, 40, 50 and 60 km/h. We have used 4-channel data acquisition A/D converts – DT 9837 and NI. Figure 5 shows one of the acceleration measurements collected from the accelerometer installed on the passenger's seat on the selected road part at the speed of 30 km/h. Our studied cases have demonstrated on the bus ISUZU NP70 that for the chosen road terrains average acceleration values on the driver's and passenger's seats and floors are considerably higher than the comfort level values of the whole body vibration stated in ISO 2631 [1].
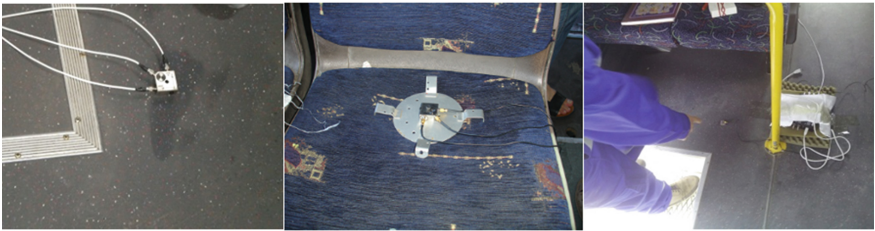
Fig. 4. Installation of accelerometers and measurements.
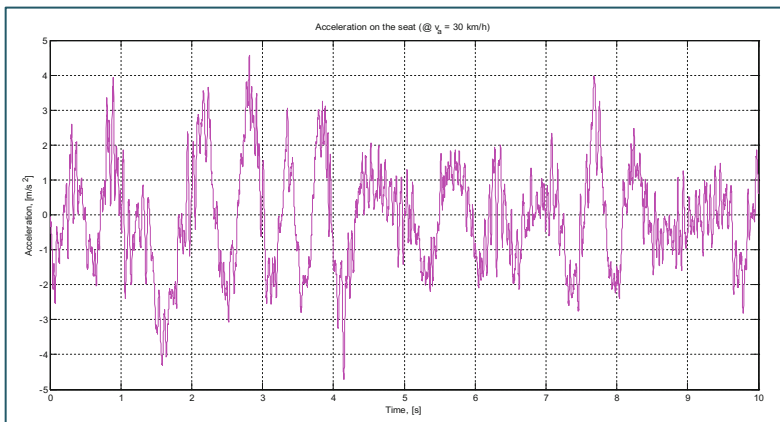

Fig. 5. Acceleration measured with an accelerometer on the passenger's seat.

For numerical simulation models, to feed the models with the road profile data, a terrain roughness is defined to be a function of time by interpolating the measured data and considering the time spent to cover the distance of 252 m at a constant velocity (e.g. 20, 30, 40, 50, 60 km/h) of the vehicle.

The interpolated road profile data are used as an input signal for $r(t)$. Besides, we have used the Heaviside step function representing a sharp uneven road profile with the magnitude of 0.075 m. The Step function is expressed by $r(t) = \begin{cases} 0, & t < 1 \\ 0.075, & t = 1 \\ 0.075, & t > 1 \end{cases}$. In our developed model simulations, we have used the Golden Car parameters taken from [13–15], driver's seat parameters given in Table 1, and MR damper parameters for the Bingham model given in Tables 2 and 3. From the simulation results of the Simulink models (Fig. 2), it is clear that the model with the MR damper suspension and MR seat damper has outperformed the passive suspension with a passively damped driver's seat considerably in damping vertical motion (displacement and acceleration). For instance, Figs. 6 and 7 show that the models with MR damper in suspension and the driver's seat dissipate the energy and diminish the undesired vertical displacements and accelerations in the vehicle's body and the driver's seat substantially higher than the passive suspension and seat damper model does. The MR damper equipped with the suspension and seat decreases the vertical accelerations within the range of $-1.3 \dots 1.5 \frac{m}{s^2}$. That means the MR damper's vibration damping efficiency is about 70% higher than the conventional passive damper. The system responses on the Heaviside (step)

Table 1. Driver's seat parameters.

Parameter name	Parameter notation	Parameter value
Mass of seat (incl. driver's mass)	m_s	90 [kg]
Stiffness of seat	k_s	2850 [N/m]
Damping coefficient of seat	c_s	135 [N·s/m]

Table 2. Suspension's MR damper parameters (for Bingham model).

Parameter name	Parameter notation	Parameter value
Damping coefficient	c_0	650 [N·s/m]
Offset force	F_0	0 [N]
Frictional force	F_c	210 [N]
Stiffness of an elastic component	k_0	300 [N/m]
Form factor	d	**10**

Table 3. Seat's MR damper parameters (for Bingham model).

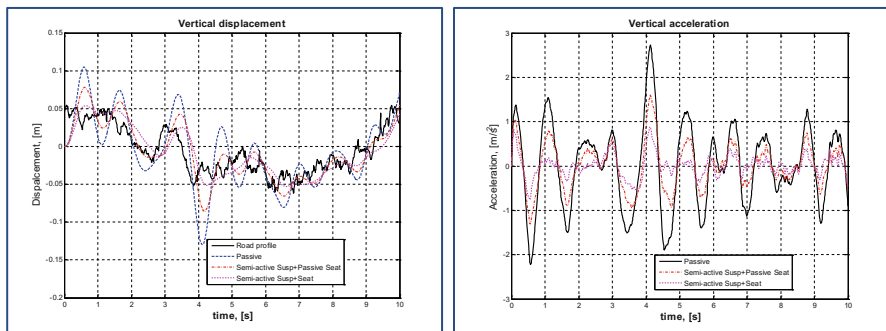| Parameter name	Parameter notation	Parameter value
Damping coefficient	c_{0s}	65 [N·s/m]
Offset force	F_{0s}	0 [N]
Frictional force	F_{cs}	21 [N]
Stiffness of an elastic component	k_{0s}	30 [N/m]
Form factor	d_s	10

Fig. 6. Vertical displacement and acceleration of driver's seat w.r.t. the measured road profile.
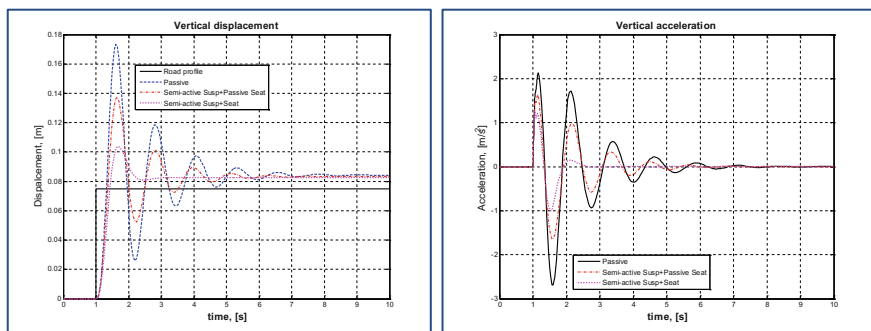

Fig. 7. Vertical displacement and acceleration of driver's seat w.r.t the step input.

function with the magnitude of 0.075 m – Fig. 7 demonstrate that the model with the MR dampers installed in suspension and driver's seat can dissipate the energy from the vertical motion in about 1.5 s whereas passive suspension does it in about 7.5 s.

5   Conclusions

From our performed experimental studies and road tests, it was clear that the medium size bus ISUZU-NP70's suspension system could not provide sufficient comfort ride on relatively poor terrain profiles. The studied models of the passive and semi-active suspension and seat models with respect to the two excitation signals, viz. measured road profile and Heaviside step function representing the terrain roughness have shown that the MR damper equipped with the suspension model outperforms passively controlled suspension model in damping undesired vibrations (vertical motion) of the car body substantially. Furthermore, the MR damper installed in the driver's seat would enhance comfort ride substantially by diminishing undesired vertical accelerations and displacements in the seat for more than 70% in comparison with the passive damper in the example of the Golden Car parameters for a quarter car model. Our further studies

will be dedicated to studying the applicability of the MR damper for the whole car model by considering other motions such as pitch, roll, and yaw, and identify rational parameter values of the semi-actively controlled MR dampers for the whole suspension system and the driver's seat.

References

1. ISO 2631.: Guide for evaluation of human exposure to whole-body vibration. 31 p. (1978)
2. Sekulic, D., Dedovic, V.: The effect of stiffness and damping of the suspension system elements on the optimization of the vibrational behavior of a bus. Int. J. Traffic Transport Eng. **1**(4), 231–244 (2011)
3. Kawamura, A., Kaku, T.: An evaluation of road roughness and the effects on riding comfort and vehicle dynamics. In: Proceedings of the JSCE, No. 359/N-2, pp. 137–147 (1985)
4. Zhao, L., et al.: A method to evaluate stiffness and damping parameters of cabin suspension system for heavy truck. Adv. Mech. Eng. **8**(7), 1–9 (2016)
5. Du, H., Li, W., Zhang, N.: Integrated seat and suspension control for a quarter car with driver model. IEEE Trans. Veh. Technol. **61**(9), 3893–3908 (2012)
6. Nagarkara, P.M., et al.: Optimization of nonlinear quarter car suspension–seat–driver model. J. Adv. Res. **7**, 991–1007 (2016)
7. Kuznetsov, A., Mammadov, M., Sultan, I., Hajilarov, E.: Optimization of a quarter–car suspension model coupled with driver biomechanical effects. J. Sound Vib. **330**, 2937–2946 (2011)
8. Gundogdu, O.: Optimal seat and suspension design for a quarter car with driver model using genetic algorithm. Int. J. Ind. Ergonom. **37**, 327–332 (2007)
9. Badran, S., Salah, A., Abbas, W., Abouelatta, O.: Design of optimal linear suspension for quarter car with human model using genetic algorithms. Res. Bull. Jordan ACM **II**(II), 42–51 (2012)
10. Sapinski, B.: Magneto-rheological dampers in vibrational control of mechanical structures. Mechanics **28**(1), 18–25 (2009)
11. Braz Cesar, M., Carneiro de Barros, R.: Properties and numerical modeling of MR dampers. In: Proceedings of 15th International Conference on Experimental Mechanics. Porto, Portugal (2012)
12. Jolly, M.R., Al-Bender, B.F., Carlsson, J.D.: Properties and applications of commercial magneto-rheological fluids. J. Intell. Mater. Syst. Struct. **10**(1), 5–13 (1999)
13. Eshkabilov, S.: Modeling and simulation of non-linear and hysteresis behavior of magneto-rheological dampers in the example of quarter-car model. Eng. Math. **1**(1), 19–38 (2016)
14. Ikhouane, F., Rodellar, J.: Systems with Hysteresis: Analysis, Identification and Control Using the Bouc–Wen Model. Wiley, Chi Chester (UK) (1987)
15. Gillespie, T.D., Sayers, M.W., Segel, L.: Calibration of response-type road roughness measuring systems. Journal: National Cooperative Highway Research Program Report 228 (December) (1980)
16. Stanway, R., Sproston, J.L., Stevens, N.G.: Non-linear modelling of an electro-rheological vibration damper. J. Electrost. **20**, 167–184 (1987)

17. Dahl, P.R.: A solid friction model. Technical Report, TOR-158(3107-18). The Aerospace Corporation, El-Segundo, CA (1968)
18. Canudas de Wit, C, Olsson, H.J., Astrom, K.J., Lischinsky, P.: Dynamics friction models and control design. In: American Control Conference, pp. 1920–1926. San Francisco, USA (1993)
19. Canudas de Wit, C., Olsson, H., Astrom, K.J., Lischinsky, P.: A new model for control of systems with friction. IEEE Trans. Autom. Control **40**(3), 419–425 (1995)
20. Bouc, R.: Forced vibrations of mechanical systems with hysteresis. In: Proceeding of the 4th Conference on Nonlinear Oscillations, pp. 315–321. Prague, Czechoslovakia (1967)
21. Wen, Y.K.: Method for random vibration of hysteretic systems. J. Eng. Mech. Div. **102**(2), 249–263 (1976)

A Semi-implicit Generalized Finite Differences Approach to Simulate Natural Convective Viscous Flows

Felix Raymundo Saucedo-Zendejo[(✉)]
and Edgar Omar Resnediz-Flores

The Technological Institute of Saltillo, Blvd. V. Carranza 2400 Col.
Tecnológico, 25280 Saltillo, Coahuila, Mexico
feliks@live.com.mx

Abstract. The purpose of this work is to carry out a Lagrangian semi-implicit Generalized Finite Differences (GFDM) implementation to simulate transient natural convective viscous flows. The solution of the incompressible Navier–Stokes equations is formulated through the first order Chorin's projection method whilst the energy equation is implicitly discretized with the first order Euler scheme. The semi-implicit set of discretized equations is solved with the Finite Point set Method where the incorporation of the boundary conditions is done in a direct and simple manner without requiring any special treatment or stabilization. The main features behind this mesh free approach as well as details of its implementation are shown. The suitability and the accuracy of this approach for the numerical simulation of the transient natural convective viscous flows are demonstrated through the solution of the two-dimensional benchmark problem. Finally, the stability of this FPM approach is studied through the variation of parameters in the two-dimensional benchmark problem, which shows that this formulation is a promising numerical tool for the simulation of the processes involving convective thermal flows.

Keywords: Mesh less method · GFDM · Thermal flow
Finite Point set Method

1 Introduction

Natural convective flow is a physical phenomenon involved in many industrial applications such as cooling devices, insulation tools, thermal energy collection devices or double glazing, to name just a few of them, and it is also involved in many material transformation processes, such as casting, mould filling and furnace treatments. Therefore, many theoretical, numerical and experimental studies on the natural convective flows and heat transfer in the two-dimensional enclosures have been performed [1]. Unfortunately, it is very difficult to improve and optimize this kind of processes with experimental techniques since it is impossible to measure velocities, temperatures and pressures exactly without interfering with the process.

2 Literature Review

Numerical simulation is commonly used to improve these processes since it provides a large amount of information that cannot be obtained through other methods. Numerical mesh-based methods such as the Finite Element Method (FEM), Finite Difference Method (FDM), and more recently, mesh free methods as Lattice Boltzmann Method (LBM), Local Radial Basis Function Method (LRBFM), Meshless Local Petrov-Galerkin Method (MLPG), Oñate's Finite Point Method (FPM) and the Local Radial Basis Function Collocation Method (LRBFCM) have already been used to analyze this kind of processes [1–6]. The advantages of the mesh free methods over mesh-based methods are in the use of the set of finite nodes to represent the problem domain and its boundaries without requiring any information about the relationship between nodes so that they do not form an element mesh which allows modeling discontinuities and deformations in the domain without the need of using the remeshing approaches. Therefore, this fact provides the flexibility to add or remove nodes wherever and whenever needed and it allows developing adaptive schemes easily.

A truly mesh free GFDM is the so-called Finite Point set Method (FPM) developed by Kuhnert [7]. It has proven to be far superior over the traditional mesh-based and some other meshless methods to treat fluid dynamics problems with rapidly changing domains, free surface or multiphase flows, and heat transfer problems [7–11]. This is a Lagrangian strong-form method which uses the weighted least squares (WLSM) interpolation scheme to approximate the spatial derivatives and to solve elliptic partial differential equations [8]. It has many advantages over other methods since it is able to incorporate any kind of boundary conditions naturally and easily without requiring any special treatment or stabilization and it is simple to implement. Therefore, in this work we propose the application of Finite Point set Method of Kuhnert to model transient natural convective viscous flows. In order to get some insight on his performance we compute the numerical solution of the benchmark test. The structure of the paper is as follows: Sect. 2 shortly describes the governing equations. Section 3 describes the basic ideas of FPM and the numerical procedure used to solve the governing equations followed by the numerical test presented in Sect. 4 with its corresponding results. Finally, some conclusions are given in last section.

3 Research Methodology

3.1 Governing Equations

The governing equations of a natural convective fluid flow are the Navier–Stokes equations with the Boussinesq approximation, which in the Lagrangian form are

$$\frac{D\mathbf{v}}{Dt} = -\frac{1}{\rho}\nabla p + v\nabla^2\mathbf{v} + \mathbf{a} + \mathbf{g}\beta(T - T_r) \tag{1}$$

$$\nabla \cdot \mathbf{v} = 0 \tag{2}$$

$$\rho c \frac{DT}{Dt} = \nabla \cdot (k\nabla T) \tag{3}$$

where ρ is the density, T is the fluid temperature, k is the thermal conductivity, $\mathbf{v}$ is the velocity, c is the effective specific heat, p is pressure, v is the kinematic viscosity, $\mathbf{a}$ is the net acceleration vector due all body forces, β is the volumetric thermal expansion coefficient, T_r is a reference temperature, $\mathbf{g}$ is the gravitational acceleration vector and t is time. The thermal problem is completed by specifying proper boundary and initial conditions. Typical boundary conditions for this kind of problem can be written as follows:

$$\mathbf{v}|_{\partial\Omega_i} = \mathbf{b} \tag{4}$$

$$T|_{\partial\Omega_i} = T_0 \tag{5}$$

$$\kappa\nabla T|_{\partial\Omega_i} \cdot \mathbf{n} = q \tag{6}$$

where $\partial\Omega$ indicates the kind of boundary, $\mathbf{b}$ is a prescribed value for the velocity, T_0 is the initial temperature, $\mathbf{n}$ is the outward unitary normal vector on $\partial\Omega$ and q is the local flux density, which could be zero for isolated boundaries or could be $q = h_c(T - T_\infty) + h_r(T - T_\infty)$, where h_c is the convective heat transfer coefficient, T_∞ is the ambient temperature and h_r is the radiative heat transfer coefficient which is proportional to the Stefan–Boltzmann constant and the surface emissivity.

3.2   Numerical Scheme

Along this section, we will describe some details regarding the numerical implementation of FPM applied to this problem. If an implicit first order Chorin's projection method is used to uncouple the velocity and pressure fields in Eqs. (1) and (2) and (3) is discretized using and implicit Euler scheme with respect to the time, we obtain the following numerical algorithm for T, $\mathbf{v}$ and p:

1. Move the point cloud:

$$\mathbf{x}^{n+1} = \mathbf{x}^n + \Delta t \mathbf{v}^n \tag{7}$$

2. Solve the new temperature:

$$\rho c T^{n+1} - \Delta t \nabla \cdot \left(\kappa\nabla T^{n+1}\right) = \rho c T^n \tag{8}$$

3. Solve the intermediate velocity:

$$\mathbf{v}^{*n+1} - \Delta t v \nabla^2 \mathbf{v}^{*n+1} = \mathbf{f} \tag{9}$$

4. Solve the pressure:

$$\nabla^2 p^{n+1} = \frac{\rho}{\Delta t} \nabla \cdot \mathbf{v}^{*n+1} \tag{10}$$

5. Compute the new velocity:

$$\mathbf{v}^{n+1} = \mathbf{v}^{*n+1} - \frac{\Delta t}{\rho} \nabla p^{n+1} \tag{11}$$

where $\mathbf{v}^*$ is an intermediate velocity, $\mathbf{f} = \mathbf{v}^n + \Delta t \mathbf{a} + \Delta t \mathbf{g} \beta (T^{n+1} - T_r)$, Δt denotes the time step and the superscripts n and $n+1$ denote the level of time. Equations (8), (9) and (10) are elliptic partial differential equations, which can be written in the following general form

$$Af + \mathbf{B} \cdot \nabla f + C\nabla^2 f = D \tag{12}$$

and the boundary conditions take the general form

$$Ef + G\nabla f \cdot \mathbf{n} = H. \tag{13}$$

3.3   The Finite Point set Method

In this section, we describe the main ideas of the FPM method proposed by [7]. The FPM is a member of the family of the GFDM and it is based on the WLSM. Following [10]:

Let Ω be a given domain with the boundary $\partial\Omega$ and suppose that a set of points $\mathbf{r}_1$, $\mathbf{r}_2$, $\cdots$, $\mathbf{r}_N$ are distributed with the corresponding function values $f(\mathbf{r}_1)$, $f(\mathbf{r}_2)$, $\cdots$, $f(\mathbf{r}_N)$. The problem is to find an approximate value of f at some arbitrary location $f(\mathbf{r})$ using its discrete values at particles positions inside a neighborhood of $\mathbf{r}$. To define the set of particles and the neighborhood of $\mathbf{r}$, a weight function w_i is introduced

$$w_i = w(\mathbf{r}_i - \mathbf{r}; h) = \begin{cases} e^{-\alpha \frac{\|\mathbf{r}_i - \mathbf{r}^2\|}{h^2}}, & \|\mathbf{r}_i - \mathbf{r}\| \leq h \\ 0, & \text{otherwise} \end{cases} \tag{14}$$

where h is the smoothing length, α is a positive constant whose value is considered to be 6.5 and $\mathbf{r}_i$ is the position of the i - th particle inside the neighborhood. A Taylor's series expansion of $f(\mathbf{r}_i)$ around $\mathbf{r}$ reads

$$f(\mathbf{r}_i) = f(\mathbf{r}) + \sum_{k=1}^{3} f_k(\mathbf{r})(r_{k_i} - r_k) + \frac{1}{2}\sum_{k,l=1}^{3} f_{kl}(\mathbf{r})(r_{k_i} - r_k)(r_{l_i} - r_l) + e_i \tag{15}$$

where e_i is the truncation error of the Taylor's series expansion, r_{k_i} and r_k represent the k - th components of the position vectors $\mathbf{r}_i$ and $\mathbf{r}$, respectively. f_k and f_{kl} ($f_{kl} = f_{lk}$)

represent a set of the first and second spatial derivatives at particle position $\mathbf{r}$. The values of f_k and f_{kl} can be computed minimizing the error e_i for the n_p Taylor's series expansion of $f(\mathbf{r}_i)$ corresponding to the n_p particles inside the neighborhood of $\mathbf{r}$. This system of equations can be written in a matrix form as $\mathbf{e} = \mathbf{M}\mathbf{a} - \mathbf{b}$, where $\mathbf{e} = [e_1, e_2, e_3, \cdots, e_{np}]^t$, $\mathbf{a} = [f, f_1, f_2, f_3, f_{11}, f_{12}, f_{13}, f_{22}, f_{23}, f_{33}]^t$, $\mathbf{b} = [f(\mathbf{r}_1), f(\mathbf{r}_2), \cdots, f(\mathbf{r}_{np})]^t$, $M = [s_1, s_2, \cdots, s_{np}]^t$, $s_i = [1, \Delta r_{1i}, \Delta r_{2i}, \Delta r_{3i}, \Delta r_{11i}, \Delta r_{12i}, \Delta r_{13i}, \Delta r_{22i}, \Delta r_{23i}, \Delta r_{33i}]^t$, $\Delta r_{ki} = r_{ki} - r_k$, $\Delta r_{kli} = (r_{ki} - r_k)(r_{li} - r_l)$ and $\Delta r_{kki} = 0.5(r_{ki} - r_k)(r_{ki} - r_k)$, for $k, l = 1, 2, 3$ and $k \neq l$. The unknown vector $\mathbf{a}$ is obtained through WLSM by minimizing the quadratic form

$$J = \sum_{i=1}^{n} w_i e_i^2 \tag{16}$$

which reads $(M^t \, W \, M)\mathbf{a} = (M^t \, W)\mathbf{b}$, where $W = \text{diag}(w_1, w_2, \cdots, w_{np})$. Therefore, $\mathbf{a} = (M^t \, W \, M)^{-1}(M^t \, W)\mathbf{b}$. Such a way we automatically get the values of the function and its derivatives at points $\mathbf{r}$.

3.4   FPM for General Elliptic Partial Differential Equations

General elliptic partial differential equations as the Eq. (12) have been already studied in [8]. Following their works, we present, for the completeness the corresponding FPM discretization under this setting. In the FPM representation for a general elliptic equation, Eq. (12) must be taken together with the system of n_p Taylor's series expansion of $f(\mathbf{r}_i)$ around $\mathbf{r}$. In this case, the matrices we need to compute by each particle in Ω take the following form: $\mathbf{b} = [f(\mathbf{r}_1), f(\mathbf{r}_2), \cdots, f(\mathbf{r}_{np}), D]^t$, $M = [s_1, s_2, \cdots, s_{np}, s_E]^t$, and $W = \text{diag}(w_1, w_2, \cdots, w_{np}, 1)$, where $s_E = [A, B_1, B_2, B_3, C, 0, 0, C, 0, C]^t$ and $\mathbf{B} = [B_1, B_2, B_3]^t$. If $\mathbf{r}_i \in \partial\Omega$, additionally, we have to add the general boundary condition (13). Therefore, in this case, the matrices we need to compute by each particle in $\partial\Omega$ take the following form: $\mathbf{b} = [f(\mathbf{r}_1), f(\mathbf{r}_2), \cdots, f(\mathbf{r}_{np}), D, F]^t$, $M = [s_1, s_2, \cdots, s_{np}, s_E, s_B]^t$, and $W = \text{diag}(w_1, w_2, \cdots, w_{np}, 1, 1)$, where $s_B = [E, n_1, n_2, n_3, 0, 0, 0, 0, 0, 0]^t$.

If we define $\mathbf{Q} = [Q_1, Q_2, \cdots Q_{10}]^t$ as the first row of $(M^t \, W \, M)^{-1}$ and the terms in the moving least squares solution $\mathbf{a} = (M^t \, W \, M)^{-1}(M^t \, W)\mathbf{b}$ are worked out, we can see that the following linear equations arises

$$f(\mathbf{r}_j) = \sum_{i=1}^{n(j)} w_i(Q_1 + Q_2\Delta r_{1_i} + Q_3\Delta r_{2_i} + Q_4\Delta r_{3_i} + Q_5\Delta r_{11_i} + Q_6\Delta r_{12_i} + Q_7\Delta r_{13_i} + Q_8\Delta r_{22_i} + Q_9\Delta r_{23_i} + Q_{10}\Delta r_{33_i})$$

$$f(\mathbf{r}_i)[AQ_1 + B_1Q_2 + B_2Q_3 + B_3Q_4 + (Q_5 + Q_8 + Q_{10})]D$$

$$\tag{17}$$

where $f(\mathbf{r}_j)$ denotes the unknown function value at particle j and $n(j)$ the number of j-th particle neighbours. Since Eq. (17) is valid for $j = 1, 2, \cdots, N$, this can be arranged in a full sparse system of the linear equations $L\mathbf{F} = \mathbf{P}$ which can be solved by iterative methods. Thus, all kind of problems such as Eqs. (8–10) can be solved in this way, just adding appropriate entries in the systems of equations [8, 9, 11].

4   Results

In order to validate the ability of this FPM formulation to simulate a natural convective flow, a simplified test is reported and compared with the corresponding FEM solution. It corresponds with a thermal flow in a squared cavity driven by natural convection produced by a temperature difference in two opposite sides of a square cavity and it was selected since it is a popular benchmark to taste numerical methods. Initially the cavity fluid is at rest and its temperature is $T_0 = T_h$. The cavity dimensions are 0.05 m $\times$ 0.05 m and it was discretized with 2600 particles with a mean spacing of 0.001 m. The smoothing length was selected as 0.0032 m. On the other hand, the material properties are: coefficient of thermal expansion $\beta = 4 \times 10^5$ °C^{-1}, dynamic viscosity $\mu = 0.0025$ kg m^{-1} s^{-1}, density $\rho = 2500$ kg m^{-3}, gravitational acceleration $g = 9.81$ m s^{-2}, heat capacity $c = 1046$ J kg^{-1} °C^{-1} and thermal conductivity $k = 104.6$ W m^{-1} °C^{-1} s^{-1}. The hot wall is maintained at $T_h = 710$ °C whilst the cold wall is at $T_c = 610$ °C. Therefore, the temperature difference between the opposite walls is $\Delta T_0 = 100$ °C. The remaining walls are thermally isolated. The time step was chosen as $\Delta t = 0.01$ s and the simulation was carried out for 21.5 s. Finally, on the cavity walls a no-slip boundary condition for the velocity was used.

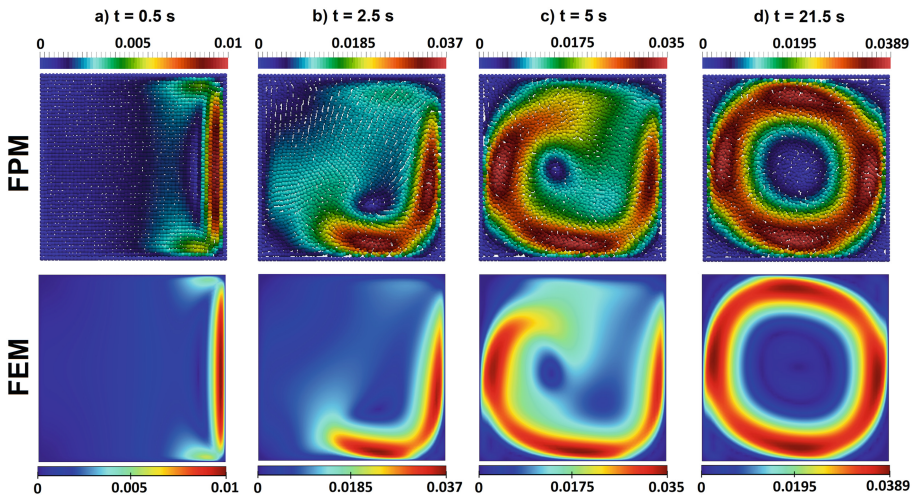The velocity and temperature profiles are shown in Figs. 1 and 2.

Fig. 1. Velocity patterns (m/s) at the selected time steps.

There, the velocity and temperature fields perfectly match the patterns predicted with FEM. These pictures indicate that this semi-implicit formulation of FPM performs well for the simulation of natural convective flows since the fluid and temperature patterns evolution is quite smooth and stable, and the accuracy of the solutions is suitable. The maximum velocity in the patch calculated with this formulation of FPM through time is shown in Fig. 3 and it has been compared with the corresponding FEM
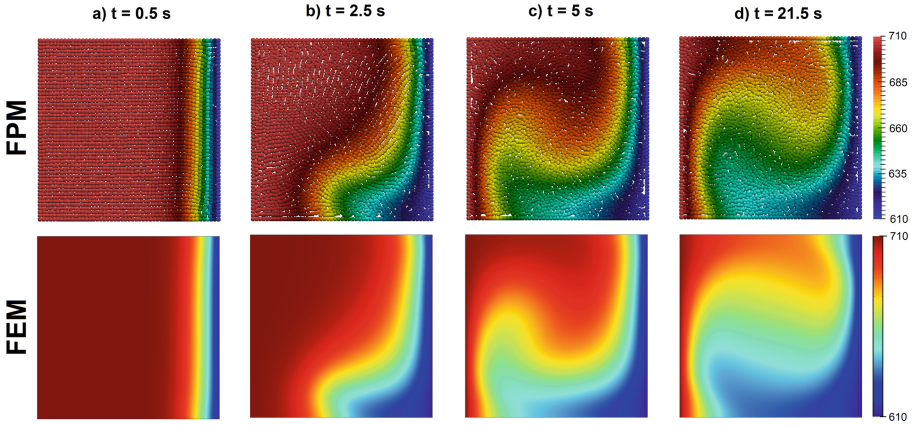
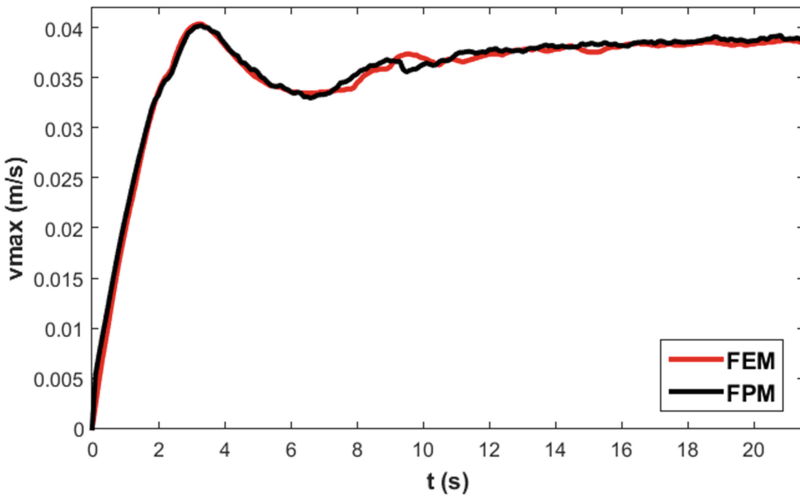**Fig. 2.** Temperature patterns (°C) at the selected time steps.

Fig. 3. Maximum velocity through time.

solution. There the effectiveness of this scheme to model this thermo hydrodynamic problem can be observed since the FPM results for the maximum velocity are quite similar to the corresponding values of the FEM computation. The small differences observed in the velocity profiles are directly attributed to the fact that our FPM solution was obtained with the complete Lagrangian and moving point cloud whilst the FEM simulation was calculated with the fixed squared mesh.

To further study the stability of this FPM approach for the simulation of natural convective flows, the previous driven cavity example was recomputed considering four different temperature differences between the opposite walls around 660 °C, which are

$\Delta T = 0.0625 \Delta T_0$, $\Delta T = 0.25 \Delta T_0$, $\Delta T = 4 \Delta T_0$ and $\Delta T = 16 \Delta T_0$, where the last and first examples were computed with a time step size of $\Delta t = 0.02$ s and $\Delta t = 0.005$ s, respectively. The velocity patterns at $t = 21.5$ s for all the previous cases are shown in Fig. 4. Here the stability of this approach can be perceived since the velocity profiles always remain smooth under different conditions. These results indicate that FPM is suitable and feasible for the simulation of natural convective flows.
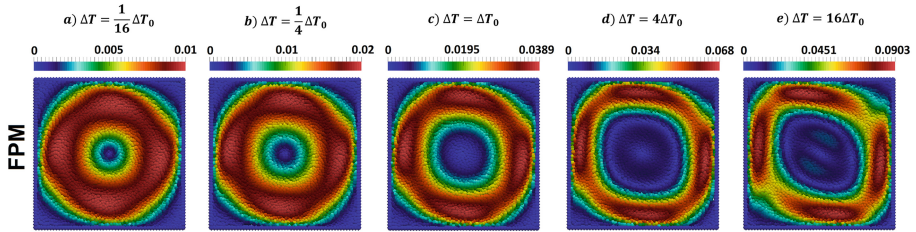

Fig. 4. Maximum velocities at $t = 21.5$ s.

5 Conclusions

The discussed semi-implict GFDM FPM approach to simulate natural convective flows has been successfully implemented and reported. Based on the numerical performance shown in the numerical examples, we can conclude that the current approach is suitable and feasible for the simulation of natural and industrial processes where natural convective flows are involved. It is stable and has enough accuracy to capture the thermal flow evolution in a smooth manner. Since this formulation is a truly mesh free method it could be used for the study and analysis of more complex problems involving high deformations and domain fragmentations with a great computational advantage because it does not need to compute any numerical quadrature and it does not need remeshing approaches. Further, it is able to handle any kind of boundary conditions naturally and easily without requiring any special treatment or stabilization and it is simple to implement. Therefore, it could be a promising numerical tool for the simulation of natural and industrial processes involving complex thermal flows and other phenomena described with elliptic partial differential equations. Consequently, it depicts a rich source of the research opportunities.

References

1. Zhang, T., Che, D.: Lattice Boltzmann simulation of natural convection in an inclined square cavity with spatial temperature variation. Numer. Heat Transf. Part A: Appl. **66**(6), 712–732 (2014)
2. Divo, E., Kassab, A.J.: Localized meshless modeling of natural-convective viscous flows. Numer. Heat Transf. Part B: Fundam. **53**(6), 487–509 (2008)

3. Arefmanesh, A., Najafi, M., Musavi, S.H.: Buoyancy-driven fluid flow and heat transfer in a square cavity with a wavy baffle—meshless numerical analysis. Eng. Anal. Bound. Elem. **37** (2), 366–382 (2013)
4. Chantasiriwan, S.: Solutions of buoyancy-driven flow problems by the local collocation method that uses multiquadrics as the radial basis function. J. Res. Dev. KMUTT **31**(4), 643–658 (2008)
5. Kosec, G., Šarler, B.: Numerical solution of natural convection problems by a meshless method. In: Convection and Conduction Heat Transfer (2011)
6. Oñate, E., Idelsohn, S., Zienkiewicz, O.C., Taylor, R.L.: A finite point method in computational mechanics. Applications to convective transport and fluid flow. Int. J. Numer. Methods Eng. **39**(22), 3839–3866 (1996)
7. Kuhnert, J.: General smoothed particle hydrodynamics, Ph.D. thesis, Technische Universität Kaiserslautern (1999)
8. Tiwari, S., Kuhnert, J.: Modeling of two-phase flows with surface tension by finite pointset method (FPM). J. Comput. Appl. Math. **203**(2), 376–386 (2007)
9. Reséndiz-Flores, E.O., Saucedo-Zendejo, F.R.: Two-dimensional numerical simulation of heat transfer with moving heat source in welding using the finite pointset method. Int. J. Heat Mass Transf. **90**, 239–245 (2015)
10. Tiwari, S., Kuhnert, J.: Finite pointset method based on the projection method for simulations of the incompressible Navier–Stokes equations. In: Meshfree Methods for Partial Differential Equations, pp. 373–387. Springer, Berlin (2003)
11. Saucedo-Zendejo, F.R., Reséndiz-Flores, E.O.: A new approach for the numerical simulation of free surface incompressible flows using a meshfree method. Comput. Methods Appl. Mech. Eng. **324**, 619–639 (2017)

Optimal Management of Small Hydroelectric Plants Power Generation in Local Electrical Systems

Petro Lezhnuk , Olexander Rubanenko[(✉)] , and Iryna Hunko

Vinnytsia National Technical University,
93 Khmelnytske Shose St., Vinnytsia 21021, Ukraine
`rubanenkoae@ukr.net`

Abstract. The number of renewable energy sources (photovoltaic power plants, small hydroelectric power plants and others) is growing rapidly. They transfer the generated electrical energy through the distribution networks of power supply companies. Therefore, the problem of calculating the normal modes of such electrical networks is urgent. This makes it possible to investigate the influence of renewable energy sources on the losses of electric power in distribution electrical networks. The given paper presents a mathematical model of active power losses of local electrical systems - electrical systems of power supply companies. The sources of electricity for such systems are not only powerful electric stations, but also renewable energy sources. Often these are distributed sources of energy. That is why optimal management of such sources is complex. The article shows the determination of insensitivity zones of the optimal points deviations in which the power fluxes are distributed to the change in the load power and generation in the nodes of local electrical systems. The mathematical expression is proposed where similarity criteria are used, it allows to analyze the influence of generation of the investigated renewable energy source on the losses of active power. The significance of these similarity criteria can be determined from the optimality conditions of the dual criterion programming problem with respect to the direct problem. It is expected that the account of calculation results of dead zones will enable to determine a renewable energy source, for instance, a small hydroelectric power station. Control of the generated power of the selected power plant at this time provides minimal losses of electrical energy of distributed electric networks.

Keywords: Renewable energy sources · District electric networks
Power lines · Distributed sources of energy · Electricity losses
Mathematical model · The country's energy · Matrix of branches in the nodes

1 Introduction

A sign of today is the ever-increasing use of renewable energy sources (RES) which are considered as one of the most promising ways to solve growing energy supply problems. Often, such features of RES as ecological cleanliness and inexhaustible resource

base become crucial to their benefits in the face of increasing rates of environmental pollution and a rapid reduction of organic fuel resources.

Ensuring the country's energy independence and joining the European Union are two of the most important strategic tasks for the development of modern Ukraine. One of the conditions for a successful solution to both tasks is the maximum increase in the share of energy in the strategic balance, produced at the expense of its own energy resources, including RES. Ukraine has a great potential for a variety of RES.

It is also known that there are problems in Ukraine due to the use of traditional energy sources. The reasons are outdated technologies and the exhaustion of equipment resources in the power industry which, together with the low efficiency of fuel usage, lead to considerable increase of harmful emissions. The significant losses during transportation, distribution and use of electricity and heat, as well as a monopoly dependence on imports of energy carriers, complicate the situation on the energy markets of Ukraine. However, an increase in the generation of distributed energy sources (DES) without taking into account the peculiarities of their operation in power grids can lead to the deterioration of the electric energy quality, and sometimes to deterioration of equipment reliability indices in local electrical systems.

Consequently, the reduction of electricity losses in local electrical systems by means of coordinated control over the generation of solar power stations and small hydroelectric stations and the optimization of power flows in local electrical systems (LES) with RES are relevant, designed to ensure reduction of electricity losses in electrical networks, maintain balance reliability and improve the quality of electric energy supply.

A characteristic feature of today is the ever-increasing use of renewable energy sources (RESs) which are considered to be one of the most promising ways of solving growing energy supply problems. Such features of RES as ecological cleanliness and inexhaustible resource base become their main advantages in the conditions of increasing rates of environmental pollution and a rapid reduction of organic fuel resources.

Providing the country's energy independence and joining the European Union are two of the most important strategic tasks of the development of modern Ukraine. One of the conditions of a successful solution of both tasks is the maximum increase in the strategic balance of the share of energy produced at the expense of its own energy resources, including RES. Ukraine has a great potential of various RES.

It is also known that there are problems in Ukraine due to the use of traditional energy sources. The reasons of this are outdated technologies, the exhaustion of equipment resources in power industry, and all of this, together with the low efficiency of fuel use, leads to significant amounts of harmful emissions. Significant losses in the process of transportation, distribution and use of electric energy and heat, as well as a monopoly dependence on imports of energy carriers, complicate the situation in the energy markets of Ukraine. However, an increase in the generation volume of distributed energy sources (DESs) without taking into account the peculiarities of their operation in power grids can lead to the deterioration of electric energy quality, and sometimes to the deterioration of reliability indices of the equipment of local electrical systems.

2   Literature Review

In [1] Anand et al. state that in order to reduce electric energy losses and improve its quality indices, it is expedient to pass to solution of the complex problem of district electric grids (DEG), which involves the implementation of efficient design solutions and the introduction of operational reconfiguration systems of RES connection by means of Smart Grid.

Consequently, the reduction of electric energy losses in local electrical systems by means of coordinated control of the generation by solar power plants and small hydroelectric power stations, and the optimization of power flows in local electric systems (LES) with RES, are urgent, intended to provide the reduction of electric energy losses in power grids, maintain balance reliability and improve the quality of power supply

For example, in [2] the need for coordinated control of automated devices and photovoltaic generators in order to reduce the negative impact of the voltage increase in circuits of DESs by RES sources is substantiated, and an algorithm for reducing power losses and voltage stabilization by using voltage regulators and reactive power compensation devices in a microcontroller is suggested. In [3], an overview of the literature on optimal energy management and control modes of DES is presented and a hierarchical energy management architecture that requires a telecommunications infrastructure for the connection of distributed control on the level of DES with the upper level of control of the energy supply company where the optimization of grid operation mode is carried out, is analyzed. In [4], the issues of autonomous operation of DEG in the directions of symmetric load distribution between parallel operating inverters and compliance with the requirements of electric power quality are studied. In [5], the issue of influence optimization of the share of RES in the balance of reactive power of DEG of wind and solar power plants is discussed. The issue of estimating the forecast characteristics of solar power plants generation is a subject of scientific work in [6]. The article proposes new economic indices for the forecasting of the production of electric energy at solar power plants, considering the consequences of forecasting errors. In [7] a methodology was proposed for the development of equivalents of electric grids of low and medium voltage electric networks to study their impact on the reliability of power systems. In [8], the attention was paid to the creation of intelligent electric grids based on the SMART GRID concept, considering the features of the energy market and RES. The ways of compensating seasonal variations of RES generation are analyzed. In [9], it is shown that the grid configuration depends on the choice of individual generators' modes which allows to reduce the power losses in the system. Inconsistencies in operating modes can lead to excessive losses. In [10], it is said that the integration of RES in the distribution grid of rural areas can significantly improve the reliability of electric energy supply. Thus, the problem of optimal control of power generation by small hydroelectric power stations in local electrical systems is relevant and actively studied in foreign and domestic scientific works.

3   Research Methodology

In order to calculate the losses of active power in District Electric Networks the node voltage method [10] is chosen. The matrix of branches in the nodes, the matrix of the branches resistance and the matrix of currents in the nodes are used as the input parameters.

To calculate the steady-state DEN with DES, the mathematical model based on the node voltage method is adapted to the form of the output data of such networks, as well as to the tasks that are solved. The method and corresponding algorithm allow counting modes when the circuit of the network is closed and open, but some of the lines (those with the RES) are lines with two-way power supply. Moreover, the individual power lines can combine several different types of DES.

The mathematical model in the matrix form, depending on the output data, is used in the form where $\mathbf{Y_n}$ – is a matrix of nodal conductivity;

$$\mathbf{Y_n} \cdot \dot{\mathbf{U}} = \hat{\mathbf{U}}_{\mathbf{d}}^{-1} \hat{\mathbf{S}} - Y_b \cdot \dot{\mathbf{U}}_b \text{ or } \mathbf{Y_n} \cdot \dot{\mathbf{U}} = \dot{J} - Y_b \cdot \dot{\mathbf{U}}_b \tag{1}$$

Y_b – is a matrix-column of nodal conductivity relative to the balancing node with voltage $\dot{\mathbf{U}}_b$; $\hat{\mathbf{S}}$ is a vector of conjugated complex capacities of nodes; $\hat{\mathbf{U}}_{\mathbf{d}}^{-1}$ – inverse diagonal matrix of nodal voltage complexes; $\dot{\mathbf{J}}$ – is a vector of nodal currents.

Capacities or currents in nodes are provided as the sum of nodal loads and generation of RES:

$$\dot{\mathbf{S}} = \dot{S}_1 - \dot{\mathbf{S}}_{\mathbf{gHES}} - \dot{\mathbf{S}}_{\mathbf{gSES}} \text{ or } \dot{J} = \dot{\mathbf{J}}_1 - \dot{\mathbf{J}}_{\mathbf{gHES}} - \dot{\mathbf{J}}_{\mathbf{gSES}} \tag{2}$$

To study the effect of the generation of RES on power losses in DEN and its selected fragments, an algorithm based on the matrix of the distribution of power losses on the circuit branches, depending on the power in its nodes, is used [10]:

$$\Delta\dot{\mathbf{S}}_{\mathbf{b}} = \dot{\mathbf{T}} \cdot \dot{\mathbf{S}}, \tag{3}$$

where $\dot{S}_1, \ldots, \dot{S}_{gHES}$; $\Delta\dot{\mathbf{S}}_{\mathbf{b}}$ – is a vector of losses in the branches of the circuit, which are determined by the capacities.

Each matrix т line is defined as

$$\dot{\mathbf{T}}_{\mathbf{i}} = (\dot{\mathbf{U}}_{\mathbf{t}}\mathbf{M}_{\mathbf{i}})\widehat{\mathbf{C}}_{\mathbf{i}}\mathbf{U}_{\mathbf{d}}^{-1}, \tag{4}$$

where $\mathbf{M_i}$ – is branches matrix of connection in the nodes; $\widehat{\mathbf{C}}_{\mathbf{i}}$ – is the i line of the matrix for the distribution of currents in the nodes $\dot{\mathbf{J}}_1, \dot{\mathbf{J}}_{\mathbf{gHES}}, \dot{\mathbf{J}}_{\mathbf{gSES}}$ on the branches of the circuit. For a fragment of a network with dedicated HES, expression (4) is converted to

$$\Delta \dot{\mathbf{S}}_{\mathbf{bf}} = \dot{\mathbf{T}}_f \cdot \dot{\mathbf{S}}_{gHES}, \tag{5}$$

where $\dot{\mathbf{T}}_f = \dot{\mathbf{T}}_{fa} + \dot{\mathbf{T}}_{fr}$ – is the power loss distribution matrix in the fragment of the network. As a rule, the dependence of losses of active power and electricity from generation of hydroelectric power stations is interesting. If the power of HES tires is balanced in such a way that it does not consume or generate reactive power, then the expression (5) for the analysis of the impact of HES on the loss is considerably simplified:

$$\Delta P_b = T_{fa} \cdot P_{gHES}. \tag{6}$$

Expressions (1÷6) are a mathematical model of LES modes that enables to study the impact of HES and SES capacities on power losses in them and determine the optimal power generated by the losses criterion taking into account voltage constraints, transmission capacities and installed HES power.

Unplugging the network trunk at the point of flow distribution provides a minimum of power losses [11]. However, network segmentation at this point is associated with a number of problems. First, optimal location of power losses may not coincide with the location of the segmentation determined from the conditions of reliability. Secondly, the point of flow distribution in the network can "float", depending on the load, in addition, the point of flow distribution of active and reactive power may not coincide. The task is to ensure that a power network, open in accordance with the requirements of reliability, provides power fluxes that correspond to the point of flow distribution in a closed network. Thus, a reduction of electric power losses in DEN without reducing its reliability is achieved. In DEN with RES, it is possible to influence the power flows by modifying the generation of small HES and SES [11, 12]. However, considering that the optimal point of power flow and, accordingly, the calculated optimal power flows may change, this task can only be realized with the help of Industrial control system (ICS).

To create the normal conditions for the functioning of ICS it is necessary to establish for it a zone of insensitivity to the input parameters, which are the power load of consumers and the generation of DES.

By its physical content, this zone of insensitivity corresponds to the optimality region of electric energy losses in DEN when the power load of consumers and the generation of DES change [13, 14].

4   Results

The insensitivity zone of the functioning of ICS can be determined in relative units in accordance with the procedure outlined in [15]. To obtain a criterial model that relates the relative total active power losses in DEN with currents set in the nodes, the following equation is written in matrix form:

$$\Delta P = \dot{\mathbf{I}}_{\mathbf{t}} \, \mathbf{r} \, \hat{\hat{\mathbf{I}}}. \tag{7}$$

Let us express the losses $\Delta \mathbf{P}$ by the currents in the nodes. The currents in the network branches, if emf is missing, are defined as $\dot{\mathbf{I}} = \dot{\mathbf{C}} \dot{\mathbf{J}}$, where $\dot{\mathbf{C}}$ – is matrix of current distribution coefficients, $\dot{\mathbf{J}}$ – is current in the nodes of load and DES generation. Then (7) will be rewritten:

$$\Delta \mathbf{P} = \dot{\mathbf{J}}_{\mathbf{t}} \left(\dot{\mathbf{C}}_{\mathbf{t}} \, \mathbf{r} \, \hat{\hat{\mathbf{C}}} \right) \hat{\hat{\mathbf{J}}} \tag{8}$$

Rewrite (8) as follows: $\mathbf{B_a} = Re\left(\dot{\mathbf{C}}_{\mathbf{t}} \, \mathbf{r} \, \hat{\hat{\mathbf{C}}} \right)$; $\mathbf{B_p} = Im\left(\dot{\mathbf{C}}_{\mathbf{t}} \, \mathbf{r} \, \hat{\hat{\mathbf{C}}} \right)$ are valid symmetric matrices.

$$\Delta P = \dot{\mathbf{J}}_{\mathbf{t}} \, \mathbf{B_a} \, \hat{\hat{\mathbf{J}}} + j \, \dot{\mathbf{J}}_{\mathbf{t}} \, \mathbf{B_p} \, \hat{\hat{\mathbf{J}}}. \tag{9}$$

Further, according to the method described in [8], expression (9) is rewritten in a canonical quadratic form and by the method of integral analogues [7] the value of power losses in relative units is written:

$$\Delta \mathrm{P}_* = \sum_{i=1}^{m} \pi_{ja} \, \bar{\mathrm{J}}_{ja^*}^2 + \sum_{i=1}^{m} \pi_{jp} \, \bar{\mathrm{J}}_{jp^*}^2 \tag{10}$$

Or

$$\Delta P_* = \sum_{j=1}^{m} \pi_{ja} \left(\sum_{i=1}^{m} v_{jia} \frac{J_{iao}}{J_{jao}} J_{ia^*} \right)^2 + \sum_{j=1}^{m} \pi_{jp} \left(\sum_{i=1}^{m} v_{jip} \frac{J_{ipo}}{J_{jpo}} J_{ip^*} \right)^2 \tag{11}$$

$\pi_{ja}^J = \frac{b_{ja} \bar{J}_{jao}^2}{\Delta P_{min}}$; $\pi_{jp}^J = \frac{b_{jp} \bar{J}_{jpo}^2}{\Delta P_{min}}$ where is caused by the active and reactive components of currents in the nodes, respectively from the general expression for DEN with DES (11), we can obtain the expression for analysis of the effect on relative power losses P_* in the network, caused by the generation of DES. For example, for j-th DES with (11) we obtain:

$$\Delta \mathrm{P}_{*j} = \pi_{ja} v_{aj}^2 J_{ja^*}^2 + \pi_{jp} v_j^2 J_{jp^*}^2 \tag{12}$$

where v_{aj}, v_{pj} – are weight coefficients of the influence of the relative change of the current in the j-th node, expressed through the branches parameters.

Another possibility of determining relative power losses, depending on the power of a small hydroelectric power station, is the usage of expression (6). In this case, the influence of HES capacity on the losses of power is determined in the part of the electrical network on which this HES is operating. In practice, as a rule, the task is set

precisely because it is necessary to determine the zone of insensitivity for ICS of HES, corrective effects of which are determined by the local parameters of the mode [8].

To construct the dependence of power losses on the power of HES and further analysis of the sensitivity, calculations are carried out according to (6). Dependence is formed in tabular form. When using the criterion method as the basis of the algorithm for assessing the sensitivity of optimal solutions, the dependence of losses on the power of HES is approximated in the criterial form. In particular, we obtain certain advantage if the dependence Pf(Pg HES) is approximated in the form of a binomial polynomial:

$$\Delta P_{*j}(P_{g\ HES^*}) = a_j P_{g\ HES^*j}^{\alpha_j} + b_j P_{g\ HES^*j}^{b_j}, \tag{13}$$

where $\Delta P_{*j}(P_{g\ HES^*})$ – is the value of the target function (minimum losses of active power in the network or its part) in relative units; $P_{g\ HES^*j} = P_{g\ HES\ j}/P_{g\ HES\ jo}$ generation capacity of HES, with the help of which the LES modes are optimized, in relative units. (taken as the basic optimal values of generating capacity of HES); a_j, b_j, α_j, β_j – are constant coefficients reflecting the dependence and the degree of influence of HES generation on the value ΔP_{*j}. The advantage of approximating the target function in the form (13) lies in the fact that the direct and inverse task of sensitivity is solved in a simplified manner [16]. If there is no problem with the direct task – $\Delta P_{*j}(P_{g\ HES^*})$ in the right side of Eq. (13) the set deviation of the generation is substituted and the corresponding value of the losses is calculated, then the inverse task of sensitivity ΔP_* is more difficult. Since the Eq. (13) is nonlinear, the inverse problem of sensitivity refers to incorrect problems [15].

Figure 1 illustrates the determination of optimal solutions area, i.e., the inverse problem of sensitivity.
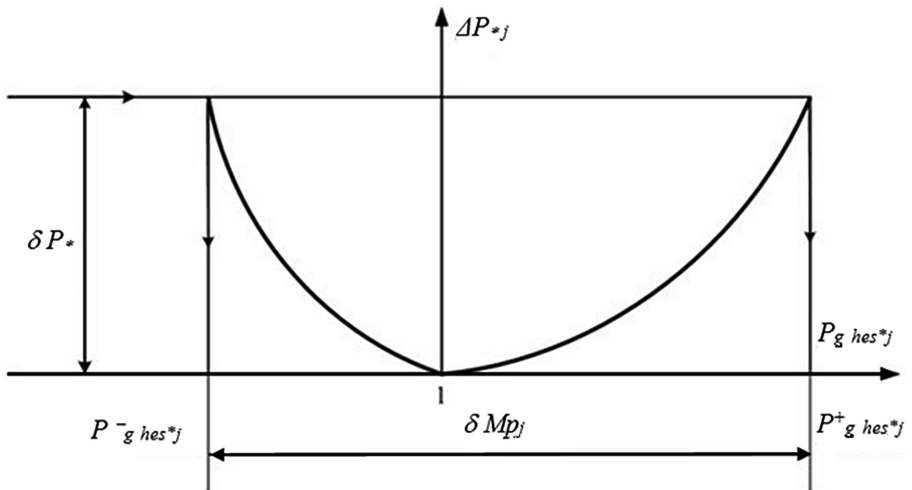

Fig. 1. Definition of optimal solution area (inverse sensitivity problem).

Limiting values of generating power with a given allowable deviation of power δP_* losses in a selected fragment of DEN [8]:

$$P^-_{g\,HES^*j} = \left(\frac{1}{\pi_{j1}} \cdot \frac{a_j}{1 + \delta P_*} \right)^{-1/\alpha}, \qquad P^+_{g\,HES^*j} = \left(\frac{1}{\pi_{j2}} \cdot \frac{b_j}{1 + \delta P_*} \right)^{-1/\beta}. \qquad (14)$$

The values of similarity criteria can be determined from the optimality conditions of the dual problem of criterion programming relative to the direct problem [15]. For (15):

$$\begin{cases} \alpha_j \pi_{j1} + \beta_j \pi_{j2} = 0; \\ \pi_{j1} + \pi_{j2} = 1. \end{cases} \qquad (15)$$

From the system of Eqs. (15) we obtain

$$\pi_{j1} = \frac{-\beta_j}{\alpha_j - \beta_j}, \ \ \pi_{j2} = \frac{\alpha_j}{\alpha_j - \beta_j}. \qquad (16)$$

Substitute in (14) the value of the similarity criteria (16) and finally observe:

$$P^-_{gHES^*j} = \left(\frac{\alpha_j - \beta_j}{-\beta_j} \frac{a_j}{1 + \delta P^*} \right)^{-1/\alpha}, \ \ P^+_{gHES^*j} = \left(\frac{\alpha_j - \beta_j}{\alpha_j} \frac{b_j}{1 + \delta P^*} \right)^{-1/\beta}. \qquad (17)$$

The resulting δM_P area of the allowable deviations of the variables from their optimal values, in essence, contains a set of possible equally-economical variants of HES generation with the set accuracy. The δM_P area is used to make decisions regarding the implementation of optimal modes, using HES.

It should be noted that the implementation of this approach is achieved by the reduction of the calculated number of impacts on DES. This is essential for GRAM systems of hydroelectric plants, since it makes the implementation of the control laws that are set for them real. In DEN, automating the process of optimal control of power flows is made possible by changing the allowable deviation of active power losses from the optimum value P to control the intensity of DES operation in order to increase the efficiency of their use. The values of the insensitivity zone of the optimality criterion P are established, based on the desire to maximize the effectiveness of each corrective effect of DES.

5   Conclusions

Since, in order to create the normal conditions for the functioning of ICS, it is necessary to establish for it a zone of insensitivity to the input parameters, which are the power load of consumers and the generation of DES, the method of determining insensitivity

areas of active power loss in DEN with RES to the change of the generated DES power was further developed. This method allows to determine the limits of insensitivity zones of active power losses in DEN with DES to the change of power generated by each HES, and choose the most influential one for reducing the losses of the hydro-electric power station.
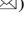
References

1. Anand, M. P., Ongsakul, W., Singh, J. G., Golshannavaz, S.: Economic operational Scheduling of a smart distribution network considering demand response, electric vehicles and network reconfiguration. In: 2015 IEEE Eindhoven, pp. 1–6. PowerTech, IEEE (2015)
2. Jung, J., Onen, A., Arghandeh, R., Broadwater, R.: Coordinated control of automated devices and photovoltaic generators for voltage rise mitigation in power distribution circuits. Renew. Energy **66**, 532–540 (2014)
3. Minchala-Avila, L., Garza-Castanon, L., Vargas-Martınez, A., Zhang, Y.: A review of optimal control techniques applied to the energy management and control of microgrids. In: The 5th International Conference on Sustainable Energy Information Technology (SEIT-2015), pp. 780–787. Elsevier, London (2015)
4. Han, H., Hou, X., Yang, J., Wu, J., Su, M., Guerrero, J.M.: Review of power sharing control strategies for islanding operation of AC microgrids. IEEE Trans. Smart Grid **7**(1), 200–215 (2016)
5. Shengqi, L., Lilin, Z., Yongan, L., Zhengping, H.: Optimal reactive power planning of radial distribution systems with distributed generation ISDEA. In: 2013 Third International Conference on Intelligent System Design and Engineering Applications, pp. 1030–1033. IEEE, Hong Kong (2013)
6. Bracale, A., Carpinelli, G., Rizzo, R., Russo, A.: Advanced method and cost-based indices for probabilistic forecasting the generation of renewable power. In: 3rd Renewable Power Generation Conference (RPG 2014), pp. 1–6. IET, Naples (2014)
7. Ilie, I., Hernando-Gil, I., Djokic, S. Z.: Reliability equivalents of LV and MV distribution networks. 2012 IEEE International Energy Conference and Exhibition (ENERGYCON), pp. 343–348. IEEE, Florence (2012)
8. Kirilenko, O.V., Pavlovskiy, V.V., Luk'yanenko, L.M., Trach, I.V.: The problem of integration of renewable source of energy into the "weak" electrical networks. Tech. Electrodyn. **3**, 25–26 (2012)
9. Tugay, Yu.I., Kozirskiy, V.V., Gay, O.V., Bodunov, V.M.: The integration of renewable energy sources in rural distribution electrical networks of village regiones. Tech. Electrodyn. **5**, 63–67 (2011)
10. Lezhniuk, P.D., Hunko, I., Kravchuk, S., Komada, P., Askarova, N., Arman, A.: Influence of distributed power sources on active power loss in electric grid. Przegląd Elektrotechniczny **93**(3), 107–112 (2017)
11. Komar, V.O., Kovalchuk, O.A., Kuzmyk, O.V.: Impact of distributed generation on the quality of distributed electric grids operation. Tech. Electrodyn. **2**, 34–35 (2012)
12. Keane, A., Ochoa, L., Vittal, E., Dent, C., Harrison, G.: Enhanced utilization of voltage control resources with distributed generation. IEEE Trans. Power Syst. **26**(1), 252–260 (2011)

13. Ardeshna, N. K., Chowdhury, B. H.: Supporting islanded microgrid operations in the presence of intermittent wind generation. In: Power and Energy Society General Meeting, pp. 1–8. IEEE, Providence (2010)
14. Keane, A., Ochoa, L. (N.)F., Vittal, E., Dent, C.J., Harrison, G.P.: Enhanced utilization of voltage control resources with distributed generation. In: Power and Energy Society General Meeting, pp. 1–8. IEEE, Providence (2010)
15. Medeiros, R., Xu, X., Makram, E.: Assessment of operating condition dependent reliability indices in microgrids. J. Power Energy Eng. **4**, 56–66 (2016)

Effect of Phase Composition on Cavitation Resistance of Ceramics

Alexander Litvinenko[1(✉)] 📖, Yuriy Boyko[1] 📖,
Bohdan Pashchenko[1] 📖, and Yuriy Sukhenko[2] 📖

[1] National University of Food Technologies,
68 Volodymyrska St., Kyiv 01601, Ukraine
litvinen@nuft.edu.ua, boykoyi@ukr.net
[2] National University of Life and Environmental Sciences of Ukraine,
15 Heroiv Oborony St., Kyiv 03041, Ukraine

Abstract. The results of the tests of technical ceramics in conditions of cavitation wear are presented. The ultrasonic frequencies of 22 and 44 kHz were used. The influence of the structural constituents of ceramics on the rate of failure is shown. Wear features are noted. The effect of additives on the durability of materials is analyzed. The nature of ceramics wear and its similarity to the mechanism of damage of metals are demonstrated. It is proposed to use the critical destruction power for the determination of intensity of ceramics wear. On the basis of structural energetic theory, an adapted formula is proposed for comparing the intensity of destruction of ceramics of different types. The results of calculations are correlated with the experimental data. In addition, the proposed approach makes it possible to use for the known materials the known dependences of the evaluation of the wear resistance of metals.

Keywords: Ceramic materials · Vibration · Wear · Specimens

1 Introduction

In various industries, it is important to use physical and mechanical effects, for example, hydrodynamic cavitation, to intensify the processes of processing the liquid-phase media. Microbubbles that arise during the decay of cavitation caverns, have an intense impact effect on the components of the medium. Such conditions accelerate the mass-exchange reactions [1, 2].

2 Literature Review

The most effective processing conditions correspond to the maximum wear of the working parts of equipment. The increase of their durability is an urgent task and requires the implementation of challenging structural materials. As such material technical ceramics can be used based on aluminum oxide [5–10]. Firm "Cerabar" produces the structural elements from practically pure Al_2O_3 [11]. That is why it was proposed to choose ceramics for valves of homogenizers [12]. Ceramics is stable in conditions of

hydroabrasive wear and in terms of durability exceeds stainless steels [12, 13]. Depending on the ratio of the phase constituents of ceramics, its types can possess different properties.

3   Research Methodology

The information on the cavitation resistance of ceramics is limited. To study the abovementioned property of ceramics, the experimental tests were carried out using a magnetostrictive vibrator with the frequency of vibration of 22 and 44 kHz.

The intensity of wear was determined by the weight method by loss of sample mass at fixed time intervals.

The main characteristics of specimens are presented in Table 1.

Table 1. Main properties of ceramic materials.

Properties	Number of specimen		
	1	2	3
Content of Al_2O_3, % mass	65	92	96
Density, g/sm^3	2,2	3,4	3,5
Elastic modulus, $E \cdot 10^2$, MPa	0,6	2,2	2,4
Impact strength, $\kappa J/m^3$	1,8	4,0	4,90

4   Results

The results of the studies are illustrated by the figures, which show the changes in the mass of the specimens at frequency of vibration of the magnetostrictive vibrator 22 and 44 kHz (Figs. 1 and 2) and the rate of loss of their mass (Figs. 3 and 4).

The analysis of obtained results makes it possible to conclude that specimen No. 1 was the least resistant. This is evident from the curve for the loss of its mass (Fig. 1), which is the largest of all the tested specimens.

Equally evident is the graph for the rate of mass loss (Fig. 3), which characterizes the cyclic nature of the process, when the kinetic energy of the impact of cavitation bubbles accumulated in the surface layers of the specimen contributes to the brittle fracture of its microvolumes. Similar dependence is observed at the frequency of vibrations 44 kHz as well (Fig. 2 and 4).

Specimens No. 2 and No. 3 demonstrated better wear resistance, with the loss of their mass being practically constant throughout the test period and was much less than the loss of specimen No. 1 at the frequency of vibrator 22 kHz. At the frequency of vibration 44 kHz, a significant difference in mass loss for all the specimens is observed after 120 min of testing, and for specimens No. 2 and No. 3, in which the content of the base component of Al_2O_3 is greater, wear is less intensive.
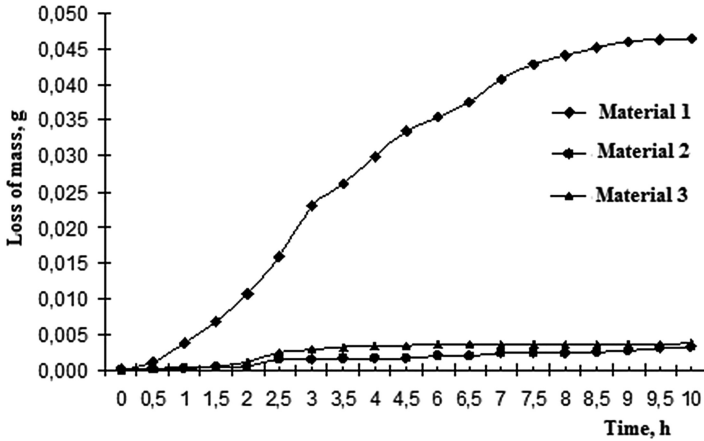
Fig. 1. Change in mass loss of material at frequency of vibrations of the magnetostrictive vibrator 22 kHz.
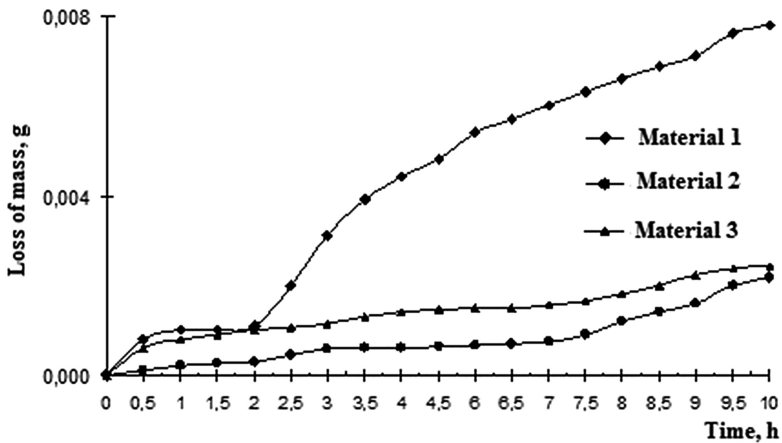

Fig. 2. Change in mass loss of material at frequency of vibrations of the magnetostrictive vibrator 44 kHz.

Figure 2 indicates that the rate of mass loss by samples is practically constant, and its increase at the beginning of the tests is mainly due to defects in the surface layer accumulated during the preparation of the specimens.

In our opinion, technological additions are the most vulnerable component of ceramics, for example in the form of silicon oxide SiO_2, which create conditions for the formation of a glass phase with distributed Al_2O_3 particles. The accumulation of stresses of the surface layer takes place namely along the boundaries of the phases, which is responsible for the cyclical nature of mass losses.
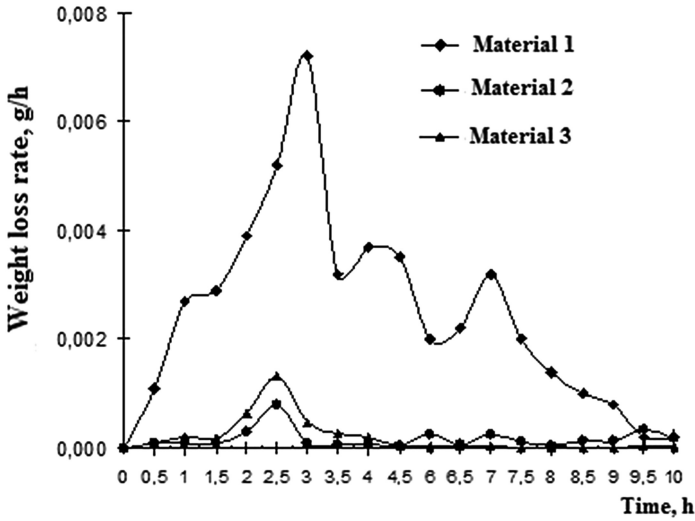
Fig. 3. Weight loss rate of specimens at the frequency of magnetostrictive vibrator 22 kHz.
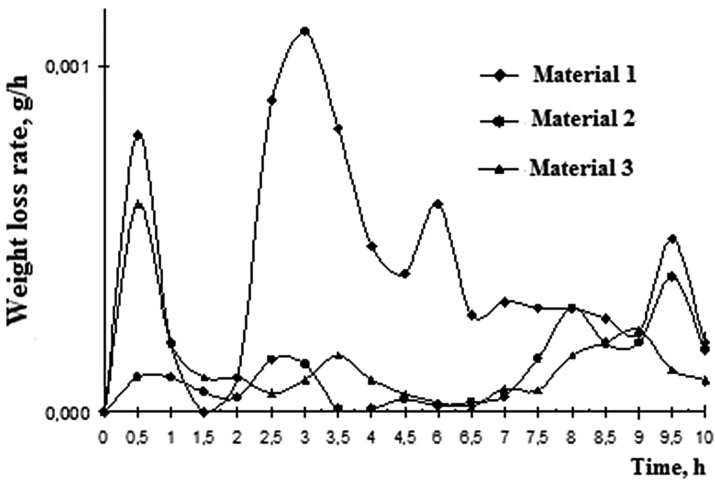

Fig. 4. Weight loss rate of specimens at the frequency of magnetostrictive vibrator 44 kHz.

Microscopic analysis showed that the destruction of specimens occurs precisely over the vitreous phase, which is contained along the grain boundaries of aluminum oxide. Specimens also contain other inclusions that affect their physical and mechanical properties and the mechanism of destruction. In addition, ceramic materials possess structural defects (pores, cracks), caused by the composition and technology of their manufacture.

When studying the size of Al_2O_3 grains, it was found that sizes up to 150 m km are optimal, which determine the resistance of the material to the propagation of cracks,

their number and determines the dependence of the energy of fracture on the grain size. Most defects of microcracks type occur during the sintering and subsequent cooling of the specimens. These microcracks will increase even under low loads and, according to the theory of A. Griffiths, their presence on the outer surface and inside the specimens contributes to the increasing of stress concentrations. This leads to the increase of the size of cracks and to subsequent destruction of a specimen.

According to the structure-energy theory of wear [14], the intensity of wear of materials under dynamic load is determined by the ratio of the strain energy density (load), which is introduced into the material by micro-impacts when bubbles or abrasive particles collapse to the critical destruction power W_{kr}^*. As the authors investigations on ceramic materials have shown, the strain power is also determined by the structure of the material and by the stress intensity factor K_{1c}. At the same time, for ceramics the cyclic character of the change in wear rate during the whole duration of the tests is observed. The high erosive activity of cavitation bubbles is in agreement with the relaxation hypothesis. According to this hypothesis the erosion damages arise as a result of their shock-wave action, the duration of which is comparable to the time of shear relaxation of the viscous fluid's strength $(1...2) \cdot 10^{-7}$ s. In this case, the mass of liquid that acts on the surface can be considered a solid body [15].

It is established that the most reliable criteria for the wear resistance of structural materials is the critical strain power density W_{cr}^* and the accumulation period of cyclic accumulation of damages. Upon reaching W_{cr}^*, visible erosion products are formed, and after the accumulation period, the wear rate sharply increases [14].

Based on the results of the conducted experiments, it is possible to assume the validity of application of the critical strain power density index for comparison of wear of ceramic materials.

Depending on the properties of materials, the power density reaches critical value at a certain velocity of impact V_{cr}.

Since $V_{cr} = f(W_{cr}^*)$, the criterion of wear resistance for the brittle fracture of the surface layer of material can be determined from the simplified Pogodaev–Nekoz formula [14]:

$$W_{cr}^* = \frac{\sigma_v^2/2E}{3} C_M \qquad (1)$$

where σ_v^2 is the ultimate strength, E is the elastic modulus, and C_M is the velocity of the propagation of shock waves in the material under study.

This makes it possible to compare the wear resistance of materials. The values in formula (1) can be simply determined experimentally. It adapts well to the results of the experimental data and makes it possible to quantify the rate of destruction of materials and to predict their durability [15].

On the basis of the proposed approach to the evaluation of wear resistance of ceramic materials, comparative wear resistance is presented in the Table 2. Calculations show the legitimacy of using the proposed approach to comparing the wear resistance of various types of ceramic materials, which is determined by their physical-mechanical properties, in particular, hardness.

Table 2. The critical strain power density W_{cr}^* for the specimens studied.

W_{cr}^*	Number of specimen		
	1	2	3
	75,6	762,3	901,6

5   Conclusions

The obtained values of the critical strain power density W_{cr}^* for the investigated specimens are in a good agreement with the results of the experiments that establish the dependence of the cavitation-erosion resistance of technical ceramics on the content of aluminum oxide.

In addition, the proposed approach makes it possible to use for the known materials the known dependences of the evaluation of the wear resistance of metals.

References

1. Vitenko, T.: Hydrodynamic Cavitation in Mass-Exchange, Chemical and Biological Processes: Monograph. TNTU named by Ivan Pul'uj, Ternopil (2009)
2. Litwinienko, A., Nekoz, A., Lukasik, K.: Technologiczne zastosovanie kavitacji hydrody-namichnej – doswiadczenia i perspektyvy. Lubielskie Towarzystwo Naukowe, Lublin (2005)
3. Grimm, A., Bast, S., Tillmanns, R., Schumacher, M.: Keramik Leichtbautiele. Keram. Z. **58**(1), 8–11 (2006)
4. Tarasov, V.: Physical mechanisms of cavitation erosion. Electron. J. Tech. Acoust. **3** (2015). http://www.ejta.org/ru/tarasov1. Accessed 21 Feb 2018
5. Meltser, A., Ananevskyi, I., Kyrychenko, I.: New control valve for waterjet environments. Armature Constr. **3**(42), 26–28 (2006)
6. Makarenko, V., Semchenko, G.: The influence of technological factors on the properties of composite materials. Refract. Tech. Ceram. **11–12**, 35–40 (2008)
7. Shtefan, E., Ryndyuk, D., Blagenko, S.: Determination of structural-mechanical and rheological properties of dispersed materials. Bull. Natl. Tech. Univ. "KhPU" **53** (1095), 141–147 (2014)
8. Semchenko, G.: Structural Ceramics and Refractories. Shtrish, Kharkov (2000)
9. Murzakova, A., Shayakhmetov, U., Valeev, I.: Ogneupory i tekhnicheskaya keramika **1–2**, 37–39 (2012)
10. Hubyn, S., Maklashova, Y., Melnykova, K., Lyubymov, A., Hubyna, V.: Evaluation of the properties of ceramics from oxides aluminum and zirconium. Mater. Sci. Nanotechnol. Bull. TSTU **1**(20), 153–158 (2014)
11. Hees, M.: Verwirbelungen halten Keramik Sauber. Ernahrungsindustrie **6**, 64–65 (2001)
12. Lukasik, K.: The comparison of a selected material for homogenizing valves. Problems and prospects for creating and implementing of the new resource and energy saving technologies equipment in the food and processing industries, vol. III, p. 94, USUFT (2000)

13. Sukhenko, Y., Miedviedieva, N., Sukhenko, V.: Analysis and choice of coatings for increasing the durability of parts of diffusion units of sugar plants. East Eur. J. Enterp. Technol. **6/12**(90), 27–34 (2017)
14. Pogodaev, L., Kuzmyn, V.: Structural-energy models of reliability of materials and machine parts. Academy of Transport of the RF (2006)
15. Litvinenko, A., Nekoz, A., Jastreba, S.: Predicting of durability of ceramic working cavitation devices. Br. J. Sci. Educ. Cult. **2**(6), 174–178 (2014)

System Dynamics Model for Continuous Review Inventory System in Demand Shock Conditions

Sławomir Luściński[1(✉)] and Dariusz Dobrowolski[2]

[1] Kielce University of Technology, 7 Tysiąclecia Państwa Polskiego al., 25314 Kielce, Poland
luscinski@tu.kielce.pl
[2] Maria Curie-Sklodowska University, Marii Curie-Skłodowskiej Pl., 00031 Lublin, Poland

Abstract. This paper deals with applying a control loop based on PID controller algorithm to dynamically setting the components of the continuous review system (Q-system) for inventory management to avoid demand shock unrequired influence on a customer service level. Through Vensim software platform, the system dynamic model of feedback system was developed, consisting of the Q-system for single echelon logistics and PID controller. Finally, operational performance results are analyzed using data of performed simulation experiments.

Keywords: System dynamics · Demand shock · Simulation

1 Introduction

Inventory management deals with a trade-off between the benefits of keeping stocks of goods that allows fulfilling the customer's demand, and the cost of carrying inventory. Moreover, inventory management is subjected to variability, both of internal and external nature. In a turbulent market environment supply chain networks are exposed to so-called "bullwhip" effect, a term coined by J. Forrester (1961). This phenomenon refers to the unexpected fluctuation of final customers' demand due to its untypical behaviour (called demand shock) that leads to amplified variability of stock replenishment orders upstream supply chain, hence unreasonable inventory of supply goods along the supply chain. The issue is the subject a lot of studies aimed to improve the understanding of nature and avoid the occurrence of the bullwhip effect; search in the Web of Science with the keyword 'bullwhip effect' returns 860 papers (access online 25.02.2018).

2   Literature Review

In the review article [1] on bullwhip effect (based on 455 papers reviewed and 150 cited) authors provide a review of the bullwhip literature which adopts various analytical, experimental and empirical methodologies. The Following elements of bullwhip modelling were highlighted: demand, delay, forecasting policy, ordering policy and information sharing mechanism. It is highlighted, that recent trends in bullwhip research are evolving towards a nonlinear and complex description of supply chain structures [1]. There is growing interest in applying control theory concepts to managing and optimizing supply chain due to dynamic nature of stock management problem [2]. System dynamics (SD) is widely recognized as a method of computer modelling and simulation for supply chain issues [3–7]. Causal presentation and quantitative means used in modelling make SD instrumental in researching on the behaviour of the modelled stock management system and its response to various policies. In [7] Proportion-Integral-Differential (PID) a controller was designed in order to control the bullwhip effect. By designing Genetic Algorithm, tuning the control parameters for the PID controller was obtained. Simulation results indicated the designed PID controller can eliminate effectively the bullwhip effect of the closed-loop supply chain.

This paper is devoted to researching the idea of employing automatic control methods for effective inventory management for Continuous Review Inventory System in Demand Shock Conditions. The Model of the feedback system consisting of a PID controller mathematical model and a single-echelon logistics system were built. To achieve simplicity and flexibility both during building the model and simulation experiments, the system dynamics approach was used through Vensim software platform.

3   Research Methodology

3.1   Continuous Inventory Review System

To achieve inventory equilibrium, inventory management systems are used. There are two general types of inventory systems: continuous review system (Q-system) and periodic review system (P-system). The application of Q-system brings lower inventory size than P-system does [8]. Generally, Q-system is applicable in computerized inventory management systems.

The continuous review system also called a reorder point policy (ROP), or fixed-order quantity system, is based on tracking the inventory level of an item to determine, whether it is time to reorder. As soon as the inventory position IP of the item reaches a predetermined minimum level R, a constant quantity Q is ordered. The inventory position is computed as follows:

$$IP = OH + SR - BO \qquad (1)$$

where OH – On-hand-inventory, SR – Scheduled receipts, BO – Backorders.

Setting the order quantity Q is subordinated to the objective of minimizing total annual inventory cost defined as annual ordering cost plus annual holding cost. There is a classical economic order quantity (EOQ) model introduced by F.W. Harris (1913) for an instantaneous resupply:

$$EOQ = \sqrt{\frac{2DS}{H}} \tag{2}$$

where D – annual demand, S – setup or ordering cost, H – holding cost (often estimated as $H = pC$ where p is a banking interest rate, C - unit cost).

The reorder point level of the stock R should cover using of inventory during the replenishment lead time L, defined as the time between when an order is placed and when it is expected to arrive. Additionally, let's assume that the demand is unpredictable. In such a case, the reorder point level should be increased by adding an extra inventory, named safety stock I_s, to buffer against uncertainty in the demand.

The R is calculated as

$$R = \bar{D}_L + I_s \tag{3}$$

where $\bar{D}_L$ stands for average demand during the lead time (L).

The service level represents a trade-off between the cost of inventory and the cost of stock-outs (which incur missed sales, lost opportunities and client frustration among others).

It is assumed that the incidence of the demand in the cycle of replenishment of inventory is represented by a normal distribution. There are two different formulas to setting appropriate safety stock balancing the risk of stock out against the cost of carrying an extra inventory derived from two different definitions of the level of service:

1. The level of service type 1 (cycle-service level) – the probability of not running out of stock during any ordering cycle (length of time between the receipt of two orders). It is applied to the supply of any materials, especially when stock-out events occurrence is more important than the amount of missed stock, for instance in continuous production.

   It is defined as the probability $F(Z)$ that a variable from a standard normal distribution will be less than or equal to Z. The amount of safety stock is calculated as [9]

$$I_s = z * \sigma_{dL} = z * \sigma_d * \sqrt{L} \tag{4}$$

   when σ_{dL} – the standard deviation of demand during the lead time L, z – the service factor (Z-score). Z- the score of 1 protects from 1 standard deviation of the demand.

2. The level of service type 2 – (fill rate) the fraction of the customer demand that is met through an immediate stock availability. It is applied for instance to the distribution, where stock out results in loss of margin are also widely used in industry (batch production). The expected backorder EBO during any ordering cycle [9]

$$EBO = L(z) * \sigma_{dL} \tag{5}$$

when $L(z)$ – the standard normal loss function, i.e. the expected number level of.

It is proposed, that $L(z)$ may be computed using approximate formula [9]

$$L(z) = 0.3536 * e^{-1.4032 * z^{1.44}} \tag{6}$$

The fill rate during any ordering cycle as a fraction of demand that is fulfilled immediately (without backorder) is calculated as

$$\text{Fill rate} = 1 - \frac{\text{Expected backorder}}{\text{Expected demand in replenishment lead time}} \tag{7}$$

Hence, in order to designate the safety stock I_s when level of service is expressed as a fill rate, calculate the expected backorder EBO (from transformed formula above) and designate the service factor with formula proposed in [9]

$$z = \left[\frac{-1.0396 - \ln(EBO)}{1,4032} \right]^{0,6944} \tag{8}$$

then use formula (4). The cycle-service level is to designate from the table of corresponding values of the cycle-service level, the z-score and the standard normal loss function (Table 1).

Table 1. Example values of z, $L(z)$, due to cycle service level.

Cycle-service level	Z-score	Standard normal loss function L(z)
90.00%	1.28	0.04758
91.00%	1.34	0.04158
92.00%	1.41	0.03581
93.00%	1.48	0.03028
94.00%	1.55	0.02500
95.00%	1.64	0.01999

The average fill rate may be measured empirically by averaging the amount of fulfilled demand over total demand during any period of time.

3.2 Feedback System

A *dynamical* system is a system which behaviour changes over time. A *feedback* system is when two or more dynamical systems are interconnected and each influences the other. The term *control* is defined as the use of algorithms and feedback loops in engineered systems [10]. An ideal closed-loop control system with continuous proportional-integral-derivative PID controller based on error feedback is shown in Fig. 1.
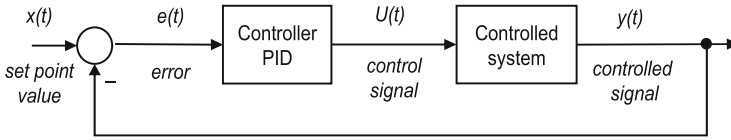
Fig. 1. The diagram of a basic control system with continuous PID controller [11].

The controller has one input, the control error $e = x - y$ and the process output y. The "textbook" input/output formula for a PID controller with error feedback is [10]

$$u = k_p \left(e + \frac{1}{T_i} \int_0^t e(\tau) d\tau + T_d \frac{de}{dt} \right) \tag{9}$$

The control action u of the PID controller is a sum of three terms: the proportional feedback, the integral term and the derivative action. The controller parameters are the proportional gain k_p, the integral time T_i and the derivative time T_d.

The PID controller is very useful and is capable of solving a wide range of control problems. More than 95% of all industrial control problems are solved by the PID control.

3.3   Dynamic System Model

3.3.1   Modeling Method and Tool

The system dynamics (SD) was introduced by J.W. Forester in 1950s. It involves mental representation of a system, qualitative dynamics (causal loop diagramming) and quantitative dynamics (stock and flow diagramming) analysis and representations of a system, formal modelling, testing, and experimenting.

The system Dynamics approach is based on the analysis of the internal logic and the structural relationships within the model. Thus, the system dynamics modelling is the process of looking for abstract mathematical representation of the reality as well as discovering and extraction of hidden knowledge on it.

The system dynamics programming environment Vensim PLP 7.2 (Ventana Systems, Inc.) was used for the purpose of computer modelling and simulation of a proposed feedback system for a single-echelon logistics system.

The model consists of a PID controller and a continuous review inventory system in the environment of uncertain and shock demand. Graphically, the model is presented as so-called Stock and Flow Diagram (SFD). To develop both graphical and mathematical aspects of the SFD, different types of variables are used: stocks, flows, auxiliaries, parameters and constants. Stocks stands for integral equations of the flows. Flows and auxiliaries are equations of other variables. Parameters and constants represent constant values over a simulation run. Each variable type is assigned a separate graphical symbol on SFD. To simplify and maintain the reliability of the developed model, it was split into sub-models related to each other by using so-called <*shadow variables*> which reflect the original variables, that are defined in particular sub-models.

3.3.2   SD Sub-models of Market Demand and Reorder Policy

Figures 2 and 3 are the stock and flow diagrams for modelling uncertain stochastic demand with a normal distribution, economic order quantity formula for reordering the size and reorder the designation of the reorder point due to the desired cycle service-level.
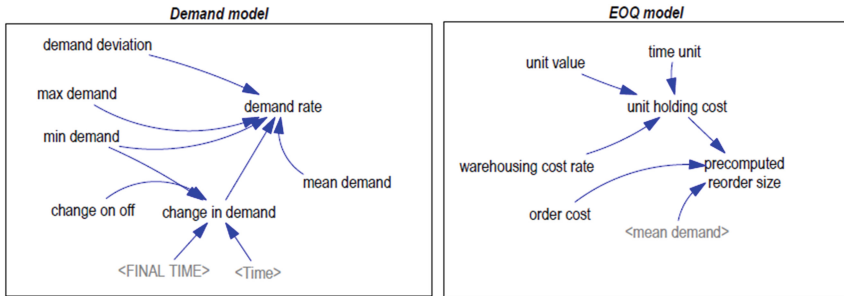
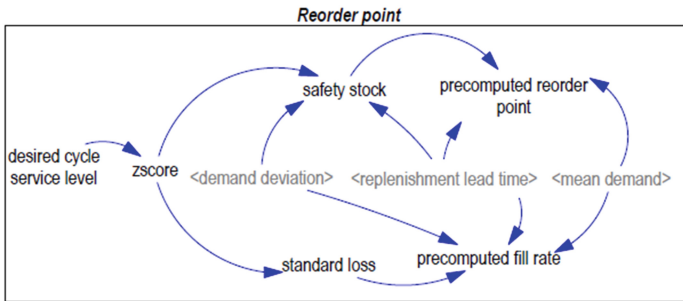

Fig. 2. SD models of market demand and EOQ policy.

Fig. 3. SD models of reordering policy.

3.3.3   SD Sub-model of Proportional-Integral-Derivative Controller

Figure 4 is the stock and flow diagrams for modelling a PID controller. The model reflects the triple-action structure of the controller.

The controlled signal is the auxiliary variable *backorder* that represents an unfilled demand in any single step time of simulation. The PID process variable input and setpoint input is stated as 0.

The proportional band (PB) for the proportional action was implemented as follows

$$\text{proportional term} = \text{error} * 100/\text{PB} \tag{10}$$

where the PB is given in %.

The higher PB, the slower but more stable the control. Typically, the PB varies from 25% to 250%. It was assumed, due to nonlinear nature of the controlled system, that the PID should not be very reactive, thus the PB was stated on 250%.
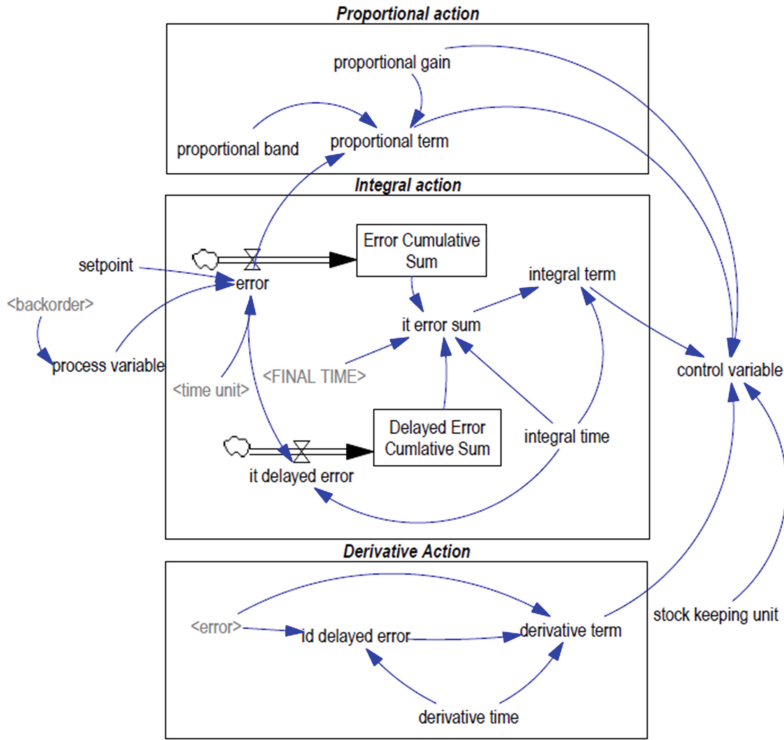
Fig. 4. SD sub-model of PID controller.

3.3.4   SD Sub-model of Single-Echelon Logistics System

Figure 5 is the stock and flow diagrams for modelling of considered single echelon logistics system. SD is split into 3 blocks: inventory management, ordering (replenishment management) and customer service tracking block.

The control signal during the PID controller action is an auxiliary variable of reorder size. Additionally, when the PID control is on, the auxiliary variable *reorder point* follows changes in *reorder size*, in proportion to the ratio *precomputed reorder point* to *precomputed reorder size*.

In order to automatically switch on the PID action when the shock-demand is detected, the SD equation for peak signal detection is as follows:

IF THEN ELSE(demand rate >= mean demand +
detection level sensivity*zscore*demand deviation, 1, IF THEN ELSE(demand rate < mean demand + detection level sensivity*zscore*demand deviation, −1, 0))
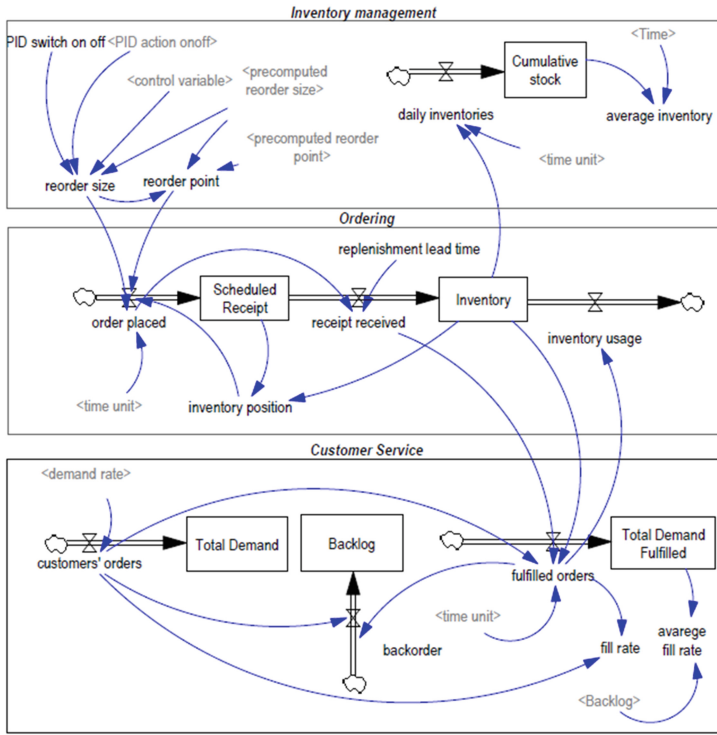
Fig. 5. SD sub-model of single-echelon logistics.

4   Results

Figures 6 and 7 show the results of the simulations applying 3 scenarios: basic case simulation (2); simulation with the demand affected by a step change in the demand (3) and with employing the PID control (1).

During preliminary simulation experiments, initial variables of the model were stated based on arbitrarily assumed values characterizing the market demand and the logistics
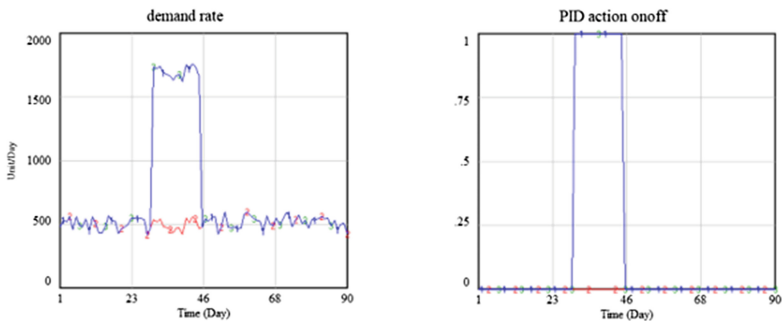

Fig. 6. Demand rate and PID action in simulation experiments with 3 different scenarios.
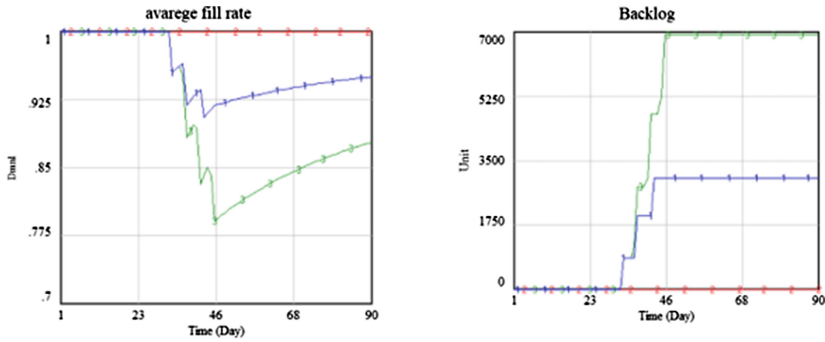
Fig. 7. Average fill rate and backlog in simulation experiments with 3 different scenarios.

costs for a single anonymous item. The time of the simulation is 90 days with time step 1 day. The mean demand is 510 units per day, varies from 400 to 610 with a standard deviation 60. The replenishment lead time is 2 days. The unit procurement price for the inventory item is 500 EUR, the warehousing unit annual cost rate (including financial cost of frozen capital) is 30%, the order cost is 100 EUR. The desired cycle service level is 95%. For implementing the demand shock, it is assumed that during a certain period of time the demand will be shifted by a factor 3 × mean demand (Fig. 7). In all scenarios the precomputed reorder point = 1159, the precomputed reorder size = 4726. The pre-computed fill rate is 0.84 (84%). There is no backlog during the basic case simulation (2), so the average fill rate = 1. The average inventory is equal to 2493.

During the next simulation (3) we may observe consequences of applying reorder policy without adapting it fully to shock-demand conditions. The backlog after the duration of a step change in the demand is levelled at 6912 units. The average fill rate initially drops to 0.80 and finally reaches 0.88. The average inventory is equal to 2235 (Fig. 8).
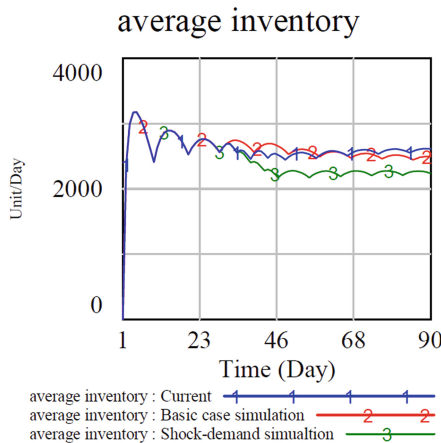

Fig. 8. Comparison of average inventory level in 3 scenarios of simulation.

In the PID control scenario (1) after tuning the parameters of the controller with the heuristic approach following the sensitive analysis of the feedback system, the PID parameters were stated as follows: proportional gain = 2.7, integral time = 3 days, derivative time = 2 days. The model of the logistics system produce simulation results as follows: average inventory = 2611, average fill rate = 0.95, backlog = 3018. The cost of warehousing based on the average inventory is higher for the PID scenario (1) than for (3) as follows: (2493 units/day − 2235 units/day) * (90 days/365 days) * 0.30 * 500 EUR/unit = 858 822 EUR.

There are 12 orders scheduled in scenario (3) and 11 orders in scenario (1), so the difference of the total cost of procurement is 858 822 EUR − 1 × 100 EUR = 858 722 EUR.

Scenario (1) product backlog is lower than scenario (3) by: 6912 units- 3894 units = 3894 units. So, the marginal operational profit per unit is 858 722 EUR/3894 units = 220.50 EUR. It makes the minimal selling price for the inventory item as follows: 500EUR + 220.50 EUR = 720.50 EUR. It makes economically realistic applying adaptive solution based on the PID controller in shock demand conditions.

5   Conclusions

One main objective of this research is to investigate the possibility to develop an adaptive algorithm for the inventory management based on a formula of the PID controller. The simulations study shows that although the logistics system with the PID control loop produces lower backlog than without it in the shock demand environment, the final results should be considered as not ambiguous if total costs of the procurement are taken into consideration. Moreover, the limited scope of the study does not provide a sophisticated method of setting parameters of the PID controller model; due to the nature of simulations, the applied parameters for the simulation scenario were established *a posteori*, after series of sensitivity analysis. However, computer simulations provide some evidence, that the PID loop is applicable to supply chain management issues, it requires future research grounded both in supply chain management and feedback systems theory.

References

1. Wang, X., Disney, S.M.: The bullwhip effect: progress, trends and directions. Eur. J. Oper. Res. **3**(250), 691–701 (2016)
2. Dorofieiev, Yu.I, Lyubchyk, L.M.: Bullwhip effect in supply chains reducing by decentralized inventory control based on invariant ellipsoids method. Radio Electr. Comput. Sci. Control **1**(40), 161–170 (2017)
3. Sterman, J.D.: Business Dynamics Systems Thinking and Modeling for a Complex World. Irwin McGraw-Hill, Boston (2000)
4. Jolly, R.: Systems Thinking for Business: Capitalize on Structures Hidden in Plain Sight, Kindle edn. Systems Solutions Press, Portland (2015)

5. Gierulski, W., Luscinski, S., Serafin, R.: Computer simulation of logistics processes using the Vensim program. In: Knosala, R. (ed.) Innovations in Management and Production Engineering, vol. I, pp. 843–854. PTZP, Nysa (2015)
6. Botha, A., Grobler, J., Yadavalli, V.S.S.: System dynamics comparison of three inventory management models in an automotive parts supply chain. J. Transp. Supply Chain Manag. **11**, a281 (2017)
7. Jing, Y., Wang, X., Li, W., Deng, L.: Simulation and PID control of bullwhip effect in closed-loop supply chain based on noise bandwidth. Int. J. Appl. Math. Stat. **11**(41), 286–294 (2013)
8. Verma, R., Boyer, K.K.: Operations and Supply Chain Management. World Class Theory and Practice, International edn. South-Western Cengage Learning, Boston (2010)
9. Krzyzaniak, S.: Service level in inventory management. Logistics **1**, 19–21 (2003)
10. Åström, K.J., Murray, R.M.: Feedback Systems. An Introduction for Scientists and Engineers. Princeton University Press, Princeton (2008)
11. Laskawski, M., Wcislik, M.: Sampling rate impact on the tuning of PID controller parameters. Int. J. Electron. Telecommun. **1**(62), 43–48 (2016)

Numerical Study of Outlet Blade Angle Effect on Impeller Characteristics of Double Entry Centrifugal Pump

Viktoriia Miltykh$^{(\boxtimes)}$ ⓘ and Mykola Sotnyk ⓘ

Sumy State University, 2 Rymskogo-Korsakova Street, Sumy 40007, Ukraine
miltykh.viktoriia@gmail.com

Abstract. The characteristics of pump performance are depended strongly on the impeller geometry. Changes in some impeller geometric parameter can improve pump performance. It is well known that outlet blade angle is one of those parameters, which has significant effect on the impeller work characteristics. This work is connected with the effect of blade outlet angle changes on the performance of double entry centrifugal pump impeller. This process is investigated via Ansys computational fluid dynamics (CFD) software. CFD method can predict well the complex internal flows in centrifugal impellers. The present paper describes the simulation of four impeller working process. The outlet blade angle was changed from 26° to 32° while all other geometrical impeller parameters were kept constant. The head-flow rate, hydraulic efficiency-flow rate and shaft power-flow rate curves are compared and discussed for each impeller. The obtained results show that even insignificant changes of the blade outlet angle effect on the impeller performance.

Keywords: Characteristic curve · Impeller geometry CFD · ANSYS-CFX
Efficiency

1 Introduction

Pump equipment's designers are challenged continually to provide customers more efficient, reliable and energy saving machines but at lower cost. It is necessary to make detailed understanding of the internal flow within its stationary and rotating passages. That is why it is required the complex internal flows investigations in centrifugal pumps impellers.

Experiment is considered as a preferable investigation method of mechanisms inside centrifugal pumps. However, today the Computational Fluid Dynamics (CFD) approach is quite common because of high cost of experiments. With the aid of CFD, the complex internal flows in centrifugal pumps can be well described. It is worth to pay special attention to internal flow in inter-blade impeller channels, as it is a key element in the entire pump unit.

2 Literature Review

There are various studies about the effect of impeller geometrical parameters on pump characteristics. Some researchers have investigated the effect of impeller outlet blade angle on centrifugal impeller in order to achieve its better performance.

Bacharoudis et al. [1] describe the flow simulation in the impeller of centrifugal pump. In this study, it is evaluated the performance of impellers with the same outlet diameter and different outlet blade angles. They conclude that increasing of outlet blade angle causes the shape of the curve which becomes smoother and flatter. 50% reduction of the volume rate from its nominal value results to 20%, 25% and 28% drop of the hydraulic efficiency relative to their nominal value for the impellers with outlet blade angle, it is equal to 20°, 30° and 50° respectively. In addition, 50% increase of the volume rate from the nominal point leads to 25%, 15% and 15% drop of the hydraulic efficiency relative to the nominal value for the 3 impellers respectively.

Djerroud et al. [2], have obtained similar study results of the outlet blade angle effect on the head and efficiency and it is noted that the increasing of outlet blade angle entails the increasing in shaft horsepower.

Shojaeefard et al. [3], and Patel et al. [4], have observed the increase in efficiency with outlet blade angle increasing.

Anagnostopoulos [5] has investigated the effect of blade geometry on pump efficiency. It is emphasized that flow rate decreases at low blade angles and increases at high blade angles with increasing the losses.

A sufficient number of such studies were conducted. Nevertheless, the results of those works cannot be generalized because those researches were conducted for different types of pumps that use different working fluid.

The study results of hydraulic performance of the double entry centrifugal pump impeller provide in this paper. The CFD code served as a tool for investigating the outlet blade angle change effect on impeller head, shaft horsepower and hydraulic efficiency.

It was studied four impellers with seven blades. All impellers have the same diameters in suction and pressure side and they vary only on the outlet blade angle, which is 26°, 28°, 30° and 32°, respectively. In the rotational speed (n) of 980 rpm, the normal operation of the original impeller is 3200 m^3/h flow rate (Q), the estimated pump's total head (H) is 75 m and the number of impeller entries (fq) is 2 that results in the value 26 for the specific speed ($n_q = n \cdot (Q/f_q)^{1/2}/H^{3/4}$). Table 1 shows the main design data of the modeled pump impeller.

Table 1. Main data design of the modeled centrifugal impellers.

Geometry variant	Im. 1	Im. 2	Im. 3 (original impeller)	Im. 4
Outlet blade angle, β_2	26°	28°	30°	32°
Impeller outlet width, b_2 (mm)	59,6			
Impeller outlet diameter, D_2 (mm)	740			
Number of blades, z	7			

3   Research Methodology

The ANSYS-CFX code consists of geometry, CFX-pre, CFX-solver, and CFX-post modules. According to the applied ANSYS-CFX code, Fig. 1 shows a block scheme which is used to obtain the numerical simulation results from impeller geometry models to impeller numerical models.
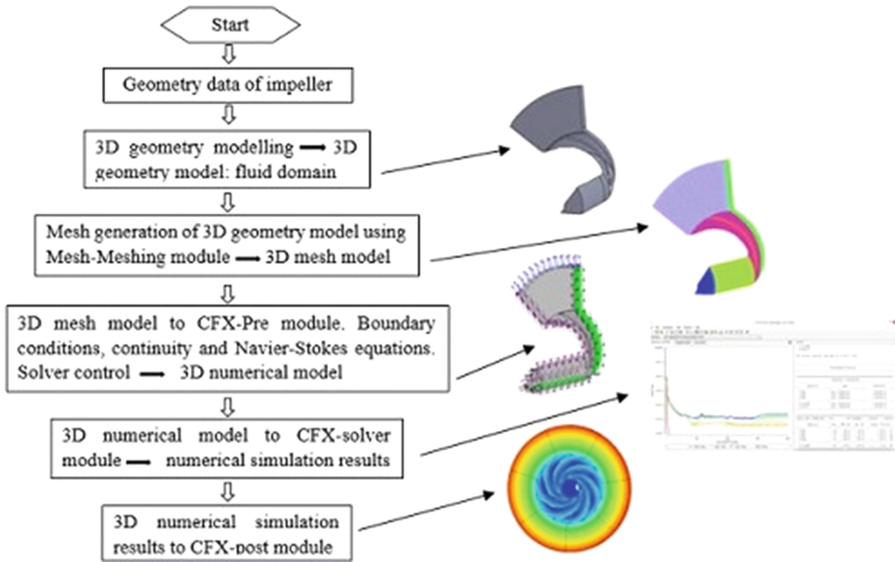

Fig. 1. The steps of study block scheme from geometry models to numerical models for impeller.

3.1   Three-Dimensional Computer Models of the Impellers

To carry out a numerical study, three-dimensional models of impellers with four different outlet blade angles were created, according to the recommendations presented in [6], and use of following assumptions: internal flow is symmetrical; internal flow at the entry to computational domain is axisymmetric; leakage through the impeller seals is neglected.

Due to assumptions above, the computational domain is a single channel of impeller half without gap seals. Inlet and outlet boundaries of the domain are spaced from the control sections at distance of 1…1,5 of impeller outlet diameter in order to get steady flow. A three-dimensional model of the computational fluid domain is shown in Fig. 2.
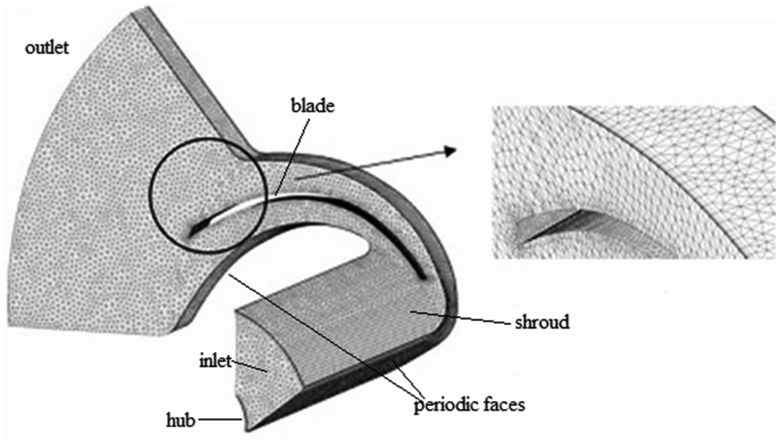
Fig. 2. A sample of the three-dimensional model of the computational fluid domain.

3.2   Mesh Structure and Boundary Conditions

The resulting geometry is used to build a mesh. The meshing is carried out using the Auto Mesh feature. The sample of mesh, which is shown in the Fig. 2, indicates that the tetrahedrons are used as the elements. A grid refinement was studied and adapted to flow morphology. Figure 3 shows the influence of the cell number on the theoretical head (H_t) which was developed by the impeller. According to this figure, the grid with about 1.5 million cells is considered enough sufficiently to ensure mesh independence.
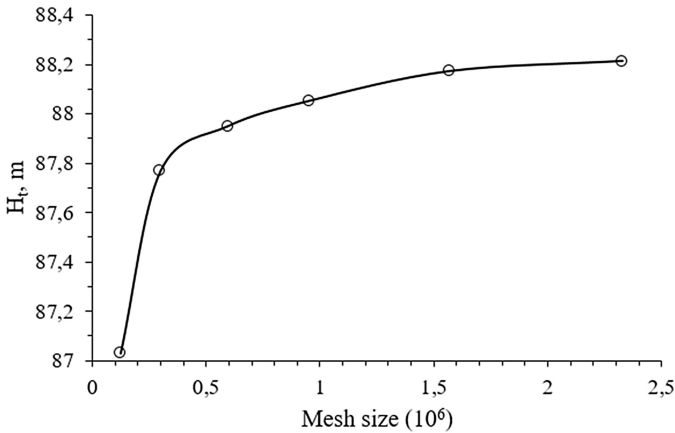
Fig. 3. The influence of grid size on the solution.

Cylindrical velocity components are specified on the computational fluid domain inlet and the static pressure is employed at the impeller outlet. The boundary condition type as "opening" is used at the outlet.

No-slip wall conditions are applied on all walls. Surface roughness is assumed as 6.3 μm for all surfaces of the wall in accordance with material properties. Water at 25 °C is specified as a working fluid.

Convergence criterion is 10^{-4}. A steady state model is used for all calculations. Inlet and outlet segments were set in stationary frame. However, the impeller is set in rotary frame. Turbulence is modeled with the selection of the standard k-ε model.

We modeled working process of four impellers at the modes from $0{,}5Q$ to $1{,}2Q$, where Q is the original impeller flow rate in the optimal point.

4   Results

The performance curves are the results through calculation of internal flow field and successful correlation of local and global parameters. Computational results, converged values are determined for each flow rate and different outlet blade angles, which is shown in Figs. 4, 5 and 6.
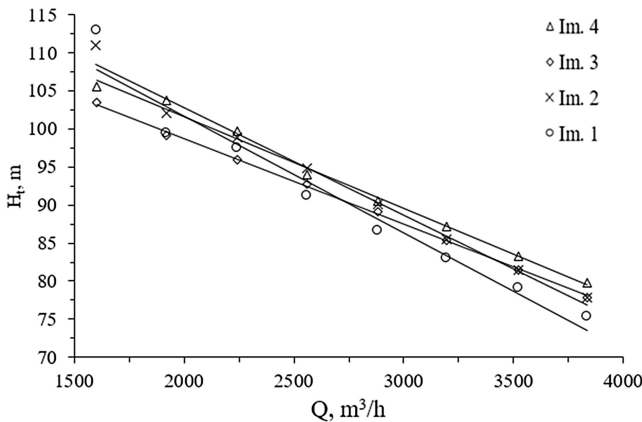

Fig. 4. The effect of outlet blade angles on the theoretical head.

Figure 4 depicts distribution of the calculated theoretical head, which is presented as a function of flow rate and with outlet blade angle as a parameter. Head increases by the increasing of the outlet blade angle. However, the theoretical head is hardly changed and we can clearly see it in flow rate range from $0{,}9Q$ to $1{,}2Q$. The gain in the head is less than 5% when the outlet blade angle increases from 26° to 32°. It proves that the impeller hydraulic loss per outlet blade angle unit differs insignificantly.

With the increase of the outlet blade angle, the impeller pressure significantly increases, according to published conducted research results [1, 4], on this study we don't see a significant increase in head and most likely because of a small range of outlet blade angle variation.
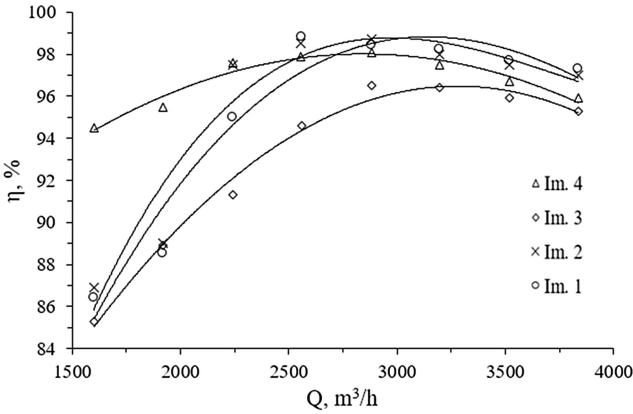

Fig. 5. The effect of outlet blade angles on hydraulic efficiency.

Figure 5 depicts distribution of the calculated hydraulic efficiency, which is presented as a function of flow rate and with outlet blade angle as a parameter. As the outlet blade angle increases, the hydraulic efficiency curves become smoother and flatter for whole range of flow rate. Those curves decrease more rapidly for the impellers with $\beta_2 = 26°$, $28°$ and $30°$ than for $\beta_2 = 32°$ at lower flow rate than the Q.

The comparison of the hydraulic efficiency of four impellers shows that the decreasing of outlet blade angle leads to increasing of the hydraulic efficiency value up to 6% for range of flow rate from $0{,}7Q$ to $1{,}2Q$. However, the operating regions near to best efficiency point (BEP) become narrower. Moreover, the efficiency curves illustrate that impeller hydraulic efficiency with $\beta_2 = 32°$ decreases slowly to the left of the BEP.
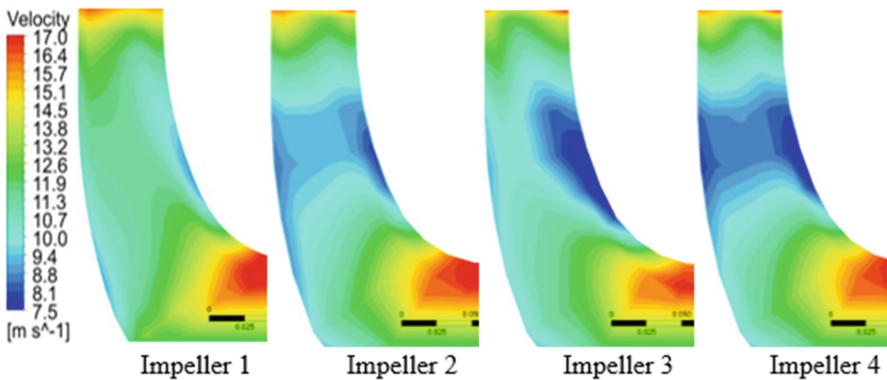

Fig. 6. Meridian view plots of velocity distribution for impellers.

Figure 6 illustrates the velocity contours in the numerical simulations which is performed at the normal operating conditions (3200 m³/h). It is noticed that zone with low velocity exists in the impeller 2, 3 and 4 but not in the impeller 1. This fact causes higher hydraulic efficiency of impeller 1.

Figure 7 depicts distribution of the calculated shaft horsepower, which is presented as a function of flow rate and with outlet blade angle as a parameter. The curves show that shaft horsepower continuously increases in the flow rate range from 0.5 Q to 1.2 Q. In addition, Fig. 6 illustrates that the shaft horsepower increases relative to the augmenting outlet blade angle for all flow rate range. We observe noticeable increase in shaft horsepower for flow rate range from 0,8Q to 1,2Q.
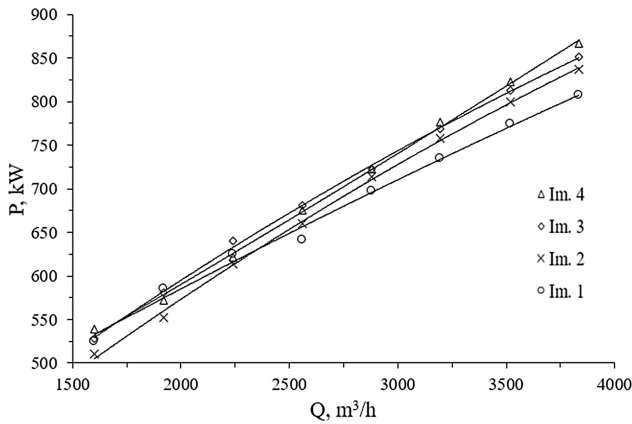

Fig. 7. The effect of outlet blade angles on shaft horsepower.

Nonetheless, the research results of the working process of the centrifugal pump impeller at the outlet blade angle change in the wide range, which is presented in [2], demonstrate a decrease in the pump power consumption at a very small outlet blade angle ($\beta_2 < 14°$) for flow rate larger than the optimal.

5   Conclusions

The investigation of impeller outlet blade angle effect on the centrifugal impeller performance has been done in this study. This study has been carried out by changing the outlet blade angle in range from 26° to 32° while all other parameters were kept constant. The centrifugal impeller hydraulic performance was studied numerically with the CFD code.

We can have following conclusions from the discussion above. The change of outlet blade angle in such small range of specified flow rate range has no significant effect on impeller theoretical head. The gain in head is less than 5% when the outlet blade angle increases from 26° to 32°. However, the decreasing of outlet blade angle

leads to the increasing of hydraulic efficiency up to 6% and depends on the flow rate value. However, the operating regions near to BEP become narrower. In addition, we can't dismiss the fact that the shaft power decrease in this case, is insignificant.

It's planned to complete this research work through the investigation the effect of outlet blade angle change in wide range on the impeller and pump hydraulic performance.

References

1. Bacharoudis, E., Filios, A., Mentzos, M., Margaris, D.: Parametric study of a centrifugal pump impeller by varying the outlet blade angle. Open Mech. Eng. J. **2**, 75–83 (2008)
2. Djerroud, M., Dituba Ngoma, G., Ghie, W.: Numerical identification of key design parameters enhancing the centrifugal pump performance: impeller, impeller-volute and impeller-diffuser. International scholarly research network. Mech. Eng. **2011**, 16 (2011)
3. Shojaeefard, M., Tahani, M., Ehghaghi, M., Fallahian, M., Beglari, M.: Numerical study of the effects of some geometric characteristics of a centrifugal pump impeller that pumps a viscous fluid. Comput. Fluids **60**, 61–70 (2012)
4. Patel, M., Doshi, A.: Effect of impeller blade exit angle on the performance of centrifugal pump. Int. J. Emerg. Technol. Adv. Eng. **3**(1), 702–706 (2013)
5. Anagnostopoulos, J.: A fast numerical method for flow analysis and blade design in centrifugal pump impellers. Comput. Fluids **38**(2), 284–289 (2009)
6. Gűlich, J.: Centrifugal Pumps. Springer, Heidelberg (2010)

Application of Artificial Neural Network for Identification of Bearing Stiffness Characteristics in Rotor Dynamics Analysis

Ivan Pavlenko[1(✉)] , Vitalii Simonovskiy[1], Vitalii Ivanov[1] ,
Jozef Zajac[2], and Jan Pitel[2]

[1] Sumy State University, 2 Rymskogo-Korsakova Street, Sumy 40007, Ukraine
i.pavlenko@omdm.sumdu.edu.ua
[2] Technical University of Kosice,
1 Bayerova Street, 08001 Presov, Slovak Republic

Abstract. In this article the implementation of the mathematical model for rotor oscillations on non-linear bearing supports for the multistage centrifugal compressor is considered by using the computer program "Critical frequencies of the rotor". It realized the finite element mathematical model, which allows taking into account the non-linear dependence of bearing stiffness on the rotor speed, as well as gyroscopic moments of inertia of impellers and shell-type parts. The artificial neural network "Virtual Gene Developer" software is proposed for evaluating the operating parameters of the approximating curve "bearing stiffness – rotor speed" by the dataset of numerical simulation results in the abovementioned software. Actual parameters of non-linear bearing stiffness are obtained by the results of the experimental research of rotor critical frequencies for the multistage centrifugal compressor 295GC2-190/44-100M on the experimental accelerating-balancing stand "Schenck". The main advantages of the proposed approach and methodology for application of Artificial Neural Networks are stated.

Keywords: Rotor vibrations · Artificial intelligence · Non-linear support
Critical frequency · Mode shape

1 Introduction

Intensification of the development in the field of power engineering occurs through the usage of the modern energy-intensive equipment, an essential role of which is performed by multistage rotor machines. Permanently raising their parameters leads to increasingly significant problems of vibration reliability. Furthermore, the problem of investigating the dynamics of flexible rotors on the system of bearings is currently actual due to the impossibility of absolutely accurate dynamic balancing. It is complemented by an acute problem of evaluation of stiffness characteristics for rotor bearings in close connection with the dependence of critical frequencies of the rotor and corresponding mode shapes [1]. However, up-to-date methods for simulating the dynamics of rotor systems are predominantly based on the use of computer programs realizing the finite element method [2], but analytical studies generally use

two-dimensional continuous mathematical models for beam elements taking into account the hypothesis of Kirhhoff [3] about the non-deformable cross-sections. Application of the three-dimensional finite element models, particularly within the use of "ANSYS" software requires a relatively large machine time, in contrast to the beam models. Moreover, available software by default cannot provide it, taking into account non-linearities, which may be inherent in rotors. Consequently, the attention of scientists is attached to the application of significant efforts to expand the capabilities of existing software products and create new ones, more often combining the fields of hard and soft modeling [4–7].

2   Literature Review

The recent achievements in the field of rotor dynamics can be marked. The research work [5] is aimed at the development of the computational techniques of rotor dynamics with the use of the finite element method. Using "Matlab" software to develop the simulation model for determining the eigenfrequencies of the elastic rotor based on the 2D beam bending model with testing by "SolidWorks" software is presented in the research [8]. The problem of determining eigenfrequencies of rotors on the basis of linear and non-linear mathematical models is well researched in the work [9]. The influence of the rotor speed on the bearing stiffness using numerical simulation with the use of "ANSYS" software is investigated in the work [10]. The approach for identification of the rotor unbalances is proposed within the work [11] for the case of a single-span rotor as an elastic Euler-Bernoulli beam with a single-disc. Techniques that allow taking into account the gyroscopic moments are considered in works [12], and the impact of the deformable parts on rotor dynamics is investigated in the article [13].

The work [14] is devoted to comprehending the inherent mechanism and the feature of the subharmonic resonance for the rotor system supported on the ball bearings using numerical analysis for the 6-degrees-of-freedom model with non-linearities, Hertzian contact forces and bearing clearance. Taking into account the random excitations for the analysis of gas turbine, the blade vibrations is presented in work [15]. The approach for experimental and numerical research of a new dynamic phenomenon for two-bladed wind turbines is stated in the article [16], and the novel methodology for the angular position identification of the unbalance force for the case of asymmetric rotors is proposed in the research paper [17]. Finally, a novel methodology for a stochastic presentation of non-linear dynamics problems is stated within the work [18]. The solution of the problem of evaluation of stiffness characteristics for the rotor bearings within the dependence of critical frequencies of the rotor has not been found. Due to the abovementioned, this paper is aimed at using the artificial neural network (ANN) for evaluating the parameters of the approximating curve "bearing stiffness – rotor speed" by the dataset of numerical simulation results in the proposed computer program. The results of the experimental research of critical frequencies allow obtaining actual parameters of bearing stiffness.

3 Research Methodology

3.1 Bearing Stiffness Characteristics

To develop a technique for determining eigenfrequencies and critical frequencies of rotor oscillations, an approximating curve for describing the dependence "rotor speed – bearing stiffness" from the recent experience in the design and calculation of compressor units can be used. It confirms the sufficiency of using quadratic polynomial to describe the dependence of the bearing stiffness c on the rotor speed ω:

$$c(\omega) = c_0 + \alpha\omega + \beta\omega^2, \tag{1}$$

where c_0 – bearing stiffness in case of the non-rotating rotor (N/m); α – initial slope (N·s/m); β – initial curvature of the curve (N·s^2/m). The following investigation is aimed at identifying parameters c_0, α, β by using ANN.

3.2 The Mathematical Model of Rotor Dynamics

The finite element mathematical model of rotor oscillations, which allows taking into consideration gyroscopic moments of inertia for impellers and shell-type parts, as well as the non-linear dependence of bearing stiffness on the rotor speed (1), is realized by the computer program [19].

Due to the finite element method, the mathematical model of rotor oscillations is described with the following equation [20, 21]:

$$\left([C(\omega)] - \omega^2[M]\right)\{Y\} = \{F\}, \tag{2}$$

where $\{F\}$, $\{Y\}$ – column vectors of amplitudes F_k and y_k of external mono-harmonic forces $F_k \sin\omega t$ and node displacements $y_k \sin\omega t$ respectively; k – node number ($k = 1, 2, \ldots, 2N - 1$); N – total number of finite elements; $[C(\omega)]$, $[M]$ – global stiffness and inertia matrices formed from local ones by summarizing at corresponding nodes k:

$$[C(\omega)]_{ij} = \sum_{k=1}^{n} \left([C(\omega)]_e\right)_{ij}^{\langle k \rangle}; \quad [M]_{ij} = \sum_{k=1}^{n} \left([M]_e\right)_{ij}^{\langle k \rangle}; \quad (i,j = 1, 2, \ldots, 2N - 1). \tag{3}$$

In case of two-nodes beam finite elements with 4 degrees of freedom, the local matrices of stiffness $[C(\omega)]_e$ and inertia $[M]_e$ for the finite element $e = (i, j)$ are determined by the following expressions:

$$C_e = \frac{EI}{l^3} \begin{bmatrix} 12 + \frac{cl^3}{EI} & 6l & -12 & 6l \\ 6l & 4l^2 & -6l & 2l^2 \\ -12 & -6l & 12 & -6l \\ 6l & 2l^2 & -6l & 4l^2 \end{bmatrix};$$

$$M_e = \frac{m}{420} \begin{bmatrix} 136 & 22l & 54 & -13l \\ 22l & \begin{matrix} -136l^2 - \\ -105r^2/4 + \\ + 420I_g/m \end{matrix} & 13l & -3l^2 \\ 54 & 13l & 136 & -22l \\ -13l & -3l^2 & -22l & 4l^2 \end{bmatrix}, \tag{4}$$

where m – finite element mass (kg); l – finite element length (m); E – Young's modulus of the material (N/m^2); I – axial moment of inertia for the cross-section (kg·m^2); r – cross-sectional radius (m); I_g – gyroscopic moment of inertia for impellers and shell-type parts (kg·m^2).

In case of free oscillations $F_k = 0$ (k = 1, 2, … $2N - 1$), and the condition of existence of non-trivial solutions of the system (2) is vanishing, the determinant

$$\det\big([C(\Omega)] - \Omega^2[M]\big) = 0, \tag{5}$$

which is the higher order non-linear algebraic equation with respect to critical frequency Ω.

As a result of the rotor dynamic modeling for the different values of parameters c_0, α, β, the dataset describing the matrix dependence $\{K\} = f\{\Omega\}$ between stiffness characteristic $\{K\} = \{c_0, \alpha, \beta\}^T$ and spectrum $\{\Omega\} = \{\Omega_1, \Omega_2, \Omega_3, …\}^T$ of critical frequencies can be obtained.

The abovementioned technique is implemented on the example of the multistage centrifugal compressor 295GC2-190/44-10M on magnetic bearings. The compressor with a capacity of 16,85 megawatt is a part of the gas pumping unit GPU-C-16/102-3,32M produced by the Public Joint Stock Company "Sumy Machine-Building Science-and-Production Association", has the operating rotor speed in the range 3710…5565 rpm.

Obtained maximum parameters $c_0^{max} = 2{,}5 \cdot 10^7$ N/m, $\alpha^{max} = 3 \cdot 10^4$ N·s/m, $\beta^{max} = 3 \cdot 10^7$ N·s^2/m and $\Omega^{max} = 536$ will be used for normalizing the dataset within the regression procedure and ANN implementation.

3.3 Regression Procedure

The dataset obtained as a result of numerical simulation of rotor dynamics by using the computer program "Critical frequencies of the rotor" can be used within the regression procedure [19, 20] for determining the linear dependence between bearing stiffness and critical frequencies in the following form:

$$\bar{\Omega}_i = a_i \bar{c}_0 + b_i \bar{\alpha} + c_i \bar{\beta}, \tag{6}$$

where i – number of critical frequency ($i = \{1, 2, 3\}$); a_i, b_i, c_i – unknown weight factors; $\bar{\Omega}_i$, $\bar{c}_0$, $\bar{\alpha}$, $\bar{\beta}$ – dimensionless normalized parameters in a range $0\ldots1$ determined by formulas:

$$\bar{\Omega}_i = \Omega_i/\Omega^{\mathrm{max}}; \quad \bar{c}_0 = c_0/c^{\mathrm{max}}; \quad \bar{\alpha} = \alpha/\alpha^{\mathrm{max}}; \quad \bar{\beta} = \beta/\beta^{\mathrm{max}}. \tag{7}$$

Dependence (6) is equal to a set of three planes in the 4D hyperspace unit "$\bar{c}_0 - \bar{\alpha} - \bar{\beta} - \bar{\Omega}_i$" after normalizing (7).

Unknown parameters a_i, b_i, c_i as a components of the column vector of weight factors $\{A\}_i = \{a_i, b_i, c_i\}^{\mathrm{T}}$ can be obtained as a result of solving the system of non-homogeneous linear equations

$$[\overline{K}]\{A\}_i = \{\bar{\Omega}\}_i, \tag{8}$$

where $[\overline{K}]$ – rectangular matrix of bearing stiffness coefficients of size $n \times 3$ (n – number of rows of numerical simulation results dataset); $\{\bar{\Omega}\}_i$ – column vector of normalized critical frequencies of size $n \times 1$:

$$[\overline{K}] = \begin{bmatrix} c_0^{\langle 1 \rangle} & \alpha^{\langle 1 \rangle} & \beta^{\langle 1 \rangle} \\ c_0^{\langle 2 \rangle} & \alpha^{\langle 2 \rangle} & \beta^{\langle 2 \rangle} \\ \ldots & \ldots & \ldots \\ c_0^{\langle n \rangle} & \alpha^{\langle n \rangle} & \beta^{\langle n \rangle} \end{bmatrix}; \quad \{\bar{\Omega}\}_i = \begin{Bmatrix} \bar{\Omega}_i^{\langle 1 \rangle} \\ \bar{\Omega}_i^{\langle 2 \rangle} \\ \ldots \\ \bar{\Omega}_i^{\langle n \rangle} \end{Bmatrix}. \tag{9}$$

Due to $n > 3$, column vectors, $\{A\}_i$ can be obtained by the formula of linear regression:

$$\{A\}_i = \underbrace{\left([\overline{K}]^T[\overline{K}]\right)^{-1}[\overline{K}]^T}_{n \times n} \underbrace{\{\bar{\Omega}\}_i}_{n \times 1}. \tag{10}$$

Critical frequencies can be determined by the linear regression model by the following formula:

$$\{\tilde{\Omega}\} = [A]\{\bar{K}\}, \tag{11}$$

where $\{\tilde{\Omega}\}$ – column vector of experimental values of critical frequencies $\tilde{\Omega}_1$, $\tilde{\Omega}_2$, $\tilde{\Omega}_3$; $\{\bar{K}\}$ – column vector of bearing stiffness parameters; $[A]$ – the rectangular matrix of weight factors determined by formula (10):

$$[A] = \begin{bmatrix} \{A\}_1 \\ \{A\}_2 \\ \{A\}_3 \end{bmatrix} = \begin{bmatrix} a_1 & b_1 & c_1 \\ a_2 & b_2 & c_2 \\ a_3 & b_3 & c_3 \end{bmatrix}; \quad \{\tilde{\Omega}\} = \begin{Bmatrix} \tilde{\Omega}_1 \\ \tilde{\Omega}_2 \\ \tilde{\Omega}_3 \end{Bmatrix}; \quad \{\bar{K}\} = \begin{Bmatrix} \bar{c}_0 \\ \bar{\alpha} \\ \bar{\beta} \end{Bmatrix}. \tag{12}$$

Unknown weight factors $\{\bar{K}\}$ are determined in Eq. (11) by the inverse matrix formula:

$$\{\bar{K}\} = [A]^{-1}\{\tilde{\Omega}\}. \tag{13}$$

3.4   Using Artificial Neural Network

Using the continuum analytical models for investigating rotor dynamics is not possible in the general form. Therefore, the finite element method is mainly applied. However, solving the inverse problem related to the identification of bearing stiffness characteristic providing the actual operating parameters or critical frequencies and form shapes is the complicated research problem that can not be solved using traditional finite element analysis due to the initial nonlinearity of the mathematical model. In this case, artificial neural networks (ANN) as universal approximators can be implemented due to their ability to provide general mechanisms for creating models with highly nonlinear relationships between input and output parameters [21].

A variety of ANN is ensured due to the specific requirements of the problems by adopting a different degree of network complexity, types of inter-connections, transfer functions, training method, etc. In this work, ANN with input, output and system of hidden layers is used, that creates a correspondence between critical frequencies of the rotor and parameters of the bearing stiffness characteristic. The procedure for identification of rotor bearing stiffness characteristic by combined using finite element model of rotor dynamics and ANN is schematically presented in Fig. 1a.
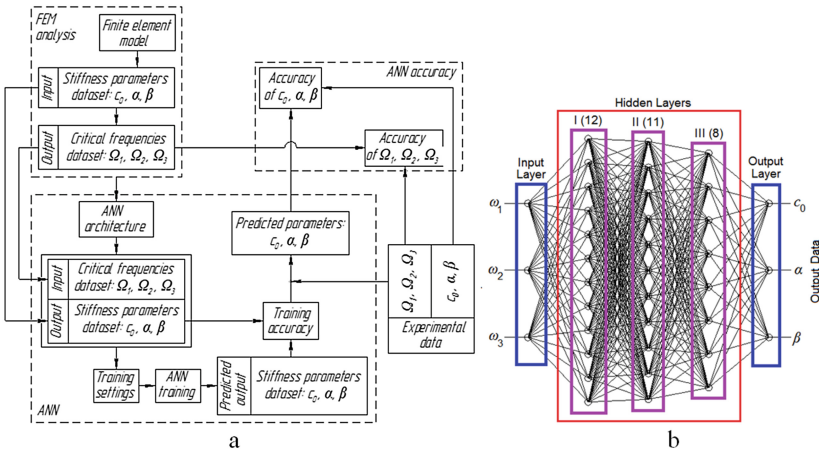

Fig. 1. The procedure of using ANN (a) and ANN architecture (b).

It should be noted that the output parameters (critical frequencies Ω_1, Ω_2, Ω_3) of numerical simulation in the computer program "Critical frequencies of the rotor" are input data for ANN training, and the output parameters of ANN (stiffness coefficients

c_0, α, β) must be compared with their corresponding actual values determining as a result of experimental research.

The configuration of ANN is presented in Fig. 1b. The number of layers and the distribution of neurons in layers are determined by the condition of full-time operating of all neurons. Decreasing the number of hidden layers and corresponding neurons leads to decreasing accuracy of the subsequent evaluation of rotor bearing stiffness characteristics, while an unreasonable increasing of neurons and layers leads to increasing the learning time and to non-involved neurons.

4 Results

4.1 Using Regression Procedure

Experimental research of the rotor dynamics for the multistage centrifugal compressor 295GC2-190/44-100M was provided on the accelerating-balancing stand "Schenck" for accelerating testing and dynamic balancing in vacuum of flexible rotors of centrifugal compressors with a mass up to 2500 kg. As a result, actual critical frequencies $\Omega_1 = 117$ rad/s, $\Omega_2 = 256$ rad/s, $\Omega_3 = 511$ rad/s were determined, and corresponding normalized parameters $\bar{\Omega}_1 = 0.218; \bar{\Omega}_2 = 0.478; \bar{\Omega}_3 = 0.953$ were calculated. Thus, due to the formula (13), the column vector $\{\bar{K}\} = \{0.817, 0.204, 0.891\}^{\mathrm{T}}$, and the evaluated bearing stiffness parameters are as follows: $c_0 = 0.817 \cdot 2.5 \cdot 10^7 = 2.179 \cdot 10^7$ (N/m); $\alpha = 0.204 \cdot (-3 \cdot 10^4) = -0.613 \cdot 10^4$ (N·s/m); $\beta = 0.891 \cdot 2 \cdot 10^2 = 1.782 \cdot 10^2$ (N·s^2/m).

All the abovementioned results are presented in Table 1.

Table 1. Comparison of achieved results.

Methods and parameters	$c_0 \cdot 10^7$	$\alpha \cdot 10^4$	$\beta \cdot 10^2$	ω_1	ω_2	ω_3
Regression analysis	2.179	−0.613	1.782	117	264	513
Artificial Neural Network	2.455	−2.682	1.996	118	256	511
Actual parameters	2.450	−2.900	2.086	117	256	511
Error in regression analysis	11.1	78.9	14.6	0.0	3.1	0.4
Error for using ANN	0.2	7.6	4.4	0.9	0.0	0.0

The verification of the results is carried out by determining the critical frequencies as a result of numerical simulation in the program "Critical frequencies of the rotor". In case of the parameters $c_0 = 2.179 \cdot 10^7$ N/m; $\alpha = -0.613 \cdot 10^4$ N s/m; $\beta = 1.782 \cdot 10^2$ N s^2/m, the critical frequencies are obtained: $\Omega_1 = 117$ rad/s, $\Omega_2 = 264$ rad/s, $\Omega_1 = 513$ rad/s, which corresponds to actual critical frequencies.

However, it should be noted that actual parameters $c_0 = 2.45 \cdot 10^7$ N/m; $\alpha = -2.9 \cdot 10^4$ N s/m; $\beta = 2.086 \cdot 10^2$ N s^2/m of bearing stiffness characteristic allow concluding that there is insufficient accuracy of the linear regression procedure due to relative errors 11.1%, 78.9% and 14.6% respectively. Thus, there is a need to use the method giving more accurate results.

4.2   Implementation of Artificial Neural Network

"Visual Gene Developer" software provides graphical visualization of ANN training procedure (Fig. 2). Lines present weight factors and nodes means threshold values. In the diagram, red color corresponds to the high positive number, and violet color means high negative number. Line width is proportional to the absolute number of weight factor or threshold value.
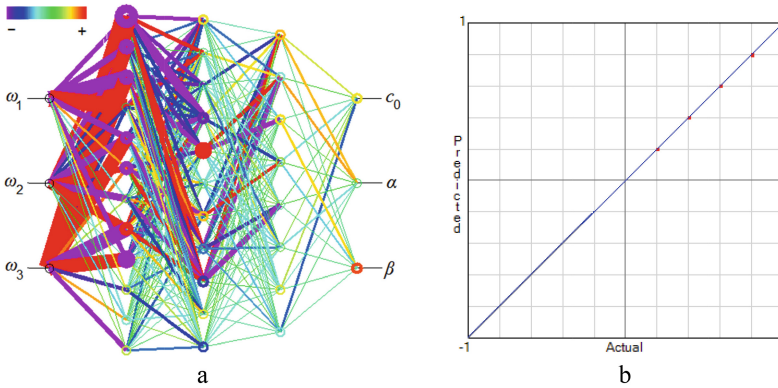

Fig. 2. ANN map analysis (a) and results of regression analysis (b).

The following training settings were selected: Learning rate – 0.001; Transfer function – Hyperbolic tangent; Total number of training cycles – $1 \cdot 10^6$; Target error – $1 \cdot 10^{-5}$; Initialization method of threshold – Random; Initialization of weight factor – Random; Analysis update interval – 500 cycles.

ANN training results include initial parameters c_0, α, β, resulting frequencies Ω_1, Ω_2, Ω_3 and predicted critical frequencies ω_1, ω_2, ω_3.

Comparison of predicted critical frequencies with the corresponding resulting critical frequencies leads to the conclusion about high accuracy (up to the third decimal place) of ANN learning process. In addition, the following training results are obtained: Sum of error – $3.5 \cdot 10^{-4}$; Average error per output per dataset – $3.6 \cdot 10^{-6}$; Regression coefficient – 0.99996.

Evaluated bearing stiffness parameters are $\bar{c}_0 = 0.982$ ($c_0 = 2.455 \cdot 10^7$ N/m); $\bar{\alpha} = 0.894$ ($\alpha = -2.681 \cdot 10^4$ N s/m); $\bar{\beta} = 0.998$ ($\beta = 1.996 \cdot 10^2$ N s^2/m). All the abovementioned results are presented in Table 1. The verification of the results is carried out by determining the critical frequencies as a result of numerical simulation in the program "Critical frequencies of the rotor". In case of the parameters $c_0 = 2.455 \cdot 10^7$ N/m; $\alpha = -2.681 \cdot 10^4$ N s/m; $\beta = 1.996 \cdot 10^2$ N s^2/m, the critical frequencies are obtained: $\Omega_1 = 118$ rad/s, $\Omega_2 = 256$ rad/s, $\Omega_1 = 511$ rad/s, which corresponds to the actual critical frequencies. However, it should be noted that actual parameters $c_0 = 2.45 \cdot 10^7$ N/m; $\alpha = -2.9 \cdot 10^4$ N s/m; $\beta = 2.086 \cdot 10^2$ N s^2/m of bearing stiffness characteristic indicates high accuracy of results obtained by using ANN due to the relative errors less than 1%. The design scheme and mode shapes obtained using

the computer program "Critical frequencies of the rotor" for bearing stiffness evaluated by the use of ANN are presented in Fig. 3.
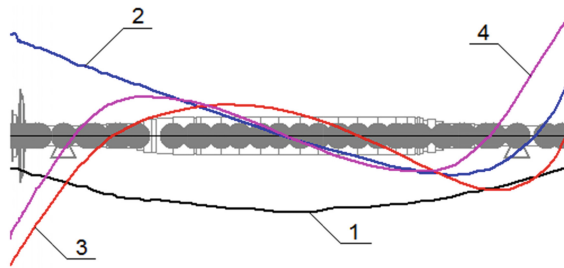

Fig. 3. Design model and mode shapes of the rotor.

The main advantages of using ANN are sufficient accuracy of the obtained results, and lack of need for the re-optimizing procedure when changing experimental values of critical frequencies within the same model of rotor dynamics.

5   Conclusions

Thus, the regression dependences for identification of bearing stiffness parameters by using numerical simulation and experimental data are proposed. The computer program "Critical oscillations of the rotor" realizes the mathematical model of rotor dynamics, which allows taking into consideration gyroscopic moments of inertia for impellers and shell-type parts, as well as the non-linear dependence of bearing stiffness on the rotor speed.

The implementation of ANN is verified on the example of the compressor 295GC2-190/44-10M on magnetic bearings with taking into account dependence of stiffness characteristics on the rotor speed. Comparison of the bearing stiffness and critical frequencies obtained with the use of ANN and physical experiment on the accelerating-balancing stand confirms the reliability of the proposed approach with sufficient accuracy for practical purposes.

There are different results of the evaluation of bearing stiffness characteristics as a result of the implementation of the linear regression procedure and artificial neural network. Moreover, sufficient accuracy of calculation of critical frequencies does not ensure a sufficient accuracy of regression procedure due to its original linearity. However, this problem is completely eliminated with the use of an artificial neural network. In addition, it should be noted that using artificial neural network significantly improves the accuracy of identification of the parameters for the mathematical model of bearing stiffness in comparison with the linear regression procedure. ANN has the advantage over traditional optimization methods due to the fact, that changing the initial data for the same model requires a new optimization procedure, while the previously trained ANN does not need this.

Achieved results allow setting directions of further research within the development an approach for implementation ANN for identification non-linear bearing stiffness characteristics by the results of numerical simulation and experimental research of forced oscillations, as well as providing virtual dynamic balancing of flexible rotor systems for multistage centrifugal machines.

References

1. Norfield, D.: Practical Balancing of Rotating Machinery. Elsevier, Amsterdam (2006)
2. Swanson, E., Powell, C.D., Weissman, S.: A practical review of rotating machinery critical speeds and modes. Sound Vib. **39**(5), 10–17 (2005)
3. Vance, J.M., Zeidan, F.Y., Murphy, B.: Machinery Vibration and Rotordynamics. Wiley, Hoboken (2010)
4. Sika, R., Rogalewicz, M., Popielarski, P., Wytyk, G.: Forecasting of steel consumption with use of nearest neighbors method. In: Proceedings of 13th International Conference on Modern Technologies in Manufacturing, Cluj-Napoca and AMaTUC, MATEC Web of Conference, vol. 137, p. 01010 (2017)
5. Sika, R., Rogalewicz, M.: Demerit Control Chart as a decision support tool in quality control of ductile cast-iron casting process. In: Proceedings of 8th International Conference on Manufacturing Science and Education (MSE 2017), Trends in New Industrial Revolution, Sibiu, MATEC Web of Conference, vol. 121, p. 05007 (2017)
6. Sika, R., Hajkowski, J.: Synergy of modeling processes in the area of soft and hard modeling. In: Proceedings of 8th International Conference on Manufacturing Science and Education (MSE 2017), Trends in New Industrial Revolution, Sibiu, MATEC Web of Conference, vol. 121, p. 04009 (2017)
7. Vollan, A., Komzsik, L.: Computational Techniques of Rotor Dynamics with the Finite Element Method. CRC Press, Boca Raton (2012)
8. Muminovic, A.J., Braut, S., Muminovic, A., Saric, I.: Numerical and analytical analysis of elastic rotor natural frequency. Technol. Educ. Manag. Inform. **3**(4), 323–328 (2014)
9. Yamamoto, T., Ishida, Y.: Linear and Nonlinear Rotordynamics: A Modern Treatment with Applications. Wiley, Hoboken (2013)
10. Jin, C., Xu, Y., Zhou, J., et al.: Active Magnetic Bearings Stiffness and Damping Identification from Frequency Characteristics of Control Systems, pp. 1–8. Hindawi Publishing Corporation, Cairo (2016)
11. Wang, A., Cheng, X., Meng, G., et al.: Dynamic analysis and numerical experiments for balancing of the continuous single-disc and single-span rotor-bearing system. Mech. Syst. Sig. Process. **86**, 151–176 (2017)
12. Wang, T., Wang, F., Bai, H., et al.: Stiffness and critical speed calculation of magnetic bearing-rotor system based on FEA. In: International Conference on Electrical Machines and Systems (**10458520**) (2008)

13. Villa, C., Sinou, J., Thouverez, F.: Stability and vibration analysis of a complex flexible rotor bearing system. Commun. Nonlinear Sci. Numer. Simul. **13**(4), 804–821 (2008)
14. Bai, C., Zhang, H., Xu, Q.: Subharmonic resonance of a symmetric ball bearing-rotor system. Int. J. Non Linear Mech. **50**, 1–10 (2013)
15. Ogbonnaya, E.A., Poku, R., Ugwu, H.U., et al.: Analysis of Gas Turbine Blade Vibration Due to Random Excitation. InTech, London (2015)
16. Larsen, T.J., Kim, T.: Experimental and numerical study of a new dynamic phenomenon for two-bladed wind turbines. In: Proceedings of the 25th International Ocean and Polar Engineering Conference, pp. 547–553 (2015)
17. Ocampo, J.C., Wing, E.S.G., Moroyoqui, F.J.R., et al.: A novel methodology for the angular position identification of the unbalance force on asymmetric rotors by response polar plot analysis. Mech. Syst. Signal Process. **95**, 172–186 (2017)
18. Sinou, J., Didier, J., Faverjon, B.: Stochastic non-linear response of a flexible rotor with local non-linearities. Int. J. Non Linear Mech. **74**, 92–99 (2015)
19. Pavlenko, I.V., Simonovskiy, V.I., Demianenko, M.M.: Dynamic analysis of centrifugal machine rotors supported on ball bearings by combined using 3D and beam finite element models. In: IOP Conference Series: Materials Science and Engineering, vol. 233, pp. 1–8 (2017)
20. Pavlenko, I.: Static and dynamic analysis of the closing rotor balancing device of the multistage centrifugal pump. Appl. Mech. Mater. **630**, 248–254 (2014)
21. Reddy, M.C.S., Sekhar, A.S.: Application of artificial neural networks for identification of unbalance and looseness in rotor bearing systems. Int. J. Appl. Sci. Eng. **11**(1), 69–84 (2013)

Movement of the Particle on the External Surface of the Cylinder, Which Makes the Translational Oscillations in Horizontal Planes

Sergiy Pylypaka[1] , Mikola Klendiy[2] ,
and Tatiana Zaharova[3(✉)]

[1] National University of Life and Environmental Sciences of Ukraine,
15 Heroiv Oborony Street, Kiev 03041, Ukraine
[2] Beregany Agricultural Institute of National University of Life
and Environmental Sciences of Ukraine, 20 Academichna Street,
Berezhany, Ternopil Region 47501, Ukraine
[3] Sumy National Agrarian University, 160 H. Kindratiieva Street,
Sumy 40021, Ukraine
t.n.zaharova@ukr.net

Abstract. Differential equations of relative displacement of a particle on the external surface of an inclined cylinder, which performs oscillatory motion, are obtained in the article. All points of the cylinder describe circles in horizontal planes. The equation has been solved numerically and trajectories of relative motion of a particle along the cylinder surface have been constructed. Graphs of other kinematic characteristics in time function are presented. Partial cases, when the axis of the cylinder is located horizontally or at an angle of friction to the horizontal plane, are considered. An experimental research to determine the soil separation efficiency by a sloping cylinder, which performs fluctuations, depending on the influence of individual factors (the coefficient of friction of the soil and the angle of inclination of the cylinder) was conducted in the article. After processing the experimental data, the regression equations were obtained to determine the separation quality and the response surface was constructed.

Keywords: Relative motion · Differential equations · Kinematic parameters
Trajectory · Angle · Friction

1 Introduction

The cylindrical surface is a universal constructive element of many agricultural machines. It moves technological material. For cylindrical moving surfaces, mainly the displacement of a particle by the inner surface is investigated. An example of such a move is the displacement of biomass fractions inside a horizontal cylinder that rotates around its axis [1]. The motion of particles by the external surface of the cylinder is interesting from the cognitive point of view, since with a large radius of the cylinder, bounded portion of its surface, where the relative motion occurs, will be close to the

plane. Accordingly, the trajectories of relative motion in this case should be similar to the trajectories on the plane.

2   Literature Review

It is easier to study the motion of particles in comparison with the motion of bodies, because in the second case it is necessary to take into account the forces of inertia from the rotation of the body. In some cases, these forces can be neglected or ignored at low angular velocities, for example, in the operation of material-handling equipment [2] or when moving on the surfaces of working bodies [3]. Movable particles can be of different nature [4]. Many researches on material particles of technological material, for example, mineral fertilizers are conducted [5–7]. The motion of particles on screw surfaces is also considered [8–10].

3   Research Methodology

First of all, place the upper half of the cylinder in such way, that its axis is inclined to the horizontal plane at an angle β (Fig. 1). Let us write the equation of the cylinder with the horizontal axis OX:

$$X = u; \qquad Y = R\cos\alpha; \qquad Z = -R\sin\alpha, \qquad (1)$$
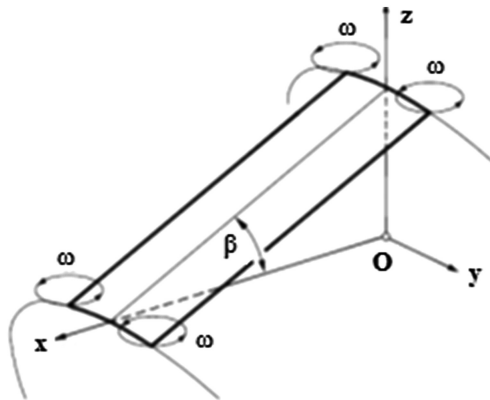
Fig. 1. Scheme of movement of the points of the slope cylinder by circles with angular velocity ω.

where R – radius of the cylinder;
α, u – independent variables of the surface:
α – the angle of rotation of the point of the cylinder around its axis;
u – length of a rectilinear generatrix of the cylinder.
Turn the cylinder (1) to the angle β around the axis OY. Parametrical equations of a rotated cylinder will be written:

$$X = u\cos\beta + R\sin\beta\sin\alpha;$$
$$Y = R\cos\alpha; \qquad\qquad\qquad (2)$$
$$Z = u\sin\beta - R\cos\beta\sin\alpha.$$

The cylinder carries progressive oscillations in such a way that all its points describe circles in horizontal planes (Fig. 1 shows the trajectories of movement of four points of the cylinder). The absolute motion of a particle will be considered in relation to a fixed coordinate system OXYZ. If the cylinder is tied to a moving coordinate system, then, the axis of motion and motionless systems will be parallel at all times, when the cylinder is oscillating. This means, that the absolute trajectory of the particle can be written as the sum of the transient motion of the cylinder, the points of which describe the circle, and the relative motion of the point along the cylinder surface:

$$x = x_n + x_\beta; \qquad y = y_n + y_\beta; \qquad z = z_n + z_\beta, \qquad (3)$$

where $x_e = x_e(t)$; $y_e = y_e(t)$; $z_e = z_e(t)$ – is the trajectory of the transient motion of a cylinder in the function of time t;

$x_r = x_r(t)$; $y_r = y_r(t)$; $z_r = z_r(t)$ – is the trajectory of relative motion of a particle on the surface of a cylinder in the function of time t.

Let us denote the radius of the circles by r, on which the points of the cylinder move, through r. Then the transient motion of the cylinder points is described by the equations:

$$x_e = r\cos\omega t; \qquad y_e = r\sin\omega t; \qquad z_e = h, \qquad (4)$$

where ω – angular velocity of rotation of points of the cylinder by circles;

h = const – height of a point of the cylinder in relation to the origin of coordinates.

On the cylinder the point slips on a certain trajectory. The equation of the trajectory can be obtained, if the independent variables α and u are interconnected (2). Let us write this connection in variable of time t, so the coordinates of the particle on the cylinder surface will be time functions: $\alpha = \alpha(t)$ and u = u(t). In this case, the relative motion of a particle is described by equations:

$$x_r = u\cos\beta + R\sin\beta\sin\alpha;$$
$$y_r = R\cos\alpha; \qquad\qquad\qquad (5)$$
$$z_r = u\sin\beta - R\cos\beta\sin\alpha.$$

Summing up the transient (4) and relative (5) motions by the formula (3), we obtain the equation of the absolute trajectory of the particle:

$$x = u\cos\beta + R\sin\beta\sin\alpha + r\cos\omega t;$$
$$y = R\cos\alpha + r\cos\omega t; \qquad\qquad (6)$$
$$z = u\sin\beta - R\cos\beta\sin\alpha + h.$$

Dependencies: $\alpha = \alpha(t)$ and $u = u(t)$, which describe the trajectory of relative motion (slipping of a particle along the cylinder surface), are unknown functions, that need to be found. After differentiating Eq. (6) by time t, we find projections of the absolute velocity of the particle:

$$\dot{x} = -r\omega \sin \omega t + \dot{u} \cos \beta + R\dot{\alpha} \sin \beta \cos \alpha;$$
$$\dot{y} = r\omega \cos \omega t - R\dot{\alpha} \sin \alpha; \qquad (7)$$
$$\dot{z} = \dot{u} \sin \beta - R\dot{\alpha} \cos \beta \cos \alpha.$$

The differentiation of expressions (7) gives a projection of absolute acceleration:

$$\ddot{x} = -r\omega^2 \cos \omega t - R\dot{\alpha}^2 \sin \beta \sin \alpha + \ddot{u} \cos \beta + R\ddot{\alpha} \sin \beta \cos \alpha;$$
$$\ddot{y} = -r\omega^2 \sin \omega t - R\dot{\alpha}^2 \cos \alpha - R\ddot{\alpha} \sin \alpha; \qquad (8)$$
$$\ddot{z} = R\dot{\alpha}^2 \cos \beta \sin \alpha + \ddot{u} \sin \beta - R\ddot{\alpha} \cos \beta \cos \alpha.$$

Let us formulate the equation of motion in the form $m\bar{w} = \bar{F}$, where m – particle mass, $\bar{w}$ – vector of absolute acceleration, $\bar{F}$ – the resulting vector applied to the particle forces. Such forces are the force of weight mg (g = 9.81 m/s^2), reaction N of the cylinder surface and friction force fN, when the particles slide along the cylinder surface (f is the coefficient of friction). All forces need to be projected on the axis of the coordinate system OXYZ.

The force of the weight is orientated down, so its projections will be the next:

$$\{0; \quad 0; \quad -mg\}. \qquad (9)$$

The reaction of the surface of the cylinder N is directed to its normal and is determined from the vector product of two vectors tangent to the coordinate lines of the cylinder. Projections of these vectors are partial derivatives of Eq. (2):

$$\frac{\partial X}{\partial \alpha} = R \sin \beta \cos \alpha; \quad \frac{\partial Y}{\partial \alpha} = -R \sin \alpha; \quad \frac{\partial Z}{\partial \alpha} = -R \cos \beta \cos \alpha;$$
$$\frac{\partial X}{\partial u} = \cos \beta; \qquad \frac{\partial Y}{\partial u} = 0; \qquad \frac{\partial Z}{\partial u} = \sin \beta. \qquad (10)$$

Vector multiplication of vectors (10) can give two oppositely directed normal vectors – either inside a cylinder, or outside. This depends on the replacement of the vectors (10) in the vector product determinant. The first product corresponds to the motion of the particle on the internal surface of the cylinder, and the second – on the external. With this in mind, the normal vector was found and reduced to a unit vector:

$$\{\sin \beta \sin \alpha; \quad \cos \alpha; \quad -\cos \beta \sin \alpha\}. \qquad (11)$$

Since the friction force is directed towards the tangent to the trajectory of the relative motion of the particle in the opposite direction, we find projections of the vector of the tangent. They are determined by the first derivatives of the Eq. (5):

$$\dot{x}_\beta = \dot{u}\cos\beta + R\dot{\alpha}\sin\beta\cos\alpha; \qquad \dot{y}_\beta = -R\dot{\alpha}\sin\alpha;$$
$$\dot{z}_\beta = \dot{u}\sin\beta - R\dot{\alpha}\cos\beta\cos\alpha. \tag{12}$$

The geometric sum of the components (12) will give the value of the particle slip velocity along the cylinder surface in relative motion:

$$V_\beta = \sqrt{\dot{x}_\beta^2 + \dot{y}_\beta^2 + \dot{z}_\beta^2} = \sqrt{\dot{u}^2 + R^2\dot{\alpha}^2}. \tag{13}$$

The unitary vector of the tangent in the projections on the axis of the OXYZ system is obtained by dividing the projections (12) by the value of the vector (13):

$$\left\{ \frac{\dot{u}\cos\beta + R\dot{\alpha}\sin\beta\cos\alpha}{\sqrt{\dot{u}^2 + R^2\dot{\alpha}^2}}; \qquad -\frac{R\dot{\alpha}\sin\alpha}{\sqrt{\dot{u}^2 + R^2\dot{\alpha}^2}}; \qquad \frac{\dot{u}\sin\beta - R\dot{\alpha}\cos\beta\cos\alpha}{\sqrt{\dot{u}^2 + R^2\dot{\alpha}^2}} \right\}. \tag{14}$$

Let us write a vector equation $m\bar{w} = \bar{F}$ in projections on the axis of the coordinate system, taking into account, that the friction force fN is directed along the unit vector (14) in the opposite direction:

$$m\ddot{x} = N\sin\beta\sin\alpha - fN\frac{\dot{u}\cos\beta + R\dot{\alpha}\sin\beta\cos\alpha}{\sqrt{\dot{u}^2 + R^2\dot{\alpha}^2}};$$
$$m\ddot{y} = N\cos\alpha - fN\frac{R\dot{\alpha}\sin\alpha}{\sqrt{\dot{u}^2 + R^2\dot{\alpha}^2}}; \tag{15}$$
$$m\ddot{z} = -mg - N\cos\beta\sin\alpha - fN\frac{\dot{u}\sin\beta - R\dot{\alpha}\cos\beta\cos\alpha}{\sqrt{\dot{u}^2 + R^2\dot{\alpha}^2}}.$$

We substitute in the Eq. (15) the second derivatives (projections of absolute acceleration) from (8) and obtain a system of three equations:

$$m(-r\omega^2\cos\omega t - R\dot{\alpha}^2\sin\beta\sin\alpha + \ddot{u}\cos\beta + R\ddot{\alpha}\sin\beta\cos\alpha)$$
$$= N\sin\beta\sin\alpha - fN\frac{\dot{u}\cos\beta + R\dot{\alpha}\sin\beta\cos\alpha}{\sqrt{\dot{u}^2 + R^2\dot{\alpha}^2}};$$
$$m(-r\omega^2\sin\omega t - R\dot{\alpha}^2\cos\alpha - R\ddot{\alpha}\sin\alpha)$$
$$= N\cos\alpha - fN\frac{R\dot{\alpha}\sin\alpha}{\sqrt{\dot{u}^2 + R^2\dot{\alpha}^2}}; \tag{16}$$
$$m(R\dot{\alpha}^2\cos\beta\sin\alpha + \ddot{u}\sin\beta - R\ddot{\alpha}\cos\beta\cos\alpha)$$
$$= -mg - N\cos\beta\sin\alpha - fN\frac{\dot{u}\sin\beta - R\dot{\alpha}\cos\beta\cos\alpha}{\sqrt{\dot{u}^2 + R^2\dot{\alpha}^2}}.$$

The system (16) includes three unknown functions: $N = N(t)$, $u = u(t)$ and $\alpha = \alpha(t)$. Solving it by relative N, $\ddot{u}$ and $\ddot{\alpha}$, we get the following expressions:

$$\ddot{\alpha} = \frac{1}{R}\left[-r\omega^2 \sin\alpha \sin\omega t + (r\omega^2 \sin\beta \cos\omega t + g\cos\beta)\cos\alpha\right]$$
$$+ \frac{Af\dot{\alpha}}{\sqrt{\dot{u}^2 + R^2\dot{\alpha}^2}};$$
$$\ddot{u} = r\omega^2 \cos\beta \cos\omega t - g\sin\beta + \frac{Af\dot{u}}{\sqrt{\dot{u}^2 + R^2\dot{\alpha}^2}}; \tag{17}$$
$$N = -mA,$$

where $A = R\dot{\alpha}^2 + g\cos\beta \sin\alpha + r\omega^2(\cos\alpha \sin\omega t + \sin\beta \sin\alpha \cos\omega t)$.

System (17) can not be integrated in analytical form. It needs to be solved numerically. Finding the dependences $\alpha = \alpha\,(t)$ and $u = u\,(t)$ and substituting them in Eq. (2), we obtain the relative trajectory of the motion of the particle along the cylinder surface, that is, the trajectory of sliding. Let us consider individual cases.

4   Results

First case. The angle $\beta = 0$, so all straight lines of the cylinder are parallel to the horizontal plane. Integration of the system (17) was carried out at $r = 0.05$ m, $R = 5$ m. At Fig. 2 the relative trajectories of a particle, which is placed on the surface of the cylinder near its highest rectilinear generatrix, are constructed. The oscillating motion of a particle occurs perpendicularly to the generatrixs of the cylinder, so in the direction of the line of greatest inclination. Depending on the incidence point, the particle moves in one or the opposite direction, and the amplitude of oscillations increases. As can be seen from Fig. 2, the relative motion of the particle is very sensitive to the frequency of oscillations: with increasing ω from 10 s^{-1} to 11 s^{-1}, the length of the traversed path increases significantly.
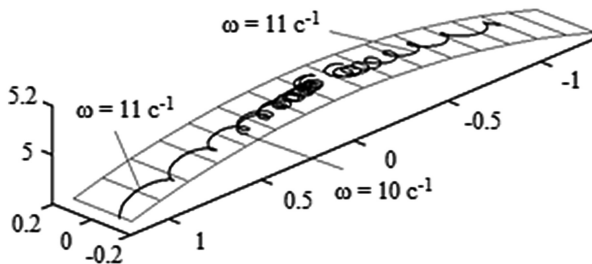

Fig. 2. Trajectories of relative motion of a particle on the surface of a horizontal cylinder, which performs oscillatory motion for 5 s at $R = 5$ m; $r = 0.05$ m; $f = 0.3$.

Second case. The cylinder is inclined at an angle β to the horizon and is immobile ($\omega = 0$).

When the angle β is equal to the friction angle (β = arctg f), the motion of a particle depends on the initial conditions. If it is given the initial velocity along the highest rectilinear generatrix of the cylinder, it will continue to move at this with such speed (Fig. 3, trajectory 1).
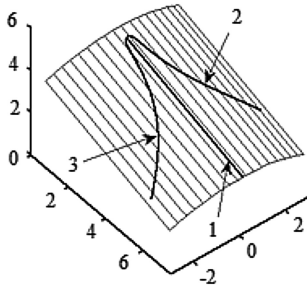

Fig. 3. Trajectory of motion of a particle on a fixed cylinder, inclined at an angle of friction (R = 5 m;   f = 0.3; β = arctg; f = 16.3°).
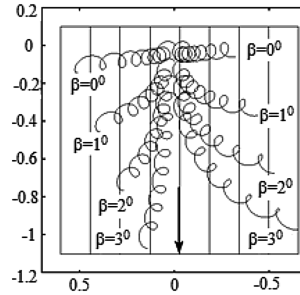
Fig. 4. Trajectories of relative motion of a particle on a cylinder, inclined at different angles β (R = 5 m; r = 0.05 m; f = 0.3; $\omega = 10 \text{ s}^{-1}$).

The numerical integration of the system of differential Eq. (17) gives this result. If the initial velocity is given in the other direction, then the trajectory of motion will be curvilinear and motion will be accelerated. At Fig. 3 two trajectories start with a common point on the upper generatrix of the cylinder. The initial velocity of the particle, which described the trajectory 2, was given by the initial values of constant integration $\dot{\alpha} = 0.2$ and $\dot{u} = 0$. These constants set the speed value in the transverse and longitudinal directions at the initial point. Trajectory 3 is built with $\dot{\alpha} = -0.15$ and $\dot{u} = 0.5$.

If the angle of inclination of the cylinder is less than the angle of friction, then there are areas on its surface, where the initial velocity decreases to zero, so the particle stops or does not begin to move from rest.

If the angle of inclination of the cylinder is greater than the angle of friction, then the particle begins to accelerate from any point of the surface, regardless of the value of the initial velocity.

Third case. The cylinder is inclined at an angle β to the horizontal plane and performs translational oscillations.

In the absence of an angle of inclination of the cylinder, the particle slides along it, moving in the transverse direction (Fig. 2). This case is also shown on the horizontal projection (Fig. 4) with $\omega = 10 \text{ s}^{-1}$. The direction of particle propagation in the oscillatory motion depends to a large extent on the angle of the β cylinder. The

inclination of the cylinder by only 1° substantially rejects the trajectory of the motion of the particle in the direction of the slope (Fig. 4, the line of inclination of the highest generatrix of the cylinder is directed towards the horizontal plane and indicated by an arrow). Obviously, this deviation also depends on the diameter of the cylinder. When the angle β is increasing, the direction of propagation of the particle in the oscillatory motion is increasingly closer to the upper generatrix of the cylinder.

It was found out, how the coefficient of friction influences the trajectory of relative motion of a particle f. At Fig. 5 trajectories for particles with different coefficient of friction are constructed. A cylinder with a radius R = 5 m and the angle of its inclination β = 10^0 was studied. The oscillation frequency ω was 20 s^{-1}. At Fig. 5, the trajectories of the particles with different friction coefficients and with different values of the radiuses r of circles, which are described by the points of the cylinder during its oscillatory motion, are constructed. The value of the coefficient of friction f was in the range from 0.25 to 0.35. On the left side of Fig. 5, trajectories are built for r = 0.02 m, which are almost merging. If the radius r of fluctuations decreases to 0.01 m, then the trajectories of the relative motion of the particles are removed from each other at a considerable distance as they slide along the surface of the cylinder. These trajectories are constructed at Fig. 5, right side. Thus, it is possible to select such parameters of the cylinder and its oscillations, which can provide separation of the technological material, depending on the coefficient of friction. Figure 5b shows the surface of the cylinder and the trajectory of the motion of particles on it at r = 0.02 m. Figures indicate the trajectory of particles with different friction coefficients: 1 − f = 0.25; 2 − f = 0.3; 3 − f = 0.35. The difference L among the distances between the extreme points is about 1 m at the moment of the acceleration of the particles from the limited compartment of the cylinder.

An experimental research was conducted to determine the soil separation efficiency by a sloping cylinder, which performs fluctuations, depending on the influence of individual factors (the coefficient of friction of the soil and the angle of inclination of the cylinder).

Soil humidity was changed from 10% to 50%, and the coefficient of friction of the soil with the steel changed from 0.4 to 0.6.

Angle of inclination of a cylinder β was in range from 0° to 3°.

After processing the experimental data, the regression equations were obtained to determine the separation quality and the response surface was constructed (Fig. 6).

$$k_1 = 0.95 + \frac{0.39}{\beta} - \frac{1.24}{f};$$
$$k_2 = 0.75 + \frac{0.39}{\beta} + \frac{1.24}{f}.$$

(17)

The main array of approximated experimental values of the separation coefficient k_1 is in the range 0.6 … 0.94, and k_2 – within the range 0.17 … 0.62.
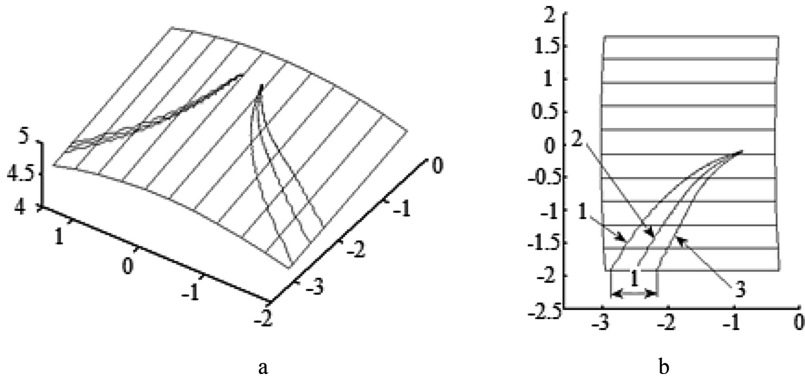
a   b

Fig. 5. Trajectories of relative motion of particles with different coefficients of friction on the surface of an inclined cylinder (R = 5 m; β = 10°; ω = 20 s⁻¹): (a) r = 0.02 m (left) and r = 0.01 m (right); (b) trajectory on a horizontal plane of projections.
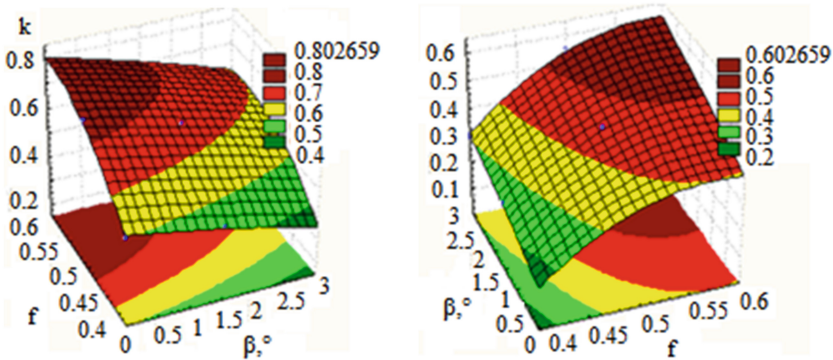

Fig. 6. Feedback surface of changing of the separation factor.

5   Conclusions

When the oscillatory motion of the horizontal cylinder takes place, the particle also performs oscillatory motion, moving along external surface of the cylinder in a transverse direction in relation to the rectilinear generatrix of the cylinder. With the inclination of the cylinder, even at a small angle, the trajectory of moving particles substantially changes, deviating from the transverse direction to the side of the cylinder slope. Particles with different friction coefficients move along different trajectories, and the distance between them increases during slipping over the surface. It can be used to separate the technological material depending on its frictional properties.

References

1. Golub, G.A., Szalay, K., Kukharets, S.M., Marus, O.A.: Energy efficiency of rotary digesters. Prog. Agric. Eng. Sci. **13**(1), 35–49 (2017)
2. Loveikin, V.S., Romesevych, Yu.O.: Dynamic optimization of a mine winder acceleration mode. Sci. Bull. Natl. Chem. Univ. **4**, 81–87 (2017)
3. Baranovsky, V.M., Potapenko, M.V.: Theoretical analysis of the technological feed of lifted root crops. INMATEH Agric. Eng. **51**(1), 29–38 (2017)
4. Batluk, V., Basov, M., Klymets, V.: Mathematical model for motion of weighted parts in curled flow. Econtechmod. Int. Q. J. **2**(3), 17–24 (2013)
5. Adamchuk, V.V.: Investigation of the general case of dispersal of mineral fertilizers by a centrifugal dispersing body. Bull. Agrar. Sci. **12**, 51–57 (2003)
6. Kobets, A.S., Ponomarenko, N.O., Kharytonov, M.M.: Construction of centrifugal working device for mineral fertilizers spreading. INMATEH Agric. Eng. **51**(1), 5–14 (2017)
7. Adamchuk, O.: Theory of dispersal of fertilizers by a dispersing working organ of the centrifugal type. Sci. Pap. Rousse Univ. **52**(1), 22–30 (2013)
8. Isaev, Yu.M., Semashkin, N.M., Nazarova, N.N.: Justification of the process of seed movement by a spiral-helical working organ. Bull. Ulyanovsk State Agric. Acad. **1**, 97–99 (2011)
9. Pylypaka, S.F., Klendiy, M.B., Klendiy, O.M.: Particle motion over the surface of a rotary vertical axis helicoid. INMATEH Agric. Eng. **51**(1), 15–28 (2017)
10. Matveev, A.I., Lebedev, I.F., Nikiforova, L.V., Yakovlev, B.V.: Simulation of the motion of particles in a screw pneumatic separator. Mt. Inf. Anal. Bull. (Sci. Tech. J.) **10**, 172–178 (2014)

Influence of the Passive Flow Initial Parameters on the Efficiency of Liquid-Vapor Ejectors

Serhii Sharapov[(✉)] [iD], Vyacheslav Arsenyev [iD], Maxim Prokopov [iD], and Viktor Kozin [iD]

Sumy State University, 2 Rymskogo-Korsakova Street, Sumy 40007, Ukraine
s.sharapov@kttf.sumdu.edu.ua

Abstract. The article deals with the issue of creating a vacuum in various industries and equipment using two-phase jet devices, namely liquid-vapor ejectors working on principle of stream thermal compression. The principle of stream thermal compression implies boiling of the working fluid in the expanding part of the active flow nozzle. The influence of the initial parameters of the passive flow on the efficiency of the mixing process is based on extensive literature analysis of the works of modern domestic and foreign authors. The character of the influence of temperature, relative humidity and the content of the passive flow at the entrance to the receiving chamber on the geometric and regime parameters of the mixing chamber is established. The results of numerical and experimental investigations of the influence of the passive flow initial parameters on the efficiency of liquid-vapor ejectors are presented. Exergetic analysis of the efficiency of these devices with various passive flow environments is performed.

Keywords: Liquid-vapor ejector (LVE) · Two-phase jet device
Active flow · Passive flow · Receiving chamber · Mixing chamber
Exergetic efficiency

1 Introduction

Now more and more technological processes, using vacuum, are becoming increasingly widespread. The efficiency of using liquid-vapor ejectors for such purposes, which working process is based on the principle of jet thermal compression, has been numerically modeled and experimentally confirmed in the scientific works [1–3].

The efficiency of mixing the active and passive flows in the mixing camera directly depends on the initial parameters of the passive flow. Thus, when water vapor is used as a passive flow that on an entrance to the reception chamber can be in a saturated or superheated state as a result of process of mixing we will receive a two-phase stream of uniform homogeneous structure. In the case where the passive flow is air or an air-vapor mixture, during the mixing process, the injected pure air or a part of it from the air-vapor mixture takes away a part of the moisture from the active flow, that is necessary to pass into the state of moist air. This increases the time required for the

process of mixing and, accordingly, entails a change in the geometric and regime parameters of the mixing chamber and LVE in general.

2 Literature Review

The scientific work [4] describes the influence of the geometric dimensions of the mixing chamber on the degree of completeness of exchange processes between the active and passive flows. In an experimental study of a water-air jet device on a transparent model, it is noted that in the vast majority of operating modes, not all trapped air is constricted in the flowing part of this device and is discharged into the injection pipe. Some of the working fluid of the passive flow returns to the receiving camera, forming reverse currents at the walls of the mixing camera of the device. This phenomenon is especially visualized in $p_c/p_н > 15$.

According to the results of experimental studies of two-phase jet devices, a large number of works have been published that describe the influence of the regime parameters (loss coefficients, compression indexes and temperature of the working fluid of the active flow) [5–8].

The calculation methods discussed above don't prove the diversity of operating modes for vacuum two-phase jet devices, don't allow us to determine the boundaries of the transition from one process of operation to another, don't describe the dependence of the characteristics of devices from the shape, the length of the mixing camera, and a number of other parameters. These techniques are applicable, as a rule, only for the selected operating process of the device in a narrow range of its parameters.

Marchenko and Prokopov approached the study of the working process of a two-phase jet device operating in a compressor process the most fundamentally [1].

The authors of the article have improved the method of calculating by Marchenko and Prokopov that can be applied to vacuum aggregates, revealed a number of peculiarities of the vacuum regime of the operation of the liquid-vapor ejector, associated with the influence of the initial parameters of the working fluid of the active flow on the efficiency of the operation of the LVE.

3 Research Methodology

3.1 Numerical Research

Liquid vapor ejectors are operating on the principle of the jet thermal compression, in which the injection of the passive flow is carried out by a working steam jet, which is formed by the boiling of liquid supplied into the active nozzle. While implementing, such active flow expansion cycle of the working stream occurs on the left of the lower boundary curve. In this case, the emergence of limiting critical flow regimes at the entrance to the mixing chamber, which significantly reduces the efficiency of steam jet ejectors, is virtually eliminated. Scheme of vacuum unit based on LVE and the representation of its workflow presented in [1].

The calculation of the mixing camera of a variable cross-sectioninduced the use of a mathematical model that is based on the equations of impulse signals and mass conservation [2, 3]. The initial parameters determining the efficiency of the mixing process are temperature, moisture content and vapor content of the passive flow at the entrance to the mixing camera.

In the general case, the expressions for the specific enthalpy h02 and entropy s02 of the passive flow at the entrance to the receiving chamber of the LVE are written as:

$$h_{02} = h'_{02} + x_n \cdot r_{02}, \tag{1}$$

$$s_{02} = s'_{02} + \frac{x_n \cdot r_{02}}{T_{02}}, \tag{2}$$

where h'_{02} – a specific enthalpy in a liquid state, J/kg, s'_{02} – a specific entropy in a liquid state, J/(kg K), x_n – a steam quality, kg/kg, r_{02} – a specific heat of a vaporization, J/kg, T_{02} – temperature, index "02" indicates the value of the parameters at the entrance to the receiving chamber.

We will consider the limited cases, when the passive flow is in the saturated vapor state ($x_n = 1$) and in the superheated vapor state.

In the first case, its temperature is a function of the thermodynamic parameters $t_{02} = f\left(P_{02}, h'_{02}, s'_{02}, r_{02}\right)$ and remains constant at a certain pressure.

In the second case, at the same pressure, its temperature can take any values, above the saturation temperature. Such parameters as enthalpy, entropy and specific volume are determined from tables of thermophysical properties.

The speed of the passive flow at the input to the reception department is:

$$w_\kappa = \varphi_1 \cdot \sqrt{2000 \cdot \left(h_{01} - h'_{02} - \left(s_{01} - s'_{02}\right) \cdot T_{02}\right)}, \tag{3}$$

where φ_1 – a coefficient of speed of the reception chamber, h_{01} – a specific enthalpy of the active flow at the input to the mixing chamber, J/kg, h_{01} – a specific entropy of the active flow at the input to the mixing chamber, J/(kg K).

You can see from the formula (3), the speed of the passive flow will increase as its temperature T_{02} grows. Since a subcritical mixing of the active and passive flows will proceed in the mixing chamber, the following condition will be observed:

$$M_2 = \frac{w_\kappa}{a_{2*}} < 1, \tag{4}$$

$$a_{2*} = \sqrt{10^5 \cdot k_2 \cdot P_2 \cdot v_2 \cdot \beta_2^{-1}}, \tag{5}$$

where a_{2*} – a local speed of the passive flow, m/s, k – a specific heats ratio, P – pressure, Pa, v – a specific heat volume, m^3/kg, β – a volumetric steam quality, index "02" indicates the value of the parameters at the entrance to the mixing chamber.

Obviously, the temperature T_{02} will influence the geometric parameters of the reception chamber and the conical tapering portion of the mixing chamber. If in the reception chamber the working medium of the passive flow is in a state of superheated steam, then at the same pressure it takes a larger specific heat volume $v_{02}{}'$, accordingly, with the same mass flow of the passive flow, the relative area of the input section of the reception chamber $\bar{f}_1$ should be larger.

$$\bar{f}_1 = \frac{v_{02}' \cdot w_a}{v_a \cdot w_\kappa} \tag{6}$$

Proportionally $\bar{f}_1$, the relative area of the entrance section of the mixing chamber also increases $\bar{f}_\kappa$. At the output from the mixing chamber the flow is a homogeneous jet, so the relative area of the mixing chamber at the output $\bar{f}_3$ remains constant for all mixing cases (passive flow states at the input to the receiving chamber). Thus, the area ratio $\bar{f}_\kappa/\bar{f}_3$ will also increase as the temperature ratio T_{02}/T_2 grows.

It should also be noted that the length of the conical convergent portion of the mixing chamber increases with increasing of the relative area $\bar{f}_\kappa$ at the entrance to the mixing chamber, with constant values of the relative area $\bar{f}_3$ and the confusion angle of the conical section of the mixing chamber. This is because the passive flow rate, which is in the superheated steam state w_κ, is higher, than in the saturated vapor state, and it takes a longer time to get the total pressure p_2, which is set at the input of the flow into the cylindrical part of the mixing chamber.

When injecting humid air or a steam-air mixture, formulas (1) and (2) are needed to find the parameters of the working environment of the passive flow at the entrance to the reception chamber are recorded in this form:

$$h_{CM} = h_{cB} + h_n, \tag{7}$$

$$\dot{m}_{CM} \cdot h_{CM} = \dot{m}_{c.B.} \cdot h_{c.B.} + \dot{m}_n \cdot h_n, \tag{8}$$

where h_{CM} – the enthalpy of the steam-air mixture at the input to the reception chamber, $h_{c.в.}$ – the enthalpy of dry air at the input to the reception chamber, h_n – the enthalpy of water vapor at the input to the reception chamber, $\dot{m}_{CM}$ – the mass flow rate of steam-air mixture at the input to the reception chamber, $\dot{m}_{c.в.}$ – the mass flow rate of dry air at the input to the reception chamber, $\dot{m}_n$ – the mass flow rate of vapor at the input to the reception chamber.

A humidity φ_n of steam-air mixture is determined by the formula:

$$\varphi_n = \frac{P_s(T_d)}{P_s(T)} \cdot 100\% \tag{9}$$

where P_s – a saturated air pressure at the appropriate temperature, T_d – the temperature of dew point T – the air temperature, that is contained in the steam-air mixture at the entrance to the reception chamber.

The vapor content of the working medium of the passive flow influences on the nature of the mixing process. The steam content of the steam-air mixture is determined from the ratio:

$$x_n = \frac{\dot{m}_n}{\dot{m}_{CM}} \tag{10}$$

The value of the gas constant of the vapor-air mixture, that determines its thermodynamic parameters, makes it possible to say sufficiently with what properties it will possess.

3.2 Experimental Research

An experimental study of liquid-vapor ejector was carried out on a transparent model according to the program and test procedure, described in the work [2]. The results of the evaluation of the influence of the initial parameters of the working fluid of the passive flow on the efficiency of the mixing process obtained experimentally, confirmed the results of numerical simulation using the calculation method proposed by the authors of the article (Fig. 1).
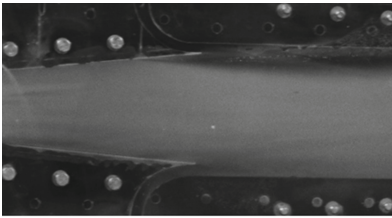
$P_{01} = 4\ bar,\ T_{01} = 130^0C,\ P_a = 0,8\ bar$
(cylindrical mixing chamber (MC))
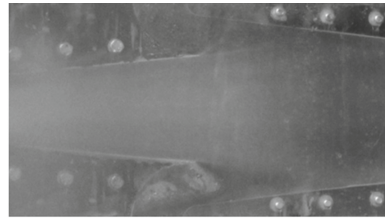
$P_{01} = 4\ bar,\ T_{01} = 130^0C,\ P_a = 0,8\ bar$
(conical MC)
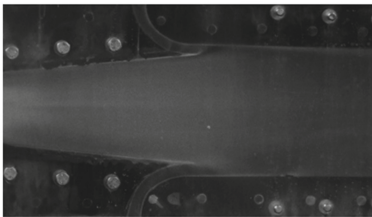
$P_{01} = 10\ bar,\ T_{01} = 175^0C,$
$P_a = 0,52\ bar$ (cylindrical MC)
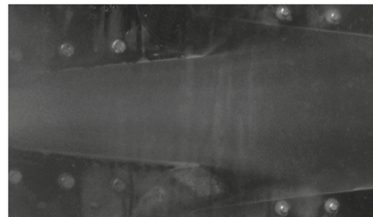
$P_{01} = 10\ bar,\ T_{01} = 175^0C,$
$P_a = 0,45\ bar$ (conical MC)

Fig. 1. The influence of the convergence degree of the conical mixing chamber to the mode of its operation.

Figure 1 presents the results of an experiment in which cylindrical and conical mixing chambers were studied in the range of the initial parameters $P_{01} = 4$–10 bar, $T_{01} = 130$–175 °C at a pressure in the output section of the nozzle $P_a = 0{,}45$–$0{,}8$ bar. In values $P_{01} < 4$ bar the active flow doesn't have sufficient energy to eject the passive flow, and at pressures $P_{01} > 10$ bar the active flow has a very high speed, as a result of which the mixing process is completed not in the cylindrical part of the mixing chamber, but in the diffuser.

Figure 1 shows that it is possible to achieve lower pressure of the passive flow with larger initial operating fluid parameters of the active flow. For the same reasons, as the convergence angle was increased, it was required to increase the initial parameters of the working fluid of the active flow, because the basic geometric parameter was decreased f_3 and in the input section of the mixing chamber was a smaller ratio of pressures P_c/P_{02}.

4   Results

The results of numerical investigations are shown in Figs. 2, 3, 4, 5 and 6. The temperature influence of the passive flow on the nature of the mixing process is shown in Figs. 2 and 3.

In general, it can be said that the geometric dimensions of the liquid-vapor ejector, operating on the superheated vapor, are larger, than LVE, that injects saturated vapor, as evidenced by the change in the basic geometric parameter of the mixing chamber at the input $\bar{f}_\kappa$ and at the output $\bar{f}_3$ while the temperature increasing of the working medium of the passive flow at the input to the reception chamber T_{02} (Fig. 2).
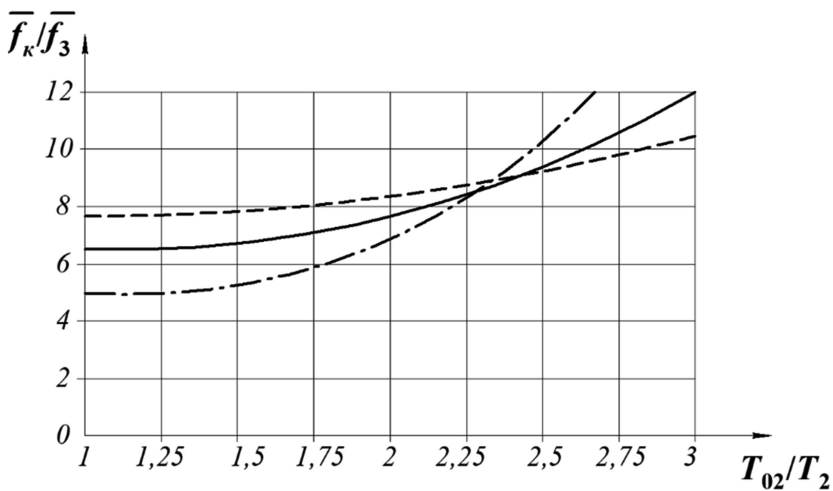

Fig. 2. Dependence of the area ratio $\bar{f}_\kappa/\bar{f}_3$ from the temperature ratio T_{02}/T_2 when: $P_a = P_{02} = 0{,}05$ bar, $T_{02} = 30$–100 °C; $- \cdot - \cdot - -$ $P_{01} = 2$ bar, ——— – $P_{01} = 4$ bar, $- - - - -$ $P_{01} = 6$ bar.
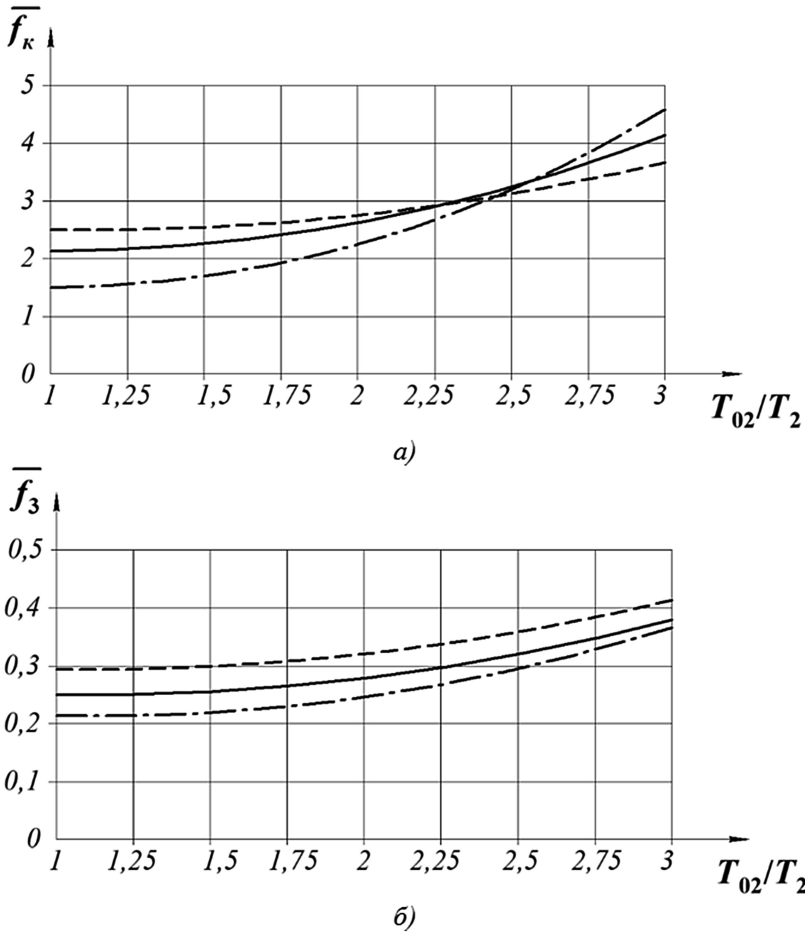
Fig. 3. The influence of the temperature ratio T_{02}/T_2 on the main geometric parameter at the input $\bar{f}_\kappa$ (*a*) and at the output $\bar{f}_3$ (*б*) when: $P_a = P_{02} = 0,05$ bar, $T_{02} = 30–100$ °C; - · - · - · − $P_{01} = 2$ bar, ——— $P_{01} = 4$ bar, - - - - - $P_{01} = 6$ *bar.*

Figure 4 shows that the higher degree of air dryiness, the more moisture will be taken away from the active stream, and the less overproduction of vapor will be at the exit from the ejector and the injection ratio.

Figure 5 shows how the vapor content of the passive flow affects the main geometric parameters of the mixing chamber at the input and output. When the air content in the vapor mixture increases, the basic geometric parameters of the mixing chamber of the liquid-vapor ejector rapidly increase, that leads to more rapid flow regimes and a lesser degree of completeness of metabolic processes between them, as in the case of a passive superheated flow as a working medium.
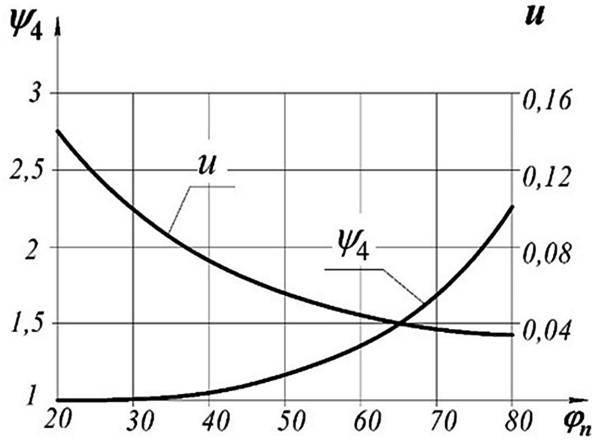
Fig. 4. Dependence of the overproduction of vapor degree ψ_4 and the injection coefficient u from the relative humidity φ_n of the passive flow ($P_a = P_{02} = 0{,}2$ bar).
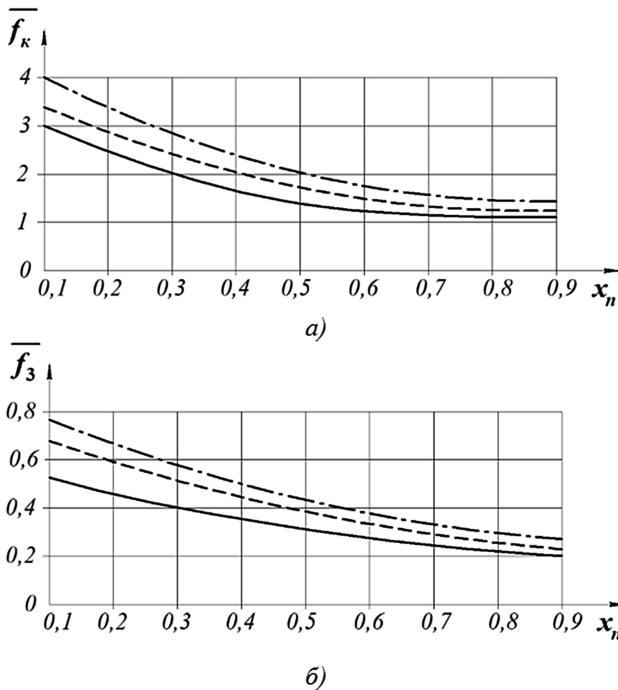

Fig. 5. The vapor content influence of the passive flow x_n on the basic geometric parameter of the mixing chamber at the input $\bar{f}_\kappa$ (а) and at the output $\bar{f}_3$ (б) when: $P_a = P_{02} = 0{,}2$ bar; - · - · - - $P_{01} = 1{,}5$ bar, ——— $P_{01} = 2$ bar, - - - - - $P_{01} = 4$ bar.

Analyzing the effect of vapor content on the geometric parameters of the mixing chamber, it can be argued that it, like the moisture content, affects the achievable parameters of the liquid-vapor ejector and the vacuum unit as a whole (Fig. 6).
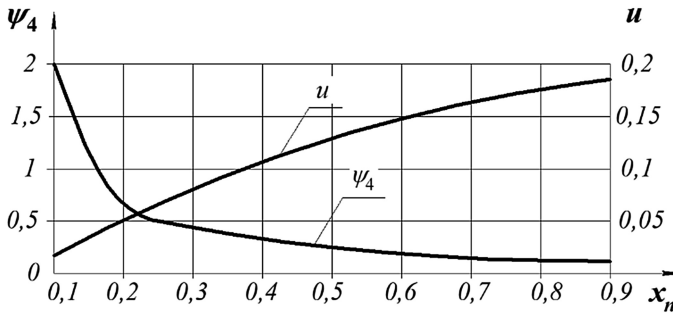

Fig. 6. The vapor content influence of the passive flow x_Π on the accessible effective figures of the liquid-vapor ejector.

5   Conclusions

As a result of the study, that touches on the influence of the initial parameters of the passive flow on the efficiency for the mixing process and the entire working process of the liquid-vapor ejector as a whole, the following conclusions can be drawn:

1. The temperature of the passive flow at the input to the reception chamber affects the geometric parameters of the mixing chamber. The more it is greater at the same pressure, that is, the greater the degree of superheat of vapor, the more time is required for the liquid phase of the passive flow to "vaporize" and complete the mixing process, and, therefore, the greater the geometric dimensions are near the mixing chamber.
2. The use of a passive vapor air mixture or air as working media also affects the geometry of the mixing chamber. Increasing the moisture content and vapor content of the passive flow also increases the time of the mixing process, which in turn leads to an increase in the geometric dimensions of the mixing chamber.

References

1. Marchenko, V., Osipov, V., Prokopov, M., Sharapov, S.: Principle of stream thermocompression: conception of energetic efficiency and prospect of realization is in small heat energetic. MOTROL. Motoryzacja i energetylca rolnictwa **11A**, 70–76 (2009)
2. Sharapov, S., Arsenyev, V.: Experimental study of a liquid-vapor ejector with a cylindrical mixing chamber. Refrig. Equip. Technol. **52**(2), 87–92 (2016). (in Russian)
3. Sharapov, S., Arsenyev, V., Kozin, V.: Experimental investigation of liquid-vapor ejector with conical mixing chamber. Technol. Audit Prod. Reserves **4**(1(30)), 50–55 (2016)

4. Tsegelskiy, V.: Two-phase jet apparatus. N.E. Bauman MSTU, Moscow (2003). (in Russian)
5. Shurchkova, Yu.: Adiabatic Boiling. Practical Use. Naukova dumka, Kyiv (1999). (in Russian)
6. Kudirka, A.A., Glants, D.M.: The jet pump designing for circulation systems of boiling water-moderated reactors. In: Energy Machines and Plants. Proceedings American Society of Mechanical Engineers, vol. 1, pp. 1312–1321 (1974)
7. Smolka, J., Bulinski, Z., Fic, A., Nowak, A.J., Banasiak, K., Hafner, A.: A computational model of a transcritical R744 ejector based on a homogeneous real fluid approach. Appl. Math. Model. 37(3), 1208–1224 (2013)
8. Hemidi, A., Henry, F., Leclaire, S., Seynhaeve, J.M., Bartosiewicz, Y.: CFD analysis of a supersonic air ejector. Part I: Experimental validation of single-phase and two-phase op-eration. Appl. Therm. Eng. 29(8), 1523–1531 (2009)

Constitutive Equation for Numerical Simulation of Elastic-Viscous - Plastic Disperse Materials Deformation Process

Evgenii Shtefan[(✉)] , Bohdan Pashchenko , Serhii Blagenko,
and Serhii Yastreba

National University of Food Technologies,
68 Volodymyrska St., Kyiv 01601, Ukraine
eshtefan@ukr.net

Abstract. During the investigation it was made the methodology of elastic - viscous - plastic disperses materials (DM), deformation processes, creation of constitutive equation. The two levels of DM structural analyses are used, such as microanalysis (separated micro-fragment (particle) of a disperse system consideration) and macro-analysis (the parameters averaging the representative element macro volume). It is considered that the parameter of the local (at micro level) energy deformation speed of the solid phase with its subsequent over the representative element volume is averaged. The constitutive equation general structure is formulated by the components of stress and deformation rates tensors due to the chosen material model. The peculiarity of this model is that the equilibrium flow concept elastic-viscous-plastic material is an alternative to its elastic-plastic deformation The proposed equations are suitable for their effective practical using for digital models creation that based on existent software for the of equilibrium processes of compact materials deformation finite-element analysis. It can be used for calculating of technological processes and designing equipment of food and other productions.

Keywords: The mathematical simulation · Non-equilibrium deformation
Mechanical behavior · Dispersible materials

1 Introduction

The research problem determination is connected with the dispersed materials (DM) non-equilibrium deformation processes which are needed to study. The mathematical simulation using as an instrumental core in modern technologies of DM processes and equipment design is impossible without taking into account the structural and mechanical characteristics of these materials and, first of all, the solid phase rheological properties of, such as, elasticity, plasticity, viscosity, etc. [1, 2]. A significant problem is the elastic – viscous – plastic porous material constitutive relations [3, 4], which is connected with the obtaining adequate results of non-equilibrium deformation processes numerical simulation in the technologies of DM mechanical processing. In order to ensure the constitutive equation effective practical using, it is

expedient to obtain them in the corresponding equation form compact material elastic-plastic rheological model [5].

For creating of the instrumental (numerical) system for DM non-equilibrium deformation processes numerical analysis, it is necessary to develop the mathematical boundary value problem of dispersed media mechanics with in the solid phase elastic – viscous–plastic deformation process regime [6, 7]. Therefore, the main task of present paper is the creation of constitutive equation methods which can describe the processes of DM elastic – viscous–plastic deformation process and can be used for computational experiments parallel with the equilibrium (elastic-plastic) rheological model constitutive equation within the framework of the common software.

2 Literature Review

The decision of the intensification and optimization problem of the manufacture technologies of the DM is impossible without establishment of the main appropriateness of the mass-exchange processes proceeding [8–10]. The mathematical imitation modeling of these processes can serve as the basis of the information practice of design (IPD) of the technological equipment [11]. One of the most effective IPD variants has the type: "mathematical model - intellectual expert system - design automation system" and considers the technological processes as multicomponental system of interconnected subjects of inquiry (SI): DM, technological equipment elements, thermomechanical loading means etc. [11–13]. IPD is based on carrying out of the computing experiments which realize the analytical, algorithm and digital models [11, 14].

The analytical model construction of the mechanical behavior of the disperse medium is suitable by using the principle of its conditional division on three groups: 1 - solid particles; 2 - water in various kinds and conditions; 3 - gaseous inclusions [2, 5]. Considering a specific processing technology we adopt the presentation of DM concept as two-phase mixtures of the porous or granular solid deformed structure with a liquid or gas [5, 11]. To describe mechanical behavior of such materials it is necessary to use the stress, deformation, density terms and changing rate of these parameters [4, 15]. These tensor and scalar characteristics are local and may be determined by operations of the boundary transition, when the space elements (volumes and surfaces) are leveled to material points [5]. In traditional continuum models the points are identified by the particles of the medium (the infinitesimal material continuum volume) [6, 7, 12]. Such particles are elementary carriers of the material properties [2, 4].

3 Research Methodology

Dynamic aspects of DM mechanical behavior are regulated by the balance equations in the form of the motion amount and mass safety laws within the DM representative element (RE). At the same time for DM each phase's relative motion equation is presented in the form [5]:

$$\alpha_1 \left(\rho_1 \frac{du}{dt} - \rho_2 \frac{dv}{dt} \right) - \nabla \sigma^f - \frac{R}{\alpha_2} - \alpha_1 (\rho_1 - \rho_2) G = 0 \tag{1}$$

$$\rho_2 \frac{dv}{dt} = -\nabla P - \frac{R}{\alpha_2} + \rho_2 G = 0 \tag{2}$$

where according to the particular DM phase's interpenetration mechanism (filtration, diffusion, etc.) the force R is taken into account, which is proportional to the relative average velocity of the gas-jet phase flux (analogous to the viscous resistance strength):

$$R = \frac{\mu}{a^2} \alpha_1 \alpha_2 (v - u) \tag{3}$$

where μ – the dynamic viscosity coefficient (kg·s/m) for the non-compressible liquid; a – a generalized coefficient that takes into account the pore configuration of the dispersion medium.

For the constitutive equation formulation (between deformations and stresses) within the limits of the DM (RE), a methodology has been developed, and it consists of the following steps:

1. The two levels of DM structural analyses are used – microanalysis (separated micro-fragment – particle of a disperse system consideration) and macro-analysis (the parameters averaging the RE macro volume). An idealized DM micro-fragment is considered – elementary volume in the form of an empty cylinder (Fig. 1). The material of this cylinder (DM solid phase on a micro level) is considered non-compressible, and its axis coincides with one of the main direction of strain rate tensor components.
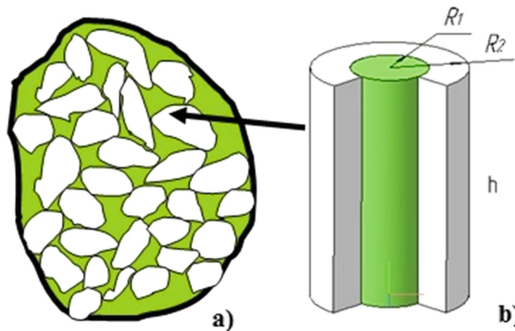

Fig. 1. The disperse material macro-fragment (a) and idealized micro-fragment (b).

In the area, is which is occupied by the cylinder $R_1 < r < R_2;\ 0 < z < h$ only two components of the material move points velocity v_r and v_z are considered:

$$\frac{\partial v_r}{\partial r} + \frac{v_r}{r} + \frac{\partial v_z}{\partial z} = 0 \tag{4}$$

2. The parameter of the local (at micro level) energy deformation speed of the solid phase with its subsequent over the entire cylinder volume averaging is considered:

$$D = \sigma_0 \gamma_0 \cdot \left(\frac{1}{\alpha_1} \sqrt{\frac{\psi e^2}{\gamma_0^2} + \frac{\varphi \Gamma^2}{\gamma_0^2}} \right)^{n+1} + \sigma_T \gamma_0 \frac{1}{\alpha_1} \sqrt{\frac{\psi e^2}{\gamma_0^2} + \frac{\varphi \Gamma^2}{\gamma_0^2}} \tag{5}$$

In Eq. (5) the material dispersion parameters are taken into account:

$$\alpha_2 = 1 - \alpha_1 = \frac{R_1^2}{R_2^2}; \quad \psi = \frac{\alpha_1}{2\alpha_2}; \quad \sigma = \sigma_0 \left(\frac{\gamma'}{\gamma_0} \right)^n + \sigma_m; \quad \gamma = \sqrt{\frac{1}{2} \frac{R_2^4}{r^4} e^2 + \Gamma^2} \varphi = \alpha_1;$$

as well as a generalized rheological model of material solid phase, where σ_m – the yield point, γ – parameter of deformation velocities intensity, σ_0, γ_0, n – constants of the experimental data approximation; e, Γ – first and second stress tensor invariants.

3. The general structure of constitutive equation is formulated by the components of stress σ_{ij} and deformation rates e_{ij} tensors [11, 15].

$$\sigma_{ij} = \left(\frac{\sigma_0 \left({w}/{\gamma_0} \right)^n + \sigma_T}{w} \right) \left[\varphi\, e_{ij} + \left(\psi - \frac{1}{3}\varphi \right) e\, \delta_{ij} \right] \tag{6}$$

$$w = \frac{1}{\alpha_1} \sqrt{\psi\, e^2 + \varphi\, \Gamma^2} \tag{7}$$

4. The relation (6) concretization due to the chosen material model. According to the dissipative determinism principle for the elastic - viscous - plastic material model it is enough to set the parameters: free Helmholtz energy Δ, which determines the reverse component of mechanical deformation power:

$$W^0 = \frac{\partial \Delta}{\partial e^e}\, e^e \tag{8}$$

with the velocities tensor of reverse (elastic) deformation e^e; generalized dissipative potential D_M with a scalar function $\lambda(\Phi)$, which determines the mechanical energy dissipation (in the Clausius-Dugem's inequality):

$$D_{\mathcal{M}} = \lambda(\Phi) \cdot \Phi = \sigma_{ij} \cdot e_{ji}^{\mathcal{H}} \tag{9}$$

From Eq. (7) we can have the following constitutive equation for the PE elastic deformation regime:

$$\dot{\sigma}_{ij} = D^{e}_{ijkl} e^{e}_{kl} \tag{10}$$

where D^{e}_{ijkl} the solid phase elastic properties tensor.

For the general form constitutive Eq. (6) construction is the functional Φ, which defines the boundary of the reversible and irreversible states in the stress space of the macro DM volume should be represented as [11]:

$$\Phi(p, \tau, \alpha_1, \kappa, t) = \frac{\tau^2}{\varphi} + \frac{p^2}{\psi} - \kappa(t) = 0 \tag{11}$$

where P – hydrostatic pressure level in the dispersive medium, τ^2 – the effective stresses second deviant invariant; $\kappa(t)$ –the loading surface size characteristic of the deformation process. Taking into account (8) and (9) we obtain the constitutive equation for the PE DM irreversible deformation regime:

$$\sigma_{ik} = \frac{1}{\lambda(\Phi)} \left[\varphi e^{\mathcal{H}}_{ik} + \left(\psi - \frac{1}{3}\varphi \right) e^{\mathcal{H}} \delta_{ik} \right] \tag{12}$$

Complete effective stresses σ of the non-equilibrium irreversible deformation process which is considered as a sum of equilibrium σ^p and non-equilibrium components σ^v:

$$\sigma = \sigma^p + \sigma^v \tag{13}$$

The peculiarity of this model is that the equilibrium flow concept elastic-viscous-plastic material is an alternative to its elastic-plastic deformation.

The equilibrium components of the stress tensor (13) are determined by the (12):

$$\sigma^{p}_{ik} = \frac{\sqrt{\rho}\kappa(t)}{\sqrt{\varphi \gamma^2 + \psi e^2}} \left[\varphi \, e^{\mathcal{H}}_{ik} + \left(\psi - \frac{1}{3}\varphi \right) e^{\mathcal{H}} \delta_{ik} \right] \tag{14}$$

where γ – is the velocity second deviator invariant. In turn, for the nonequilibrium component of the stress tensor on the basis of (11) we have:

$$\sigma^{v}_{ik} = 2\eta \left[\varphi e^{\mathcal{H}}_{ik} + \left(\psi - \frac{1}{3}\varphi \right) e^{\mathcal{H}} \delta_{ik} \right] \tag{15}$$

where η is the coefficient of viscosity of the material solid phase.

Equation (13) with (14) and (15) determine the irreversible component of the DM deformation rate:

$$e^{\mathcal{H}}_{ik} = \frac{\sqrt{\varphi\gamma^2 + \psi e^2}}{\varphi\psi \left(\sqrt{\rho}\kappa + 2\eta_k \sqrt{\varphi\gamma^2 + \psi e^2} \right)} \left[\varphi\sigma_{ik} + \left(\frac{1}{3}\varphi - \psi \right) p\delta_{ik} \right] \tag{16}$$

or in matrix form

$$\{e^{\mathcal{H}}\} = [Z^{\mathcal{H}}]\{\sigma\} \tag{17}$$

where $[Z^{\mathcal{H}}]$ a matrix which components determine the parameters of the viscoelastic DM model.

5. The constitutive equation formulation for the elastic-viscous-plastic deformation regime material solid phase. To do this, we use the Taylor series decomposition for vector $\{e^{\mathcal{H}}\}$ (16) in the time argument $t_n < t < t_n + \Delta t_n$ in the neighborhood of the moment t_n in the smallness assumption for Δt_n:

$$
\begin{aligned}
\{e^{\mathcal{H}}\}_{n+1} &= \sum_{n=0}^{m} \frac{d^{m-1}}{dt^{m-1}}\{e^{\mathcal{H}}\}\,|_{t_n}\, \frac{(\Delta t_n)^m}{m!} + 0(\Delta t_n)^{m+1} \\
&\approx \{e^{\mathcal{H}}\}_n + \left([\dot{Z}^{\mathcal{H}}]_n\{\sigma\}_n + [Z^{\mathcal{H}}]_n\{\dot{\sigma}\}_n\right)\Delta t_n
\end{aligned} \tag{18}
$$

Taking into account the additive decomposition of the rate of deformation $e = e^e + e^{\mathcal{H}}$ and linear interpolation (18) in time layers t_n and t_n+1 $\{e^{\mathcal{H}}\} = (1-\omega)\{e^{\mathcal{H}}\}_n + \omega\{e^{\mathcal{H}}\}_{n+1}$ from (10) follow the relation in the matrix form:

$$\{\dot{\sigma}\} = [D^{evp}]_n\{e\} - \{VP\}_n \tag{19}$$

where $[D^{evp}]_n$ – the constitutive matrix of elastic-viscous-plasticity, $\{VP\}_n$ is the vector of stresses "rheological" correction.

4   Results

The constitutive Eqs. (19) for the accepted solid phase deformation models definite form are obtained:

1) elastic-plastic (equilibrium) in a cylindrical coordinate system:

$$
[D^{ep}] = \frac{E}{(1+v)(1-2v)}
\begin{bmatrix}
1-v & v & v & 0 \\
v & 1-v & v & 0 \\
v & v & 1-v & 0 \\
0 & 0 & 0 & \frac{1-2v}{2}
\end{bmatrix}
- K_f
\begin{bmatrix}
S_r^2 & S_r S_z & S_r S_\alpha & S_r \tau_{rz} \\
S_z S_r & S_z^2 & S_z S_\alpha & S_z \tau_{rz} \\
S_\alpha S_r & S_\alpha S_z & S_\alpha^2 & S_\alpha \tau_{rz} \\
\tau_{rz} S_r & \tau_{rz} S_z & \tau_{rz} S_\alpha & \tau_{rz}^2
\end{bmatrix}
$$

$$
- K_s
\begin{bmatrix}
2S_r & S_r + S_z & S_r + S_\alpha & \tau_{rz} \\
S_z + S_r & 2S_z & S_z + S_\alpha & \tau_{rz} \\
S_\alpha + S_r & S_\alpha + S_z & 2S_\alpha & \tau_{rz} \\
\tau_{zr} & \tau_{zr} & \tau_{zr} & 0
\end{bmatrix}
- K_p
\begin{bmatrix}
1 & 1 & 1 & 0 \\
1 & 1 & 1 & 0 \\
1 & 1 & 1 & 0 \\
0 & 0 & 0 & 0
\end{bmatrix}
\tag{20}
$$

$$K_f = \frac{27G^2\psi^2}{9(\xi+3G)\psi^2\tau^2 + \left(2\xi + \frac{3E}{1-2v}\right)\varphi^2 P^2} \tag{21}$$

$$K_s = \frac{9GPE\psi\varphi}{(1-2v)\left[9(\xi+3G)\psi^2\tau^2 + \left(2\xi + \frac{3E}{1-2v}\right)\varphi^2 P^2\right]} \tag{22}$$

$$K_p = \frac{3P^2E^2\varphi^2}{(1-2v)^2\left[9(\xi+3G)\psi^2\tau^2 + \left(2\xi + \frac{3E}{1-2v}\right)\varphi^2 P^2\right]} \tag{23}$$

where K_f – the plastic forming coefficient of the given DM volume; K_S – plastic shear deformation coefficient; K_p – the DM plastic volume change coefficient; S_i – components of the stress tensor deviator; ξ – coefficient of plastic rigidity of the material solid phase. As can be seen from (19) in the case $K_f = K_s = K_p = 0$ we have elastic properties $[D^e]$ DM solid phase matrix.

2) elastic-viscous-plastic (non-equilibrium) in a cylindrical coordinate system:

$$[D^{evp}]_n = \left[[D^e]^{-1} + [V]_n\right]^{-1} \tag{24}$$

where

$$[V]_n = \bar{\omega}\,\Delta t_n \left(\frac{\sqrt{\varphi\gamma^2 + \psi e^2}}{\left(\sqrt{\rho}\kappa + 2\eta\sqrt{\gamma^2 + \psi e^2}\right)}\right) \begin{bmatrix} \frac{2}{3\varphi}+\frac{1}{3\psi} & -\frac{1}{3\varphi}+\frac{1}{9\psi} & -\frac{1}{3\varphi}+\frac{1}{9\psi} & 0 \\ & \frac{2}{3\varphi}+\frac{1}{3\psi} & -\frac{1}{3\varphi}+\frac{1}{9\psi} & 0 \\ & & \frac{2}{3\varphi}+\frac{1}{3\psi} & 0 \\ & \textit{symmetrically} & & \frac{1}{\varphi} \end{bmatrix} \tag{25}$$

The equations system (1)–(25) must be supplemented by the initial and boundary conditions formulation that reflected the specifics DM technological processing.

5   Conclusions

The presented system of equations forms the basis of the boundary value problem of the DM mechanics. By using of these equations it is possible to create the mathematical model of deformation processes, which allows the structural-mechanical and rheological parameters of the material solid phase accounting. The form of the obtained constitutive equation allows them to be used effectively for DM mechanical behavior finite-element analysis as the physical basis for existing well-tested digital models of equilibrium (elastic-plastic) processes of compact materials deformation [5].

References

1. Rindyuk, D., Lementar, S.: The method of determination of the optimal parameters of dispersed materials granulation through consolidation. Food Environ. Saf. J. **2**(11) (2014)
2. Camanho, P., Davila, G., de Moura, F.: Numerical simulation of mixed-mode progressive delamination in composite materials. J. Compos. Mater. **37**(16), 1415–1438 (2003)
3. HartleyaI, P., Pillingerb, I.: Numerical simulation of the forging process. Comput. Methods Appl. Mech. Eng. **195**(48–49), 6676–6690 (2006)
4. Bui, Q., Ponthot, J.: Numerical simulation of cold roll-forming processes. J. Mater. Process. Technol. **202**(1–3), 275–282 (2008)
5. Shtefan, E.: Development of information technologies for the design of machinery and equipment for food production. Sci. Works. ONAFT **28**(2), 222–223 (2006)
6. Samarskyi, A., Mikhailov, A.: Mathematical Modeling: Ideas, Methods, Examples. Fizmatlit, Moscow (2002)
7. Kazuyoshi, I., Masanobu, O.: Micro-deformation mechanism of shear banding process based on modified distinct element method. Powder Technol. **109**(1–3), 192–205 (2000)
8. Yelkin, V., Mikhailov, V., Mikhailova, T.: Numerical simulation of plastic flow localization under simple shear. Phys. Mesomech. **7**(1), 184–187 (2004)
9. Smolin, A., Stefanov, Yu., Psakhie, S.: Combined discrete-continual method for simulation of deformation and fracture in the contact zone. **7**(1), 70–73 (2004)
10. Korolev, A.: Computer modeling of processes with distributed parameters. Technical science. Mech. Eng. Eng. Sci. **1**, 138–150 (2008)
11. Shtefan, E., Rindyuk, D., Kadomsky, S.: Mathematical simulation of the organic disperse material mechanical manufacturing. East. Eur. J. Enterp. Technol. **2**(12(68)), 55–61 (2014)
12. Norenkov, I.: Fundamentals of Computer Aided Design. MSTU named by N. Bauman, Moscow (2002)
13. Chempynskiy, L.: Computer Drawing and Graphic Systems for the Development of Design and Technological Documentation in Mechanical Engineering. Academy, Moscow (2002)
14. Horodetskyi, D., Lazniuk, M., Rasskazov, A., Yusypenko, S.: Examples of Calculation and Design. Fakt, Kyiv (2006)
15. Ambrogio, G., Costantino, I., De Napolia, L., Filice, L., Fratini, L., Muzzupappa, M.: Influence of some relevant process parameters on the dimensional accuracy in incremental forming: a numerical and experimental investigation. J. Mater. Process. Technol. **153–154**, 501–507 (2004)

Determination of Transfer Functions
for Electrohydraulic Servo Drive
of Technological Equipment

Volodymyr Sokolov[(✉)] and Oleg Krol

Volodymyr Dahl East Ukrainian National University, 59-a Central Av.,
Severodonetsk 93400, Ukraine
sokolov.snu.edu@gmail.com

Abstract. An electrohydraulic servo drive with throttling regulation of technological equipment is considered. The following basic elements are distinguished in the drive: hydraulic cylinders, the electrohydraulic amplifier including the electromechanical transducer and the hydraulic amplifier, the feedback gauge, the electronic block. To study the dynamic characteristics of the drive a typical mathematical model of non-stationary work processes occurring in the drive is presented. The linearization of the mathematical model is carried out, the structural scheme of the drive is constructed, the transfer functions are obtained for the control signal and the loading influence. The main parameters of the drive are the time constant of the control winding, the time constants of the electrohydraulic amplifier, the time constants of the hydraulic cylinder, the coefficient of relative damping of the hydraulic cylinder, the feedback coefficient, the drive transfer coefficient by the control signal, and the drive transfer coefficient by the loading influence. The proposed linear mathematical model and transfer functions are adapted to the drives of the technological equipment. The main advantage of the presented mathematical description of the characteristics of the electrohydraulic servo drive with the throttle regulation is the ability to perform the stability evaluation, quality of control and correction of the dynamic properties of the drive using the technical certificate data of the drive elements and devices.

Keywords: Electrohydraulic servo drive · Throttle regulation
Structural scheme · Transfer functions

1 Introduction

Modern technological equipment for the mechanical processing of the materials (equipment for processing materials with pressure, metal-cutting machine tools and systems, tool production equipment, etc.) makes high demands on the characteristics of drives for the accuracy of the implementation of the prescribed laws of motion of the output unit, which is achieved by using an electrohydraulic servo drive (EHSD) [1–4].

2 Literature Review

An important stage in EHSD designing is the estimation of stability, quality of control and correction of dynamic properties of a drive. Performance of the given stage is connected with working out of the mathematical model of the non-stationary working processes proceeding in a drive. The mathematical models of dynamic processes presented in the literature [5–8], cannot be generalized to all the class considered EHSD. A number of them are focused on certain designs of devices of a drive, in particular, electrohydraulic amplifier. In the majority of a model definition of parameters which cannot be estimated from the technical certificate data of standard devices demand or are revealed at a stage of preliminary designing.

At small deviations of parameters of the system from static values use of linear models for the mathematical description of non-stationary processes is admissible. It allows receiving the analytical decisions, giving the chance to find out and present prominent features of the studied process for any combination of parameters of the system [9–12]. Besides, analytical decisions are "standards" for an estimation of the accuracy of analytical decisions.

The work purpose is to develop a linear mathematical model and determination of transfer functions for EHSD with the throttle regulation, adapted on drives of the technological equipment, constructed on the basis of standard modules, using an estimation of dynamic characteristics of the technical certificate data of the drive elements and devices.

3 Research Methodology

We allocate basic elements of the EHSD: hydraulic cylinders (HC), an electrohydraulic amplifier (EHA), including an electromechanical transducer (EMT) and a hydraulic amplifier (HA), a feedback gauge (FB), and an electronic block (EB). Further, consider the settlement scheme of a drive presented in Fig. 1.
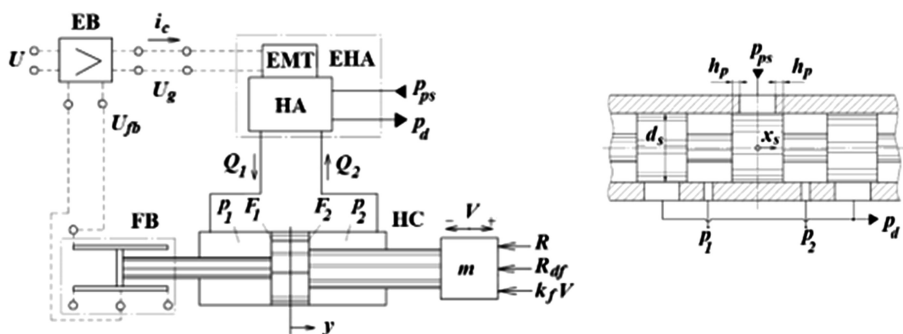

Fig. 1. Settlement scheme of the EHSD and output cascade of the EHA

Based on the works [13–16], we can propose a typical nonlinear mathematical model of the EHSD with the throttle regulation, which includes following equations and dependences:

$$U_{fb} = k_{fb}Y; U_g = k_g(U - U_{fb});$$ (1)

$$L_c\frac{di_c}{dt} + R_e i_c = U_{fb};$$ (2)

$$T_{2a}^2\frac{d^2x_s}{dt^2} + T_{1a}\frac{dx_s}{dt} + x_s = k_{xi}i_c;$$ (3)

$$Q_1 = \begin{cases} \mu_s\pi d_s k_c(x_s - h_p)\sqrt{\frac{2}{\rho}|p_{ps} - p_1|}sign(p_{ps} - p_1), x_s > h_p; \\ 0, |x_s| \le h_p; \\ \mu_s\pi d_s k_c(x_s + h_p)\sqrt{\frac{2}{\rho}|p_1 - p_d|}sign(p_1 - p_d), x_s < -h_p; \end{cases}$$ (4)

$$Q_2 = \begin{cases} \mu_s\pi d_s k_c(x_s - h_p)\sqrt{\frac{2}{\rho}|p_2 - p_d|}sign(p_2 - p_d), x_s > h_p; \\ 0, |x_s| \le h_p; \\ \mu_s\pi d_s k_c(x_s + h_p)\sqrt{\frac{2}{\rho}|p_{ps} - p_2|}sign(p_{ps} - p_2), x_s < -h_p; \end{cases}$$ (5)

$$m\frac{dV}{dt} = p_1 F_1 - p_2 F_2 - k_f V - R - R_{df}signV;$$ (6)

$$\frac{dy}{dt} = V, \quad -H/2 \le y \le H/2;$$ (7)

$$\frac{W_p + F_1(H/2 + y)}{E_f}\frac{dp_1}{dt} = Q_1 - F_1 V;$$ (8)

$$\frac{W_d + F_2(H/2 - y)}{E_f}\frac{dp_2}{dt} = -Q_1 + F_1 V;$$ (9)

where U – input (control) voltage; U_{fb} - FB voltage; U_g - voltage on EB exit; k_{fb} - transfer coefficient of FB; k_g - EB gain coefficient; i_c - current in the control winding; L_c - inductance of the control winding; R_e - active resistance of the electrical circuit; k_{xi} - transfer coefficient of EHA; T_{2a}, T_{1a} - time constants, which are defined on frequencies ν_1, ν_2 of the phase shift on 45 and 90 degrees:

$$T_{2a} = \frac{1}{2\pi\nu_2}; T_{1a} = \frac{1}{2\pi\nu_1} - \frac{2\pi\nu_1}{(2\pi\nu_2)^2};$$ (10)

Q_1, Q_2 – flow rates in the lines of the EHA; c - positional load stiffness; p_{ps}, p_d – pressure of the pump station and drain; p_1, p_2 – pressure in the hydraulic cylinder cavities; h_p – size of a positive overlap (Fig. 1); μ_s – flow coefficient of a spool slot; d_s – diameter of a spool; k_c – coefficient of the completeness of the spool perimeter use;

ρ – density of a working fluid; y, V – displacement and speed of the piston; m – reduced mass of the moving parts; F_1, F_2 - effective areas; κ_f - coefficient of the force of a viscous friction; R_{df} – force of a dry friction; R – loading; H – piston stroke; E_f – module of elasticity of a working fluid; W_p, W_d – "dead" volumes of the pressure head and drain lines.

We linearize the result nonlinear mathematical model, first eliminating the dry friction force and the positional load in the first approximation. Usually, in the compilation of the linear mathematical models of hydraulic drives [1, 4, 10, 11], it is assumed that the "dead" volumes of the pressure head and drain lines are equal

$$W_p = W_d = W_0 \tag{11}$$

and the continuity equations are written for the average position of the piston, as well as the equality of the effective areas of the hydraulic cylinder

$$F_1 = F_2 = F. \tag{12}$$

The last assumption is the most significant, but it allows significantly simplifying the model due to the ensuing of the possibility to allow the equality of flow rates in the lines of the EHA

$$Q_1 = Q_2 = Q. \tag{13}$$

Then, the equations of motion and the balance of flow rates assume the form:

$$m\frac{dV}{dt} = (p_1 - p_2)F - k_f V - R; \tag{14}$$

$$\frac{dy}{dt} = V; \tag{15}$$

$$\frac{W_0 + FH/2}{E_f}\frac{dp_1}{dt} = Q - FV; \tag{16}$$

$$\frac{W_0 + FH/2}{E_f}\frac{dp_2}{dt} = Q + FV. \tag{17}$$

The linear units (1, 2) describe FB, EB and the control winding of the EHA. The linear connection is the displacement of the spool of the HA with the current in the control winding (3). We use the traditional approach [1, 4, 17, 18] to linearize the flow rates characteristics of EHA

$$Q = k_{Qx}x_s - k_{Qp}(p_1 - p_2), \tag{18}$$

where the transfer coefficients are determined by the expressions

$$k_{Qx} = \left.\frac{\partial Q}{\partial x}\right|_{\substack{x_s=x_{s0} \\ p_1=p_{10} \\ p_2=p_{20}}}; k_{Qp} = \left.\frac{\partial Q}{\partial(p_1 - p_2)}\right|_{\substack{x_s=x_{s0} \\ p_1=p_{10} \\ p_2=p_{20};}} \tag{19}$$

where x_s, p_{10}, p_{20}- static values of variables.

In the first approximation in the calculations, we can put the values k_{Qx} and k_{Qp}, determined for $x_{s0} = 0, p_{10} = 0, p_{20} = 0$ and for a spool HA with a zero overlap [1, 4]

$$k_{Qx} = \mu_s \pi d_s k_c \sqrt{\frac{p_{ps} - p_d}{\rho}}; k_{Qp} = 0. \tag{20}$$

For deviations of variables from static values, we have the following system of linear equations:

$$\Delta U_{fb} = k_{fb}\Delta y; \Delta U_g = k_g(\Delta U - \Delta U_{fb}); \tag{21}$$

$$L_c \frac{d\Delta i_c}{dt} + R_e \Delta i_c = \Delta U_{fb}; \tag{22}$$

$$T_{2a}^2 \frac{d^2 \Delta x_s}{dt^2} + T_{1a} \frac{d\Delta x_s}{dt} + \Delta x_s = k_{xi}\Delta i_c; \tag{23}$$

$$\Delta Q = k_{Qx}\Delta x_s - k_{Qp}(\Delta p_1 - \Delta p_2), \tag{24}$$

$$\frac{W_0 + FH/2}{E_f}\frac{d\Delta p_1}{dt} = \Delta Q - F\Delta V; \tag{25}$$

$$\frac{W_0 + FH/2}{E_f}\frac{d\Delta p_2}{dt} = \Delta Q + F\Delta V; \tag{26}$$

$$m\frac{d\Delta V}{dt} = (\Delta p_1 - \Delta p_2)F - k_f\Delta V - \Delta R; \tag{27}$$

$$\frac{d\Delta y}{dt} = \Delta V. \tag{28}$$

Subtract (26) from (25), substitute the result in (24), after which the system is transformed according to Laplace [1, 4] under the null initial conditions and reduces to the form

$$\Delta U_{fb}(s) = k_{fb}\Delta y(s); \Delta U_g(s) = k_g(\Delta U(s) - \Delta U_{fb}(s)); \tag{29}$$

$$\Delta i_c(s) = \frac{1/R_e}{T_{cw}s + 1}\Delta U_g(s); \tag{30}$$

$$\Delta x_s(s) = \frac{k_{xi}}{T_{2a}^2 s^2 + T_{1a}s + 1}\Delta i_c; \tag{31}$$

$$(\Delta p_1(s) - \Delta p_2(s)) = \frac{1}{\frac{FH}{4E_c}s + k_{Qp}}[k_{Qx}\Delta x_s(s) - F\Delta V(s)];\,; \tag{32}$$

$$\Delta V(s) = \frac{1}{ms + k_f}[F(\Delta p_1(s) - \Delta p_2(s)) - \Delta R] \tag{33}$$

$$\Delta y(s) = \frac{1}{s}\Delta V(s); \tag{34}$$

where s – the Laplace variable; T_{cw} – time constant of the control winding

$$T_{cw} = L_c/R_e; \tag{35}$$

E_c – reduced elastic modulus of HC

$$E_c = E_f \left/ \left(1 + \frac{2W_0}{FH}\right).\right. \tag{36}$$

The system (29)–(34) corresponds to the structural scheme shown in Fig. 2.
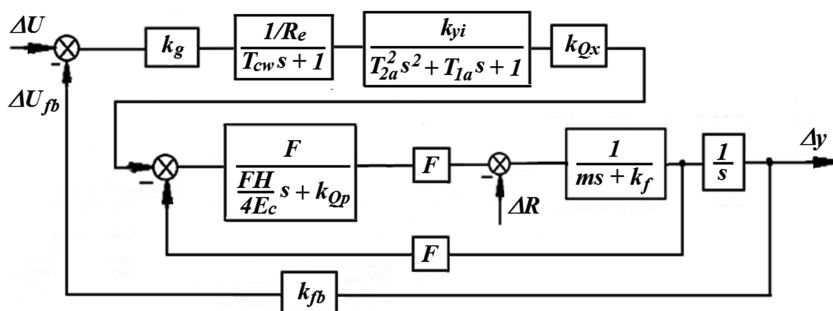
Fig. 2. Structural scheme

For the further conversion structural scheme, we introduce a transfer coefficient of EB

$$k_{eb} = k_g/R_e \tag{37}$$

and EHA gain a coefficient by the flow rate

$$k_{Qi} = k_{xi}/k_{Qx}. \tag{38}$$

The value k_{Qi} can be established according to the technical certificate data of EHA [9]

$$k_{Qi} = Q_{nom}/i_{nom}, \tag{39}$$

where Q_{nom}, i_{nom} – a nominal flow rate and nominal control current control of EHA. Also, we define the hydromechanical time constant of HC

$$T_c = \sqrt{\frac{mH}{4E_cF}} \tag{40}$$

and the coefficient of a relative damping of HC

$$\zeta_c = \frac{1}{T_c}\left[\frac{k_{Qp}m}{F^2} + \frac{Hk_f}{2E_cF}\right]. \tag{41}$$

In real drives [1, 19, 20]

$$k_{Qp}k_f/F^2 << 1. \tag{42}$$

4 Results

With the allowance for (37–42), we have the structural scheme of the control signal transfer shown in Fig. 3.
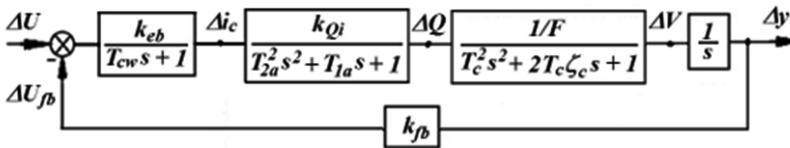
Fig. 3. Structural scheme of the control signal transfer

According to the structural scheme, we establish the transfer function of EHSD according to the control signal

$$W_{yu}(s) = \frac{k_{yu}}{\frac{s}{D_{EHSD}}(T_{cw}s+1)(T_{2a}^2s^2+T_{1a}s+1)(T_c^2s^2+2T_c\zeta_cs+1)+1}, \tag{43}$$

where k_{yu}- transfer coefficient of EHSD by the control signal

$$k_{yu} = 1/k_{fb}; \tag{44}$$

D_{EHSD}- drive quality factor (open-loop gain)

$$D_{EHSD} = k_{eb}k_{Qi}k_{fb}/F. \tag{45}$$

According to Fig. 2 and (37)–(42) we obtain the structural scheme of the control signal transfer by loading influence, shown in Fig. 4. In the scheme a time constant of the precursor unit is designated

$$T_R = \frac{FH}{4E_c k_{Qp}}. \tag{46}$$

According to the structural scheme, we find the transfer function of EHSD by loading influence

$$W_{yR}(s) = \frac{k_{yR}(T_R s + 1)(T_c^2 s^2 + 2T_c \zeta_c s + 1)(T_{cw} s + 1)}{\frac{s}{D_{EHSD}}(T_{cw} s + 1)(T_{2a}^2 s^2 + T_{1a} s + 1)(T_c^2 s^2 + 2T_c \zeta_c s + 1) + 1}, \tag{47}$$

where k_{yR}- transfer coefficient of the EHSD by loading influence

$$k_{yR} = \frac{k_{Qp}}{F^2 D_{EHSD}}. \tag{48}$$

The output value is determined in the general case by the result of the control signal and loading influence according to the principle of superposition

$$\Delta y(s) = W_{yu}(s)\Delta U(s) - W_{yR}(s)\Delta R(s). \tag{49}$$

The results of calculations of the dynamic characteristics of EHSD on the basis of the obtained transfer functions were compared with the results of calculations based on adequate nonlinear mathematical models of a number of authors [8, 12, 15], as well as the data from experimental research [5, 11, 20]. As an example, in Fig. 5 shows the results of the calculation of the transient processes for the displacement of the piston according to (43) (solid line) and according to the nonlinear mathematical model [15] (dotted line). The calculations were made for the following basic parameters: $F_1 = F_2 = 9,15.10^{-3}$ m^2 (diameter of piston 125 mm and diameter of the stocks 63 mm);
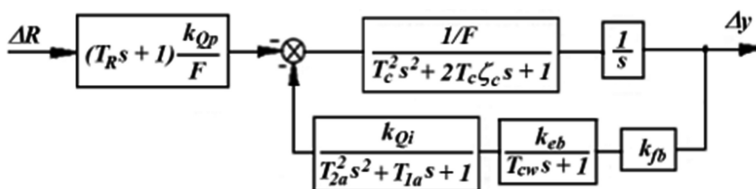

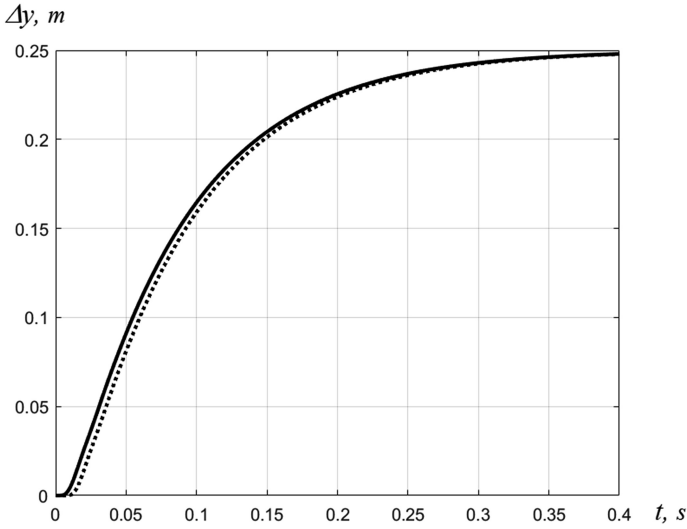**Fig. 4.** Structural scheme of the loading influence transfer

Fig. 5. Displacement of the piston according to (43) (solid line) and [15] (dotted line)

H = 0,5 m; p_{ps} = 32.10^6 Pa; E_c = 9,9.10^8 Pa; κ_f = 5.10^4 kg/s; m = 500 kg; Q_{nom} = 6,38.10^{-3} m³/s; i_{nom} = 0,3 A; T_{1a} = 1,17.10^{-3} s; T_{2a} = 1,27.10^{-3} s (phase shift -45° and − 90° at frequencies v_1 = 80 Hz and v_2 = 125 Hz); L_c = 1,0 H; R_e = 100 Ω; D_{EHSD} = 10,7 1/s; T_{cw} = 0,01 s; ζ_c = 0,25; T_c = 2,62.10^{-3} s.

In general, the results of calculations based on the obtained transfer functions are in good agreement with the theoretical and experimental data of other authors, which allows us to state the adequacy of the presented mathematical description of EHSD.

5   Conclusions

Thus, we consider a mathematical model of non-stationary work processes occurring in the EHSD. The linearization of the mathematical model is carried out, the structural scheme of the drive is constructed, the transfer functions are obtained for the control signal and the loading influence. The main parameters of the drive are the time constant of the control winding, the time constants of the electrohydraulic amplifier, the time constants of the hydraulic cylinder, the coefficient of relative damping of the hydraulic cylinder, the feedback coefficient, the drive transfer coefficient by the control signal, and the drive transfer coefficient by the loading influence. The proposed linear mathematical model and transfer functions are adapted to the drives of technological equipment for mechanical processing of materials, in particular, equipment for processing materials with pressure, metal-cutting machine tools and systems, tool production equipment, etc. The main advantage of the presented mathematical description of the characteristics of the electrohydraulic servo drive with the throttle regulation is the ability to perform stability evaluation, quality of control, and correction of the dynamic properties of the drive using the technical certificate data of the drive elements

and devices. A good coincidence of the calculated dynamic characteristics with other theoretical and experimental data makes it possible to consider the obtained transfer functions the basis for further research on improving the technological equipment.

References

1. Popov, D.: Dynamics and Regulation Hydro-and Pneumatic Systems. Machinery Engineering, Moscow (1987)
2. Navrotsky, K.: Theory and Designing Hydro- and Pneumodrives. Machinery Engineering, Moscow (1991)
3. Popov, D.: Mechanics of Hydro- and Pneumodrives. MGTU, Moscow (2005)
4. Sveshnikov, V.: Hydrodrives in modern mechanical engineering. Hydraul. Pneum. **28**, 10–16 (2007)
5. Azarenko, N., Rasskazova, Y., Stepanova, O.: Perfection of Machine-Building Equipment with Electrohydraulic Drive. V. Dahl EUNU, Severodonetsk (2015)
6. Sokolov, V., Rasskazova, Y.: Automation of control processes of technological equipment with rotary hydraulic drive. East. Eur. J. Enterp. Technol. **2**(2 (80)), 44–50 (2016)
7. Popov, D.: Non-stationary Hydromechanical Processes. Machinery Engineering, Moscow (1982)
8. Sokolova, Y., Tavanuk, T.: Modeling of Automatic Electrohydraulic Drives of Special Technological Equipment. Knowledge, Donetsk (2013)
9. Lutsenko, I., Fomovskaya, E., Koval, S., Serdiuk, O.: Development of the method of quasioptimal robust control for periodic operational processes. East. Eur. J. Enterp. Technol. **4**(2 (88)), 52–60 (2017)
10. Kreynin, G., Krivts, I.: Hydraulic and Pneumatic Drives of Industrial Robots and Automatic Manipulators. Machinery Engineering, Moscow (1993)
11. Azarenko, N., Sokolova, Y., Tavanuk, T.: Research of Electrohydraulic Drives of Technological Equipment. V. Dahl EUNU, Severodonetsk (2014)
12. Rasskazova, Y., Stepanova, O., Azarenko, N.: Perfection of Electrohydraulic Drives of Machine-Building Equipment. V. Dahl EUNU, Severodonetsk (2016)
13. Emtsev, B.T.: Technical Hydromechanics. Machinery Engineering, Moscow (1978)
14. Lojtsjansky, L.: Mechanics of Liquid and Gas. Science, Moscow (1987)
15. Ramazanov, S., Sokolova, Y., Tavanuk, T.: Nonlinear modeling of the electrohydraulic watching drive. TEKA Comm. Mot. Energ. Agric. **XC**, 234–241 (2010)
16. Sokolova, Y., Azarenko, N.: The synthesis of system of automatic control of equipment for machining materials with hydraulic drive. East. Eur. J. Enterp. Technol. **2**(2 (68)), 56–60 (2014)
17. Sokolov, V., Krol, O.: Installations criterion of deceleration device in volumetric hydraulic drive. Procedia Eng. **206**, 936–943 (2017)
18. Sokolova, Y., Tavanuk, T., Greshnoy, D.: Linear modeling of the electrohydraulic watching drive. TEKA Comm. Mot. Energ. Agric. **XIB**, 167–176 (2011)
19. Bogdanovich, L.: Hydraulic Drives. High School, Kiev (1980)
20. Sveshnikov, V.: Hydrodrives of Tools. Machinery Engineering, Moscow (2008)

Influence of the Stochastic Nature Parameters of Throttle Channels on Characteristic of Automatic Balancing Device of the Centrifugal Pump

Yuliia Tarasevych[✉], Nataliia Sovenko, and Ievgen Savchenko

Sumy State University, 2 Rymskogo-Korsakova St., Sumy 40007, Ukraine
y.tarasevich@omdm.sumdu.edu.ua

Abstract. Automatic balancing device is used to balance the axial force. Moreover, this device acts as an end-seal of centrifugal pump and about 5% of whole power can be lost on it. Operating characteristics of automatic balancing device are determined by cylindrical and face throttles geometrical characteristics that have stochastic nature. It caused by the real constructional form of inlet in annular and face throttles, possible deformations, initial manufacturing, and installation misalignment and deviations depend on different stochastic factors. Using the example of static characteristic calculating of an automatic balancing device for a centrifugal pump, it is shown that considering the stochastic nature of the geometric characteristics of the throttle channels, the losses in the face throttle, gives a random character to the variation of the balancing device parameter. Obtained results showed not only the qualitative but also quantitative influence of the random changes of the hydraulic resistances on the values of the balancing axial force and the face gap (about 10–13%). The deviation of the gap value from the calculated one leads in any case to negative consequences: a decreasing - to scuffing and a complete failure of the whole device, increasing - to reducing the volume efficiency of the pump. Presented calculating technique can be recommended as easy-to-use and simple way to consider local losses in automatic balancing device.

Keywords: Face throttle · Cylindrical throttle · Axial balancing force
Random parameters · Static characteristic · Coefficients of local losses

1 Introduction

Special automatic balancing devices (Fig. 1) are used in modern high-pressure multi-stage centrifugal pumps to unload the rotor from the axial forces. Driving wheels of multi-stage centrifugal pumps are made with internal radius of basic disk less than internal radius of covering disk to provide liquid to the subsequent stage. Therefore, pressure on the sides of wheel is distributed differently. The difference of pressure distributions (area S_T) determines unstable axial force of pressure, operating on a wheel and directed toward an inlet (T). Value of this force is proportional to pump head, which in turn is proportional to the square of frequency of rotation ω and area of outer

radius of wheel, and also depends on the other factors. Therefore, axial force value can significantly change on different pump operating modes.
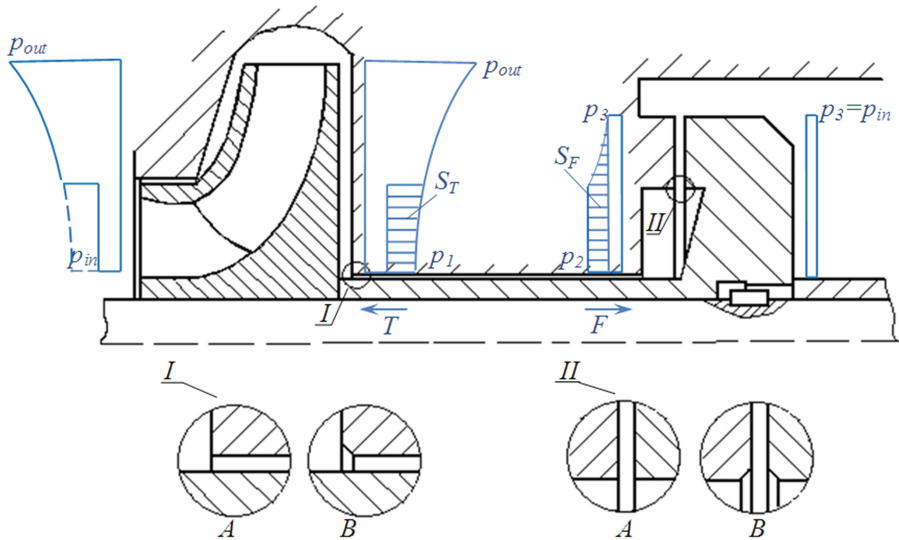

Fig. 1. Automatic balancing device.

Automatic balancing device is the most effective unloading system because acts both thrust bearing with automatic load capacity control, which is capable of operating over a wide range of axial force variation, as well as the end seal through which the almost whole pump head is throttled.

The manufacturing and installation deviations lead to a non-flatness of the working surfaces. The unloading disc of automatic balancing device and the fixed disk are set with some declination to an axis of rotation. As a result, the middle gap increases, and the resistance of the face throttles decreases. Force deformations of the balancing device disc form a diffuse form of the face throttle. The hydrostatic force decreases as a result and the face gap of the balancing device decreases consequently. This can lead to an undesirable contact operation mode. It can be shown that the initial declination and deformation of the rotating and non-rotating disc significantly affect to the balancing device operation. Therefore, special attention is paid to ensure that the face throttle surfaces are parallel when designing a balancing device.

In practice calculation of static and dynamic characteristics of a balancing device is carried out in deterministic statement without considering random change of parameters of the device and the probabilistic nature of its geometric characteristics. As a rule, accepted in the pump building tolerances for the sizes of working surfaces are commensurated with the size of the throttle channel gaps in the seals. It nullifies any efforts to improve the accuracy of the calculation. Given the above, consideration of the probabilistic nature of throttle channel parameters on the characteristics of the automatic balancing device of centrifugal pump is an important practical problem.

2   Literature Review

As the initial misalignment and deformations of the rotating and non-rotating disk significantly influence on operation of the balancing device, special attention should be paid to its design. One of the possible solutions to ensure the parallel form of the face throttle surfaces of the balancing device is to design one with a resilient-fixed on a rotating disc or in the housing rings. As a result, the movable ring tracks the initial misalignment in the balancing device [1].

Engineering calculation of the balancing device as an automatic control system includes static and dynamic analysis. For the conventional design the calculation procedure was considered in detail in [2–4]. Wherein, the coefficients of local losses at the inlet and outlet of the cylindrical and face throttle, which depend on the geometry of the sealing surfaces, are widely used in the calculation of the balancing device. Accounting local throttling losses in channels is discussed in [5–8]. As generally a rectangular shape of the input and output is adopted, and the values of the corresponding coefficients are established empirically. Considering lack of requirements to a form of input cross-section of cylindrical and face throttles, their real form can significantly differ from calculated. Different forms of input sections will be in different assemblies and constructions of the balancing device disc installation. Furthermore, during operation of the pump, the sealing surfaces may change shape significantly due to wear. And it means that local losses coefficients are also random variables by the nature and stochastic functions if change of surface wear in time is considered.

Unfortunately, works that take into account the stochastic nature of change of parameters of the device and the probabilistic nature of its geometrical characteristics are practically absent. One of such works devoted to the calculation of the effect of a random change in the parameters of annular seal on its flow rate characteristic is presented in [9] by authors of this article.

3   Research Methodology

Calculated model of hydraulic balancing device is shown in Fig. 2.

Static characteristic of the balancing device is determined by the equilibrium conditions of the axial discharge disc:

$$T = F, \tag{1}$$

Where $F = p_2 S_2 + F_f - p_3 (S_f - S_3)$ - total axial force of pressure acting on the rotor, which consists of the pressure force in the chamber ($p_2 S_2$) and the pressure force in the face gap, taking into account the deformation of the disk β - taper angle of face throttle):

$$F_f = S_f \left[\frac{p_2 + p_3}{2} + \frac{p_2 - p_3}{2} \left(\frac{2\Lambda + 3\bar{\beta}}{3} \frac{\zeta_{2f}}{\zeta_f} - \frac{\zeta_{if} + \zeta_{of}}{\zeta_f} \right) \right], \tag{2}$$
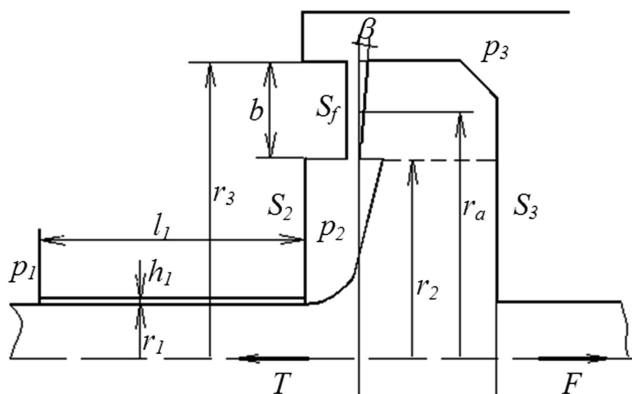
Fig. 2. Calculated model of hydraulic balancing device.

Where $\Lambda = b/2r_a$, $\bar{\beta} = b\beta/2r_a$ - relative taper, $\zeta_f = \zeta_{if} + \zeta_{2f} - \zeta_{of}$ - total throttle loss factor, ζ_{if}, ζ_{of} - local loss factors at the inlet and outlet of the face throttle, $\zeta_{2f} = \lambda b/(2h_f)$ - the loss factor for the length of the face throttle, λ- friction factor.

The dependence of the pressure in the discharge chamber p_2 on the face gap is found from the balance of fluid flow through the cylindrical Q_1 and face Q_2 throttles:

$$Q_1 = Q_2, \tag{3}$$

Which can be represented as

$$Q_1 = g_1\sqrt{p_1 - p_2} \text{ and } Q_2 = g_2\sqrt{p_2 - p_3},$$

Where $g_1 = 2\pi r_1 h_1 \sqrt{2(p_1 - p_2)/(\rho\zeta_c)}$ and $g_2 = 2\pi r_a h_a \sqrt{2(p_2 - p_3)/(\rho\zeta_f)}$ - conductivity of the cylindrical and face throttle respectively, $\zeta_c = \zeta_{ic} + \zeta_{2c} - \zeta_{oc}$ - total loss factor of a cylindrical throttle, ζ_{ic} and ζ_{oc} - local losses factor at the inlet and outlet of the cylindrical throttle, $\zeta_{2c} = \lambda l_1/(2h_1)$ - loss factor along the length of the cylindrical throttle.

The conductivity of the face throttle g_2 depends on the face gap value and determines the dependence of the pressure in the discharge chamber p_2 on the face gap value. The dependence of the axial force on the face gap value is obtained from Eqs. (1) and (3):

$$F = p_2\left[S_2 + \frac{S_f}{2}\left(1 - \frac{2\Lambda + 3\bar{\beta}}{3}\frac{\zeta_{2f}}{\zeta_f} - \frac{\zeta_{if} + \zeta_{of}}{\zeta_f}\right)\right]$$
$$- p_3\left[S_3 + \frac{S_f}{2}\left(1 - \frac{2\Lambda + 3\bar{\beta}}{3}\frac{\zeta_{2f}}{\zeta_f} - \frac{\zeta_{if} + \zeta_{of}}{\zeta_f}\right)\right], \tag{4}$$

Where $p_2 = \left(p_1 + p_3\frac{\zeta_c}{\zeta_f}\frac{r_a^2 h_a^2}{r_1^2 h_1^2}\right) / \left(1 + \frac{\zeta_c}{\zeta_f}\frac{r_a^2 h_a^2}{r_1^2 h_1^2}\right)$.

As noted above, the local loss factors in expression (2), (3) and (4) depend on the geometry of the sealing surfaces and are random variables or random functions.

The normal distribution law is used as a first approximation based on central limit theorem of probability theory.

In this case the empirical values of the factor considered in deterministic calculations are taken as mean values [8]: $\langle \zeta_{if} \rangle = 1,5$, $\langle \zeta_{of} \rangle = 0,2\langle \zeta_{if} \rangle$, $\rangle \zeta_{ij} \rangle = \int_{-\infty}^{\infty} f_i(\zeta_{ij})\zeta_{ij}d\zeta_{ij}$, $f_i(\zeta_{ij})$ - probability density of corresponding loss factor [10]. Due to the lack of information on the corresponding standard deviations, they will be given by using the percentage deviation of the random variable values from its mean values.

Let's consider the effect of random changes in hydrodynamic local loss factors on the conductivity of the face throttle. Total hydraulic loss factor $\zeta_f = \zeta_{if} + \zeta_{2f} - \zeta_{of}$ is a linear function of normal random variables ζ_{if}, ζ_{of}, ζ_{2f}. Consequently, it is also normally distributed value with parameters:

$$\langle \zeta_f \rangle = \langle \zeta_{if} \rangle + \langle \zeta_{2f} \rangle - \langle \zeta_{of} \rangle,$$

$$D_{\zeta_f} = \langle \zeta_{if}^2 \rangle - \langle \zeta_{if}^2 \rangle + \langle \zeta_{of}^2 \rangle - \langle \zeta_{of}^2 \rangle + \langle \zeta_{2f}^2 \rangle - \langle \zeta_{2f}^2 \rangle,$$

$$f_1(\zeta_f) = \frac{1}{\sqrt{2\pi D_{\zeta_f}}} exp\left[-\frac{(\zeta_f - \zeta_f)^2}{2D_{\langle \zeta_f \rangle}} \right].$$

Since the conductivity of the face throttle is monotone non-random function of random argument, the probability density can be written:

$$f_2(g_2) = f_1(\psi(g_2))\left| \psi(g_2)' \right|.$$

Since the probability density function is known, the corresponding moment characteristics can be determined in a such way

$$\langle g_2 \langle = \int_0^\infty f_2(g_2)g_2 dg_2, D_{g_2} = \langle g_2^2 \rangle - \langle g_2^2 \rangle = \int_0^\infty f_2(g_2)g_2^2 dg_2 - \langle g_2^2 \rangle.$$

The joint probability density $f_3(\zeta_{if}, \zeta_{of}, \zeta_{2f})$ is introduced to determine the effect of a random change in the local hydraulic loss factors on the value of the axial force (4). Considering the stochastic independence of the random variables $\zeta_{if}, \zeta_{of}, \zeta_{2f}$ it can be represented in the form

$$f_3(\zeta_{if}, \zeta_{of}, \zeta_{2f}) = f_4(\zeta_{if})f_5(\zeta_{of})f_6(\zeta_{2f}), \tag{5}$$

where $f_i(\zeta_j)$ - the probability density of the normal distribution of local hydraulic loss factors at the inlet, outlet and along the length, respectively.

The problem of finding the probability density of the axial force in the form (4) is rather complicated. However, it is not necessary to know the probability density of the axial force to find the first two moment characteristics. It is sufficient to have an

analytical force dependence on the corresponding random variables (4), which denoted as $f_7\left(\zeta_{if}, \zeta_{of}, \zeta_{2f}\right)$, and their joint probability density (5).

In this case, the mean value of the axial force may be obtained based on the formula

$$\langle F \rangle = \int_{\zeta_{2f1}}^{\zeta_{2f2}} \int_{\zeta_{of1}}^{\zeta_{of2}} \int_{\zeta_{if1}}^{\zeta_{if2}} f_7\left(\zeta_{if}, \zeta_{of}, \zeta_{2f}\right) f_3\left(\zeta_{if}, \zeta_{of}, \zeta_{2f}\right) d\zeta_{if} d\zeta_{of} d\zeta_{2f}. \tag{6}$$

Dispersion:

$$D_F = \int_{\zeta_{2f1}}^{\zeta_{2f2}} \int_{\zeta_{of1}}^{\zeta_{of2}} \int_{\zeta_{if1}}^{\zeta_{if2}} \left(f_7\left(\zeta_{if}, \zeta_{of}, \zeta_{2f}\right) - \langle F \rangle\right)^2 f_3\left(\zeta_{if}, \zeta_{of}, \zeta_{2f}\right) d\zeta_{if} d\zeta_{of} d\zeta_{2f}. \tag{7}$$

4   Results

Calculation of the moment characteristics of the face throttle conductivity was carried out for the following values of the parameters: $r_1 = 55$ mm, $r_2 = 77,5$ mm, $r_3 = 100$ mm, $h_1 = 200$ μm, $l_1 = 210$ mm, $p_1 = 35 \cdot 10^6$ Pa, $p_3 = 3 \cdot 10^6$ Pa. It was obtained: $g_2 = 3,7 \cdot 10^{-3}$ m³/(s·Pa^{0,5}) for turbulent flow regimes. Table 1 presents the standard deviations $\zeta_{if}, \zeta_{of}, \zeta_{2f}$ accepted in the calculations, and the values obtained for standard deviation of the face throttle conductivity. The calculations showed that the maximum possible deviation of the face throttle conductivity value is approximately 9% from its deterministic value. The increase in the standard deviation values of the local hydraulic loss factors significantly effects on the conductivity value.

Table 1.

Tolerance	$\sqrt{D_{\zeta_{of}}}$	$\sqrt{D_{\zeta_{if}}}$	$\sqrt{D_{\zeta_{2f}}}$	$\sqrt{D_{g_2}}$
5%	$3,16 \cdot 10^{-3}$	$0,042$	$0,211$	$2,65 \cdot 10^{-5}$
10%	$6,32 \cdot 10^{-3}$	$0,084$	$0,422$	$5,322 \cdot 10^{-5}$
15%	$9,5 \cdot 10^{-3}$	$0,126$	$0,633$	$1,072 \cdot 10^{-4}$

In practical applications, face throttle is used not only in the hydraulic balancing device for which turbulent flow regimes are prevailing. Therefore, the effect of a random change in the hydraulic loss factor on the conductivity characteristics for laminar flow regimes has also been studied.

It was found that for the geometric parameters given above (the middle gap did not change), the mean value of conductivity for the laminar flow regime is smaller by an order than for the turbulent regime:

$$\langle g_2 \rangle_{turb} = 3,7 \cdot 10^{-3}\,\mathrm{m^3/(s \cdot Pa^{0,5})},$$

$$\langle g_2 \rangle_{lam} = 2,6 \cdot 10^{-4}\,\mathrm{m^3/(s \cdot Pa^{0,5})}.$$

Also, the conductivity value changes by 1,2 times for the case when the tolerance for $\zeta_{if}, \zeta_{of}, \zeta_{2f}$ is 15%.

It should be noted that the change of the pressure in the balancing device chamber was not considered in this article. With axial oscillations of the rotor the flow in the throttling channels becomes unsteady and calculation of pressure p_2 is substantially more complicated.

According to the conducted studies, the maximum deviation of the value of the axial force from its deterministic value (tolerance 10% for $\zeta_{if}, \zeta_{of}, \zeta_{2f}$) is 10%.

Analysis of the deviation of the gap value in the face throttle is not analytically possible because of its implicit connection with the loss factors. However, it is possible to estimate the probable deviations of the gap with the obtained change in the axial force. The static characteristic of the balancing device used in the calculation is shown in Fig. 3. It represents the connection between the axial force and the face gap value. According to the calculation the deviation in the axial force from the calculated value in the range $\pm 10\%$ gives a change in the corresponding gap in the range $\pm 12\%$.

Dimensionless face gap
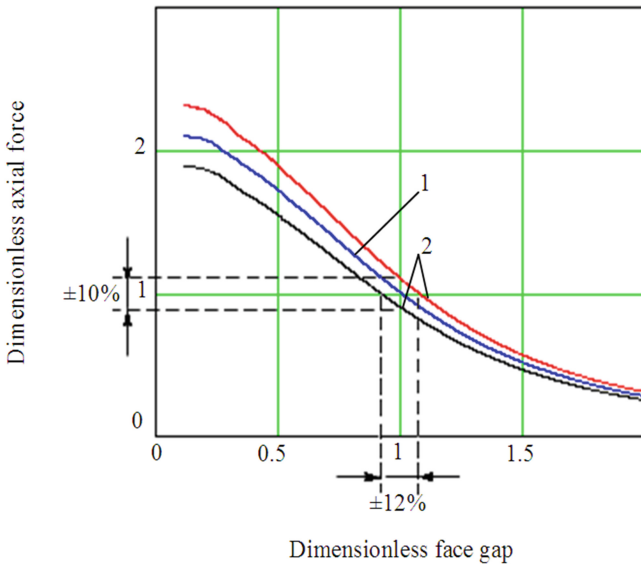
Fig. 3. Static characteristic of the balancing device: 1 – for mean value of axial force (F), 2 – for force with allowance for deviation $\left(F \pm 3\sqrt{D_F}\right)$.

Taking into account the fact that the face gap values are measured in micrometers the deviating of the gap value in the smaller direction can lead to negative consequences such as scuffing and total failure of the device. An increase in the calculated gap values significantly affect the reduction in volumetric efficiency of the pump due to increased fluid flow through the hydraulic balancing device.

5   Conclusions

The results obtained in the article confirmed the necessity to consider the stochastic nature of the geometric characteristics of the throttle channels and the random nature of the changes in the parameters of the automatic balancing device in the calculation of its static characteristics and in future the dynamic ones. At the moment, an experimental validation of the obtained results is not possible, since there is no sufficient statistical information on the characteristics of local loss factors. The calculations given in this paper can be regarded as the first approximation to the solution of this problem. There are presently no reliable data and methods that allow to calculate the effect of local hydraulic resistances in the literature. So the technique developed by the authors can be recommended as a simple and easy-to-use tool to take into account the effect of these resistances. The result showed not only the qualitative but also quantitative influence of the random changes of the hydraulic resistances on the values of the counterbalancing axial force and the face gap. It is important to note that the deviation of the gap value in a smaller side from the calculated value will lead to negative consequences such as scuffing and total failure of whole device, and, to a greater extent, a decrease in the volumetric efficiency of the pump. In subsequent studies, one should take into account the effect of a random change in the parameters of the cylindrical gap of the balancing device to its characteristics. The hydrodynamics of a cylindrical gap largely determines the pressure in the discharge chamber p_2, which in turn is determined by the face gap value.

References

1. Korczak, A.: Badania ukladow rownowazacych napor osiowy w wielostopniowych pompach odsrodkowych. Wyd. Politechniki Slaskiej, Gliwice (2005)
2. Martsinkovski, V.A., Vorona, P.N.: Pumps of Nuclear Power Plants. Energoatomizdat, Moscow (1987)
3. Jedral, W.: Metody obliczania sil wzdluznych i ukladow odciazajacych w pompah wirowych, Prace Naukowe. Mechanika z.110, Wydawnictwa PW (1988)
4. Korczak, A., Martsynkovskyy, V., Peczkis, G., Zahorulko, A.: Diagnosis of the phenomenon of flow as an inspiration to inventions in the domain of constructing hydraulic machines. Procedia Eng. **39**, 286–302 (2012)
5. Korczak, A., Papierski, A.: The flow through the face clearance of disk relieving the axial force in multi-stage centrifugal pump. Trans. Inst. Fluid Flow Mach. **115**, 125–142 (2004)
6. Zueva, N.V.: Accounting for local losses in calculating of the hydrodynamic characteristics of the face throttles. Bull. Sumy Natl. Agric. **9**(15), 42–48 (2006)
7. Karaskiewicz, K.: Badanie przeplywow wewnetrznych w pompach pod katem obliczania sil hydraulicznych. Oficyna wydawnicza Politechniki Warszawskiej, Warszawa (2013)
8. Jedral, W.: Turbulentny przeplyw cieczy w hydraulicznie gladkich szczelinach poprecznych. Archiwum budomy maszyn **T.XXVIII**(1), 39–53 (1981)
9. Tarasevych, Y., Savchenko, I., Sovenko, N., Savchenko, A.: Research of influence of random change of annular seal parameters on efficiency of centrifugal pump. East. Eur. J. Enterp. Technol. **6**(7–84), 37–42 (2016)
10. Bolotin, V.V.: Metody teorii verojatnostej i teorii nadeznosti v rasczotah sooruzenij. Strojizdat, Moscow (1982)

Comparative Tribological Tests for Face Impulse Seals Sliding Surfaces Formed by Various Methods

Viacheslav Tarelnyk[1(✉)] , Ievgen Konoplianchenko[1] ,
Vasyl Martsynkovskyy[1] , Aleksey Zhukov[1], and Piotr Kurp[2]

[1] Sumy National Agrarian University,
160 H. Kindratiieva St., Sumy 40021, Ukraine
`tarelnik@i.ua`
[2] Kielce University of Technology,
aleja Tysiąclecia Państwa Polskiego 7, 25-314 Kielce, Poland

Abstract. The article shows the analysis of change of face impulse seal rings, which are completely made of expensive wear-resistant materials, such as tungsten carbide, silicon carbide, various kinds of graphite on rings, which are made of less expensive but not less qualitative materials. It has been established that the seal rings surfaces are in contact for a very short time, only at the time of starting and stopping the unit. Therefore, it is proposed to use metal base-coating composite materials for such surfaces, which combine the protective properties of coatings and the mechanical strength of the surface base. Metallographic and tribological research were carried out on samples of heat-resistant steel 38X2MUA (41CrAlMo7), high-speed steel P6M5 (HS6-5-2C) and stainless steel 12X18H10T (X6CrNiTi18-10KT). Various variations of the samples heat treatment were used: steel 38X2MUA after thermal treatment, thermal treatment + ion nitriding, thermal treatment + carbonitriding; steel P6M5 after thermal treatment, thermal treatment + condensed ion bombardment; steel X6CrNiTi18-10KT after thermal treatment; thermal treatment + condensed ion bombardment. It was found that the greatest thickness of hardened layers (up to 500 μm) is achieved with hardening of 41CrAlMo7 steel by ion nitriding and carbonitriding methods; the greatest of the surface layers microhardness for samples of steels HS6-5-2C and X6CrNiTi18-10KT, which were subjected to hardening by the method of condensed ion bombardment (18.3 and 16.4 GPa, respectively); The lowest frictional force was shown in samples of steel 41CrAlMo7, slightly higher in high-speed steel HS6-5-2C, and the highest in steel - X6CrNiTi18-10KT.

Keywords: Face seal · Strengthening · Ring · Wear · Surface layer
Tribological tests

1 Introduction

Creating of reliable sealing units that ensure long-term tightness under condition of a wide range of temperature and pressure changes is one of the main problems arising at designing pump and compressor machines and aggregations.

A face seal (FS) is one of the most common seals, and it comprises a sealing device consisting of two parts in the form of rings, one of which rotates together with the shaft and the other one is fixedly connected to the body [1].

In the designs of high-speed pumps and high-pressure compressors, there have been widely used the face impulse seals, the ring surfaces of which are in contact with each other for a very short period of time, only at the moment of a machine starting and/or shutting down [2]. The availability of the guaranteed clearance of 0.003–0.004 mm results in the fact that the sealing surfaces of the rings almost do not wear out. Despite this, the sealing rings are entirely made of wear-resistant materials, such as tungsten carbide, silicon carbide, various kinds of graphite. The costs of the rings of those materials reach hundreds and thousands of US dollars. Therefore, the researches aimed at ensuring the effectiveness of the operation of the face impulse seals made of less expensive, but rather qualitative materials, are relevant and well-timed.

2   Literature Review

In the course of choosing a FS design, the correct choice of a proper material for seal rings and its mechanical and physical characteristics are of significant importance. In this case, the decisive role is not provided by the choice of the friction pair materials themselves, but their combinations. When choosing the optimal sliding pairs, it is necessary to take into account the corrosion resistance and wear resistance of the materials, the possibility of heat removal from the friction zone, and also the compatibility of the materials, i.e., the ability to work without grasping and jamming [3].

According to the reference [4], the rotor seals must satisfy two main conditions: to possess the required tightness and increased reliability for given pressure drops, rotation frequencies, temperatures and physical properties of the medium being sealed.

Any changes in protective and tribological properties of part surfaces can be achieved while creating special reliefs of friction pair surfaces [5–8] or when forming combined multilayer coatings, for example, by electroerosive alloying method.

As a reserve for improving the FS quality it is possible to use composite materials in alloyed steel parts. The use of the method for alloying parts with the materials having special properties makes it possible to create designs providing for the necessary strength, reliability and durability [9].

With the improvement of technology, it becomes necessary to use high and ultra-high pressures, extreme temperatures (from high to cryogenic ones), aggressive media, and the like. The influence of these operating conditions on the leakproofness of the detachable joints is very large. Therefore, at manufacturing FS rings, it is expedient to use metal composite materials of the "base-coating" type, which combine the protective properties of coatings with the mechanical strength of the base [10].

Taking into considering that not all materials can be used for creating the surfaces of the FS, their choice is crucial. Therefore, the comparative tribological tests of the friction surfaces of the FS rings, formed by various methods on steel substrates, will make it possible to facilitate the choice of one or another method of strengthening them for specific operating conditions in some extent.

The purpose of this work is to reduce the cost and increase the durability of the face impulse seals rings by conducting the studies of tribotechnical characteristics of steel sliding surfaces, formed by various methods.

3   Research Methodology

The specimens of heat-resistant structural steel 38X2MUA (EU analogue - 41CrAlMo7), high-speed steel P6M5 (EU analogue - HS6-5-2C) and stainless steel 12X18H10T (EU analogue - X6CrNiTi18-10KT) were made for carrying out metallographic and tribological studies. The following series of specimens were used: Steel grade 41CrAlMo7 after thermal processing (TP); TP and ionic nitriding (IN); TP and carbonitriding (CN); Steel grade HS6-5-2C after TP; TP and condensed ion bombardment (CIB); Steel grade X6CrNiTi18-10KT after TP; TP and CIB.

To carry out the experimental study on ionic nitriding (IN), there was used the electric ionic vacuum and bell-shaped furnace of «NGV - 6, 6/6 - I1» model.

The electric ionic vacuum and bell-shaped furnace of « GV - 6, 6/6 - I1» model was used to carry out the experimental study on ionic nitriding (IN). The rectangular specimens of $15 \times 15 \times 8$ mm size were made for metallographic studies. To determine the tribological properties according to the "ball-disk" scheme at the T - 01 M tester, the rings of $42 \times 25 \times 6$ mm size were made (Fig. 1). The IN process lasted 12 h on the average. It should be noted that, with the IN process, the saturation rate is of 2 to 4 times higher than with the gas nitriding (GN) process, and the absence of deformation allows it to be carried out after machining.
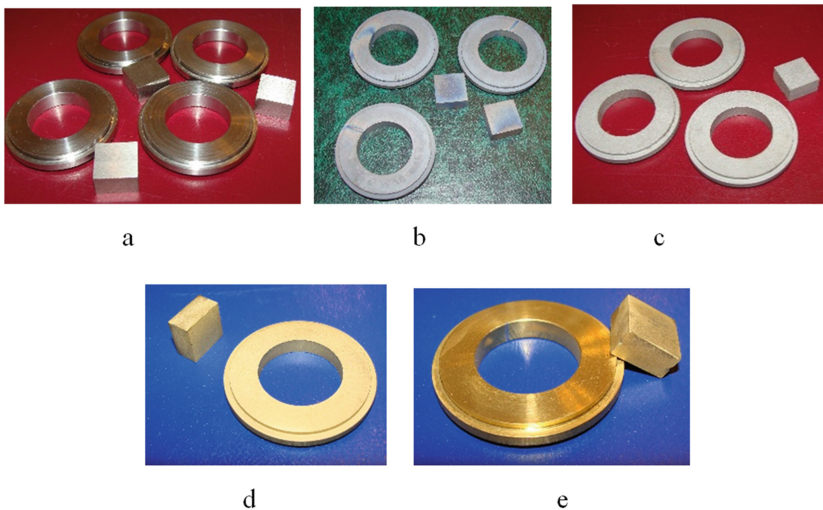
Fig. 1. The rectangular specimens and rings made of steel 41CrAlMo7 after TP (a), IN (b), carbonitration (c); steels X6CrNiTi18-10KT and HS6-5-2C after processing by CIB, respectively (d) and (e).

The carbonitriding or so-called "liquid" nitriding process is used to increase wear resistance and fatigue strength of steel and cast iron products. This technology is an alternative to such well-known processes as nitriding, surface hardening by high-frequency currents, carburization, nitrocarburization, galvanic chromium plating, wear-resistant gas spraying, etc.

The CN method consists in strengthening the surface layer of steel products by diffusion saturation with nitrogen and carbon in the melt of salts at the temperature of 560–580 °C. The total time of conducting the process of CN is 7.0 h. The specimens were directly kept in the melt of salts for 4.0 h.

The essence of the CIB method consists in the fact that the process comprises the procedures of spraying the cathode refractory metal, creating ions in low-temperature plasma, and bombarding the surface being strengthened therewith. The cathode material (material being sprayed) evaporates in the form of high-speed jets (speed of 1×10^6 cm/s) containing both charged and neutral particles. The jets are plasma streams of atoms and ions with a high degree of ionization.

The method makes it possible to create metal and wear-resistant coatings consisting of such chemical compounds as carbides, nitrides, oxides, carbonitrides of refractory metals: titanium, molybdenum, chromium, tungsten, vanadium, etc., as well as multilayer and multicomponent (composite) coatings.

The coating of the specimens made of steel HS6-5-2C and X6CrNiTi18-10KT was produced at the installation of the NNV-66-I1 model (Fig. 2a). Titanium was used as a cathode, and nitrogen was used as a reactant gas.

a   b

Fig. 2. Installation for applying coatings using the CIB method (a) and a chamber with a device for fixing the specimens (b).

The temperature during heating and performing the deposition of the wear-resistant coating was controlled by means of an infrared pyrometer of Smotrych 1-1-03 model.

Thus, the rectangular specimens and the rings have been coated with titanium nitride for 25 min at the temperature of 520 ± 20 and of 800 ± 20 °C, respectively, for the materials of HS6-5-2C and X6CrNiTi18-10KT with preliminary cleaning the surfaces to be strengthened in a glow discharge for 10 min.

The tribological properties of the formed surface layers were determined at a T-01 M tester made by the Radom Institute of Technology (Poland) in Ball-on-disc friction system (DIN-50324:1992-07 standard Tribology) (Fig. 3). The ball $\varnothing$ = 6.3 mm, made of 100Cr6 material (Table 1), was changed after each test.
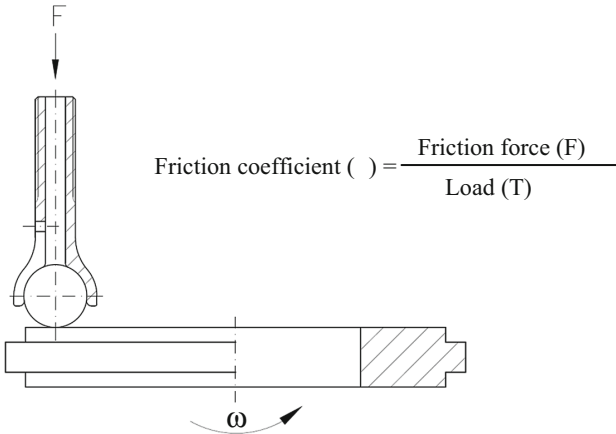

$$\text{Friction coefficient ( ) } = \frac{\text{Friction force (F)}}{\text{Load (T)}}$$

Fig. 3. Diagram of the friction pair of the tribological tester of T-01 M model: ball-on-disk.

While studying, there were used the following operating parameters of the tester: the rotation speed ω = 360 rpm; the test time (t) for the wear radius r = 17 and 12 mm was 95 and 135 s, respectively; the load (T) varied after every 60 m and was: 0.5 kgf (4.91 N); 1.0 kgf (9.81 N); 2.0 kgf (19.62 N); and 4.0 kgf (39.24 N). In addition, for Series No. 4, the additional load of 6.0 kgf (58.86 N) was used.

The specimens were lubricated with a drop of paraffin oil before each load increase. During the test, friction force F was recorded.

Table 1. Composition of the ball material.

	C	Si	Mn	Cr	Mo	Ni	S max	P max
Min	0.95	0.15	0.20	1.35	–	–	–	–
Max	1.10	0.35	0.40	1.60	0.10	0.40	0.025	0025

4   Results

As a result of metallographic and durametric studies, there were obtained the data on the hardness of the base of the heat-treated specimens and the ones strengthened by various methods, on the thickness and microhardness of the strengthened layers (Table 2).

Table 2. Qualitative parameters of various series of specimens for tribological studies.

Series No.	Material	Type of thermal processing (TP)	Type of strengthening	Thickness of strengthened layer, μm	Hardness
1	41CrAlMo7	Hardening, °C 940 ± 10, Oil; Tempering, °C 600–670, Oil	–	–	302–341 HB
2	41CrAlMo7	Hardening, °C 940 ± 10, Oil; Tempering, °C 600–670, Oil	IN	500	9950 MPa
3	41CrAlMo7	Hardening, °C 940 ± 10, Oil; Tempering, °C 600–670, Oil	CN	500	10000 MPa
4	HS6-5-2C	Hardening, °C 1220, Oil; Tempering, °C 560, Oil, 3 times	–	–	61–63 HRC
5	HS6-5-2C	Hardening, °C 1220, Oil; Tempering, °C 560, Oil, 3 times	CIB	3.0–3.5	17,5…18,3 GPa
6	X6CrNiTi18-10KT	Hardening, °C 1000–1080, Water	–	–	140–170 HB
7	X6CrNiTi18-10KT	Hardening, °C 1000–1080, Water	CIB	2.0–2.5	12,1…16,4 GPa

In addition, the table provides information on the nature of the heat treatment and the type of strengthening the test specimens.

During the tests recorded of the change in friction force for all series of the specimens at the steel ball passing a friction distance equal to 60 m for each load. In this case, as a load changed, the contacting surfaces of the ball and specimen did not change. Figure 4 shows the nature of the change in frictional force for the samples of the first series. For those friction pairs in Table 3, there are represented average values for friction forces F and friction coefficients μ.

Figure 5 is a summary graph of the applied load dependence of the friction forces of a steel ball over the surface of disc.

It should be noted that in experiments No. 1–5, there was normal friction, because at the point of contact the surface of the ball was polished by the surface of the disk (Fig. 6a). As a rule, normal friction is accompanied by a slight mechanical and oxidative wear.

In experiments Nos. 6 and 7, the ball had been rotating inside its own fixation during the process. Depending on a load, the ball wear looked like an abrasive one. At the low load (0.5 kg), there was occurred a partial wear of the friction track and the surface of the ball, and with increasing the load, there was occurred a complete wear, (Fig. 6b, c), respectively. After the test termination, there were found wear products in the form of small metal chips and grains.
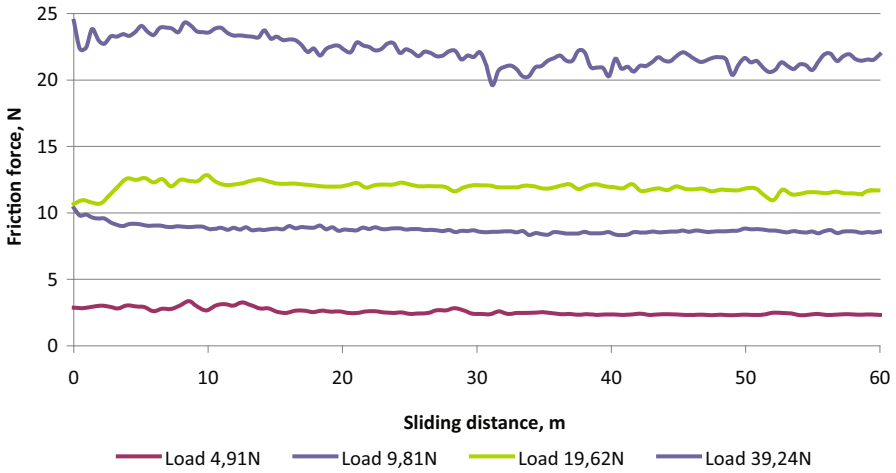
Fig. 4. Load and values.

Table 3. Friction force and friction coefficient for steel ball over the surface of steel specimens strengthened in various ways.

Load, T (N)	Average friction force, F (N)	Friction coefficient $\mu = F/T$	Standard deviation of average friction force
Specimen No 1-41CrAlMo7			
4.91	0.56	0.114	0.0035
9.81	5.47	0.558	0.0068
19.62	6.68	0.340	0.0293
39.24	8.46	0.216	0.0440
Specimen No 2-41CrAlMo7			
4.91	0.59	0.120	0.0057
9.81	5.44	0.554	0.1132
19.62	6.40	0.326	0.0321
39.24	8.09	0.206	0.0844
Specimen No 3-41CrAlMo7			
4.91	0.55	0.112	0.0180
9.81	5.55	0.566	0.0550
19.62	6.41	0.327	0.1022
39.24	8.09	0.206	0.2018
Specimen No 4 - HS6-5-2C			
4.91	0.63	0.128	0.0102
9.81	5.55	0.566	0.0238
19.62	6.79	0.346	0.0591
39.24	8.82	0.225	0.1122
58.86	11.42	0.291	0.7874

Table 3. (*continued*)

Load, T (N)	Average friction force, F (N)	Friction coefficient μ = F/T	Standard deviation of average friction force
Specimen No 5 - HS6-5-2C			
4.91	0.65	0.132	0.0056
9.81	5.54	0.565	0.0156
19.62	6.45	0.329	0.0257
39.24	8.53	0.217	0.0675
Specimen No 6 - X6CrNiTi18-10KT			
4.91	2.18	0.443	0.1758
9.81	8.74	0.891	0.2513
19.62	14.16	0.722	0.4780
39.24	21.87	0.557	0.5906
Specimen No 7 - X6CrNiTi18-10KT			
4.91	2.57	0.522	0.2555
9.81	8.75	0.892	0.3052
19.62	11.91	0.607	0.4075
39.24	22.10	0.563	1.0429
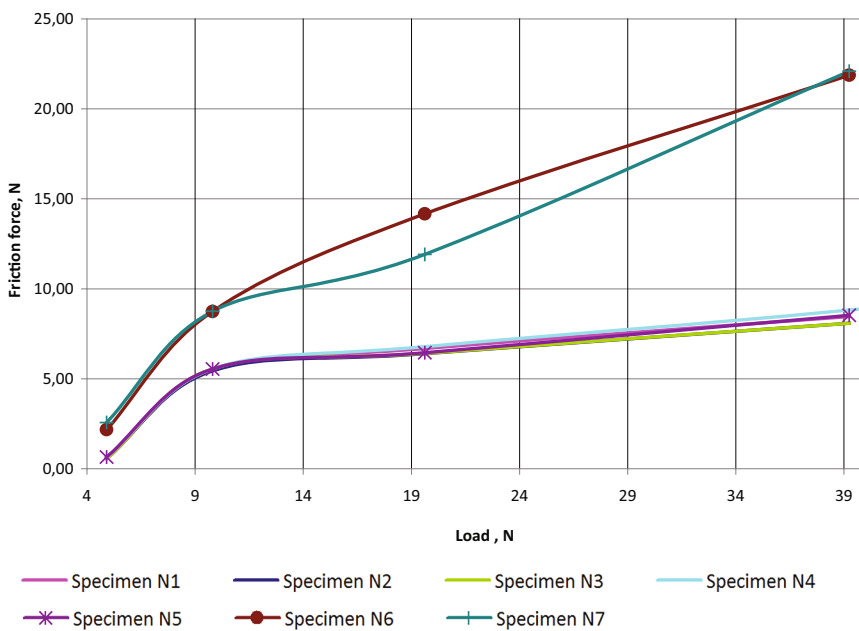
Fig. 5. Load dependence of the friction force.
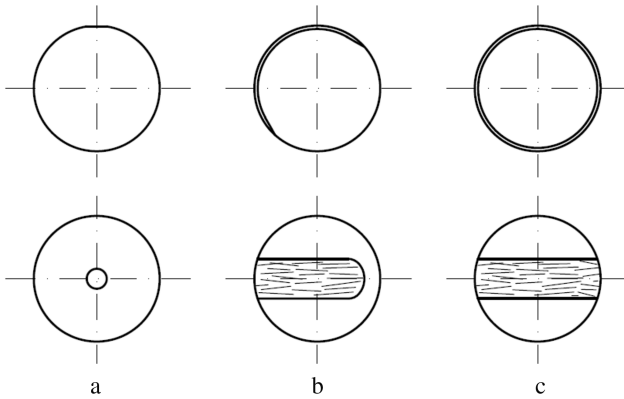
Fig. 6. Wear of the ball surface: a - normal wear, b - partial wear of the friction track with scratches, c - complete wear of the friction track with scratches.

Figure 7 represents a diagram that allows to compare the frictional forces of all series of samples from the maximum load of 39.24 N.
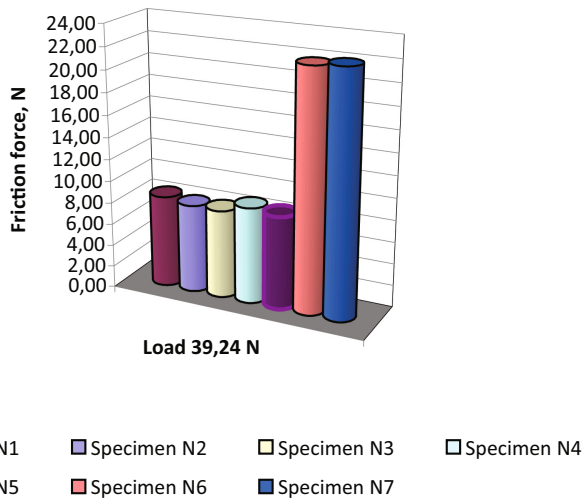
Fig. 7. Specimen and No.

5   Conclusions

As a result of carrying out the metallographic and durametric studies it has been set as follows: - the maximum thickness of the strengthened layers (up to 500 µm) was achieved when strengthening steel 41CrAlMo7 using ionic nitriding and carbonitriding methods; - the greatest microhardness of the surface layers was found out for the

specimens of steels HS6-5-2C and X6CrNiTi18-10KT, (18.3 and 16.4 GPa, respectively), which had been strengthened by the method of condensed ion bombardment.

As a result of carrying out the tribological studies, it has been set: - the friction force increases with increasing the loads for all series of the specimens; - the smallest friction force is found out for the specimens of steel 41CrAlMo7, a slightly higher one is for the specimens of high-speed steel HS6-5-2C, and the highest one is for steel X6CrNiTi18-10KT. In experiments No. 1-5 (steels 41CrAlMo7 and HS6-5-2C), there was determined normal friction, accompanied by a slight mechanical and oxidative wear. In experiments No. 6 and No. 7 (steel X6CrNiTi18-10KT) there was determined abnormal friction accompanied by abrasive wear.

References

1. Blasiak, S., Zahorulko, A.V.: A parametric and dynamic analysis of non-contacting gas face seals with modified surfaces. Tribol. Int. **94**, 126–137 (2016)
2. Zahorulko, A.: Theoretical and experimental investigations of face buffer impulse seals with discrete supplying. East. Eur. J. Enterp. Technol. **4**(7), 45–52 (2015)
3. Zakharov, B., Zakharov, I.: Seals for Oil Centrifugal and Piston Pumps. OAO VNIIOENG, Moscow (2011)
4. Martsynkovskyy, V.: Dynamics of Rotors of Centrifugal Machines: Monograph. SumSU, Sumy (2012)
5. Antoszewski, B.: Influence of laser surface texturing on scuffing resistance of sliding pairs. Adv. Mater. Res. **874**, 51–55 (2014)
6. Adamczak, S., Kundera, C., Swiderski, J.: Assessment of the state of the geometrical surface texture of seal rings by various measuring methods. In: IOP Conference Series: Materials Science and Engineering, vol. 233(1), paper No 012031 (2017)
7. Błasiak, S., Kundera, C.: A numerical analysis of the grooved surface effects on the thermal behavior of a non-contacting face seal. Procedia Eng. **39**, 315–326 (2012)
8. Zahorulko, A., Kundera, C., Hudkov, S.: Determination of mechanical characteristics of stuffing box packings. In: IOP Conference Series: Materials Science and Engineering, vol. 233(1), paper No 012039 (2017)
9. Kirik, G.: New Composite Materials: Monograph. University Book, Sumy (2011)
10. Tarelnik, V.B., Martsinkovskii, V.S., Zhukov, A.N.: Increase in the reliability and durability of metal impulse seals. Part 2. Chem. Pet. Eng. **53**(3–4), 266–272 (2017)

Effect of the Parameters at the Inlet to the Rotor of the Jet-Reactive Turbine on Its Efficiency

Serhiy Vanyeyev[(✉)] , Stanislav Meleychuk , Vadim Baga ,
and Tetiana Rodymchenko

Sumy State University, 2 Rymskogo-Korsakova St., Sumy 40007, Ukraine
s.vaneev@kttf.sumdu.edu.ua

Abstract. The article shows that the amount of motive force of the traction nozzle is directly affected by the total pressure recovery factor in the flow part of the jet-reactive turbine and its elements, which characterizes the energy losses. The effect of various gas-dynamic and geometric parameters on the total pressure recovery factor in the flow part of the jet-reactive turbine is studied. In order to increase the total pressure recovery factor in the flow part of the jet-reactive turbine, it is necessary to install a diffuser sleeve with a cylindrical part where there is a transition from a supersonic flow velocity to a subsonic flow and a diffuser part where a further subsonic flow velocity decreases. Element-by-element analysis of gas flow in the flowing part of the jet reactive turbine with a diffuser sleeve at the entrance to the rotor is performed. It is established that the reduced flow velocity at the inlet to the rotor should be as low as possible, based on the location of the shock wave in the inlet part of the diffuser sleeve, and the opening angle of the diffuser part of the diffuser sleeve should be no more than $10°$.

Keywords: Jet-reactive turbine · Flow part · Diffuser sleeve
Total pressure recovery factor · Reduced velocity · Available pressure ratio

1 Introduction

One of the ways to solve the problem of energy saving and rational use of the energy potential of our planet is the usage (utilization) of the secondary energy resources. Today, a large amount of energy of compressed gases and vapors is lost on reducers and pressure regulators in the gas, chemical and other industries. The power that can be utilized at these throttling nodes is often not more than 500 kW [1–3]. To solve this problem, it is promising to create turbo-expanded units of low power based on the jet-reactive turbines (JRT) for the utilization of energy of compressed gases and vapors at throttling junctions with a payback period of no more than 2 years [4].

Another urgent task of the modern gas transportation industry is to increase the safety of operation of the main gas pipelines by creating the pneumatic (gas), the efficient, reliable and easy-to-use drive of ball valves of large cross-sections ($D_N > 300$ mm) instead of the currently used pneumatic hydro actuators [5]. This task is also solved by the creation of the pneumatic actuators based on the jet-reactive turbines [5, 6].

The aim of the study is to estimate the influence of different parameters (in particular, the gas velocity at the inlet to the turbine rotor) on the total pressure recovery factor in the flow part of the JRT.

2   Literature Review

The principle of the jet-reactive turbine functioning is to convert the potential energy of the compressed fluid into the kinetic energy of the supersonic jet, which flows out of the traction nozzle (TN). As a result, the reactive traction force on the traction nozzle and the corresponding torque on the turbine shaft are formed, and when the shaft rotates, the mechanical work is performed. The process of transforming the potential energy of the fluid into the kinetic energy of the outflowing jet is the main one and occurs in the TN.

Typically, JRTs operate at supercritical pressure ratios and a supersonic flow of gas is formed at the inlet to the rotor.

The very principle of the JRT functioning supposes that in order to obtain the high efficiency of the turbine, it is necessary to bring the flow of the fluid with as little energy loss as possible to the traction nozzle. The energy losses in the section "inlet to the turbine - inlet to the traction nozzle" depend on a variety of geometric and gas dynamic parameters.

The theory of JRT (Segner wheel) has been considered in a number of works, however, either the process of a gas flow in the flow part is assumed to be isentropic [7] or friction losses in the gas path are assumed to be equal to a certain fraction of the torque obtained in the isentropic flow process in the gas path turbines (for example, 10–20% in the work [8]).

In the literature, no studies have been made of the effect of the gas parameters at the entrance to the JRT (in particular, on the JRT rotor), as well as the geometric parameters of the flowing part, on the coefficient of restoring the total pressure in the flowing part of the JRT.

The article also considers the influence of the total pressure recovery factor in the flow part of the JRT on the value of the motive force of the traction nozzle and the influence of various gas dynamic and geometric parameters on this ratio.

3   Research Methodology

The driving torque on the rotor shaft of the JRT in the steady mode $\omega = const$, with equal gas flow through the feed and traction nozzle $G_{ih} = G_t$, c, taking into account the resistance of the ambient viscous gas to the rotor rotation, is determined by the Eq. [8]

$$M = \left[G_t w_{out.t} + f_{out.t} \left(p_{out.t} - p_{a.p} \right) \right] \cdot L - G_t L^2 \omega - K_{r.r} \omega^2, \tag{1}$$

where L is the distance from the axis of the rotor rotation to the axis of the traction nozzle (the arm of the action of the motive force on the TN relative to the axis of the rotor), ω is the angular velocity of the rotor, $K_{r.r}$ is the ratio of resistance to rotation,

and $w_{out.t}, f_{out.t}, p_{out.t}$ are the velocity, the area and the pressure in the outlet section (on the cut) of the traction nozzle, respectively; $p_{a.p}$ is the ambient pressure.

The accuracy and reliability of the calculated determination of the output characteristics of the JRT according to the Eq. (1) depend to the greatest extent on the accuracy of the design determination of the starting torque corresponding to $\omega = 0$:

$$M_n = L \cdot P_{d.t.s=0} = L \cdot \left[G_t \cdot c_{d.t.s=0} + f_{out.t} \cdot \left(p_{out.t} - p_{a.p} \right) \right], \tag{2}$$

where $P_{d.t=0}$ is the draft of the traction nozzle for the starting mode, it is equal to:

$$P_{d.t=0} = p^*_{in.d.t=0} \cdot f_{kr.d} \cdot \lambda_{gr.t.s=0} \cdot k \cdot \beta_{kr} + f_{out.t} \cdot \left[p^*_{in.d.t=0} \cdot \pi(\lambda_{d.t.s=0}) - p_{a.p} \right] \tag{3}$$

where $p^*_{in.d.t=0}$ is the pressure of the blocked flow (full pressure) at the inlet to the traction nozzle for the starting mode; $f_{kr.d}$ is the area of the critical section of the traction nozzle; $\lambda_{dr.t.s=0}$ is the reduced gas flow velocity at the cut of the traction nozzle for the starting mode; $\pi(\lambda)$ is the gas dynamic function; k is adiabatic exponent (isentropic) gas; β_{kr} is the critical pressure ratio.

It can be noted that the accuracy of determining the draft of the TN, and therefore of the starting torque, depends entirely on the accuracy of determining the total pressure at the inlet of the TN: the higher the total pressure is, the greater the draft is.

The aerodynamic perfection of the flow part is estimated by the total pressure recovery coefficient:

$$\sigma_{t=0} = p^*_{in.d.t=0} / p^*_{in.t}, \tag{4}$$

considering it the expression (5) takes the form of:

$$\begin{aligned} P_{d.t=0} = p^*_{in.t} \cdot \sigma_{t=0} \cdot f_{kr.t} \cdot \lambda_{d.t.s=0} \cdot k \cdot \beta_{kr} + f_{out.t} \\ \times \left[p^*_{in.t} \cdot \sigma_{t=0} \cdot \pi(\lambda_{d.t.s=0}) - p_{a.p} \right], \end{aligned} \tag{5}$$

where $p^*_{in.t}$ is the total pressure at the inlet to the feed nozzle.

It follows from the Eq. (5) that the higher the total pressure recovery factor in the flowing part of the JRT is $\sigma_{t=0}$, the greater the draft of the traction nozzle is.

In a first approximation, the gas path of the JRT rotor can be considered as a tube (pipe) of a certain length (Fig. 1), in which an adiabatic flow with friction occurs under the action of the pressure and the specific velocity at the inlet to the rotor.

The equation connecting the reduced velocities at the inlet and outlet of the pipe with the reduced pipe length [9]

$$\frac{1}{\lambda_1^2} - \frac{1}{\lambda_2^2} - ln\frac{\lambda_2^2}{\lambda_1^2} = \chi, \tag{6}$$

where λ_1, λ_2 – the dimensionless (reduced) velocity at the inlet and outlet of the pipe, respectively; χ – the reduced pipe length:
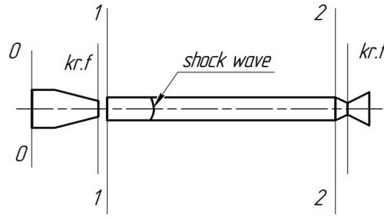
Fig. 1. Scheme of the gas path of JRT in the first approximation.

$$\chi = \frac{2k}{k+1} \xi \frac{L}{D_{tr}}, \tag{7}$$

where L – the pipe length; D_p – the pipe diameter; ξ – the coefficient of friction in the pipe.

The equation connecting the reduced velocities in the inlet and outlet sections of the pipe with the available pressure ratio Π_o (total pressure recovery factor at the inlet to the rotor to the static pressure in the environment) from which the reduced velocity can be determined λ_2:

$$y(\lambda_2) = \frac{p_1^*}{p_2} \cdot q(\lambda_1) = \Pi_0 \cdot q(\lambda_1) \tag{8}$$

The equation to determine the total pressure recovery factor for the pipe

$$\sigma = \frac{p_2^*}{p_1^*} = \frac{q(\lambda_1)}{q(\lambda_2)} = \frac{\lambda_1}{\lambda_2} \cdot \left(\frac{1 - \lambda_1^2 \cdot \frac{k-1}{k+1}}{1 - \lambda_2^2 \cdot \frac{k-1}{k+1}} \right)^{\frac{1}{k-1}} \tag{9}$$

4 Results

According to the formulas given above, the airflow parameters were calculated for a flow in a pipe of length $L = 150$ mm, diameter $D_p = 5$ mm with a resistance ratio $\xi = 0.015$, different values of the dimensionless velocity at the inlet to the rotor λ_1 and the available pressure ratio Π_0.

The results of calculations in the form of dependence of the change in the reduced velocity along the reduced pipe length for the practically real range of reduced supersonic velocities at the inlet are shown in Fig. 2.

Notably that in the given pipe, flows are possible, both with shock waves inside the tube, and supersonic flows along the entire length of the tube. The flow mode depends on the reduced velocity at the inlet to the tube $\lambda 1$ and the available pressure ratio Π_0.

At $\lambda_1 = 1.5495$, the shock wave is located at the inlet to the tube, while the available pressure ratio is equal to $\Pi_0 = 2.8$. At $\lambda_1 = 1.853$ and $\Pi_0 = 5.4$, the supersonic flow is decelerated to the critical velocity at the outlet of the pipe. At $\lambda_1 > 1.853$,
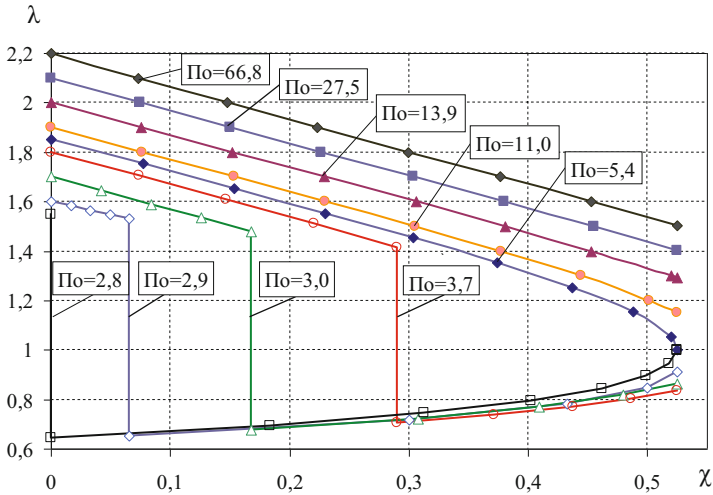
Fig. 2. Change in the reduced velocity along the tube for different values of λ_1 and Π_0.

a supersonic flow is possible over the entire length and at the exit from the tube (i.e., in the JRT design, in this case, there is no need to use a supersonic traction nozzle, but the total pressure losses will be large in this case).

The change in the total pressure recovery factor along the reduced pipe length for the dependencies depicted in Fig. 2 is shown in Fig. 3.

Notably, the smaller the reduced velocity at the inlet to the pipe and the available pressure ratio are, the higher the total pressure recovery factor for the pipe is, and therefore it is less than the loss of the total pressure and flow energy.

The dependence of the change in the available pressure ratio on the reduced velocity at the inlet to the pipe for the graphs drawn in Fig. 2 is shown in Fig. 4. With increasing λ_1, especially in the area of the supersonic flows along the entire length of the pipe, the required available pressure ratio sharply increases.

The dependence of the total pressure recovery factor for the pipe on the reduced velocity at the inlet to the pipe, $\sigma_{\text{тр}} = f(\lambda_1)$ is shown in Fig. 5. Notably, that $\lambda_1 > 1{,}7$ $\sigma_{\text{тр}}$ becomes less than 0.5, that is more than 50% of the initial value of the total pressure is lost.

The research shows that the smaller the supersonic speed at the entrance to the gas path of the rotor and the available pressure ratio are, the closer the shock wave to the inlet section of the pipe is and less the total pressure loss in the pipe is as a whole. However, they remain all the same large. In particular, for the studied pipe, the reduced input velocity λ_1 cannot be less than 1.5495 and the total pressure recovery factor σ is greater than 0.7.

To obtain large σ, it is necessary to decrease λ_1, which requires a change in the geometry of the pipe (length and/or pipe diameter). Figure 6 shows the dependence of the minimum possible reduced supersonic velocity at the inlet to the tube $\lambda_{1\text{min}}$, by which the shock wave is located at the inlet to the tube (Fig. 6a), the available pressure ratio (Fig. 6b), and the total pressure recovery factor in the pipe (Fig. 6c) of the relative
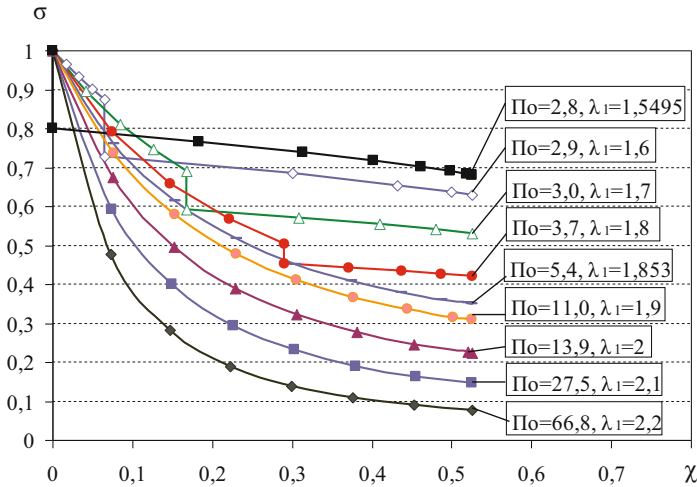
Fig. 3. Change in the total pressure recovery factor along the tube for different values of λ_1 and Π_0.
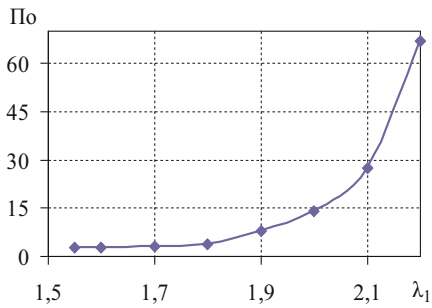

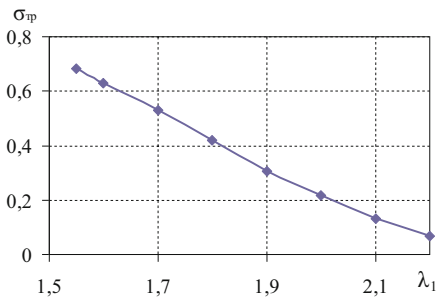**Fig. 4.** Change in the available pressure ratio from the reduced velocity at the inlet to the pipe.

Fig. 5. Dependence of total pressure recovery factor in the pipe on the reduced velocity at the inlet to the pipe.

length of the tube. Notably that with decreasing the relative length of the tube, λ_{1min}, decreases, as well as the required available pressure ratio, and the total pressure recovery factor in the pipe increases.

Since the diameter of the axial channel of the JRT rotor is determined by the parameters of the supply nozzle, the flow part of which, in turn, is determined by the specified gas flow, it is necessary to reduce the length per tube (the flow part of the JRT). However, the total length of the flow part in the JRT is related to the creation of the necessary torque on the JRT shaft. It was sufficient to install a diffuser sleeve in the axial channel of the JRT rotor (Fig. 7) which has a cylindrical part smaller than the diameter of the main gas path of the rotor and the length that depends on the gas
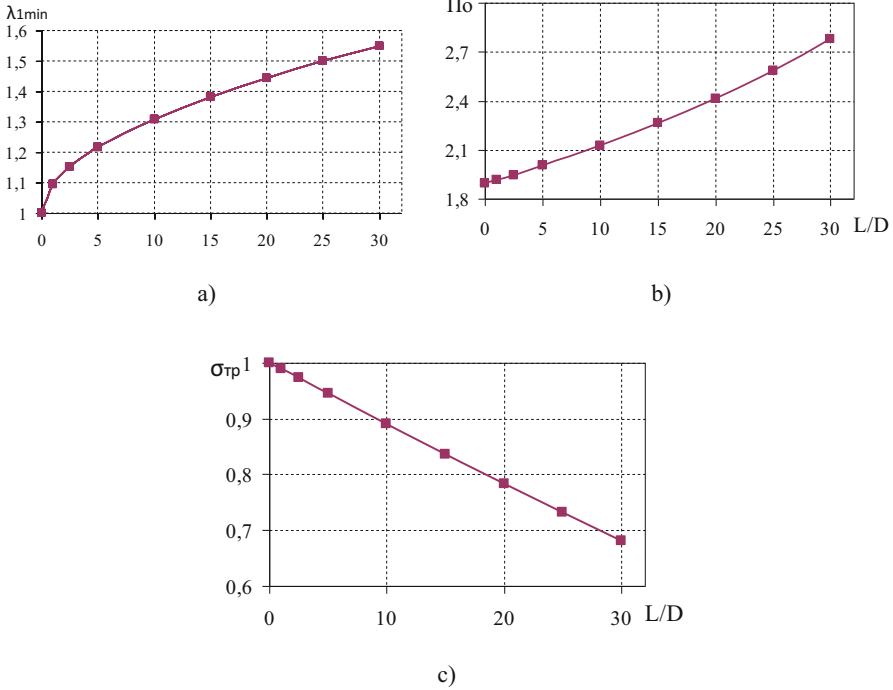
a)

b)

c)

Fig. 6. Dependence of the minimum possible reduced supersonic velocity at the inlet to the pipe (a), the available pressure ratio (b), the total pressure recovery factor in the pipe (c) from the relative length of the pipe
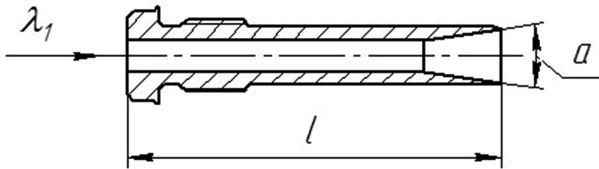
Fig. 7. Scheme of the diffuser sleeve at the inlet to the JRT rotor.

velocity at the input to the rotor; where there is a transition from supersonic to subsonic velocity, and the diffuser part, where a further decrease in the subsonic flow velocity occurs.

The research is conducted on the effect of the opening angle α of the diffuser, the length of the cylindrical part of the sleeve-diffuser l and the dimensionless (reduced) velocity at the entrance to the rotor λ_1 (Fig. 7) on the total pressure recovery factor in the elements of the JRT gas path and in the gas path as a whole from the inlet to the rotor to the inlet to the traction nozzle, therefore splitting the flow part into a number of sections (Fig. 8). The inlet cylindrical part of the rotor (cylindrical section of the
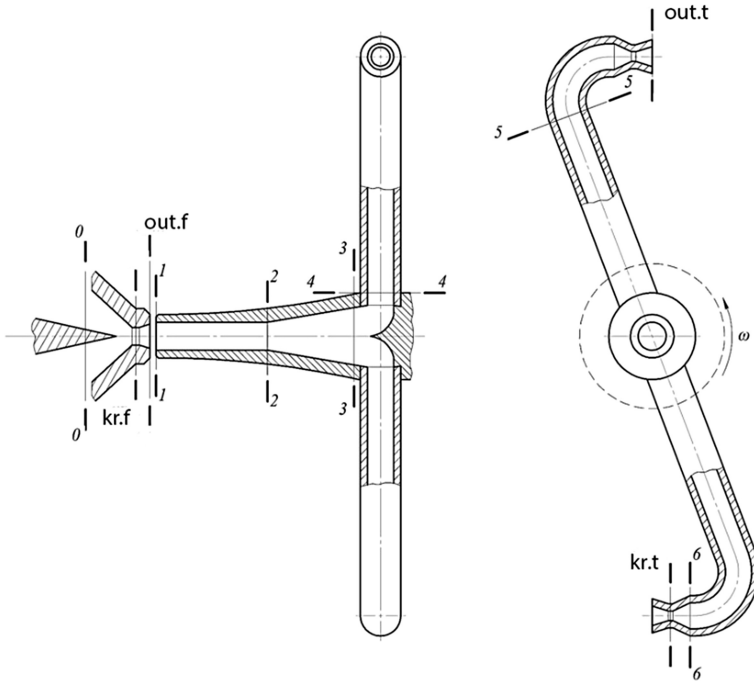
Fig. 8. Calculation scheme of the JRT flow part.

diffuser sleeve) is σ_{1-2}; the diffuser (diffuser section of the diffuser sleeve) - σ_{2-3}; turning the section from the axial to radial direction - σ_{3-4}; the radial section of the shoulder-console of the rotor - σ_{4-5}; The turning area before the traction nozzle is σ_{5-6}.

Consider, for example, the flow part of the JRT for the driving ball valve at the inlet pressure of the 2 MPa JRT, the outlet pressure of the 0.1 MPa JRT, the inlet temperature at the inlet to the 300 K JRT:

- diameter of the cylindrical part of the diffuser sleeve is $d_1 = 5$ mm;
- output diameter of the cylindrical part of the diffuser sleeve is $d_{out.d} = 10$ mm;
- length of the cylindrical part of the diffuser sleeve is $l = 30$ mm;
- angle of the diffuser opening is $\alpha = 10°$;
- diameter of the inlet to the radial part of the rotor is $d_{in.r} = 10$ mm;
- radius of rotation of the rotor arms $R_0 = 15$ mm;
- rotation angle of the rotor arms is $\alpha_0 = 90°$;
- distance from the rotor axis to the axis of the traction nozzle is 100 mm.

The fluid is natural gas. The reduced flow velocity at the inlet to the cylindrical section of the diffuser sleeve is $\lambda_1 = 1.25$.

The total pressure recovery factors are calculated for the diffuser opening angles, 3°, 5°,10°, 15°, 20°, 25°, 30° and the reduced flow velocities at the inlet to the cylindrical section of the diffuser sleeve $\lambda_1 = 1,25$, $\lambda_1 = 1,29$.
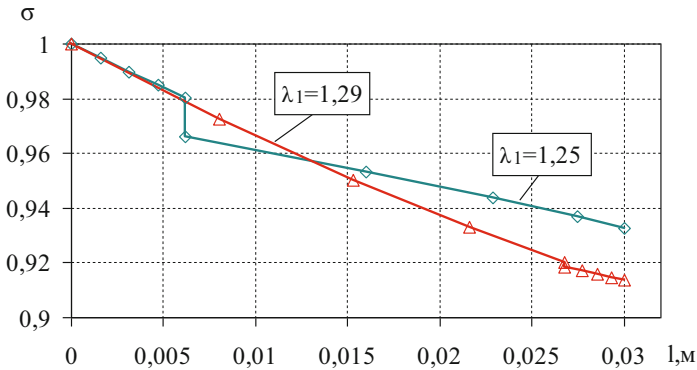
Fig. 9. Dependence of the total pressure recovery factor on the length of the cylindrical section of the diffuser sleeve (l = 30 mm) for $\lambda_1 = 1.25$.

Based on the results of calculations for the cylindrical section of the diffuser sleeve, with the opening angle of the diffuser 10°, the dependences of the change in the total pressure recovery factor along the cylindrical section of the diffuser sleeve are obtained (Fig. 9).

It should be noted that at $\lambda_1 = 1.25$ the shock wave is 6 mm from the inlet to the rotor, that is, at the inlet section of the diffuser sleeve, and the total pressure recovery factor is 0.9328. At $\lambda_1 = 1.29$ the shock wave is located 27 mm from the inlet to the cylindrical section of the diffuser sleeve, which is practically at the entrance to the diffuser. This fact is adverse, since with an insignificant increase in λ_1 there can be a sharp increase in energy losses, as the diffuser in this case can become a supersonic part of the Laval nozzle and the flow will not be decelerated but accelerated there, the total pressure recovery fact here is 0.9136.
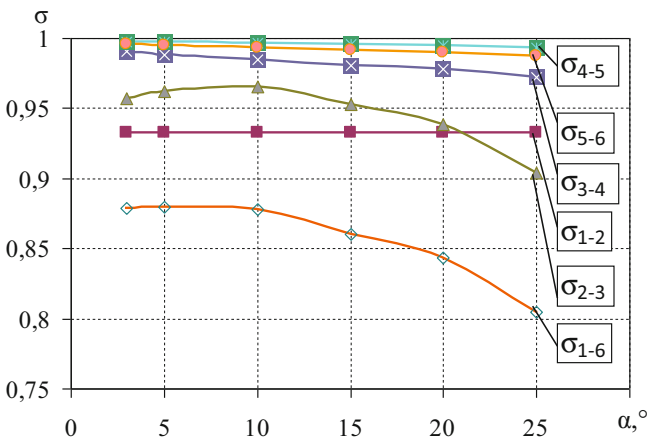
Fig. 10. Dependences of the change in the total pressure recovery factor on the angle of the diffuser opening on the elements of the flow part and for the JRT rotor on the whole at $\lambda_1 = 1.25$.

Dependences of the total pressure recovery factor on the opening angle of the diffuser by the above-mentioned elements of the flowing part of the JRT and overall from the inlet to the rotor to the inlet of the traction nozzle σ_{1-6} are shown in (Fig. 10).

5 Conclusions

1. The total pressure losses in the flow part of the JRT essentially depend on the reduced velocity at the inlet to the rotor λ_1 and the available pressure ratio Π_0. With the correct choice of λ_1, Π_0 and the geometrical sizes of the flow part at the inlet to the rotor, they can be significantly reduced.
2. To increase the total pressure recovery factor in the flow part of the JRT in the axial channel of the rotor, it is necessary to install a diffuser sleeve with a cylindrical part where the transition from supersonic to subsonic velocity and the diffusor part where a further subsonic flow velocity decrease occurs.
3. The reduced flow velocity at the inlet to the rotor should be as small as possible, based on the location of the shock wave in the inlet part of the diffuser sleeve.
4. The opening angle of the diffuser part of the diffuser sleeve should be no more than 10°.
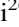
References

1. Kudrya, S.O., Yatsenko, L.V., Dushina, H.P., et al.: Atlas of Energy Potential of Renewable and Non-traditional Energy Sources of Ukraine. Instytut elektrodynamiky NAN, Ukraine (2001)
2. Shchokin, A.R.: State and problems on the way of development of cogeneration systems in Ukraine. Informational and analytical reference book. Energy Saving in Regions, pp. 38–41 (2003)
3. Tarshevsky, V.S., Bondarenko, V.S., Ogorodnik, V.A.: Realization of energy saving policy in NAC «Naftogaz of Ukraine». Oil Gas Ind. **1**, 3–6 (2009)
4. Vanyeyev, S., Getalo, V.: Jet-reactive turbine: experimental researches and calculations by means of softwares. Appl. Mech. Mater. **630**, 66–71 (2014)
5. Moroz, V.V.: Jet drive—unrealized possibilities. Part I. Review of piston actuators. Armaturostroyeniye **2**(83), 50–63 (2013)
6. Sayapin, V.V., Baklanov, Y.H., Belousov, V.A., Nabiev, R.M., Korotkov, V.P., Mutallim-Zade, I.F.: Pneumatic actuator for ball valves. Gazov. Promushlennost **8**, 54–55 (1999)
7. Chashin, V.A., Kamladze, O.H., Kondratyev, A.B., et al.: Pneumatic Control Systems for the Aircrafts. Mashinistroyeniye, Moscow (1987)
8. Sayapin, V.V.: Optimization of pneumatic actuator with jet engine. Pnevmatika i gidravlika. Privody i sistemy upravleniya **10**, 58–63 (1984)
9. Abramovich, G.N.: Applied Gas Dynamics. Nauka, Moscow (1969)

Chemical Engineering

Modeling of the Heating for Cladded Powder in Plasma Jet at Spraying of Coating

Andrii Andreytsev[1] , Igor Smirnov[2] , Andrii Chornyi[2(✉)] ,
Mykhailo Yelysieiev[2] , and Nikolay Dolgov[3]

[1] State University of Infrastructure and Technology,
19 Ivan Ogienko St., Kyiv 02000, Ukraine
[2] National Technical University of Ukraine "Igor Sikorsky Kyiv
Polytechnic Institute", 37 Peremohy Ave., Kyiv 03056, Ukraine
black803@gmail.com
[3] Pisarenko Institute for Problems of Strength of the National Academy
of Sciences of Ukraine, 2 Timiriazevska St., Kyiv 01014, Ukraine

Abstract. The paper is devoted to solving the problem of determining the temperature of cladded particles with a shell in a plasma jet taking into account the change in their aggregate state. The features of heating of the cladded particles during plasma spraying of functional coatings are considered. The analytic solution of the boundary problem for the heat equation in the case of a variable temperature of the plasma jet, which was approximated by cubic splines, was obtained. The mathematical model of heating of powder particle with a sheath during plasma spraying taking into account the time matching of plasma jet temperature and particle is generalized. Formulas for determining the melting time of the metal sheath and the ceramic core were given. Influence copper sheath thickness on heating of alumina kernel of the cladded particle by an analytical solution is set. The results of testing coated samples confirmed that the developed cladded powder improves the physical and mechanical properties of the plasma sprayed composite coatings.

Keywords: Plating sheath · Coated particle · Cladded powder
Plasma jet · Heat conductivity · Boundary problem

1 Introduction

During plasma spraying much attention is paid to setting an optimum temperature condition of particles of the sprayed powder that depends on a set of factors connected first of all with kinetic and thermophysical parameters, both a plasma jet, and the sprayed material. The aim becomes complicated in case of use for a spraying of ceramic powders because of their specific physical properties and thermodynamic instability. Even thermodynamic resistant oxides are inclined to considerable dissociation during a particles heating temperature that is close to melting temperature. Correlation is observed between degree of dissociation and heat of oxides formation. Temperature drops in particles of oxides can reach 10^7–10^9 W/m^2 during heat streams of about 10^8–10^9 K/m that are realized during plasma spraying. In this case temperature of a

particle surface can exceed melting temperature with preservation in the centre of a firm core. Existence of such gradients of temperature leads to considerable increase of heating time of the whole particle up to the necessary melting temperature.

The metal sheath on a ceramic particle and providing increase of adhesive and cohesive properties of raised sprayed coating, can have considerable influence on development of temperature processes and as a result on phase transformations. Changing heat exchange conditions by means of a cladded sheath on powder particles, it is possible to pull together or divide processes of their heating, melting and evaporation during spraying [1].

2 Literature Review

Theoretical and experimental researches of temperature conditions of the sprayed particles in a plasma jet were studied earlier [2–4]. Temperature and time dependences matching temperature of a plasma jet and residence time of a sprayed particle in a high-temperature zone were insufficiently considered. Existing dependences can be used only at the initial stage of particle stay in a plasma jet when the difference between temperatures and velocities of the jet and particle is great enough.

It is necessary to know a structure of a plasma jet, laws of temperature change and speed alone radius and axis of the jet in order to solve the tasks connected with a thermal spraying. Results of these studies including using of mathematical modelling are presented in research works [5, 6]. Complex computer modelling of both plasma jet, and the process of spraying is implemented in software packages such as CSPSP, Plasma 2000, MARC. However, the limitation of material databases, constructive and technological parameters of plasma torches in these packages doesn't allow conducting the study of process of spraying in nonstandard conditions outside of offered ranges and when using the composite (cladded) powders.

The detailed analysis of physical and chemical aspects of spraying and use of the cladded powders and mathematical modelling and consideration of physics of processes of drawing plasma-sprayed coating of the composite cladded powders is shown earlier [7]. These studies show the solution of Stephan's problem for the condition of melting of a two-layer composite particle during its transportation in a plasma jet of an arc plasma torch and define the range of the parameters that provides melt-through of the Ni sheath and heating of a solid core of particles from the titanium-chrome carbide. Thus, it is shown that heating of the cladded powders in a plasma jet should be within a certain interval for providing the melt-through of a refractory ceramic core on the one hand, and on the other hand, reduction of losses of a metal sheath by evaporation.

3 Research Methodology

The aim of this research paper is to study influence of a cladded sheath on temperature conditions of ceramic particles in a plasma jet by means of mathematical models of heat conductivity.

The majority of ceramic oxides are spectrally partially transparent. Therefore, their heating is described by the equation containing conductive and radiation components in general. However, a radiation component in the energy equation can be not taking into account for particles with a diameter less than 100 μm at any period of heating and particles with a diameter less than 3 μm at the heating time not more than 3 μs. In this case, the energy equation for the particle results into the heat conductivity equation specific type of which depends on a structure and shape of the particle.

During modelling the heating process of the particle in a plasma jet proceeded from the following assumptions: the particle has a spherical shape and temperature distribution is spherically symmetric in it; the particle is a homogeneous, isotropic body; internal sources of heat are absent. Calculations have shown that time of spheroidization of the particle in the plasma jet was about 10^{-8} s whereas, heating time of the particle exceeded 10^{-4} s. Therefore, the assumption about a spherical shape of the particle is reasonable.

If it is granted that all thermodynamic coefficients at a certain stage of flight of the particle in the plasma jet are constant and equal to average values in the considered range of temperatures, the mathematical model can be formulated as follows

$$\frac{\partial(rT)}{\partial t} = a \frac{\partial^2(rT)}{\partial r^2}, \text{ when } r \in [0, R] \tag{1}$$

$$\frac{\partial(rT_1)}{\partial t} = a_1 \frac{\partial^2(rT_1)}{\partial r^2}, \text{ when } r \in [R, R_1] \tag{2}$$

$$T_1(R, t) = T(R, t) \tag{3}$$

$$\lambda_1 \frac{\partial T_1}{\partial r}|_{r=R} = \lambda \frac{\partial T_1}{\partial r}|_{r=R} \tag{4}$$

$$\lambda_1 \frac{\partial T_1}{\partial r}|_{r=R_1} = \left[\alpha\left(T_g - T_1\right)\right]|_{r=R_1} \tag{5}$$

$$\lambda_1 \frac{\partial T}{\partial r}|_{r=0} = 0, T < \infty \tag{6}$$

$$T_1(r, 0) = T(r, 0) = T_0 \tag{7}$$

Where T, T_1, $a = \frac{\lambda}{c\rho}$, $a_1 = \frac{\lambda_1}{c_1\rho_1}$; λ, c, ρ and λ_1, c_1, ρ – temperature, heat conductivity coefficient, specific heat capacity, density of material of a core and sheath, respectively; α – heat exchange coefficient; T_0 – the initial temperature of a particle; R_1, R – external and internal radiuses of a sheath, respectively T_g – temperature of a plasma jet.

It was found that for making exact calculations of heating temperature of ceramic particles it is necessary to match temperature of a plasma jet and residence time of a sprayed particle in a high-temperature zone [8]. For this purpose dependences of changing of plasma jet temperature T_{pl} on t – residence time of sprayed particle in the plasma jet were constructed. Then the received dependences were approximated by a quadratic polynomial. In [8] temperature distribution in a thin sheath is presented as the

two first expansion terms $T_1(t, r)$ as series in powers of $1/r$ and it is the solution of the third boundary problem for the heat conductivity equation that describes core temperature changing in a plasma jet of constant temperature. It is given the analytical solution of this boundary problem on condition of changing of plasma temperature, which is approximated by squared polynomial [9]. This solution allows to determine the temperature in a two-layer cladded particle in cases of variable radius and sheath thickness.

In this paper, the plasma temperature is approximated by cubic polynomials.

$$P_3(t) = At^3 + Bt^2 + Ct + D \tag{8}$$

Then a solution is obtained.

$$T(r,t) = T_0 \sum_{n=1}^{\infty} A_n(r) e^{-\frac{\mu_n^2 a^2 t}{R^2}} + \int_0^t \left(P_3(\tau) - P_3'(\tau) \frac{k_c''}{Bi} \right) \frac{a^2 \mu_n^2}{R^2} \sum_{n=1}^{\infty} A_n(r) e^{-\frac{\mu_n^2 a^2 t}{R^2}} d\tau \tag{9}$$

$$A_n(r) = \frac{2R \sin \mu_n \frac{r}{R}}{\mu_n r} \frac{Bi}{\mu_n \left[\left(1 + k_c' + \frac{Bi-1}{\mu_n^2} \right) \sin \mu_n + \left(k_c' \mu_n - \frac{Bi-1}{\mu_n} \right) \cos \mu_n \right]} \tag{10}$$

where $k_c' = k_c \left(1 - \frac{Bi_1}{6} \right)$; $k_c'' = k_c \frac{Bi_1}{6}$; $k_c = \frac{c_1 \rho_1 h}{c \rho R}$; μ_n – the roots of equation $\cos \mu_n = \left(k_c' \mu_n + \frac{1-Bi}{\mu_n} \right) \sin \mu_n$.

Since the change in the plasma temperature along the total deposit distance cannot be approximated by cubic polynomials, we split the distance into sections and reconcile the plasma temperature with the time of the particle in it.

The description of this process is given in [10].

Then, in the case of continuity of the approximating function at the nodes, the solution takes the form

$$T = \sum_{n=1}^{\infty} A_n(r) \left(T_0 e^{-\frac{\mu_n^2 a^2 t}{R^2}} + \sum_{j \geq 0} \left(\eta(t - t_j) - \eta(t - t_{j+1}) \right) I_{j,\mu_n} \right) \tag{11}$$

Here $\eta(t)$ – Heaviside function;

$$\eta(t) = \begin{cases} 0, & t < 0 \\ 1, & t \geq 0 \end{cases} \tag{12}$$

$$I_{j,\mu_n} = \int_{t_j}^t \left(P_{3j}(\tau) - P_{3j}'(\tau) \frac{k_c''}{Bi} \right) \frac{a^2 \mu_n^2}{R^2} e^{-\frac{\mu_n^2 a^2 t}{R^2}} d\tau, \quad t_0 = 0 \tag{13}$$

For approximation, we used Hermitian cubic splines that are continuously differentiable functions (see formulas (7), (8) in [10]).

4   Results

Thus, we receive the curve of changing of temperature maximum reached by a particle of aluminium oxide with the radius of 25 μm of the cladded sheath from copper depending on external radius, i.e. when the radius of core is invariable and core thickness is changing (Fig. 1).
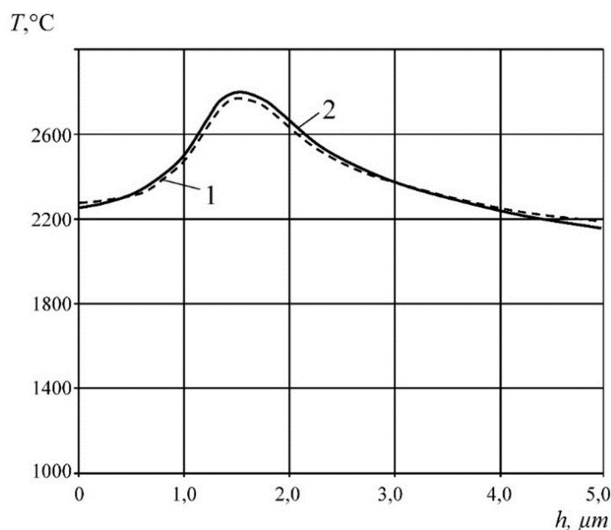

Fig. 1. Dependence of temperature maximum reached by a particle of aluminium oxide with the radius of 25 μm of the cladded sheath from copper on its external radius: 1 – for quadratic approximation of plasma jet temperature, 2 – for approximation by cubic splines.

It follows from Fig. 1 that existence of a copper sheath with thickness of 1.5 μm serves to the maximum temperature increase of a core, and with a core thickness more than 4 μm, a particle of alumina may not melt. Applying various diameters of the cladded particle with the constant diameter of a core, it is possible to determine an influence of thickness of a core on the timespan when the cladded particle reaches the required temperature, for example temperature of the core melting.

Determination of an optimum thickness of the core is shown at Fig. 2 which show the curves of change of particles temperature until reaching the maximum and temperature of a plasma jet on the particle surface depending on time, the curves do not show the decrease of temperature not to overload Fig. 2.

The change of heating temperature of the cladded particles that is connected with dynamic motion is shown at Fig. 2. In this case change of speed of particles happens at the expense of increase of their weight in proportion to sheath thickness.
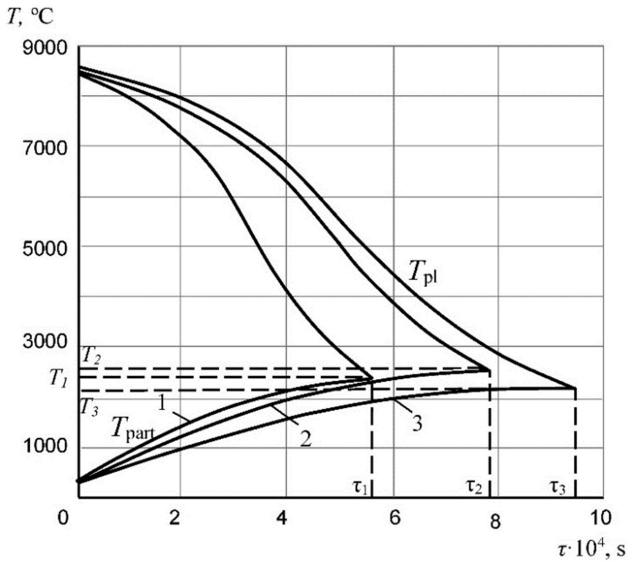
Fig. 2. Change of temperature of the plated particle T_{part} and plasma jet T_{pl} within time: indexes 1, 2, 3 correspond to thickness of a shell 1, 1.5, 3 μm respectively.

5   Conclusions

A mathematical model of heating of a powder particle with sheath during plasma spraying, which considers correlation between plasma jet temperature and particle temperature, as well as time, based on what the determined influence of sheath thickness on core heating of the cladded particle was developed. As a result, the optimum thickness of a copper sheath at the level of 1.5 μm (48% wt.) for a alumina particle with a diameter of 50 μm, which provides the maximum heating of a refractory ceramic core that results into qualitative plasma coatings was defined. The results of testing coated samples confirmed that the developed cladded powder improves the physical and mechanical properties of the plasma sprayed composite coatings.

References

1. Pawlowski, L.: The Science and Engineering of Thermal Spray Coatings, 2nd edn. Wiley, Australia (2008)
2. Remesh, K., Yu, S.C.M., Ng, H.W., Berndt, C.C.: Computational study and experimental comparison of the in-flight particle behavior for an external injection plasma spray process. J. Therm. Spray Technol. **12**(4), 508–522 (2003)
3. Mostaghimi, J., Pasandideh-Fard, M., Chandra, S.: Dynamics of splat formation in plasma spray coating process. Plasma Chem. Plasma Process. **22**(1), 59–84 (2002)
4. Borisov, Yu., Bushma, A., Krivtsun, I.: Modeling of motion and heating of powder particles in laser, plasma, and hybrid spraying. J. Therm. Spray Technol. **15**(4), 553–558 (2006)

5. Lee, Y.C., Chyou, Y.P., Pfender, E.: Particle dynamics and particle heat and mass transfer in thermal plasmas. Part II. Particle heat and mass transfer in thermal plasmas. Plasma Chem. Plasma Process. **5**(4), 391–414 (1985)
6. Cheng, K., Chen, X., Pan, W.: Comporson of laminar and turbulent plasma jet characteristics – a modeling study. Plasma Chem. Plasma Process. **26**, 211–235 (2006)
7. Barvinok, V.A., Bogdanovych, V.I., Dokukina, I.A., Kytaykin, V.L., Plotnikov, A.N.: Mathematical modelling of heating of powder composite material in plasma jet. In: News Samara Scientific center at Russian Academy of Science, vol. 2, pp. 197–203 (2001)
8. Smirnov, I.V., Andreytsev, A.Y., Chornyi, A.V.: Analytic definition of speed and temperature of the oxide ceramic particles in the process of plasma spraying. Bull. KhNTU **2**(35), 403–410 (2009)
9. Andreytsev, A.Y., Smirnov, I.V.: Modelling of a powder particle heating with a shell during gas-thermal coatings. In: International Scientific Conference "Actual Mathematic Problems and Its Applications in Natural Sciences and Information Technologies", 17–22 April 2011, pp. 215–216. V. N. Karazin Kharkiv National University, Kharkiv (2011)
10. Andreytsev, A.Y., Kryukov, N.N., Smirnov, I.V., Zashchepkina, N.N.: Numerically-analytical determination of the particle temperature for plasma spraying (Refined model). Bull. KhNTU **3**(54), 326–331 (2015)

Information Support of Optimization Calculation of Vortex Type Granulation Devices

Artem Artyukhov[(✉)]

Sumy State University, 2 Rymskogo-Korsakova St., Sumy 40007, Ukraine
artyukhov@pohnp.sumdu.edu.ua

Abstract. The paper studies the hydrodynamic conditions of gas flow motion and vortex granulator workspace design optimization. A comprehensive approach for determination of the hydrodynamic characteristics of a vortex gas flow and their visualization is proposed. The mathematical approach, based on Reynolds equations for turbulent flows solution, is presented. The mathematical model of equations solution with the definition of gas flow velocity components in any point on the radius and height of vortex granulator is obtained. The value of gas flow components of velocity, received by the results of analytical solution, and experimental data has a high degree of compliance. There is mutual rejection that numerical value of velocities and overall graphic image of diagrams of components of gas flow velocities have the same character. For rate and radial velocity components of gas flow for the initial conditions and changing set of geometrical and technological conditions does not cause such significant change of quantitative distribution value along the radius and height for angular velocity component gas stream. The obtained results form the basis of original algorithm for calculating of vortex granulator hydrodynamic calculation and its basic dimensions optimization selection.

Keywords: Software · Modeling · Vortex granulator · Hydrodynamics
Optimization

1 Introduction

Flows of single-phase and multiphase medium play a key role in the working process of many contemporary engineering devices. The design of these devices for the required operating parameters is impossible without a reliable prediction of the characteristics of these flows. Since many modern engineering devices are expensive and time consuming to manufacture, physical modeling with the experimental determination of the parameters of their work in different modes, as a rule, requires a lot of time and cost. In addition, because of limited possibilities of modern experimental sensors and measuring instruments, experimental observations do not provide a complete picture of the phenomenon being investigated.

2   Literature Review

Because of nature of these environments, flow of liquids and gases often varies in complex manner to form nonstationary effects, "dead" zones and vortex structures [1]. The situation is further complicated by the presence of heat transfer, in considering flows of several substances mixture, flows with free surfaces, weighted particles in stream, flows with cavitation, boiling, condensation, combustion, chemical reactions [2–8]. These factors lead to the growing interest of mathematical modeling tools for flows of liquids and gases, which allows to predict the flow characteristics and parameters of the devices at design stages and stages of manufacturing in the metal [9–12].

Software can adequately simulate the complex physical effects taking place in flows motion in vortex granulator, and perform calculation of flows within the reasonable time [13, 14]. They provide the user with the convenient tools of data preparation and analysis of calculations results, and are a powerful tool for accurate prediction of the characteristics of hydraulic parts flow at a design stage, saving the resources to conduct a physical experiment [15, 16].

Methods CFD (Computational Fluid Dynamics) suggest calculation of flows of liquids and gases through the numerical solution of equations of Navier-Stokes and continuity, describing the most general case of this medium motion (for turbulent flows - Reynolds equations).

The purpose of the work is creation of vortex granulator optimization calculation algorithm. The created algorithm is based on the author's software and calculation data visualization using software for calculation of flows hydrodynamics.

3   Research Methodology

The simulation of flows is based on the finite-volume method of solving equations of hydrodynamics and the use of a rectangular adaptive grid with local grinding. For the approximation of the curvilinear geometry with increased accuracy, the technology of the substrate density of geometry is used. This technology allows importing geometry from CAD systems and transferring information with finite element analysis systems.

Given that, in practice interest it usually deals with not instantaneous, but with the average in time velocity value, for mathematical description of turbulent swirling motion of gas flow Reynolds equation as modification of Navier-Stokes equations is used [17, 18].

$$\frac{\partial}{\partial t}\left(\rho \overline{V_i}\right) + \frac{\partial}{\partial q_j}\left(\rho \overline{V_i V_j}\right) + \frac{\partial}{\partial q_j}\left(\rho \overline{V_i' V_j}\right) = -\frac{\partial p}{\partial q_i} + \frac{\partial}{\partial q_j}\left[\mu\left(\frac{\partial \overline{V_i}}{\partial q_j} + \frac{\partial \overline{V_j}}{\partial q_i}\right)\right] + f_i \quad (1)$$

where $\overline{V}$- average in time values of velocity; $\overline{V}'$- components of velocity pulsations; µ - coefficient of turbulent viscosity; t - time; ρ - gas density; p - pressure; f_i – element, characterizing the mass forces effect; q_j - coordinate axes (in the case of hydrodynamic modeling in granulator working volume as it is shown above, it is advisable to use

curvilinear coordinate system), i, j − 1 … 3; for cylindrical coordinate system (Fig. 1) code "1" – axial direction (z), code "2" – radial direction (r), code "3" – circular direction (φ) (Figs. 1 and 2).
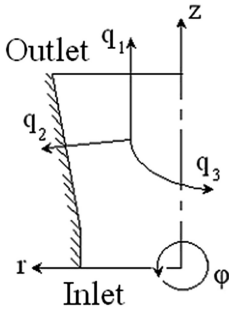

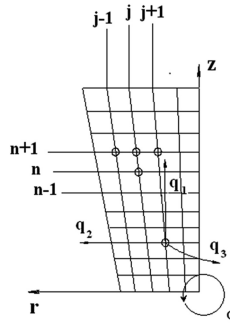**Fig. 1.** Scheme of vortex granulator workspace and coordinate system.

Fig. 2. Construction of calculation grid.

The main advantages of description and problem solving hydrodynamics method, based on numerical solution of Reynolds complete equations, are accuracy and versatility.

The Reynolds equations system is supplemented with flow continuity equation

$$\frac{\partial \rho}{\partial t} + \frac{\partial}{\partial q_j}\left(\rho V_j\right) = 0. \tag{2}$$

For Reynolds Eq. (1) solving Boussinesq hypothesis [17] is used. According to this hypothesis, the members with velocity pulsations $\left(\rho \overline{V_i' V_j'}\right)$ in Eq. (3) are associated with the averaged flow characteristics in such relation:

$$\rho \overline{V_i' V_j'} = -\mu\left(\frac{\partial \overline{V_i}}{\partial q_j} + \frac{\partial \overline{V_j}}{\partial q_i}\right) + \frac{2}{3}\rho \delta_{ij} k, \tag{3}$$

where $k = 0,5\left(\overline{V_j' V_j'}\right)$ – turbulence kinetic energy, $\delta_{ij} = 1$ when i = j, $\delta_i = 0$ when i ≠ j.

The Reynolds system of equations is elliptic. It is used to calculate the trends in those cases where flow characteristics at arbitrary point area depend on the structure of flow both above and downstream, i.e. when the dominant direction of the fluid is absent or weakly expressed. Ellipticity system of equations means that it is necessary to set the boundary conditions for all variables in all the borders of calculation area.

When axisymmetrical flow modeling equation of motion (1) and continuity of flow (2) are significantly simplified. For curved (cylindrical) coordinate system they are as follows (with the introduction of Eq. (3) Reynolds number $Re = V_0 D / \nu$ where characteristic parameters D – diameter of input cross section calculation area; V_0 - average rate velocity in the input section; ν - kinematic viscosity):

– Reynolds equations projected on the axial direction q1:

$$
\begin{aligned}
&\frac{V_1}{H_1}\frac{\partial V_1}{\partial q_1} + \frac{V_2}{H_2}\frac{\partial V_1}{\partial q_2} - \frac{V_2^2}{H_1 H_2}\frac{\partial H_2}{\partial q_1} - \frac{V_3^2}{H_1 H_3}\frac{\partial H_3}{\partial q_1} + \frac{1}{H_2}\frac{\partial\left(\overline{V_1'V_2'}\right)}{\partial q_2} + \frac{\left(\overline{V_1'V_2'}\right)}{H_1^2 H_2 H_3}\frac{\partial\left(H_1^2 H_3\right)}{\partial q_2} \\
&+ \frac{1}{H_1}\frac{\partial\left(\overline{V_1'V_1'}\right)}{\partial q_1} + \frac{\left(\overline{V_1'V_1'}\right)}{H_1^2 H_2 H_3}\frac{\partial(H_1 H_2 H_3)}{\partial q_1} - \frac{\left(\overline{V_2'V_2'}\right)}{H_1 H_2}\frac{\partial H_2}{\partial q_1} - \frac{\left(\overline{V_3'V_3'}\right)}{H_1 H_3}\frac{\partial H_3}{\partial q_1} = -\frac{1}{H_1}\frac{\partial p}{\partial q_1} \\
&+ \frac{1}{Re}\left(\frac{1}{H_1^2}\frac{\partial^2 V_1}{\partial q_1^2} + \frac{1}{H_2^2}\frac{\partial^2 V_1}{\partial q_2^2} + \frac{1}{H_1 H_2 H_3}\frac{\partial V_1}{\partial q_1}\frac{\partial(H_2 H_3/H_1)}{\partial q_1} + \frac{1}{H_1 H_2 H_3}\frac{\partial V_1}{\partial q_2}\frac{\partial(H_1 H_3/H_2)}{\partial q_2} \right. \\
&- \frac{2}{H_1 H_2^2}\frac{\partial H_2}{\partial q_1}\frac{\partial V_2}{\partial q_2} + \frac{V_1}{H_1}\frac{\partial}{\partial q_1}\left(\frac{1}{H_1 H_2 H_3}\frac{\partial(H_2 H_3)}{\partial q_1} \right) \\
&+ \left. \frac{V_2}{H_1}\frac{\partial}{\partial q_1}\left(\frac{1}{H_1 H_2 H_3}\frac{\partial(H_1 H_3)}{\partial q_2} \right) - \frac{V_2}{H_2 H_3}\frac{\partial}{\partial q_2}\left(\frac{H_3}{H_1 H_2}\frac{\partial H_2}{\partial q_1} \right) \right);
\end{aligned} \tag{4}
$$

– Reynolds equations projected on the radial direction q2:

$$
\begin{aligned}
&\frac{V_1}{H_1}\frac{\partial V_2}{\partial q_1} + \frac{V_2}{H_2}\frac{\partial V_2}{\partial q_2} - \frac{V_1 V_2}{H_1 H_2}\frac{\partial H_2}{\partial q_1} - \frac{V_3^2}{H_2 H_3}\frac{\partial H_3}{\partial q_2} + \frac{1}{H_1}\frac{\partial\left(\overline{V_1'V_2'}\right)}{\partial q_1} + \frac{\left(\overline{V_1'V_2'}\right)}{H_1 H_2^2 H_3}\frac{\partial\left(H_2^2 H_3\right)}{\partial q_1} \\
&+ \frac{1}{H_2}\frac{\partial\left(\overline{V_2'V_2'}\right)}{\partial q_2} + \frac{\left(\overline{V_2'V_2'}\right)}{H_1 H_2^2 H_3}\frac{\partial(H_1 H_2 H_3)}{\partial q_2} - \frac{\left(\overline{V_3'V_3'}\right)}{H_2 H_3}\frac{\partial H_3}{\partial q_2} = -\frac{1}{H_2}\frac{\partial p}{\partial q_2} \\
&+ \frac{1}{Re}\left(\frac{1}{H_1^2}\frac{\partial^2 V_2}{\partial q_1^2} + \frac{1}{H_2^2}\frac{\partial^2 V_2}{\partial q_2^2} + \frac{1}{H_1 H_2 H_3}\frac{\partial V_2}{\partial q_1}\frac{\partial(H_2 H_3/H_1)}{\partial q_1} + \frac{1}{H_1 H_2 H_3}\frac{\partial V_2}{\partial q_2}\frac{\partial(H_1 H_3/H_2)}{\partial q_2} \right. \\
&+ \left. \frac{2}{H_1 H_2^2}\frac{\partial H_2}{\partial q_1}\frac{\partial V_1}{\partial q_2} + \frac{V_2}{H_2}\frac{\partial}{\partial q_2}\left(\frac{1}{H_1 H_2 H_3}\frac{\partial(H_1 H_3)}{\partial q_2} \right) \right);
\end{aligned} \tag{5}
$$

– Reynolds equations projected on the circular direction q3:

$$
\begin{aligned}
&\frac{V_1}{H_1}\frac{\partial V_3}{\partial q_1} + \frac{V_2}{H_2}\frac{\partial V_3}{\partial q_2} + \frac{V_1 V_3}{H_1 H_3}\frac{\partial H_3}{\partial q_1} + \frac{V_2 V_3}{H_2 H_3}\frac{\partial H_3}{\partial q_2} + \frac{1}{H_2}\frac{\partial\left(\overline{V_2'V_3'}\right)}{\partial q_2} + \frac{\left(\overline{V_2'V_3'}\right)}{H_1 H_2 H_3^2}\frac{\partial\left(H_1 H_3^2\right)}{\partial q_2} \\
&+ \frac{1}{H_1}\frac{\partial\left(\overline{V_1'V_3'}\right)}{\partial q_1} + \frac{\left(\overline{V_1'V_3'}\right)}{H_1 H_2 H_3^2}\frac{\partial\left(H_2 H_3^2\right)}{\partial q_1} = \frac{1}{Re}\left(\frac{1}{H_1^2}\frac{\partial^2 V_3}{\partial q_1^2} + \frac{1}{H_2^2}\frac{\partial^2 V_3}{\partial q_2^2} \right. \\
&+ \left. \frac{1}{H_1 H_2 H_3}\frac{\partial V_3}{\partial q_1}\frac{\partial(H_2 H_3/H_1)}{\partial q_1} + \frac{1}{H_1 H_2 H_3}\frac{\partial V_3}{\partial q_2}\frac{\partial(H_1 H_3/H_2)}{\partial q_2} + \frac{V_3}{H_1 H_2}\frac{\partial}{\partial q_2}\left(\frac{H_1}{H_2 H_3}\frac{\partial H_3}{\partial q_2} \right) \right);
\end{aligned} \tag{6}
$$

– continuity equation:

$$
\frac{1}{H_1 H_2 H_3}\left(V_1\frac{\partial(H_2 H_3)}{\partial q_1} + V_2\frac{\partial(H_3 H_1)}{\partial q_2} \right) + \frac{1}{H_1}\frac{\partial V_1}{\partial q_1} + \frac{1}{H_2}\frac{\partial V_2}{\partial q_2} = 0, \tag{7}
$$

where H1, H2, H3 – Lamé coefficient [17].

Further simplification of system of Eqs. (4)–(7) for simulating the vortex flow of gas phase in the workspace granulator is possible using the following assumptions [19, 20]:

- the expected presence of dominant flow direction along with the axial component of gas flow velocity is everywhere positive and far exceeds the radial;
- gas flow velocity component in the axial direction varies considerably slower than in the radial;
- velocity and pressure values in every elementary volume of gas flow depend only on the conditions downstream and do not depend on the conditions upstream.

These assumptions allow to conduct analysis of components in Eqs. (4)–(7) and discard those that provide significant impact on the result of the calculation.

After accounting assumptions for axially symmetric gas flow Eq. (4)–(7) can be written as

$$
\frac{V_1}{H_1}\frac{\partial V_1}{\partial q_1} + \frac{V_2}{H_2}\frac{\partial V_1}{\partial q_2} - \frac{V_3^2}{H_1 H_3}\frac{\partial H_3}{\partial q_1} + \frac{1}{H_2}\frac{\partial\left(\overline{V_1' V_2'}\right)}{\partial q_2} + \frac{\left(\overline{V_1' V_2'}\right)}{H_1^2 H_2 H_3}\frac{\partial\left(H_1^2 H_3\right)}{\partial q_2}
$$
$$
= -\frac{1}{H_1}\frac{\partial p}{\partial q_1} + \frac{1}{\mathrm{Re}}\left(\frac{1}{H_2^2}\frac{\partial^2 V_1}{\partial q_2^2} + \frac{1}{H_1 H_2 H_3}\frac{\partial V_1}{\partial q_2}\frac{\partial(H_1 H_3/H_2)}{\partial q_2}\right);
\tag{8}
$$

$$
\frac{\partial p_r}{\partial q_2} = \frac{V_3^2}{H_3}\frac{\partial H_3}{\partial q_2};
\tag{9}
$$

$$
\frac{V_1}{H_1}\frac{\partial V_3}{\partial q_1} + \frac{V_2}{H_2}\frac{\partial V_3}{\partial q_2} + \frac{V_1 V_3}{H_1 H_3}\frac{\partial H_3}{\partial q_1} + \frac{V_2 V_3}{H_2 H_3}\frac{\partial H_3}{\partial q_2} + \frac{1}{H_2}\frac{\partial\left(\overline{V_2' V_3'}\right)}{\partial q_2} + \frac{\left(\overline{V_2' V_3'}\right)}{H_1 H_2 H_3^2}\frac{\partial\left(H_1 H_3^2\right)}{\partial q_2}
$$
$$
= \frac{1}{\mathrm{Re}}\left(\frac{1}{H_2^2}\frac{\partial^2 V_3}{\partial q_2^2} + \frac{1}{H_1 H_2 H_3}\frac{\partial V_3}{\partial q_2}\frac{\partial(H_1 H_3/H_2)}{\partial q_2} + \frac{V_3}{H_1 H_2}\frac{\partial}{\partial q_2}\left(\frac{H_1}{H_2 H_3}\frac{\partial H_3}{\partial q_2}\right)\right);
\tag{10}
$$

$$
\frac{1}{H_1 H_2 H_3}\left(V_1\frac{\partial(H_2 H_3)}{\partial q_1} + V_2\frac{\partial(H_3 H_1)}{\partial q_2}\right) + \frac{1}{H_1}\frac{\partial V_1}{\partial q_1} + \frac{1}{H_2}\frac{\partial V_2}{\partial q_2} = 0.
\tag{11}
$$

This system of equations is closed equation sustainability costs:

$$
\int_0^{Q_2} V_1 H_2 H_3 dq_2 = const,
\tag{12}
$$

where Q2 - coordinate q2 on the wall of working volume of vortex granulator.

Obtained system of Eqs. (8)–(11) has a parabolic character, and its decision based on the method proposed by Patankar and Spalding [20] and realized in SIMPLE (Semi-Implicit Method for Pressure-Linked Equations) procedure and its modifications.

Numerical solutions of mathematical models equations are performed in one marching passage from the working volume input cross section to output using finite

volumes method with the elements of finite-element approach. Before calculating the estimated grid is constructed (Fig. 2), and unknown values of velocity and pressure are found in the nodes of this grid.

The program «Conical channel» © is designed to calculate axial symmetric gas flows in channels, including the swirling flows in the diffuser on the base of the model [21].

Initial data for calculation are geometric configuration of channel properties and parameters of gas and parameters of flow in the input cross-section. The calculation objective is to determine the fields of velocity and pressure in full range of calculated area and, consequently, the determination of energy losses between the input and output cross sections of the channel. The program displays the calculation data as graphic dependencies.

Program's work starts with opening or creating a new file of calculated area configuration. Example of calculation area configuration is shown in Fig. 3.
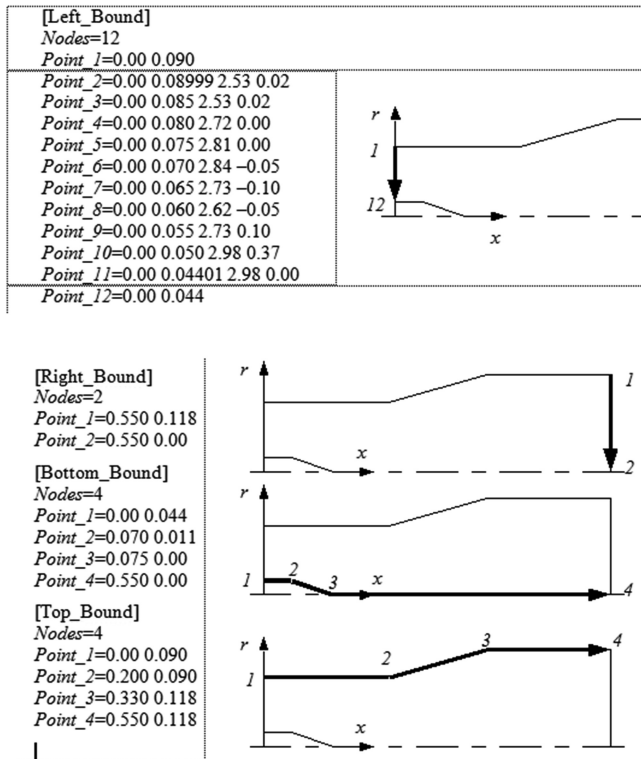
Fig. 3. Example of calculation area configuration.

After selecting the necessary parameter for calculation the program «Conical channel» © builds an estimated grid (Fig. 2).

4   Results

For the analysis of motion velocity components it is necessary to define the nature of dependencies of the graphical components and match them within a comparative graph as it is shown in Figs. 4, 5, 6.
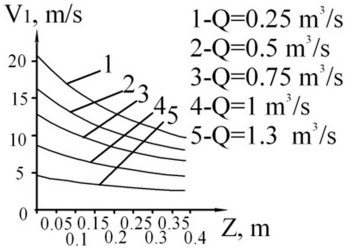
Fig. 4. Calculated change of the longitudinal velocity of the gas flow.
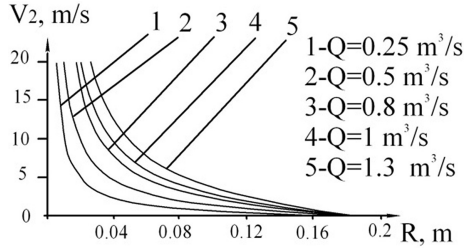
Fig. 5. Calculated change of the radial velocity of the gas flow.
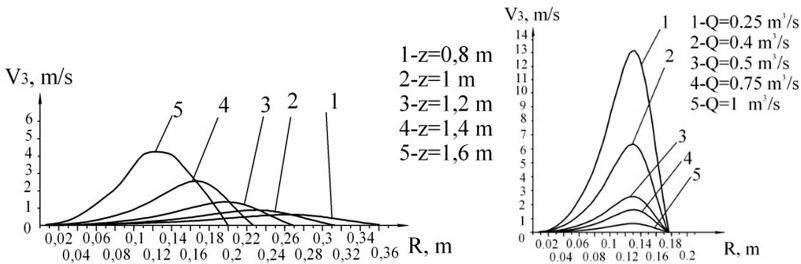
Fig. 6. Calculated change of the circumferential velocity of the gas flow.

Analysis of graphic dependences of gas flow rate velocity under various conditions has identified monotonous nature of rate velocity reduction under all calculations of the conducting conditions.

Comparison of theoretical calculation for different cross sections of working space and different opening cone angles shows that the area of maximum circular speed for the arbitrarily chosen section is r = 0.66–0.72 R.

Analysis of graphical dependencies shows the reduction zone of circular velocity growth by increasing the gas flow rate and narrowing the range of maximum speed. This velocity peak remains constant at geometric place in the working space of vortex granulator.

The value of circular velocity with increasing the gas flow rate increases faster. At the same time, with the increasing gas flow rate in the workspace of vortex granulator the angular velocity slow growth zone is growing. Thus, the vortex is moving toward the solid wall and has a greater intensity.

Analysis of dependences of circular velocity changes under different conditions identified pattern of velocity distribution by the radius of device and its quality change according to the set of parameters.

Given the results of analysis of circular velocity peak of gas flow in cross section of the device workspace for the granular product from the melt (solution) device (or group of devices) for spraying it is advisable to locate within the working space of vortex granulator in specified range of current radius at random selected height and cone opening angle the received results of experiment (optimal height of location sprayer is defined to be h = 0.6–0.8 H).

Continuous increase of the circular velocity of gas flow before reaching its peak and reduction after passing its peak had obtained confirmation by the experiment and defined the range of gas distribution unit operation with maximum efficiency. In the area of minimum circular velocity the granules motion intensification and "dead" zones prevention, that is possible in the range up to r = 0.25 R, are achieved by reasonable selection of gas-distributing unit with additional elements for flow swirling.

According to the analysis the influence of conical workspace opening angle on the possibility of reverse vortex in the center of a weighted layer and place a geometric location of individual elements of the weighted layer connection place and the transition region combining the weighted layer connection was identified. With the
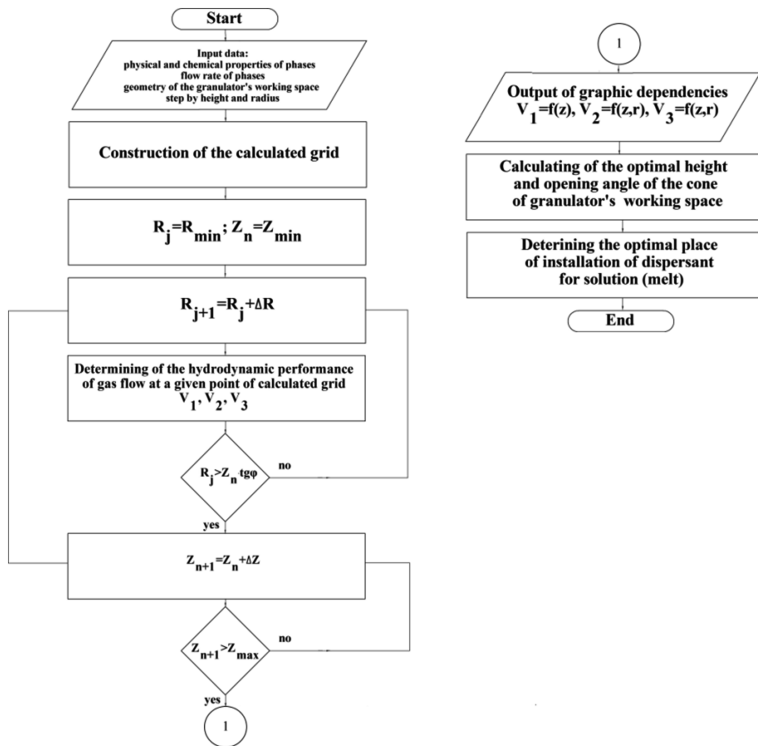
Fig. 7. An algorithm for vortex granulator hydrodynamic calculating.

increasing of cone opening angle (up to 10–13°) zone of reverse vortex has a constant value and is determined within r = (0.15–0.25) R. This situation is observed before h = (0.3–0.4) H. Recirculation zone is located in the inlet of diffuser.

Based on the analysis of hydrodynamic properties of gas flow due to certain variables the rational selection of geometry workspace vortex granulator becomes possible (opening angle α and height z).
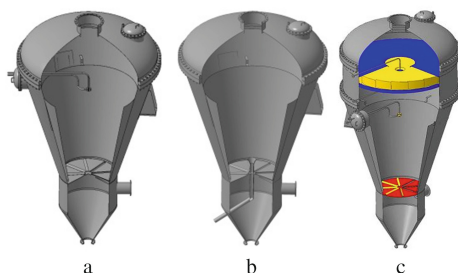

Fig. 8. Vortex granulator designs: a – with spraying of the melt; b – with a previous wetting of granules and simple inner case; c – with separating device for exhaust gases cleaning.

5   Conclusions

Simulation results allowed us to develop an algorithm for vortex granulator hydrodynamic calculating, which is represented on Fig. 7.

Example of granulator design based on hydrodynamic calculation (porous ammonium nitrate production, final product performance 3000 kg/day, commodity fraction – granules 2–3 mm) is shown in Fig. 8.

References

1. Artyukhov, A.E., Sklabinskyi, V.I.: Experimental and industrial implementation of porous ammonium nitrate producing process in vortex granulators. Naukovyi Visnyk Natsionalnoho Hirnychoho Universytetu **6**, 42–48 (2013)
2. Ashcraft, R., Heynderickx, G., Marin, G.: Modeling fast biomass pyrolysis in a gas-solid vortex reactor. Chem. Eng. J. **207–208**, 195–208 (2012)

3. Khalatov, A.: Heat transfer and hydrodynamics in the fields of mass forces. J. Eng. Phys. Thermophys. **83**(4), 794–808 (2010)
4. Kaewklum, R., Kuprianov, V., Douglas, P.: Hydrodynamics of air-sand flow in a conical swirling fluidized bed: A comparative study between tangential and axial air entries. Energy Convers. Manag. **50**, 2999–3006 (2009)
5. Volchkov, E., Dvornikov, N., Lukashov, V., Abdrakhmanov, R.: Investigation of the flow in the vortex chamber with centrifugal fluidizing bed with and without combustion. Thermophys. Aeromech. **20**(6), 663–668 (2013)
6. Shi, D.-P., Luo, Z.H., Guo, A.Y.: Numerical Simulation of the gas – solid flow in fluidized-bed polymerization reactors. Ind. Eng. Chem. Res. **49**(9), 4070–4079 (2010)
7. Pandaba, P., Sukanta, K.D.: Numerical simulation for hydrodynamic analysis and pressure drop prediction in horizontal gas-solid flows. Part. Sci. Technol. **32**(1), 94–103 (2014)
8. Feldmann, F., Hagemann, B., Ganzer, L., Panfilov, M.: Numerical simulation of hydrodynamic and gas mixing processes in underground hydrogen storages. Environ. Earth Sci. **75**, 1165–1172 (2016)
9. Kwauk, M.: Fluidization: Idealized and Bubbleless, with Application. Science Press, Beijing (1992)
10. Gidaspow, D.: Multiphase Flow and Fluidization: Continuum and Kinetic Theory Descriptions with Applications. Academic Press, San Diego (1994)
11. Salman, A., Hounslow, M., Seville, J.: Granulation. Elsevier Science, London (2006)
12. Yang, W.: Handbook of Fluidizaition and fluid-Particle Systems. Marcel Dekker, New York (2003)
13. Artyukhov, A.E., Fursa, A.S., Moskalenko, K.V.: Classification and separation of granules in vortex granulators. Chem. Pet. Eng. **51**(5–6), 311–318 (2015)
14. Crowe, C.: Multiphase Flow Handbook. Taylor & Francis Group, Boca Raton (2006)
15. Dvornikov, N., Belousov, P.: Investigation of a fluidized bed in a vortex chamber. J. Appl. Mech. Tech. Phys. **52**(2), 206–211 (2011)
16. Caiyuan, Y., Tao, Q., Xizhong, W.: Heat and mass transfer in process of fluidized bed spray granulation. Chin. J. Chem. Eng. **16**(6), 836–839 (2004)
17. Sinaiski, E.G.: Hydromechanics: Theory and Fundamentals. Wiley-VCH Verlag GmbH & Co. KGaA, Weinheim (2010)
18. Tenneti, S., Subramaniam, S.: Particle-resolved direct numerical simulation for gas-solid flow model development. Annu. Rev. Fluid Mech. **46**, 199–230 (2014)
19. Yang, J., Wang, Q., Zeng, M., Nakayama, A.: Computational study of forced convective heat transfer in structured packed beds with spherical or ellipsoidal particles. Chem. Eng. Sci. **65**(2), 726–738 (2010)
20. Patankar, S.V.: Numerical Heat Transfer and Fluid Flow. Hemisphere Publishing Corp, Washington (1980)
21. Artyukhov, A., Sklabinskyi, V.: Theoretical analysis of granules movement hydrodynamics in the vortex granulators of ammonium nitrate and carbamide production. Chem. Chem. Technol. **9**(2), 175–180 (2015)

The Carrier Development for Biofilms on the Basis of Technogenic Wastes for Pollutants Treatment in the Environmental Protection Technologies

Yelizaveta Chernysh(✉) and Leonid Plyatsuk

Sumy State University, 2 Rymskogo-Korsakova St., Sumy 40007, Ukraine
e.chernish@ssu.edu.ua

Abstract. The advantages of the environment protection systems operated with the use of cell immobilization were analyzed. This paper focuses on the determination of the formed features of mineral carrier based on the technogenic secondary resource use (phosphogypsum and fly ash) for hydrogen sulfide removal technologies. The results of research show that oxygen diffusion was difficult at a depth of penetration of a bacterial matrix around 1.5–2.5 mm in the phosphogypsum granules of large size (diameter > 5 mm). The main processes of aerobic conversion occurred in the granules from 3 to 5 mm with the oxidation of sulfur compounds, hydrogen sulfide and sulfur oxides, to produce biosulfur. The depth of bacterial matrix penetration increased with diameter increase, because the components of the granules were transformed as a mineral substrate. Various mechanisms of fixing biomass on carriers based on technogenic mineral resource was studied for assessment of biomass productivity out of the carrier layer. The optimal hardening time for the granules stabilization was determined under an internal interlayer of the immobilized biomass conditions and the efficiency of sulfide oxidation was estimated.

Keywords: Environmental protection · Technogenic secondary resource
Phosphogypsum · Immobilization

1 Introduction

The use of support medium for the immobilization of microorganisms is widely known to provide a surface for microbial growth and a shelter that protects the microorganisms from inhibitory compounds.

One of the most promising areas of research is using this technology to reduce environmental pollutions through biodegradation of many harmful compounds. Immobilized microbial systems currently offer various advantages over free systems. The application of immobilization technology to environmental area is in its preliminary stages, but the results seen so far are promising. The immobilized cells will be useful to treat the waste to convert the toxicant into nutrient, biomass and CO_2 via biodegradation through their intermediates. Better biodegradation rate was observed in immobilized cells due to absence of internal and external mass transfer resistance. The

features of the process based on immobilized biomass include enhancing microbial cell stability, allowing the continuous process operation and avoiding the biomass - liquid separation requirement [1].

2   Literature Review

For wastewater and gas purification treatment, support materials need to meet the following criteria: insoluble, non-toxic, nonpolluting, light weight; flexibility in overall shape, high mechanical and chemical stability, high diffusivity, simple immobilization procedure, high biomass retention, minimal attachment of other organisms and preferably low cost price [1–4]. The carriers are classified as inorganic material (zeolite, clay, anthracite, porous glass, activated charcoal, and ceramics) and organic polymers. Inorganic carriers were selected to immobilize microorganisms because they can resist microbial degradation and are thermostable. Granular activated carbon is often used for immobilization of microorganisms. The organic polymeric carriers are more abundant than inorganic carriers and can be natural and synthetic polymeric carriers [5–15]. In this way the search for the new support mediums is an important task nowadays.

In the work [10], a sulfur-oxidizing bacteria, Thiobacillus thioparus was immobilized on Mavicell B support. It was employed to develop a microaerobic, biotrickling filter reactor for the efficient elimination of H_2S from synthetic (bio)gas.

Regarding 5% (v/v) addition of synthetic and biological materials, the maximum cumulative hydrogen production using immobilizing synthetic material of ball-shaped hydrophobic polyethylene (1256.5 ml H_2/l wastewater) was a two-fold increase of cumulative hydrogen production when compared to its production using immobilizing biological material of rope-shaped hydrophilic ramie (609.8 ml H_2/l wastewater) [11].

The research reports [12] on the pilot plant scale study of the impact of 20% to 50% CO_2 on biogas into the growing medium of microalgae which obtained bio-methane purification results as gaseous bio-fuels. Microalgae, Scenedesmus sp., in laboratory experiments using biogas slurry as growing medium and biogas are given periodically generating 21% of CO_2 compared with 24% of control. Arthrospira sp., Chlorella sp., Chlamydomonas sp. and Scenedesmus sp. were reported as a positive synergy with biogas. However, used pure cultures of microalgae even mutant might not be applied to small-scale digester households, especially in rural areas. The H_2S reduction levels being made to minimize corrosion must be solved.

The study [13] focused on the scaffold for cell propagation should mimic, as much as possible, the native extracellular matrix and also illustrated the efficiency of using polyurethane chemistry for covalent immobilization. Studies of immobilization are very useful and demonstrate the efficacy and ease to which the technique is performed, particularly with prepolymers. In contemplating immobilization, one must be prepared to optimize the competing effects to yield an economic advantage.

On the other hand, inventing new ways to recycle and reuse waste is a major task today.

Millions of tons of phosphogypsum is stacked worldwide every year and is progressively considered as an asset rather than an environmental burden. Phosphogypsum is a waste by-product from the processing of phosphate rock by the "wet acid method"

of fertilizer production, which currently accounts for over 90% of phosphoric acid production. World phosphogypsum production is variously estimated to be around 100–280 Mtons per year and the main producers of phosphate rock and phosphate fertilizers are in the USA, China, Russia, Africa and the Middle East. In Ukraine the most common of all kinds of gypsum wastes is phosphogypsum.

This paper focuses on the determination of formed features of mineral carrier based on technogenic secondary resources use (phosphogypsum and fly ash) for hydrogen sulfide removal systems for environmental protection technologies. To achieve the aim, the following tasks were set:

– determination of the specific features of the biofilm growth in the surface of the granulated carrier based on phosphogypsum for environmental protection technologies;
– influence of the diameter of immobilized granules on the sulfide oxidation;
– effect of granules hardening time on sulfide oxidation.

3   Research Methodology

3.1   Experimental Set-up of Aerobic Hydrogen Sulfide Removal

Figure 1 shows the experimental set-up that was used in this work.

Mineral granules previously inoculated biomass sulfideoxidizing microorganisms.

Concentration of H_2S gas in biogas and bacterial population at a regular interval (5, 10, 15 h) of contact time consisted of 30 tests for each interval. The pH was constant at level 5.0–5.5.

3.2   Method for Producing a Granulated Carrier Containing Immobilized Microorganisms

The method includes the microorganism's immobilization in the form of a suspension in a gel forming reagent, using 3–5% solution of sodium alginate with subsequent granulation. In addition, phosphogypsum was added to the gelling agent. The granulation is carried out in a rotating plate granulator with mixing of immobilized microorganisms and mineral powder, which was made on the basis of fly ash from thermal power plant (TPP) for water resistance increase. The initial ratio of components, mass particles [14]: suspension of microorganisms 10–15; 3–5% solution of sodium alginate 3–5; phosphogypsum 15–20; fly ash 7–10.

In addition, the concentration of the microorganism's suspension should be 10^{10}– 10^{11} CFU/g granules.

3.3   Analytical Methods

Study of the gaseous phase was carried out on a laboratory gas chromatograph SelmiChrom-1 (Ukraine). The thermal conductivity detector (katharometer) was used. Argon was chosen as the mobile phase.
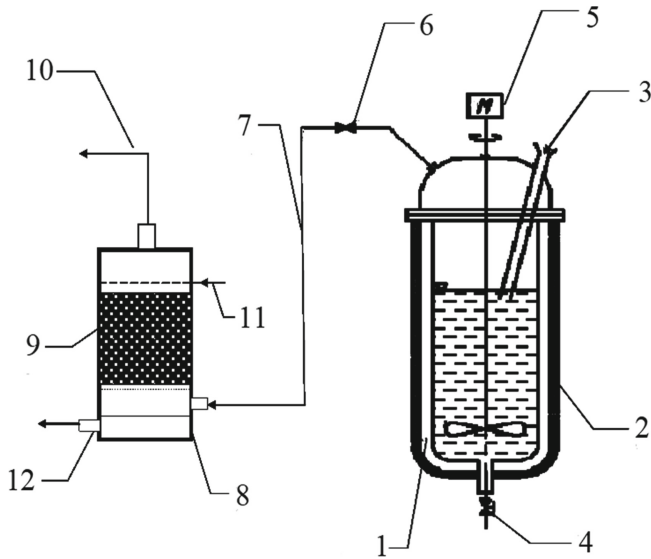
1 – anaerobic bioreactor; 2 – insulation; 3 – opening for sewage sludge loading; 4 – port for sludge removal; 5 – mix device; 6 – control valve; 7 – biogas inflow; 8 – biofilter; 9 – granulated phosphogypsum; 10 – purified biogas outflow; 11 – water supply for irrigation; 12 – removal of biosulfur suspension

Fig. 1. Experimental set-up of aerobic hydrogen sulfide removal from biogas.

The quality analyses of materials were performed on the scanning electron microscope-microanalyzer REMMA-102 (Ukraine). Measurements were performed at five points on each sample. The sensitivity of the measurement was at 1%. Additionally, elemental composition of waste was surveyed by X-ray fluorescence analysis, which made it possible to determine the concentration of elements in the ppm level. Photomicrographs were received and processed using the digital output of image «SEO Scan ICX 285 AK-F IEE-1394» and morphometric program «SEO Image Lab 2.0» and on the scanning electron microscope (SEM) REMMA-102.

pX-150 ionometer (Belarus) was used to analyze pH.

Sieve analysis included the calculation of the number of granules of different size and the mass fraction dimension of the different fractions of the granules.

Measurement of optical density (OD) of cell suspensions was performed by the method of photometric absorption of cultures on the Multiscan analyzer. The optical density, measured at 600 nm, reflects the concentration of cells in the nutrient medium. The absorption spectrum was obtained as a result of automatic measurement with a duration of 100 ms. Determination of the concentration of cells in the medium can be carried out in dishes in a volume of 200 μl (optical path length of 1 mm) or 1000 μl (optical path length 10 mm).

3.4　Microbiological Investigation

Isolation of sulfide oxidizing bacteria is done out of aerobic sewage sludge collected from municipal wastewater treatment plant. The aerobic sludge samples were collected and screened for the removal of solid particles. Then the sludge is kept in aerobic conditions by continuous aeration in order to prevent growth of any anaerobic bacteria for a period of 10 days at the temperature of 35 °C.

Thiobacillus enrichment medium has the following composition NH_4Cl, 1.0 g; K_2HPO_4, 0.6 g; $CaCl_2·2H_2O$, 0.2 g; $FeCl_3·H_2O$, 0.02 g; we tacked such sulfates: $ZnSO_4·7H_2O$, 40 mg; $CaSO_4·2H_2O$, 70 mg; $MnSO_4$, 15 mg; $Na_2B_4O_7$, 10 mg; distilled water, 1000 ml; pH, 5.

4　Results

4.1　Determination of the Specific Features of the Biofilm Growth in the Surface of the Granulated Carrier Based on Phosphogypsum for Environmental Protection Technologies

In accordance with the task of research and the use of phosphogypsum granules, the rationalization of their size should be based on the determination of the penetration depth of the bacterial matrix.

The aerobic groups of sulfur oxidizing bacteria were used for the process of gas streams purification from sulfur compounds. The mineral components of phosphogypsum (calcium, phosphorus, sulfur, potassium, magnesium, etc.) can be effectively used as aerobic and anaerobic microorganisms of various ecological trophic groups. Therefore, it is important to determine the optimal size of the granules and to limit the diameter in accordance with the nature of the thiobacteria development to stimulate their dominance among other types of microorganisms.

In phosphogypsum granules were of a rather large size (diameter > 5 mm) at a depth of penetration of a bacterial matrix around >1.5–2.5 mm, where oxygen diffusion was difficult. Thus, the aerobic respiration was changed on anaerobic direction from the surface to the bottom of the granule. There is a stratification of the oxygen concentrations, nitrates, sulfates and products of their recovery along the profile of granules with biofilm. Accordingly, when implementing the gas purification system in biofilters or purifying the aqueous medium from sulfur compounds in bioscrubbers, it is necessary to consider the dependence of the conversion processes of electrons acceptors in biofilm on the size of the granules. Figure 2 shows that the anaerobic zone of sulfate reduction development, which restores SO_2, SO_4^{2-} to hydrogen sulfide was formed with an increase in the depth of the biofilm penetration in the middle of the granules.

The main processes of conversion occurred in aerobic conditions were observed in granules on average from 3 to 5 mm, with the oxidation of sulfur compounds, hydrogen sulfide and sulfur oxides, to biosulfur production. According to diameter increase of the granules the depth of bacterial matrix penetration increased too as a result of the components transformation of phosphogypsum granules as a mineral substrate. Thus, the penetration depth was around 0.95–1.25 mm under granules
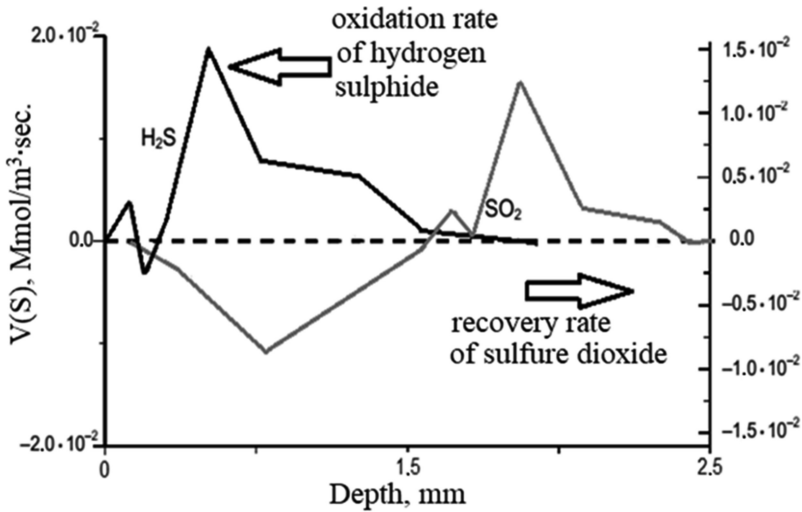
Fig. 2. Profiles of concentration and speed of H_2S oxidation and SO_2 reduction at different depth of the biofilm penetration into phosphogypsum granules.

diameter of 4 mm and radius of 2 mm, 1.00–1.54 mm under the diameter of 5 mm, and 1.56–2.00 mm under 6 mm diameter.

4.2 Influence of the Diameter of Immobilized Granules on the Sulfide Oxidation

Figure 3 shows the effect of the diameter on the sulfide oxidation. The results showed that the maximum sulfide oxidation of 98.7% can be achieved with the diameter of granules of carrier no more than 4 mm. Granules on average of 2–4 mm showed better oxidation of sulfides compared to large sized with diameter of 6 mm and more. Sulfide oxidation with granules of 1, 2, 4 and 6 mm in diameter was 91%, 96%, 92% and 81%, respectively. Figure 3 shows that as the size of the granules increases, leakage of immobilized biomass increases too. For granules with a large size (6 mm), the leakage of cells was greater than for all subsequent granules with a diameter of 2–4 mm. Based on the results of the research (Fig. 3), the following dependencies approximated by the regression equations were found:

– efficiency of sulfide oxidation (M_S) from the granules diameter from technogenic waste ($d_{\phi 2}$)

$$M_S = -0,9286d_{\phi 2}^2 + 4,6571d_{\phi 2} + 92,4; \tag{1}$$

($R^2 = 0,9872$);

– an increase in the leakage of bacterial cells (M_{OD}) from the granules diameter from technogenic waste ($d_{\phi 2}$)
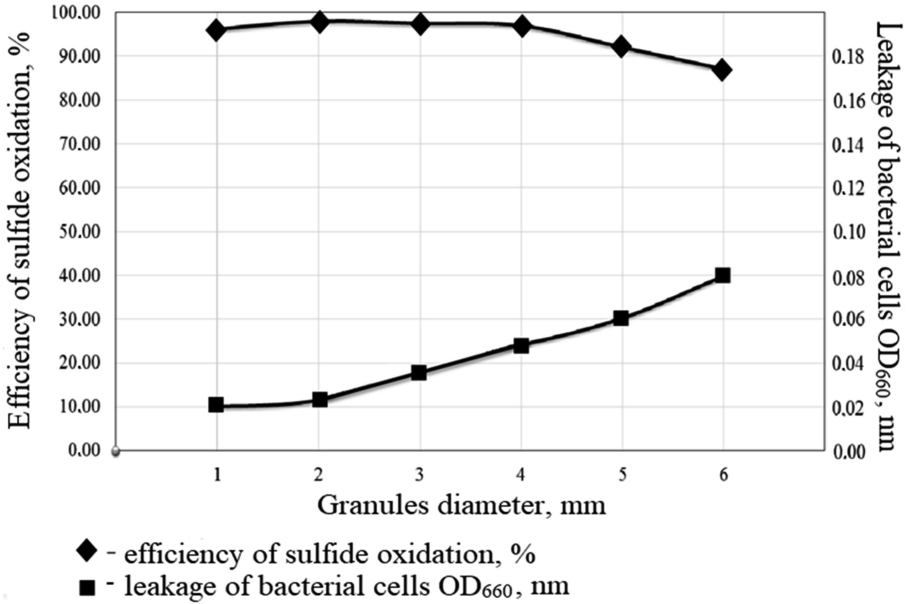
Fig. 3. Effect of granules diameter on sulfide oxidation.
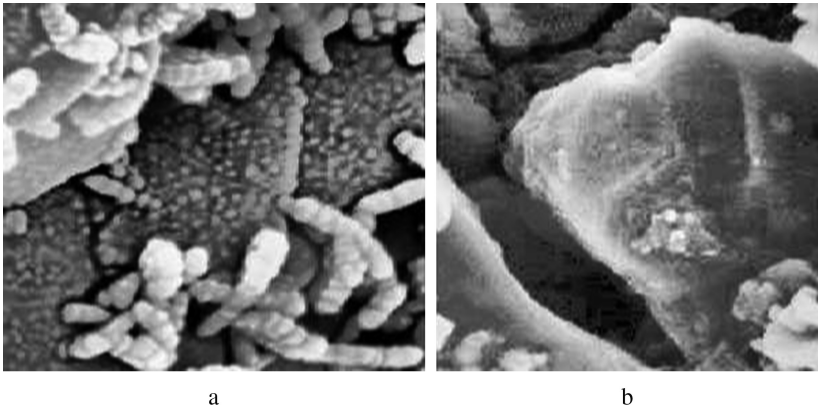

a   b

Fig. 4. SEM of immobilized granules for detecting cell leakage: a - clusters of cells are visible in the interlayer between phosphogypsum and alginine of the carrier; b - leakage of bacterial cells from the carrier layer.

$$M_{OD} = 0,5018d_{\Phi2}^2 + 2,4732d_{\Phi2} + 6,55; \qquad (2)$$

$(R^2 = 0,9831)$.

SEM was used for studying the immobilized surface of granules (Fig. 4).

In this case, the immobilized granules were cut through the cross-section and fixed with 2% glutaraldehyde and dehydrated in gradient ethanol (10–100%). The sample was dried and observed with an electron microscope (SEM).

It must be noted that during the sulfide oxidation, a loss of the cells from the granules occurred, which was due to their removal from the system together with metabolites. Samples of cell loss from granules based on $CaSO_4 \cdot 2H_2O$ (phosphogypsum) with alginate matrices didn't exceed 0.08 OD_{660} and accordingly show that the rationalized conditions were suitable for sulfide oxidation process during long-term using.

Experimental study compared results of two kinds of support medium such as lavsan fiber and GAC was performed in [15]. After Thiobacillus biomass immobilized on lavsan fiber bacterial growth reached maximum ($3.5 \cdot 10^{10}$ CFU/g) with maximum efficiency of H_2S oxidation 89.78% at initial culture pH 5.0 at optimum contact time of 10 h. Immobilization of microorganisms on GAC has shown that the total immobilized biomass at the end of batches was of $1.6 \cdot 10^9$ CFU/g. Biochemical reactions were aggressive (pH = 4.5–5.0) for GAC and its structure was quickly destroyed during biofilter operation (after 30 days of exploitation).

The usage of a new type of carrier such as phosphogypsum granules proves to be more effective than that of GAC and lavsan fiber in terms of bio-desulfurization system performance and immobilized biomass viability. In addition, phosphogypsum granules are the resource of necessary nutrients and mineral elements for bacteria growth (Ca, Mn, Fe, Cu, Zn etc.).

Note that the indicators of the dependence of the sulfide oxidation effectiveness on the granules size with immobilized microorganisms differ from phosphogypsum granules studied in [16] with sorption immobilization on the surface. Thus, under the internal immobilization it's rational to choose a granules diameter in the range from 3 to 4 mm and with sorption surface immobilization from 4 to 5 mm. This is due to various mechanisms of fixing biomass on carriers of phosphogypsum and changing the value of productive biomass out of the carrier layer.

The vital activity of chemolithoautotrophic microorganisms, oxidizing ammonia and sulfur compounds leads to the dissolution of carbonates. Therefore, the negative effect of carbonate film formation can be excluded. The dissolution of phosphogypsum components was provoked by organic substances of microbiological origin. Such as exopolysaccharides (the main component of bacterial biofilms), siderophores and other chelating compounds formed in the process of metabolic activity.

4.3   Effect of Granules Hardening Time on Sulfide Oxidation

The granules of immobilized thiobacteria prepared on the basis of dihydrate phosphogypsum were tested for 1, 2, 4, 6 and 8 h to stabilize and assess the increase in sulfide oxidation (Fig. 5).

After curing for different periods, the granules were transferred to the medium and incubated.

Based on the results of the research (Fig. 5), the following dependencies approximated by the regression equations were found:
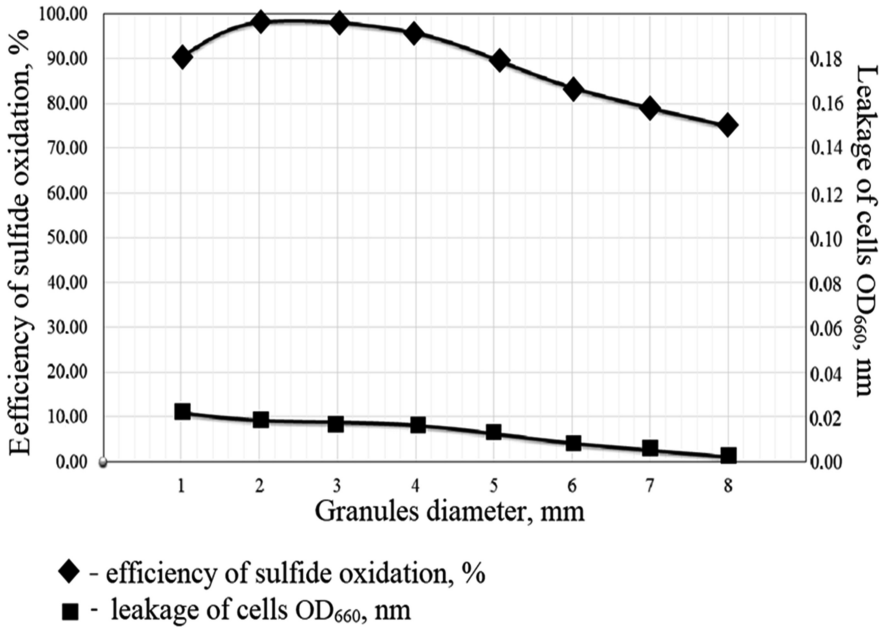
Fig. 5. Effect of granules hardening time on the sulfide oxidation.

– efficiency of sulfide oxidation (M_S) from the hardening time (τ_3)

$$M_S = 1,125\tau_3^3 - 16,507\tau_3^2 + 69,682\tau_3 + 7,98; \qquad (3)$$

($R^2 = 0,9933$)

– an increase in the leakage of bacterial cells (M_{OD}) from the hardening time (τ_3)

$$M_{OD} = -0,4071\tau_3^2 + 0,7671\tau_3 + 11,02; \qquad (4)$$

($R^2 = 0,9882$)

Thus, the hardening time was rational in the range of 2 to 4 h. At the same time, in 2 h, a high stability was achieved with respect to loss of cells during oxidation with a low content of sulfur oxides. The granules obtained with a 2-h curing time resulted in a maximum oxidation of the sulfide by 98% than the granules obtained with other curing times. Leakage of cells decreased with an increase of the curing time. The hardening time of 1 h or less resulted in a low stability of the granules, which led to their early disintegration. With an increase of the curing time of more than 4 h, an increase in the drying zone, which leads to a slow development of the bacterial mass and the oxidation efficiency of the sulfides decreases. Although the leakage of bacterial cells was minimal (Fig. 5). Thus, for granules obtained with curing times of 1, 2, 4, 6 and 8 h the sulfide oxidation was 96.0%, 98.7%, 95.7%, 83.4% and 75.0% respectively for purification systems of biogas with a hydrogen sulfide concentration of 850 ppm.

5 Conclusions

The biochemical features of carrier based on technogenic mineral wastes was studied for hydrogen sulfide removal systems for environmental protection technologies. In the granules on average from 3 to 5 mm, the main processes of conversion occurred in aerobic conditions, with the oxidation of sulfur compounds, such as hydrogen sulfide and sulfur oxides, to produce biosulfur. The depth of bacterial matrix penetration increased with the granules diameter increase, as a result of the components transformation of phosphogypsum granules as a mineral substrate. Thus, the penetration depth was around 0,95–1,25 mm under granules diameter of 4 mm and radius of 2 mm, 1,00–1,54 mm under the diameter of 5 mm, and 1,56–2,00 mm under 6 mm diameter. Noted that under the internal immobilization it's rational to choose the granules diameter in the range from 3 to 4 mm and with sorption surface immobilization on average from 4 to 5 mm. This is due to various mechanisms of fixing biomass on carriers and the productive biomass changing out of the carrier layer. The optimal hardening time of 2 h for forming the stable granules with an internal interlayer of immobilized biomass and the efficiency of sulfide oxidation were determined.

References

1. Cláudia Silveira, S.M., Claudia, M.M., Cidrão Guedes Fiúza, L.M., Tédde Santaella, S.: Immobilization of microbial cells: a promising tool for treatment of toxic pollutants in industrial wastewater. Afr. J. Biotech. **12**(28), 4412–4418 (2013)
2. Kourkoutas, Y., Bekatorou, A., Banat, I.M., Marchant, R., Koutinas, A.A.: Immobilization technologies and support materials suitable in alcohol beverages production: a review. Food Microbiol. **21**(4), 377–397 (2004)
3. Manju, N.J., Deepesh, V., Achuthan, C., Rosamma, Ph., Bright Singh, I.S.: Immobilization of nitrifying bacterial consortia on wood particles for bioaugmenting nitrification in shrimp culture systems. Aquaculture **294**, 65–75 (2009)
4. Zacheus, O.M., Iivanainen, E.K., Nissinen, T.K., Lehtola, M.J., Martikainen, P.J.: Bacterial biofilm formation on polyvinyl chloride, polyethylene and stainless steel exposed to ozonated water. Water Res. **34**, 63–70 (2000)
5. Górecka, E., Jastrzębska, M.: Immobilization techniques and biopolymer carriers. Biotechnol. Food Sci. **75**, 65–86 (2011)
6. Verma, M., Brar, S.K., Blais, J.F., Tyagi, R.D., Surampalli, R.Y.: Aerobic biofiltration processes-advances in wastewater treatment. Pract. Period. Hazard Toxic Radioact. Waste Manage. **10**, 264–276 (2006)
7. Andersson, S., Nilsson, M., Dalhammar, G., Kuttuva Rajarao, G.: Assessment of carrier materials for biofilm formation and denitrification. Vatten **64**, 201–207 (2008)
8. Andersson, S., Dalhammar, G., Land, C.J., Kuttuva Rajarao, G.: Characterization of extracellular polymeric substances from denitrifying organism *Comamonas denitrificans*. Appl. Microbiol. Biotechnol. **82**(3), 535–543 (2009)
9. Alejandro Dinamarcaa, M., Rojasa, A., Baezab, P., Espinozaa, G., Ibacache-Quirogaa, C., Ojeda, J.: Optimizing the biodesulfurization of gas oil by adding surfactants to immobilized cell systems. Fuel **116**, 237–241 (2014)

10. Tóth, G., Nemestóthy, N., Bélafi-Bakó, K., Vozik, D., Bakonyi, P.: Degradation of hydrogen sulfide by immobilized Thiobacillus thioparus in continuous biotrickling reactor fed with synthetic gas mixture. Int. Biodeterior. Biodegrad **105**, 185–191 (2015)
11. Wongthanate, J., Polprasert, Ch.: Immobilized biofilm in thermophilic biohydrogen production using. Synth. Versus Biol. Mater. **58**(1), 124–130 (2015)
12. Setyobudib, R.H., Wahono, S.K., Nindita, A., Adinurani, P.G., Nugroho, Y.A., Sasmito, A., Liwang, T.: Biological purification system: integrated biogas from small anaerobic digestion and natural microalgae. Proc. Chem. **14**, 387–393 (2015)
13. Thomson, T.: Polyurethane Immobilization of Cells and Biomolecules: Medical and Environmental Applications. Wiley, London (2018)
14. Chernysh, Y.Y., Plyatsuk, L.D.: Method for Producing a Granulated Carrier Containing Immobilized Microorganisms. Patent of Ukraine No. 114664 (2017)
15. Ye, C., Plyatsuk, L.: Opportunity of biochemical process for phosphogypsum utilization. J. Solid Waste Technol. Manag. **42**(2), 108–115 (2016)
16. Plyatsuk, L.D., Chernysh, Y.Y.: The removal of hydrogen sulfide in the biodesulfurization system using granulated phosphogypsum. Eurasian Chem. Technol. J. **18**(1), 47–54 (2016)

The Use of Waveguides with Internal Dissectors in the Process of Regeneration of Industrial Adsorbents by Means of the Energy of Ultrahigh-Frequency Radiation

Sergey Dobrotvorskiy [ID], Ludmila Dobrovolska [ID],
Borys Aleksenko [(✉)] [ID], and Yevheniia Basova [ID]

National Technical University «Kharkiv Polytechnic Institute»,
2 Kyrpychova St., Kharkiv 61002, Ukraine
`ttm777@ukr.net, e.v.basova.khpi@gmail.com`

Abstract. Waveguide structures that can be used in the adsorption columns of compressed air dehumidifiers for the purpose of molecular sieve regeneration by using microwave energy in the process of desorption are considered. Mathematical models of the electromagnetic field in waveguides of various designs are constructed. A study was carried out to select the best design of the waveguide irradiating the volume of the adsorbent in the cavity of the adsorption tower of the adsorption desiccant. In general, the conducted studies have shown the possibility and expediency of using X-shaped waveguides with excitation from an exciting waveguide or a coaxial cable in the construction of adsorption columns with microwave regeneration of the adsorbent, as well as the applicability of an internal dissector installed inside the waveguide to create a traveling wave in the column cavity with different the intensity of the microwave radiation of the electric field in order to increase the uniformity of the influence of microwave energy on the volume of the adsorbent. Theoretically, the possibility of using internal dissectors has been confirmed in order to increase the uniformity of the distribution of microwave energy in the cavity of the adsorption column of the desiccant. The presented theoretical experiment opens the prospect for further practical studies of the effect of microwave radiation on the process of molecular sieve desorption under conditions of the adsorption column operation as part of the adsorption dryer, and shows the creation of an effective innovative sample of industrial equipment.

Keywords: Heating · Microwave · Adsorption · Desiccant · Silica gel
Computer modeling

1 Introduction

Mathematical modeling of physical processes is an actual and rapidly developing field of scientific knowledge. Modern software products can be used to obtain S-parameters [1], create SPICE (Simulation Program with Integrated Circuit Emphasis) models and

three-dimensional modeling of the electromagnetic field by the finite element method, which greatly facilitates and accelerates the development of new equipment, which uses microwave energy (Microwave radiation). The article consideres the problem of using microwave energy for the regeneration of an adsorbent in the cavity of an adsorption column [2–4].

Modern trends in the development of technological processes of heat treatment are aimed at using the energy of microwave radiation as a source of heat. The use of microwave radiation in the process of heat treatment of materials makes it possible to improve the technical characteristics of the processed materials due to the volume and uniform nature of heating, and also to raise the indicators of the technological processes themselves, characterized by ecological purity, absence of thermal inertia and high efficiency.

2   Literature Review

The main task of the developers [5] is to improve the efficiency of the microwave heater by increasing the uniformity of the distribution of microwave energy inside the heating chamber, increasing the efficiency and stabilizing the heat treatment of the processed materials. The equipment for microwave drying of dielectric materials [6] is known as one in which the regulation of the power of the action of the energy of microwave radiation is carried out by alternately removing or approximating the processed material to the zone of the highest radiation intensity of the microwave energy; however, a significant drawback of this design is the small volume of the dried product in the chamber and the technical complexity of implementing the technology in the adsorption tower of the desiccant. In other designs [7] microwave generators with a multiple number of transmitting antennas are connected by outputs to the input of a transmitting antenna, with the antennas arranged to rotate their electric axes on both sides relative to the normal to the irradiated material surface. Similar designs with the number of radiators multiples of the number of microwave generators are characterized by increased energy costs, a complex process of uniform distribution of electromagnetic radiation in the processed material and low operational reliability. Attempts to realize the technical task to improve the uniformity of energy distribution by the volume of the chamber due to the movement of radiating antennas in a heat-insulated electro-hermetic chamber lead to increasing costs of hardware, reducing reliability and reduce the occupancy of the volume of the drying chamber.

Irradiation of the dried volume of the adsorbent on only one side (from above) [8] causes a decrease in the transparency of the upper layers for the electromagnetic field, while the top-layed adsorbent heats to the overheats temperature with uneven drying of the lower layers, which leads to loss of adsorbent useful properties and longer drying times.

In this article we consider the problem of creating an adsorption column (Fig. 1), which provides drying of dielectric materials (KCMG adsorbent) using microwave energy. The design of the adsorption column should provide for the intensification of drying using the energy of microwave radiation due to redistribution of electromagnetic radiation in the chamber in the entire volume of the dried material without its local overheating and with less hardware costs.
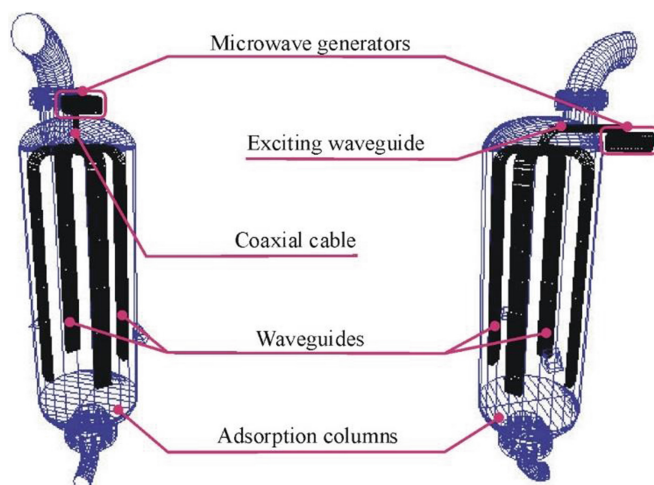
Fig. 1. Adsorption columns with microwave generators and mounted waveguide systems.

3   Research Methodology

Microwave energy reaches different coordinates of space in different ways. The electric field strength in a given volume region is the vector sum of the fields formed by the waves of all directions, and, in the process of addition, the spatial orientation of the field must be also taken into account along with the numerical value of the field. Thus, the aggregated field may turn out to be smaller than each of the additions. In order to achieve uniformity of the field, it is necessary to divide in time the waves, which is propagated in different directions. Also, a certain leveling of the heating temperature in the column volume is facilitated by the appearance in the chamber of hybrid modes, characterized by the presence of magnetic and electric field components in three coordinates.

It is possible to improve the uniformity of heating if the available modes of oscillation or some of them are switched in turn. Adding or, conversely, the removal of any mode leads to a change in the overall structure of the electric field. Areas with the maximum and minimum amplitude are displaced in space and can change places. As a result, each section of the column volume is alternately subjected to the influence of fields of different configuration and intensity. The effect of microwave energy can be fairly uniform with a large number of combinations [9].

The present research is devoted to the study of the effect on propagation of microwave energy in the adsorbent volume of the internal dissector and the configuration of the exciting waveguide channel. The principle of operation of an internal dissector consists in disturbing the electro-magnetic field structure. As a result, some of the existing modes can be suppressed. Under the action of the dissector the excitation conditions for different modes vary, depending on the relative turn of the dissector. Therefore, the spectrum of electromagnetic oscillations, and, accordingly, the structure of the field is constantly changing. Also, the effect of the dissector lies in its effect on

the resonant frequencies, but this effect is reduced when an internally dissector mounted inside the waveguide.

Calculation of the parameters of the waveguide and the power allocated at the ports of the waveguide is performed in the software Ansys HFSS™. The modelling method used by the program to calculate the total three-dimensional electromagnetic field inside the structure is based on the finite element method. The pattern of the traveling wave field inside the waveguide can be determined by solving the Maxwell equation [10].

Different types of microwave devices can be described with the help of falling and reflected waves that propagate. The relationship between these waves is described by the scattering wave matrix or the matrix of S-parameters, the elements of which describe the physical parameters of the scattering. In microwave technology, the scattering matrix is used to describe microwave devices and the linear amplitude-dependent complex amplitudes of the incident and reflected waves.

It is very important that an HFSS™ simulation encompasses a volume within which electric and magnetic fields exist. These volumes generally include conducting materials as well as the dielectric materials, including air, that surround the conductors [11–14].

A generalized S-matrix describes what fraction of power associated with a given field excitation is transmitted or reflected at each port.

The S-matrix for a three-port structure is as follows:

$$
\begin{bmatrix} b_1 \\ b_2 \\ b_3 \end{bmatrix} = \begin{bmatrix} b_{11} & b_{12} & b_{13} \\ b_{21} & b_{22} & b_{23} \\ b_{31} & b_{32} & b_{33} \end{bmatrix} \cdot \begin{bmatrix} a_1 \\ a_2 \\ a_3 \end{bmatrix}, \tag{11}
$$

where:

- All quantities are complex numbers.
- The magnitudes of a and b are normalized to a field carrying one watt of power.
- $|a_i|^2$ represents the excitation power at port i.
- $|b_i|^2$ represents the power of the transmitted or reflected field at port i.
- The full field pattern at a port is the sum of the port's excitation field and all reflected/transmitted fields.
- The phase of a_i and b_i represents the phase of the incident and reflected/transmitted field at $t = 0$.
- $<a_i$ represents the phase angle of the excitation field on port i at $t = 0$. (By default, it is zero for lossy port modes and lossless propagating modes. For lossless cut-off modes, it is 90.)
- $<b_i$ represents the phase angle of the reflected or transmitted field with respect to the excitation field.
- S_{ij} is the S-parameter describing how much of the excitation field at port j is reflected back or transmitted to port i. For example, S_{31} is used to compute the amount of power from the port 1 excitation field that is transmitted to port 3. The phase of S_{31} specifies the phase shift that occurs as the field travels from port 1 to port 3 [15, 16].

3.1   Model Definition

In the present study 3D calculation of models of rectangular waveguides, operating on the main type of wave H10, is performed at a fundamental frequency of 2.45 GHz with different waveguide drive modes. The radiating antennas are made in the form of output channels of H-flat tees.

Several waveguide constructions are considered:

1. 4-arm X-shaped rectangular H10 waveguide (Fig. 2) with excitation from the exciting waveguide;
2. a similar design, excited by a coaxial cable (Fig. 3);
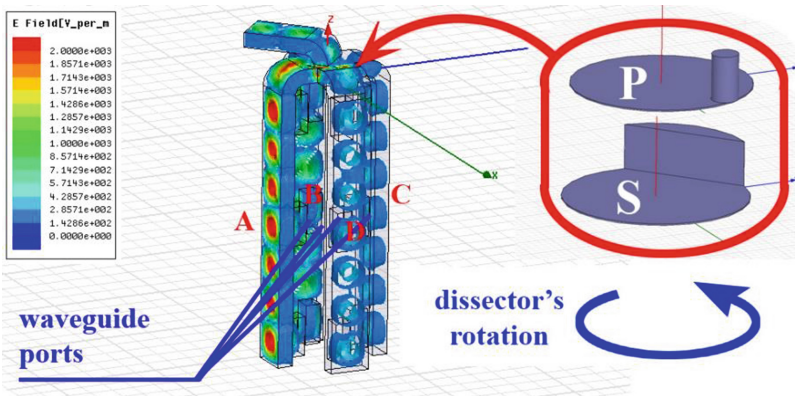
Fig. 2. X-shaped rectangular waveguide with excitation from an exciting waveguide. Letters "P" and "S" denotes the Pin type dissector and the Segment type dissector, respectively.
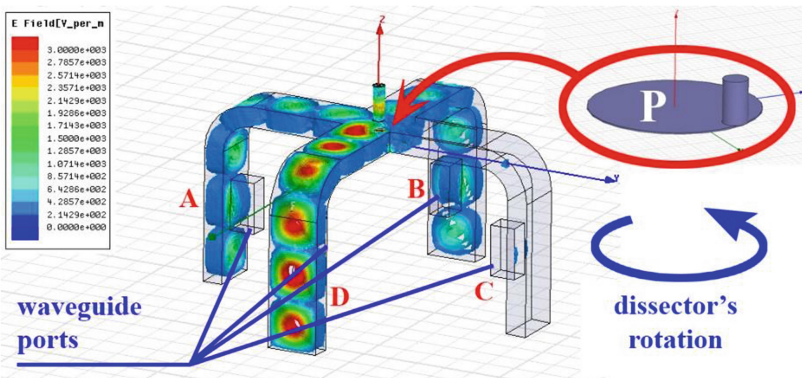
Fig. 3. X-shaped rectangular waveguide with excitation from a coaxial cable. The letter "P" denotes the Pin type dissector.

Initially, the geometry of the waveguide models under investigation is optimized using the Optimetrics module in order to obtain the maximum level of electromagnetic field strength in the waveguide. For this purpose, the parametrized geometry of each model is calculated in the selected range of values of optimization variables. The objective function is compiled on the basis of the value of the electromagnetic field for each model change in the investigated range. Optimization is performed by comparing the results of calculating various variants of the model with choosing the best values of optimization variables.

The linear dimensions of waveguide models optimized using the Optimetrics module are given in the table (Table 1).

Table 1. Linear dimensions of waveguide models.

Parameter	Dimension	Value
X-shaped rectangular waveguide with excitation from an exciting waveguide		
Waveguide height	mm	34
Waveguide width	mm	88
Length of the exciting waveguide	mm	187
Rotation of the exciting waveguide (Fig. 2) along the axes		
X	deg	90
Z	deg	45
Quantity of arms of the waveguide	n	4
The angle of intersection of the arms of the waveguide	deg	90
Arms Length	mm	743
X-shaped rectangular waveguide with excitation from a coaxial cable		
Waveguide Height	mm	35
Waveguide Width	mm	88
Quantity of arms of the waveguide	n	4
The angle of intersection of the arms of the waveguide	deg	90
Arms Length	mm	547

As shown above, obtaining the maximum level of electromagnetic field strength in the waveguide is not a sufficient condition for achieving maximum efficiency of the microwave heater. The most important task of stabilizing the heat treatment regime is to increase the uniformity of the distribution of microwave energy inside the heating chamber, which is facilitated by a change in the overall structure of the electric field.

4   Results

The optimized waveguide models (Figs. 2 and 3) serve as a basis for investigating the effect of the internally dissector, placed in the waveguide, with a step-by-step simulation of the power distribution between the waveguide ports, depending on the position of the dissector.

The Figures show the distribution of the electromagnetic field strength in the investigated waveguide models using dissectors of various designs (Figs. 4, 6 and 8).

It has been established that when a segment-type dissector is excited in an X-shaped waveguide with excitation from the exciting waveguide (Fig. 4), a significant change in the overall structure of the electric field is observed (Fig. 5).
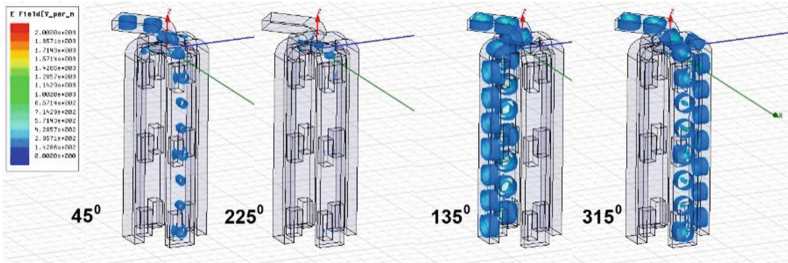

Fig. 4. The pattern of the electromagnetic field in the arms of an X-shaped waveguide with excitation from a coaxial cable when the segmental dissector rotates to different positions with respect to the axis of the exciting waveguide.
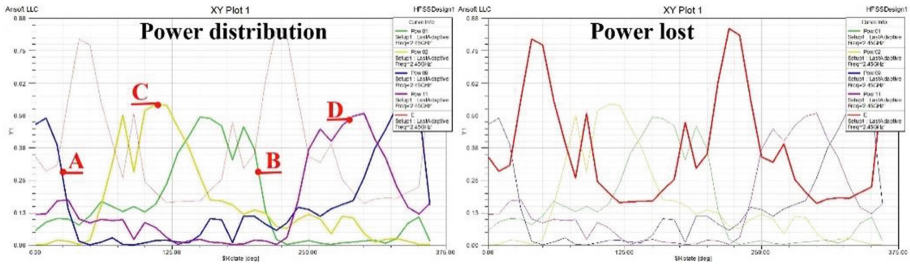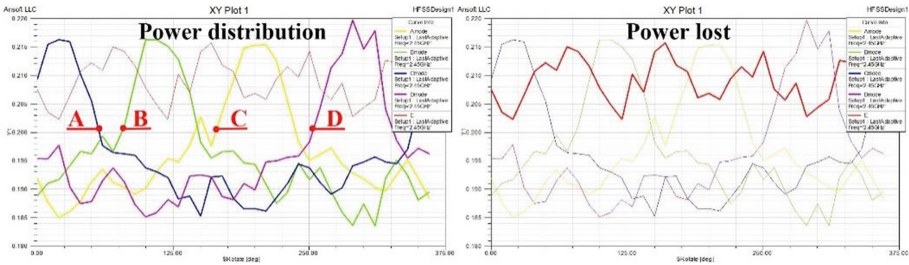

Fig. 5. The graph of power distribution in the ports (A, B, C, D) and power loss in the X-shaped waveguide with excitation from the exciting waveguide during the rotation of the segmental dissector.
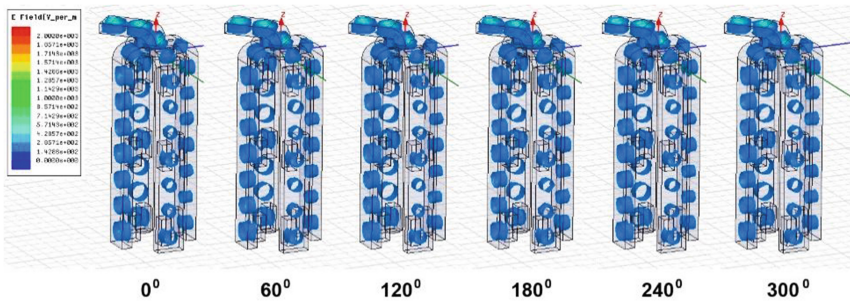
Fig. 6. The pattern of the electromagnetic field in the arms of the X-shaped waveguide with excitation from the exciting waveguide, depending on the angle of rotation of the pin-type dissector.

Pictures of the electromagnetic field (Fig. 4) correlates with the power distribution graphs from the ports of each of the four arms of the waveguide (Fig. 5). On the power loss graph (Fig. 5 Power lost) it is clearly seen that when the dissector rotates to positions 45° and 255° close to the axis parallel to the axis of the exciting waveguide (see Appendix 1. Linear dimensions of waveguide models: waveguide along the Z axis.) the power losses in the waveguide reach a maximum. In cases of perpendicular positioning of the chord of the segment of the dissector (rotation by 100°… 170° and 280°… 350°), the energy is distributed relatively evenly over symmetrical shoulders (Fig. 5 Power lost).

The use of a pin-type dissector in the X-shaped waveguide (Fig. 6) causes less pronounced changes in the microwave intensity (Fig. 7 Power distribution) and a more even cyclic redistribution of power in the ports.

Fig. 7. The graph of power distribution in the ports (A, B, C, D) and power loss in the X-shaped waveguide with excitation from the exciting waveguide during the rotation of the pin dissector.

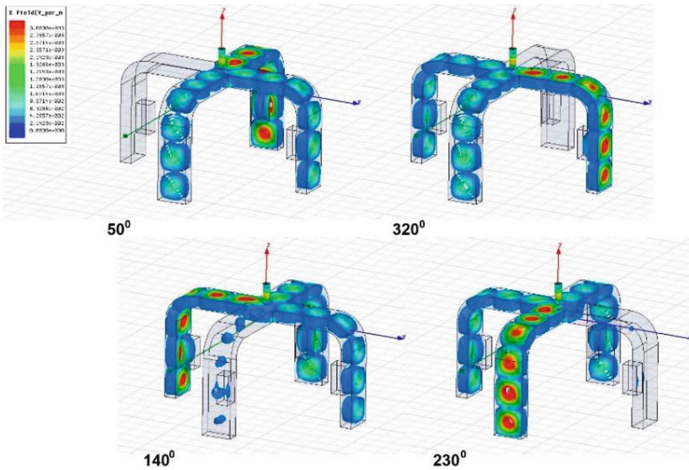However, the power losses in the waveguide are large compared to the transmitted power (Fig. 7).

Fig. 8. The pattern of the electromagnetic field in the arms of the X-shaped waveguide with excitation from the coaxial cable, depending on the angle of rotation of the pin-type dissector.

Model X-shaped waveguide with a pin-type dissector (Fig. 8). The waveguide is excited by a coaxial cable.

In this case, the most uniform cyclic redistribution of energy in the arms of the waveguide is observed (Fig. 9 Power distribution) with relatively small power losses (Fig. 9 Power lost).
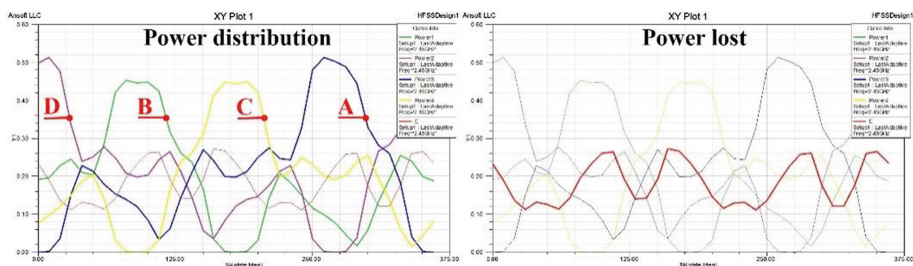

Fig. 9. The graph of power distribution in the ports (A, B, C, D) and power loss in the X-shaped waveguide with excitation from the coaxial cable during the rotation of the pin dissector.

5   Conclusions

In general, the conducted studies have shown the possibility and expediency of using X-shaped waveguides with excitation from an exciting waveguide or a coaxial cable in the construction of adsorption columns with microwave regeneration of the adsorbent, as well as the applicability of an internal dissector, which is installed inside the waveguide, to create a traveling wave in the column cavity with different the intensity of the microwave radiation of the electric field in order to increase the uniformity of the influence of microwave energy on the volume of the adsorbent.

However, it should be taken into account that some amount of electromagnetic energy emitted by the magnetron, fails to penetrate into the chamber with the adsorbent and is not used in the desorption process (Fig. 5, and also Figs. 7 and 9), but returns back to the magnetron, leading to overheating of this node and its failure. Therefore, when building adsorption dryers regenerating the adsorbent using microwave energy, it's necessary to give increased attention to the issue of choosing the type and con-figuration of the waveguide and dissector. Also the experiment shows, that the use of an X-shaped waveguide in the excitation of a coaxial cable in conjunction with an internal pin dissector should receive preference.

Performed theoretical experiment opens the prospect for further practical studies of the effect of microwave radiation on the process of molecular sieve desorption under conditions of the adsorption column operation as part of the adsorption dryer, and the creation of an effective innovative sample of industrial equipment.

References

1. Sophocles, J.O.: Electromagnetic Waves and Antennas. Rutgers University, Newark (2016)
2. Jones, S.: Comparing Microwave to Conventional Heating and Drying Systems. Features Advantages Economics (2012)
3. Gao, F.: Comparison of Microwave Drying and Conventional Drying of Coal. Science Queen's University, Kingston (2010)
4. Tanaka, K., Asakuma, Y., Saptoro, A., Phan C.: Surface tension profiles of nanofluid containing surfactant during microwave irradiation. In: 29th Symposium of Malaysian Chemical Engineers (SOMChE) 2016, vol. 206, pp. 101–105. Miri, Malaysia (2017)
5. Gareev, F.H.: Pat. 2199064 RF. Installation for drying dielectric materials with microwave power (2003)
6. Monolakov, V.A., Yudin, V.V.: Method of drying lumber. Patent No. 2113666, Russian Federation (1998)
7. Valeev, G.G.: Drying plant. Patent No. 2115073, Russian Federation (1998)
8. Vergasov, A.A.: Universal super high frequency microwave dryer (options). Patent No. 2111631, Russian Federation (1998)
9. Dobrotvorskiy, S.S., Dobrovolska, L.G., Aleksenko, B.A.: Computer simulation of the process of re-generating the adsorbent using microwave radiation in compressed air dryers. In: Hamrol, A., Ciszak, O., Legutko, S., Jurczyk, M. (eds.) Advances in Manufacturing, pp. 511–519. Springer, Berlin (2018)
10. Berezin, A.V., Markov, M.B., Plyushchenkov, B.D.: Locally One-Dimensional Finite-Difference Scheme for the Electrodynamic Problems with Given Wavefront. Russian Academy of Science, Moscow (2005)
11. Bankov, S.E., Kurushin, A.A., Razevig, V.D.: Analysis and Optimization of Three-Dimensional Microwave Structures Using HFSS™. Solon-Press, Moscow (2004). (in Russian)
12. ECE-329 Fields and Waves I. 21: Monochromatic waves and phasor notation. In: Phasor form of Maxwell's Equations and Damped Waves in Conducting Media: Lecture Notes. ECE ILLINOIS Department of Electrical and Computer Engineering. University of Illinous, Urbana (2013)
13. Balanis, K.A.: Antenna Theory: Analysis and Design, vol. 2. Wiley, London (1997)
14. Solovyanova, I.P., Naymushin, M.P.: Theory of Wave Processes. Electromagnetic Waves: A Training Manual. GOU VPO UGTU, Ekaterinburg (2005). (in Russian)
15. An Introduction to HFSS™: Fundamental Principles, Concepts, and Use. Ansoft, LLC., Pittsburgh (2009)
16. HFSS™: High Frequency Structure Simulation. Manuals. Ansoft, Pittsburgh (2004)

Obtaining of Multilayer Granules in a Vortex Gas Flow: Automated Complex for Technological Calculation

Andrii Ivaniia and Artem Artyukhov[(✉)]

Sumy State University, 2 Rymskogo-Korsakova St., Sumy 40007, Ukraine
{a.ivaniya, a.artyukhov}@pohnp.sumdu.edu.ua

Abstract. The article describes theoretical bases of the process of obtaining multilayer granules and mathematic model for software realization. The program Multilayer Granules® that carries out technological calculation of the solution for the filming process of the granule surface, is represented in the article. The optimal construction of the vortex granulator is achieved, based on technological calculation results of the granulating process and hydrodynamic calculations, using the computer modeling (based on the author's model for calculating the hydrodynamic conditions of gas flow and granules movement, classification and separation processes of granules in a vortex granulator, kinetics of granules heating and removing moisture from the granules). The calculation results become the base for vortex granulators engineering calculation methodology to obtain the multilayer granules. The work shows industrial application of the investigated software products – production of the porous ammonium nitrate (PAN). A porous multilayer granules sample, obtained in the vortex granulator, is demonstrated in the article. Multilayer Granules® allows conducting optimization of vortex granulator calculation according to the criteria of minimum required residence time of granules in device workspace.

Keywords: Software · Modeling · Vortex granulator · Multilayer granules
Optimization

1 Introduction

Currently, in order to obtain multilayer granules, one uses several ways [1–4]:

1. Ways, related to the process, when granule is covered with a solid film of another substance's solution (fusion), with further crystallization:

– Obtaining of multilayer granules in devices, which look like the circulatory sloping drum, with atomizers fixed inside for solution (fusion) spraying. Initial granules are moving from the entry side through distributor. The drum body is heated, and it provides the drying and crystallization process.
– Ways, when an initial granule is moving through one or several solid films of other substances, with further drying and crystallization.

2. Producing in devices with fluidized bed. This method consists in the process, when solution (fusion) of one substance is being sprayed with simultaneous process of crystallization on another substance's granule surface, which is in the fluidized state.

The process of obtaining multilayer granules in the fluidized bed is distinguished by high efficiency and enables to receive wide assortment of fertilizers with different balance of nutrients, to reduce hygroscopity of granules and to improve their quality [5, 6]. It is also possible to obtain granules with developed porous structure of the surface and near-surface layers [7].

2 Literature Review

Although there is high efficiency of phases contact in the three-phase flow "gas-liquid-solid" in devices with classical fluidized bed, it is difficult to provide stability of their work in the load ranged by phases [8–10]. In order to solve this problem, one has to use the technology of directed swirling gas flow movement for granulating with formation of the vortex fluidized bed. The authors of this research propose the way to obtain multilayer granules in vortex granulators with fluidized bed [11].

Vortex granulators-dryers are characterized by the following advantages [12–19]:

– high specific volume and specific performance;
– availability of granule's residence time and trajectory in the workspace of device management mechanism;
– universality, i.e. ability of granulation, classification, separation, drying and cooling processes in the volume of one device;
– possibility of quick changeover, changing design and technological parameters according to the task.

Carrying out the drying process in these devices with active hydrodynamic mode, according to which the increasing of relative velocity of interacting phases is ensured, which helps to intensify the process without reducing the economic efficiency of the device. The advantages of an active hydrodynamic mode also include [20]:

– hydrodynamic stability of the process;
– provision of advanced surface interaction of contacting phases;
– reduction of energy intensity of the process and metal consumption for the devices.

Construction of the multistage vortex granulator, which enables to obtain multilayer granules, is demonstrated in the Fig. 1.

One can observe the processes of crystallization, drying and classification in the workspace of the proposed device. Thanks to these processes, we have the multilayer granules, consisting of core (substance A), intermediate layer (substance B) and external layer (substance C) [21]. Owing to the peculiarities of the mentioned processes in the vortex devices with fluidized bed, the final product's granulation structure consistency and its high consumer qualities are achieved.
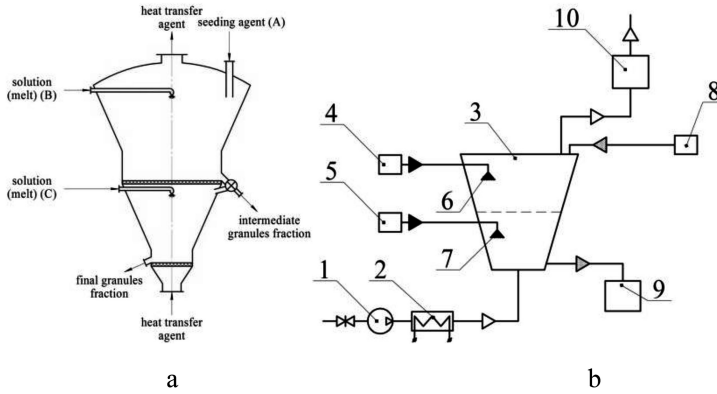
Fig. 1. Multistage granulator: a – basic construction; b – experimental installation. Installation equipment: 1 – compressor; 2 – heat exchanger; 3 – vortex granulator; 4, 5 – unit for preparation and supplying the solution to the upper and lower sections of the granulator; 6, 7 – injectors; 8 – feed unit of the loop; 9 – bunker of the finished product; 10 – exhaust gas cleaning unit.

The granulators of this type can be used to produce multi-layer granules of porous ammonium nitrate, organic-mineral fertilizers, mineral fertilizers with various nutrients in each layer (for example, nitrogen, phosphorus, potassium). The proposed capacity of the unit is 3000–5000 kg/h.

3   Research Methodology

This section demonstrates (in short) technological calculation of the multistage granulator section, which is based on the author's mathematic model [22, 23].

Hydrodynamics of gas flow motion

The Navier-Stokes equation for the motion of the real gas flow in the diffuser, complementing it with flow continuity equations

$$\left.\begin{aligned}
H_{V_r} - \frac{V_\varphi^2}{r} &= F_r - \frac{1}{\rho}\frac{\partial p}{\partial r} + E(\Delta v_r - \frac{V_r}{r^2} - \frac{2}{r^2}\frac{\partial V_\varphi}{\partial \varphi}), \\
H_{V_\varphi} + \frac{V_r V_\varphi}{r} &= F_\varphi + E(\Delta V_\varphi - \frac{V_\varphi}{r^2} + \frac{2}{r^2}\frac{\partial V_r}{\partial \varphi}), \\
H_{V_z} &= F_z - \frac{1}{\rho}\frac{\partial p}{\partial z} + E\Delta V_z,
\end{aligned}\right\} \tag{1}$$

$$\frac{\partial V_r}{\partial r} + \frac{1}{r}\frac{\partial V_\varphi}{\partial \varphi} + \frac{\partial V_z}{\partial z} + \frac{V_r}{r} = 0, \tag{2}$$

where E – a coefficient of turbulent viscosity according to the Boussinesq hypothesis; H, Δ – differential operators.

Hydrodynamics of Granules Motion

Theoretical calculations of the components of the granule rate were based on the mathematical instrument describing the hydrodynamic characteristics of the granules in the working space of the vortex granulator:

$$
\left.
\begin{array}{r}
m\dfrac{d^2 r}{d\tau^2} = \dfrac{W_\varphi^2}{r} + \psi \cdot \dfrac{\pi \cdot \mu_{gs} \cdot d_{gr}}{8 \cdot m}(V_r - W_r), \\[2mm]
m\dfrac{d^2 \varphi}{d\tau^2} = -\dfrac{W_r W_\varphi}{r} + \psi \cdot \dfrac{\pi \cdot \mu_{gs} \cdot d_{gr}}{8 \cdot m}(V_\varphi - W_\varphi), \\[2mm]
m\dfrac{d^2 z}{d\tau^2} = -g + \psi \cdot \dfrac{\pi \cdot \mu_{gs} \cdot d_{gr}}{8 \cdot m}(V_z - W_z),
\end{array}
\right\}
\tag{3}
$$

where m - mass of the granules, τ- the time; r - the current radius of the working space of the vortex granulator; W_r, W_φ, W_z - radial, circumferential and longitudinal/perpendicular components of the velocity of the granules, respectively; g - acceleration of gravity; ψ - linear coefficient of the granule's resistance to the gas flow; μ_{gs}- viscosity of the gas stream; d_{gr} – diameter of the granule.

Solution of the target substance (concentration of the target component in solution x_1) and ammonium nitrate granules (seeding agent) with mid-diameter d_1 move to the granulator as an outgoing raw material.

Mathematic model [22, 23] together with the standard techniques of technological calculation [9] are completely realized in the software product Multilayer Granules®. The main windows of this software product (basic data input, results of calculation) are presented in Figs. 2 and 3.
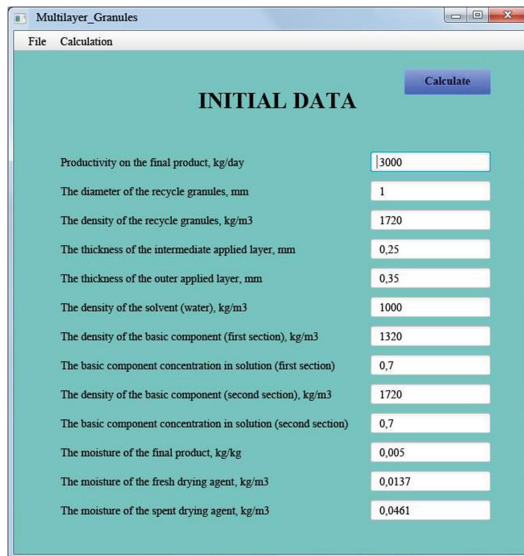

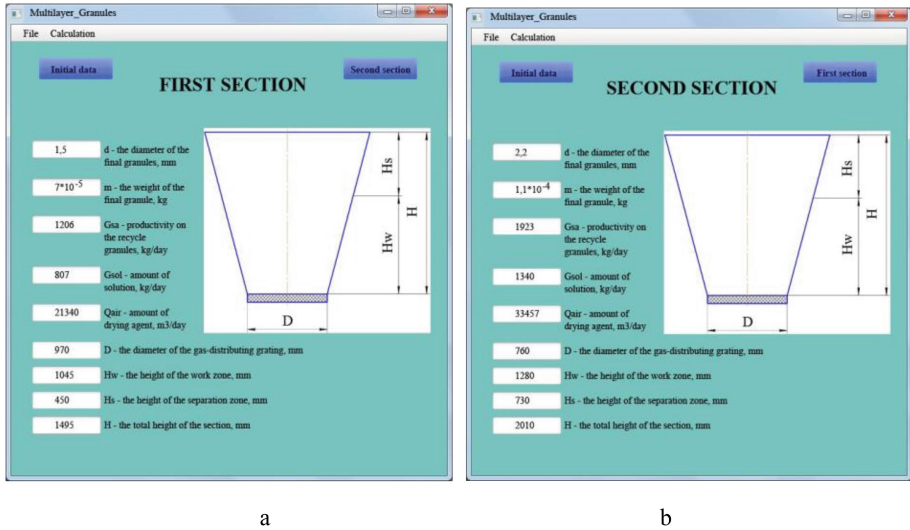**Fig. 2.** Multilayer Granules® (basic data input).

Fig. 3. Multilayer Granules®: a – calculation of the first section; b – calculation of the second section.

The results of the technological calculation, particularly (necessary amount of air) are the base for further hydrodynamic and constructive calculation of the vortex granulator section. The vortex granulator workspace construction is selected, based on the provision of conditions regarding the fluidized bed (diapason between the first and second crucial velocities of air, given for granules drying).

In this research carrying out the optimization calculation of the vortex granulator sections construction is proposed with the help of complex ANSYS CFX [24] based on the original mathematic model [22, 23]. The results of the optimization calculation are given in the next section.

4   Results

The main results of visualization are shown in Figs. 4, 5, 6, 7 and 8.

Analysis of simulation using the visualization software ANSYS CFX has showed:

– depending on gas flow velocity the component value trajectory of its movement has a different configuration with the predominance of one or another direction;
– when the axial velocity component predominance the area of gas flow movement is narrowed;
– when velocity circular component predominance we observe an increasing zone of gas flow vortex motion in height;
– when the velocity radial component predominance gas flow movement to the wall of the vortex granulator is made more intense;
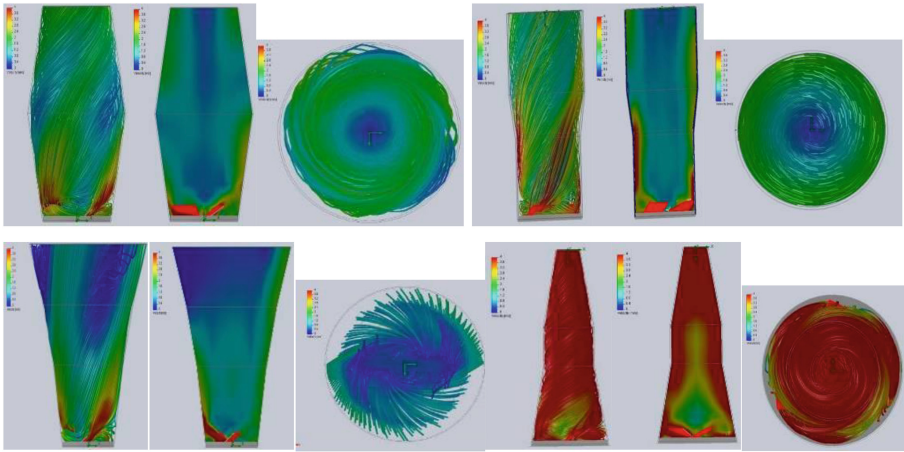
Fig. 4. Filling the gas flow velocity field when installing the gas-distributing unit with blades and various configuration of granulator workspace with blades inclination angle $\alpha = 30°$ and their number n = 3.
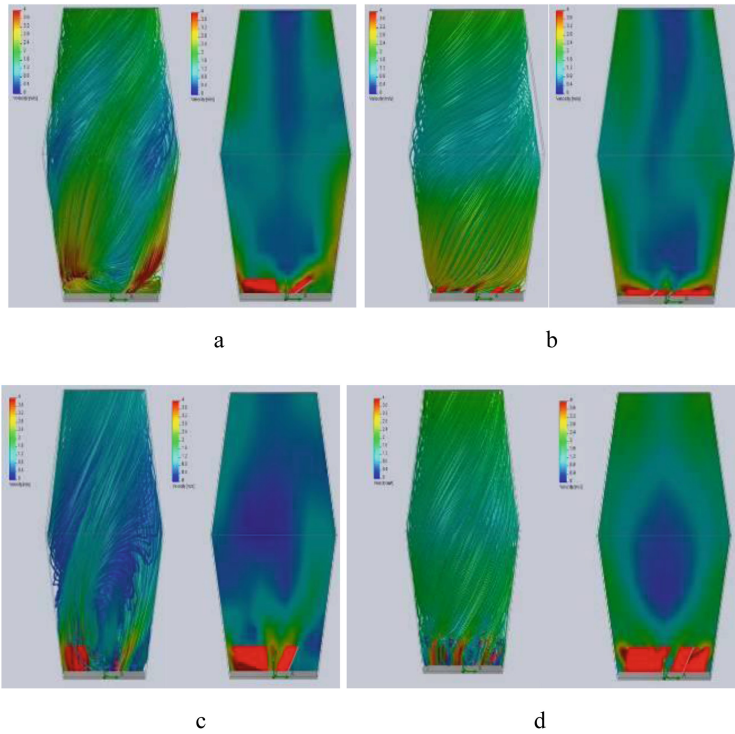

a   b

c   d

Fig. 5. Filling the gas flow velocity field when installing the gas-distributing unit with blades: a – $\alpha = 30°$, n = 3; b – $\alpha = 30°$, n = 8; c – $\alpha = 60°$, n = 3; d – $\alpha = 60°$, n = 8.
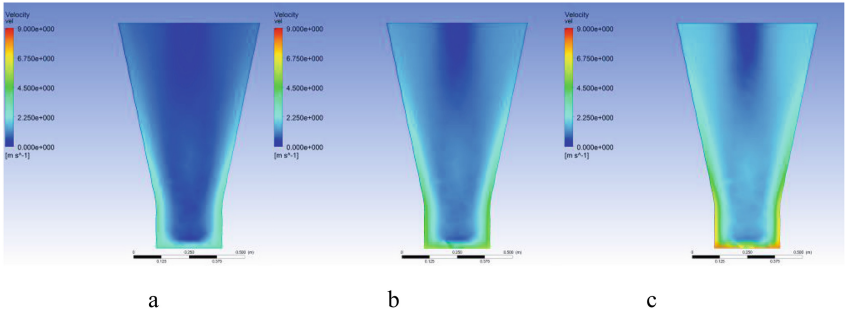
Fig. 6. The impact of granulator workspace design and gas flow velocity components on the gas flow total velocity and gas movement trajectory (working space "diffuser" with cylindrical insertion in the lower part), d = 300 mm; lc = 200 mm; L = 1000 mm, φ = 12°: a – Vr = Vz = 1 m/s; Vφ = 3 m/s; b – Vr = Vz = 1 m/s; Vφ = 5,2 m/s; c – Vr = Vz = 1 m/s; Vφ = 8 m/s.

Values of velocities	The direction of gas flow motion (axonometry)	The direction of gas flow motion (space)
V_z=1 m/s; V_r=1 m/s; V_φ=15 m/s		
V_z=15 m/s; V_r=1 m/s; V_φ=1 m/s		
V_z=15 m/s; V_r=1 m/s; V_φ=15 m/s		
V_z=8 m/s; V_r=15 m/s; V_φ=8 m/s		
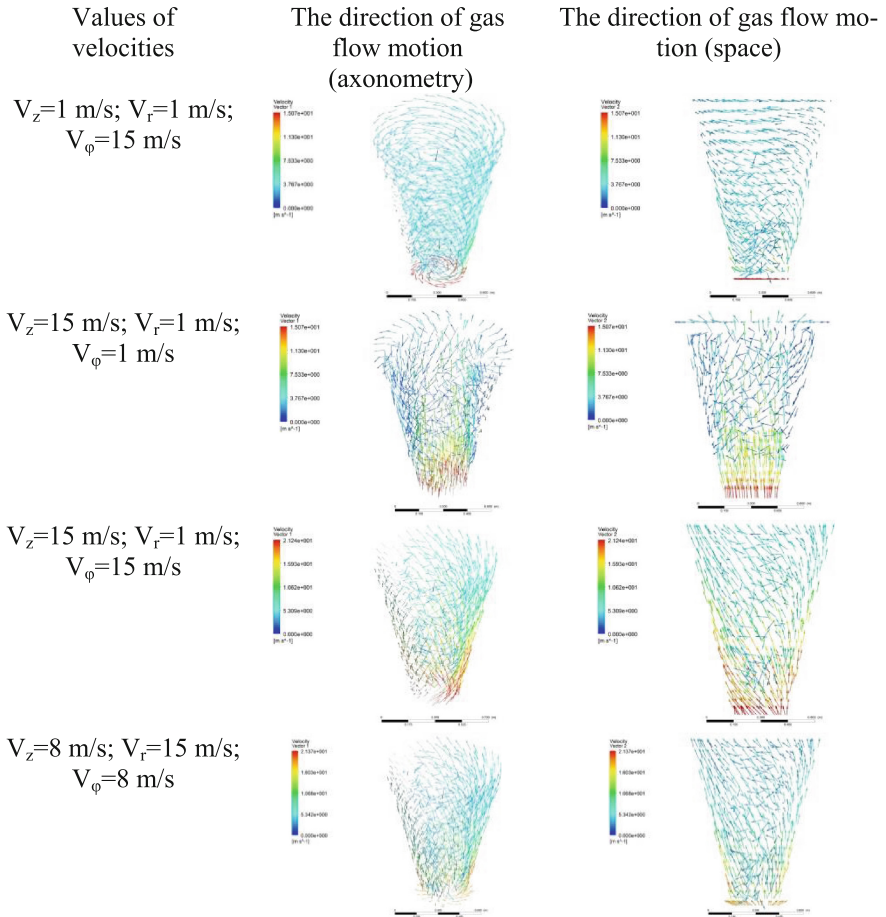
Fig. 7. Gas flow movement vectors for different values of speed components.

V_z=1 m/s; V_r=1 m/s;
V_φ=15 m/s

Vz=8 m/s; Vr=1 m/s;
Vφ=15 m/s

Vz=15 m/s; Vr=1 m/s;
Vφ=15 m/s

V_z=8 m/s; V_r=15 m/s;
V_φ=8 m/s
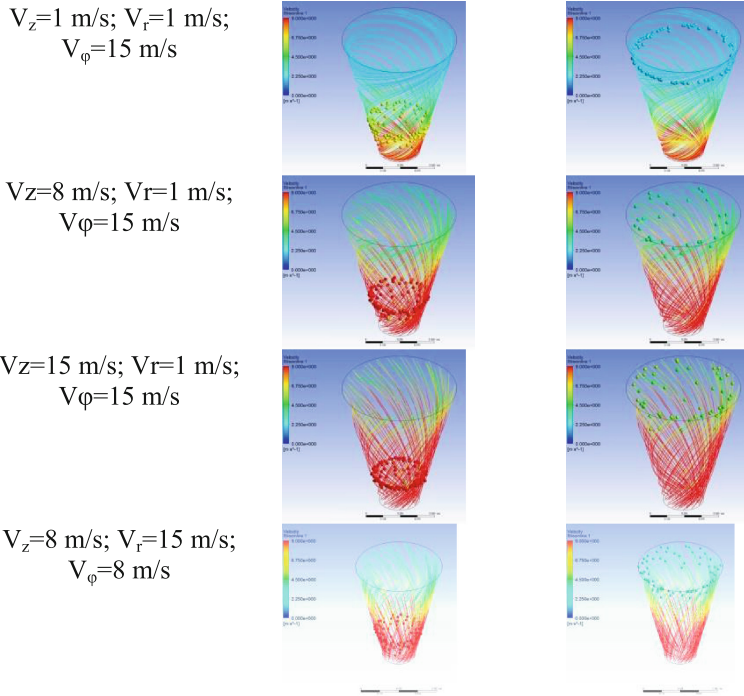
Fig. 8. Gas flow movement trajectory for different values of speed components.

- under certain conditions the intensity of gas flow initial twisting does not affect the trajectory of its movement, and affects only the value of gas flow resulting velocity;
- the velocity radial component is characterized by maximum value on the axis of the device.

The results of calculation allowed to project two-stage vortex granulator to produce granules with porous structure (porous ammonium nitrate for mining industry). Two layers of solution with its further crystallization were put on the seeding agent. The calculation of the process of material balance and selection of technological parameters were fulfilled with the help of the program Multilayer Granules®. The optimal hydrodynamic regime of work and granulator's construction is determined, based on the results of computer modeling.

Owing to the optimization of granulator's structural design, the "soft" hydrodynamic regime of its work was achieved (high intensity of granules moving and dehydration; therefore, granules are not damaged thanks to abrasion and collision). In this regime near-surface nanostructured layer (Fig. 9a) is received on the granule core (Fig. 9b) with micropores (in order to retain diesel fuel distillate) and surface nanostructured layer (Fig. 9c) is received with meso- and macropores (for the diesel fuel distillate free penetration inside the granule).
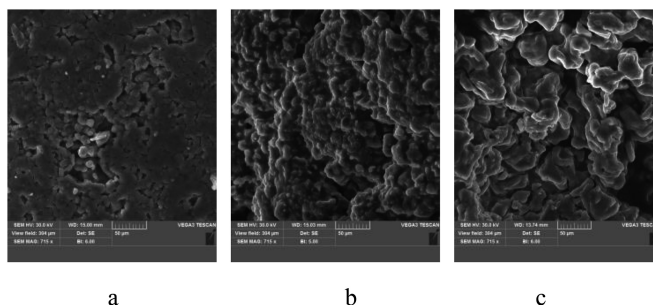
Fig. 9. Structure of the porous ammonium nitrate granule: a – core of the granule (ammonium nitrate); b – near-surface layer (ammonium nitrate); c – surface layer (ammonium nitrate + urea).

5   Conclusions

The demonstrated complex algorithm of calculation of the multistage vortex granulator sections enables to: select an optimal hydrodynamic regime of every section work (minimum hydraulic resistance); define an optimal structural design of section (minimum material intensity); carry out combined technological and constructive calculation with data transfer between blocks. It should be mentioned that this algorithm allows to fulfill calculations of one-section devices more accurately. Thus, it is possible to receive an optimal construction of the vortex granulator to produce multilayer granules, on the projecting stage without an expensive multifactorial experiment.

References

1. Wang, J., Liu, S., Qin, Y., Chen, X., Xing, R., Yu, H., Li, K., Li, P.: Preparation and characterization of controlled-release fertilizers coated with marine polysaccharide derivatives. Chin. J. Oceanol. Limnol. **35**(5), 1086–1093 (2017)
2. Neamţu, C., Popescu, M., Oancea, F., Dima, Ş.-O.: Synthesis optimization and characterization of microencapsulated N–P–K slow-release fertilizers. Open Chem. **13**, 813–823 (2015)
3. Noppakundilograt, S., Pheatcharat, N., Kiatkamjornwong, S.: Multilayer-coated NPK compound fertilizer hydrogel with controlled nutrient release and water absorbency. J. Appl. Polym. Sci. **132**(2), 41249 (2015)
4. Kornienko, Y., Raida, V., Sachok, R., Tsepkalo, O.: Mathematical modelling of continuous formation of multilayer humic-mineral solid components. Chem. Chem. Technol. **3**(4), 335–338 (2009)
5. Solanki, H., Basuri, T., Thakkar, J., Patel, C.: Recent advances in granulation technology. Int. J. Pharm. Sci. Rev. Res. **5**(3), 48–54 (2010)

6. Patel, P., Telange, D., Sharma, N.: Comparison of different granulation techniques for lactose monohydrate. Int. J. Pharm. Sci. Drug Res. **3**, 222–225 (2011)
7. Artyukhov, A.E., Sklabinskyi, V.I.: Experimental and industrial implementation of porous ammonium nitrate producing process in vortex granulators. Naukovyi Visnyk Natsionalnoho Hirnychoho Universytetu **6**, 42–48 (2013)
8. Stahl, H.: Comparing Granulation Methods. GEA Pharma Systems, Hürth (2010)
9. Litster, J., Ennis, B.: The Science and Engineering of Granulation Processes. Springer, Berlin (2004)
10. Salman, A.D., Hounslow, M.J., Seville, J.P.K.: Granulation. Elsevier, London (2006)
11. Artyukhov, A., Sklabinskiy, V., Ivaniia, A., Moskalenko, K.: Software for calculation of vortex type granulation devices. In: CEUR Workshop Proceedings, vol. 1761, pp. 374–385
12. Zardi, F.: Vortex granulation: the new route to high-quality solid nitrogen fertilizers. In: Nitrogen and Syngas Conference and Exibition, 15 p. (2011)
13. Bedetti, G.: Fluid bed granulation of urea and related apparatus. Patent No. 2013/0316078 A1, US (2013)
14. Funder, C.R., Mourits, J., Hansen, M.M.: Apparatus and a process for the preparation of an agglomerated material. Patent No. 5695701, US (1997)
15. Delves, J.L., Young, N.K., Drew, D.O.: Fluidizing apparatus with swirl-generating means. Patent No. 8628276, US (2014)
16. Changzhou Fengqi Drying Equipment Co. Ltd. (Electronic resource). http://czfengqi.en.alibaba.com/
17. Yixin Drying Equipment Co. Ltd. (Electronic resource). http://yixindrying.en.alibaba.com/
18. Wong, P., Chan, L., Heng, P.: Investigation on side-spray fluidized bed granulation with swirling airflow. AAPS PharmSciTech **14**(1), 211–221 (2013)
19. Wakamatsu, Y., Watano, S.: Device for treating powder particles by rotary flow. Patent No. 1020040047753 A, KR (2004)
20. Dvornikov, N., Belousov, P.: Investigation of a fluidized bed in a vortex chamber. J. Appl. Mech. Tech. Phys. **52**(2), 206–211 (2011)
21. Artyukhov, A., Sklabinskyi, V., Moskalenko, K.: Vortex granulator. Patent No. 113141, Ukraine (2017)
22. Artyukhov, A., Sklabinskyi, V.: Theoretical analysis of granules movement hydrodynamics in the vortex granulators of ammonium nitrate and carbamide production. Chem. Chem. Technol. **9**(2), 175–180 (2015)
23. Artyukhov, A., Sklabinskyi, V.: Hydrodynamics of gas flow in small-sized vortex granulators in the production of nitrogen fertilizers. Chem. Chem. Technol. **9**(3), 337–342 (2015)
24. Computational Fluid Dynamics: ANSYS CFX and FLUENT CFD Software (Electronic resource). https://caeai.com/ansys-software-support/ansys-software/computational-fluid-dynamics-ansys-cfx-and-fluent-cfd-software

Simulation and Design of Welded Plate Heat Exchangers with Channels of Different Corrugation Height

Gennadii Khavin[(✉)] [iD]

National Technical University "Kharkiv Polytechnic Institute",
2 Kyrpychova St., Kharkiv 61002, Ukraine
gennadii.khavin@gmail.com

Abstract. A method of using a different height of the corrugation along the side of the heating and incalescent heat carriers to intensify the heat transfer process in the channels of heat exchangers with a circular plate is proposed. The use of such construction leads to equalization of the flow rates in the channels, a reduction in the number of channels, and an increase in the shear stress on the heat transfer surface of the plates. The search for the solution is based on the determination of the velocity of the heat carriers in the channels of the heat exchanger, when the pressure drop in the channels is complete satisfaction. The algorithm for solving the problem of finding the best solution is combinatorial. The problem of finding the optimal integer value (number of plates) is solved on a limited set of possible combinations of continuous design parameters – the height and angle of corrugation. The influence of the geometric parameters of the corrugation on its heat transfer capacity is investigated. A specific application for the calculation of the heat exchangers with different height channels of the corrugation was considered.

Keywords: Plate heat exchangers · Height of corrugation
Heat transfer analysis

1 Introduction

Increasing the efficiency of operating production and building new capacities requires not only improvement of the available technologies but also creation of new equipment that implements these changes. Modernization of enterprises in the petrochemical, chemical, and other industries is connected with an increase in the share of heat recovery, which is accompanied by an increase in operating temperature regimes and pressures, installation of heat exchange equipment in the new heat exchange positions. The basic nomenclature of the heat-exchange equipment, for example, in the oil refineries are shell-and-tube devices. Despite the high reliability in of operation under the conditions of high temperatures and pressures, they have large dimensions and a low heat transfer coefficient. The requirements for increasing the efficiency of heat transfer, reducing the size, reducing the fouling of the heat transfer surface and minimizing stops for cleaning the units created the prerequisites for replacing the shell-and-tube equipment with the plate heat exchangers or their installation in parallel.

2 Literature Review

As such heat exchangers, a welded plate and spiral heat exchangers [1] were proposed to use. Welded units allow for the heat exchange at high temperatures of ~ 300–350 °C, high pressures of ~ 32 bars, and also work with poisonous and hazardous media. At present, there is a fairly wide range of welded heat exchangers of the cross-flow type "Compobloc" [2, 3], produced serially by various manufacturers. The main advantage of these devices is their compactness, the possibility of assembling multi-pass units to increase the speed in the channels, semi-dismountable wash and the presence of a small amount of heat carrier in the device. Their main disadvantage is high cost and worsening of hydraulic characteristics (an increase of pressure drops) due to fouling of the heat transfer surface during the operation.

A completely welded plate heat exchanger AlfaRex is an efficient laser welding, which allows working under conditions of up to 40 bar and 350 °C. AlfaRex has all the advantages of a plate heat exchanger, including a compact and flexible design, high heat transfer coefficient and availability of service. AlfaRex is well suited for working with aggressive media or high temperatures/pressures, cyclic in temperature and/or pressure, as well as for the heat recovery. The typical AlfaRex PHE occupies only one-sixth of the area and weighs only one-sixth of the comparable shell-and-tube heat exchanger.

In addition, other types of the welded plate-type heat exchangers of a mixed type, such as plate-and-shell HE (PSHE) are being currently developed and successfully operated [1, 5]. Devices of this construction design were developed by Vahterus Oy Company [5] and are also produced by Alfa Laval, Gea, Tranter and etc. These devices use round plates with a round or square corrugated heat exchange surface. The main advantage of such units is one-pass grouping, high heat transfer coefficient and low manufacturing cost [1, 6].

The efficient use of welded PHEs in different recuperation systems and heat exchanger networks (HENs) require a reliable method for their rating and sizing. This analysis and correct design can differ significantly from the known plate-and-frame PHE calculation methods, a modern analysis of which is presented, for example, in [1, 7]. However, the features of welded PHEs construction introduce some additional specifics in their design procedure. PSHE with parallel flow of heat exchanging streams can be modeled in the same way as plate-and-frame PHE [8].

A fairly complete analysis of the mathematical modeling of heat transfer and pressure drops in the channels of plate heat exchangers is presented in [9, 10]. A general statement problem of numerical modeling based on the application of CFD technology and the volume element method is presented. Numerous studies in this direction are mainly devoted to the evaluation of the efficiency of heat transfer in the channels of various geometries. The process of flow in channels is studied and analyzed [11, 12]. These models allow us refining the calculation of the plate package in each particular case, using more advanced relationships to determine the quantitative characteristics of the heat transfer and pressure drop.

3 Research Methodology

There are a large number of applications in the industry where, in terms of energy recovery, there is a significant difference between the flow rates of hot and cold heat carriers. In this case, the velocity in the channels of the heat exchanger drops sharply along the side of the heat carrier with a lower flow rate. This condition leads to a decrease in the heat transfer coefficient from the side of this heat carrier, the overall heat transfer coefficient of the device and to the intensification of the heat exchange surface fouling during the operation. In this case, the conditions of its operation are extremely disadvantageous because of the large heat exchange surface caused by the use of a carrier with a large flow rate, which leads to a drop in the carrier velocity alongside with low flow rate.

3.1 Mathematical Formulation

Taking into account the above-mentioned, the question arises of the creation of PHE structures with different corrugation height in the channels (different cross-sectional area of the channels), that make it possible to overcome the imperfections of using the traditional plate-frame devices in various applications. To realize the design of welded plate heat exchangers with the channels of different cross-sections (different heights and corrugation pitch), a mathematical model to calculate such devices was developed by analogy with the calculation of traditional plate devices [1].

To calculate the heat transfer coefficient and pressure drops, the relationships given in [13, 14] were used. To calculate the heat transfer coefficient on the cold and hot sides, an expression is as follows

$$Nu_i = \alpha_i \cdot d_{ekvi}/\lambda_i = 0,065 \cdot Re_i^{6/7} \cdot (\psi_i \cdot \zeta_i/\Phi_i)^{3/7} \cdot \Pr_i^n \cdot (\mu_i/\mu_{wi})^{0.4}, \qquad (1)$$

where Nu is the Nusselt number; λ is the thermal conductivity of the stream, W/(m·°K); δ is the corrugation height, $d_{ekv} = 2 \cdot \delta$ diameter of channel, m; δ is the corrugation height, m; α is the film heat transfer coefficient, W/(m·°K); Pr is the Prandtl number; Re is the Reynolds number; Φ is the coefficient of increase in the area of the plate due to corrugation; μ is coefficient dynamic viscosity, Pa·s; μ_w is coefficient dynamic viscosity, calculated at the wall temperature of the plate, Pa·s. The coefficient n is determined from expression $n = \exp [64/(Pr + 30)]/(1–0.012 \cdot Re^{0.27})/3$. The value of ψ can be estimated by the following equation $\psi = (Re/A)^{-0,15 \cdot \sin \beta}$ at the Re > A and $\psi = 1$ at Re $\leq$ A, where $A = 380/(tg\beta)^{1,75}$, where β is a corrugations inclination angle. The empirical equation to calculate the friction factor ξ in the criss–cross flow channels was reported by [7]. It enables to predict the friction factors at corrugated field of the criss–cross flow channels formed by plates with inclined corrugations in wide range of corrugation parameters. The equation for ξ is as follows

$$\zeta = 8 \cdot \left[\left(\frac{12 + p_2}{Re} \right)^{12} + \frac{1}{(K_1 + K_2)^{3/2}} \right]^{1/12}, \qquad (2)$$

$$K_1 = \left[p_4 \cdot \ln \left(\frac{p_5}{\left(\frac{7 \cdot p_3}{\mathrm{Re}} \right)^{0.9} + 0.27 \cdot 10^{-5}} \right) \right]^{16}, \quad K_2 = \left(\frac{37530 \cdot p_1}{\mathrm{Re}} \right)^{16}, \quad (3)$$

where p_1, p_2, p_3, p_4, p_5 are the parameters defined by channel corrugation form $p_1 = \exp(-0.15705 \cdot \beta)$, $p_2 = \pi \cdot \beta \cdot \gamma^2/3$, $p_3 = \exp(-\pi \cdot \beta/\gamma^2/180)$, $p_4 = [0.061 + (0.69 + \mathrm{tg}\,\beta)^{-2.63}] \cdot [1 - 0.9 \cdot (1-\gamma) \cdot \beta^{0.01}]$, $p_5 = 1 + \beta/10$, where $\mathrm{tg}\,\gamma = 2\delta/(\Lambda/2)$, Λ – pitch of corrugation, m, Fig. 1.
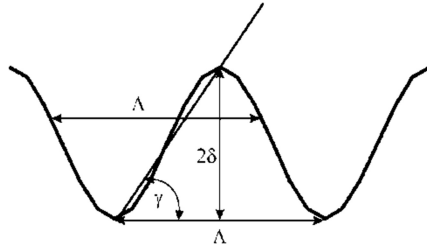
Fig. 1. Basic parameters of a sinusoidal corrugation.

The total pressure drop in the PHE channel can be calculated as follows

$$\Delta p = \zeta \cdot \frac{l_f}{d_{ekv}} \cdot \frac{\rho w^2}{2} + \zeta_{neck} \cdot \frac{\rho w^2}{2}, \quad (4)$$

where w is the stream velocity in the channel, m/s; l_f is a reduced length of the corrugated field, m, which is equal to $l_f = f_{pl}/b$, where f_{pl} is the corrugated area of plate, m^2; b is the width of the plate, m; ρ is the fluid density, kg/m^3. The corrugated area of the plate may be calculated using the coefficient of increase in the area of the plate due to corrugation Φ as $f_{pl} = l_0 \cdot \Phi \cdot b$. The coefficient of increase in the area of the plate due to corrugation Φ determined by formula

$$\Phi = \frac{1}{6} \left(1 + \sqrt{1 + \eta^2} + 4\sqrt{1 + \eta^2/2} \right),$$

where $\eta = 2\pi \cdot \delta/\Lambda$ or $\eta = \pi/2 \cdot \mathrm{tg}\,\gamma$; l_0 is the linear length of corrugated area, m.

The paper [15] shows that for the plates investigated there with different forms of corrugations, but with similarly constructed distribution zones, the coefficients ζ_{neck} are close in values. For different plates the values of such coefficients from 25 to 110 were obtained. For four out of six investigated plates the average value was 27.25. For those plates, the ratio of the length of corrugated field l_f to effective plate length l_{ef} used in the ζ_{neck} calculations was equal to 0.72. The value of coefficient from the paper [13] should be divided by this ratio to use it in the Eq. (4).

The experimental data generalized by the Eq. (1) were obtained for the models of criss-cross flow channels formed by the plates with the height of corrugations from 1.5 mm to 10 mm. It confirms that the scale factor in the investigated range of the corrugations sizes is accounted by Eq. (1) due to its dimensionless form and also allows modeling the influence of the inter-plate spacing on the PHE hydraulic performance. To account for the pressure losses in the distribution zones [6, 14] of the inter-plate channel formed by commercial plates, it has been introduced the coefficient of local hydraulic resistance in those zones ζ_{neck}, assuming that these coefficients for the inlet and outlet zones are equal. The average velocity of stream at the main corrugated field w is assumed as characteristic velocity in determining these coefficients [14].

3.2 Design Algorithm

The problem of designing a plate heat exchanger is now precisely formulated and consists of determining the minimum number of channels (plates) of a given standard size, the set of which ensures the given heat transfer conditions, and the pressure drops in the devise when the heat carriers pass through it, and they do not exceed those specified by the conditions of the problem. The problem of finding the optimal integer value (number of plates) is being solved on a limited set of possible combinations of continuous design parameters.

At the same time, if the pressure drop condition for the heat carrier with a high flow rate is satisfied, then on the other side they will certainly be less than the allowable one. From (4) it is fairly clear that the best result can be obtained with one pass counter current PHE, as for the multiple passes it increases the number of distribution zones through which the stream flows. In addition, the additional pressure drops are added owing to the turning flow in collectors between the passes. The special case when unsymmetrical passes number may be necessary is not considered here. Let us assume that to satisfy process conditions for the given geometry of corrugations on the main heat transfer field of the plate, the plate length should be changed. It is similar to the design approach proposed by Picon-Nunez et al. [16] in a graphical form.

When pressure drop condition for the hot stream is satisfied completely, from the (4) one can get

$$l_f = \frac{d_{ekv}}{\zeta(w)} \cdot \left(\frac{2 \cdot [\Delta p]}{\rho w^2} - \zeta_{neck} \right), \tag{5}$$

where $[\Delta p]$ is the maximum allowable pressure loss by the condition of the problem, Pa. Using this expression and the ε-NTU method, one can obtain a nonlinear equation to determine the value of the velocity in the channel satisfying expression (4) and further the plate area and the number of channels (plates), as described in [6, 7, 14].

To design the welded plate heat exchangers with channels of different cross-sections (different heights and corrugation pitch), the software to implement the possibility of such modeling was developed. The basis for calculating the heat transfer through the wall of the corrugated plate is the availability of criterion equations describing the dependence of the heat transfer coefficients on the thermal and hydraulic

parameters of the heat carriers. In fact, for each plate size with different corrugation geometry, the relationship for calculating the heat transfer coefficients and pressure drops must be known. However, in design practice the generalized relations are also used, which, with varying degrees of accuracy, allow calculating the necessary coefficients for a group of plate sizes with similar corrugations.

The general idea of the calculation algorithm is to find the optimal value of the plate length and determine its area, the number of plates, provided all the required conditions of heat transfer and hydraulic losses in the apparatus be satisfied. The length of the plate (5) is a function of the plate corrugation and, accordingly, determines the velocity of the heat carrier in the channels and their ability to the heat transfer. It is well known that the intensity of the heat transfer increases with an increase in the angle of inclination and a decrease in height of the corrugation [1, 7, 13]. It is natural to assume that the best solution, from this point of view, will be a combination of the maximum angle of inclination and the minimum corrugation height. However, such a solution is not always correct, since in this case, the pressure drops in the devise increase significantly on the side with a large flow rate of the heat carrier, and to satisfy the condition for the permissible pressure drops a large number of channels (plates) or the realization of multi-pass in the unit are needed. An increase in the number of channels (a package of plates as a whole) leads to a drop in the speed alongside with the carrier of a low flow rate, a decrease in the heat transfer coefficient, and a worsening in the efficiency operation of the heat exchanger. In addition, the loss of speed causes an intensification of contamination on the heat transfer surface in the unit. To ensure the distribution of the flow over the width and length of the plate, it is necessary to maintain the length-to-width ratio. Usually, this value for the industrial-grade plates is $k_{pl} = l_0/b = 1.5 - 2.5$. In addition, if the plate has a distribution part, then it participates in the work and it must be taken into account as a part of the heat transfer surface. According to [15, 17] for the industrial plates, this value is no more than 15% ($k_{neck} = 1.15$). Then the heat transfer surface of the plate can be calculated by the formula $f_{pl} = l_0 \cdot b \cdot \Phi \cdot k_{neck} = l_0^2/k_{pl} \cdot \Phi \cdot k_{neck}$.

4 Results

To determine the degree of influence of different corrugation height in the process of designing devices with a circular plate, a number of numerical experiments were carried out to calculate various heat exchangers from the data of heating crude and desalted oil.

Consider, as an application, the use of a plate welded heat exchanger with a circular plate [6] having a square configuration of the heat transfer surface, for a position of the crude oil heating by the desalted oil. The design characteristics were: thermal load 840.5 kW; input and output temperatures of the heating (hot) carrier (bottom T-101) are respectively 346 °C and 300 °C; input and output temperatures of the heated (cold) carrier (oil) are 269.3 °C and 284 C, respectively; permissible pressure drops on the hot and cold sides were assumed to be equal to 100 kPa. In this example, the ratio of the mass flow rates on the hot G_h and cold G_c sides is $G_h/G_c = 0,3$. The average

values of thermo physical properties of heat carriers in the calculations are presented in Table 1.

Table 1. Thermo physical properties of heat carriers

Name	T, °C	ρ, kg/m³	Cp, kJ/(kg·K)	λ, W/(m·K)	μ, cP
Oil	250	579.0	3.081	0.0605	0.2898
Bottom T-101	320	550.6	3.280	0.0640	0.2260

When designing heat exchangers with circle plates, the corrugation of plates with the parameters shown in Table 2 was considered, the surface area of the plate was calculated from the ratio (5) by the formula $f_{pl} = l_0^2 \cdot \Phi$. It was assumed that the range of variation of the corrugation height is from 0.002 to 0.006 m and the angle of inclination of the corrugation is 25 to 65°. Corrugation parameters are presented in Table 2.

Table 2. Parameters of circular plate's corrugation with a square area of the heat transfer surface

Parameters	Quantities values				
tg γ	0.65	0.70	0.75	0.80	0.85
η	1.021	1.100	1.178	1.257	1.335
Φ	1.227	1.259	1.292	1.326	1.362

To study the effect of tg γ on the heat exchange surface area and the plate area, several heat exchangers were calculated, for which the height of the corrugation was assumed equal to 2 mm on the hot side, and the angle of inclination of the corrugation along the hot and cold side was 65°. The maximum area of the plate does not exceed 1 m² and the number of plates in the device is not more than 200. The results of the calculations are shown in Fig. 2.
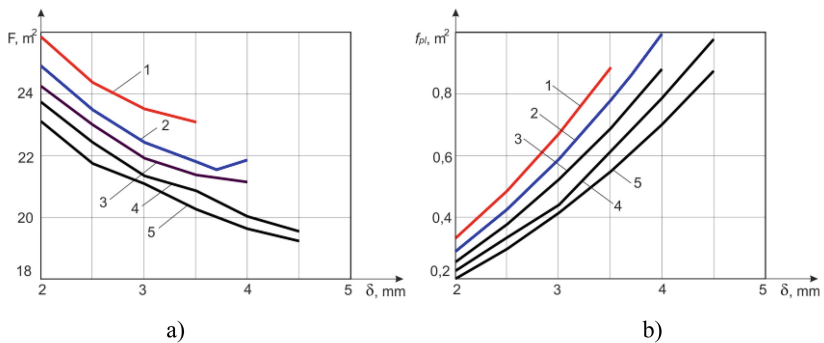
Fig. 2. Dependence of the total heat exchange surface – (a) and the heat exchange area of the plate – (b) on the height of the corrugation δ for different values of the corrugation parameter tg γ: 1 – 0.65; 2 – 0.70; 3 – 0.75; 4 – 0.80; 5 – 0.85.

As it can be seen from Fig. 2, with increasing tg γ the heat exchange rate is improved and a smaller heat exchange surface is required to ensure the heat transfer. It obvious that an increase in the height of the corrugation on the cold side results in a decrease in the heat transfer surface from about 12 to 17% for different values tg γ.

Figure 2 shows the change in the heat transfer area of a single plate as a function of the corrugation height for different values of the parameter tg γ. Analyzing the results, a conclusion can be made that at the same height of the corrugation, the larger the value of the parameter tg γ is, the smaller the heat exchange area of the plate is. The latter circumstance makes it possible to design the heat exchangers with a smaller plate surface, though the number of it will be more.

To investigate the effect of the corrugation inclination angle β on the heat exchange surface value and the heat exchange area of the plate, a number of calculations of heat exchangers with a change in the angle inclination were carried out, the results are shown in Fig. 3.

a)   b)
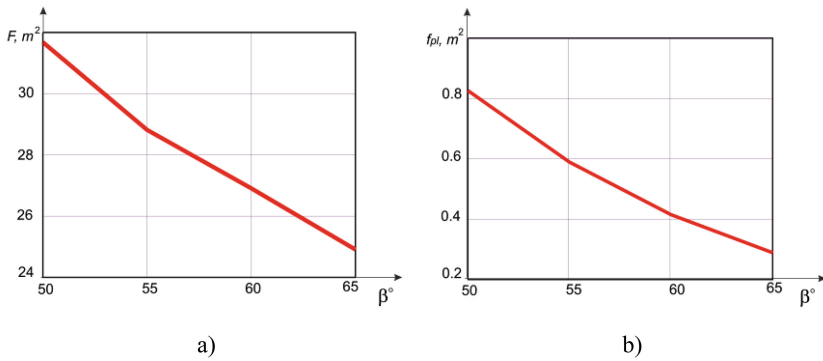
Fig. 3. Influence of the inclination angle corrugation: a – by an amount of the heat transfer surfaces; b – plate heat transfer area.

As it was known before, an increase in the corrugation angle leads to an improvement in the heat transfer capacity of the corrugated plate and a decrease in the heat exchange area of the single plate. It can also be seen from the calculated data that the dependence of the heat transfer surface and the heat exchange area of a single plate is practically linear.

Calculations of the heat exchangers with different corrugation height are given in Table 3, which shows that the minimum heat exchange area is reached at a corrugation height of 3.7 mm with the limitations on the area of the plate being 1 m^2.

The value of the shear stress on the plate wall is an indication of the tendency of the heat exchanger to contaminate during operation. Then this value is higher, the probability of appearance and growth of deposits is lower. In most industrial applications with calculating plate heat exchangers, this value should not be below a certain threshold value at which the device is allowed to work.

Table 3. The calculations results of heat exchangers with different corrugation height.

Corrugation Height, mm	Plate area, m^2	Plate number	Heat transfer surface, m^2	Velocity in the channels, m/s		Shear stress on the wall, Pa	
				Hot	Cold	Hot	Cold
2.0	0.290	86	24.92	0.289	0.916	12.52	97.88
2.5	0.427	55	23.49	0.373	0.946	17.92	96.51
3.0	0.590	38	22.42	0.459	0.970	24.08	95.33
3.5	0.779	28	21.80	0.547	0.990	30.78	94.17
3.7	0.861	25	21.53	0.582	0.997	33.65	93.72
4.0	0.994	22	21.86	0.635	1.006	38.12	93.06
4.5	1.235	17	21.00	0.724	1.020	46.03	91.99
5.0	1.505	14	21.06	0.814	1.032	54.48	90.96
5.5	1.802	12	21.62	0.904	1.042	63.42	89.98

In all cases, an increase in the height of the corrugation on the side with a high flow rate causes an increase in the shear stress on the wall. This indicates a positive effect of using the grouping of a plate heat exchanger with different channel widths (different corrugation heights).

5 Conclusions

An analysis of the obtained results made it possible to conclude that for a fixed height of the corrugation on the side of one of the heat carrier (with a lower flow rate), the change in the total area of the heat transfer surface is extreme. The extremal relation of the dimensions of the corrugation height is characterized by an approximate equality of the pressure drops along the hot and cold sides.

The design of the welded plate heat exchangers with a circle plate and the use of plates with different corrugation heights along the hot and cold side is one of the promising directions for designing heat exchangers of this class. This approach, due to the effect of equalizing the velocities in the channels, can lead to a significant reduction of the heat transfer surface of the device and, consequently, reduces its cost. In addition, in this design, the shear stress on the plate walls increases, which has a positive effect on the resistance to contamination during the operation.

References

1. Klemes, J., Arsenyeva, O., Kapustenko, P., Tovazhnyanskyy, L.: Compact Heat Exchangers for Energy Transfer Intensification: Low Grade Heat and Fouling Mitigation. CRC Press, Boca Raton (2015)
2. AlfaLaval Welded Plate-and-Block Heat Exchangers. http://www.alfalaval.com. Accessed 11 Apr 2017
3. Andersson, E., Quah, J., Polley, G.T.: Experience in application of Compabloc heat exchangers in refinery pre-heat trains. In: Muller-Steinhagen, H., Malayeri, Watkinson, A.P. (eds.) Proceedings of the International Conference on Heat Exchanger Fouling and Cleaning VIII-2009, pp. 39–43, Schladming, Austria (2009)

4. Rugged, Efficient and Trouble-Free AlfaRex: All-Welded Plate Heat Exchanger. http://www.alfalaval.com. Accessed 11 Apr 2017
5. Vahterus O.: Plate and Shell Heat Exchanger. www.vahterus.com/en/node/528 (2016). Accessed 11 April 2017
6. Arsenyeva, O.P., Tovazhnyanskyy, L.L., Kapustenko, P.A., Khavin, G.L., et al.: Two types of welded plate heat exchangers for efficient heat recovery in industry. Appl. Therm. Eng. 105, 763–773 (2016)
7. Arsenyeva, O.P., Tovazhnyansky, L.L., Kapustenko, P.A., Khavin, G.L.: Optimal design of plate-and-frame heat exchangers for efficient heat recovery in process industries. Energy 36(8), 4588–4598 (2011)
8. Arsenyeva, O., Tovazhnyansky, L., Kapustenko, P., Khavin, G.: Mathematical modeling and optimal design of plate-and-frame heat exchangers. Chem. Eng. Trans. 18, 791–796 (2009)
9. Talakala, M.S., Babu, T.P.: Use of a CFD code in the analysis of heat transfer surfaces international refrigeration and air conditioning. In: Conference at Purdue (2008)
10. Egeregor, D.: Numerical Simulation of Heat Transfer and Pressure Drop in Plate Heat Exchanger Using Fluent as CFD Tool. Department of Mechanical Engineering Blekinge Institute of Technology, Karlskrona (2008)
11. Fadl, M.S.: A numerical simulation of heat transfer performance using different corrugated surface shape. In: Eleventh International Conference of Fluid Dynamics. Alexandria, Egypt (2013)
12. Zimmerer, C., Gschwind, P., Gaiser, G., Kottke, V.: Comparison of heat and mass transfer in different heat exchanger geometries with corrugated walls. Exp. Thermal Fluid Sci. 26, 269–273 (2002)
13. Arsenyeva, O.P., Tovazhnyansky, L.L., Kapustenko, P.A., Demirskiy, A.V.: Heat transfer and friction factor in criss-cross flow channels of plate-and-frame heat exchangers. Theor. Found. Chem. Eng. 46(6), 634–641 (2012)
14. Arsenyeva, O., Tovazhnyansky, L., Kapustenko, P., Khavin, G.: The influence of plate corrugations geometry on plate heat exchanger performance in specified process conditions. Energy 57, 201–207 (2013)
15. Tovazhnyansky, L.L., Kapustenko, P.A., Tsibulnic, V.A.: Heat transfer and hydraulic resistance in channels of plate heat exchangers. Energetika 9, 123–125 (1980)
16. Picon-Nunez, M., Polley, G.T., Jantes-Jaramillo, D.: Alternative design approach for plate and frame heat exchangers using parameter plots. Heat Transfer Eng. 31(9), 742–749 (2010)
17. Muley, A., Manglik, R.M.: Experimental study of turbulent flow heat transfer and pressure drop in a plate heat exchanger with chevron plates. ASME J. Heat Transfer 121, 110–117 (1999)

Granulation Process of the Organic Suspension: Fluidized Bed Temperature Influence on the Kinetics of the Granule Formation

Ruslan Ostroha[1]([✉]) , Mykola Yukhymenko[1] ,
Andrii Lytvynenko[1] , Jozef Bocko[2] , and Ivan Pavlenko[1]

[1] Sumy State University, 2 Rymskogo-Korsakova St., Sumy 40007, Ukraine
r.ostroga@pohnp.sumdu.edu.ua
[2] Technical University of Košice, Letná 9/B, 042 00 Košice, Slovak Republic

Abstract. The authors of the article present and prove the possibility of reducing the economic and environmental indicators in the processes of mineral fertilizers granulation by means of recycling and using organic agricultural waste. It is shown that such waste products are in the form of very moist suspensions, therefore, in order to minimize energy consumption for their processing, the optimal technology for granular product preparation is granulation in the fluidized bed apparatus. For this purpose there has been conducted the physical modelling of the granule formation process and one found out the conditions of suspended layer formation, which determine the nature of the dispersed suspension and dispersed solid phase interaction. One has experimentally established the temperature regimes of organic suspensions granulation and determined the operating parameters of the process. The kinetics of coarsening of granules was studied depending on the temperature of dehydration of organic suspensions. Analytical dependencies that are determined by the heat transfer coefficient are obtained to determine the time and temperature of granule heating.

Keywords: Nitrogen fertilizers · Encapsulation · Carbamide · Chicken manure
Temperature regime · Parameter · Granule

1 Introduction

Ammonia nitrate and carbamide prevail in the range of nitrogen fertilizers which are used in all soil-climatic zones. They are transformed in soil-plant system, and get actively involved in the general biological nitrogen cycle, providing the needs of growing plants in nitrogen. But along with the known advantages of these nitrogen fertilizers they have significant disadvantages: high water solubility and washing off from the arable layer, which leads to contamination of surface and groundwater. In addition, the use of high doses of nitrogen fertilizers leads to accumulation of a significant amount of nitrate nitrogen in the main agricultural products, as well as in the soil, which leads to soil degradation and product quality fall-off [1].

Consequently, the task of developing and creation of the nitrogen fertilizers, which have the prolonged effect and provide the efficient use of nitrogen during the growing season, is very up-to date.

Methods of improving fertilizers quality, the production process of which is not very complicated and does not require unavailable and expensive reagents and conditioning additives, are of great interest. Therefore, one can solve the mentioned up-to-date problems by coating the granules surface with protective shells. Protective shell, covering the particles surface, creates additional resistance to mass transfer in the process of dissolution. As a result, the fertilizers efficiency coefficient increases, and one can reduce their quantitative introduction into the soil.

2   Literature Review

Various materials can be used for the encapsulation of granular fertilizers. For example, for the encapsulation of carbamide at PJSC «Severodonetsk Azot Association» (Ukraine), amino-formaldehyde resin of KFS-K grade is used. Its main disadvantage is the high content of highly toxic substance – formaldehyde.

As shell materials one also uses epoxide, polyester, carbamide resins, sulfur, phosphor-gypsum, paraffin, etc. [2–5]. Most of the used substances are not dissolved in the soil. As a consequence, every introduction of such fertilizers increases soil pollution which has negative effect to its further exploitation.

Formation of a continuous coating on the mineral granules surface can take place as a result of two or more substances reaction. An example of such technology is an encapsulated particle [6], which consists of a core and a shell disposed around it.

The main and significant disadvantage of capsulated materials in comparison with non-capsulated, is higher energy consumption and additional material costs for their production [7]. To improve the encapsulated fertilizer competitiveness it is necessary to use cheap materials and compositions on their basis.

In the industry two ways of cleaning the litter are used – mechanical and water washing. Due to this one distinguishes: natural liquid manure with humidity 65–70%, semisolid manure – 91–95% and waste water – more than 95% of water. Thus, the most appropriate technology for the production of organic and organo-mineral granules is their granulation in a fluidized bed apparatus with air nozzle [8].

3   Research Methodology

Study of the basic laws of the chicken manure suspension granulation was conducted on a laboratory stand (see Fig. 1). The setup includes the working chamber, which is made of organic glass that enables visualization of the process under study. Granulation is fulfilled directly in the fluidized bed. For this purpose one forms a zone, which is limited with:
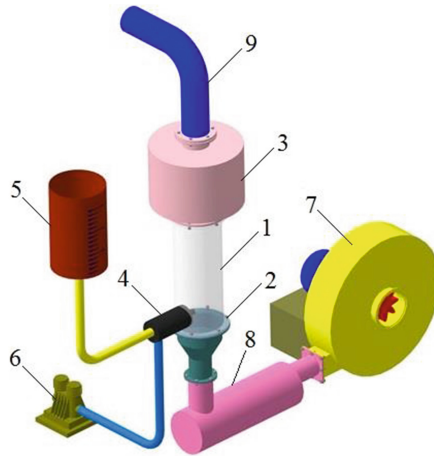
Fig. 1. Model of laboratory stand: 1 – working chamber; 2 – air distributor plat; 3 – device head; 4 – pneumatic nozzle; 5 – measuring tank; 6 – compressor; 7 – blower; 8 – heater; 9 – air corrugation.

– air distributor plate at the bottom; which is the sheet with holes of small diameter through which gas is outflowing in the form of separate vertical jets;
– vertical walls of the working chamber on the sides.

On top there is a free space – separation zone, where granules can come up to a certain height and then come down into the layer.

Alongside of the device, at about the average height of the layer, there placed an air nozzle, which is supplied with the compressed air and liquid organic (chicken manure). Previously, before coming into the measuring tank, the output organic is processed to obtain fine homogeneous mass.

Device head is attached to the top of the working chamber with the flange connections; the diameter of which (head) is approximately two times bigger than the diameter of the working chamber. Thus, the space inside of the head is a separation zone.

These steps ensure minimization of granules entrainment with the exhaust air. However, some suspension drops together with air are taken outside the device, and liquid chicken manure has a specific and unpleasant odor. To solve this problem the exhaust air is sent to the laboratory exhaust device through air corrugations.

Experimental study of the formation and enlargement of polydispersed particles dispersed in the fluidized bed is carried out by means of supplying the chicken manure suspension at a rate of 25 ml/min. The suspension of granulated chicken manure, the so-called seed is loaded onto the air distributor plate of the laboratory setup. Then one by one the blower and the heater are turned on. One sets the necessary speed of the upward air flow which creates the fluidized bed.

Chicken manure suspension is sprayed into the layer of the suspended granules with the air nozzle and the compressor. After each 20 min of the setup operation one turned it off and conducted the sieve analysis of the formed granules. Then the setup

was put into operation again and one continued the experiment. Thus, for each subsequent 20-min process the output granules loaded into the working chamber were the final granules obtained in the previous experiment.

4   Results

4.1   Temperature Regimes for Organic Suspension Granulation in the Fluidized Bed Apparatus

A feature of using the chicken manure is that one disperses not a solution into the fluidized bed, as in the case of mineral fertilizers granulation, but a suspension. In this case, the mechanism of granule enlargement is complex and it essentially depends on the suspension specifics and on the process condition, which determine the interaction nature of the suspension and dispersed solid phase. That is, the granule growth rate depends on: drop spreading time and evaporation rate of the suspension liquid phase.

During laboratory tests the temperature under the air distributor plate was controlled in the range of 50–100 °C, while the air temperature in the granules layer was in the range of 40–80 °C. Temperature drop occurs because the granules boiling layer is constantly supplied with the wet substance which evaporates and removes heat. Therefore, the changing air temperature under the plate, and thus in the layer, controls the whole process. There have been experimentally determined the following temperature regimes of the granulation process:

– shell mode – when the air temperature in the layer is in the range of 60–65 °C the suspension spreads over the granule surface and moisture begins to evaporate rapidly, forming a solid layer of dry organic matter;
– nonuniform shell mode (with crackles) – an increase of bed temperature to 70–80 °C leads to the formation of an uneven surface with deep cracks. It is followed by the cleavage of solids in some places of the granules surface, which provides the formation of new organic granulation centers.

The main indicator of coating quality, in the case of fertilizer granules encapsulating with chicken manure, is the shell of certain thickness which is uniformly distributed over the granule surface and which completely covers mineral core with solid organic layer (see Fig. 2a). Thus, the shell mode is a working mode which allows growing all the granules to marketable size.

If one maintains air temperature within 70–80 °C, two processes simultaneously occur in the layer – granules build-up (enlargement) and the formation of a small amount of fine particles. This temperature regime is the operating mode for the preparation of organic fertilizers and it provides constant operation of the apparatus for a long time with continuous producing of granules of marketable size. As a result one obtains the multi-layered granules of given particle size distribution, having very high density and strength (see Fig. 2b).

a)   b)
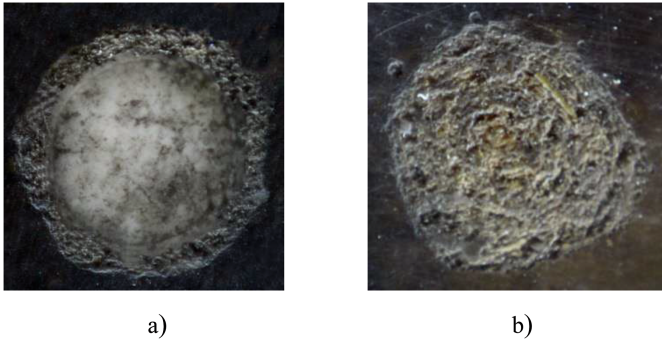
Fig. 2. Granules cuts (20 times magnified): a – two-component organo-mineral granules (carbamide + chicken manure); b – organic granules (chicken manure).

4.2 Theoretical Regularities of Granule Temperature Change in a Fluidized Bed

Heat transfer and, consequently, change in granule temperature in the selected volume of the fluidized bed ΔV along the direction of «x» is effected due to: (1) heat entering the volume of granules from the nearest layers; (2) heat, which leaves the elemental volume of granules; (3) heat from the drying agent, which is brought to the surface of granules due to convection; (4) heat leaving the volume with small particles, that are driven by a gas flow in the vertical direction of «y».

Thus, the equation of temperature change in a layer of granules will be written as:

$$\int_V \frac{\partial t(\tau)}{\partial \tau}\left(N \cdot \rho_G \cdot c_G \left[\int_0^\infty f(R)dR\right] \cdot V_G\right)dV = \int_V \frac{\partial t(x)}{\partial x}\left(N \cdot \rho_G \cdot c_G \cdot u_G \left[\int_0^\infty f(R)dR\right] \cdot V_G\right)dV -$$

$$- \int_V \frac{\partial t(\Delta x)}{\partial x}\left(N \cdot \rho_G \cdot c_G \cdot u_G \left[\int_0^\infty f(R)dR\right] \cdot V_G \cdot \theta_i\right)dV + \int_V \alpha(R,w) \cdot N \cdot F_G[t(R) - t_S] \tag{1}$$

$$\times \left[\int_0^\infty f(R,\tau)dR\right]dV - \int_V \frac{\partial t(y)}{\partial y}\left(N \cdot \rho_G \cdot c_G \cdot u_G \left[\int_0^\infty f(R)dR\right] \cdot V_G \cdot \theta_i\right)dV$$

In the Eq. (1), particle quantity in the layer of granules (pcs/m^3) is represented by [9]:

$$N = \frac{n \cdot \rho_G}{V_A \cdot \rho_A} = \frac{G_C}{V_G \int_0^\infty f(R)dR} \tag{2}$$

where n – number of particles per unit of time, s^{-1}; V_A – consumption of drying agent, m^3/s; ρ_G, ρ_A – density of granules and drying agent, respectively, kg/m^3; G_C – consumption concentration of the suspended layer of granules, kg/kg; V_G – initial volume of granules, m^3; $f(R)$ – function of radial distribution of granules.

Specific surface of granules in the selected layer volume, m^2/m^3:

$$F_{SP} = N \cdot F_T = \frac{6 \cdot (1 - \varepsilon)}{D} \tag{3}$$

where ε –singularity of the fluidized bed; D – diameter of granules, m.

We believe that in the fluidized bed, as a result of the active mixing of particles there is no heat transfer and no change in the layer temperature due to the convective movement of solid particles in the direction of «x». The transfer of particles from the gas flow layer is also neglected. Then, rejecting the integration symbols due to the randomness of the chosen volume and taking into account the normalization condition of the granule size distribution, one obtains the Eq. (1) in the following form:

$$G_C \cdot \rho_G \cdot c_G \frac{dt}{d\tau} = \frac{\alpha(R, w) \cdot 6 \cdot (1 - \varepsilon) \cdot [t(R) - t_S]}{D} \tag{4}$$

Solving the Eq. (4) under the initial and boundary conditions, one obtains the equation for determining the temperature of granules in the fluidized bed (5) or heating temperature of the granule (6):

$$t(\Delta\tau) = t(\tau) \cdot \exp\left(\frac{\alpha(R, w) \cdot 6 \cdot (1 - \varepsilon)}{G_C \cdot \rho_G \cdot c_G \cdot D}\right) \cdot \tau \tag{5}$$

$$t_K = t_I \cdot \exp\left(\frac{\alpha(R, w) \cdot 6 \cdot (1 - \varepsilon)}{G_C \cdot \rho_G \cdot c_G \cdot D}\right) \cdot \tau_H \tag{6}$$

where τ_H – duration of granule heating to reach the predetermined temperature when moisture starts evaporating from the suspension film on the surface of the granule, s.

Dependences (5) and (6) are obtained under the boundary conditions of the third order andare the function of the Bio criterion [9]. Analysis of the dependence (6) shows that the change in the temperature of the granule surface depends primarily on the coefficient of heat transfer from the drying agent, as surface area and the properties of granules.

4.3   Study Results of Temperature Influence on the Kinetics of Granule Formation in a Fluidized Bed

Experimental results of the granulation kinetics of chicken manure suspension in the fluidized bed are shown in Figs. 3 and 4.

The shell mode allows obtaining two component fertilizers that combine the nutrients of organic and mineral origin in the quantity required for their application with respect to the agronomic conditions in the region. Organic shell of the dry chicken manure laid on the surface of the mineral granules modifies them into a new product with the new physical and chemical properties.

Effective period of the encapsulated fertilizers is very important and it is determined by the time the target component is released from the containment. Thus, by changing
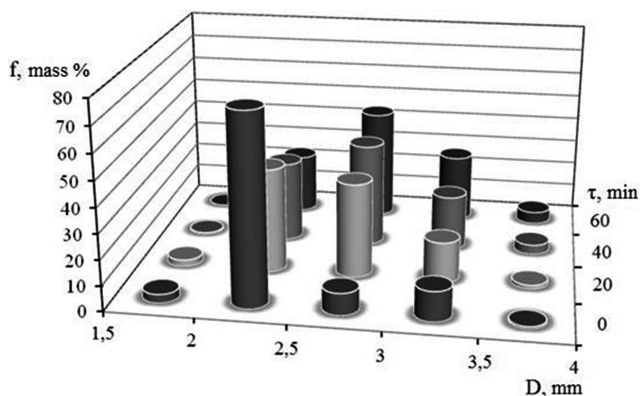
Fig. 3. Histograms of the particle size distribution at different times during encapsulation of the carbamide granules with the chicken manure shell.
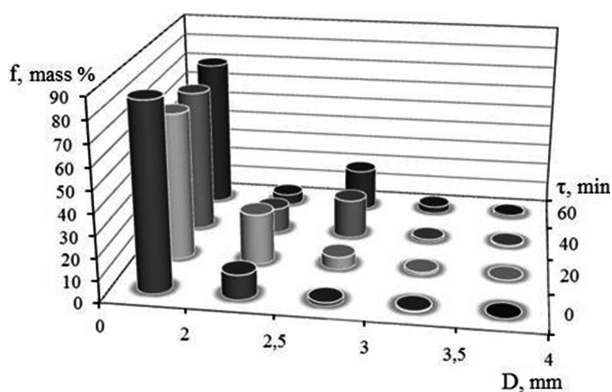
Fig. 4. Histograms of the particle size distribution at different times during granulation of the chicken manure.

the organic coating thickness we can receive three types of the encapsulated granules with the effective period: 3–4, 5–6 and 12–14 months [10].

Histograms of the particle size distribution (see Fig. 3) show that in the process of encapsulation maximum of a function is shifted towards increasing the granules size. This distribution curve changes its shape and has one maximum value. It means that in the shell mode the organic substance is attached to the particle surface and forms a solid layer and this layer does not chip on the granules surface.

If granulation process is carried out under the conditions typical for the unstable shell mode – it favors the bimodal processes (see Fig. 4): when the particle size is increased and also the reverse processes take place, due to abrasion and chipping from the granules surface, new granulation centers are formed which provide the formation of fine particles in the layer.

Harmonious combination of these processes provides the continuous operation of the apparatus and unit as a whole. And the resulting multi-layer single-component product has increased strength and density.

5   Conclusions

The proposed technology for producing the organic-based granules in a fluidized bed apparatus enables to increase the obtained fertilizers efficiency and to minimize the quantitative incorporation of fertilizers into the soil, and so it provides much less environmental pollution.

The operating temperature regimes of suspension granulation in the fluidized bed are experimentally determined, namely: at the air temperature of 60–65 °C in the layer of granules, a solid layer of organic shell is formed on the surface of the mineral particle. The temperature of 70–80 °C ensures the continuous operation of the plant to produce complete organic granules.

Analytical dependencies are obtained to determine the time and temperature of granule heating, which makes it possible to predict the energy costs of granular fertilizer production, to increase the economic indices of this production and to optimize the process.

References

1. Jarchow, M.E., Liebman, M.: Nitrogen fertilization increases diversity and productivity of prairie communities used for bioenergy. GCB Bioenergy **5**(3), 281–289 (2012)
2. Goertz, H.M., Timmons, R.J., Johnson, W.R.: Precoated controlled release fertilizers and processes for their preparation. Patent No. 6039781 A, United States (2008)
3. Gupta, S.K., Singhvi, I.J., Shirsat, M.K., Karwani, G., Agarwal, A.: Microencapsulation techniques and its application in pharmaceutical. Asian J. Pharm. Sci. Clin. Res. **1**(3), 67–77 (2011)
4. Politi, G., Heilakka, E.: Granules, tablets and granulation. Patent No. 20080111269, United States (2008)
5. Jordon, S., Jordan, J.: Controlled release fertilizer and system and method. Patent No. 7674313 B2, United States (2010)
6. Mente, D.: Encapsulated Particle. Patent No. 2396237, Russia, Ch. (2010)
7. Izquierdo-Barrientos, M.A., Sobrino, C., Almendros-Ibàñez, J.A.: Thermal energy storage in a fluidized bed of PCM. Chem. Eng. J. **230**, 573–583 (2013)
8. Niedziela, D., Schmidt, S., Steiner, K., Zausch, J., Zemerli, C.: Continuum numerical simulation of multiphase granular suspension flow in the context of applications for the mechanical processing industry. Int. J. Miner. Process. **136**, 50–55 (2015)

9. Ostroha, R.O., Yukhymenko, M.P., Mikhajlovskiy, Y.E., Litvinenko, A.V.: Technology of producing granular fertilizers on the organic basis. East. Eur. J. Enterp. Technol. Ser. Technol. Organ. Inorgan. Subst. **1/6**(79), 19–26 (2016)
10. Nawozy wolnodzialajace: Oznaczanie uwalniania skladnikow odzywczych. Metoda dla nawozow otoczkowanych. Norma europejska EN 13266:2001, 12, Poland (2003)

Design and Study of Conical Pressure-Swirl Atomizers

Marek Ochowiak[1]([✉]), Olha Lytvynenko[2], Sylwia Włodarczak[1],
Magdalena Matuszak[1], and Andżelika Krupińska[1]

[1] Poznan University of Technology,
4 Berdychowo, 61131 Poznan, Poland
`marek.ochowiak@put.poznan.pl`
[2] Sumy State University,
2 Rymskogo-Korsakova Street, Sumy 40007, Ukraine

Abstract. The paper shows the results of experimental studies for two-phase swirl atomizers with two inlet ports different in terms of design. The effect of volumetric liquid and gas flow rate and the height and diameter of mixing chamber on the discharge coefficients, histograms, radial distributions of mean droplet diameters in the drop stream and the mean Sauter diameter were determined. The studies were conducted within the air flow rates not exceeding $5.6 \cdot 10^{-4}$ [m³/s] and water flow rate $1.11 \cdot 10^{-5}$ [m³/s]. It was shown that the discharge coefficient increases with the higher Reynolds number for the liquid and decreases with the higher gas flow rate. The increased liquid flow rate caused greater drop diameters and increased gas flow rate allowed to obtain droplets with smaller sizes. The value of Sauter means that the diameter is dependent on the ratio of height to the diameter of mixing chamber. The rapid increase in the mean droplet diameter occurs above the value of $H_S/D_S \approx 2.75$. It was further noted that higher gas flow rate within the aerosol axis gives rise to the drops with smaller diameters and there is a clear difference in the size of droplets between the central stream area and its edges. In addition, the empirical correlation was proposed for the discharge coefficient as a function of work characteristics and geometric dimensions of the atomizer. The obtained data can be used for designing new atomizers and are essential from the viewpoint of agriculture or combustion processes.

Keywords: Construction of atomizer · Discharge coefficient
Droplet size histogram · Sauter mean diameter

1 Introduction

Atomizers are mainly designed based on the experimental data and the design comes down to the initial technical documentation, constructing an atomizer and conducting experimental tests. The analysis of current work on dispersing liquid with the use of swirling motion indicates that we know the method of basic calculations of pressure-swirl atomizers with a relatively simple design quite well. Only in this case, we can use the theoretical formulas in which, however, not all the structural features and properties of the dispersed liquid are taken into account [1, 2]. Other data come

only from the results of the experimental methods. The main reason for this approach is the complexity of the flow and in case of two-phase atomizers – the interaction between the gas and the liquid phase and an unclear character of this phenomenon. Despite the growing number of scientific works on this issue, there are still no works that would allow summarizing the achievements in this field. It should be stated that the existing works in many cases are only fragmentary and discuss the specific geometric solutions of dispersing systems failing to cover the issue comprehensively [3].

The atomizer designing process consists of several stages:

1. placing the diameter of atomizer outlet of the pressure-swirl atomizer;
2. calculating discharge coefficient;
3. calculating the filling degree of the atomizer outlet of the atomizer by the liquid;
4. calculating geometric constants of the atomizer;
5. possible attempt to determine the characteristics of the dispersed stream, such as the spray angle and mean droplet diameter.

2 Literature Review

2.1 Discharge Coefficient

The discharge coefficient is one of the most important characteristics of pressure-swirl atomizers including their efficiency:

$$C_D = \frac{w_L \cdot \rho_L}{(2\rho_L \cdot \Delta P)^{0.5}} \tag{1}$$

It defines the atomizer's capacity at the given injection conditions [14]. The analysis of literature data conducted by Hong et al. [4] showed that the discharge coefficient can be described with one generalized dependency:

$$C_D = a \left(\frac{nA_k}{d_0^2} \right)^{n_1} \beta'^{-n_2} \tag{2}$$

in which the exponents n_1 and n_2 are greater than 0. Values of exponents are shown in Table 1.

The most common equation in designing is the Jones equation [13]:

$$C_D = 0.45 \left(\frac{w d_0 \rho_L}{\eta_L} \right)^{-0.02} \left(\frac{l_0}{d_0} \right)^{-0.03} \left(\frac{H_s}{D_s} \right)^{0.05} \left(\frac{nA_k}{D_s d_0} \right)^{0.52} \left(\frac{D_s}{d_0} \right)^{0.23} \tag{3}$$

Table 1. Values of exponents from Eq. (5) [4]

Equation	n_1	n_2	C_D
Abramowicz [5]	0.64	0.64	$f(A)$
Kulagin and Moroshkin [6]	0.69	0.69	
Khavkin [7]	$\frac{1.345}{\beta'^{0.874}}$	$\frac{1.345}{\beta'^{0.874}}$	
Taylor [8] (Lefebvre [1], Rizk and Lefebvre [9])	0.5	0.5	$f\left(K, \frac{D_s}{d_0}\right)$
Carlisle [10]	1.0	0	
Eisenklam [11]	1.0	0.1–0.5	
Dombrowski and Hasson [12]	1.0	0.5	
Jones [12]	0.52	0.29	
Rizk and Lefebvre [9]	0.5	0.25	

2.2   Sauter Mean Diameter

The most important general aerosol characteristic is considered the Sauter mean diameter (SMD, D_{32}), which defines the dependence:

$$SMD = \frac{\sum_{i=1}^{i=j} n_i d_i^3}{\sum_{i=1}^{i=j} n_i d_i^2} \qquad (4)$$

For pressure-swirl atomizers, there is a generalized correlation for anticipating the mean size of droplets as follows [15–17]:

$$SMD \propto \sigma^a \cdot \rho_C^b \cdot \eta_C^b \cdot \dot{m}_C^c \cdot \Delta P^d \qquad (5)$$

Wang and Lefebvre [17] showed the correlation for pressure-swirl atomizers with a different design that considers liquids with a viscosity and surface tension:

$$SMD = 4.52 \left(\frac{\sigma \cdot \eta_L^2}{\rho_G \cdot \Delta P_i^2}\right)^{0.25} \left(t \cos \frac{\theta}{2}\right)^{0.25} + 0.39 \left(\frac{\sigma \cdot \rho_L}{\rho_G \cdot \Delta P}\right)^{0.25} \left(t \cos \frac{\theta}{2}\right)^{0.75} \qquad (6)$$

where t is the thickness of liquid film at the atomizer outlet.

The paper shows the design of a conical swirl-pressure atomizer and discusses the literature data and own studies on the parameters characteristic for the atomization process, i.e. discharge coefficient, mean droplet diameter and liquid distribution in a dispersed stream.

3   Research Methodology

The experimental set-up consisted of pressure-swirl atomizers, container, rotameters of Krohne Messtechnik type VA 40, pump CHI 2-30 by Grunfos Poland, compressor Metabo Mega350-100D digital thermometer Center 309, coil, digital pressure meter DigiComb 1900, camera Canon EOS-1D Mark III with stroboscopic lamp and a PC with appropriate software. Tested were swirl atomizers with two inlet ports with a diameter $d_p = 0.0025$ m (Fig. 1). The diameter of swirl chamber D_s (used as a mixing chamber of gaseous and liquid phase) was 0.02 m and its height H_s ranged of 0.02 to 0.08 m. The diameter of outlet hole d_0 was 0.0025 m. The tests were conducted within the air flow rates not exceeding $5.6 \cdot 10^{-4}$ [m^3/s] and water flow rate $1.11 \cdot 10^{-5}$ [m^3/s]. Tests were conducted at $T = 20 \pm 1$ °C. For determining the diameters of droplets, Image-Pro Plus by Media Cybernetics software was used.

Atomizer	H_s [m]
CSA1	0.02
CSA2	0.04
CSA3	0.06
CSA4	0.08
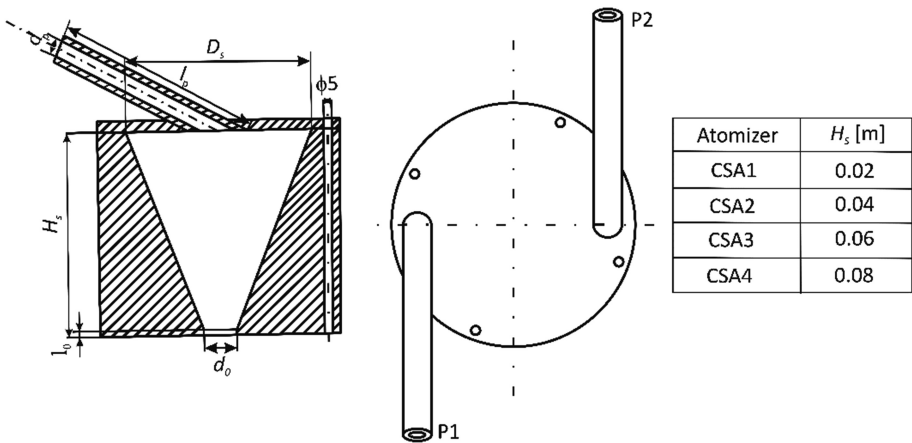
Fig. 1.   Pressure-swirl atomizers tested.

4   Results

To Know the discharge coefficient is very important for designing the atomizers [1]. Figure 2a shows an example dependence of the discharge coefficient from the Reynolds number for gas and liquid for CSA2 atomizer. It was shown that the liquid discharge coefficient for analyzed atomizer structures increases with the higher Re_L, and with the increased Re_G – it is smaller. It was further showed that the discharge coefficient increases with the decreased chamber height H_s (Fig. 2b). However, the effect of the chamber is small.

The analyzed experimental data of the dependence of the discharge coefficient from dimensionless numbers Re_G, Re_L, Fr_G and the atomizer's geometrical module H_s/d_0 provided the following empirical relation:
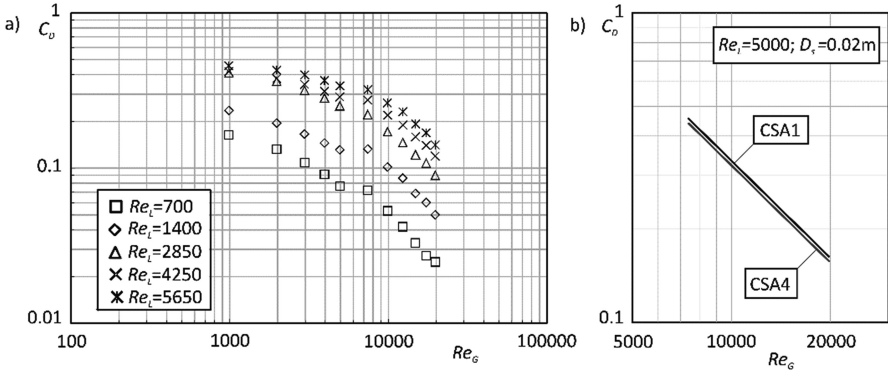
Fig. 2. Example relations between discharge coefficient and gas and liquid Reynolds numbers: (a) for CSA2 atomizer; (b) for atomizers differing in height of mixing chamber.

$$C_D = 0.701 \cdot Re_G^{0.77} \cdot Re_L^{-0.94} \cdot Fr_G^{0.14} \cdot \left(\frac{H_s}{d_0}\right)^{-0.03} \pm 15\% \tag{7}$$

in which the Reynolds number for liquid was defined as follows:

$$Re_L = \frac{w_L \cdot d_0 \cdot \rho_L}{\eta_L} \tag{8}$$

gas Reynolds number:

$$Re_G = \frac{w_G \cdot d_0 \cdot \rho_G}{\eta_G} \tag{9}$$

and Froude number:

$$Fr_G = \frac{w_G^2}{g \cdot d_0} \tag{10}$$

The offered equation is true within variable numbers of $Re_L \in (1000; 5500)$, $Re_G \in (5000; 20000)$, $Fr_G \in (70000; 500000)$, and the geometric module $H_s/d_0 \in (8; 32)$. It is used to develop a non-linear estimation with smallest squares method with Levenberg-Marquardt non-linear optimization algorithm. The discrepancies between the experimental values and equation values (7) do not exceed $\pm15\%$.

In this paper, the relations of H_s/D_s were 1 to 4. The relations of the height to the diameter of the swirl chamber should be low to minimize any friction loss. However, a proper height should be planned to separate the streams flowing out through the liquid inflow inlet ports. For many designs, the relations of H_s/D_s from 0.5 to 1.0 were assumed although it was suggested that higher values of H_s/D_s, up to the value of less than 2.75, may improve atomizing [18, 19].
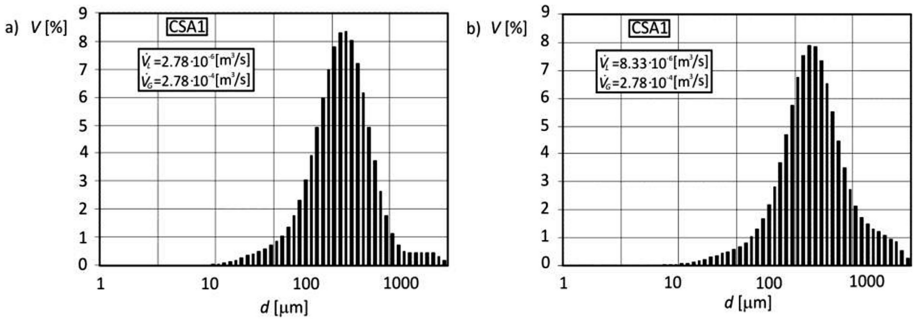
Fig. 3. Example droplet size distributions for CSA1 atomizer at a volumetric gas flow rate $\dot{V}_G = 2.78 \cdot 10^{-4}$ [m³/s]: (a) at $\dot{V}_L = 2.78 \cdot 10^{-6}$ [m³/s]; (b) at $\dot{V}_L = 8.33 \cdot 10^{-6}$ [m³/s].

Figure 3 shows the example of the droplet size distributions. Based on the results, it can be noted that for the higher liquid flow rate there are more droplets with higher diameters at a lower number of droplets with medium sizes. At the same gas and liquid flow rate and higher relation H_s/D_s more droplets were formed with greater diameters and more droplets of medium sizes

Figure 4 shows some radial distributions of mean droplet diameters within a liquid stream. The relation H_s/D_s impacts the radial distribution, which can be seen particularly within the central aerosol area. Smaller droplet diameters are obtained for the atomizer with higher H_s/D_s.
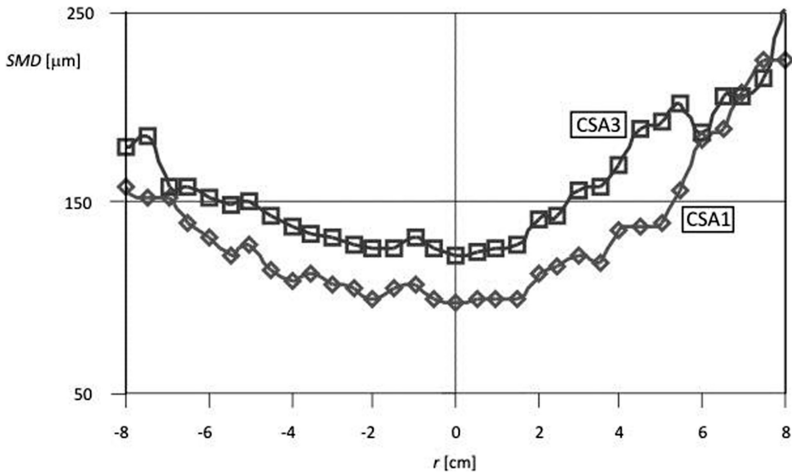
Fig. 4. Distribution of mean droplet diameters within liquid stream at volumetric liquid flow rate $\dot{V}_L = 8.33 \cdot 10^{-6}$ [m³/s] and volumetric gas flow rate $\dot{V}_G = 2.78 \cdot 10^{-4}$ [m³/s] (r – distance from aerosol axis).

Figure 5 shows the dependence between the mean droplet diameter and the relation H_S/D_S and from the gas flow rate at the constant liquid flow rate. Based on achieved results, it can be concluded that the relation H_s/D_s has a considerable effect on the mean value of the Sauter diameter only after exceeding a certain constant value (ca. $H_s/D_s = 2.75$). The increased mean drop diameter is then observed. These results partially correspond to the literature data shown by Elkotb et al. [19], where the smallest droplets were obtained for $H_s/D_s = 2.75$ for atomizers with the relation H_s/D_s of 0.25 to 0.4. The increased gas flow rate causes the formation of droplets with smaller diameters. It can be further observed that along with the higher volumetric gas flow rate, the Sauter mean diameter decreases.
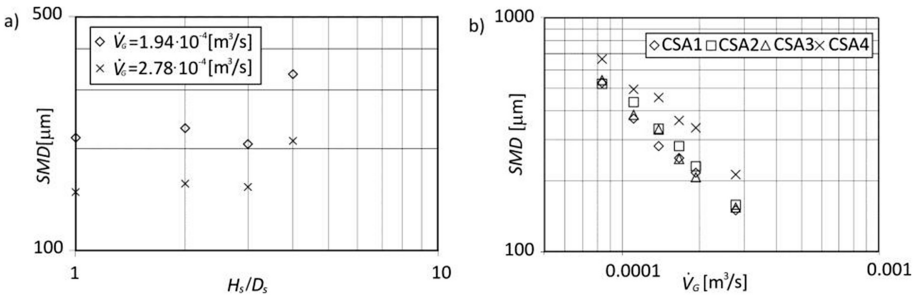
Fig. 5. Dependence of Sauter mean diameter from: a – H_s/D_s at liquid flow rate $\dot{V}_L = = 8.33 \cdot 10^{-6}$ [m³/s]; b – gas flow rate at volumetric liquid flow rate $\dot{V}_L = 8.33\cdot10^{-6}$ [m³/s].

5   Conclusions

The paper determines the discharge coefficient values, volumetric and radial distribution, sizes of the droplets in the liquid stream and mean values of Sauter mean diameter achieved during the atomization with two-phase pressure-swirl atomizers. Atomizers differ in terms of the relation of the height to the mixing chamber diameter. Studies were conducted at variable liquid and gas volumetric flow rate.

It was shown that the discharge coefficient depends on the Reynolds number for gas and liquid. The increase of Reynolds number for the liquid cases the increase of discharge coefficient and the increase of Reynolds number for the gas causes its decrease. A small effect of the mixing chamber height was also observed. Reduced height resulted in higher discharge coefficient. In addition, a correlation equation was offered that describes the discharge coefficient in the function of Reynolds number for the gas and liquid, Froude number and relation of the mixing chamber height to the atomizer outlet diameter.

It was also shown that the increased gas flow rate causes filling of the central stream area with the drops of lower diameters and decreased Sauter mean diameter. The analysis of diameters of forming drops showed that the mean droplet diameter depends on the value of H_s/D_s. It should be noted that a sudden increase of the Sauter mean

diameter occurs above the value of $H_s/D_s \approx 2.75$. Based on the obtained volumetric distributions it was shown that with the increased liquid flow rate there are more droplets with higher diameters at a lower share of droplets with medium sizes. A similar dependence was observed along with the decreased relation H_s/D_s.

The results allow enlarging the knowledge on the phenomenon of two-phase atomization and the principle of operation of pressure-swirl atomizers, which may contribute to a more precise selection of atomizers and their wider application.

References

1. Lefebvre, A.H.: Atomization and Sprays. Hemisphere Publishing Corporation, New York (1989)
2. Orzechowski, Z., Prywer, J.: Wytwarzanie i zastosowanie rozpylonej cieczy. WNT, Warszawa (2008)
3. Ochowiak, M.: Analiza procesu rozpylania cieczy w rozpylaczach pęcherzykowych i pęcherzykowo-wirowych. Rozprawy Nr 519, Wydawnictwo Politechniki Poznańskiej, Poznań (2014)
4. Hong, M., Jeon, J., Lee, S.Y.: Influence of ambient air pressure on effervescent atomization. J. Propuls. Power **28**(1), 13–217 (2012)
5. Abramovich, G.N.: The Theory of Swirl Atomizer. Industrial Aerodynamics, Bureau of Advanced Technology, pp. 114–285. Central Institute of Aerohydrodynamics, Moscow (1944)
6. Kulagin, L.W., Moroshkin, M.I.: Atomization for Heavy Fuel Oil. Mashinostroenie, Moscow (1966)
7. Khavkin, Y.I.: Theory and Practice of Swirl Atomizers. Taylor & Francis, New York (2004)
8. Taylor, G.I.: The mechanics of swirl atomizers. In: Proceedings of the Seventh International Congress of Applied Mechanics. Cambridge University, New York, vol. 2, pp. 280–285 (1948)
9. Rizk, N.K., Lefebvre, A.H.: International flow characteristics of simplex swirl atomizers. J. Propul. Power **3**, 193–199 (1985)
10. Carlisle, D.R.: Communication on the performance of a type of swirl atomizer, by A. Radcliffe. Proc. Inst. Mech. Eng. **169**, 101–106 (1955)
11. Eisenklam, P.: Atomization of liquid fuels for combustion. J. Inst. Fuel **34**, 130–143 (1961)
12. Dombrowski, N., Hasson, D.: The flow characteristics of swirl (centrifugal) spray pressure nozzles with low viscosity liquids. AIChE J. **15**(4), 604–611 (1969)
13. Jones, A.R.: Design optimization of a large pressure jet atomizer for power plant. In: Proceedings of the Second International Conference on Liquid Atomization and Spray Systems, ICLASS-82, Madison, pp. 181–185 (1982)
14. Som, S.K., Mukherjee, S.G.: Theoretical and experimental on the coefficient of discharge and spray cone angle of swirl spray atomizing nozzle. Acta Mech. **32**, 79–102 (1980)
15. Radcliffe, A.: Fuel injection, High Speed Aerodynamics and Jet Propulsion, vol. XI, Sect. D. Princeton University Press, Princeton, NJ (1960)
16. Jasuja, A.K.: Atomization of crude and residual fuel oils. J. Eng. Gas Turbines Power **101**, 250–258 (1979)

17. Wang, X.F., Lefebvre, A.H.: Mean drop sizes from pressure-swirl nozzles. J. Propul. Power **3**, 11–18 (1987)
18. Jones, A.R.: Design optimization of a large pressure jet atomizer for power plant. In: Proceedings of the Second International Conference on Liquid Atomization and Spray Systems, ICLASS-82, Madison, pp. 181–185 (1982)
19. Elkotb, M.M., Rafat, N.M., Hanna, M.A.: The influence of swirl atomizer geometry on the atomization performance. In: Proceedings of the 1st International Conference on Liquid Atomization and Spray Systems, Tokyo, pp. 109–115 (1978)

Investigation of the Process of Saturation of the Filter Liquid of Soda Production with Ammonia and Carbon Dioxide in the Production of Ammonium Chloride

Inna Pitak[(✉)] , Valery Shaporev , Oleg Pitak , Alina Hrubnik ,
and Viktor Moiseev

National Technical University, "Kharkiv Polytechnic Institute", 2 Kirpichova St.,
Kharkiv 61002, Ukraine
ipitak5@gmail.com

Abstract. This paper is focused on the saturation process of the filter liquid of soda production with ammonia and carbon dioxide in the production of ammonium chloride. In the world practice, there are many ways to produce ammonium chloride from the filter liquid. These ways of ammonium chloride production suppose progressive saturation of the filter liquid with ammonia and carbon dioxide. This paper is focused on identifying the optimal conditions for conducting the process. For this purpose, the saturation of the filter liquid with gases both in sequential and simultaneous feeding to the apparatus at total flow of 1.5–6.0 dm^3/min and at temperature of test solution of 15–50 °C was studied. The comparison of material balances of consecutive and simultaneous supply of ammonia and carbon dioxide shows that the process in one apparatus allows reducing the gas consumption factor by approximately 14.4%. Thus, as a result, the method for simultaneous supply of gases is proposed in order to obtain high degree of saturation with ammonia and carbon dioxide of the filter liquid followed by the production of ammonium chloride by the salting out method.

Keywords: Process · Liquid of soda · Ammonium chloride

1 Introduction

Mass exchange processes of gas absorption by liquid solutions are accompanied by physico-chemical transformations in liquid with the formation and crystallization of a new solid phase. These processes are widespread in chemical and processing industries. Such processes are referred to as combined reaction-mass-exchange processes. The organization of most of these processes is based on empirical approach. The research of processes in soda production resulted in the limited data. Although, these data could reveal mechanisms of processes intensification that occur in the apparatus and their mutual influence on each other. There are no reliable data on the kinetics of processes and the influence of hydrodynamic factors on the kinetics. The mechanism of chemical transformations is not fully understood, the complex analysis of hydrodynamics, the

---

energy distribution in the system, and the characteristics of the gas phase, their effect on the kinetics of the absorption and crystallization processes have not been carried out.

In this regard, this research is aimed at clarifying the features of the flow of directed-organized combined processes and the development of specific technological methods, which constitute the relevance of the paper.

2   Literature Review

In soda production, one of the intermediate products is ammonium chloride, which is contained in the filter liquid. In the world practice, there are several ways to produce ammonium chloride from the filter liquid [1–3]. These ways of ammonium chloride production suppose progressive saturation of the filter liquid with ammonia and carbon dioxide. This is a link to the need to install additional column equipment, which presents certain difficulties in its maintenance [1, 4–6].

On favorable conditions of the process, the rate and degree of interaction of low-level lime grows and the process ends in 5–10 min. After that, the interaction speed drops rapidly. This is due to the development of side processes. As a result of hydration, dissolution and crystallization of hydrates, calcium ions bind to difficult soluble hydrosilicates of calcium and others.

In order to increase the degree of use of lime milk, it is advisable to process the decomposition of ammonium chloride in several stages. Thus, an increase in the degree of use of lime milk is aimed at creating conditions, when the inactive lime could participate in the reaction with ammonium chloride [5, 6].

It is known, that the process of interaction of low-activity lime with ammonium chloride takes place in the diffusion region and consists of several stages. This is due to the multilayer arrangement of impurities in the polydisperse lime granules [7].

It should be noted, that insufficient certainty of the kinetic patterns of ammonia use in the process of regeneration in the reactor of the injection-type would require additional research in this direction [8–11].

The most promising way to produce ammonium chloride is the method of salting out with a preliminary preparation of the filter liquid by simultaneous saturation with ammonia and carbon dioxide [12–16].

3   Research Methodology

This paper is focused at identifying the optimal conditions for conducting the process. For this purpose, it was studied the saturation of the filter liquid with gases both in sequential and simultaneous feeding to the apparatus at total flow of 1.5–6.0 dm^3/min and at temperature of the test solution of 15–50 °C. For the stuy we used a filter liquid with a molar concentration of equivalents: NH_{3total} 59.92; Cl $\sim$ 76.00; CO_2 20.47; direct titre 13.73. We have carried out experiments in a column with capacity of 4 L; we took the samples from the top and bottom of the column every 10 min. The duration of the experiments was 60–200 min.

To intensify the process of NH_3 and CO_2 sorption, the following hydrodynamic factors are used: liquid circulation in column or its pulsation with vibration amplitude of 460 mm, which corresponds to frequency of 0.8 Hz.

Figure 1 shows carbonization degree over time of liquid saturation with ammonia up to 96.82 n.p., depending on its temperature.

$1 - 40^oC; 2 - 30^oC; 3 - 50^oC; 4 - 15^oC$
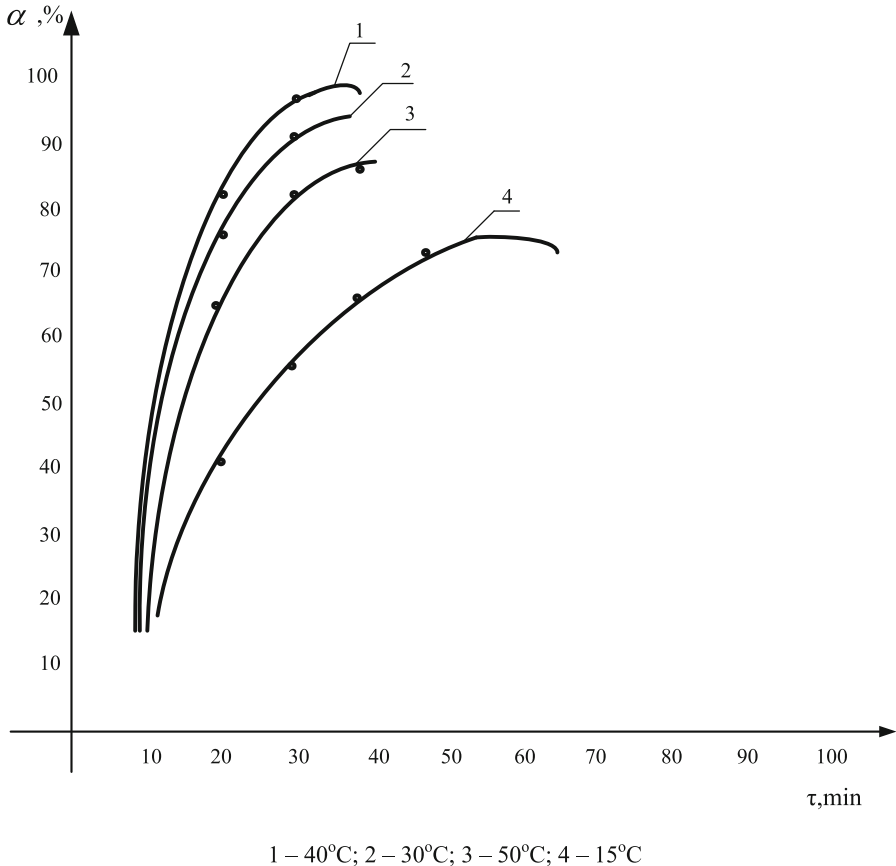
Fig. 1. Effect of temperature on carbonization kinetics of filter liquid.

4   Results

The results analysis shows that the process of carbonization is the most expedient to conduct at the temperature range 30–40 °C, since specified degree of carbonization of 80–90% has been achieved in 30 min. All curves show inflection, which corresponds to an intensive precipitation of the solid precipitate, which is identified as NH_4HCO_3. The increase in temperature above 60 °C led to significant decomposition of carbonate compounds and decrease in mass concentration of NH_3 and CO_2. The results of the

studies carried out during the sequential and simultaneous saturation of the filter liquid with ammonia and carbon dioxide using the circulation regime are shown in Fig. 2.
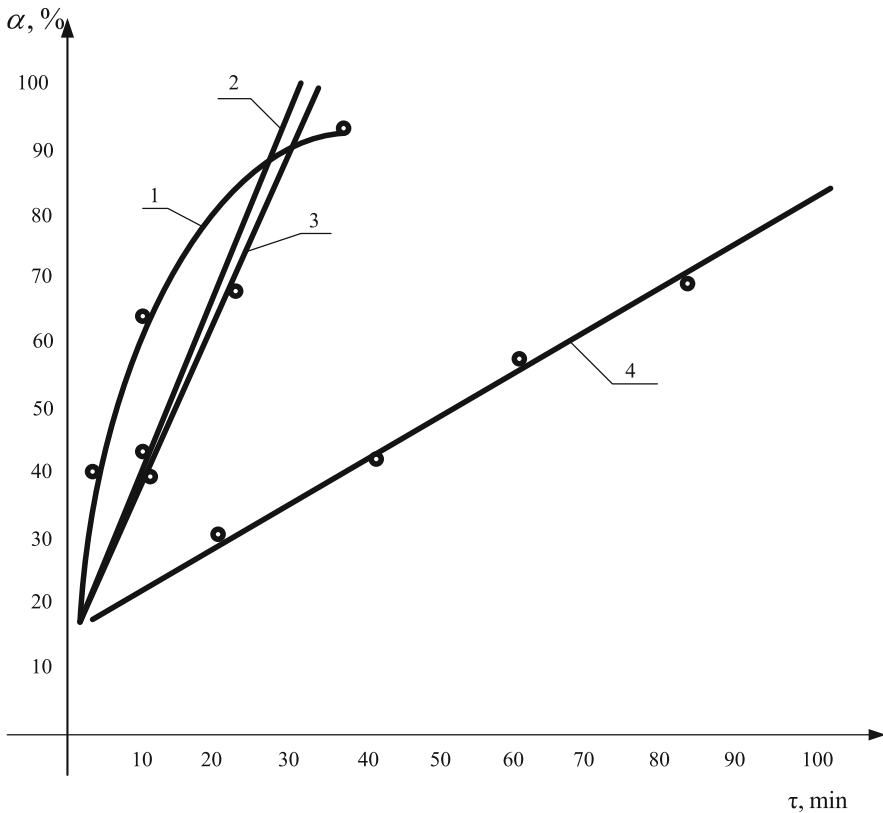
Fig. 2. Dependence of the degree of carbonization and ammoniation of the filter liquid in time on the gas supply method: 1 − carbonization in the sequential supply of gases; 2 − the same for simultaneous supply; 3 − ammoniation with simultaneous supply of gases; 4 − the same for sequential supply.

From the data in Fig. 2, it follows that ammonia saturation of the filter liquid occurs evenly and is characterized on the graph by a straight line both with consecutive and simultaneous gas supply to the column. The saturation with carbon dioxide is characterized by a straight line only in the case of simultaneous gas supply. In the case of their sequential feeding, an inflection is observed which is characteristic for the given process temperature and corresponds to the onset of precipitation of NH_4HCO_3.

With simultaneous supply of gases and temperature of 40 °C, the entire process ends in 30 min, during this time mass concentration of NH_3 and CO_2 reaches the optimum values of 102 and 85 n.p., respectively.

The technological cycle of saturation with ammonia and then with carbon dioxide ends only in 170 min.

In addition, at CO_2 concentration above 80 n.p., ammonium bicarbonate begins to precipitate, which complicates the process.

The data on the effect of solution mixing on its saturation rate with ammonia and carbon dioxide in the column using the circulation or pulsation regime are shown in Fig. 3.
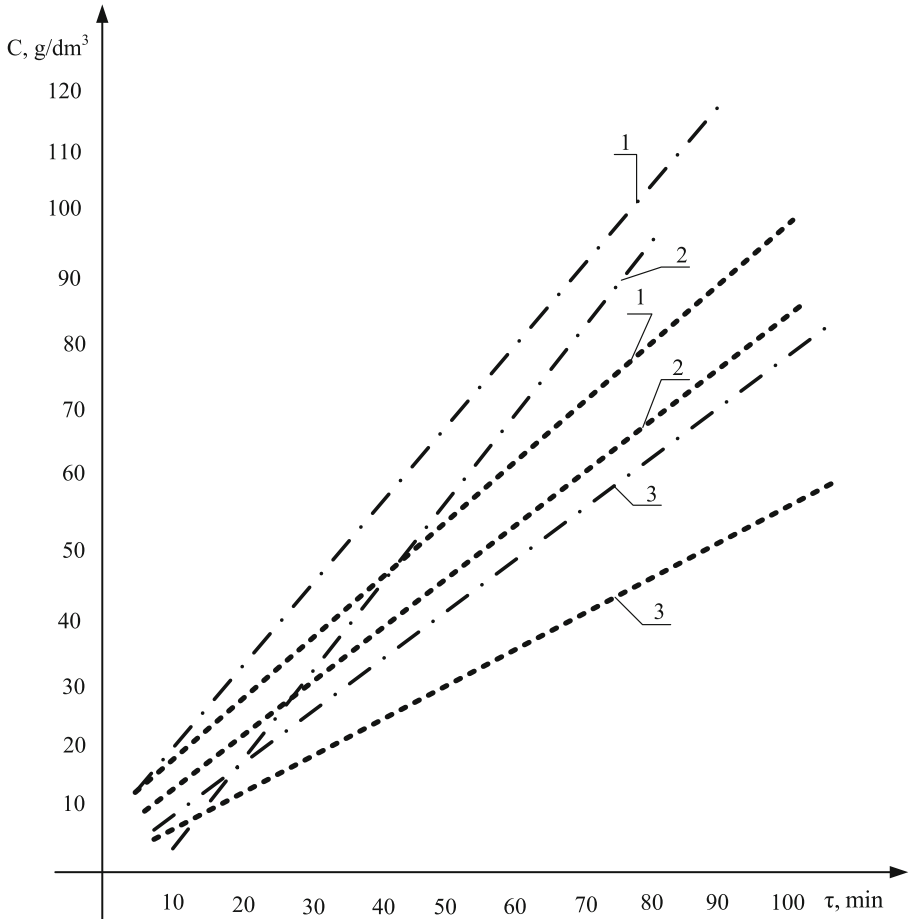
Fig. 3. Influence of the mixing method on the saturation rate of the filter liquid with ammonia and carbon dioxide: 1 − when the liquid is circulating; 2 − when the liquid is pulsed; 3 − without mixing ●●●●● − direct titer, ▬▬ − mass concentration of CO_2.

The analysis of the curves shown in the figure indicates positive effect on the process of hydrodynamic factors − circulation and pulsation, which significantly

accelerate it and allow to obtain uniform composition of the solution along the entire height of the column.

The study results of the effect of the ratio of the simultaneously supplied gases at 20 °C are presented in the Table 1. From the table, it follows that the required degree of carbonization (82%) is achieved at ratio of gas flow rates NH_3; and CO_2, equal to 1:0.75. With their ratio of 1:1, supersaturation of carbon dioxide rapidly sets in, which adversely affects the release of ammonium chloride during the salting out stage.

Table 1. Parameters of carbonization degree and ratio of NH_3 and CO_2 fed to the column.

Ratio NH_3: CO_2	Duration experience, mines	Ratio of NH_3:CO_2 in the liquid leaving the column		Degree of carbonation
		Column top	Bottom of the column	
1:0.5	0	1.09	1.09	–
1:0.5	20	0.86	0.64	63.64
1:0.5	100	0.80	0.72	71.59
1:0.75	0	1.09	1.09	–
1:0.75	30	0.62	0.48	46.74
1:0.75	60	0.69	0.66	66.18
1:0.75	90	0.86	0.78	78.85
1:0.75	100	0.86	0.80	82.0
1:1	0	1.09	1.09	–
1:1	30	1.17	1.30	130.22
1:1	60	1.08	1.08	108.76
1:1	90	1.01	0.98	99.15
1:1	100	1.01	0.88	88.27

The foregoing indicates that the highest degree of saturation of the filter liquid with ammonia and carbon dioxide can be obtained by simultaneous supply of gases at ratio of NH_3: CO_2 = 1:0.75 and process temperature of 30–40 °C.

The use of circulation and pulsation of the solution significantly accelerates the process and allows obtaining homogeneous composition of the solution. Based on the carried out study, the schematic diagram of a process unit for saturating the filter liquid with ammonia and carbon dioxide and its subsequent direction to an apparatus for NH_4C1 salting is proposed in Fig. 4. The installation consists of the capacity of the initial solution – the absorber column.

The latter is a vertical cylindrical vessel consisting of a rods set, which are connected together by rings. Between the regiments there are plates that serve to distribute the gas uniformly in the column and increase the contact surface of the gas and liquid. The structure of the plant includes a liquid collector 4 for saturated liquid with ammonia and carbon dioxide.
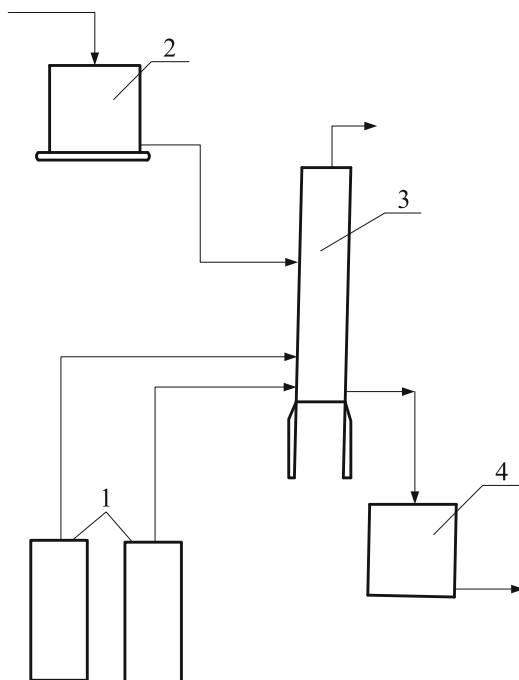
Fig. 4. Scheme of the process unit for saturation of the filter liquid with ammonia and carbon dioxide: 1 − cylinders with NH_3 and CO_2; 2 − reservoir with filter liquid; 3 − carbonation column; 4 − liquid collector.

5   Conclusions

The comparison of material balances of consecutive and simultaneous supply of ammonia and carbon dioxide shows that the process in one apparatus allows reducing the gas consumption factor by approximately 14.4%.

Thus, as a result of study, the method for simultaneous supply of gases is proposed to obtain high degree of saturation with ammonia and carbon dioxide of the filter liquid followed by the production of ammonium chloride by the salting out method. The obtained results can be used in modernization of soda production, in order to increase the productivity of carbonization columns and improve the quality of products.

References

1. Frumin, V.M., Gut, V.M., Burin, V.L., Oleichenko, T.V., Rida, M.R., Rezanov, M.R.: Methods of dry cleaning of calcination gas from soda dust chemistry and technology of production of the main chemical industry. Collect. Sci. Works GU NIOCHIM **78**, 52–57 (2016). (in Russian)
2. Yakimenko, Ya.: Some regularities of calcium oxide hydration activity. Eastern Eur. J. Enterp. Technol. **4**(6(70), 30–35 (2014). https://doi.org/10.15587/1729-4061.2014.26239

3. Shaporev, V., Pitak, I., Pitak, O., Briankin, S.: Study of functioning of vortex tube with a two-phase flow. East.-Eur. J. Enterp. Technol. **4**(10–88), 51–60 (2017)

4. Kasikowski, T., Buczkowski, R., Lemanowska, E.: Cleaner production in the ammonia-soda industry: an ecological and economic study. J. Environ. Manag. **73**, 339–356 (2004)

5. Mikhailova, E.N., Gridasov, V.N., Annopolsky, V.F., et al.: Increase in the use of carbonate raw materials in the regeneration of ammonia in soda production. Proc. NIOCHEM **73**, 64–65 (2003). (in Russian)

6. Zaikin, A.P.: Dispersion of the lime slurry used to decompose ammonium chloride in the distillation stage in soda production. Proc. NIOCHEM **76**, 25–31 (2010). (in Russian)

7. Zubakhin, Z.K., Gerasimenko, E.I., Revenko, S.S.: Interaction of low-active lime with ammonium chloride. Chem. Ind. **6**, 47 (1978). (in Russian)

8. Onac, B.P., Forti, P.: Minerogenetic mechanisms occurring in the cave environment: an overview. Int. J. Speleol. **40**(2), 79–98 (2011)

9. Kasikowski, T., Buczkowski, R., Dejewska, B., Peszynska-Bialczyk, K., Lemanowska, E., Iglinski, B.: Utilization of distiller waste from ammonia-soda processing. J. Clean. Prod. **12**(7), 759–769 (2004)

10. Kuzenko, Y.N., Olesyuk, V.I., Rusina, E.L., Kukhtenkov, K.M.: On the issue of improving the technology of lime milk for distillation in the Sterlitamak JSC "Soda". Proc. NIOCHEM **73**, 77–86 (2003). (in Russian)

11. Filonenko, D.V., Shestopalov, O.V.: On the issue of decomposition of ammonium chloride in the mixer reactor of the distillation unit of soda production. Bull. Natl. Tech. Univ. **7**, 120–126 (2014). (in Ukraine)

12. Kuzenko, Yu.N., Lebedenko, Yu.P., Mikhailova, E.N., Panasenko, V.A: Purification of solid sodium chloride in low-waste soda technology. Bull. Belgorod State Technol. Univ. named after V.G. Shukhov (1), 149–151 (2014) (in Russian)

13. Kathryn, S., Ash Khana, U.G., Simionia, M., Endoa, K., Zhaob, X., Zhaob, S.K., Qadera, A., Hoopera, B., Stevensa, G.: Recent developments in solvent absorption technologies at the CO_2. Energy Procedia **1**, 16 (2009)

14. Benkovsky, S.V., Krugly, S.M., Secovanov, S.K.: Technology of soda products. Chemistry, Moscow (1972). (in Russian)

15. Chernov, V.F.: Production of soda ash. Goskhimizdat, Moscow (1956). (in Russian)

16. Grinev, N.: The role of innovation in improving the efficiency of chlor-alkali industry enterprises. J. Legal Econ. Stud. **3**, 122–125 (2016). (in Russian)

Modelling of Liquid's Distribution and Migration in the Fibrous Filter Layer in the Process of Inertial-Filtering Separation

Vsevolod Sklabinskyi , Oleksandr Liaposhchenko ,
Ivan Pavlenko , Olha Lytvynenko(✉) ,
and Maryna Demianenko

Sumy State University, 2 Rymskogo-Korsakova St., Sumy 40007, Ukraine
{o.liaposhchenko, o.lytvynenko}@pohnp.sumdu.edu.ua

Abstract. The obtained solution of the mathematical model of liquid's distribution and migration in the filter layer as flow model in the fibrous environment, which describes the non-pressure filtration motion in the gravity field of the separated liquid film from the gas-drop flow, allows to determine the saturation conditions of the free volume of the filter layer, distribution of speed and pressure under the conditions of free liquid's movement in the filter layer, as well as to calculate the required cross-sectional area of the thin-layer fibrous filter element and the optimum height of the location of the overflow chutes for draining the separated liquid from the inertial-filtering to the drainage channels in order to avoid the secondary removal of droplets with the turbulent gas flow. As a result, the application rate of the separated liquid which falls from the filter element of the inertial-filtering separation channel to the drainage channels is obtained, as well as the dependence for the overflowed gutter of diverting the separated liquids from the inertial-filtering to the drainage channels is presented.

Keywords: Separation · Filtration · Gas–liquid flow · Filter element
Thin layer · Drainage channel

1 Introduction

The main process of dropping liquid separation from the gas-dropwise flow in the inertial-filtering separation channels occurs by the inertial mechanisms, and an additional level of separation is reached by the layout of the filtering elements and their partial passing through the gas-dropwise flow. The basic purpose of using these elements is the control of favorable conditions for extraction (drainage) of separated liquid in order to avoid its secondary removal with a turbulent gas flow. The main mechanisms of disperse particle settling on the fibers of filtering materials (contact effect or gearing, sieving effect, inertial collision, Brownian diffusion as the heat motion of highly dispersed particles, gravitational deposition, etc.) were studied by Fuks M.A., Uzhov V.M., Waldberg A. Yu., Miahkov B.I., Kirsh A.A. and others, whose works laid the foundations of the theory of filtration of aerodisperse systems [1–3].

2 Literature Review

The recent achievements in the field of modelling the processes of separation can be described and analyzed. Thus, research paper [4] is aimed at general approach for modelling of inertial-filtering gas separators and condensers, as well as for designing these devices for compressor units of oil and gas industry. The kinematic characteristics, such as radial relative velocity between particles suspended in turbulent flow for droplet collision and growth are presented in work [5, 6]. Analysis of the physical conditions of phase equilibrium is described in paper [7], as well as the impact of the heat and mass transfer on the reliability of separation processes in inertial-filtering separators is investigated. The experimental approach and numerical simulations are compared in work [8, 9] for evaluation the accuracy of the Stokes-drag model used for the investigation of inertial particles under the turbulent flow mode. In addition, paper [10] is devoted to the measurements of the evolution of lines, planes and volumes in the intensely turbulent laboratory flow using high-speed particle tracking. Sling effect in collisions of water droplets in turbulent clouds is investigated in work [11], and paper [12] is devoted to the effects of gravity on the acceleration and pair statistics of inertial particles in homogeneous isotropic turbulence. Statistical approach for the modelling turbulent collision of inertial particles in the turbulent flow is proposed in work [13]. Finally, research papers [14, 15] are devoted to realizing the numerical analysis of the separation process of gas-liquid mixtures, and experimental investigations of the two-phase gas-liquid flow in the divergent channels respectively.

3 Research Methodology

Based on the scientific works of predecessors, the following research is aimed at the modeling of the distribution and migration of the separated liquid in the fibrous filter layer located on the curvilinear sections of the inertial-filtering separation channel (Fig. 1).

The above mentioned design scheme is used for determining the saturation conditions of the free volume layer of the filter (carrying capacity) and obtaining the dependence describing the speed of the liquid's free flow in the filter layer. During the mathematical modelling of the hydrodynamics of the liquid flow in the curvilinear inertial-filtering separation channels and in accordance with the previous assumptions, a simplified case of the flow is considered, and the curved section of the separation channel is represented by the formed louver walls with the constant radius (inner r_1 and outer r_2) according to Fig. 1 [4, 17].

Only after determining the conditions of the free volume layer saturation of the filter (carrying capacity), as well as based on the dependence for calculating the free flow rate of the liquid in the filter layer, it is possible to determine the required cross-sectional area S_f of the thin-layer filter element (Fig. 1), which is geometrically identified by the segment area [7]:
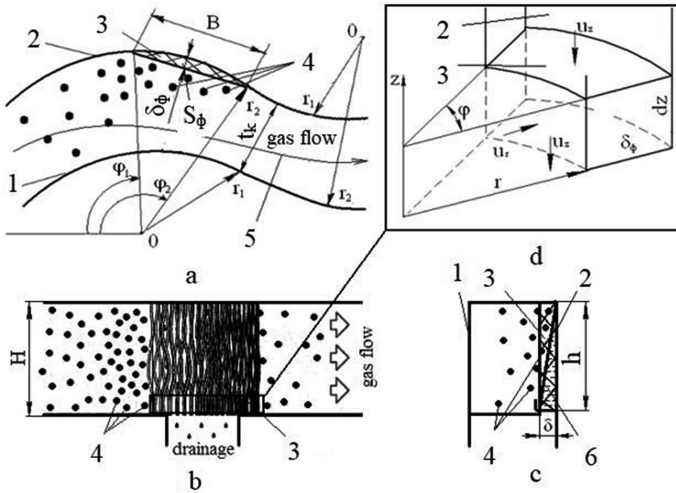
Fig. 1. Design model of the thin-layer filter element on the curvilinear part of the separation channel [4, 10]: horizontal (a) and vertical (b, d) sections of the curvilinear inertial-filtering separation channel, and infinitesimal element (c) in the strip of the filter element (elementary volume); 1, 2 – inner and outer walls on the corresponding curved sections of the channel; 3 – thin-layered filter element; 4 – dispersed particles (droplets); 5 – streamlines of the gas; 6 – film of the separated liquid.

$$S_f = \frac{r_2^2}{2}\left[\frac{\pi}{180}(\varphi_2 - \varphi_1) - \mathrm{Sin}(\varphi_2 - \varphi_1)\right] = \frac{r_2^2}{2}\left(\frac{\pi}{180}\varphi - \mathrm{Sin}\varphi\right), \qquad (1)$$

or

$$S_f = \frac{1}{2}\left(\pi r_2^2 \frac{\varphi}{180} - B(r_2 - \delta_\Phi)\right), \qquad (2)$$

where r_2 – outer radius of the curvilinear separation channel; $\varphi = \varphi_2 - \varphi_1$ – segment angle; B and δ_f – stripe width and thickness of the filtering element layer.

The geometrical sizes of the filtering elements, that determine the total volume taking into account the free volume and structure of fibrous materials, specify the absorbing ability of filters as the maximum amount of the carried liquid without reaching the flooding modes with the subsequent secondary removal of splashes due to the critical accumulation of the separated liquid in the filter layer at a certain height of the channel with the appearance of a fluid film on the surface of the filter element stripes (Fig. 1c).

A possible heterogeneity of the structure of the fiber filter determines local liquid accumulation and formation of ways for its stimulated extraction from the layer under the pressure of the gas stream. Therefore, considering the conditions of free volume saturation of filters layer and the condition of liquid's drainage, it allows solving the

problem of the determination of the setout optimum height of the overflow chute h in the curvilinear inertial–filtering separation channels for removing the separated liquid into the drainage channels within the process of the filter layer saturation along the height of the separation channel H (Fig. 1).

In the process of inertial-filtering separation two stages can be distinguished. The first stage is the initial (non-stationary), which constitutes the capture of the highly dispersed fluid particles by the filtering elements, that is accompanied by a change in their structure. This stage is followed by the second stage - stationary filtration (self-cleaning mode), which is the result of the pressure drops increasing in the filter layer, therefore changes in the efficiency of the separation take place. In this case, the hydraulic resistance, separation efficiency and the amount of fluid retained in the filter layer, as well as the amount of flowing fluid remain unchanged with the constant flow-rate of gas-liquid flow and the content of the dispersed phase at the inlet of the inertial-filtering separation channel. Moreover, the constant filtering rate is kept. While the quantity of the migrated (drained) liquid is equal to the amount of the liquid entered the elementary volume of the filter layer from the curvilinear separation channel and from the upper layer (Fig. 1d):

$$q_z + dz = q_r + q_z. \tag{3}$$

During the development of a mathematical model for describing the distribution and migration of liquid in an infinitesimal element (Fig. 1c) of the filter layer (flow model in the fibrous environment), the following simplifications and assumptions are proposed [4, 14]:

- filtering elements operate in the self-cleaning mode;
- distribution of the liquid along the height of the filtering layer within the infinitesimal elemental of the fibrous filter is uniform, and the structure of the fibrous material is regular;
- thickness of the filtering element layer is insignificant in comparison with the width of the curvilinear inertial-filtering separation channel $\delta_f << t$ (Fig. 1), that allows not considering the gas flow compression in the curvilinear channel;
- the liquid flows down in the filtering elements under the gravity force;
- isothermal filtration model is described by the equations of conservation of mass and the Darcy's law.

All the mathematical formulations describing the isothermal filtration of the compressed gas-disperse flow in the fibrous filter elements of the inertial-filtering separation channels are presented by the equation of the Darcy's law [16, 17]:

$$\frac{\partial m\rho}{\partial t} + \mathrm{div}\rho\vec{u} = 0, \tag{4}$$

$$\vec{u} = -\frac{k}{\mu}\mathrm{grad}\, p, \tag{5}$$

where m is sponginess of the fibrous material of the filter element; u – vector of the filtration speed; k – permeability of the fibrous material.

If the compressibility of the gas flow is much bigger than the compressibility of the porous environment (the fibrous filter material), the Eq. (4) takes the form:

$$m\frac{\partial \rho}{\partial t} + \text{div } \rho\vec{u} = 0. \tag{6}$$

The system of three scalar Eqs. (5) is unconstrained. Under the assumption of the isothermal model of the filtration process (T = const), the density ρ and the dynamic viscosity μ in the Eqs. (5) and (6), can be represented as functions of pressure:

$$\rho = \rho(p); \mu = \mu(p). \tag{7}$$

This simplification allows to reduce the system of Eqs. (6) to one equation for one function, which contains the density ρ and pressure p:

$$m\frac{\partial \rho}{\partial t} + \text{div}\left(-\rho\frac{k}{\mu}\text{grad p}\right) = 0. \tag{8}$$

Therefore, the filtration process is considered in the stationary mode of self-purification:

$$\frac{k}{\mu}\text{div}(\rho\,\text{grad p}) = 0. \tag{9}$$

Further transformations of the last equation are related to the introduction of the Leibenzon's function, that allows linearizing the expression under the divergence operator:

$$\begin{cases} \Delta P = 0, \\ \rho\vec{u} = -\frac{k}{\mu}\text{grad P}, \\ \rho = \rho(p), \\ P = \int \rho dp. \end{cases} \tag{10}$$

Thus, it is possible to determine the distribution of speed and pressure in the filter layer in the set mode of filtration after the substitution of the first equation of the system (11) as the Laplace equation to the Leybenzon's function [17].

4   Results

From the comparison of the systems of the equations for the models of the steady filtration process in case of the one-dimensional flow scheme for incompressible liquid and gas it follows that they are equivalent to change the pressure p by Leibenzon's function P, as well as the filtration rate u by the mass filtration rate ρ_u.

Taking this into account, the mathematical model for the solution of the problem of determining the characteristics (the pressure distribution p and filtration velocity u) of the steady filtration motion of fluid in the filter element layer is given by the system of equations:

$$\begin{cases} \Delta p = 0, \\ \vec{u} = -\frac{k}{\mu}(\text{grad } p - \rho g), \end{cases} \tag{11}$$

or in terms of projections on a cylindrical coordinate system (Fig. 1):

$$\begin{cases} \frac{1}{r}\frac{\partial}{\partial r}\left(r\frac{\partial p}{\partial r}\right) + \frac{1}{r^2}\frac{\partial^2 p}{\partial \varphi^2} + \frac{\partial^2 p}{\partial z^2} = 0, \\ u_r = -\frac{k}{\mu}\frac{\partial p}{\partial r}, u_\varphi = -\frac{k}{\mu}\frac{\partial p}{\partial \varphi}, u_z = \frac{k}{\mu}\left(\frac{\partial p}{\partial z} + \rho g\right). \end{cases} \tag{12}$$

According to the accepted design scheme of the liquid movement in an infinitesimal element of the fibrous filter layer (Fig. 1d) and by assuming the non-weep condition through the side faces from the next elements due to the anisotropy of the fibrous filter material:

$$\frac{1}{r}\frac{\partial}{\partial r}\left(r\frac{\partial p}{\partial r}\right) + \frac{\partial^2 p}{\partial z^2} = 0, \tag{13}$$

$$u_r = -\frac{k}{\mu}\frac{\partial p}{\partial r}, \tag{14}$$

$$u_z = \frac{k}{\mu}\left(\frac{\partial}{\partial z} + \rho g\right). \tag{15}$$

In accordance with the assumption of the pressure distribution in the separated liquid film along the thickness of the fiber filter layer (in the radial direction) and on the free surface of phases' differentiation, the system of Eqs. (15) and (16) takes the form:

$$u_r(z) = \frac{k}{\mu}\frac{\rho g z}{\delta(z)}, \tag{16}$$

$$u_z(r, z) = \frac{k}{\mu}\rho g\left(1 - \frac{r_2 - r}{\delta(z)} + z(r_2 - r)\frac{\frac{d\delta(z)}{dz}}{\delta^2(z)}\right). \tag{17}$$

The analysis of the components of the continuity equation (integrity, wholeness) of the flow for the stationary process of running down a liquid film in a layer of the fibrous filter under conditions, which are determined by the dependences with account for $u_z = \text{const}$, and after the integration:

$$\ln \delta = \frac{\mu}{k\rho g} u_z \ln z + \ln C, \tag{18}$$

$$\delta = C Z^{\frac{\mu}{k\rho g} u_z}. \tag{19}$$

Based on the boundary condition, when the fiber filter layer is completely saturated with the entrapped liquid ($\delta = \delta_f$) at the corresponding optimum height of installation of the overflowed gutter ($z = h$) for tapping the separated liquid from the inertial-filtering channels to the drainage ones:

$$\delta_f = C h^{\frac{\mu}{k\rho g} u_z}. \tag{20}$$

The last correlation allows obtaining the integration constant C:

$$C = \frac{\delta_\Phi}{h^{\frac{\mu}{k\rho g} u_z}}. \tag{21}$$

Substituting the obtained constant C to the dependence (21) allows receiving the distribution of the liquid thickness in the fibrous filter layer:

$$\delta = \delta_f \left(\frac{z}{h}\right)^{\frac{\mu}{k\rho g} u_z}. \tag{22}$$

Equation for dropping liquid q_r, which falls into the filter layer from the curvilinear separation channel, and the amount of the separated liquid that flows from the above filter layers q_z (Fig. 1d) allows to obtain the following formulas. After the substitution of the dependence (21) to the Eq. (18), as well as integration and simplifying:

$$\frac{q_r}{\rho r \varphi} = \frac{k}{\mu} \rho g \int_0^h \frac{z}{\delta_\Phi \left(\frac{z}{h}\right)^{\frac{\mu}{k\rho g} u_z}} dz = \frac{k}{\mu} \rho g \frac{h^{2-\frac{\mu}{k\rho g} u_z}}{2 - \frac{\mu}{k\rho g} u_z} \frac{h^{\frac{\mu}{k\rho g} u_z}}{\delta_\Phi} = \frac{k\rho g}{\mu} \frac{\frac{h^2}{\delta_\Phi}}{2 - \frac{\mu}{k\rho g} u_z}. \tag{23}$$

From the Eq. (24) it is possible to receive the dependence for the determination of the necessary height of arrangement of the overflowed gutter h for diverting separated liquids from the inertial-filtering to drainage channels:

$$h = \sqrt{\frac{\mu}{k} \frac{q_r}{\rho^2 gr\varphi} \left(2 - \frac{\mu}{k\rho g} u_z\right) \delta_\Phi}. \tag{24}$$

The specific flow rate of the liquid dq_r falls into the elementary volume dV of the filter layer from the curvilinear separation channel and is determined according to the Dupuit's formula [16, 17], that is obtained from the system of Eqs. (12) for the one-dimensional flat-radial filtration flow of the incompressible liquid through the side surface of the fibrous filter element:

$$dq_r = \frac{2\pi\varphi k}{360\mu} \frac{(p_r - p(z))dz}{\ln(r_2/r)}. \tag{25}$$

The application rate of the separated liquid q_z, which falls from the filter element of the inertial-filtering separation channel to the drainage channels:

$$q_z = \rho u_z S_f = \rho u_z \frac{1}{2}\left(\pi r_2^2 \frac{\varphi}{180} - B(r_2 - \delta_f)\right). \tag{26}$$

For the known value of the separation efficiency η of the gas-droplet flow, the Eq. (26) determines the required cross-sectional area S_f of the thin-layer filter element that ensures the effective removal of the separated liquid film avoiding the direct contact with the gas-droplet flow in the inertial-filtration separation channel.

5   Conclusions

The obtained solution of the mathematical model of liquid's distribution and migration in the filter layer (flow model in the fibrous environment), which describes the non-pressure filtration motion in the gravity field of the separated liquid film from the gas-drop flow, allows to determine the saturation conditions of the free volume of the filter layer, distribution of speed and pressure under the conditions of free liquid's movement in the filter layer, as well as to calculate the required cross-sectional area of the thin-layer fibrous filter element and the optimum height of the location of the overflow chutes for draining the separated liquid from the inertial-filtering to the drainage channels in order to avoid the secondary removal of droplets with the turbulent gas flow.

As a result, the dependence for the overflowed gutter of diverting the separated liquids from the inertial-filtering to the drainage channels is presented, and the application rate of the separated liquid which falls from the filter element of the inertial-filtering separation channel to the drainage channels is obtained.

References

1. Setnickova, K., Sima, V., Petrychkovych, R., Reznickova, J., Uchytil, P.: Separation of gas mixtures by new type of membranes: dynamic liquid membranes. Sep. Purif. Technol. **160**, 132–135 (2016)
2. Liaposhchenko, O., Nastenko, O., Pavlenko, I.: The model of crossed movement and gas-liquid flow interaction with captured liquid film in the inertial-filtering separation channels. Sep. Purif. Technol. **173**, 240–243 (2017)
3. Jia, W., Murad, S.: Separation of gas mixtures using a range of zeolite membranes: a molecular-dynamics study. J. Chem. Phys. **122** (2005)
4. Sklabinskyi, V., Liaposhchenko, A., Nastenko, O., Al-Rammahi, M.: Modelling and design of inertial-filtering gas separators-condensers for compressor units of oil and gas industry. Appl. Mech. Mater. **630**, 117–123 (2014)
5. Bragg, A.D., Collins, L.R.: New insights from comparing statistical theories for inertial particles in turbulence: part II. Relative velocities. New J. Phys. **16**, 055014 (2014)
6. Dou, Z., Ireland, P.J., Bragg, A.D., Liang, Z., Collins, L.R., Meng, H.: Particle-pair relative velocity measurement in high-Reynolds-number homogeneous and isotropic turbulence using 4-frame particle tracking velocimetry. Exp. Fluids **59**(2), 30 (2018)
7. Liaposhchenko, O., Nastenko, O.: Analysis of the conditions of phase equilibrium and influence of the United Heat and Mass transfer on the effectiveness of separation in the inertial-filtering separator. Chem. Chem. Technol. **9**(1), 125–130 (2015)
8. Saw, E.-W., Bewley, G.P., Bodenschatz, E., Sankar, R.S., Bec, J.: Extreme fluctuations of the relative velocities between droplets in turbulent airflow. Phys. Fluids **26**(11), 111702 (2014)
9. Salazar, J.P.L.C., De Jong, J., Cao, L., Woodward, S.H., Meng, H., Collins, L.R.: Experimental and numerical investigation of inertial particle clustering in isotropic turbulence. J. Fluid Mech. **600**, 245–256 (2010)
10. Xu, H., Ouellette, N.T., Bodenschatz, E.: Evolution of geometric structures in intense turbulence. New J. Phys. **10**, 013012 (2008)
11. Falkovich, G., Pumir, A.: Sling effect in collisions of water droplets in turbulent clouds. J. Atmosp. Sci. **64**(12), 4497–4505 (2007)
12. Parishani, H., Ayala, O., Rosa, B., Wang, L.-P., Grabowski, W.W.: Effects of gravity on the acceleration and pair statistics of inertial particles in homogeneous isotropic turbulence. Phys. Fluids **27**(3), 033304 (2015)
13. Wang, L.-P., Wexler, A.S., Zhou, Y.: Statistical mechanical description and modelling of turbulent collision of inertial particles. J. Fluid Mech. **415**, 117–153 (2000)
14. Huang, L., Deng, S., Chen, Z., Guan, J., Chen, M.: Numerical analysis of a novel gas-liquid pre-separation cyclone. Sep. Purif. Technol. **194**, 470–479 (2018)
15. Mansour, M., Kovats, P., Wunderlich, B., Thevenin, D.: Experimental investigations of a two-phase gas/liquid flow in a diverging horizontal channel. Exp. Therm. Fluid Sci. **93**, 210–217 (2018)
16. Basniyev, K., Dmitriyev, N., Rozenberg, G.: Oil and gas hydromechanics (2005)
17. Leontyev, N.: Fundamentals of Filtration Theory. Institute for Computer Research, Moscow (2009)

CFD Simulation of Ammonium Nitrate Melt in a Perforated Rotating Bucket

Maksym Skydanenko[1]($\boxtimes$) , Vsevolod Sklabinskyi[1] ,
and Saad Saleh[2]

[1] Sumy State University, 2 Rymskogo-Korsakova St., Sumy 40007, Ukraine
m.skydanenko@pohnp.sumdu.edu.ua
[2] Tikrit University, 42, Tikrit, Iraq

Abstract. In this paper, a computational fluid dynamics (CFD) model was developed to study the influence of the flow pattern of ammonium nitrate melt on the jet emerging from the perforations located on the wall surface of the rotating bucket. The numerical simulations were carried out using ANSYS CFX software in which a three dimensional model closed via a k-ε turbulence model was adopted. To improve the performance of the bucket, design parameters such as a number of blades setting up in the bucket and selecting their geometrical shape were examined in depth. It was found that these parameters had a crucial impact on the velocity of the melt jet. While increasing the jet velocity, the probability of plugging and alteration of geometrical sizes of perforations decreases. This enables using the bucket for dispersing melts with solid impurities. The results of CFD simulation were applied for developing a modified rotating perforated bucket of the melt with nitrogen fertilizers, which has passed experimental and industrial tests.

Keywords: Priller · Blades · Design · Monodispersity · Hydrodynamics

1 Introduction

The request on nitrogen fertilizers is growing dynamically in today's agriculture throughout the world. Economic and social development trends influence the development of the market for mineral nitrogen fertilizers. Growth in demand for nitrogen fertilizers is facilitated by: the problem of food security of countries; the necessity to maintain and increase the yield of the agricultural land, which possibilities of expansion is very limited; an active search for renewable energy sources and plans on bioenergy development. In the coming years, active investment and growth of world consumption of mineral fertilizers is expected. There are currently 250 projects under construction. IFA experts estimate the total cost of constructing new plants at $88 billion. Their implementation will lead to an increase in production capacity in 2020 by 183 million tons of mineral fertilizers [1].

In the world practice of chemical industry, the most common methods of producing nitrogen fertilizers are methods of prilling in towers and granulation (by applying layers of melt on the remained fine particles in the fluidized bed of the drum or plate granulators) [2–5]. Prilling method involves spraying the melt of mineral fertilizers

(disintegration of jets into drops that come out from the dispersing device) into the air, cool-down of melt spherical droplets, that are in free fall, and their crystallization in the counter flow of cooling air. Each of the considered methods have advantages and disadvantages, however, as the world practice shows, 70% of nitrogen fertilizers are produced in the form of prills [6].

2 Literature Review

Prilling tower is an engineering and technical building with a height of 30–114 m and a diameter of 8–22 m, depending on the productivity. In the lower part of the tower there is a built-in cooling device practically all over the cross-section in the boiling layer, equipped with forced air ducts and fans to supply air to the cooling device. Above it, there are windows for additional supply of atmospheric air, and, if necessary, there can be installed a guide cone. In the upper part of the tower, there is an overlap ceiling, in the center of which a device for dispersing the melt is placed [7, 8].

Several types of devices (granulators) are used for dispersion of melts: centrifugal, static and combined apparatus, wherein vibrations can be applied to the centrifugal and static devices. In addition, centrifugal mechanical nozzle granulators are used there (not commonly used due to the considerable scatter of granulometric composition) [9]. Centrifugal granulators are the most commonly used [10–12]. The main structure elements of melt granulators are perforated bucket, which are usually axially symmetric. The main purpose of the bucket is to disperse melt into drops.

Designing a dispersion bucket is the first and the main stage in calculating the process of melt granulation in the prilling towers. There are many works of scientists and researchers devoted to the development of theoretical foundations of hollow perforated rotary buckets.

However, until recently, this theory is not completed. Thus, in calculating the throughput capacity (productivity) of such shells it was suggested to use empirical dependences obtained for conditions of relative rest of the liquid in the shell. In practice, in many cases, liquid inside the hollow perforated rotary bucket moves at a rate that is lower than the rotational velocity of the bucket [13]. Therefore, the above-mentioned dependencies do not reflect in general the physical nature of the internal hydrodynamics of these shells and can only be applied in cases limited by the scope of experiments. The significant contribution to the development of the theory of hollow perforated rotary buckets was made by Kholin [14, 15]. He studied the patterns of internal hydrodynamics of these buckets. The authors [16] supplemented the description of the internal hydrodynamics of a hollow perforated rotary bucket, confirming their proposals by theoretical and experimental investigations. However, the hypotheses presented by the authors [14–16] can only be used for large Reynolds values.

The monodispersed droplets formation and crystallization is influenced by the formation conditions of the melt jet which is dispersed (nature of outflowing from the bucket hole and breaking). Uniform outflow of liquid is determined by the nature of its distribution velocity in the working chamber of the bucket and near the discharge hole. On the basis of the studied theoretical works on hollow perforated rotary buckets, dispersers (centrifugal vibratory granulators) for the production of ammonium nitrate

were developed [2]. These devices made it possible to obtain the product of the following grain size composition: the weight fraction of granules in the size less than 1.0 mm – 0.7–1.5%; the weight fraction of granules in the size of 1.0–2.0 mm – 3.0–6.0%; the weight fraction of granules in the size of 2.0–3.0 mm – 80–85%; the weight fraction of granules in the size of 2.0–4.0 mm – 90–96%; the weight fraction of granules in the size of more than 4.0 mm – less than 1% [2]. In order to create competition in the market with the growth in demand for mineral nitrogen fertilizers, there is a need to increase their monodispersed composition, which ensures higher productivity of agricultural crops and their flowability as well as eliminates their losses during transportation and caking during storage.

Study of liquid motion hydrodynamics in a hollow perforated shell with a small Reynolds value is very up-to-date. It is necessary to know the nature of rotary motion and distribution of velocities in the melt that fills the volume of the perforated rotating bucket and to specify velocity of the melt jet outflowing from the holes of the granulator bucket. This will make it possible to determine the nature of the liquid velocity distribution in the chamber of the bucket and near the discharge openings, thus one can work out the right constructive solutions for obtaining the monodispersed product. Performance of a perforated bucket may also be improved by modifying the internal design of the perforated bucket using a specified number of blades assisted in discharging of melt jet from the perforations with higher velocity.

3   Research Methodology

In order to determine accurately the melt flow features inside the bucket, CFD simulation was used with the software ANSYS CFX. A prilling bucket model has been constructed based on the data in [11], (diameter of the priller – 500 mm; number of holes in a priller – 2300 pcs). Simulation was provided for a mass flow of ammonium nitrate 27,000 kg/year at temperature 180 °C. The number of radial blades was varied from 0 to 7 at shell rotation frequency 50 rpm. Priller was simulated with six radial blades, rotational speed was varied from 50 to 90 rpm, also curved forward and backward blades (angle 135°) was considered with rotational speed 50 rpm. Geometry of the bucket was created by ICEM CFD module with a maximum value of Y+ = 36. Three-dimensional structured mesh, wich was constructed, has 1,592,811 hexahedral cells as indicated in Fig. 1a. The melt flow in bucket was modelled using the Eulerian approach with the Reynolds Averaged Navier-Stokes (RANS) equations. Modelling of turbulence was performed using k-ε turbulence model [17, 18].

In order to reduce the computation time, some of assumptions have been introduced, such that steady state was assumed and the hydrodynamics was considered in the lower part of the bucket near the discharge holes.

The setting of boundary conditions for the model was implemented according to the following scheme in Fig. 1b. The flow rate value, corresponding to the granulator operating mode, was set on the surface of the Inlet, through which the flow enters the computed domain. The granulator bucket rotates around its axis. Taking into account that at the outflow influenced by centrifugal forces, the velocity and pressure values near the discharge holes were not known, the boundary condition of the type outflow was used.
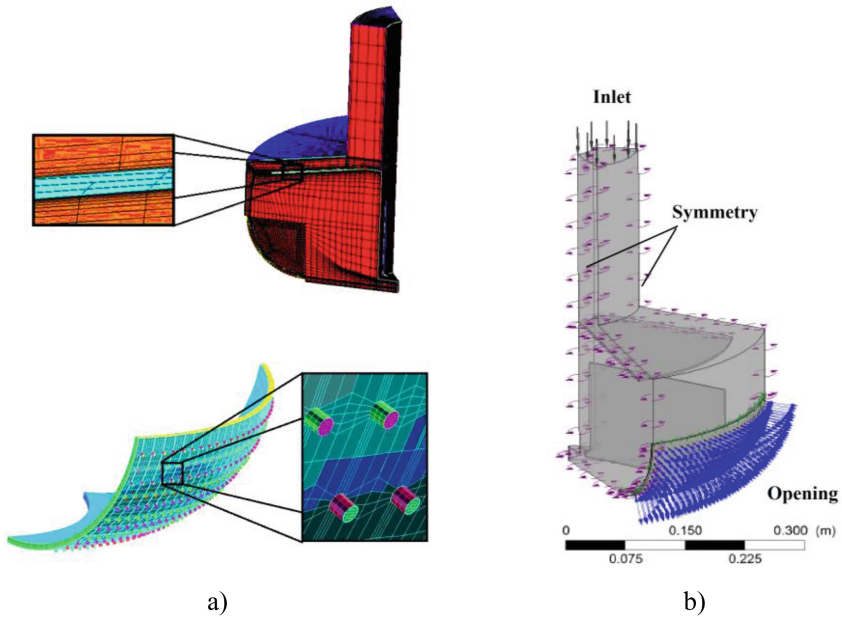
a)   b)

Fig. 1. Computational grid for CFD simulation (a) and boundary conditions (b).

Calculations were made for various values of the granulator rotation frequency, number of blades and their shape. Convergence criterion of the calculation was not only basic equations, but also integral characteristics of the flow at the discharge holes at reaching the value of the mean-root-square residual errors according to the main parameters at the level $(1 \cdot 10^{-3})$ [19].

4   Results

The simulated results of the numerical modeling of liquid flow hydrodynamics in the bucket without blades show that the main mass of fluid, except for a very thin boundary layer adjacent to the inner surface of the bucket (Fig. 2a), moves far behind the bucket. In each separate period, there will be some new amount of liquid in the area of the discharge hole. During this time, due to excess pressure, an impulse moves in the direction of the opening. Liquid discharge from the hole takes place at this moment. Radial component of the liquid velocity, which failed to enter the hole due to lack of time, at the next moment becomes zero again, since liquid enters the section of non-perforated part of the bucket wall. To obtain monodispersed droplets as well as increase productivity and improve the load distribution, it was suggested to place pressure blades in the granulator bucket. Then, there comes a new hole to the area of considered liquid and the next portion is out. As the liquid mass has inertia, the radial component of velocity will increase in time from zero at the front edge of the hole, to a certain maximum at the opposite edge of the discharge hole. Excessive pressure in the

granulator bucket is small, and therefore, impulse force value is low in the axis direction to the hole. With an increase in the shell rotation velocity the liquid residence time over the hole decreases, while the pressure increases insignificantly. Liquid flies over the hole under its own inertia in relative motion, having no time to fill the hole. In order to obtain monodispersed droplets, increase productivity and improve the load distribution, it was proposed to place pressure blades with a gap in the granulator bucket, which follow the perforated bottom shape, and rotate together with the granulator housing. A numerical simulation of granulator operation with radial, forward-curved and back-curved blades was carried out. Partitions cause rotation of the melt, which increases centrifugal pressure and velocity of the jet termination from the bucket holes. At the first stage of research, the effect of the number of radial blades (from 4 to 7) on the velocity of outflowing under constant initial conditions was investigated (Fig. 2).

As a result of simulation, as it can be seen from the graph in Fig. 3, an increase in the number of blades causes an increase in absolute velocity and pressure. To explain the obtained dependencies one should consider physics of the process. Let one assume the ideal case when the granulator consists of an infinite number of infinitely thin blades. In this case, a trajectory of the liquid flow follows completely the trajectory of the blades. In actual life, with a decrease in the number of blades in the channel between the blades, one obtains rotation of the liquid in the direction, which is reverse to the granulator bucket rotation. Vortical relative motion of the liquid in the channel between the blades has velocity that coincides in the direction with the main flow from the suction side of the blade and with the velocities in reverse direction to the main flow from the pressure side of the blade. Axial vortex of the transport motion is imposed on the main flow, which leads to an increase in relative velocities on the suction side and to a decrease in their pressure (Fig. 2). Consequently, the smaller the number of blades is in the granulator bucket, the greater is the velocity on the pressure side of the blade, and, consequently, the velocity of liquid outflow from the holes will decrease. This assumption is confirmed by the equation of theoretical pressure, taking into account the finite number of blades as per Stodola and Meizel scheme [20]. At the second stage, the dependence of the average velocity of the liquid outflow from the holes of granulator bucket was studied. As we see from the graph on Fig. 4, when granulator rotation frequency increases, the average liquid velocity rises according to the linear dependence. With the development of circumferential velocity, the theoretical pressure rises, which, in turn, increases the velocity of liquid outflow from the hole of the perforated shell. At the third stage, the velocity of liquid outflow from the holes was investigated, depending on the geometric shape of the blades.

The tests were carried out on the radial (the output angle of the blades of 90°) Fig. 2d, forward-curved (the output angle of the blades of 135°) blades Fig. 2e, and back-curved (exit angle of the blades 135°) blades Fig. 2f, while they follow the shape of the perforated bottom of the bucket. All tests were conducted in identical conditions. The replacement of radial blades on the forward-curved increases the velocity of liquid outflow from the holes by 37%.
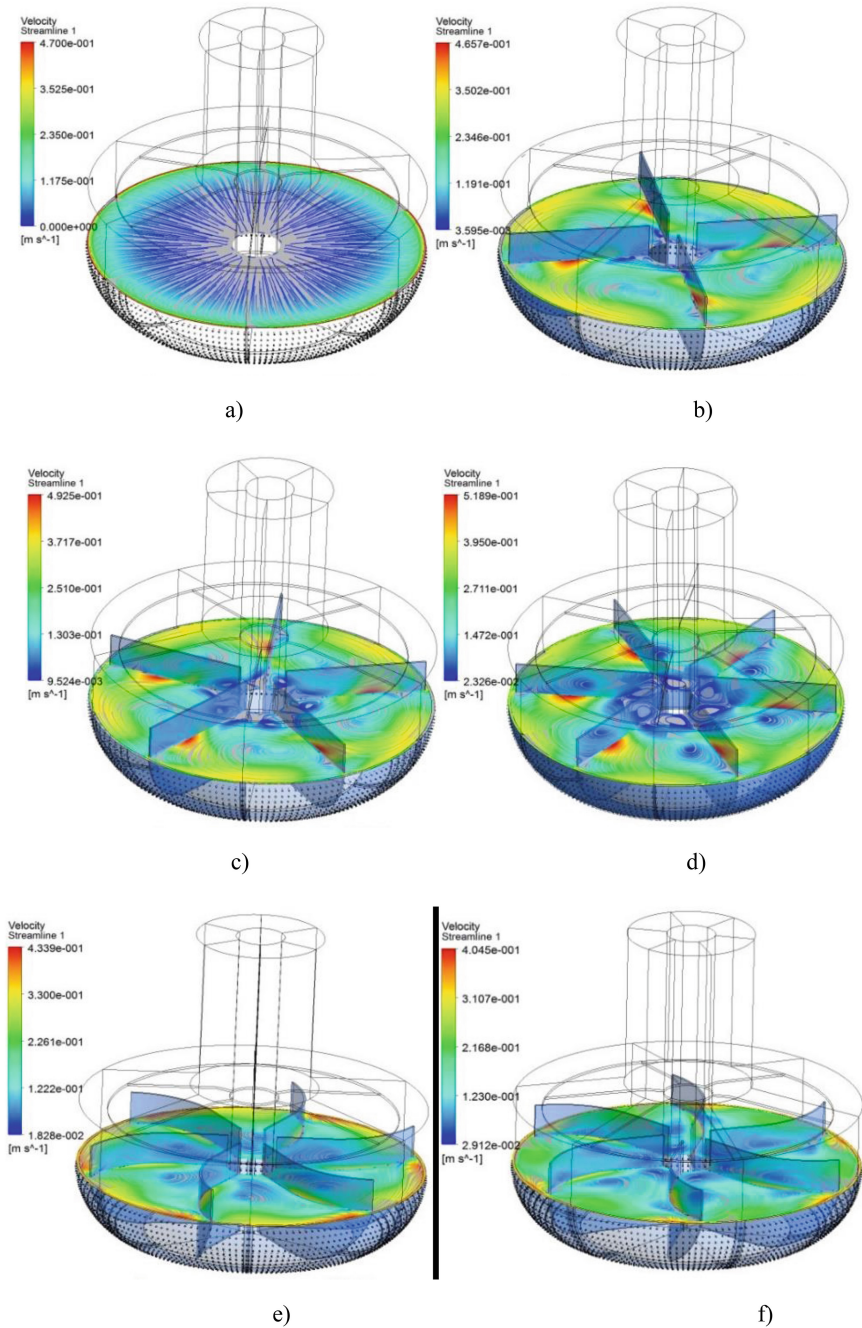
Fig. 2. Streamlines of the liquid motion in the rotary bucket with rotational velocity of 50 rpm: a – without blades; b – with 4 radial blades; c – with 5 radial blades; d – with 6 radial blades; e– forward-curved blades; f – back-curved blades.
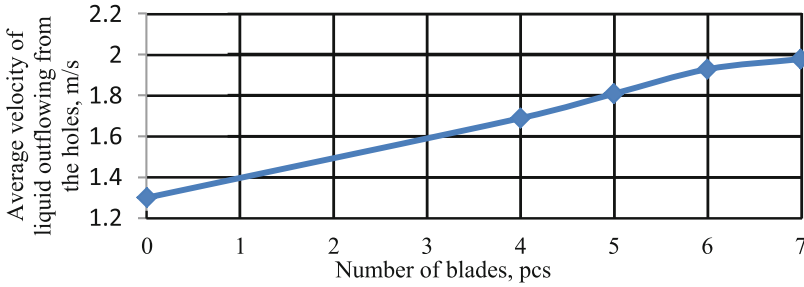
Fig. 3. Dependence of the average velocity by area of liquid outflowing from the holes of the cup-shaped bucket bottom on the number of radial blades at a bucket rotational velocity of 50 rpm.
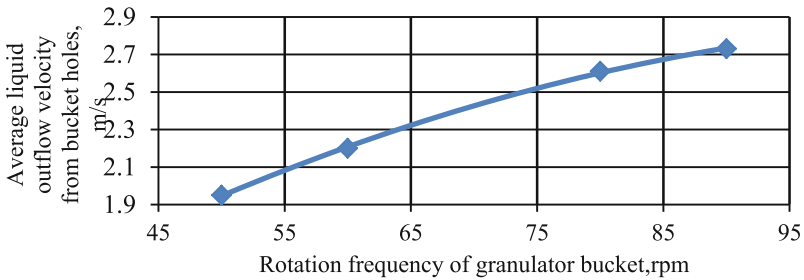

Fig. 4. Dependence of the average velocity by area of liquid outflow from the holes of granulator bucket with 6 radial blades on the bucket rotation velocity.

In accordance with the rules for constructing a velocity plan, the absolute velocity V_i in the blade section is the vector sum of the relative W_i and the circumferential U_i velocity. When using a radial blade, the absolute velocity V_1 is less than that one of the forward-curved V_2.

The simulation results were analyzed and applied in the development of a modified centrifugal vibratory granulator for nitrogen fertilizers which passed pilot-industrial tests in the composition of aggregate for production of ammonium nitrate at PJSC Concern Stirol [10].

5   Conclusions

A numerical simulation of liquid motion hydrodynamics in a perforated rotating bucket was carried out using the ANSYS CFX software product, which demonstrates the distribution character of the velocity in the granulator working chamber and near the discharge hole. A numerical study made it possible to specify velocity of melt jet and to find a way to increase the outflow velocity (pressure) of the melt from the holes of the granulator bucket, by modernizing a design of the vibratory granulator, increasing the

number of blades or selecting the geometric shape of blades, depending on the working parameters of the granulator.

As a result of the simulation, the optimal number of blades in the distributor for the given granulator design is 6 pieces. A further increase of the blade number slightly increases the velocity of fluid outflow, as well as complicates the manufacturing of priller. As can be seen from the results analysis, the use of bent forward blades increases the velocity of fluid outflow from the holes by 37%, in comparison with the radial ones. That is, the design of priller with forwarding curved blades allows reducing the rotation speed, herewith it provides the required melt atomization; consequently, the air influence on the decomposition of a jet of melt ammonium nitrate is decreased, which leads to the secondary fragmentation or coagulation that degrade the quality and product monodispersity factor. Also, it was defined that there is much less clogging with the increasing pressure and the geometric sizes of discharge openings stay the same.

This makes it possible to use a granulator to disperse melts containing solid admixtures (additives).

References

1. Food and Agriculture Organization of the United Nations: World Fertilizer Trends and Outlook to 2018. FAO, Rome (2015)
2. Chernyshev, A.K., Levin, B.V., Tugolukov, A.V.: Ammonium nitrate: properties, manufacturing, usage. In: INFOCHIM, Moscow (2009)
3. Rahmanian, N., Naderi, S., Supuk, E., Abbas, R., Hassanpour, A.: Urea finishing process: prilling versus granulation. Procedia Eng. **102**, 174–181 (2015)
4. Anderzhanov, R., Shestakov, N.: Stepping up prilling and granulation. World Fertilizer, 89–94 (2017)
5. Taran, A.L., Ostanina, O.I., Taran, A.V., Bespalova, V.O.: Analysis of the national and foreign quality requirements for basic mineral nitrogenous fertilizers, and technical solutions for improving their quality. Chem. Pet. Eng. **52**, 10–14 (2016)
6. European Fertilizer Manufacturers' Association. Production of ammonium nitrate and calcium ammonium nitrate: Booklet No. 6 of 8. Fisherprint Ltd, Peterborough, England (2000)
7. Skydanenko, M., Sklabinskyi, V., Saleh, S.N., Barghi, S.: Reduction of dust emission by monodisperse system technology for ammonium nitrate manufacturing. Processes **5**(3), 37 (2017)
8. Mehrez, A., Ookawara, Sh, Hamza, A.H., Suzuki, M.: A numerical study on cooling-solidification process of urea particles in prilling tower. J. Chem. Eng. Jpn. **47**(1), 1–8 (2014)
9. Taran, A.L., Dolgalov, E.V., Taran, YuA: Algorithm for calculating nozzle granulator for production of lime-ammonium nitrate in towers. Vestnik Moscow State Univ. Fine Chem. Technol. **3**, 42–46 (2006)
10. Skydanenko, M.S., Sklabinskyi, V.I.: Analysis of hydrodynamics of stationary flow discharge. Visnyk Sumy State University, Series "Technical Sciences" **1**, 79–85 (2013)
11. Hassanpour, A., Pasha, M., Susana, L., Rahmanian, N., Santomaso, A.C., Ghadiri, M.: Analysis of seeded granulation in high shear granulators by discrete element method. Powder Technol. **238**, 50–55 (2013)

12. Muhammad, A., Rahmanian, N., Pendyala, R.: Flow analysis of melted urea in a perforated rotating bucket. Appl. Mech. Mater. **372**, 340–345 (2013)
13. Kholin, B.G.: On the theory of liquid motion in hollow perforated rotating shell. Visnyk Charkiv Polytech. Inst. **12**(60), 45–56 (1966)
14. Kholin, B.G.: On hydrodynamic paradox of centrifuge. Intensif. Tech. Process. Chem. Eng. Ind. **5**, 7–13 (1970)
15. Kholin, B.G.: Centrifugal and Vibratory Melting Granulators and Liquid Sprays. Mashinistroyeniye, Moscow (1977)
16. Baranov, E.I., Yakushko, S.I.: Justification and calculation of the hydrodynamic paradox arising when liquid flows out of holes of perforated rotating shell. Visnyk Sumy Sumy State Univ. Ser. Tech. Study **4**, 7–12 (2012)
17. Spalart, P.R.: Strategies for turbulence modelling and simulations. Int. J. Heat Fluid Flow **21**(3), 252–263 (2000)
18. Ngб, B.H., Ding, Y.L., Ghadiriб, M.: Modelling of dense and complex granular flow in high shear mixer granulator: a CFD approach. Chem. Eng. Sci. **64**(16), 3622–3632 (2009)
19. Kuz'minovб, A.V., Lapinб, V.N., Chernyiб, S.G.: The calculation method for turbulent flows of an incompressible liquid on the basis of a two-layer (k-ε) model. Comput. Technol. **6**(5), 73–86 (2001)
20. Mikhailov, A.K., Malyushenko, V.V.: Designs and Calculation of High-Pressure Centrifugal Pumps. Mashinostroyeniye, Moscow (1971)

Mathematical Model of Corrosive-Mechanic Wear Materials in Technological Medium of Food Industry

Yuriy Sukhenko[1] , Vladislav Sukhenko[1] ,
Mikhailo Mushtruk[1(✉)] , and Alexander Litvinenko[2]

[1] National University of Life and Environmental Sciences of Ukraine,
15 Heroiv Oborony St., Kiev 03041, Ukraine
`mixej.1984@ukr.net`
[2] National University of Food Technologies,
68 Voloymyrska St., Kiev 01601, Ukraine

Abstract. Using the thermodynamic methods of the irreversible process proved that the speed of corrosive-mechanical metals wear in the technological media of electrolytes of food industry depends on the linearly loads and speed of the slip and depends parabolically on the loss of strength of the materials by a corrosive-active medium. The influence of the electrode potential of metals in technological environments of food industries and the magnitude of their change in the friction of contacting surfaces of parts on the intensity of wear are determined. The methods of control over the process about corrosive-mechanical wear are pointed. The validation of a mathematical model of wear for adequacy was conducted in the technological medium of food industry. The methods of controlling the intensity of the process of corrosion-mechanical wear due to the strengthening of the friction pairs in the cathode or anode area, the selection of the composition of contact materials, and the inhibition of technological environments are proposed. The corrosion-mechanical wear of the surfaces in aggressive technological environments of food production are proven not to be regarded as a simple summary of mechanical and electrochemical factors.

Keywords: Corrosion · Wear · Mechanical factors · Catalyst
Fatigue · Durability · Electrochemistry · A potential of the metal

1 Introduction

Unlike other industries, the work of food industry equipment is characterized by a direct contact of parts surfaces with raw materials, semi-finished products and products that can be in different aggregate state (mostly liquid) [1]. Therefore, in the first place, the properties of technological environments and their interaction with the surface layers of parts determine the nature and characteristics of the wear components of the equipment [2].

A lot of food environments are electrolytes. These include various sour and alkaline environments, neutral solutions, water with different chemical compositions, food products and intermediates [3]. When friction of metals in solutions of electrolytes

accurs, two-phase (metal-solution) or three-phase (metal 1 - solution - metal 2) systems should be considered specific electrochemicals, to which appropriate electrochemical laws and methods of research can be applied [4].

2 Literature Review

The high durability of tribo couplings will be achieved when the surface of contacting parts is characterized not only by a high wear resistance but also by the maximum resistance to the corrosion damage [5]. The complexity in solving such problems is connected, first, with the lack of a sufficient theoretical basis for the investigations of processes of corrosion-mechanical wear of the materials [6]. In some current works there is a simplified representation, which is described as the process of formation of films of the corrosion products and their periodic detachment in the mechanical interaction of the surfaces of friction. No less important is the question of the role of mechanical and corrosive factors and their mutual influence [7].

Mechanical properties of most crystalline materials are known to be characterized by the behaviour of dislocations. Therefore, the influence of the medium on the mechanical properties of solids can be related to the motion of dislocations on the surface [8]. Electrode potentials of the friction surfaces are the fundamental characteristics of electrochemical systems, which indicate the intensity of corrosion and mechanical wear of food processing equipment [9].

There is an understanding of the corrosion-mechanical wear of materials when rubbed enough to take into account the impact of the processed fluids and recycled raw materials. To open the mechanism of corrosion-mechanical wear of the materials and coatings in liquid aggressive media of food industries, it is necessary to consider a thermodynamic system that binds the microscopic parameters of the object and loads with the electrochemical processes of the internal interaction and fracture. The variety and quality of the differences in the nature of the physical and chemical processes that accompany the corrosion-mechanical wear, make it difficult to explain the mechanism of this phenomenon and its quantitative description. Joint quantitative analysis of various processes is possible by carrying out the universal criteria using the methods of thermodynamics of the irreversible processes [10].

The purpose of this work is to create a mathematical model for the corrosion-mechanical wear of the materials and aggressive liquid media of food industries and to test its adequacy.

To achieve this goal, the most important factors were taken into account: the electrochemical interaction of metals and the environment; the energy dissipation rate at the deformation and the density of the dislocation flow; transformation of electrode potentials at friction.

The results, which broaden the idea of corrosion and the mechanical wear of materials in the technological environments, have allowed developing theoretical foundations and experimentally substantiate the new conceptual approach to solving the problem of increasing the durability of the equipment of processing and food industries of the agro industrial complex, which confirms the relevance of the research.

3   Research Methodology

The process of material wear is accompanied by an irreversible loss of mechanical energy and its conversion into other types of energy. The mechanism of corrosive-mechanical wear of materials in corrosive food medium-electrolytes may be considered based on the thermodynamic system analysis which connects the micro-scope parameter of the rubbing pair with the electrochemical characteristics of inter-action and material destruction in a special technological medium.

By considering the fixed process of the corrosive-mechanical wear of metals in a technological medium of food industry the thermodynamically system can be defined by the aggregate of the contacting the destructive bulk of the metal, with the medium and the grits. This system can be divided into two parts: one is the destructive process and the other is connected with the chemical reaction and the transformation of a free surface owing to destruction.

During the corrosive-mechanical abrasion, the quantity of dissipation is defined not only by plastic deformation but even intensity by electrochemical processes and quantity of modification of a free surface area.

Joint quantitative analysis of heterogeneous processes is possible by introducing universal power criteria using the methods of thermodynamically irreversible processes.

Such processes can be described by a dissipative function [11]:

$$\overline{\psi} = T\frac{diS}{dt} = \sum \frac{d\overline{W}^i_{dis}}{dt} + \overline{I_C}A_C, \tag{1}$$

where $\psi = \psi/S_K$ - dissipative function (speed of dissipated energy in system) related to the unit of contact surface S_k; T - the temperature of the systems; $d i\overline{S}/dt = diS/S_K dt$ - the modifying entropy of system; $d\overline{W}^i_{dis}/dt$ - the energy dissipation speed for a process which takes place in the system; $\overline{I_C}A_C = \frac{I_C}{S_K}A_C$ - the power of chemical reaction; $\overline{I}_c$ - chemical reaction speed; A_c - chemical affinity of the reaction.

Energy dissipation speed which is connected with plastical deformation and formation of a new surfaces makes:

$$\sum_i \frac{dW^i_{dis}}{dt} = \frac{d\overline{W}_{pl}}{dt} + \sum_j \frac{d\overline{W}^j_S}{dt} \tag{2}$$

Dissipation function of the plastification process is as follows [11]:

$$\overline{\psi}_{pl} = \frac{dW_{pl}}{dt} = \overline{I}dA_\alpha \tag{3}$$

where $\overline{I}_\alpha = I_\alpha/S_K$ - density dislocation of the flow; $A_\alpha = \Delta\tau/\alpha$ - chemical affinity of the process of formation and dislocation transfer; $\Delta\tau$ - loss of material strength; α - number of dislocations fitted on the material deformation.

Taking surface abrasive wear process as spalling of the units on maximum distorted and loosened (dislocation boundaries), the dissipative power of the process of free surface formation can be defined by the following model:

$$\sum_j \frac{d\overline{W}_S^j}{dt} = I_{S0}\Delta\sigma_0 + \overline{I}_{sm}\Delta\sigma_m, \tag{4}$$

where $I_{so} = dS_o/S_k \cdot dt$ i $I_{sm} = d_{sm}/S_k \cdot dt$ - the changing speed of free surface of oxides and non-oxides; $\Delta\sigma_0$ i $\Delta\sigma_m$ - the work of formation of a new unit of the free surface, new free surface oxides and the proceed into consideration points of the material.

Taking into consideration the Eqs. (2)–(4), the Eq. (1) can be presented as follows:

$$\overline{\psi} = \overline{I}_\alpha \frac{\Delta\tau}{\alpha} + \overline{I}_{S0}\Delta\sigma_0 + I_{sm}\Delta m + \overline{I}_C A_C \tag{5}$$

Based on the linearity law and Eq. (5), the relations with Onsager [12] reciprocity in the system of the linearly phenomenological equation is as follows:

$$\overline{I}_\alpha = C_1 \frac{\Delta\tau}{\alpha} + C_2 A_C + C_3\Delta\sigma_0 + C_4\Delta\sigma_m \tag{6}$$

$$\overline{I}_c = C_2 \frac{\Delta\tau}{\alpha} + C_5 A_C + C_6\Delta\sigma_0 + C_7\Delta\sigma_m \tag{7}$$

$$\overline{I}_{so} = C_3 \frac{\Delta\tau}{\alpha} + C_6 A_C + C_8\Delta\sigma_0 + C_9\Delta\sigma_m \tag{8}$$

$$\overline{I}_{sm} = C_4 \frac{\Delta\tau}{\alpha} + C_7 A_C + C_9\Delta\sigma_0 + C_{10}\Delta\sigma_m \tag{9}$$

where $C_1...C_{10}$ - phenomenological coefficient.

The brought wear speed must $\overline{I}$ be defined by summing up of fluxes densities mass of oxided $\overline{I}_0$ and non-oxided I_m wear products:

$$\overline{I} = \overline{I}_0 + \overline{I}_m \tag{10}$$

The fluxes I_0 and I_m may be acquired based on the Eqs. (5)–(9). So as $\overline{I}_0 = \overline{I}_c v_o$, the Eq. (7) is the quantity of the fluxes of the oxide metal:

$$\overline{I}_0 = I_C v_0 = v_0(C_2 A\alpha + C_5 A_C + C_6\Delta\sigma_0 + C_7\Delta\sigma_m) \tag{11}$$

where v_o - is stoichiometric coefficient of oxide in the equation of the chemical reaction.

Substituting the Eqs. (6) and (7) into (5) and taking into consideration, that $(\overline{I}_m = I_{sm}/C_{11}$ where, C_{11} - the coefficient, which depends on the properties of the wearing material) [11], and in such a way we get:

$$\bar{I}_m = \frac{1}{C_{11}\Delta\sigma_m}[\bar{\psi} - C_1\left(\frac{\Delta\tau}{\alpha}\right)^2 - (2C_3\Delta\sigma_0 + 2C_2A_C + C_4\Delta\sigma_m)\frac{\Delta\tau}{\alpha} -$$
$$- \left(C_5A_C + C_8\Delta\sigma_0^2 + 2C_6\Delta\sigma_0A_C + C_7\Delta\sigma_mA_C + C_9\Delta\sigma_0\Delta\sigma_m\right)] \tag{12}$$

We define the value ψ. The whole outer work which was carried out with the rubbing system is as follows:

$$W = P \cdot f_{mp} \cdot L \tag{13}$$

where P - the unit loads; f_{mp} - the coefficient of rub slips; L - the course of rub.
Then the dissipative function is:

$$\psi = K \cdot P \cdot f_{mp} \cdot V \tag{14}$$

where K - constant which is characterizing the fraction of dissipative energy during the wearing; V - the speed of relative slipping of particles of wearing medium on the rubbing surface.

Excretions (11), (12) and (14) can give us the quantity of the wear speed which is brought to the unit of the surface:

$$\bar{I} = \bar{I}_0 + \bar{I}_m = K_1 \cdot P \cdot V + K_2\Delta\tau + K_3(-\Delta\tau)^2 \tag{15}$$

where K1, K2, K3 - is the constant, which includes the quantity $C_i, f_{mp}, v_0, \Delta\sigma_0, \Delta\sigma_m, \alpha$.

The Eq. (15) shows that the speed of the corrosive mechanical wear depends linearly on the load and speed of sliding and parabolically on the material loss of strength by a corrosive active medium.

The electrochemistry [13] proves that

$$\Delta\tau = \frac{\Delta\varphi_0 \cdot n \cdot F}{V_M}, \tag{16}$$

where: $\Delta\varphi_0$ - is the quantitave of the balanced electrode potential during the wear; n - metal valence; F - Faraday constant; V_m - male volume of the material.

Substituting the expression (16) into (15) we have:

$$\bar{I} = K_1 \cdot P \cdot V - K_2\frac{\Delta\varphi_0 \cdot n \cdot F}{V_M} + K_3\left(\frac{\Delta\varphi_0 \cdot n \cdot F}{V_M}\right)^2 \tag{17}$$

4   Results

4.1   Simulation Results

Given mathematical model (17) of quantity P and V characterizes the outside influence upon the wear surface, and the potential $\Delta\varphi 0$ quantitative depends on the material qualities of rubbing details as well as the qualities of a corrosive medium. If the pair of rubbing consists of heterogeneous metals, each of others metals has its own electrode properties. In this case the control pair is characterized by mimed electrode potential.

Pushing the potential of the pair rubbing together with an external power supply into the cathode or /and sphere, we may control over the process of corrosive-mechanical wear within the defined limits without changing the conditions of the rubbing joint load. This move may be realized by changing the structure of the rubbing materials by protecting coating, by the changing the rubbing regime, or by the inhibition of a technological medium, that is proven by many investigators.

4.2   Verifying the Adequacy of the Model

The verification of the adequacy of the mathematical model of the metals wear in the food environments (17) was carried out by comparing the calculations and the results obtained during the experiments of the value of the samples' demolition.

The regression procedure for estimating the method of the least squares of the coefficients K_1, K_2, K_3 and calculating the size of the wear, depending on the change in the friction pair potential in the processing environments, was performed using the computer program Microsoft Excel following output data: the bronze valence $-$ 2; constant Faraday F = 96485.3 K/mol; molar volume of samples Vm = $7.53 \cdot 10^{-6}$ m^3/mol. In this case the confidence intervals were chosen for the probability level 0.95.

Simultaneously, practical tests of bronze examples (Pb5Zn5Sn5) on the "bush-bush" scheme on the plant of face rubbing [3] were carried out. The experiments were carried out in the media of beer-non-alcohol industry (Table 1). The slipping speed was 0.2 m/s, specific load was 0.92 MN/m^2. The speed of the potential sweep was 2 mW/s during the removal of the polarisable curve. The example wear was defined by a gravimetrical method. The results of analytical and experimental tests were tabulated.

To verify the adequacy of the model (17) for the drinking water, we will conduct 3 experiments (Table 1).

Media error $S = \sqrt{\sum\limits_{i=1}^{n} (X_i - \bar{X})^2 \Big/ (n-1)} = 0,25$. Given the small sample size, multiply S by the Student coefficient t. Then corrected S: $S = 0.25 \cdot 4.3 = 1.08$. That is, the measurement results are $S = 10.95 \pm 1.08$. The upper limit of wear is 12.03 mg. In such a case, a theoretically determined result of the deterioration of 11.80 mg falls into the confidence interval with a probability of 0.95. A similar check for the wear in beer $S = 0.2$, and, taking into account the Student's criterion, $S = 0.02 \cdot 4.3 = 0.086 \approx 0.09$. Consequently, with a probability of 0.95, the theoretical result of 0.24 mg falls into the confidence interval, because its lower limit is 0.21 mg.

Table 1. Tribotecnical and electrochemical characteristics of bronze examples received by calculative and experimental methods.

Technological environment	Change the potential at wear and tear, mW	Demolition of samples in mg per 10 km of friction				
		The upper	The bottom	Average	Average for all experiments	Calculated
Hard water (drinking)	100	11.20	10.70	10.95	10.95	11.8
		11.22	10.72	10.97		
		11.18	10.68	10.93		
Beer is light (brewery "Obolon", Kyiv)	15.0	0.33	0.29	0.31	0.30	0.24
		0.32	0.27	0.29		
		0.32	0.28	0.30		

5 Conclusions

The results of analytical and experimental studies confirm the adequacy of the developed mathematical model. They also indicate that the technological environment can vary ten times during the wear and tear of the materials. Corrosive and mechanical wear of surfaces in aggressive technological environments of food industries cannot be considered as a mere summing up of mechanical and electrochemical factors. This is a more complex process in which electrochemical dissolution serves as a catalyst for a fatigue failure. Rubbing h in turn contributes to the development of electrochemical corrosion. In all these processes, the potential of the system and its displacement during the friction plays a significant role.

References

1. Sukhenko, Yu., Litvinenko, O., Sukhenko, V.: Reliability and durability of the equipment of food and processing industries. NUFT, Kiev (2010)
2. Sukhenko, Y., Sukhenko, V., Mushtruk, M., Vasuliv, V., Boyko, Y.: Changing the quality of ground meat for sausage products in the process of grinding. East. Eur. J. Enterp. Technol. **411**(88), 56–63 (2017)
3. Dziub, A., Sukhenko, V., Manuilov, V., Sukhenko, Yu.: Method of investigation of processes of corrosion-mechanical wear of equipment of food and processing industries. Motrol **16**(3), 74–81 (2014)
4. Pamfilov, E., Prozorov, I.: On the issue of modeling of corrosion-mechanical wear. Frict. Wear **3**, 288–297 (2012)
5. Landolt, D., Micshler, S.: Tribocorrosion of passive metals and coatings. Wood-head Publishing Limited, Cambridge (2011)
6. Diomidis, N., Celis, J., Ponthiaux, P., Wenger, F.: Tribocorrosion of stainless steel in sulfuric acid: identification of corrosion- wear components and effect of contact area. Wear **269**(1–2), 93–103 (2010)
7. Bayer, G.: Mechanical Wear Fundamentals and Testing. Marcel Dekker, New York (2004)
8. Karpenko, G.: Influence of the medium on the strength and durability of metals. Scientific Missionary, Kiev (1976)

9. Stechyshyn, M., Aleksandrenko, V., Bilyk, Yu.: Corrosion and Corrosion Protection. NHU, Khmelnytsky (2015)
10. Haase, R.: Thermodynamics of Irreversible Processes. World, Moscow (1967)
11. Golego, N., Alyab'ev, A., Shevel, V.: Frating-Corrosion of Metals. Technics, Kiev (1974)
12. Groot, C.: Thermodynamics of Irreversible Processes. GITTL, Moscow (1956)
13. Gutman, E.: Mechanochemistry of Metals and Corrosion Protection. Metallurgy, Moscow (1974)

Light and Heavy Pollutant Removal by Modified Swirl Sedimentation Tank – Design and Study

Sylwia Włodarczak[(✉)], Marek Ochowiak, Małgorzata Markowska,
Szymon Woziwodzki, and Magdalena Matuszak

Poznan University of Technology, 4 Berdychowo, 61131 Poznan, Poland
sylwia.wlodarczak@put.poznan.pl

Abstract. The paper shows the effect of volumetric flow rate of liquid and diameters of solid particles in the sedimentation tank for the water contaminated with sediment and oil substances on the effectiveness of the tank. The effect of liquid flow rate on liquid damming has been studied. It has been shown that the liquid damming in the tank increases with increasing a volumetric flow rate of liquid at the inlet. The determined value of the loss coefficient is 3.06. The effectiveness of sedimentation tank for heavy fraction increases with the diameter of solid particles. It has been shown that an increase in the liquid flow rate reduces the effectiveness of the tank, both for the heavy and the light fractions. The vortex sedimentation tank of the proposed construction allows for the simultaneous removal of the heavy and light fractions from water and their partial separation.

Keywords: Swirling flow · Separation process · Oil fraction · Solid particle
Construction effect

1 Introduction

Solid-oil-water separators are in-line devices used to remove suspended solids and light substances from agricultural and industrial waste streams and storm-water discharges. The separators operate by employing various physicochemical separation methods e.g. sedimentation and flotation, coagulation and flocculation, and filtration. The use of any separation process depends on the properties of the contamination [1–4]. The process is applied in different chemical engineering operations and processes such as filtration, fluidization, multiphase flow and environmental engineering [5–8]. The swirl sedimentation tanks are proprietary underground devices designed to remove floatable debris and to remove suspended solids in the treatment of water (storm-water runoff), agricultural fluids, sewage and industrial effluents [9–14]. During the flow of water through the tank, mechanical impurities, sand, soil, paraffin, asphalt as well as other heavy oil component contained in the oil product will settle naturally, because of the occurrence of the specific gravity difference.

2   Literature Review

The tanks are designed for storm-water treatment in urban areas to meet tight space constraints [10, 12, 15]. The sedimentation tanks of various shapes are used, but the principal configurations are tanks with tangential inlet [12, 16, 17]. The simple construction of the sedimentation tank allows separate contaminated liquid from solid particles and oils at a relatively low cost (conventional clarifiers, enhanced gravity separators, and lamella gravity settlers) [1, 5, 10, 12, 18, 19]. Detailed classification and description of the tanks are shown in the earlier articles [20, 21].

The measure of effectiveness of sedimentation tanks is the degree of removing contaminants (liquids or solids) [12, 22, 23]: The effectiveness of the process depends on many factors, including the size, structure, density, and concentration of the contaminant's particles, temperature of water, and process parameters [10, 15]. From the point of view of the purification of liquids, it is appropriate to combine the sedimentation and the flotation processes. The swirl sedimentation tanks offered by many corporations are designed only to collect solid. But, small changes in the sedimentation tank design contribute to the improvement of the effectiveness and/or the possibility of removing the liquids of lower density than water from the waste streams [10, 17, 24, 25]. It should be emphasized that the studies of the reduction of concentrations of light substances (e.g. oils: olive oil, rapeseed oil, rice oil, coconut oil, linseed oil, hemp oil, almond oil, black cumin oil; light fraction) come down to the laboratory tests of apparatus.

This study was concerned with the determining of the effect of volumetric flow rate of liquid and diameters of solid particles in a modified swirl sedimentation tank for water contaminated with sediment and light substances on the effectiveness of the tank. In addition, studies on the effect of the volumetric flow rate of the liquid on the liquid damming in the sedimentation tank were carried out. The vortex sedimentation tank of the proposed construction allows for the simultaneous removal of the heavy and light fractions from the water and their partial separation.

3   Research Methodology

The main elements of the experimental set-up (Fig. 1) were the studied swirl sedimentation tank, VA-40 liquid flow meter (Krohne Messtechnik GmbH&Co KG), a Center 309 multi-point electronic thermometer (Center), an Ebara Optima MA rotary pump, digital laboratory scale PS 210/C/2 (Radwag). The weight of solid was measured with an accuracy of ± 0.001 g. For the measurement of the oil volume, the measuring cylinders of different nominal volumes were used.
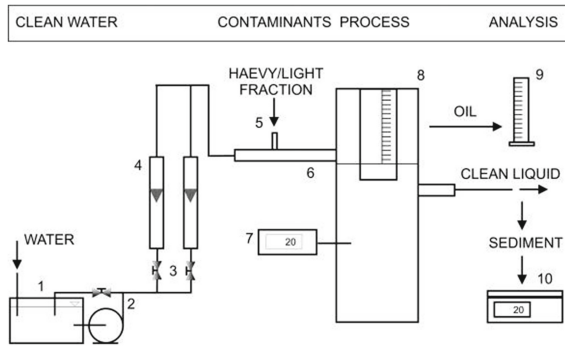
Fig. 1. Main elements of the experimental set-up of sedimentation tank system: 1 – water tank, 2 – pump, 3 – valves, 4 – rotameters, 5 – heavy/light fraction feeder, 6 – inlet pipe, 7 – thermometer, 8 – sedimentation tank, 9 – measuring cylinder, 10 – small-capacity scales.

The swirl sedimentation tank of the studied construction is shown in Fig. 2 [26]. Experimental studies were conducted on the cylindrical tank with an inner cylinder. The active volume of the tank is $V = 0.0116$ m^3. The removal of the heavy fraction from the water takes place in the entire volume of the tank, and the removal of the light fraction takes place in the annular zone, i.e. between the outer and inner cylinders. The inner cylinder acts as a baffle at the exit of the sedimentation tank, which takes flotation substances (light fraction) and calms the liquid stream. The values measured were: diameters of solid particles, the mass of the solid, the volume of oil, the volumetric flow rate of liquid ($\dot{V}$), water damming (ΔH) and liquid temperature (T). The liquid temperature was 20 °C. The tests were carried out within the range of the volumetric flow rate of liquid from $2.2\cdot10^{-4}$ to $7.2\cdot10^{-4}$ (m^3/s).
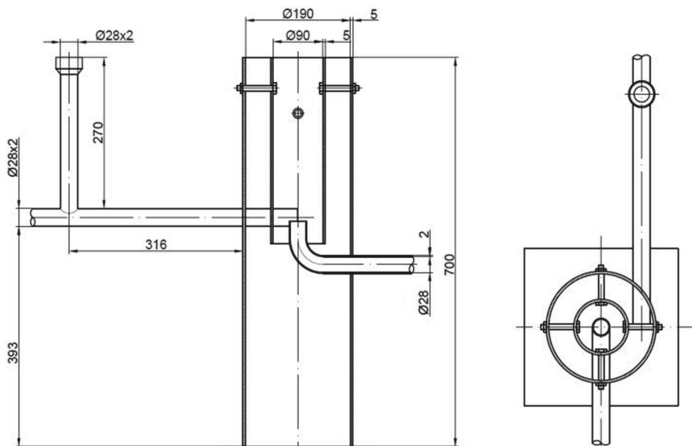
Fig. 2. Construction of analysed swirl sedimentation tank.

The contaminants were coastal beach sands with well-rounded grains from the area of Mielno (Poland). Quartz and feldspar grains are almost the main components of sand. The average content of heavy minerals of density above 2800 (kg/m^3) in these sands is 1–1.5% of mass [17, 27]. The sands sieve analysis was performed using a set of sieves and the vibratory sieve shaker AS 200 basic delivered by Retsch GmbH, and the division included fractions with 100–150, 150–200, 200–300, 300–500 μm. The sands were dried in a laboratory drying oven SL (Pol-Eko-Aparatura Sp.j.) at temperature 90 °C before and after the process. Assessment of the effectiveness of the sedimentation tank was conducted for the heavy fractions of sand with mean grain diameters of 125, 175, 250 and 400 μm. The density of the sand is 2620 (kg/m^3). The settling efficacy studies for the light fraction were made for oil of type of 20–70 delivered by Instytut Nafty i Gazu (Krakow, Poland). The viscosity of the oil used in the tests was 0.060 (Pa·s), and density was 865 (kg/m^3).

Tests of settling tank efficiency were conducted for volumetric flow rate: from $2.2 \cdot 10^{-4}$ to $7.2 \cdot 10^{-4}$ (m^3/s). The separation process was carried out at constant temperature $T = 20$ °C. the analysis came down to addition precise mass of sand (20 g) into water stream before it enters the tank and then to catch contaminants on filter outside the tank. Efficiency was determined as a water stream purification degree expressed percentage.

4   Results

The relationship between the liquid damming vs. volumetric liquid flow rate has been shown that the liquid damming increases with an increase of the liquid flow rate. The values of liquid damming are similar to those observed in standard swirl sedimentation tank and the swirl sedimentation tank with a directional elbow [17].

The detailed statistical analysis of the loss coefficient showed that $\xi = 3.06 \pm 0.31$. In the earlier article, it has been shown that for classical sedimentation tank of similar construction $\xi = 4.34 \pm 0.45$ [17]. In the classical separator, the liquid flowing by the tangential inlet port collides with the layer of liquid rotating inside the tank, which consequently leads to an increase in loss coefficient. In the studied case, the collision of the liquid jets was eliminated by suitable design of the internal cylinder and the inlet pipe.

Figure 3a shows the relation between the removal efficiency and the volumetric flow rate of liquid and diameters of solid particles for the predetermined fraction of the solid. It has been shown that the effectiveness decreases with increasing the liquid flow rate at the inlet. For liquid flow rate values below the $4.4 \cdot 10^{-4}$ (m^3/s) the efficiency significantly decreases with increasing the flow rate, and above the $4.4 \cdot 10^{-4}$ (m^3/s) efficiency decreases more slowly. At the least liquid flow rate used, the tank caught over 94% of sand. The increase in flow rate of liquid reduces the effectiveness due to the turbulent flow of liquid that carries away solid particles and leaches them outside the purification system. It can also be observed that the efficiency of the settling tank increases with increasing the diameter of the solid particles. The particles of smaller diameters, due to their low weight, are more difficult to separate from the liquid. The efficiency for smaller

particles is high only at small flow rates of the contaminated liquid. Larger particles are more likely to settle at the bottom of the tank. For example, for particles of the diameter of $d > 300$ µm the efficiency was more than 90%. The observed values of the efficiency of separation of the suspended solids at high hydraulic loads are relatively high ($E > 50\%$) for such a simple construction of the sedimentation tank.
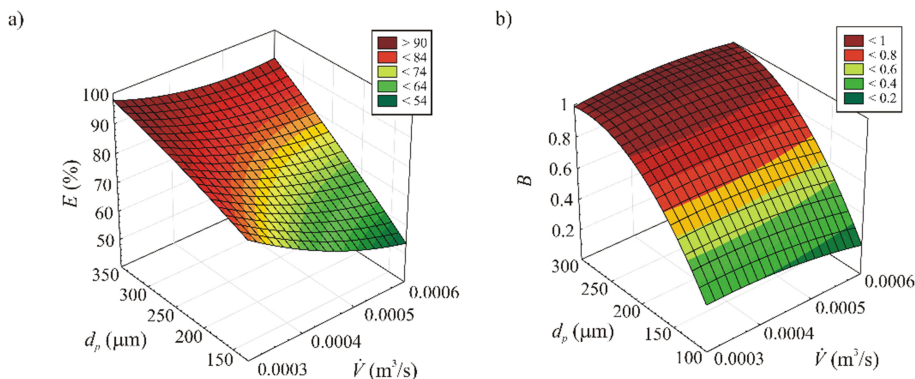
Fig. 3. The relation of volumetric liquid stream and particle size in reference to: (a) efficiency of purifying the stream from contaminants, (b) correction coefficient.

According to the United States Environmental Protection Agency which developed water quality criteria, the effectiveness of sedimentation tank is defined as [17]:

$$E = \frac{100 \cdot P}{1 + P}[\%] \tag{1}$$

where gravity separation parameter (ideal settling parameter) P:

$$P = \frac{w_g \cdot A}{V} \tag{2}$$

where: A—water surface area in chamber, w_g—rate of particle gravity settling in water [17], V—volumetric flow rate of liquid.

The values of correction coefficient (B) are greater than zero, and for the tested construction averaged values of B equal 0.76. The value is smaller than value B observed for classical sedimentation tank ($B = 0.86$). The smaller values of B indicate greater values of the effectiveness of sedimentation tank. The relation of the correction coefficient B vs. the volumetric flow rate of liquid and the diameter of the particles is shown in Fig. 3b. It has been shown that the coefficient B does not depend on the liquid flow rate. Its value increases with increasing the particle diameter. Each tank is characterized by only one value B. In reality, the suspension (sand) introduced into the sedimentation tank is a mixture of sand of different diameters of particles, and the value of B should be determined for a given fraction of solid particles. Hence, there are large differences

between the results obtained from the Eq. (1) for $B = 0.76$ and the results obtained for the particular fractions.

Figure 4 shows the relationship between the efficiency of separation of the light fraction from the liquid and its flow rate. The increase in volumetric flow rate of the liquid stream reduces the efficiency of the settling tank.
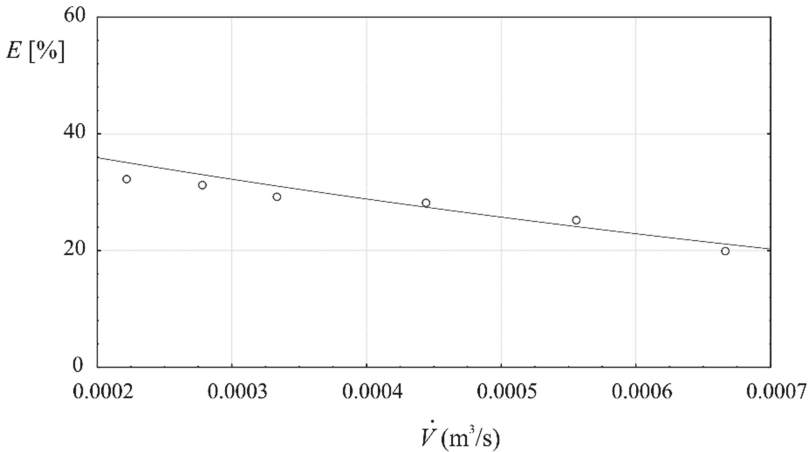
Fig. 4. Dependence of purification for fluid contaminated with the light fraction on the volumetric fluid stream for swirl settling tank.

The tested tank, despite its simple construction, is characterized by the efficiency that equals similar design solutions. Analysis of experimental data has been shown that it is possible to obtain a satisfactory effectiveness of sedimentation tanks, even at high hydraulic loads. It is well known that the smaller the oil globules are, the more difficult the purification process becomes. Nither without significance also the viscosity and density of oil are. These parameters of oil, in addition to the operating parameters of the process, and the geometric dimensions and design of the sedimentation tank, can significantly affect the effectiveness of the settler. In this case, the estimated mean diameter of oil globules is $d_l = 240\ \mu m$, but in fact, the oil droplets have very different diameters.

Based on the experimental data, the dependence of the efficiency on the particle size and the volumetric liquid stream of the following form was proposed as follows:

$$E = A \cdot \left(\frac{d_p}{\dot{V}}\right)^B \tag{3}$$

where constant $A = 95.41$ and exponent $B = 0.31$. Nonlinear estimation by least squares method was used. The Levenberg–Marquardt algorithm of estimation was used. The value of R equals 0.922. Figure 5 shows the comparison of values obtained from the Eq. (3) with the values obtained experimentally.
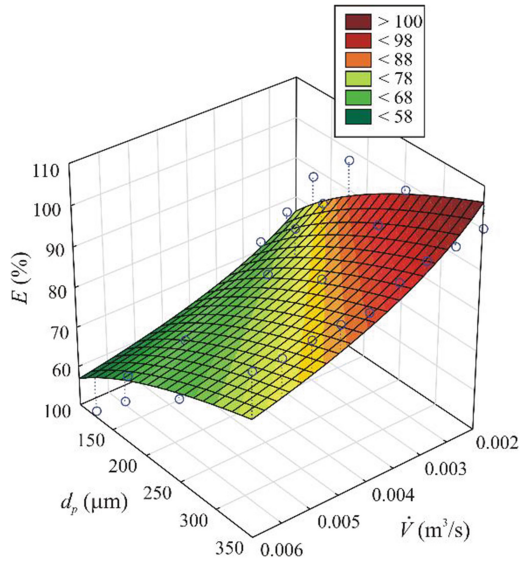
Fig. 5. Dependence of efficiency on the particle size and the volumetric liquid stream.

5   Conclusions

The paper presents the design and results of the studies of modified vortex sedimentation tank. The modification allowed for the simultaneous removal of the sand and oil from the water and additionally their partial separation.

The analysis of the results shows that:

- liquid damming in the tank increases with increasing the volumetric flow rate of liquid at the inlet;
- for the tank studied the loss coefficient is $\xi = 3.06 \pm 10\%$ and does not depend on the liquid flow rate;
- the effectiveness of sedimentation tank for heavy fraction increases with the diameter of solid particles;
- at higher values of the flow rate of liquid lighter particles are washed away from the tank;
- the value of correction coefficient should be determined for a given fraction of solid particles or for specific contamination;
- increase in the liquid flow rate reduces the effectiveness of the tank, both for the heavy and the light fractions.

The sedimentation could be more effective taking into account negligible modifications of constructions of the swirl sedimentation tanks. Therefore, further experimental studies of other constructions of the tanks in the laboratory scale are purposeful. The purified liquids should be studied because they may have different physical and chemical properties of other liquids. Further research seems to be appropriate and justified,

especially if we take into account the environmental aspect and the future of our environment.

References

1. Bandrowski, J., Merta, H., Zioło, J.: Sedimentation of suspension. The rules and design. Wydaw. Politech. Śląskiej, Gliwice (1995)
2. Bień, J.B., Wystalska, K.: Sewage sludge: theory and practise. Wydawnictwo Politechniki Częstochowskiej, Częstochowa (2011)
3. Cywiński, B., Gdula, S., Kempa, E., Kurbil, J., Płoszański, H.: Urban sewage treatment plants: technological basics and design rules. Arkady, Warszawa (1972)
4. Kowal, A.L., Świderska-Bróż, M.: Water purification. PWN, Warszawa (2000)
5. Chhetri, R.K., Bonnerup, A., Andersen, H.R.: Combined sewer overflow pretreatment with chemical coagulation and a particle settler for improved peracetic acid disinfection. J. Ind. Eng. Chem. **37**, 372–379 (2016)
6. do Amaral, L.G.H., Righes, A.A., e Souza Filho, P.D.S., Dalla Costa, R.: Automatic regulator for channel flow control on flooded rice. Agric. Water Manag. **75**, 184–193 (2005)
7. McCabe, W.L., Smith, J.C., Harriott, P.: Unit Operation of Chemical Engineering. McGraw Hill, New York (2005)
8. Wu, J., He, C.: Experimental and modelling investigation of sewage solids sedimentation based on particle size distribution and fractal dimension. Int. J. Environ. Sci. Technol. **7**(1), 37–46 (2010)
9. Benjamin, M.M., Lawler, D.F.: Water Quality Engineering: Physical/Chemical Treatment Processes. Wiley, London (2013)
10. Davidson, J., Summerfelt, S.T.: Radial flow vs. tangential flow. Glob. Aquac. Advocate **8**(3), 56–57 (2005)
11. Diaz, F.J., O'Geen, A.T., Dahlgrena, R.A.: Agricultural pollutant removal by constructed wetlands: Implications for water management and design. Agric. Water Manag. **104**, 171–183 (2012)
12. Field, R., O'Connor, T.: Swirl technology: enhancement of design, evaluation and application. J. Environ. Eng. **122**(8), 741–748 (1996)
13. Li, Y., Kang, J., Lau, S., Kayhanian, M., Stenstrom, M.: Optimization of settling tank design to remove particles and metals. J. Environ. Eng. **134**(9), 885–894 (2008)
14. Wilson, M.A., Mohseni, O., Gulliver, J.S., Hozalski, R.M., Stefan, H.G.: Assessment of hydrodynamic separators for storm-water treatment. J. Hydraul. Eng. **135**(5), 383–389 (2009)
15. Mołoniewicz, W., Sędzikowski, T., Bonikowski, T.: Small Sewagge Treatment Okants. Design and Construction, Arkady (1979)
16. Ancukiewicz, M.: The study of vortex settling tanks with tangential inlet of liquid stream. M.Sc. Thesis, Poznan University of Technology (2016)
17. Ochowiak, M., Matuszak, M., Włodarczak, S., Ancukiewicz, M., Krupińska, A.: The modified swirl sedimentation tanks for water purification. J. Environ. Manage. **189**, 22–28 (2017)
18. Patziger, M., Kainz, H., Hunze, M., Jozsa, J.: Influence of secondary settling tank performance on suspended solids mass balance in activated sludge systems. Water Res. **46**, 2415–2424 (2012)

19. Tarpagkou, R., Pantokratoras, A.: The influence of lamellar settler in sedimentation tanks for potable water treatment: a computational fluid dynamic study. Powder Technol. **268**, 139–149 (2014)
20. Heidrich, A., Witkowski, A.: Equipment for Sewage Treatment Design, Calculation Examples. Wydawnictwo Seidel Przywecki Sp. z o.o., Warszawa (2005)
21. Królikowska, J.: Swirl chamber equipment applied in sewage networks for decreasing suspended particle load in stormwater sewage. Ecol. Eng. **26**, 156–170 (2011)
22. Kuropka, J.: Purification of Waste Gases from Gas Pollutants. Basic Processes. Wydawnictwo Politechniki Wrocławskiej, Wrocław (1988)
23. Luyckx, G., Berlamont, J.: Removal effieciency of swirl/vortex separators. Urban Water J. **1**(3), 251–260 (2004)
24. Davidson, J., Summerfelt, S.T.: Solids removal from a coldwater recirculating systems: comparison of swirl separator and a radial-flow settler. Aquac. Eng. **33**, 47–61 (2005)
25. Veerapen, J.P., Lowry, B.J., Couturier, M.F.: Design methodology for the swirl separator. Aquac. Eng. **33**, 21–45 (2005)
26. Kołak, J.: The study of the effectiveness of the removal of heavy suspension from liquid in vortex settling tank. Eng. Thesis, Poznan University of Technology, Poznan (2017)
27. Ochowiak, M., Broniarz-Press, L., Nastenko, O.V.: Air purification in the cylindrical chamber separator. Chem. Eng. Equip. **2**, 66–67 (2016)

Investigation of Hydrodynamics During Continuous Vibroextraction in a Liquid–Solid Body System

Vladimir Zavialov[(✉)] , Taras Misyura , Nataliya Popova , Yuliya Zaporozhets ,
and Vadim Dekanskiy

National University of Food Technologies of Ukraine, 68 Volodymyrska St., Kyiv 01601, Ukraine
`zavialov@nuft.edu.ua`

Abstract. Results of investigations of the hydrodynamics of flows in a counterflow continuous column-type vibroextractor for a liquid–solid body system and their generalization in the form of a mathematical description are presented. An equation for calculating the distance of propagation of pulsating turbulent jets formed by original vibrating transporting elements in a nonflowing medium, which can be taken as a scale factor in modeling the process, has been obtained. An analysis has been carried out, and a mathematical model of the structure of real flows in the vibroextractor has been developed on the basis of a combined model for the conditions of pulse perturbation of the hydrodynamic system of the apparatus. The mathematical description of the structure of flows can be taken as a base for the solution of optimization problems. We propose a new design of a vibratory extractor with a transporter for industry, which provides efficient separation of phases under the conditions of counterflow vibratory extraction of desired components from vegetable raw materials.

Keywords: Extraction · Intensification · Plant raw material · Hydrodynamic flow
Longitudinal mixing · Mathematical modeling

1 Introduction

The development of industry under new economic conditions is characterized by the creation of complex technological systems for the rational use and deepened processing of raw materials and their waste. Despite the diversity of designs of modern periodic and continuous extractors, there exist general disadvantages, the practical assurance of the conditions of optimal realization of the extraction process.

2 Literature Review

In this regard, vibroextractors can operate in a regime of intensive alternating turbulization of the working flow by jets of the mixture of vibration mixing devices, which are located in the working volume of the apparatus [1–3]. At the same time, the development and extensive commercial application of this type of apparatuses are slowed down by the insufficient knowledge of their hydrodynamics and mass transfer.

It should be noted that the construction of the main units of visbroextraction apparatuses differ substantially from those of traditional extractors, which causes the necessity to model and develop their vibromixing system and, in individual cases, vibrotransporting system [4–6].

3   Research Methodology

The methods of investigations include analytic modeling and multifactor experiments.

The distance of propagation of turbulent pulsating jets generated by the elements of vibrating mixing devices was determined with the help of a Pitot–Prandtl tube from the indications of a differential manometer [7]. The processing of experimental data and calculations were carried out with the use of the following modern integrated systems. The rotational frequency of the drive system was controlled by a LATR–1–5-type autotransformer and a tachometer.

The continuous vibroextraction process was investigated on a continuous vibroextractor model manufactured under conditions of the National University of Food Technologies according to a scheme shown in Fig. 1.
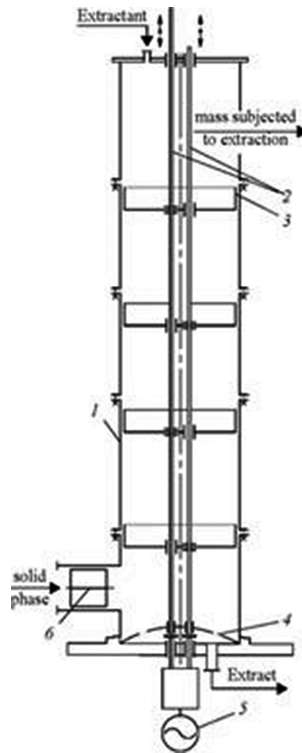
Fig. 1. Scheme of a vibratory extractor: 1 - apparatus body; 2 - rods; 3 - vibratory transport plate; 4 - filter; 5 - vibratory drive; 6 - weigher.

The apparatus is filled by an extractant, which is fed to the level of the upper plate. A specified amplitude-frequency regime of vibration of the vibrotransporting system is simultaneously set. The ground raw material prepared for extraction is directed through charging weigher 6 under the lower vibrotransporting plate. Then it moves continuously along the apparatus in the direction opposite to the direction of feeding the extractant with gradual extraction of desired components, and finally it is discharged from the apparatus in the form of an extraction cake in its upper part. The finished extract is removed from the apparatus through filter 4. The counterflow separation of phases is realized due to the difference in the hydraulic resistances of the overflow of the working medium through transporting open elements A, the filtering effect through the filtering elements **B,** and sedimentation of particles of the solid phase on the surface of the plates 1 (Fig. 2). Flange 2 mounted on the periphery of the plates is intended for keeping the solid phase on their surface, enhancing the separating effect, and preventing the flushing of fine fractions of the solid phase under the plate.
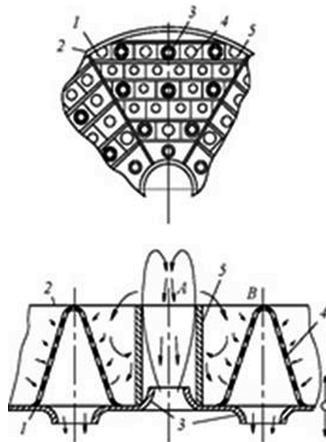
Fig. 2. Vibrotransporting plate: 1 - disk with jets; 2 - flange; 3 - jet; 4 - filtering element; 5 - branch pipe.

The mechanism of separation of the phases for plates with branch pipes of different rigidity is as follows. As the plate moves downwards, the suspension is displaced through open transporting elements in the form of nozzles 3 that fits tightly in the branch pipes 5. The suspension plume formed in this case expands, approaching the periphery edge of the branch pipe, and goes beyond it.

As the plate moves upwards, the central part of the suspension plume, which has the least concentration of the solid phase, closes and returns to the opposite side of the plate through the transporting, open, and filtering nozzles, which are covered by filtering element 4 and are directed in the direction of movement of the extractant. The branch pipes set on the plates enhance the hydraulic resistance to the overflow of the working medium in the direction opposite to the direction of transportation of the solid phase, thus increasing the production rate of the apparatus in terms of the solid phase,

decreasing the distance of propagation of the turbulent pulsating jet, and, as a result, reduces the general level of longitudinal mixing in the apparatus. The indicated effects depend not only on the operating regime of the apparatus, but also to an equal extent on the geometry of the transporting and filtering elements elements of vibromixing and on simultaneously transporting plates, which is the object of investigations of the present paper.

4 Results

4.1 Investigation of the Propagation of Pulsating Turbulent Flows in a Nonflowing Liquid Medium

The objective of the paper is to develop a mathematical model and carry out the fundamental description of the regularities of propagation of pulsating jets generated by the structural components of vibromixing devices [8, 9].

The difference between the complete (hydrodynamic) and static pressure in the flow was measured with the help of the liquid differential manometer. The velocity of the pulsating flow was established from the value of this difference [10].

The rotational frequency of the shaft of the electromotor and, at the same time, the frequency f of vibrations of the vibrotransporting system was changed in the range to 10 Hz by an autotransformer; the amplitude A was fixed and equal to 5×10^{-3}, 10×10^{-3}, and 15×10^{-3} m.

In measurements of the range of action of pulsating jets L and their velocities, the Pitot–Prandtl tube was set in the working volume of the apparatus along the axis of a transporting open element, namely, a nozzle (Fig. 3).

The ratio of the diameters of the branch pipes to diameters of the nozzles and the ratio of their heights to their diameters were varied in the ranges $D/d = 1$–3 and $H/d = 1$–4, respectively. Nozzles with a diameter of 15, 20 and 32 mm were mounted in branch pipes with a diameter of 36 and 56 mm and a height of 45 and 60 mm. Constructions of plates with a flow cross-section ranging from 5.5 to 14.2% were investigated.

From indications of the diffraction manometer we calculated the velocity of pulsating flows mean-integral over the period of vibrations and mean over the cross-section of the jet at a distance of L of the measuring tube from the mean position of the plate

$$w_L = 2 \Big/ \left(\pi \left(k \sqrt{2gh} \right) \right), \tag{1}$$

where $k = w_L / w_{\max}$ is the ratio of the mean velocity over the cross-section of the jet to the maximum value of the velocity at the center (for a laminar flow, $k = 0.5$; for a turbulent flow, $k = 0.75$–0.87; h is the difference between the levels of the liquid in the Pitot-Prandtl tube; g is the acceleration of gravity. The value of w_L obtained in such a way was referred to the initial mean-integral velocity of pulsating flows over the period of vibration:

$$w_0 = 2Af(1 - \varepsilon)/\varepsilon, \tag{2}$$
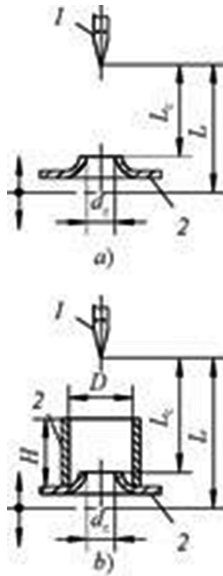
Fig. 3. Scheme of measurement of the velocity of pulsating flows: 1 - Pitot–Prandtl tube; 2 - open element; 3 - element with a flexible branch pipe.

where A and f are the amplitude and frequency of vibrations of the vibrating partition, respectively, ε is the general effective cross-section (the ratio of the area of the holes in the plate and clearance to the cross-sectional area of the apparatus).

The distance L was determined by analogy with stationary turbulent jets

$$L = L_c + 4,5r_c, \tag{3}$$

where L_c is the distance from the point of measurement to the nozzle section for the mean position of the vibrating partition; r_c is the radius of the nozzle.

After analysis of the results of experimental data obtained during investigations under plant condition of constructions of plates with proposed optimal ratios: $D/d_c = 1.5$–2.5 and $\underline{H}/D = 1.5$–3, it was established that the relative velocity w_L/w_0 for $Re_p > 5000$, where

$$Re_p = 4^2 f(1 - \varepsilon)/(\varepsilon v), \tag{4}$$

is the Reynolds pulsation criterion, and v is the kinematic viscosity of water, is determined by the value of the relative distance from the vibrating plate L/d_c.

In Fig. 4, experimental data for a nozzle 15×10^{-3} m in diameter mounted in a branch pipe with a diameter $(36 \times 45) \cdot 10^{-3}$ m are shown.
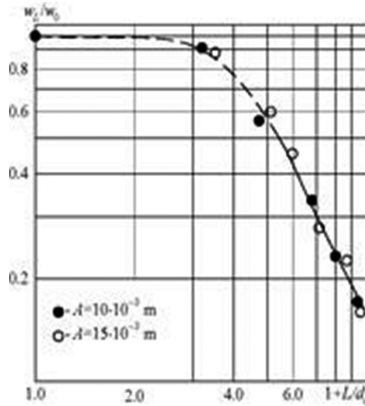
Fig. 4. Generalization of data on vanish at a substantial distance from the source of vibration.

The dashed line shows the universal profile of the relative velocity in the cross-section of the stationary turbulent jet calculated by the Schlichting equation:

$$w_L/w_0 = \left[1 - (L/L)^{1,5}\right]^2, \tag{5}$$

where $L_m = 2.44\ L_{0,5}$ is the theoretical distance of propagation of the jet; $L_{0,5}$ is the distance from a plate at which $w_L/w_0 = 0.5$.

The distance of propagation of the jet depends on the taken limiting degree of vanish

$$\beta = 1 - w_L/w_0, \tag{6}$$

The value of L_m is determined at $\beta = 0.983$.

In view of the complexity of measuring the velocity of pulsating flows, the distance of action in the given experiments was determined for $\beta = 0.85$. The quantity L_0 measured in such a way can be used for the determination of $L_{0,5} \approx 0.5L_0$, which is necessary for the calculation of the relative velocity by Eq. (4).

It was established that the experimental data correspond predominantly to the universal profile of the relative velocity in the cross-section of turbulent jets calculated by the Schlichting equation. However, the deviations from the universal profile have a systematic character. This is why to describe the regularities of vanish of pulsating flows for $\beta > 0.5$, we proposed the dependence

$$w_L/w_0 = 0,5(1 + L_{0,5}/d_c)^2/(1 + L/d_c)^2. \tag{7}$$

Results of experimental investigations were generalized by a graphical S-like dependence (Fig. 5), from which the influence of the Reynolds criterion in the laminar and turbulent regions is seen

$$\text{Str} = z\text{Re}^m(d_c H)/D^2 \left[d_c \varepsilon/2A(1 - \varepsilon)\right]^{0,85}, \tag{8}$$

$$z = 7,37 \cdot 10^{-4}; m = 1,05, \quad \text{for Re}_p < 2300$$

$$z = 2,95 \cdot 10^{-6}; m = 1,76 \quad , \text{ for } \quad \text{Re}_p = 2300 - 5000$$

$$z = 8,15; m = 0, \text{ for } \quad \text{Re}_p > 10000$$
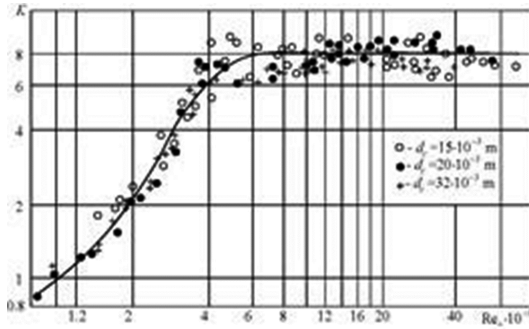
Fig. 5. Generalization of experimental data on determination of the distance of propagation of pulsating jets in a two-phase pulsating flow at different parameters of vibration for constructions of plates with nozzles.

The unknown quantity L_0 enters into the Strouhal criterion, which is the ratio of the time of movement of pulsating jets over a distance L_0 at a velocity w_0 to the period of vibration of the plate.

$$\text{Str} = L_0 \cdot \varepsilon / 2A(1 - \varepsilon), \tag{9}$$

Thus, the distance of propagation of pulsating flows increases as Re_p rises, attains the limiting value for $\text{Re}_p = 5000$, and practically does not depend on the parameters of vibrations.

The computational equations can be used in design and optimization of operation of vibroextractors.

4.2 Investigation of the Structure of Flows Under Continuous Vibroextraction

In vibroextraction continuous apparatuses, the interphase interaction is determined by the hydrodynamic conditions of the process and manifests itself in the character of distribution of the residence time of individual particles in the flow of the working system. This is why insufficient information on the mechanism of this process leads to the incomplete use of its possibilities in the stage of design and operation [11, 12].

The longitudinal mixing in the vibroextractor was realized on the basis of a diffusion model with the use of the method of pulse tracing of the flow by a substance chemically indifferent to the medium. In view of the dimensionless coefficients, this method provides direct obtaining of an experimental function of the residence time distribution in the form of a C-curve, the shape of which is determined by the following equation:

$$S = S(t) = \left(2\sqrt{\pi t / \text{Pe}}\right)^{-1} e^{-\frac{(1-t)^2}{4t/\text{Pe}}}, \tag{10}$$

where $S = cV_{ap}/Q = c/\bar{c}$ is the dimensionless concentration; $t = \tau/\bar{\tau}$ is the dimensionless time; V_{ap} is the working volume of the apparatus, m³; Q is the amount of the introduced tracer agent, kg; c is the mean concentration of the tracer, kg/m³; $\bar{\tau}$ is the mean residence time of the tracer in the apparatus, s: $\bar{\tau} = V/V_{ap}$; W is the consumption of the medium flowing through the apparatus, m³/s.

In this case, at large Peclet numbers (Pe > 2500), the shape of the C-curve tends to the symmetric form relative to $t = 1$; with decrease in the Peclet number Pe, the deviation from the normal distribution increases and, for Pe < 40, becomes pronounced.

Differentiating Eq. with respect to t and equating the derivative to zero, we can determine the time t_{max} that corresponds to the maximum dimensionless concentration S_{max}

$$t_{max} = \sqrt{\text{Pe}^{-2} + 1} - \text{Pe}^{-1} \tag{11}$$

The concentration S_{max} is obtained at values of t ranging from 0 to 1; at very large Pe numbers, the value S_{max} is obtained at the moment $t \approx 1$. Substituting $t = t_{max}$ into Eq. we get S_{max}.

For the channel of infinite length, the variance of the C-curve is related to the Pe number by the equation

$$\sigma^2 = 8/\text{Pe}^2 + 2/\text{Pe}. \tag{12}$$

where σ^2 is the variance of the dimensionless C-curve.

For the known mean residence time of the tracer, its mean concentration can be determined from the equation

$$\bar{c} = \sum c_i \Delta\tau / \bar{\tau} = Q/V_{ap}, \tag{13}$$

where $\Delta\tau$ is the time interval of taking samples.

Investigations were carried out by the method of pulse tracing of the flow by a substance chemically indifferent to the medium. For this purpose, it is assumed that, at the initial moment of time $\tau_n = 0$, the tracer (sugar beet with a weight $G = 0.5$ kg ground in a screw-type crusher with a diameter of the outlet holes of 12 mm) is introduced into the working flow that moves at a volume velocity specified according the regime V_p, into the initial cross-section $L_{in} = 0$ of an experimental section of length $L = 1$ m; samples are taken in amounts $G_i = 0.1$ kg of the tracer with a time interval $\tau_i = 5$ min from the moment the tracer appears at the end of the experimental section (Fig. 6).
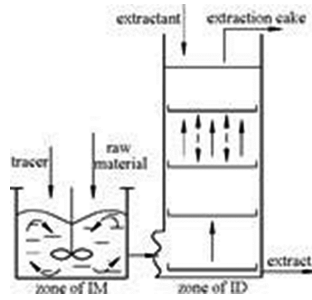
Fig. 6. Measurement scheme of the tracer concentration in investigations.

The frequency range was maintained within 2–5 Hz, and the amplitudes were equal to 5.0×10^{-3}, 10.5×10^{-3}, and 16.0×10^{-3} m. The tracer was introduced through charging device 10, and samples were taken from discharging tray II from the moment of its appearance in amounts of 0.1 kg after 2–3 min. Experimental curves of the system response to the pulse concentration perturbation are shown in Fig. 7 and indicate that with increase in the frequency vibration of the plate from 2 to 4 Hz, the longitudinal mixing increases by a factor of 7. The amplitude exerts even a larger influence on the mixing of the phases along the axis of the apparatus.
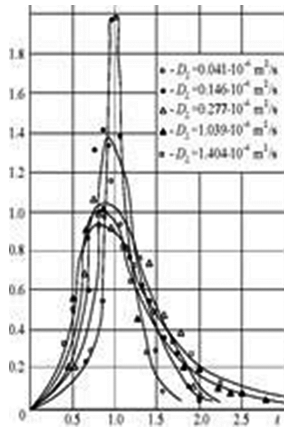
Fig. 7. Experimental curves of system response to pulse concentration perturbation/ C - curves/: (1) A = 5×10^{-3} m, f = 4.67 Hz; (2) A = 10.5×10^{-3} m, f = 2.00 Hz; (3) A = 10.5×10^{-3} m, f = 2.67 Hz; (4) A = 10.5×10^{-3} m, f = 4.00 Hz; (5) A = 16×10^{-3} m, f = 2.67 Hz.

With change in the vibration amplitude of the plate from 5×10^{-3} m up to 16×10^{-3} m, the mixing increases by a factor of 34.

The cause of the decrease in the longitudinal mixing at small amplitudes is that, in this operating regime, the vibratory motions of the plate produce small-scale turbulence, which favors the smoothening of the profile of velocities in the cross-section of the

column. However, for an amplitude of 5×10^{-3} m, the transportation of the phase begins at frequencies above 4.5 Hz.

Thus, the optimal operating regime of the vibroextractor provides the required production rate with low longitudinal mixing and is observed at an amplitude of 10.5×10^{-3} m and a frequency of 2.67 Hz. These parameters can be recommended as the best ones.

4.3 Mathematical Analysis of the Structure of Flows

In view of the realities of the hydrodynamic conditions that arise in the continuous apparatus with vibroturbulizing and, at the same time, vibrotransporting working elements, it was assumed that the apparatus consists of zone of ideal mixing (IM) and ideal displacement (ID), complicated by elements of reverse mixing. Note that the second zone belongs to the main working part of the apparatus, which provides directly the counterflow separation of phases. The apparatus is conventionally divided into two successively joined zones with different mechanisms and degree of mixing (Fig. 6): ideal mixing in the charging part of the apparatus and ideal displacement in the working part of the apparatus complicated by longitudinal mixing [11, 12].

From the material balance conditions for each zone, we have (Fig. 6):

$$\begin{cases} \dfrac{dS}{dt} = \dfrac{v}{V}(S^* - S), \\ \dfrac{\partial c}{\partial t} = -u\dfrac{\partial c}{\partial x} + D_L\dfrac{\partial^2 c}{\partial x^2}, \end{cases} \tag{14}$$

where S is the current concentration of the substance in the charging device; S^* is the equilibrium concentration of the substance in the charging device; t is the time; x is the varying coordinate of the length of the working part of the apparatus; D_L is the coefficient of longitudinal mixing; v and u are the volume velocity and linear velocity of the two-phase flow; V is the volume of the working zone of the apparatus; c is the current concentration of the substance in the apparatus (in the zone of ID), which depends on its concentration S in the charging part (in the zone of IM).

Let's consider a mathematical description of each of the zones. The zone of IM is described by the following model:

$$\begin{cases} \dfrac{dS(t)}{dt} = -\beta S(t), \\ S(0) = S_0, \end{cases} \tag{15}$$

where $\beta = v/V$ is the quantity equivalent to the inverse mean residence time of the tracer in the apparatus, i.e., $\beta = 1/\bar{\tau}$; v is the volume velocity of the flow; V is the volume of the zone of IM; S_0 and $S(t)$ are, respectively, the initial concentration and current concentration of the substance in the zone of IM.

The zone of ID, which is complicated by reverse mixing, can be described by the following boundary-value problem:

$$\frac{\partial c(x,t)}{\partial t} = D_L \frac{\partial^2 c(x,t)}{\partial x^2} - u\frac{\partial c(x,t)}{\partial x}, \ 0 \le x \le L \tag{16}$$

with the initial condition $c(x,0) = 0, 0 \le x \le L$ and boundary conditions at the left end

$$-D_L \frac{\partial c(x,t)}{\partial x} = u(S(t) - c(x,t)) \text{ for } x = 0 \text{ and, at the right end of the area of the area of}$$

the working volume of the apparatus, $\frac{\partial c(x,t)}{\partial x} = 0$ for $x = L$.

To solve the equations, we perform the replacement of the variables

$$c(x,t) = e^{kt+qx} \cdot w(x,t), \tag{17}$$

where $k = -u^2 / (4D_L); q = u / (2D_L)$.

Note that is easy to check that the function $w(x,t)$ satisfies the equation

$$\frac{\partial w(x,t)}{\partial t} = D_L \frac{\partial^2 w(x,t)}{\partial x^2}. \tag{18}$$

Using the method of separation of variables to solve the equation of parabolic type with regard for the real physical coordinates of the length x and time t, we obtain

$$c(x,t) = 2S_0 e^{\frac{Pe}{2}\left(\frac{x}{L} - \frac{1}{2}\frac{t}{\bar{t}}\right)} \sum_{n=1}^{\infty} \frac{1}{A_n} y_n(x) e^{-\frac{1}{Pe}\lambda_n^2 \frac{t}{\bar{t}}} r_n(t), \tag{19}$$

where
$$y_n(x) = \cos\left(\lambda_n x / L\right) + Pe \cdot \sin\left(\lambda_n x / L\right) / 2\lambda_n,$$
$$r_n(t) = \left(e^{(\gamma_n - \beta\bar{t})t/\bar{t}} - 1\right) / (\gamma_n - \beta\bar{t}),$$
$$A_n = 1 + Pe(1 + Pe/4) / \lambda_n^2,$$

$\gamma_n = Pe/4 + \lambda_n^2 / Pe$ are Eigen functions of the one-parameter diffusion model with the boundary conditions and $\lambda_n > 0$ are the roots of the transcendental equation: $tg(\lambda_n) / \lambda_n = 4Pe / (4\lambda_n^2 - Pe^2)$ is the quantity equivalent to the inverse mean residence time of the tracer in the apparatus: $\beta = 1/\bar{t}$

Thus, the obtained analytic model can be used for the determination of the current concentration of the substance at a random time at a random point of the working zone of the apparatus, and it can be taken as a base in solving optimization problems.

5   Conclusions

Turbulent pulsating jets generated by vibrating elements (nozzles) at a frequency to 4 Hz and amplitude to 15 mm create optimal hydrodynamic conditions for counterflow mass exchange of separation of the phase due to intensive micromixing in the cross-section of the working volume of the apparatus and with minimum longitudinal mixing. The large interface developed in this case under extremely high turbulization in the zone of the plate creates conditions for intensive mass exchange with a low longitudinal mixing.

For instance, the coefficients of longitudinal mixing D_L calculated from the obtained data and ranging from 1.32×10^{-4} to 2.02×10^{-4} m^2/s, are at a level admissible for extraction apparatuses.

References

1. Pavliuk, I., Dyachok, V., Novikov, V.: Kinetics of biologically active compound extraction from hops strobiles extraction cake. Chem. Chem. Technol. **11**(4), 487–491 (2017)
2. Semenishyn, E.M., Huglich, J., Trocki, W., Broda, O.: Model matematvczna procesu eksrakcji w aparatach o dzialaniu ciaglym. In: Materialy XV OGOLNOPOLSKA konferencia naukowa inzymeriu chemicznej 1 procesowej, pp. 71–75. Gdansk (1995)
3. Zavialov, V., Bodrov, V., Misyura, T., Popova, N., Zaporozhets, Y., Dekanskiy, V.: Development of mathematical models of external mass exchange under conditions of vibroextraction from vegetable raw materials. Chem. Chem. Technol. **9**(3), 367–374 (2015)
4. Bertrand, J., Conderc, J.P., Angelino, H.: Pover consumption, pumping capacity and turbulence intensity in buffled stirred tanks: comparison between several turbines. Chem. Eng. Sci. **35**(10), 2157–2163 (1980)
5. Dyachok, V., Ivankiv, O.: Kinetic equlibrium of phospholipids extraction from organic substances. Annaies universitatis Mariae Curie-Sklodowska. Pharmacia **XV**, 371–373 (2002)
6. Hoflez, B., Buhlemann, S., Lohz, B.: Experimentelle Untezsuchung der turbulenten Stromungsfeld in Ruhzzeaktoren Verfahrenstechnik. Chem. Eng. Res. Des. **13**(2), 80–84 (1979)
7. Oldshue, J.: Fermentations: mixing scale - up techniques. Biotech. Bioeng., 881–889 (1966)
8. Kakyji, T., Kei, M., Takeo, Y.: Axial mixing in a multistage vibrating disc column. Ind. Chem. Eng. Jpn. **8**(2), 122–126 (1975)
9. Nagarajan, K., Renganathan, T., Krishnaiaha, K.: Hydrodynamics of a continuous countercurrent liquid–solid system: experiments and modeling. RSC Adv. **42** (2016)
10. Sano, Y., Usui, H.: Interrelation among mixing time, power number and discharge flow rate number in buffled vessels. J. Chem. Eng. Jpn. **18**(1), 47–52 (1985)
11. Zavialov, V.L., Bodrov, V.S., Misyura, T.G., Popova, N.V., Zaporozhets, Yu.V: Mathematical description of the process of counterflow transportation of the solid phase during continuous vibroextraction. Vibratsii Tekh. Tekhnol. **3**(63), 102–107 (2011)
12. Zavialov, V.L., Bodrov, V.S., Misyura, T.G., Popova, N.V.: Development of an algorithm for determining the type of the model of the hydrodynamic structure of two-phase flow in the working volume of a continuous column vibroextractor. Nauk. Pratsi Nats. Univ. Kharch. Tekhnol. **33**, 63–67 (2010)

Correction to: Model of Thermal State of the System of Application of Coolant in Grinding Machine

Mykhaylo Stepanov 🆔, Larysa Ivanova 🆔, Petro Litovchenko 🆔, Maryna Ivanova 🆔, and Yevheniia Basova 🆔

Correction to:
Chapter 17 in: *Advances in Design, Simulation and Manufacturing*, **LNME,**
https://doi.org/10.1007/978-3-319-93587-4_17

In the original version of the book, the ninth reference of the reference list of chapter 17 was not correctly written. This reference was revised, and the chapter and the book were updated with this change.

The updated version of this chapter can be found at
https://doi.org/10.1007/978-3-319-93587-4_17

Correction to: Investigation of the Process of Saturation of the Filter Liquid of Soda Production with Ammonia and Carbon Dioxide in the Production of Ammonium Chloride

Inna Pitak , Valery Shaporev , Oleg Pitak , Alina Hrubnik ,
and Viktor Moiseev

Correction to:
Chapter 50 in: V. Ivanov et al. (Eds.): *Advances in Design,*
Simulation and Manufacturing, **LNME,**
https://doi.org/10.1007/978-3-319-93587-4_50

In the original version of the chapter, reference 2 was incorrect in the initially published version. It has been corrected as below;

Yakimenko, Ya.: Some regularities of calcium oxide hydration activity. Eastern Eur. J. Enterp. Technol. 4(6(70), 30–35 (2014). https://doi.org/10.15587/1729-4061.2014.26239

Author Index